

# ANNUAL REPORT

2009

and list of publications



Bayerisches Forschungsinstitut  
für Experimentelle Geochemie und Geophysik  
Universität Bayreuth

Bayerisches Geoinstitut  
Universität Bayreuth  
D-95440 Bayreuth  
Germany

Telephone: +49-(0)921-55-3700  
Telefax: +49-(0)921-55-3769  
e-mail: [bayerisches.geoinstitut@uni-bayreuth.de](mailto:bayerisches.geoinstitut@uni-bayreuth.de)  
www: <http://www.bgi.uni-bayreuth.de>

Editorial compilation by: Stefan Keyssner and Petra Buchert  
Section editors: Andreas Audétat, Tiziana Boffa Ballaran, Leonid Dubrovinsky,  
Dan Frost, Florian Heidelbach, Hans Keppler, Falko Langenhorst,  
Catherine McCammon, Nobuyoshi Miyajima, Dave Rubie,  
Henri Samuel, Gerd Steinle-Neumann, Nicolas Walte



**Staff and guests of the Bayerisches Geoinstitut in July 2009:**

**Die Mitarbeiter und Gäste des Bayerischen Geoinstituts im Juli 2009:**

First row, from left (1. Reihe, v. links) Florian Heidelberg, Vincenzo Stagno, Sushant Shekhar, Davide Novella, Yuan Li, Wei Sun, Qingguo Wei, Holger Kriegel

Second row, from left (2. Reihe, v. links) Nicole Behringer, Katja Etzel, Anke Potzel, Rekha Sharma, Iris Buisman, Sabrina Filippi, Livia Nardini, Geertje Ganskow, Martha Pamato, Linda Lerchbaumer, Federica Schiavi, Aleksandra Trzaskowska, Olga Narygina

Third row, from left (3. Reihe, v. links) Evgeniya Zarechnaya, Tiziana Boffa Ballaran, Juliane Hopf, Geeth Manthilake, Ahmed El Goresy, Uwe Dittmann, Julien Chantel, Petra Buchert, Heinz Fischer, Dan Frost, Mainak Mookherjee

Fourth row, from left (4. Reihe, v. links) Stefan Keyssner, Henri Samuel, Nico Walte, Hubert Schulze, Yoichi Nakajima, Andreas Audétat, David Dolejš, Huaiwei Ni, Kilian Pollok, Roman Skála

Fifth/Sixth row, from left (5./6. Reihe, v. links) Willem van Mierlo, Eran Greenberg, Svyatoslav Shcheka, Giacomo Pesce, Kurt Klasinski, Patrick Cordier, Detlef Krauße, Alexander Kurnosov, Nobuyoshi Miyajima, Clemens Prescher, Sergey Ovsyannikov, Konstantin Glazyrin, Zhengning Tang, Hans Keppler, Dennis Harries, Gerd Ramming, Stefan Übelhack, Craig Manning, Falko Langenhorst

Absent (Es fehlten) Enikő Bali, Diego Bernini, Ulrich Böhm, Zurab Chemia, Nico de Koker, Leonid Dubrovinsky, Alberto Escudero, Gertrud Gollner, Shantanu Keshav, Lydia Kison-Herzing, Sven Linhardt, Micaela Longo, Catherine McCammon, Oliver Rausch, Dave Rubie, Gerd Steinle-Neumann, Coralie Weigel



## Contents

Foreword/Vorwort .....	9/I
1. Advisory Board and Directorship .....	11
1.1 Advisory Board .....	11
1.2 Leadership .....	11
2. Staff, Funding and Facilities .....	13
2.1 Staff .....	13
2.2 Funding .....	13
2.3 Laboratory and office facilities .....	18
2.4 Experimental and analytical equipment .....	18
3. Forschungsprojekte - Zusammenfassung in deutscher Sprache .....	III
3. Research Projects .....	21
3.1 <i>Earth's Structure and Geodynamics</i> .....	21
a. Electrical conductivity of the lower continental crust (X.-Z. Yang, H. Keppler, and H. Ni) .....	22
b. An alternative model for the origin of metaigneous lower crust beneath the Pannonian basin (E. Bali, in collaboration with J. Degi, K. Török, and C. Szabo/Budapest) .....	23
c. What do garnet pyroxenites represent in the lithospheric mantle of the Pannonian basin? (E. Bali, in collaboration with J. Degi, K. Török, and C. Szabo/Budapest) .....	26
d. Resolving sediment subduction (Z. Chemia, G. Steinle-Neumann, D. Dolejš/Prague, and S. Buiter/Trondheim) .....	29
e. Latent heat and volume work in the mantle transition zone (T. Chust, G. Steinle-Neumann, and H.-P. Bunge/München) .....	31
f. Nominally anhydrous minerals and dense hydrous Mg-Fe silicates in a hydrous Martian mantle (G. Ganskow, F. Langenhorst, and D.J. Frost) .....	32
g. Fragmentation of sinking iron diapirs in a terrestrial magma ocean (H. Samuel, D. Rubie, and H.J. Melosh/Tucson) .....	33
h. Iron carbide (Fe <sub>7</sub> C <sub>3</sub> ), an inner core candidate? (M. Mookherjee, G. Steinle-Neumann, and X. Wu/Beijing) .....	35
3.2 <i>Geochemistry</i> .....	38
a. Accretion of volatile elements to the Earth and Moon (D.C. Rubie, and D.J. Frost; F. Nimmo/Santa Cruz, D. O'Brien/Tucson, U. Mann/Zürich, and H. Palme/Frankfurt) .....	39
b. The partitioning of alkali metals between liquid metallic Fe and silicate melt (K. Tsuno/Houston, D.J. Frost, and D.C. Rubie) .....	41

c.	The effect of Si on O partitioning between the Earth's silicate mantle and core (K. Tsuno/Houston, D.J. Frost, and D.C. Rubie) .....	43
d.	An associated solution model describing the Si and O content of liquid core-forming metal at high pressure and temperature (D.J. Frost, D.C. Rubie, and K. Tsuno/Houston) .....	44
e.	Element partitioning between metal and silicates at high pressure during formation of the Earth's core (Y. Nakajima, D.J. Frost, and D.C. Rubie) .....	46
f.	The carbon/carbonate equilibria in the Earth's mantle as a function of pressure, temperature, oxygen fugacity and melt composition (V. Stagno, and D.J. Frost) .....	47
g.	High pressure and temperature experiments on a carbonated lower mantle assemblage using sintered diamond anvils in a multianvil apparatus (V. Stagno, and D.J. Frost; Y. Tange, and T. Irifune/Ehime) .....	50
h.	$Fe^{3+}/Fe_{tot}$ measurements on garnets in carbon-bearing lherzolite assemblage and implications for the redox conditions of the Earth's upper mantle (V. Stagno, C.A. McCammon, and D.J. Frost) .....	51
i.	Oxygen fugacities determined from iron oxidation state in natural (Mg,Fe)O ferropericlase: new insights into lower mantle diamond formation (M. Longo, C.A. McCammon, G. Bulanova/Bristol, F. Kaminsky/West Vancouver, and R. Tappert/Adelaide) .....	54
j.	Investigation of diamond-forming media by transmission electron microscopy of sections produced by focused ion beam technique (V. Stagno, N. Miyajima, and C.A. McCammon; H. Ohfuji, T. Sanehira, and T. Irifune/Ehime; A. Shiryayev/Moscow) .....	56
k.	Highly calcic carbonatites at moderate depths in the Earth and solidus reactions of simplified carbonated peridotite in the system CaO-MgO-Al <sub>2</sub> O <sub>3</sub> -SiO <sub>2</sub> -CO <sub>2</sub> (S. Keshav, G.H. Gudfinnsson/Reykjavík, and D.C. Presnall/Texas) .....	58
l.	Some complications in the melting of carbonated peridotite at 2-3 GPa (D. Novella, and S. Keshav) .....	61
m.	Partitioning of U and Th between diopside, pyrope and aqueous fluid, and its implication to the composition of island arc magmas (E. Bali, A. Audétat, and H. Keppler) .....	64
n.	Partitioning of Nb and Ta between rutile and felsic melt and the fractionation of Nb/Ta during slab melting (X.L. Xiong, H. Keppler, A. Audétat, H. Ni, and Y. Li) .....	66
o.	Sulphide-silicate melt partitioning of ore metals during partial melting of the metasomatized lithospheric mantle (Y. Li, and A. Audétat) .....	68
p.	Molybdenite solubility in hydrous, pyrrhotite-saturated rhyolite melt at 2 kbar/800 °C (W. Sun, and A. Audétat) .....	71
q.	The formation of iron sulphide in sediments: Abiotic anaerobic sulphur oxidation by ferric (oxyhydr)oxides (K. Pollok, K. Hellige, and S. Peiffer) ...	73

3.3	<i>Mineralogy, Crystal Chemistry and Phase Transformations</i> .....	75
a.	Phase relations in the Al <sub>2</sub> O <sub>3</sub> – TiO <sub>2</sub> system at pressures up to 20 GPa (A. Escudero, K. Tsuno, and F. Langenhorst) .....	76
b.	Effect of carbon on the phase relations in Fe-Ni system at high pressures and temperatures (O. Narygina, L. Dubrovinsky, C.A. McCammon, and D.J. Frost; N. Dubrovinskaia/Heidelberg, I.Yu. Kantor/Chicago, and V. Dmitriev/Grenoble) .....	78
c.	High-pressure induced polymorphism on gypsum (S. Nazzareni and P. Comodi/Perugia; L. Bindi/Firenze, and L. Dubrovinsky) .....	81
d.	Insight on the low-temperature – high-pressure phase diagram of wüstite (K. Glazyrin, and L. Dubrovinsky; S. Klotz/Paris) .....	83
e.	High-pressure Mössbauer spectroscopy studies of $\gamma$ -Fe <sub>2</sub> SiO <sub>4</sub> ringwoodite (E. Greenberg, L.S. Dubrovinsky, and C.A. McCammon) .....	84
f.	The structure of a super-aluminous version of the dense hydrous magnesium silicate phase D (T. Boffa Ballaran, and D.J. Frost) .....	86
g.	The crystal chemistry of wadsleyite hydration (J.R. Smyth, and Y. Ye/Boulder; D.J. Frost) .....	88
h.	NMR studies of anhydrous and hydrous forsterite, wadsleyite and ringwoodite (Mg <sub>2</sub> SiO <sub>4</sub> ) (J.R. Smyth/Boulder, D.J. Frost, W.R. Panero/ Columbus, and J.F. Stebbins/Stanford) .....	89
i.	TEM study of natural non-integral NC-pyrrhotites (D. Harries, K. Pollok, and F. Langenhorst) .....	90
j.	Application of <sup>29</sup> Si and <sup>27</sup> Al MAS-NMR spectroscopy to the study of the reaction mechanism of kaolinite to illite/muscovite (M. Mantovani/Sevilla, A. Escudero, and A.I. Becerro/Sevilla) .....	92
k.	TEM study of hydrothermally altered pyrochlore from Zomba Malosa, Malawi (A. Soman, and T. Geisler/Münster; K. Pollok) .....	95
3.4	<i>Physical Properties of Minerals</i> .....	98
a.	V <sub>p</sub> and V <sub>s</sub> measurements of polycrystalline pyrope (Mg <sub>3</sub> Al <sub>2</sub> Si <sub>3</sub> O <sub>12</sub> ) up to 16 GPa (J. Chantel and D.J. Frost) .....	99
b.	Bulk sound velocity measurements of lower mantle phases at high P,T using nuclear inelastic scattering (C. McCammon, L. Dubrovinsky, K. Glazyrin, O. Narygina, and E. Greenberg; I. Sergueev, and A. Chumakov/ Grenoble) .....	100
c.	Elastic behaviour of nanocrystalline anatase TiO <sub>2</sub> under compression (A. Kantor, I. Kantor, and V. Prakapenka/Chicago) .....	102
d.	Effect of iron on the compressibility of hydrous ringwoodite (G. Ganskow, T. Boffa Ballaran, and F. Langenhorst) .....	104
e.	Equation of state of Fe <sub>2</sub> SiO <sub>4</sub> ringwoodite (F. Nestola/Padova, T. Boffa Ballaran, and M. Koch-Müller/Potsdam) .....	105

f.	Compressibility of the $\text{Ca}_2\text{Sb}_2\text{O}_7$ weberite-like compound: In situ high-pressure single-crystal X-ray diffraction study (L. Chelazzi/Firenze, T. Boffa Ballaran, F. Nestola/Padova, L. Bindi/Firenze, and P. Bonazzi/Firenze) .....	106
g.	Thermal diffusivity of $\text{CaGeO}_3$ perovskite (G. Manthilake, N. de Koker, and D.J. Frost) .....	107
h.	Lattice thermal conductivity in $\text{MgO}$ periclase computed using equilibrium first-principles molecular dynamics (N. de Koker) .....	109
i.	The magnetic signature of basal plane anisotropy in hematite (K. Fabian, P. Robinson, and S.A. McEnroe/Trondheim; F. Heidelbach) .....	111
3.5	<i>Fluids and their Interaction with Melts and Minerals</i> .....	115
a.	An equation of state for mineral dissolution in aqueous fluids at high temperatures and pressures (D. Dolejš/Prague, and C.E. Manning/Los Angeles) .....	116
b.	Aluminium speciation in aqueous fluids at high pressures and high temperatures (M. Mookherjee, H. Keppler, and C. Manning/Los Angeles) ....	120
c.	Partitioning of Cu in a two-phase fluid system at 600 °C and 700 bar (L. Lerchbaumer, and A. Audétat) .....	122
d.	Partitioning of sulfur dioxide between dacitic melt and aqueous fluid phases (L. Hobbs, and H. Keppler) .....	124
e.	Adsorption of HCl onto volcanic ash (L. Hobbs, and H. Keppler) .....	125
f.	Dissolution experiments on sphalerite and galena and the role of secondary phases (K. Etzel, and K. Pollok) .....	126
g.	Oxidative dissolution of pyrrhotite by <i>Acidithiobacillus ferrooxidans</i> (J. Hopf, D. Harries, F. Langenhorst, and K. Pollok; M.F. Hochella/Blacksburg) .....	127
3.6	<i>Physics and Chemistry of Melts and Magmas</i> .....	130
a.	Transport properties of $\text{Mg}_2\text{SiO}_4$ melt at high pressure – Viscosity of the magma ocean (O. Adjaoud/Potsdam, G. Steinle-Neumann, and S. Jahn/Potsdam) .....	131
b.	Observation of low-anisotropy crystal aggregates undergoing static grain growth and melting in the moissanite cell (F. Schiavi, N. Walte, and H. Keppler) .....	133
c.	Electrical conductivity of anhydrous and hydrous albite-composition melts at high pressures (H. Ni, and H. Keppler) .....	135
3.7	<i>Rheology</i> .....	138
a.	High pressure and temperature deformation experiments on San-Carlos olivine and implications for upper mantle anisotropy (S. Shekhar, D.J. Frost, N. Walte, N. Miyajima, and F. Heidelbach) .....	139

b.	Deformation and crystallographic preferred orientation of coesite and retrograde quartz (N. Walte, F. Heidelbach, P. Cordier/Lille, and D. Rubie) .....	141
c.	Characterization of the dislocations and slip systems in lingunite (P. Cordier, and A. Mussi/Lille; D.J. Frost) .....	143
d.	Burgers vector determination in deformed materials using thickness-contour fringes in weak-beam dark-field TEM images (N. Miyajima, and N. Walte) .....	145
e.	Magnetofabric and textural analysis from highly anisotropic magnetite-bearing mylonitic garnet micaschist of the Scandinavian Caledonides (R. Engelmann, A. Kontny, and J. Grimmer/Karlsruhe; F. Heidelbach) .....	147
3.8	<i>Metamorphism</i> .....	150
a.	Diffusion of majorite in garnet (W. van Mierlo, F. Langenhorst, N. Miyajima, D.J. Frost, and D. Rubie) .....	151
b.	Fe <sup>3+</sup> /Fe <sup>2+</sup> equilibria in subduction zone metasomatized garnet peridotites (N. Malaspina, S. Poli, and P. Fumagalli/Milano; F. Langenhorst) .....	152
c.	Experimental study on shock metamorphism of anhydrite (C. Prescher, F. Langenhorst, and U. Hornemann/Weil am Rhein) .....	154
d.	Ample evidence for shock-induced melting of labradorite and quenching to maskelynite glass in Martian shergottites: Fundamental consequences to equilibrium shock pressure estimates and to the age conundrum of Martian meteorites (A. El Goresy; M. Miyahara, E. Ohtani, and S. Ozawa/Sendai; P. Gillet/Lyon, P. Beck/Grenoble, G. Montagnac/Lyon, and T. Nagase/Sendai) .....	155
e.	First natural occurrence of ringwoodite exsolution lamellae in fractionally crystallized Mg-rich wadsleyite from shock-induced olivine melts in L6 chondrites (A. El Goresy; M. Miyahara, E. Ohtani, S. Ozawa, T. Nagase, and M. Nishijima/Sendai) .....	158
f.	Coherent ringwoodite growth in olivine of Yamato 791384 L6 chondrite (M. Miyahara, and E. Ohtani/Sendai; M. Kimura/Mito; A. El Goresy; S. Ozawa, T. Nagase, M. Nishijima, and K. Hiraga/Sendai) .....	162
3.9	<i>Materials Science</i> .....	165
a.	Assignment of Raman active modes of B <sub>28</sub> (E.Yu. Zarechnaya, L. Dubrovinsky, and N. Dubrovinskaia/Heidelberg) .....	165
b.	Synthesis and equation of state of a high density phase Ni <sub>3</sub> S (D. Chareev, in collaboration with E. Osadchii, and Yu. Litvin/Chernogolovka; L. Dubrovinsky, A. Kurnosov, E. Zarechnaya, O. Narygina) .....	167
c.	Pressure-induced phase transitions of iron-phosphor alloys: Ab initio calculations (X. Wu, G. Steinle-Neumann, L. Dubrovinsky, M. Kanzaki/Misasa, S. Qin/Beijing) .....	169

d.	Compression of Pnma-structured $Ti_2O_3$ to 67 GPa: X-ray diffraction and Raman studies (S.V. Ovsyannikov, X. Wu, L. Dubrovinsky, and N. Dubrovinskaia/Heidelberg) .....	170
e.	Pressure-induced structural phase transition in $YMnO_3$ (D.P. Kozlenko, and E.V. Lukin/Dubna; L.S. Dubrovinsky; B.N. Savenko/Dubna, and J.-G.Park/Suwon) .....	172
f.	A high-pressure Raman investigation of $CaFe_2O_4$ (E. Greenberg, L.S. Dubrovinsky, and C.A. McCammon) .....	173
g.	Optical and volumetric measurements on glass densified by high pressure annealing (D.J. Frost, in collaboration with U. Fotheringham, O. Sohr, P. Fischer, G. Westenberger/Schott AG, Mainz; C. Bienert, and R. Weißmann/Erlangen; K. Richardson/Clemson) .....	175
3.10	<i>Methodological Developments</i> .....	177
a.	Application of portable laser heating system for in situ diamond anvil cell experiments at synchrotron radiation facilities (L. Dubrovinsky, K. Glazyrin, O. Narygina, and C. McCammon; N. Dubrovinskaia/Heidelberg; A.I. Chumakov, and S. Pascarelli/Grenoble; J. Bock/Gaggenau) .....	177
b.	Development of synchrotron Mössbauer source for geophysical studies at the ESRF (V. Potapkin, A.I. Chumakov, and R. Rüffer/Grenoble; G.V. Smirnov, and S.L. Popov/Moscow; L. Dubrovinsky, and C. McCammon) .....	180
c.	Neutron diffraction at high pressures using Stress-Spec diffractometer at FRM II (N. Dubrovinskaia/Heidelberg, M. Hofmann/Garching, and L. Dubrovinsky) .....	182
d.	The design and calibration of a multianvil press employing six independently acting 800 tonne hydraulic rams (D.J. Frost, and G. Manthilake, in collaboration with the firm of Voggenreiter GmbH/Mainleus) .....	184
e.	Single-crystal diffractometer with an ultrahigh intensity rotating anode X-ray source (D. Trots, A. Kurnosov, T. Boffa Ballaran, and D.J. Frost) .....	187
f.	On-line Brillouin spectroscopy at BGI: Development of in-house research facility for simultaneous measurement of acoustic velocities and densities at high pressures (A. Kurnosov, A. Trzaskowska/Poznań, D. Trots, D.J. Frost, and T. Boffa Ballaran).....	189
g.	Design and calibration of a new D-DIA assembly for conducting deformation experiments in simple shear up to 8 GPa (S. Shekhar, and D.J. Frost) .....	190
h.	FIB-SEM preparation of nm-sized alteration layers and adsorbed nanoparticles on sulfide surfaces for TEM study (D. Harries, K. Pollok, and F. Langenhorst).....	193
i.	Fast and accurate modelling of sharp discontinuities in geophysical flows using Lagrangian implicit surfaces (H. Samuel) .....	194

4.	International Graduate School	
	"Structure, Reactivity and Properties of Oxide Materials" .....	197
5.	Publications, Conference Presentations, Seminars .....	201
5.1	Publications (published); Refereed international journals .....	201
	a) Refereed international journals .....	201
	b) Popular scientific magazines .....	209
5.2	Publications (submitted, in press) .....	209
5.3	Presentations at scientific institutions and at congresses .....	214
5.4	Lectures and seminars at Bayerisches Geoinstitut .....	227
5.5	Conference organization .....	234
6.	Visiting scientists .....	235
6.1	Visiting scientists funded by the Bayerisches Geoinstitut .....	235
6.2	Visiting scientists supported by other externally funded BGI projects .....	236
6.3	Visitors (externally funded) .....	237
7.	Additional scientific activities .....	241
7.1	Theses .....	241
7.2	Honours and awards .....	241
7.3	Editorship of scientific journals .....	241
7.4	Membership of scientific advisory bodies .....	242
8.	Scientific and Technical Personnel .....	243
	Index .....	247



## Foreword

Research into the deep interior of the Earth is strongly connected with new developments in high-pressure technology. In the last ten years, the Bayerisches Geoinstitut has developed numerous new experimental methods and established their use in the laboratory. A new milestone in 2009 was the installation of a new type of multianvil press with six anvils that can be moved completely independently of each other in a cubic geometry. This press was developed by the Bayerisches Geoinstitut in collaboration with Max Voggenreiter GmbH, a small local company. Each of the six independently driven anvils of this press can exert a force of 800 tonnes; at the same time, the position of each anvil can be determined to within a fraction of a micron using optical interferometry. Using this apparatus, it will be possible, for the first time, to perform deformation experiments under pressure-temperature conditions of the Earth's lower mantle, thus enabling the dynamics of a large part of the planet to be simulated directly in the laboratory. The new press will also enable the accessible pressure region to be increased in static experiments.

Experiments at high pressures and temperatures are, however, only one aspect of the scientific activities of the Geoinstitut. It has always been the philosophy of the institute to pursue experimental Earth sciences in the broadest sense – with scientific questions that range from interplanetary regions, to the Earth's surface and down to the centre of the planet. The current Annual Report presents a broad overview of such activities. Important new findings have not necessarily been obtained only under extreme temperatures and pressures. Micro-organisms play an important role in processes that take place close to the Earth's surface and many processes that might appear purely inorganic, such as the weathering of minerals, are in reality controlled by micro-organisms. Through the establishment of a new microbiological laboratory, such processes can now be studied at the Geoinstitut. The current Annual Report contains some of the first results in this research area. An interesting observation is that the same bacteria show a completely different affinity for two forms of the iron sulphide mineral pyrrhotite, even though the mineral structures are only slightly different.

The Geoinstitut is primarily a research institution. At the same time, research cannot be separated from the education of young scientists. In 2009, Li Yuan was the first student at the Geoinstitut to graduate in the Masters Programme "Experimental Geosciences". This new Masters course introduces young students to research in the very first semester and therefore extends and complements the long-established education of graduate students and postdocs at the institute.

The vast majority of scientists at the Geoinstitut originate from outside of Germany and the institute cooperates with numerous institutions in Europe, USA and Japan. Collaboration with Japanese scientists is viewed as being especially important. It was with the assistance of Japanese colleagues, more than twenty years ago, that the first multianvil press was installed and made operational at the Geoinstitut. A highpoint of such collaboration in 2009 was a joint

workshop involving scientists from the Bayerisches Geoinstitut and colleagues from the Geodynamic Research Center, Ehime University, that was held in June 2009 at the Eremitage in Bayreuth. More than 30 colleagues from Japan travelled to Bayreuth to participate in this workshop.

As in previous years, and also on behalf of my colleagues, I would like to thank the *Free State of Bavaria* as represented by the *Bayerisches Staatsministerium für Wissenschaft, Forschung und Kunst* as well as the *Kommission für Geowissenschaftliche Hochdruckforschung* of the *Bavarian Academy of Sciences* for their continuing support and strong commitment to the Bayerisches Geoinstitut. We also gratefully acknowledge generous support from external funding agencies, in particular the *Alexander von Humboldt Foundation*, the *European Union*, and the *German Science Foundation*, which have also contributed greatly to the development and success of the Institute.

Bayreuth, March 2010

Hans Keppler

## **Vorwort**

Die Erforschung des tiefen Erdinnern ist wesentlich verknüpft mit neuen Entwicklungen in der Hochdrucktechnik. Das Bayerische Geoinstitut hat in den vergangenen Jahrzehnten zahlreiche experimentelle Methoden entwickelt und erstmals im Labor angewandt. Ein neuer Meilenstein im Jahr 2009 war die Installation einer neuartigen Presse mit sechs völlig unabhängig voneinander bewegbaren Stempeln in kubischer Geometrie. Diese Presse wurde vom Bayerischen Geoinstitut entwickelt in Zusammenarbeit mit der Max Voggenreiter GmbH, einer lokalen mittelständischen Firma. Jeder der sechs hydraulischen Stempel dieser Presse kann eine Kraft von bis zu 800 Tonnen erzeugen; gleichzeitig kann durch optische Interferometrie die Position der einzelnen Stempel mit einer Genauigkeit von einem Bruchteil eines Mikrometers bestimmt werden. Mit dieser Apparatur wird es erstmals möglich sein, Verformungsexperimente unter den Druck- und Temperaturbedingungen des tieferen Erdmantels durchzuführen und damit die Dynamik großer Teile unseres Planeten direkt im Labor zu simulieren. Gleichzeitig soll die Presse den zugänglichen Druckbereich für statische Experimente erweitern.

Experimente unter extremen Drücken und Temperaturen sind jedoch nur ein Teilaspekt der wissenschaftlichen Aktivitäten am Geoinstitut. Es war stets die Philosophie des Instituts, experimentelle Geowissenschaften im weitesten Sinne zu betreiben – mit Fragestellungen, die vom interplanetaren Raum über die Erdoberfläche bis zum Zentrum unseres Planeten reichen. Der vorliegende Jahresbericht bietet einen breiten Überblick über diese Aktivitäten. Wichtige neue Erkenntnisse werden hier nicht notwendigerweise nur unter extremen Druck- und Temperaturbedingungen gewonnen. Mikroorganismen spielen eine große Rolle bei Prozessen, die in der Nähe der Erdoberfläche ablaufen und viele scheinbar rein anorganischen Vorgänge, wie die Verwitterung von Mineralen, werden in der Realität von Mikroorganismen gesteuert. Durch die Einrichtung eines neuen mikrobiologischen Labors können solche Zusammenhänge auch am Geoinstitut untersucht werden. Der vorliegende Jahresbericht enthält einige erste Resultate aus diesem Bereich. Eine bemerkenswerte Beobachtung ist hier, dass das gleiche Bakterium offenbar einen höchst unterschiedlichen Appetit auf zwei Formen des Eisen-Sulfids Pyrrhotin entwickelt, die sich in der Struktur nur minimal voneinander unterscheiden.

Das Geoinstitut ist primär eine Forschungseinrichtung. Gleichzeitig ist jedoch Forschung untrennbar mit der Förderung des wissenschaftlichen Nachwuchses verbunden. Im Jahr 2009 hat Li Yuan als erster Student am Geoinstitut seinen Master-Abschluss in „Experimental Geosciences“ erhalten. Dieser neue Master-Studiengang führt junge Studenten bereits ab dem ersten Semester direkt an die Forschung heran und er ergänzt damit die bereits gut etablierte Ausbildung von Doktoranden und Postdoktoranden am Institut.

Die weit überwiegende Mehrheit der Wissenschaftler am Geoinstitut stammt aus dem Ausland und das Institut kooperiert mit zahlreichen Institutionen in Europa, den USA und Japan. Insbesondere die Zusammenarbeit mit Japan war für das Geoinstitut stets besonders

wichtig. Vor mehr als zwei Jahrzehnten wurde die erste Mehrstempel-Pressen am Institut installiert und mit Hilfe japanischer Kollegen in Betrieb genommen. Zahlreiche Besucher aus Japan haben seitdem am Geoinstitut ihre Forschungen vorangetrieben. Ein Höhepunkt dieser Zusammenarbeit in 2009 war ein gemeinsamer Workshop des Bayerischen Geoinstituts zusammen mit unseren Kollegen des Geodynamics Research Centers der Ehime-Universität, der im Juni in der Eremitage in Bayreuth stattfand. Mehr als 30 Kollegen aus Japan reisten zu diesem Treffen nach Bayreuth.

Wie in den vorangegangenen Jahren möchte ich auch im Namen meiner Kollegen dem *Freistaat Bayern*, vertreten durch das *Bayerische Staatsministerium für Wissenschaft, Forschung und Kunst*, als auch der *Kommission für Geowissenschaftliche Hochdruckforschung* der *Bayerischen Akademie der Wissenschaften* danken für ihre fortwährende Unterstützung und ihre enge Verbundenheit mit dem Bayerischen Geoinstitut. Wir sind auch sehr dankbar für die großzügige Förderung durch externe Geldgeber, insbesondere durch die *Alexander von Humboldt-Stiftung*, die *Europäische Union* und die *Deutsche Forschungsgemeinschaft*, die ebenfalls wesentlich zur Entwicklung und zum Erfolg des Bayerischen Geoinstituts beigetragen haben.

Bayreuth, im März 2010

Hans Keppler

## 1. Advisory Board and Directorship

### 1.1 Advisory Board

The *Kommission für Geowissenschaftliche Hochdruckforschung der Bayerischen Akademie der Wissenschaften* advises on the organisation and scientific activities of the institute. Members of this board are:

Prof. Dr. G. BREY	Institut für Geowissenschaften der Johann Wolfgang Goethe-Universität, Frankfurt am Main
Prof. Dr. U. CHRISTENSEN	Max-Planck-Institut für Sonnensystemforschung, Katlenburg-Lindau
Prof. Dr. R. KNIEP	Institut für Chemische Physik fester Stoffe der Max-Planck-Gesellschaft, Dresden
Prof. Dr. H. PALME	Institut für Mineralogie und Geochemie der Universität zu Köln
Prof. Dr. R. RUMMEL	Institut für Astronomische und Physikalische Geodäsie der TU München
Prof. Dr.-Ing. G. SACHS (Chairman)	Lehrstuhl für Flugmechanik und Flugregelung der TU München
Prof. Dr. E. SALJE, FRS, FRSA	Department of Earth Sciences, University of Cambridge
Prof. Dr. H. SOFFEL	Emeritus, Institut für Allgemeine und Angewandte Geophysik der Universität München

The Advisory Board held meetings in Bayreuth (17.04.2009) and in Munich (27.11.2009).

### 1.2 Leadership

Prof. Dr. Hans KEPPLER (Director)  
Prof. Dr. David C. RUBIE  
Prof. Dr. Falko LANGENHORST



## 2. Staff, Funding and Facilities

### 2.1 Staff

At the end of 2009 the following staff positions existed in the Institute:

- Scientific staff \*: **12**
- Technical staff: **13**
- Administrative staff: **2**
- Administrative officer: **1**

\* Including a tenure-track junior professorship in geodynamic modeling initially funded by *Stifterverband für die Deutsche Wissenschaft* for 6 years, started in 2007.

During 2009, 29 scientific (238 months) positions were funded by grants raised externally by staff members of the institute. In addition 10 long-term scientific positions (94 months) were funded by the resources of the BGI Visiting Scientists' Programme (see Sect. 8) which also supported short-term visits for discussing future projects or presenting research results (see Sect. 6). Positions for 5 Ph.D. students and 1 co-ordinator were funded under the BGI International Graduate School under the Elitenetzwerk Bayern "Structure, Reactivity and Properties of Oxide Materials" (see Sect. 4). 5 scientists (31 months) were supported by personal grants (stipends).

### 2.2 Funding

In 2009, the following financial resources were available from the Free State of Bavaria:

- Visiting Scientists' Programme: 368.000 €
- Consumables: 476.000 €
- Investment Funding: 418.000 €

The total amount of national/international external funding ("*Drittmittel*") used for ongoing research projects in 2009 was 2.791.000 € (Positions: 1.230.000 €; equipment, consumables and travel grants: 1.561.000 €).

	positions	equipment, consumables, travel grants	total
• ENB	226.000 €	127.000 €	353.000 €
• AvH	62.000 €	18.000 €	80.000 €
• DFG	294.000 €	296.000 € <sup>*)</sup>	590.000 €
• EU	490.000 €	1.058.000 €	1.548.000 €
• BMBF	98.000 €	11.000 €	109.000 €
• Stifterverband	51.000 €	30.000 €	81.000 €
• Others	9.000 €	21.000 €	<u>30.000 €</u>
			<b>2.791.000 €</b>

(ENB = Int. Graduate School "Oxides" in the Elite Network of Bavaria; AvH = Alexander von Humboldt Foundation; DFG = German Science Foundation; EU = European Union; BMBF = Federal Ministry of Education and Research; Stifterverband = Stifterverband für die Deutsche Wissenschaft; Others: Europ. Science Found, Deutscher Akad. Austauschdienst, Industrie)

<sup>\*)</sup> includes Federal contribution to investment funding (§91B GG)

In the following list only the BGI part of the funding is listed in cases where joint projects involved other research institutions. Principal investigators and duration of the grants are listed in brackets. Total project funding refers to the funding over the entire duration of this project.

<b>Funding institution</b>	<b>Project, Funding</b>	<b>Total Project Funding</b>
BCTC <sup>*1)</sup>	(G. Steinle-Neumann, A.v.d. Walle/California Institute of Technology – 1.09. - 6.10) "Ternary solid solutions in mineral physics from ab initio computations" Travel funding: 4.800 € <sup>*1)</sup> Bavaria California Technology Center	4.800 €
BMBF	03G0718A (K. Pollok – 10/08 - 9/11) Nachwuchsgruppe "Microstructural Controls on Monosulfide Weathering" (MIMOS) Positions: 3 x E 13/2, each 36 months 294.235 € student assistant, (19,75h/month), 48 months 7.920 € Consumables and travel funding: 57.550 € (in 2009: 106.259 €) Total:	359.705 €
DAAD	(D. Dubrovinsky) Grant for resistivity studies at high pressure	2.500 €
DFG	Au 314/1-1 (A. Audétat – 9.08 - 8.10) "Fractionation of sulfur, copper and gold in two-phase fluids" Positions: E 13/2, 24 months 65.385 € Consumables and travel funding: 21.000 €	86.385 €
DFG	Du 393/6-1 (L.S. Dubrovinsky, H.F. Braun – 9.08 - 8.09) "Synthesis and in situ characterization of boron-doped superhard nanodiamond materials" Positions: E 13/2, 12 months 32.695 € Consumables and travel funding: 3.600 €	36.295 €
DFG	Du 393/7-1 (L.S. Dubrovinsky, N.A. Dubrovinskaia – 6.09 - 5.12) "Elasticity of iron and iron-based alloys at conditions of the Earth's and planetary cores" Positions: student assistant (80 h/month), 36 months 23.760 € Consumables and travel funding 42.017 € Publication costs 1.500 € Overhead: 18.600 €	85.877 €
DFG	Fr 1555/4-1 (D.J. Frost – 7.08 - 6.09) "Systematics of the post-spinel transition in Fe-bearing compositions" Consumables and travel funding:	1.815 €

DFG	INST 91/204-1 (H. Keppler) Co-financing of a multianvil press with 6 independent anvils 50 % of 830.918 €	415.459 €
DFG	Ke 501/5-3 (H. Keppler – 1.07 - 12.09) "Übergangsmetallionen und Wasser im Erdmantel" 1 position: E 13, 36 months 196.155 € Consumables and travel funding: 25.200 € Overhead 10.480 €	231.835 €
DFG	KE 501/8-1 (H. Keppler – 8.09 - 7.11) "Untersuchungen der Kristallisationskinetik und Gefüge- entwicklung von Basalten mit einer neuartigen Moissanit- Sichtzelle" 1 position: E 13, 24 months 130.770 € Consumables and travel funding: 27.690 € Publication costs 800 € Overhead 32.200 €	191.460 €
DFG	KE 501/9-1 (H. Keppler – 2010 - 2012) "Noble gases in silicate perovskite: Solubility, dissolution mechanism and influence on the equation of state" 1 position: E 13, 36 months 196.155 € Consumables and travel funding: 15.000 € Overhead 38.300 €	249.455 €
DFG	Ke 1351/1-1 (H. Keppler – 3.07 - 10.09) ESF-Verbundprojekt "Hydrogen in Minerals" 1 position: E 13/2, 36 months 98.080 € Consumables and travel funding: 15.000 € Overhead 6.800 €	119.880 €
DFG	La 830/9-1 (F. Langenhorst, D.J. Frost, D.C. Rubie – 2.08 - 10.09) "Stability and structures of hydrous minerals in the transition zone of the Martian mantle" Positions: E 13/2, 9 months 24.520 € Consumables and travel funding: 19.150 € Equipment: 50.000 €	93.670 €
DFG	La 830/10-1 (F. Langenhorst, D.J. Frost, D.C. Rubie – 2.08 - 10.09) "Oxygen solubility in Fe-Ni-S alloy at high pressure and implications for the formation and compositions of planetary cores" Positions: student assistant 4.300 € Consumables and travel funding: 8.450 €	12.750 €
DFG	La 830/12-1 (F. Langenhorst, A. Deutsch – 2.08 - 6.09) "Mineralogical and geochemical studies of impact melt products from the Chesapeake Bay impact structure" Positions: E 13/2, 2 months 5.450 € Consumables and travel funding: 8.100 €	13.550 €

DFG	La 830/13-1 (F. Langenhorst, A. Woodland, D.J. Frost – 2.08 - 7.09) "Systematics of the post-spinel transition in Fe-bearing compositions" Positions: E 13/2, 10 months 27.245 € Consumables and travel funding: 6.350 €	33.595 €
DFG	La 830/14-1 (F. Langenhorst – 2.08 - 9.14) Gottfried Wilhelm Leibniz-Preis 2007	2.489.000 €
DFG	La 830/15-3 (F. Langenhorst, A. Deutsch – 2.08 - 1.10) "Mineralogical and geochemical studies of impact melt products from the Chesapeake Bay and the Lake Bosumtwi impact structures (ICDP)" Consumables and travel funding: 10.800 €	10.800 €
DFG	Mc 3/16-1 (C.A. McCammon, L.S. Dubrovinsky – 10.06 - 9.09) "High-pressure high-temperature <sup>57</sup> Fe Mössbauer spectroscopy in laser-heated diamond anvil cells: Applications for the mineralogy of Earth's lower mantle and core" Positions: student assistant (80 h/month), 36 months 23.760 € Consumables and travel funding: 45.800 € Overhead: 3.900 €	73.460 €
DFG	Mc 3/16-2 (C.A. McCammon, L.S. Dubrovinsky – 10.09 - 9.12) "High-pressure high-temperature <sup>57</sup> Fe Mössbauer spectroscopy in laser-heated diamond anvil cells: Applications for the mineralogy of Earth's lower mantle and core" Positions: student assistant (80 h/month), 36 months 23.760 € Consumables and travel funding: 30.000 € Overhead: 15.400 €	69.160 €
DFG	STE 1105/6-1 (G. Steinle-Neumann – 3.09 - 8.10) DFG SPP 1375 SAMPLE "Mineralogical and Dynamic Origin of the South African Superplume" Positions: E13/2, 18 months 49.040 € Consumables and travel funding: 4.654 €	53.694 €
DFG	(G. Steinle-Neumann, H. Samuel) Computer cluster funds raised by a joint proposal between several UBT departments (BGI, physics, chemistry, computer center). Total funding: 260.000 € BGI funding:	38.000 €

EU	Marie Curie Intra European Fellowships – People "From Planetary to the Nanoscale: Magnetism at the Interface" (F. Langenhorst – 10.09 - 10.11) Positions, consumables and travel funding	231.000 €	231.000 €
EU	Marie Curie Research Training Network "Crust to core: the fate of subducted material" (2.07 - 1.11) G. Steinle-Neumann (coordinator), G. Fiquet (Paris, France), F. Langenhorst (Bayreuth, Germany), A.I. Beccero (Sevilla, Spain), S. Buiter (Trondheim, Norway), O. Cadek (Prague, Czech Republic), D. Dobson (London, UK), D. Andrault (Clermont-Ferrand, France), P. Jochym (Krakow, Poland), S. Poli (Milan, Italy) and M.W. Schmidt (Zurich, Switzerland) Total funding: 3,3 Mio €	BGI funding:	740.000 €
EU	Marie Curie Host Fellowships for Early Stage Research Training "Atomic to Global" (C.A. McCammon – 01.06 - 12.09) Positions, consumables, equipment, travel:		677.952 €
Stifter- verband	Stifterverband für die Deutsche Wissenschaft Junior-Professur Geodynamische Modellierung Positions: W1, 72 months Consumables and travel funding:	245.200 € 120.000 €	365.200 €
Industry	Unrestricted Industrial grants (L.S. Dubrovinsky)		60.000 €
Industry	Collaboration with Fa. Dorfner-Anzaplan, Hirschau (F. Heidelberg)		1.400 €

### *2.3 Laboratory and office facilities*

The institute occupies an area of

ca. 1300 m<sup>2</sup> laboratory space

ca. 480 m<sup>2</sup> infrastructural areas (machine shops, computer facilities, seminar room, library)

ca. 460 m<sup>2</sup> office space

in a building which was completed in 1994.

### *2.4 Experimental and analytical equipment*

The following major equipment is available at Bayerisches Geoinstitut:

#### I. High-pressure apparatus

6x800 tonne independently acting-anvil press (25 GPa, 3000 K)

5000 tonne multianvil press (25 GPa, 3000 K)

1200 tonne multianvil press (25 GPa, 3000 K)

1000 tonne multianvil press (25 GPa, 3000 K)

500 tonne multianvil press (20 GPa, 3000 K)

500 tonne press with a deformation DIA apparatus

4 piston-cylinder presses (4 GPa, 2100 K)

Cold-seal vessels (700 MPa, 1100 K, H<sub>2</sub>O), TZM vessels (300 MPa, 1400 K, gas), rapid-quench device

Internally-heated autoclave (1 GPa, 1600 K)

High-pressure gas loading apparatus for DAC

#### II. Structural and chemical analysis

2 X-ray powder diffractometers

1 X-ray powder diffractometer with furnace and cryostat

Single-crystal X-ray cameras

2 automated single-crystal X-ray diffractometers

High-brilliance X-ray system

Single crystal X-ray diffraction with super-bright source

1 Mössbauer spectrometer (1.5 - 1300 K)

3 Mössbauer microspectrometers

2 FTIR spectrometers with IR microscope

FEG transmission electron microscope, 200 kV analytical, with EDS and PEELS

FEG scanning electron microscope with BSE detector, EDS, EBSD and CL

3 Micro-Raman spectrometers with ultraviolet and visible lasers

Tandem-multipass Fabry-Perot interferometer for Brillouin scattering spectroscopy

JEOL JXA-8200 electron microprobe; fully-automated with 14 crystals, 5 spectrometer configuration, EDX, capability for light elements  
193 nm Excimer Laser-Ablation ICP-MS  
ICP-AES sequential spectrometer  
Water content determination by Karl-Fischer titration  
GC/MS-MS for organic analyses  
Confocal 3D surface measurement system

### III. *In situ* determination of properties

Diamond anvil cells for powder and single crystal X-ray diffraction, Mössbauer, IR, Raman, optical spectroscopy and electrical resistivity measurements up to at least 100 GPa  
Facility for in situ hydrothermal studies in DAC  
Externally heated DACs for in situ studies at pressures to 100 GPa and 1200 K  
1-atm furnaces to 1950 K, gas mixing to 1600 K, zirconia  $fO_2$  probes  
1-atm high-temperature creep apparatus  
Gigahertz ultrasonic interferometer with interface to resistance-heated diamond-anvil cells  
Heating stage for fluid inclusion studies  
Impedance/gain-phase analyser for electrical conductivity studies  
Apparatus for in situ measurements of thermal diffusivity at high P and T  
Laser-heating facility for DAC  
Portable laser heating system for DAC

### IV. Computational facilities

9 node linux cluster (2x3.0 GHz Xeon Woodcrest Dual Core, 8 Gb memory), InfiniBand  
8 node linux cluster (16x2.83 GHz Xeon 5440 Quad Core, 64 Gb memory), InfiniBand  
RAID System (6 + 7 Tb storage)

The Geoinstitut is provided with well equipped machine shops, an electronic workshop and sample preparation laboratories. It has also access to the university computer centre.



The newly installed six-ram multianvil press "LPQ6" in the deformation laboratory of BGI: Six independently acting 800 tonne hydraulic rams are used to compress an inner cubic high pressure chamber. The pressure and position of each hydraulic ram can be precisely controlled such that linear deviations from cubic symmetry are less than 0.2 micrometers. When used with an inner set of sintered diamond anvils pressures in excess of 50 GPa should be possible for which the high level of symmetry in the distribution of force is required in order to prevent tensile stresses from damaging the anvils. Rheological experiments can also be performed on cubic assemblies at pressures compatible with the Earth's transition zone (400-660 km of depth).

"LPQ6", die neue 6-Stempel-Pressen (Typ Multianvil) am Bayerischen Geoinstitut:

In der Presse wirken sechs hydraulische Kolben unabhängig voneinander mit je 800 Tonnen Presskraft auf eine Hochdruck-Probenkammer von kubischer Symmetrie. Presskraft und Position jedes einzelnen Kolbens können sehr präzise gesteuert werden, so dass lineare Abweichungen von der kubischen Symmetrie geringer als 0,2 Mikrometer sind. Die Verwendung von gesinterten Diamanten als innere Druckstempel sollte es ermöglichen, mit der neuen Presse in Druckbereiche oberhalb von 50 GPa vorzustoßen. Für diese Zielsetzung ist eine hohe Symmetrie in der Kräfteverteilung notwendig, um die Zerstörung der Druckstempel durch Zugspannungen zu verhindern. Die kubische Anordnung der Stempel erlaubt auch Deformationsexperimente bei Drücken, wie sie in der Übergangszone (400-660 km Tiefe) herrschen.

### 3. Forschungsprojekte

Es wird an dieser Stelle nur über die wichtigsten, derzeit laufenden Projekte berichtet. Informationen über abgeschlossene Teilprojekte sind in den Abschnitten 5.1 und 5.2 in Form von Literaturzitataten angegeben. Die Beiträge des Kapitels 3 sollen nicht zitiert werden.

#### *3.1 Aufbau der Erde und Geodynamik*

Dynamische Prozesse formen fortlaufend die Kruste, den Mantel und den Kern der Erde um. Ein Verständnis dieser Veränderungen erfordert das Zusammenführen von Oberflächenbeobachtungen und geodynamischen Überlegungen, sowie die Charakterisierung von thermodynamischen und anderen Materialeigenschaften unter Druck und Temperatur des Erdinnern. Beispiele dieser Herangehensweise werden in diesem Kapitel vorgestellt.

Im ersten Beitrag wird der Einfluss von Wasser auf die elektrische Leitfähigkeit von natürlichem Klinopyroxen betrachtet, einem wichtigen Mineral in der tiefen Erdkruste unter Kontinenten. Die vorläufigen Ergebnisse deuten darauf hin, dass Wasserstoff und Eisen zu einer stark erhöhten elektrischen Leitfähigkeit führen, und damit Ergebnisse magnetotellurischer Messungen über Kontinenten erklären können.

Mantel-Xenolithe aus dem karpatischen Becken, die aus großer Tiefe an die Oberfläche gebracht wurden, bieten Einblicke in die Struktur und Entwicklung der Erdkruste. Petrographische Beobachtungen und geochemische Analysen dieser Xenolithe führen zu einem alternativen und verbesserten Verständnis über den Ursprung und die Entwicklung der tiefen Kruste unterhalb dieser Region in Zentraleuropa, was in den beiden darauf folgenden Beiträgen vorgestellt wird.

Geochemische Beobachtungen an Ozeaninsel-Basalten haben ergeben, dass Sedimente in Subduktionszonen in den Erdmantel transportiert werden; der Umfang dieses Transports ist jedoch weitgehend unbekannt. Der vierte Beitrag dieses Kapitels versucht dieser Frage nachzugehen, indem er ein lithochemisches Modell für die subduzierte Platte erstellt und mit Hilfe von thermodynamischen Daten Phasenübergänge als Funktion von Druck und Temperatur untersucht.

Der dynamische Zustand des Erdmantels resultiert aus dem Zusammenspiel von Mineralogie, Druck und Temperatur, wobei in geodynamischen Modellen mineralogische Parameter oft stark vereinfacht werden. Ein Beitrag untersucht den Effekt von mineralogischer Thermodynamik auf Mantelkonvektion mit Hilfe von 2D-Simulationen systematisch und betrachtet im Besonderen die thermischen Profile, die sich aus einer solchen Kopplung ergeben.

Wasser hat einen wichtigen Einfluss auf die physikalischen Eigenschaften und die Rheologie von Silikaten im Erdmantel. Das Volumen an Wasser, das in einem planetaren Mantel gespeichert werden kann, ist deshalb von zentraler Bedeutung für das Verständnis der Entwicklung erdähnlicher Planeten. In einem Beitrag wird diese Frage für eine marsähnliche

Zusammensetzung mit Hilfe von Experimenten in der Viel-Stempel-Pressen untersucht. Die Ergebnisse zeigen, dass erhebliche Mengen an Wasser im Mantel des Mars gespeichert sein können.

Der Mechanismus der zur Differenzierung von Kern und Mantel in erdähnlichen Planeten führt, bestimmt den Ausgangspunkt der thermischen Entwicklung von Planeten. Planeten von der Größe der Erde oder Mars haben zumindest eine Episode eines Magmaozeans durchlebt, in dem Eisen und Silikate sich in Kern und Mantel getrennt haben. Der vorletzte Beitrag untersucht den Vorgang der Differenzierung, indem die Bedingungen für die Fragmentierung eines sinkenden Eisendiapirs in einem Magmaocean simuliert werden.

Während der innere Erdkern zweifelsohne hauptsächlich aus Eisen besteht, ist die Frage des leichten Elements im Erdkern weiter offen, und damit auch die Mineralphase, die dieses leichte Element im inneren Erdkern annimmt. Der letzte Beitrag des Kapitels betrachtet  $\text{Fe}_7\text{C}_3$  als eine mögliche Phase des inneren Erdkerns. Dazu werden mit Hilfe der Dichtefunktionaltheorie die elastischen Konstanten unter hohem Druck berechnet. Ein Vergleich der Dichte und akustischen Geschwindigkeiten von  $\text{Fe}_7\text{C}_3$  mit denen des Erdkerns zeigt, dass  $\text{Fe}_7\text{C}_3$  eine mögliche Mineralphase des inneren Erdkerns sein kann.

### *3.2 Geochemie*

Die frühen Differentiations-Prozesse, welche die heutige Zusammensetzung der Erde beeinflusst haben, sind Thema der ersten Beiträge dieses Kapitels. Unser Sonnensystem entstand aus Gasnebeln, die bei der Abkühlung kondensierten. Die heißen Gase waren ursprünglich als Folge starker Sonnenaktivitäten aus dem inneren Sonnensystem herausgeschleudert worden, bevor sie sich soweit abkühlten dass es zur Kondensation kommen konnte. Dieser Differenzierungsprozess bewirkte in der Umgebung der sich bildenden Erde eine Abreicherung der Elemente, die bei Temperaturen unterhalb von 1200 K kondensieren, hier als volatile (leichtflüchtige) Elemente bezeichnet. Viele volatile Elemente sind jedoch auch „siderophil“ (Metall-liebend); sie wurden durch Differentiation aus dem silikatischen Erdmantel herausgetrennt und sanken in den zunehmend metallischeren Erdkern hinab. Der erste Beitrag dieses Kapitels zeigt, wie sich Unterschiede im Gehalt volatiler Elemente in der Erde und im Mond mit Kern/Mantel-Fraktionierung unter sehr hohen Drücken in der Erde erklären lassen. Daraus lässt sich schließen, dass ein Teil der volatilen Elemente in der Erde möglicherweise erst in ihrer jüngeren Geschichte aufgenommen wurde, nachdem sich ein bestimmter Druck im Erdinneren eingestellt hatte. Der zweite Beitrag zeigt auf, dass die relative Abreicherung des Erdmantels an Alkalien (K, Rb und Cs) eher eine Folge der Erdkern-Bildung ist, und nicht durch die im vorhergehenden Artikel angeführte Volatilität verursacht wurde. Drei weitere Beiträge befassen sich mit der Möglichkeit, dass Si und O als leichte Elemente im Erdkern vorhanden sein könnten. Ein interessantes Ergebnis ist, dass der Metall/Silikat-Verteilungskoeffizient stark durch die Präsenz von Sauerstoff beeinflusst wird. Es scheint, dass bei hohem Druck sowohl Si als auch O in den Kern gewandert sein können, während sich bei niedrigem Druck diese beiden Elemente gegenseitig ausschließen.

Die nächsten sieben Artikel konzentrieren sich auf Kohlenstoff, ein bedeutsames Element des Erdmantels. Kohlenstoff ist volatil wenn er in oxidischer Form als  $\text{CO}_2$  oder als Karbonat vorliegt. In reduzierter Form, als Graphit oder Diamant, verhält sich Kohlenstoff jedoch refraktär. Die ersten drei Artikel befassen sich mit der Bestimmung der Redox-Bedingungen, bei denen der Übergang des Kohlenstoffs von einer reduzierten Form (Diamant) in eine oxidische (in Mineralen und Schmelzen mit Karbonaten) auftritt. Auffällig ist, dass karbonatische Minerale bei Redox-Bedingungen des tiefen unteren Erdmantels wahrscheinlich stabiler sind als Diamant. Um die Redox-Bedingungen, bei denen Diamanten entstehen, sowie die Quelle, von der sie abstammen, zu identifizieren, wurden Mineraleinschlüsse in natürlichen Diamanten untersucht. In zwei weiteren Beiträgen werden das Schmelzverhalten von karbonatisiertem Peridotit und die Genese karbonatführender Schmelzen (Karbonatite) untersucht. Die Schmelztemperatur karbonatischer Gesteine nimmt in der Übergangszone (zwischen dem oberen und unteren Erdmantel) ab, was die Ursache für reduzierte Geschwindigkeiten seismischer Wellen in dieser Zone sein könnte. Außerdem wurden Belege dafür gefunden, dass nicht mischbare Silikat- und Karbonatitschmelzen unter denjenigen Bedingungen koexistieren könnten unter denen die Hauptmasse der auf der Erdoberfläche austretenden Basalte produziert wird.

Es schließen sich zwei Beiträge an, die sich mit dem Ursprung der Spurenelement-Verteilungsmuster in Inselbögen-Magmen befassen. Experimentell bestimmte Fluid/Schmelze- und Fluid/Mineral-Verteilungskoeffizienten erklären das oft hohe U/Th-Verhältnis von Inselbögen-Magmen im Vergleich zu Magmen welche an mittelozeanischen Rücken produziert wurden. Es zeigt sich, dass hohe U/Th-Verhältnisse dort entstehen, wo saline und oxidierte Fluide die Schmelzbildung bewirken. Auf ähnliche Weise wird das Nb/Ta-Verhältnis in Subduktionszonen-Magmen durch Temperatur und  $\text{H}_2\text{O}$ -Gehalt der Schmelze beeinflusst. Die Resultate erklären auch das niedrige Nb/Ta-Verhältnis in kontinentaler Kruste und archaischen Granitmagmen.

Die Metallverteilung zwischen Sulfidphasen und Silikatschmelzen wird in zwei weiteren Projekten untersucht. Eine Studie befasst sich mit der Verteilung erzbildender Elemente zwischen mafischer, alkalireicher Schmelze und Sulfidmineralen sowie Sulfid-Schmelzen unter Bedingungen des zur Lithosphäre zählenden oberen Erdmantels. Diese Resultate sind sowohl für die Lagerstättenbildung wie auch für die Verteilung chalkophiler (Schwefel-liebender) Elemente während der Differentiation der Erde von Bedeutung. Die andere Studie untersucht die Löslichkeit von Molybdänit ( $\text{MoS}_2$ ) in Silikatschmelzen mit dem Ziel, ein thermodynamisches Modell abzuleiten, das eine Abschätzung der Sauerstoff- und Schwefelfugazitäten natürlicher, Molybdänit-gesättigter Schmelzen zulässt.

Sulfide werden durch Redoxreaktionen an der Grenze von sauerstoffhaltigem und sauerstofffreiem Wasser in marinen und Süßwasser-Sedimenten gebildet. Der letzte Beitrag dieses Abschnitts beschäftigt sich mit Experimenten zur Bestimmung der Reaktionspfade, die zur Bildung von Eisensulfiden in diesem Milieu führen. Die Reaktionen sind komplex und führen zur Bildung von zahlreichen metastabilen und nanoskaligen Zwischenprodukten, die dennoch erfolgreich mit der Transmissionselektronenmikroskopie (TEM) identifiziert werden können. Die Ergebnisse liefern wichtige Einblicke in die Stabilität und Wachstums-

mechanismen von Eisensulfiden, die besonders in Bergbauregionen für die Sanierung kontaminierter Gewässer von Interesse sind.

### 3.3 Mineralogie, Kristallchemie und Phasenumwandlungen

Untersuchungen zu Reaktionen kristalliner Materie auf veränderte Umgebungsbedingungen (Druck, Temperatur und chemischer Zusammensetzung) sind wichtig, um das Verhalten gesteinsbildender Minerale in der Erde nachvollziehen zu können. Ein Hauptziel mineralogischer Untersuchungen liegt darin, die gegenseitigen Beziehungen der Mineralphasen zu bestimmen, um die Phasenstabilität unter Bedingungen des Erdinneren besser einzugrenzen. Diese Informationen können nicht durch direkte Beobachtungen an Gesteinen an der Erdoberfläche gewonnen werden. Die Phasenbeziehungen sowie Phasenübergänge in Hochdruck-Polymorphen werden direkt durch den Atomaufbau der Materie beeinflusst. Es überrascht daher nicht, dass Untersuchungen zur Kristallstruktur einen Schwerpunkt bei den Beiträgen dieses Kapitels darstellen. Die folgenden elf Beiträge bedienen sich verschiedener Techniken bei der Synthese bzw. Analyse von Kristallstrukturen, Phasenübergängen und chemischen Reaktionen einer Vielzahl von Mineralen.

Die ersten vier Beiträge dieses Kapitels widmen sich Phasenbeziehungen bei hohen Drücken. Um Phasenbeziehungen unter extremen Bedingungen zu untersuchen, müssen die Minerale entweder bei den gewünschten Bedingungen mittels verschiedener Hochdruck-Apparaturen (zum Beispiel Stempelzylinder- oder Vielstempel-Pressen) synthetisiert und die abgeschreckten Versuchsprodukte anschließend analysiert werden oder unter extremen Bedingungen in Diamantstempel-Pressen (DAC) *in situ* bestimmt werden.

Die Aluminiumlöslichkeit in  $\text{TiO}_2$ -Modifikationen und strukturell verwandten Modifikationen wurde in einem System  $\text{Al}_2\text{O}_3$ - $\text{TiO}_2$  untersucht, um Ultra-Hochdruck-Metamorphose besser zu verstehen. Die Kristallstruktur der Hochdruck-Modifikationen von Gips und ihr Verhalten wurden *in situ* mit Synchrotron-Röntgenbeugungsmethoden bestimmt. Eine Neutronenbeugungsstudie über Wüstit bei niedrigen Temperaturen liefert Erkenntnisse über die magnetischen und strukturellen Phasenübergänge. Genauere Eingrenzungen der Hauptbestandteile des Erdkerns werden durch *in situ*-Untersuchungen der Kohlenstofflöslichkeit in  $\text{Fe}_{1-x}\text{Ni}_x$ -Legierungen bei hohen Drücken und Temperaturen ermöglicht. Allerdings beeinträchtigt eine nachweisbare Kontamination mit Kohlenstoff (die bei den Experimenten während des Aufheizens der Probe mittels Laser in einer DAC auftritt) die Phasenbeziehungen im System der Fe-Ni-Legierungen.

Die folgenden fünf Beiträge stellen experimentelle Untersuchungen zur Kristallstruktur und Kristallchemie von wasserfreien und wasserführenden  $(\text{Mg,Fe})_2\text{SiO}_4$ -Polymorphen, von dichten, Al-reichen wasserführenden Phasen und von inkommensuraten Pyrrhotinen vor. Neue Ergebnisse der Mössbauer-Spektroskopie an der  $\gamma$ - $\text{Fe}_2\text{SiO}_4$ -Phase deuten einen magnetischen Übergang bei hohen Drücken an. Die Entdeckung einer super-aluminiumhaltigen Phase D kann für den Wassertransport von der Erdkruste in den unteren Erdmantel wichtig sein. Um der Einlagerung von Wasser sowie Ordnungs-/Fehlorderungsprozessen in  $\text{Mg}_2\text{SiO}_4$ -Wadsleyit und -Ringwoodit auf die Spur zu kommen, werden Methoden der

Röntgenbeugung und die  $^{29}\text{Si}$  NMR-Technik eingesetzt. Mit einer umfangreichen Elektronenbeugungsstudie (TEM) gelang es, eine Methode zur Indizierung und Parametrisierung der komplizierten Anordnung von Satelliten-Reflexen für Überstrukturen der NC-Pyrrhotine zu entwickeln.

Die letzten drei Beiträge dieses Kapitels befassen sich mit chemischen Reaktionen in Kationenlagen von Alumosilikatmineralen und der Alteration von Pyrochlor. Dafür werden die MAS-NMR-Spektroskopie und die Transmissionselektronenmikroskopie (TEM) eingesetzt. Es zeigt sich, dass die NMR-Spektroskopie ein wirkungsvolles Werkzeug für die Bestimmung der lokalen Umgebung von Al und Si ist, während sich TEM als unverzichtbar für Untersuchungen von Alterationen in Pyrochlor im Nanometer-Maßstab erweist.

### *3.4 Physikalische Eigenschaften von Mineralen*

In den Erd- und Materialwissenschaften haben Beziehungen zwischen Gefüge und Eigenschaften von Feststoffen große wissenschaftliche und technische Bedeutung. Die physikalischen Eigenschaften von Mineralen im Erdmantel spielen bei der Deutung von Struktur, Dynamik und Prozessen im Erdinneren eine wichtige Rolle. So beruht zum Beispiel die Interpretation seismischer Messdaten aus dem tiefen Erdinneren auf Labormessungen von Schall- und Scherwellengeschwindigkeiten an Mantelmineralen im Labor. Die Datenbasis für derartige physikalische Eigenschaften von Mantelmineralen ist jedoch schmal und oft nicht aussagekräftig; *in situ*-Messungen bei hohen Drücken und Temperaturen an sehr kleinen Proben stellen stets eine große experimentelle Herausforderung dar. Allerdings lieferten in letzter Zeit neue Ansätze im experimentellen Aufbau sowie die gezielte Nutzung von Synchrotron- und Neutronenstrahl-Einrichtungen genauere Daten auf diesem Forschungsfeld.

Beispiele für derartige Untersuchungen folgen in diesem Kapitel. Die ersten drei Beiträge konzentrieren sich auf die experimentelle Bestimmung von Schall- und Scherwellengeschwindigkeiten in Mantelphasen mit Hilfe von Ultraschallinterferometrie, inelastischer Kernstreuung und Brillouin-Spektroskopie in Vielstempel- oder Diamantstempel-Pressen. Der erste Artikel stellt Geschwindigkeitsmessungen von seismischen Wellen in Granat vor, einer der Hauptphasen zwischen unterer Erdkruste und der Übergangszone zwischen oberem und unterem Erdmantel. Da Granat im Erdinneren Majorit-Pyrop-Mischkristalle bildet, soll geklärt werden, wie ihre Zusammensetzung die elastischen Eigenschaften dieser Mantelphase beeinflusst. Der zweite Beitrag thematisiert Ferroperiklas und die potentiellen Auswirkungen von Spinübergängen auf die elastischen Eigenschaften dieses eisenführenden Minerals als Phase des unteren Erdmantels. Ein dritter Beitrag widmet sich dem Einfluss eines Glas/Glas-Übergangs in  $\text{TiO}_2$  auf die Schallwellengeschwindigkeiten.

Die Kompressibilität ist eine weitere fundamentale Eigenschaft, die im Zusammenhang mit der Interpretation seismischer Daten benötigt wird. Das Kompressionsvermögen von Ringwoodit und die Auswirkung eines Mg-Fe-Austauschs auf den Kompressionsmodul wurden in zwei Röntgenbeugungsstudien untersucht. Derartige Untersuchungen sind besonders für Planeten wie dem Mars mit Fe-reicherem Mantel und ausgedehnter Übergangszone von Bedeutung. Die Ergebnisse der Röntgenanalysen zeigen, dass der Fe-

Einbau in die Ringwooditstruktur den Kompressionsmodul nicht signifikant beeinflusst und dass das Sauerstoff-Teilgitter der begrenzende Faktor für die Komprimierbarkeit ist.

Themenbereiche des dritten Teils dieses Kapitels sind thermisches Diffusionsvermögen und thermische Leitfähigkeit sowie magnetische Eigenschaften. Diffusionsvermögen und Leitfähigkeit sind Kenngrößen, die für die modellhafte Darstellung von Temperaturzustand und Temperaturprofil des Erdinneren benötigt werden. Experimentelle Bestimmungen dieser Eigenschaften an Phasen des unteren Erdmantels gelten wegen des sehr kleinen Probenvolumens als äußerst anspruchsvoll. Es werden hier zwei Methoden vorgestellt, mit der sich die geschilderten Schwierigkeiten umgehen lassen: Durchführung der Experimente bei geringerem Druck mit Analogmaterial ( $\text{CaGeO}_3$ -Perowskit) und Simulationen durch Molekulardynamik. Der abschließende Beitrag dieses Kapitels veranschaulicht, dass die Anisotropie der Hämatit-Kristallstruktur seine magnetischen Eigenschaften kontrolliert. Daher weisen metamorphe Gesteine mit einer ausgeprägten Textur möglicherweise eine starke Ausrichtungs- bzw. Lagenabhängigkeit ihrer magnetischen Eigenschaften auf.

### *3.5 Fluide und ihre Wechselwirkung mit Schmelzen und Mineralen*

Wässrige Fluide spielen eine große Rolle beim chemischen Transport und der Energieübertragung im Erdinneren. Stofftransport durch Fluide äußert sich in charakteristischen Anreicherungsmustern von Spurenelementen in metamorphen Gesteinen aus Subduktionszonen und in den Magmen von Inselbögen. Die Bildung von Adern in metamorphen Gesteinen, Kontakt-Metasomatose und die Alteration des Nebengesteins bei der Bildung von Erzlagerstätten sind ebenso das Resultat von Fluid-Transport wie mikroskopische Auflösungs- und Ausfällungs-Phänomene in Gesteinen.

Die Struktur und thermodynamische Eigenschaften von Fluiden sind bei hohem Druck und hoher Temperatur generell nicht gut bekannt. Zwei Beiträge in diesem Abschnitt des Jahresberichtes beschäftigen sich mit diesem Problem. Im ersten Beitrag wird eine neue Zustandsgleichung für gelöste Spezies in wässrigen Fluiden entwickelt. Die Löslichkeiten von Mineralen, die von dieser Zustandsgleichung vorhergesagt werden, korrelieren mit der Speziation im Fluid: Während die Löslichkeiten neutraler Spezies nur mit der Dichte des Fluids nur schwach ansteigt, ist diese Zunahme der Löslichkeit mit der Dichte sehr viel stärker ausgeprägt für Minerale, die in Form von Ionen oder Ionenpaaren gelöst werden. Eine andere interessante Vorhersage dieses Modells ist, dass bei konstantem Druck die Löslichkeiten von vielen Mineralen mit der Temperatur erst ansteigen, dann aber wieder abfallen. Die Beziehung zwischen Löslichkeit und Speziation wird in einem zweiten Beitrag weiter untersucht. Messungen der Raman-Spektren wässriger Fluide im Gleichgewicht mit Korund zeigen, dass der Lösungsmechanismus von Aluminium fundamental verschieden ist vom Lösungsverhalten von Silizium. Während Kieselsäure vorwiegend als  $\text{Si(OH)}_4$  gelöst wird, liegt Aluminium bei hohen Temperaturen vorwiegend in polymerisierter Form vor. Diese Tendenz von Aluminium, Polymerisationsreaktionen in der Lösung zu begünstigen, könnte wichtig sein für die Mobilisierung von „high field strength“-Elementen sowie für den Beginn von kritischem Verhalten in Silikat-Wasser-Systemen.

Wässrige Fluide in vulkanischen und subvulkanischen Systemen sind verantwortlich für die Bildung hydrothermaler Erzlagerstätten, für die globale Abkühlung des Klimas nach explosiven Vulkaneruptionen und möglicherweise auch für die Zerstörung von Ozon in der Stratosphäre nach solchen Ereignissen. Neue Daten in einem Beitrag in diesem Abschnitt des Jahresberichtes zeigen, dass Kupfer im Gleichgewicht mit einer Salzlösung in der Gasphase stark angereichert werden kann, wobei Komplexe mit Schwefelwasserstoff wohl eine entscheidende Rolle spielen. Zwei kleine Forschungsprojekten wurden von einer Studentin während eines Praktikums im Rahmen der EU Marie Curie-Förderung durchgeführt. Die Resultate zeigen, dass HCl in erheblichem Umfang von vulkanischen Aschen in einer Eruptionssäule adsorbiert wird und dass Schwefel bevorzugt in eine wässrige Fluidphase extrahiert wird, selbst wenn diese im Gleichgewicht ist mit einer eisenhaltigen Silikatschmelze. Diese Daten sind nützlich zur Vorhersage der Auswirkung von Vulkaneruptionen auf das Klima.

Die Verwitterung von Sulfiden und insbesondere die Rolle von Mikroorganismen bei diesen Prozessen ist das Thema der beiden letzten Beiträge in diesem Abschnitt. Eine sehr interessante Beobachtung ist hier, dass *Acidithiobacillus ferrooxidans* die Verwitterung von Pyrrhotin nicht nur stark beschleunigt, sondern dieses Bakterium entwickelt auch ein sehr unterschiedliches Auflösungsvermögen für verschiedene Strukturtypen dieses Minerals.

### 3.6 Physik und Chemie von Schmelzen und Magmen

Im Verlauf der Erdgeschichte haben Schmelzprozesse und die Entstehung von Magmen eine wichtige Rolle in der Evolution des Planeten gespielt. Die Migration von Magmen sowie die nachfolgende Kristallisation stellen die Hauptprozesse dar, die zur Differenzierung des Erdkörpers, d.h. zu seinem Schalenaufbau geführt haben. Auf diese Weise trennte sich zum Beispiel eine deutlich anders zusammengesetzte Erdkruste vom Erdmantel ab. Auf der Erdoberfläche sind Vulkanausbrüche Folgen der Magmenentstehung in der Erdkruste oder im Mantel. Durch die vulkanischen Aktivitäten werden auch große Mengen an Gasen in die Atmosphäre freigesetzt, die die Klimaentwicklung stark beeinflussen.

Erzeugung, Migration und Verfestigung von Magmen in der Erde sind Prozesse, die von den physikalischen und chemischen Merkmalen der Schmelzen kontrolliert werden. Dazu zählen Transporteigenschaften wie Viskosität, chemische Diffusion und elektrische Leitfähigkeit als auch allgemeine physikalische Eigenschaften wie zum Beispiel die Dichte. Für ein umfassendes Verständnis magmatischer Prozesse im Erdinneren wird in Laborexperimenten und mit Hilfe computergestützter Berechnungen der Einfluss verschiedener Parameter wie Temperatur, Druck und Zusammensetzung auf die Schmelzeigenschaften untersucht. Über drei derartige Projekte wird hier berichtet.

Die Frühgeschichte der Erde war durch gewaltige Impakte anderer planetare Körper auf der Erde bestimmt. Diese hoch-energetischen Kollisionen führten zu einer großräumigen Aufschmelzung der frühen Erde; es bildeten sich ein oder mehrere „Magmaozeane“, Hunderte von Kilometern tief. Die Entstehung eines Magmaozeans wird stark durch die Dynamik von Konvektionsprozessen beeinflusst, die wiederum in erster Linie durch die Viskosität

kontrolliert wird. Auch experimentelle Viskositätsbestimmungen an Silikatschmelzen bei Drücken oberhalb von 12 GPa stellen eine große Herausforderung dar. Eine Alternative bieten computergestützte *ab initio*-Berechnungen. In dem ersten folgenden Beitrag werden Ergebnisse derartiger Viskositätsberechnungen an  $\text{Mg}_2\text{SiO}_4$ -Schmelzen bis zu Drücken von 35 GPa vorgestellt und Konsequenzen für einen tiefen Magmazoan diskutiert.

Bisher ist nicht im Detail verstanden, wie Magma auskristallisiert, da während eines Kristallisationsexperiments mit Schmelzen direkte Beobachtungen des Gefüges schwierig sind. Ein alternativer Ansatz wird im zweiten Beitrag beschrieben, bei dem für das Experiment Analogmaterialien verwendet wurden, die schon bei relativ niedrigen Temperaturen kristallisieren. Die Verwendung von Nitrat- und Chlorid-Salzen führte bei mäßig hohen Temperaturen (250-900 °C) zu sehr detaillierten Ergebnissen über die Gefügeentwicklung bei der Kristallisation. Derartige Studien machen Interpretationen des Gefüges magmatischer Gesteine hinsichtlich ihrer Kristallisationsgeschichte zuverlässiger.

Der abschließende Beitrag dieses Kapitels stellt Ergebnisse einer Untersuchung zur elektrischen Leitfähigkeit in Silikatschmelzen bei hohem Druck vor. Dadurch sollen Daten produziert werden, die mit Ergebnissen geophysikalischer Messungen kombiniert werden können, um den Zustand von Magmenkörpern im Untergrund vulkanischer Regionen zu überwachen. Letztendlich wären derartige Methoden bei der Prognose über die Art bevorstehender Vulkanausbrüche hilfreich.

### 3.7 Rheologie

Die Rheologie der Minerale und Gesteine im tiefen Erdinneren hat direkte Konsequenzen für eine Reihe von Prozessen, die sowohl die Entwicklungsgeschichte der Erde als auch ihren gegenwärtigen Zustand geprägt haben. Dynamische Vorgänge wie die Mantelkonvektion oder die Drift tektonischer Platten sind eine Funktion der Rheologie, die auch die chemische Durchmischung des Erdmantels und die mechanische Kopplung zwischen verschiedenen Bereichen des Erdinneren (z. B. zwischen Kern und Mantel) beeinflusst. Zwei Aspekte der Gesteinsdeformation sind von besonderem Interesse in den Erdwissenschaften: 1) das mechanische Verhalten des Gesteins (d.h. die Deformationsrate) auf eine angewandte Spannung, wie es in Fließgesetzen beschrieben wird und 2), die Veränderung des deformierten Materials im Bezug auf seine Mikrostruktur und seine physikalischen Eigenschaften (insbesondere deren Orientierungsabhängigkeit oder Anisotropie), die häufig durch größere Deformationsbeträge verursacht wird. Die physikalischen Anisotropien können oft durch geophysikalische Methoden detektiert werden, was dann wieder Rückschlüsse auf Deformationsvorgänge in unzugänglichen Regionen des tiefen Erdinneren zulässt. Ist dagegen Probenmaterial (natürlich oder experimentell erzeugtes) vorhanden, kann eine detaillierte Gefügeanalyse in Kombination mit der Messung oder Berechnung von physikalischen Gesteinseigenschaften erlauben, die Deformationsgeschichte zu rekonstruieren bzw. mögliche Gesteinsanisotropien zum Vergleich mit geophysikalischen Messungen bereitzustellen.

Da die derzeitige experimentelle Ausrüstung des Geoinstituts nicht dafür ausgelegt ist, quantitative Deformationsexperimente (z. B. zur Ableitung von Fließgesetzen) durchzuführen,

konzentrieren sich die Deformationsexperimente auf die Wirkung von Deformation unter hohem Druck auf die Mikrostrukturen (z. B. intrakristalline Gleitsysteme) und möglichen Anisotropien in Mineralen und Gesteinen des Erdmantels. So kann gezeigt werden, dass der druckabhängige Übergang von Gleitsystemen in Olivin das Vorhandensein unterschiedlicher seismischer Anisotropien im oberen Erdmantel sowie ihr Verschwinden mit größerer Tiefe erklären kann. Coesit ( $\text{SiO}_2$ ) und Lingunit ( $\text{KAlSi}_3\text{O}_8$ ) sind zwei Hochdruckminerale, die sich in felsischen oder  $\text{SiO}_2$ -reichen Gesteinen bilden, die während kontinentaler Plattenkollisionen in große Tiefen subduziert werden. Ihr Deformationsverhalten sowie ihre Fähigkeit, ihre Deformationsgefüge auf dem retrograden Metamorphosepfad an ihre Niedrigdruckpolymorphe weiterzugeben, sind wichtige Faktoren, wenn wir versuchen, p,T-Pfade von tief subduziertem kontinentalen Material zu verstehen und zu rekonstruieren.

Die Bestimmung der intrakristallinen Gleitsysteme in Hochdruckmineralen ist essentiell für das Verständnis des Materialverhaltens während des Versetzungskriechens, einem im Erdinneren vermutlich weit verbreitetem Deformationsmechanismus, der auch für die Bildung charakteristischer Gesteinsanisotropien verantwortlich ist. Nur Transmissionselektronenmikroskopie (TEM) ist in der Lage, solche Gleitsysteme direkt und eindeutig zu bestimmen, aber sie muss bei der Untersuchung von Hochdruckmineralen speziell angepasst werden, da diese sehr oft metastabil sind und sehr empfindlich auf Bestrahlung mit Elektronen reagieren.

Magnetische Anisotropien (insbesondere die Anisotropie der magnetischen Suszeptibilität, AMS) in deformierten Gesteinen ermöglichen oft eine gute Abschätzung des Deformationsbetrages und der Deformationsgeschichte. Allerdings ist eine detaillierte Gefügeanalyse der unterschiedlichen magnetischen Komponenten eines Gesteins nötig, um die teilweise komplexen Signale, die aus gesteinsmagnetischen Messungen gewonnen werden, korrekt zuzuordnen und quantitativ im Bezug auf den Deformationsbetrag hin zu interpretieren.

### *3.8 Metamorphose*

Im Verlauf der Metamorphose wird terrestrisches und planetares Material veränderten Druck- und Temperaturbedingungen ausgesetzt, wodurch sich die Mineralzusammensetzung der Gesteine verändern kann. Metamorphe Phasenaggregate sind häufig in Gesteinen des oberen Erdmantels und in Meteoriten erhalten, wodurch eine Untersuchung ihrer Entstehungsbedingungen ermöglicht wird.

Festkörperdiffusion ist ein wichtiger metamorpher Prozess, der die Rate der Mineralreaktionen mitsteuert. In der ersten Studie dieses Kapitels wurde die Diffusion der sogenannten Majoritkomponente im Granat untersucht. Diffusion ist eine der wichtigen Reaktionen, die im tieferen Bereich des oberen Mantels und in der Übergangszone in 410-660 km Tiefe abläuft. Es zeigte sich, dass die Diffusionskoeffizienten für Pyrop und Majorit-Granat ähnlich sind und dass Diffusion in Granat stark druckabhängig ist, was frühere Studien im BGI bestätigt. Eine weitere detaillierte Untersuchung befasst sich mit  $\text{Fe}^{3+}/\Sigma\text{Fe}$ -Verhältnissen in verschiedenen Mineralen eines metasomatisierten Mantelperidotits. Hier

wurde eine erhöhte Sauerstoff fugazität im Vergleich zu normalen Peridotiten in alten Festlandskernen der Kontinente bestätigt. Allerdings wurde auch gezeigt, dass die  $\text{Fe}^{3+}/\Sigma\text{Fe}$ -Verteilung zwischen verschiedenen Mineralen sehr komplex ist und durch verschiedene Faktoren beeinflusst wird.

Während die Metamorphose normalerweise in langen geologischen Zeiträumen über Millionen von Jahren abläuft, geschehen metamorphe Mineralreaktionen während des Einschlag eines planetaren Körpers, der eine Schockmetamorphose ausgelöst, in Sekunden. Die Freisetzung von  $\text{SO}_x$ -Gas bei einem gigantischen Impakt vor 65 Millionen Jahren wird als Hauptauslöser für eines der größten Aussterbeereignisse in der Erdgeschichte angesehen. Um diesen Prozess quantifizieren zu können, wurde Anhydrit ( $\text{CaSO}_4$ ) einer experimentellen Schockmetamorphose ausgesetzt. Es hat sich gezeigt, dass Anhydrit in Übereinstimmung mit thermodynamischen Modellierungen bei einem Schockdruck von 31-40 GPa in  $\text{CaO}$  und  $\text{SO}_3$  dissoziiert.

Weitere Studien befassen sich mit durch Schockmetamorphose geprägten Meteoriten. Diese Meteorite sind die einzigen natürlichen Proben, an denen Mineralreaktionen direkt untersucht werden können, die normalerweise in über 400 km Erdtiefe ablaufen. Ein interessantes Beispiel für die Wichtigkeit detaillierter petrographischer Untersuchungen ist eine Studie von Maskelynitglas in einem Marsmeteorit. Es wird bisher generell angenommen, dass Maskelynit direkt durch Festkörperamorphisierung von Feldspat beim Impakt entsteht, weshalb dieses Glas als Druckindikator genutzt werden kann. Die neue Studie ergab jedoch Hinweise auf Fließstrukturen in dem Glas, was auf einen Zwischenzustand in Form einer Schmelze hindeutet. Aus diesem Grund wird Maskelynit als zuverlässiger Druckindikator in Frage gestellt.

### *3.9 Materialwissenschaften*

Historisch betrachtet dienten Hochdruck-/Hochtemperaturexperimente zuerst überwiegend dazu, Prozesse, die im tiefen Erdinneren ablaufen, im Labor nachzustellen. Später setzten Physiker, Chemiker und Materialkundler diese von Geowissenschaftlern entwickelte Methodik ein, um das Verhalten unterschiedlichster Verbindungen bei extremen Bedingungen zu erforschen. Das Bayerische Geoinstitut, zu dessen Forschungszielen die apparative und methodische (Weiter-) Entwicklung auf dem Gebiet der experimentellen Hochdruckforschung zählt, befasst sich auch an vorderster Front mit Materialforschung unter extremen Bedingungen.

Bor gilt als eines der rätselhaftesten Elemente im Periodensystem; sogar die Struktur seines Grundzustandes ist bisher nicht vollkommen verstanden. In letzter Zeit gelang es, mit einer neu entwickelten Methode eine Hochdruck-/Hochtemperatur-Phase von Bor ( $\text{B}_{28}$ ) herzustellen, die eine Reihe von nützlichen Eigenschaften kombiniert: Sie ist superhart, halbleitend und optisch transparent. Derart erzeugte Einkristalle der  $\text{B}_{28}$ -Phase ermöglichen detaillierte Ramanspektroskopie-Messungen sowie die Zuordnung von Schwingungsmodi und erlauben, das Verhalten von Bor bei hohen Drücken zu untersuchen.

Titanoxide finden aufgrund ihrer potentiellen technischen Bedeutung für Wasserstoffbrennstoffzellen und anderer elektrochemischer Anwendungsmöglichkeiten Beachtung. Die Synthese einer neuen dichten, halbleitenden  $Ti_2O_3$ -Phase mit geringer Kompressibilität und mit einer Struktur vom  $Th_2S_3$ -Typ stellt einen großen Fortschritt in der Kristallchemie von Übergangsmetall-Sesquioxiden dar.

Seltene Erden-Manganit weist zahlreiche physikalischen Eigenschaften auf, die von der chemischen Zusammensetzung beeinflusst werden. Verbindungen mit größeren Lanthaniden kristallisieren in einer orthorhombischen Struktur; dagegen zeigt Manganit mit Seltene Erden-Elementen mit kleineren Ionenradien eine hexagonale Struktur. Hexagonaler Manganit gehört einer ungewöhnlichen Klasse multiferroischer Materialien an, bei denen ferroelektrisches Verhalten und eine magnetische Ordnung koexistieren. Neue Experimente mit  $YMnO_3$  ergeben, dass der Übergang von der hexagonalen zur orthorhombischen Struktur Druckbeeinflusst ist.

Die Anwendung von hohen Drücken ermöglicht nicht nur Synthesen neuer Verbindungen und Phasen; sie erlaubt auch drastische Veränderungen der Eigenschaften bei bekannten Stoffen. Ein bedeutendes Ziel in der Technologie optischer Gläser liegt darin, Materialien mit einem hohen Brechungsindex unter Beibehaltung einer geringen Lichtstreuung zu entwickeln. Mit am Markt käuflichen Gläsern von SCHOTT konnte experimentell gezeigt werden, dass Hochdruck-Tempern einen deutlichen Anstieg im Brechungsindex bei unveränderter Streuung bewirkt. Die Behandlung bei hohem Druck ermöglicht somit Zugang zu bestimmten Glaseigenschaften, die anders kaum erreichbar sind.

### *3.10 Methodische Entwicklungen*

Die Forschung in den Geowissenschaften, insbesondere die Hochdruck- und Hochtemperaturforschung, hat in der vergangenen Dekade wegen der Verfügbarkeit zunehmend hochentwickelterer Werkzeuge und Apparaturen zur Untersuchung von Materialeigenschaften unter extremen Druck- und Temperaturbedingungen einen drastischen Wandel erfahren. Das Leistungsspektrum von Großforschungseinrichtungen, wie zum Beispiel von modernen Synchrotronanlagen und Neutronenquellen, eröffnet neuartige Experimente bei hohen Drücken. Das Bayerische Geoinstitut ist in eine Reihe dieser neuen Entwicklungen eng eingebunden. Über viele Jahre hinweg stellte die Aufheizung von Materie mit Lasern die beste Methode dar, um in einer Diamantstempelzelle (DAC) Temperaturen wie im Erdmantel bei gleichzeitig hohen Drücken zu erzielen; jedoch hat die Unbeweglichkeit des Versuchsaufbaus die Einsatzmöglichkeiten begrenzt. Hier wird nun ein neu entwickeltes tragbares System vorgestellt und erste Ergebnisse von Röntgenabsorptionsspektren bei Drücken und Temperaturen des Erdmantels präsentiert. Eine weitere Innovation für Synchrotronmessungen stellt die Entwicklung einer Energie-aufgelösten Synchrotron-Mössbauer-Spektroskopie dar. Diese Methode wird die erforderliche Energieauflösung liefern, um vielphasige Mineralvergesellschaftungen des Erdmantels zu untersuchen und in Kombination mit hoher Intensität eine Datenerfassung bei Drücken im Megabar-Bereich ermöglichen. Weiterhin werden erste Hochdruck-Neutronenbeugungsexperimente in Diamantzellen am Forschungsreaktor München II beschrieben.

Das Bayerische Geoinstitut führt die Weiterentwicklung der institutsinternen Ausstattung erfolgreich fort. Zu den neu installierten Apparaturen zählt eine Großpresse vom Typ „Multianvil“ mit sechs individuell steuerbaren hydraulischen Stempeln, die neuartige Verformungsexperimente ermöglicht. Mit Hilfe von Stempeln aus gesintertem Diamant soll diese Presse außerdem Experimente bei Drücken bis zu 50 GPa ermöglichen. Ein anderer, neuer Versuchsaufbau besteht aus der Kombination von Brillouinspektroskopie und hochauflösender Röntgenbeugung. Dieses System ermöglicht gleichzeitige Bestimmung von Struktur und elastischen Eigenschaften und soll dazu dienen, eine absolute Druckskala festzulegen sowie einen deutlich besseren Lösungsansatz zur Interpretation seismischer Daten zu liefern.

Verbesserte Bauteile für die Verformungspresse vom D-DIA-Typ ermöglichen die Überwindung bisheriger experimenteller Grenzen; sie ermöglichen einfache Scherexperimente bis in Druckbereiche, die im unteren Teil des oberen Erdmantels herrschen. Eine neu eingeführte Methode der Probenvorbereitung erlaubt eine detaillierte Betrachtung von Mineralreaktionen an Mineraloberflächen im Profil. Schließlich wird ein neuer Ansatz für die Modellierung von Grenzflächen in geodynamischen Prozessen vorgestellt.

### 3.1 Earth's Structure and Geodynamics

Dynamic processes constantly reshape the Earth's crust, mantle and core. Constraining the complementary histories of these main Earth envelopes requires combining surface observations and geodynamic considerations, together with a good knowledge of the Earth's material properties and thermodynamics at high pressure and temperature. This is the approach adopted by the contributions to this chapter.

The opening contribution focuses on determining the effect of water on electrical conductivity of natural clinopyroxene, a major mineralogical component of the Earth's lower continental crust. The first results indicate that the presence of H and Fe in the crust would yield high electric conductivity, which could provide an explanation the magneto-telluric data collected in continental regions.

Mantle xenoliths of the Carpathian-Pannonian region are a window into the Earth's lithospheric structure and evolution. Combining petrographic and geochemical analysis on these unique xenoliths, the next two contributions present an improved alternative model to explain the origin and evolution of the lower crust beneath this region of central Europe.

Although geochemical observations indicate the presence of recycled sediments in Oceanic Island Basalts, the amount of sediments that can be transported into a subduction zone remains poorly constrained. The fourth contribution to this chapter aims to address this important question using a litho-chemical model for an oceanic subducting plate, where the mineralogical changes as a function of pressure and temperature can be investigated.

The Earth's mantle's dynamic evolution is the result of various couplings between mineralogy, temperature and pressure, which are often simplified in geodynamic models. In order to study the effect of self-consistent coupling between mantle flow and mineral physics one contribution considers 2D convection simulations with various degrees of coupling between mantle mineralogy and thermodynamics, with a specific focus on the Earth's mantle transition zone bounded by phase changes.

Water can have a predominant influence on the physical properties and on the rheology of mantle silicates. The knowledge of water storage capacity in planetary mantles is therefore key to understanding the evolution of terrestrial planets. One contribution to this chapter aims at addressing this question for Martian-like mantle compositions by the means of multianvil experiments. The results suggest that the water storage capacity of a Martian mantle could be substantially large.

Understanding the dynamical mechanisms that took place during the early stages of terrestrial planets is necessary to constrain their subsequent long-term evolution. Mars- or Earth-sized

planets are likely to have experienced at least one magma ocean stage during which iron and silicates segregate into a core and a mantle. One contribution focuses on this early major differentiation event by investigating the conditions for the fragmentation of iron diapirs sinking through a terrestrial magma ocean.

While the main component in the Earth's inner core is undoubtedly iron, the nature of minor phases remains debated. The last contribution considers  $\text{Fe}_7\text{C}_3$  as a potential inner core phase. In order to assess this possibility, electronic structure calculations are used to determine the full elastic constant tensor of  $\text{Fe}_7\text{C}_3$  at high pressure. The resulting computed density and seismic velocities compared with PREM profiles indicate that  $\text{Fe}_7\text{C}_3$  could be a potential minor phase in the Earth's inner core.

**a. *Electrical conductivity of the lower continental crust (X.-Z. Yang, H. Keppler, and H. Ni)***

The lower crust of continental regions, as the interface between the continental crust and upper mantle, is of critical importance in the tectonic evolution of the continents. Knowledge of the composition, evolution, structure and dynamics of this area plays a fundamental role in understanding the geochemical and dynamic models of the whole crust, the continents and the bulk Earth.

Magneto-telluric deep sounding around the world demonstrated that the lower crust is characterized by relatively high electrical conductivity, usually in the range of  $10^{-4}$  to  $10^{-2}$  S/m, which are typically 100-1000 times more conductive than dry rocks measured in the laboratory, and 10-100 times more conductive than the middle to upper crust. Despite great efforts devoted in the past two decades, finding a mechanism for this increased conductivity remained elusive. Many explanations, such as inter-connected free fluids, graphite films and melts, have been proposed. However, they can only be applied regionally and critical limitations are involved with each of them.

The presence of H in minerals (or more commonly water), even in small amounts, can largely enhance their electrical conductivity. The lower crust consists mainly of granulite phases (*e.g.*, pyroxenes, feldspar and garnet) and they generally contain trace amounts of H as reported for xenoliths, which have usually been neglected in previous studies. We measured the electrical conductivity of a natural clinopyroxene of lower crustal composition by impedance spectroscopy over the frequency range of  $10^{-2}$  to  $10^6$  Hz, at 15 kbar and 300-1200 °C, and fitted the impedance semi-circle arc of the high frequency branch for resistivity. The preliminary data indicate that high Fe and H in lower crustal clinopyroxene can result in high electrical conductivity, similar to those determined by geophysical methods (Fig. 3.1-1).

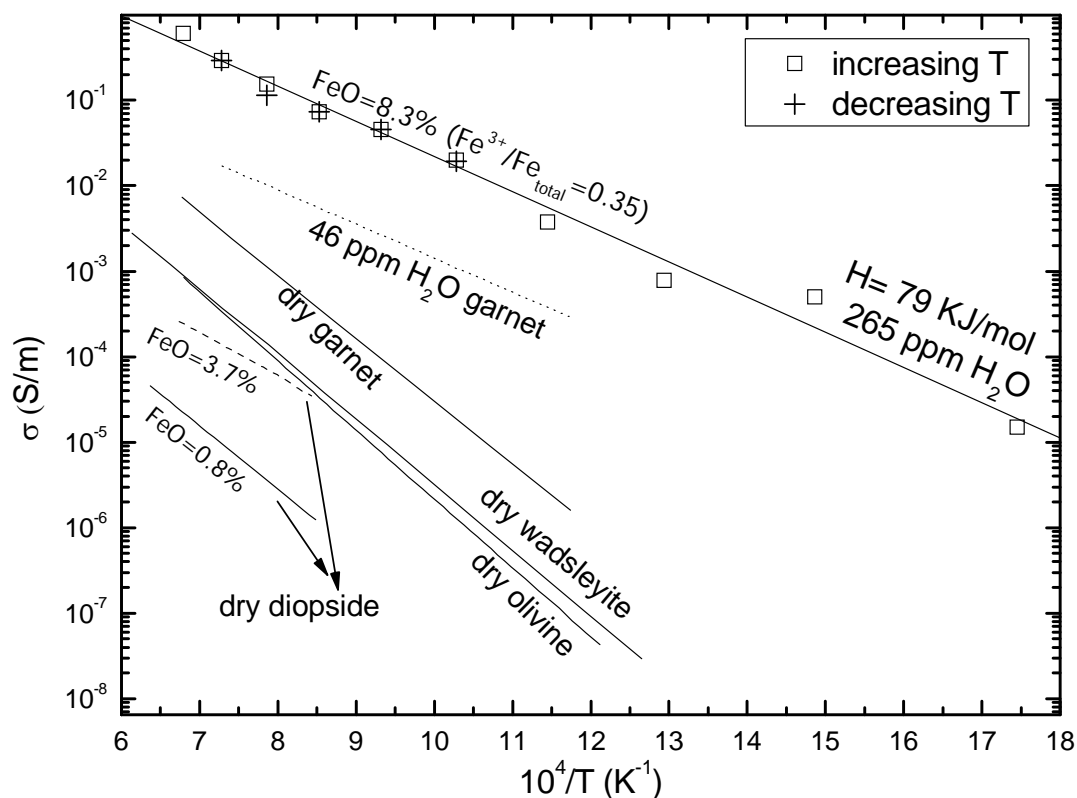


Fig. 3.1-1: Electrical conductivity of a natural clinopyroxene of lower crustal composition including H. Conductivity of other minerals reported in the literature are included for comparison.

**b. An alternative model for the origin of metaigneous lower crust beneath the Pannonian basin (E. Bali, in collaboration with J. Degi, K. Török, and C. Szabo/Budapest)**

The Pannonian basin (Central Europe) is a unique place in Europe where xenoliths from both the upper mantle and the lower crust occur in alkaline mafic magmas of different ages (from Cretaceous to Pliocene). This provides us with a possibility to study the evolution of the deep lithosphere both in time and space. There are only few areas on Earth where time evolution of the deep lithosphere can be studied from mantle xenoliths (*e.g.*, East China, South Africa or Siberia), and all of these areas provide information on the early history of the lithosphere. By contrast, the xenolith suite of the Carpathian-Pannonian area records more recent processes. For the current study we selected garnet pyroxenites of crustal origin from the Neogene alkaline basaltic volcanites of the Bakony-Balaton Highland Volcanic Field, Hungary. We carried out a detailed petrographic and geochemical study on these rocks. We integrated the new study with available data on garnet-bearing and garnet-free metaigneous granulites and we developed a new model for the origin and evolution of lower crust beneath the region. In our view this model improves the explanation of the texture as well as major and trace element geochemical characteristics of these rocks over previous models.

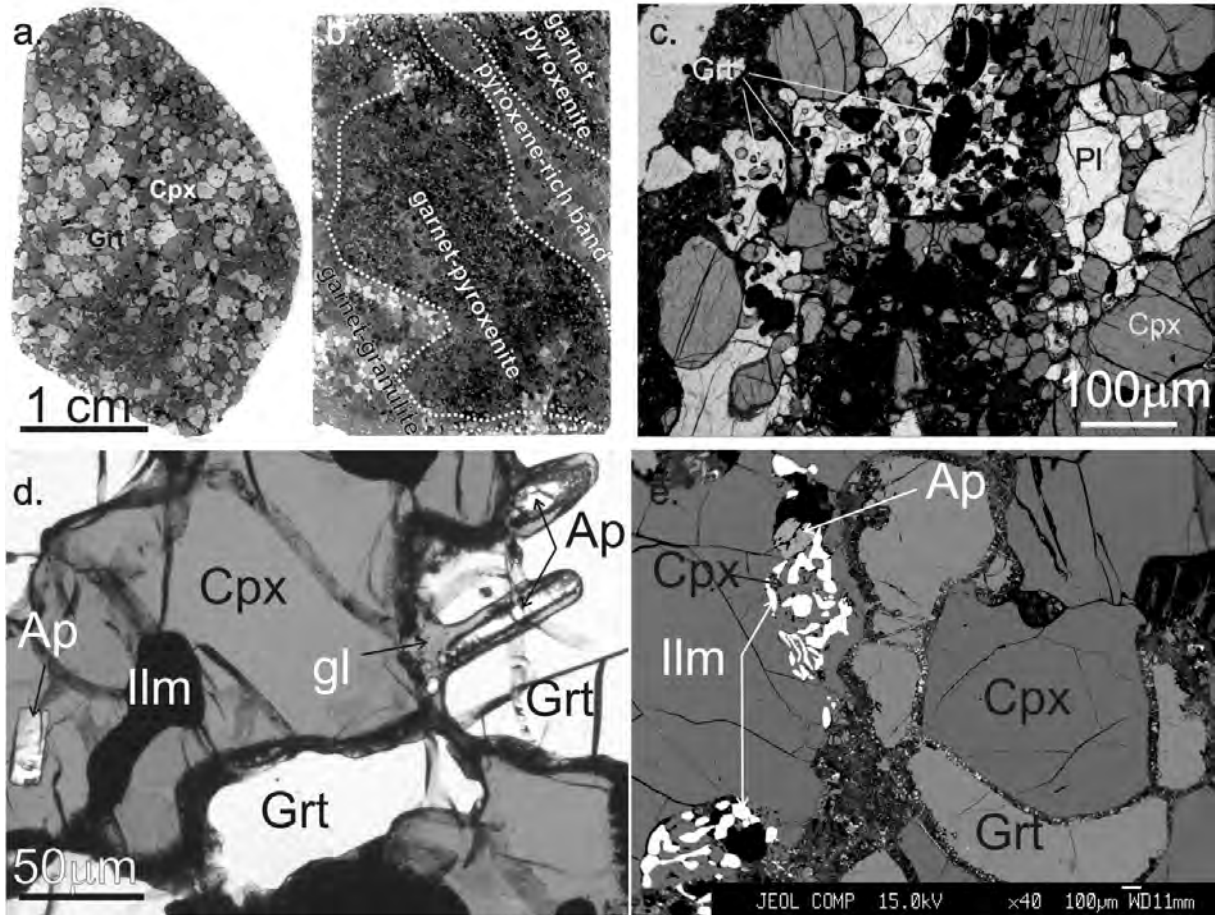


Fig. 3.1-2: Textural features of garnet pyroxenites. a-b: Scanned thin section of a single garnet pyroxenite and a banded garnet pyroxenite xenolith. c: Photomicrograph of fine grained clinopyroxene-garnet-plagioclase aggregate in coarse grained garnet pyroxenite. d: Photomicrograph of apatite and vermicular ilmenite inclusion in clinopyroxene. e: Back-scattered electron image of vermicular intergrowth of ilmenite and clinopyroxene mimicking former titanite. Labels: Grt-garnet, Cpx-clinopyroxene, Pl-plagioclase, Ap-apatite, Ilm-ilmenite, Gl-silicate glass.

The garnet pyroxenites studied have granoblastic microstructure (Fig. 3.1-2 a, d, e). They occur as single xenoliths (Fig. 3.1-2 a) or as lenses in banded granulites (Fig. 3.1-2 b). They are dominantly built up by coarse grained (up to 6 mm) clinopyroxene (cpx) and garnet (grt). Accessory apatite and spinel are common as inclusions in the silicate phases (Fig. 3.1-2 c). Amphibole (amp) is present in rock-forming amounts only in one pyroxenite; in the other xenoliths it occasionally occurs as inclusion in cpx and grt. Vermicular ilmenite is also common in all xenoliths (Fig. 3.1-2 d), occasionally showing intergrowths with cpx mimicking former titanite (tit) shape (Fig. 3.1-2 e). Small pockets of finer grained plagioclase (plag)-cpx-grt intergrowths might also be present in the coarse grained assemblage (Fig. 3.1-2 b). These features resemble former melt pockets.

As the rocks have metamorphic texture, they cannot be considered direct cumulates. The presence of completely crystallized melt pockets suggest that the protolith should have undergone (at least one significant) partial melting (event), producing cpx and grt. In most cases, the felsic melt has left the system leaving behind cpx+grt. The presence of amp inclusions in silicate porphyroblasts indicate that amp might have been a more common phase in these rocks prior to partial melting. Thus we suggest that these garnet pyroxenites ultimately formed by the partial melting of an originally amp- and plag-rich assemblage (cpx60-40%+amp21-31%+plag19-29%) by the following melting reaction due to temperature increase above 850 °C at pressures > 11 kbar:



Based on the modal composition and the chemical composition of the mineral assemblage we calculated the trace element compositions (Fig. 3.1-3). Similar to the granulites, the bulk Rare Earth Element (REE) composition of garnet pyroxenites (Fig. 3.1-3 a) shows a pattern very similar to that of Mid Oceanic Ridge Basalts (MORB). This MORB-like trace element pattern and the peculiar low  $\delta\text{O}^{18}$  composition led to the suggestion that lower crustal granulites represent former mid-oceanic ridge basalt or gabbro sheared into the lower crust during a subduction event. All xenolith compositions are strongly enriched in Ca relative to Al

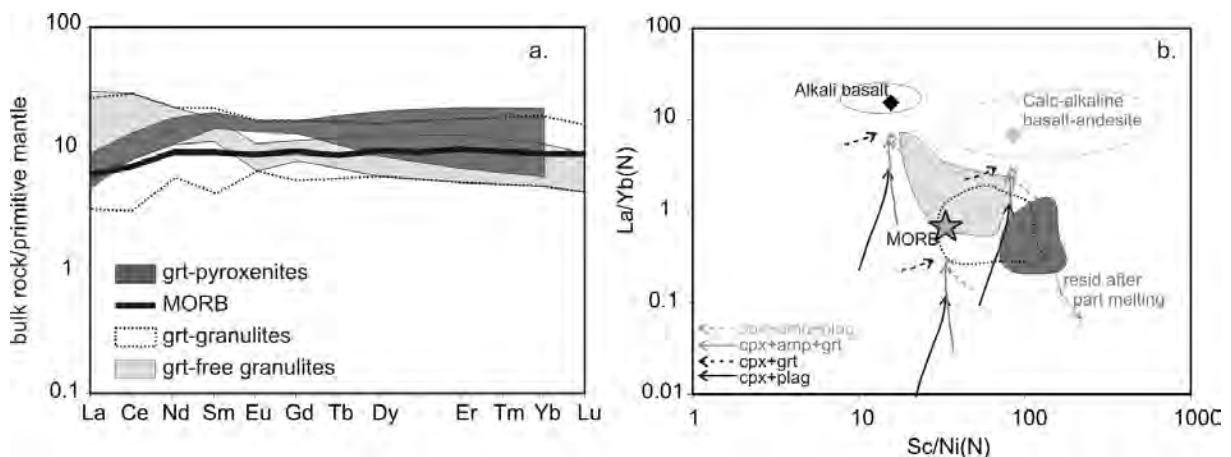


Fig. 3.1-3: Major and trace element composition of garnet pyroxenites compared to garnet-bearing and garnet-free granulites from the same locality. a: Primitive mantle normalized REE-patterns of garnet pyroxenites, garnet-bearing, garnet-free granulites and average Mid-Oceanic Ridge Basalt (MORB). b: REE vs compatible element (Sc/Ni) modeling of fractional crystallization and subsequent partial melting of variable mineral assemblages of alkali basalts, calc-alkaline andesite and MORB origin. Residual compositions after partial melting were calculated by 1 to 50 % batch partial melting of a cpx+plag+amp assemblage crystallized from calc-alkaline andesite. Mineral name abbreviations are as in Fig. 3.1-2. Granulite compositions are from Kempton, Downes, Embey-Isztin *J Pet*, 38, 941-970, 1997; and Embey-Isztin, Downes, Kempton, Dobosi, Thirlwall, *CMP*, 144, 652-670, 2003.

compared to the array drawn by peridotites and different mafic and felsic magmas (not shown), indicating that they represent either crystal cumulates or having gone through partial melting after the protolith had crystallized. Thus, the bulk trace element composition of these rocks should not be compared directly to any primary melt composition. Figure 3.1-3 b shows that the bulk composition of neither the garnet pyroxenites nor mafic granulites can be reproduced by the segregation of gabbro (cpx+plag) from MORB or alkali basaltic source. Most of the compositions can be modeled as being crystallized as garnet amphibolites from alkaline or calc-alkaline melts, or alternatively crystallized as plag-bearing amphibolite that has gone through subsequent partial melting to produce a grt-bearing assemblage (Fig. 3.1-3 b).

Based on incompatible elements, such as REE, it is very difficult to draw conclusions on the protolith of a metamorphic rock that has potentially gone through partial melting or metasomatism, because the abundance of these elements is very sensitive for the processes mentioned above. Figure 3.1-3 d demonstrates how the Sc/Ni ratio in the cumulate phase changes due to variable degree of crystal fractionation and partial melting. According to our calculation, fractional crystallization and/or subsequent partial melting can account for a change in Sc/Ni ratios by a factor of 5 (depending on the degree of fractionation, and subsequent partial melting) compared to the source melt. This means that the studied mafic granulite and grt-pyroxenite series cannot be originated from a single source as there is more than an order of magnitude difference in their Sc/Ni ratios (Fig. 3.1-3 b). Thus we suggest that the protolith of the current mafic lower crust was heterogeneous. It has formed by the crystallization of mafic melts of both alkaline and calc-alkaline affinity. This heterogeneous lower crust should have undergone at least one significant partial melting event that produced the current granulitic and pyroxenitic assemblage.

**c.** *What do garnet pyroxenites represent in the lithospheric mantle of the Pannonian basin? (E. Bali, in collaboration with J. Degi, K. Török, and C. Szabo/Budapest)*

In recent years garnet pyroxenites have been at the focus of attention after their role in the genesis of ocean island basalts (OIBs) has been discussed in the literature. Although there is debate on their petrogenetic importance for OIBs there is no doubt that they comprise a significant volume of the upper mantle. Based on our current knowledge most pyroxenites can be regarded as crystal segregates of silicate liquids precipitating in cracks of the upper mantle at variable PT conditions. In general, the most important questions to be answered are: 1) were the pyroxenites or their wall rock significantly modified after segregation; 2) what is source of these precipitating liquids; 3) can they be directly linked to geodynamic processes?

Three xenoliths were selected for this study. Two of them are single xenoliths, one of them is a vein in a spinel peridotite wall-rock (Fig. 3.1-4 a). They have granoblastic (Fig. 3.1-4 a) and granoblastic-equigranular microstructure and are mainly composed of large (up to 10 mm)

clinopyroxenes (cpx) and garnets (grt). Grt is always surrounded by a thick kelyphitic rim (Fig. 3.1-4 a). Based on their major element compositions all three xenoliths can originate from the upper mantle. The pyroxenite vein (AT01, in Fig. 3.1-5) and one of the single xenoliths (Szb42) show an extremely high equilibrium temperature (~ 1250 or ~ 1100 °C, depending on the applied thermometer), whereas the third one was equilibrated at lower temperature (by ~ 150 °C).

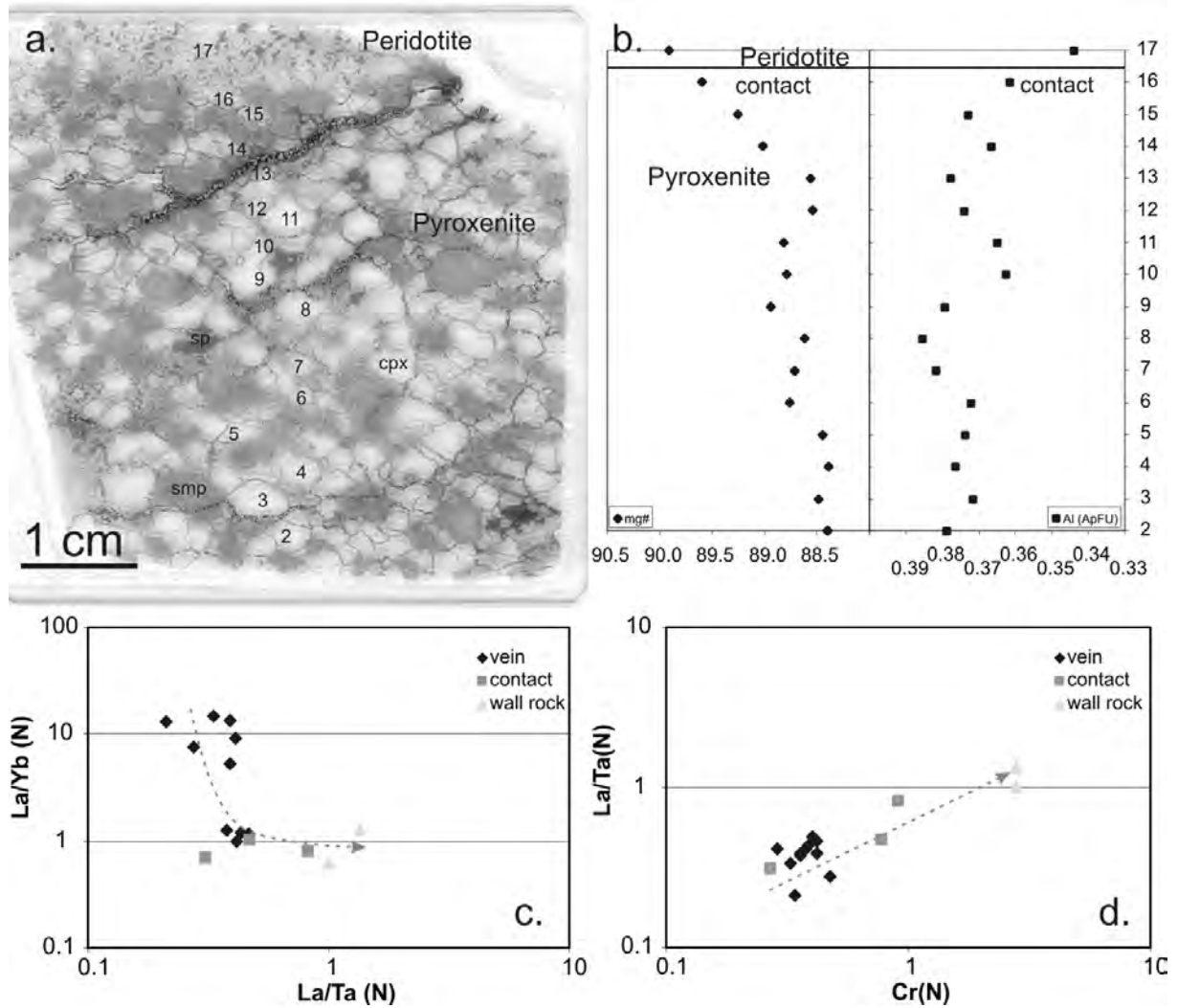


Fig. 3.1-4: Spatial variation of major and trace elements inside a garnet pyroxenite vein. (a) Scanned thin section of the garnet pyroxenite vein. Numbers indicate the analyzed minerals in panel b. cpx-clinopyroxene, smp-fine grained symplectite formed by the break-down of former garnet, sp-spinel. (b) Spatial variation of mg-number and Al-content in clinopyroxenes of the garnet pyroxenite vein of panel (a). (c-d) Spatial variation of trace element abundance in clinopyroxenes. Arrows show the general change from the center of the vein towards the peridotite wall rock.

It has been observed that the peridotitic wall-rock around clinopyroxenite veins might be strongly modified by diffusion-controlled processes, with the veins acting as a source of

major and trace elements for depleted peridotite. For the pyroxenite vein investigated here we found that the vein was also significantly modified after its precipitation. Figure 3.1-4 b shows how the Mg- and Al-contents of cpxs change from the central part of the vein (bottom) towards the peridotite wall-rock (top). Al- and Mg-content are relatively constant only between points 2 to 5, in the central part of the vein. From point 13 to 17 (last one in the peridotite) the Mg# steadily increases and a significant decrease in Al-content can be observed. A similar systematic change can be observed in the trace element composition of cpxs (Fig. 3.1-4 c, d).

Although we used trace element compositions analyzed from the central part of the vein to determine the bulk rock composition, our attempt to identify the parental melt of this vein failed. The equilibrium melt compositions calculated cannot be matched with the trace element abundance of any well known terrestrial melt (Fig. 3.1-5 a). The high concentrations of incompatible elements in these hypothetical melts (Rb to Nb in Fig. 3.1-5) reveals that that the parental melt is inconsistent with MORB, the high Nb-content suggest that the melt can not have been contaminated by slab derived components that are expected to show low Nb-content. Due to the diffusive loss of REE, however, a better constraint cannot be given based on trace element data. For the single xenolith (Szb42) showing similar high equilibrium temperature the same conclusions can be drawn (Fig. 3.1-5 a).

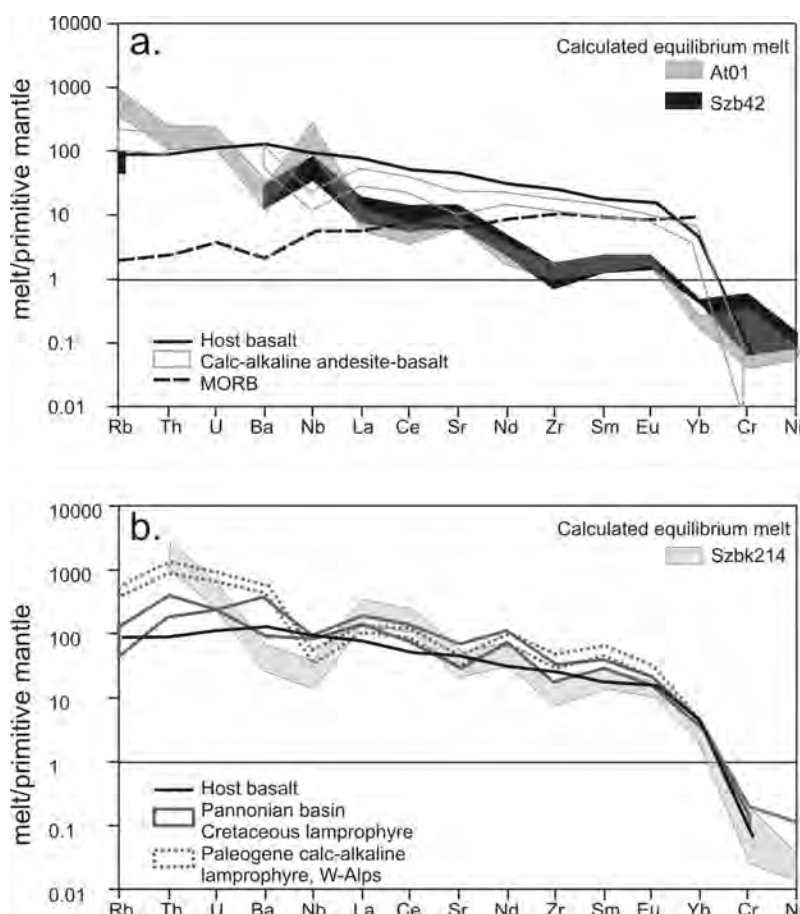


Fig. 3.1-5: Trace element composition of silicate melts in equilibrium with the studied garnet pyroxenites. (a) The trace element abundance of hypothetical silicate melts in equilibrium with high-temperature garnet pyroxenites AT01 and Szb42. (b) The trace element abundance of hypothetical silicate melts in equilibrium with the low-temperature garnet pyroxenite Szbk214.

By contrast, the calculated equilibrium melt composition for the low-temperature xenolith (Szbk214) agrees well with Cretaceous and Paleogene lamprophyres studied in the Pannonian basin and the Western Alps (Fig. 3.1-5 b). This means that precipitation/equilibration at reduced temperature protected this rock from significant diffusive loss of most trace elements. Considering that lamprophyric rocks younger than Paleogene are not known in Europe, this rock might have been preserved relatively unmodified in the mantle for tens of million years before Pliocene magmatism brought it to the surface. Furthermore, it might be another essential piece of mantle rock that confirms the recent geodynamic model for the Alpine-Carpathian-Pannonian area that states that the Paleogene to Miocene extrusion of the Northern tectonic unit of the Pannonian basin should have occurred at a lithospheric scale.

**d. Resolving sediment subduction (Z. Chemia, G. Steinle-Neumann, D. Dolejš/Prague, and S. Buiter/Trondheim)**

Geochemical tracers demonstrate that elements of subducted crust are recycled in oceanic island basalt (OIB). In addition it was stressed recently that recycling of basalt alone is not sufficient to reproduce the isotopic signature of oceanic rocks (mantle array). Studies of OIB hafnium (Hf) and neodymium (Nd) isotopic compositions show that oceanic basalt and depleted mantle peridotite need to be mixed with sediments to produce Hf-Nd isotopic compositions compatible with the mantle array. In addition, several studies have suggested sediment melting as a requirement for efficient transfer of the critical elements (Th and Be) to arc volcanism. However, experimentally determined sediment solidi ( $> 750\text{ }^{\circ}\text{C}$ ) are  $\sim 100\text{ }^{\circ}\text{C}$  higher than temperatures at the top of the slab in thermal models of subduction zones. This observation places important constraints on subduction models.

Few numerical studies have addressed the problem of subducting sediments, perhaps because of the numerical difficulties associated with large scale modeling of very detailed features. However, a “realistic” model of subducting crust should contain a layer of sediments, about 500-700 m thick on average, but highly variable with increasing crustal age. Sediments may play an important role in phenomena such as decoupling between the plates, metamorphism, subduction dynamics, and the geothermal gradient in the forearc.

We aim to quantify the amount of sediment that can be transported into a subduction zone and estimate the maximum depth to which sediments can be subducted. As a first step, we developed a litho-chemical model for the oceanic subducting plate and investigated the mineralogical changes as a function of pressure and temperature. The litho-chemical model of the subducting lithosphere consists of a relatively thin (1 km) layer of global oceanic subducting sediment (GLOSS), 7 km of oceanic basalt supercomposite (OBSC) and 50 km of serpentinized harzburgite (SHB) (Table 3.1-1).

Table 3.1-1: Model rock composition (wt.%)

	SiO <sub>2</sub>	TiO <sub>2</sub>	Al <sub>2</sub> O <sub>3</sub>	FeO	MgO	CaO	Na <sub>2</sub> O	K <sub>2</sub> O	H <sub>2</sub> O	CO <sub>2</sub>
GLOSS	58.57	0.62	11.91	5.21	2.48	5.95	2.43	2.04	7.68	3.01
OBSC	47.32	0.63	16.11	7.21	9.27	12.17	1.65	47.32	2.68	2.95
SHB	44.01	0.08	1.20	8.22	45.38	1.11			6.8	

Phase diagrams of metamorphic facies provide a useful framework to discuss the evolution of subducting oceanic crust. Thus, incorporating phase equilibria computed from thermodynamic data in geodynamic modeling can account for new types of behaviour induced by phase transformations (Fig. 3.1-6). However, full coupling between the geodynamic and thermodynamic models requires calculating a large number of parameters and is highly inefficient for large dimensional problems. A pragmatic alternative, which we use, is to calculate phase relations over the range of pressure-temperature conditions of interest. We use numerical interpolation to generate tables of any thermodynamic property as a function of any state variables.

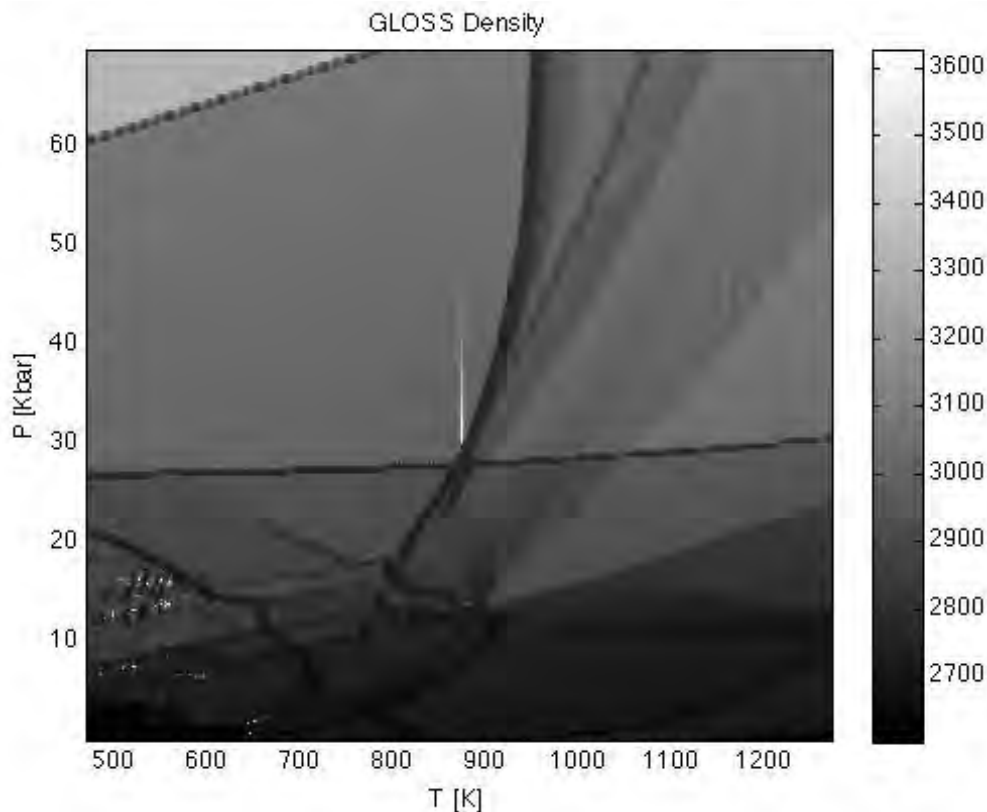


Fig. 3.1-6: Computed sediment density ( $\text{g}/\text{cm}^3$ ) as a function of pressure and temperature. Calculations are carried by free energy minimization from thermodynamic data (Connolly, 2005)

e. *Latent heat and volume work in the mantle transition zone (T. Chust, G. Steinle-Neumann, and H.-P. Bunge/München)*

The depths of phase transitions in the Earth's mantle are governed by competing effects of temperature and chemistry, which affect the dynamics of mantle convection through the release or consumption of latent heat and buoyancy due to density differences between the phase assemblages. These competing effects are of particular importance in the transition zone and have been incorporated in mantle convection models through approximations to the equation-of-state formulations and imposed Clapeyron slopes of the phase transitions. In reality, however, pressure and temperature fields in the Earth's interior determine the stable phase assemblage of a chemical mantle model through thermodynamics, and as a consequence its physical properties. Here, we combine the Gibbs free energy minimization for a pyrolitic model of the mantle with the conservation equations for mantle convection through a look-up table that records the density of the stable phase assemblage.

Using 2D convection simulations we explore the behaviour of flow with different levels of interaction with mineral physics. The simulations were run in a  $1.156 \cdot 10^7$  m wide and  $2.890 \cdot 10^6$  m high box subdivided into 1024 by 256 cells. Temperatures are set to 300 K at the top and 4000 K at the bottom; boundary conditions for the sides are reflective. Internal heat generation of  $10^{-11}$  W/m<sup>3</sup> and thermal conductivity of 4 W/Km are assumed. The material has a constant viscosity of  $10^{21}$  Pa s. Figure 3.1-7 show temperature statistics obtained from these simulations. The frequencies of temperatures in each depth layers are encoded in the background color shades, and layer mean temperatures are plotted as a continuous line. An adiabatic temperature profile is included as a thin dashed line for comparison.

Figure 3.1-7 a shows results from a simple simulation using the extended Boussinesq approximation with a Birch-Murnaghan equation of state for density of the mantle material. In Figure 3.1-7 b temperature-dependence has been added to the density field via the pre-computed table of stable phase assemblages for given points in pressure, temperature space and a pyrolite bulk mantle composition, based on the thermodynamic model by Stixrude and Lithgow-Bertelloni. In Figure 3.1-7 c a parameterization of latent heat has been added using fixed Clapeyron slopes of  $1.6 \cdot 10^6$  Pa/K and  $-2.5 \cdot 10^6$  Pa/K for the 410 km and 660 km discontinuities, respectively. The phase changes in the mantle transition zone cause jumps in the mean layer temperature: In Figure 3.1-7 b the temperature jump around layer 200, corresponding to the 660 km discontinuity, is about 236 K, while it drops to about 153 K in Fig. 3.1-7 c. It turns out that the magnitude of these temperature differences can be analyzed using basic thermodynamic theory.

Not taking into account latent heat (Fig. 3.1-7 b) a phase change can still cause a temperature jump as the density difference (volume work) changes the internal energy of the phase assemblage. To first order the phase change happens at constant external pressure  $p$ , and the volume work becomes a simple function of the volume difference  $dV$  between the associated

phases. Using the first law of thermodynamics  $pdV = mC_p dT_V$ , with  $m$  the mass and  $C_p$  the heat capacity at constant pressure, we obtain an expression for the temperature increase of  $dT_V = \frac{p}{C_p} d\left(\frac{1}{\rho}\right)$ . At the 660 km discontinuity the relevant parameters of  $p \approx 24$  GPa,  $C_p \approx 1$  J/gK, and  $d(1/\rho) \approx (1/4.1-1/4.3)\text{cm}^3/\text{g}$  yield  $dT_V \approx 270$  K, similar to the simulation results of  $dT_V \approx 236$  K.

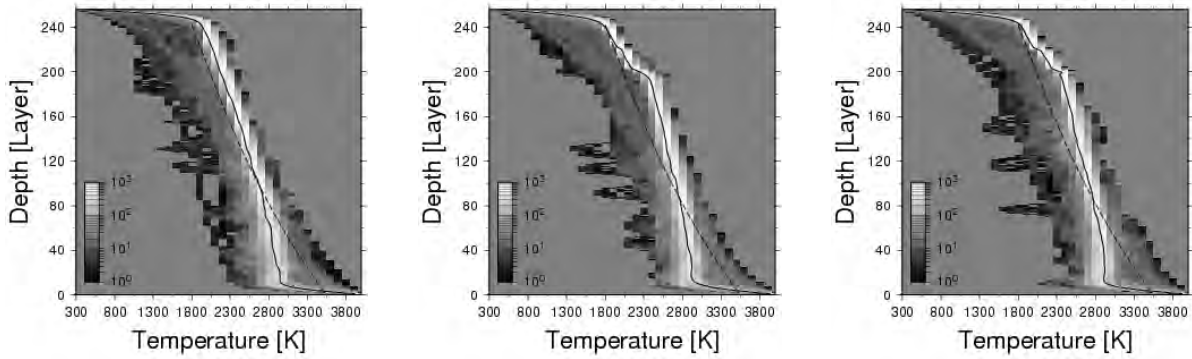


Fig. 3.1-7: Simulated temperature statistics for (left, a) the anelastic approximation, with the solid line indicating the average temperature at each depth, (middle, b) taking into account density differences from the petrological model, and (right, c) also considering the latent heat effect of the phase transition. The dashed lines indicate a reference adiabat with a footing temperature of 1800 K at layer 240.

Once the latent heat of the phase change  $L$  is taken into account, the internal energy of the phase assemblage also changes by that amount, again resulting in a temperature change. For the post-spinel transition (660 km discontinuity) the Clausius-Clapeyron relation yields a temperature decrease of  $dT_L \approx -65$  K (for a reference temperature of 2300 K at the transition), again similar to the simulated decrease of  $dT_L = dT_V - dT \approx -83$  K.

These estimates show that two competing thermodynamic processes at phase transitions influence the temperature field in convection simulations and will also affect the geotherm in the Earth's mantle.

**f. Nominally anhydrous minerals and dense hydrous Mg-Fe silicates in a hydrous Martian mantle (G. Ganskow, F. Langenhorst, and D.J. Frost)**

High-pressure and -temperature experiments have revealed that nominally anhydrous magnesium-dominated ringwoodite and wadsleyite can accommodate up to 2-3 wt.%  $\text{H}_2\text{O}$ , implying that the Earth's transition zone has an enormous potential for water storage. Comparatively little is known, however, about the solubility and incorporation mechanism of  $\text{H}_2\text{O}$  in the more iron-rich compositions that are relevant to the Martian mantle. Similarly, the effect of  $\text{H}_2\text{O}$  on phase stabilities in more Fe-rich systems is also unexplored. This knowledge

is essential, however, for modeling the past mineralogical structure of Mars and for assessing the possibility that water has been liberated from the Martian interior in the past. We have, therefore, conducted a series of multianvil experiments with hydrous Mars-like bulk composition (hydrous FMAS) aiming at estimating the water storage capacity of the Martian mantle.

High-pressure, high-temperature experiments were carried out at pressures from 6 to 23 GPa and temperatures between 1150 °C and 1500 °C. The composition of the powdered starting material was a simplified hydrous Martian mantle composition based on the model by Dreibus and Wänke: 48.6 %  $\text{Mg}(\text{OH})_2$  + 14.1 % FeO + 34.8 %  $\text{SiO}_2$  + 2.5 %  $\text{Al}_2\text{O}_3$ . Recovered samples were examined using electron microprobe (EPMA), analytical transmission electron microscopy (TEM), X-ray diffraction, RAMAN- and FTIR spectroscopy.

Hydration of the Martian mantle causes major differences to the current mineralogical models in terms of phase stabilities. The experiments show that dense hydrous Mg-Fe silicates such as superhydrous B and phase D are stable up to 1450 °C at 20.5 GPa. At transition zone pressures ringwoodite has the highest water storage capacity with up to 1.14 wt.%  $\text{H}_2\text{O}$  at 20.5 GPa for the nominally anhydrous portion of the phase assemblage. At lower pressures wadsleyite incorporates about 0.6 wt.%  $\text{H}_2\text{O}$ . The uptake of water in ringwoodite is considerably reduced compared to the Mg-endmember.

On Mars the transition zone spans ~ 900-1900 km depth, a significant portion of its interior. Due to the potential presence of the dense hydrous phases at these conditions, and despite the decrease of water solubility in the nominally anhydrous portion of the phases assemblage relative to the Mg-endmember, Mars has a strong potential for storing water in its mantle.

**g.** *Fragmentation of sinking iron diapirs in a terrestrial magma ocean (H. Samuel, D. Rubie, and H.J. Melosh/Tucson)*

Understanding the dynamics of core formation is fundamental for constraining the initial state and the subsequent long-term evolution of terrestrial planets. One plausible scenario of core formation involves the sinking of iron diapirs through a liquid magma ocean. In such context, several key questions remain unanswered: 1) under what conditions do iron diapirs emulsify during their sinking; (ii) what is the timing for diapir fragmentation and what are the subsequent stable diapir sizes; (iii) how efficient are metal-silicate equilibration processes and how does viscous heat partition during the fragmentation of the iron diapirs?

We have initiated a parameter study in order to address these questions. The dynamics of such a core formation scenario can be described by the following dimensionless set of conservation equations for mass, momentum, energy and multi-component composition, under the assumption of the extended Boussinesq approximation:

$$\begin{aligned} \nabla \cdot \mathbf{U} &= 0, \\ P_r^{-1}(\partial_t \mathbf{U} + \mathbf{U} \cdot \nabla \mathbf{U}) \mathbf{P} &= -\nabla p + \nabla \cdot \overline{\boldsymbol{\tau}} + (RaT - RbC)\overline{\mathbf{g}} - \Gamma \kappa \nabla \phi, \\ \partial_t T + \mathbf{U} \cdot \nabla T &= \nabla \cdot (k \nabla T) + (Di/Ra) \Phi_v + Di U_z T, \\ \partial_t C + \mathbf{U} \cdot \nabla C &= 0, \end{aligned}$$

where  $t$  is time,  $\mathbf{U}$  the velocity vector,  $p$  the dynamic pressure,  $C$  composition ( $C=1$  for metal and 0 for silicates),  $T$  temperature,  $\overline{\mathbf{g}}$  a unit vector in the direction of the gravity field,  $k$  the dimensionless thermal conductivity,  $\overline{\boldsymbol{\tau}}$  the deviatoric viscous stress tensor,  $\kappa$  the curvature of the metal-silicate interface(s), and  $\Phi_v$  the viscous dissipation function.

The parameter space is defined by five dimensionless numbers: the thermal and compositional Rayleigh numbers  $Ra$  and  $Rb$ , the dissipation number  $Di$ , the Prandtl number  $Pr$ , and a modified surface tension number  $\Gamma$ . Solving this set of equations is numerically challenging due to the presence of sharp interfaces between the metal and silicate phases and their respective properties (*e.g.*, viscosity, density, thermal conductivity), the presence of surface tension, combined with the influence of both viscous and inertial forces, and the non-linear dependence of material properties on temperature or stress. In addition, the process of fragmentation by definition requires a multi-scale resolution of the conservation equations. These complexities are successfully handled by the new version of the finite difference-finite volume code *STREAMV* (see last year report), which now makes use of Lagrangian Implicit surfaces, Total Variation Diminishing advection schemes, along with Adaptive Mesh Refinement (see section 3.10).

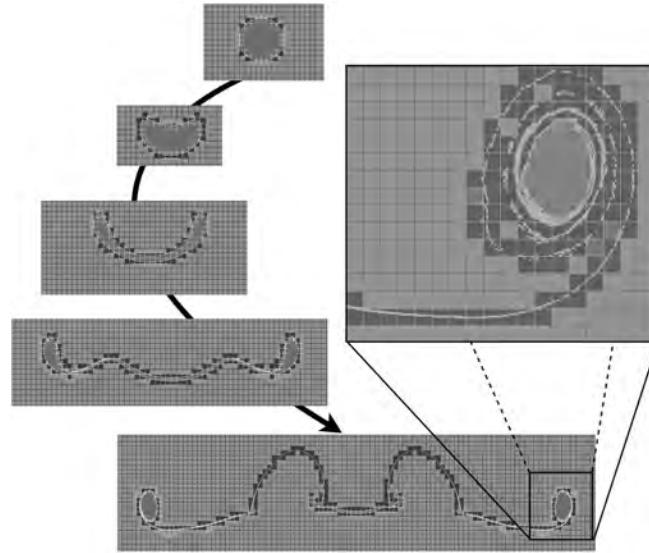


Fig. 3.1-8: Time evolution of an emulsifying iron diapir sinking through a liquid silicate magma ocean. The diapir rapidly fragments into smaller bodies which give birth in turn to smaller diapir generations, following a cascade-type mechanism. The fingering observed in few intermediate stages at the edges of diapirs is produced by shearing (*i.e.*, Kelvin Helmholtz) instabilities. A zoom (on the right) on one resulting diapir reveals the Adaptive Mesh Refinement implemented in *STREAMV* necessary to resolve accurately the processes acting on continuously decreasing length scales.

The numerical setup consist of following the gravitational sinking of an iron diapir until it fragmentates (or not) into smaller bodies due to Kevin Helmholtz shearing instabilities. An example of such an emulsification/fragmentation process is shown in Fig. 3.1-8. Our ongoing systematic exploration of the parameter space will determine the conditions and the timing of metal diapir emulsification in a magma ocean context.

**h. Iron carbide ( $Fe_7C_3$ ), an inner core candidate?** (M. Mookherjee, G. Steinle-Neumann, and X. Wu/Beijing)

$Fe_7C_3$  is a potential inner core phase and its thermoelastic parameters at inner core pressures are of significant geophysical and geochemical interest. Using electronic structure calculations we determine the full elastic constant tensor of  $Fe_7C_3$  at high pressure. Similar to the behaviour of  $Fe_3C$  under compression, a high spin – low spin transition has a significant effect on elastic parameters of  $Fe_7C_3$ . We examine the behaviour of both the magnetic and non-magnetic phases of  $Fe_7C_3$  at high pressure. Results of compression for ferromagnetic (*fm*)  $Fe_7C_3$  is well represented by a third order Birch Murnaghan finite strain equation of state with  $V_0^{fm}=9.1 \text{ \AA}^3/\text{atom}$ ,  $K_0^{fm}=275 \text{ GPa}$  and  $K_0'^{fm}=2.6$ . Under compression the magnetic moment gradually decreases and at  $\sim 67 \text{ GPa}$  the magnetic moment is lost. The high-pressure nonmagnetic phase (*nm*) has distinct finite strain parameters with  $V_0^{nm}=8.77 \text{ \AA}^3/\text{atom}$ ,  $K_0^{nm}=291 \text{ GPa}$  and  $K_0'^{nm}=4.5$ .

The computed static P-wave velocity agrees well with the reference Earth model while the calculated S-wave velocity is considerably faster (by  $\sim 30 \%$ ) than PREM (Fig. 3.1-9). It is worth noting that the temperature is likely to reduce the seismic wave velocity by a few percent, which will reduce the agreement of the P-wave velocity and reduce the discrepancy between the S-wave velocity and PREM. Similarly, the difference of shear wave velocity of pure iron at high temperatures and the reference Earth model is pronounced, and a number of possible causes for the discrepancy between material properties and seismically observed shear wave velocity have been discussed. It could be related to linear or non-linear thermoelastic effects at core conditions, attenuation in the inner core with quality factor (Q)  $\sim 200-400$ , or partial melting of around 3-10 %.

The extrapolated density of  $Fe_7C_3$  to high temperature using a Debye model is lower than that of the inner core, which implies that the presence of  $Fe_7C_3$  cannot be ruled out (Fig. 3.1-9).  $Fe_7C_3$  could occur as a minor component with iron, as the presence of carbides has been predicted stable over the substitutional incorporation of C in the Fe lattice, correcting for the excess density of Fe when compared to the inner core (Fig. 3.1-9). We determine the maximum volume fraction of  $Fe_7C_3$  in the inner core at 6000 K and ICB pressure using the relation  $\rho_{PREM} = x\rho_{Fe} + (1-x)\rho_{Fe_7C_3}$ ; with densities of  $\sim 12.9 \text{ g cm}^{-3}$ ,  $\sim 12.1 \text{ g cm}^{-3}$  and  $\sim 12.76 \text{ g cm}^{-3}$ , respectively, we find  $x=18 \text{ vol.}\%$ .

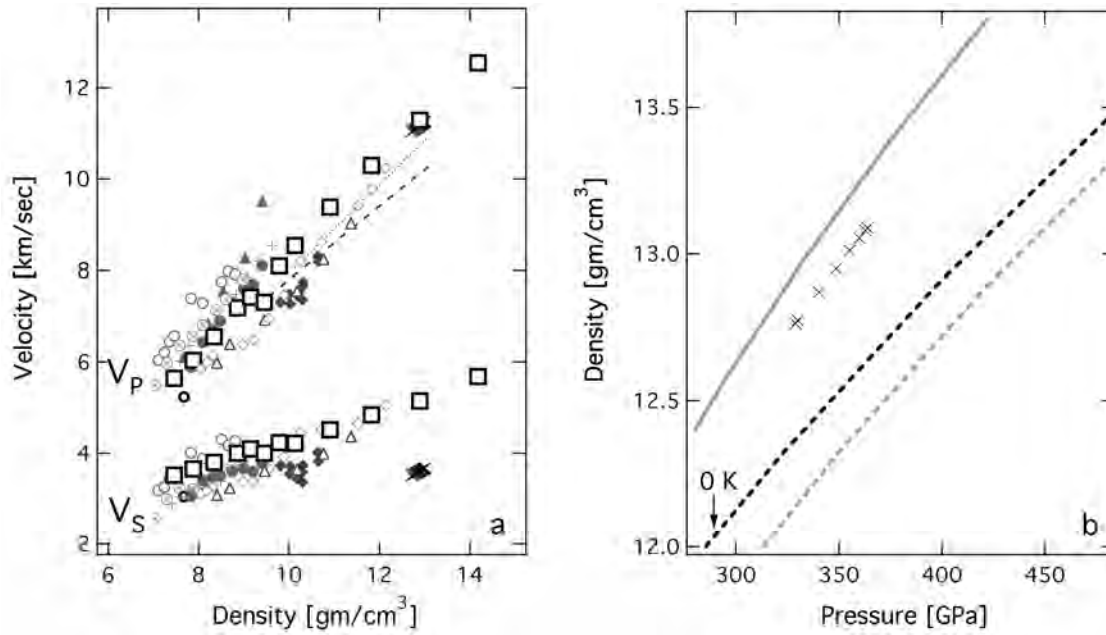


Fig. 3.1-9: a) Velocity-density systematics for iron rich alloys. Primary wave velocity ( $V_p$ ) and shear wave velocity ( $V_s$ ) are plotted with respect to density for  $Fe_7C_3$  (present study, open square). Also shown are various iron alloys:  $Fe_3C$ -grey filled circles;  $Fe_3C$ -black open circle;  $FeH_x$ -grey open circle;  $Fe_{0.85}Si_{0.15}$ -grey plus sign;  $Fe_{0.92}Ni_{0.08}$ -grey open triangle;  $Fe_3S$ -grey open circle with a cross; hexagonal closed pack (hcp)-Fe (700-1700 K)-grey filled rhombs; hcp-Fe-open rhombs; shock wave data on Fe-dotted line; inelastic X-ray scattering data on Fe- dashed grey line. Large crosses refers to PREM; b) Variation of density with pressure, grey solid line (Fe) at 6000 K, black dashed line (static, 0 K) density results on  $Fe_7C_3$ ; grey dashed lines are at 6000 K; crosses represent PREM.

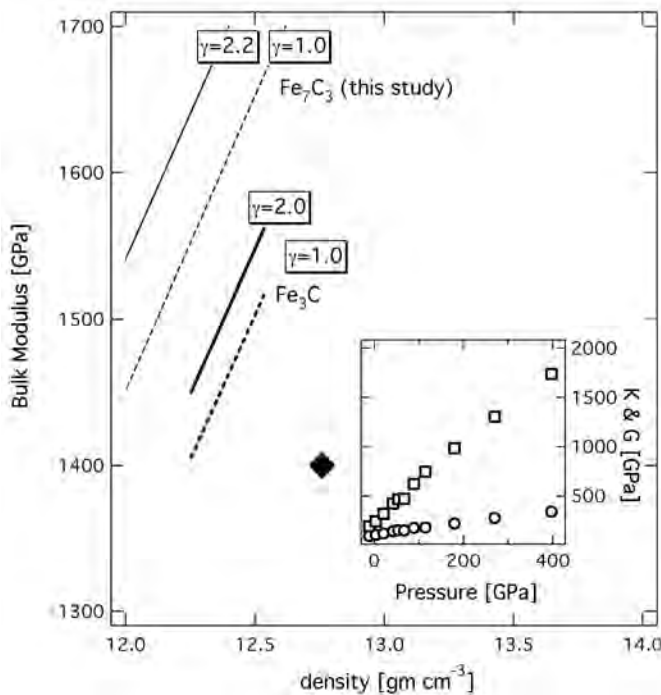


Fig 3.1-10: Adiabatic bulk modulus  $K_s$  vs density  $\rho$ . The solid line is for  $Fe_7C_3$  with a Grüneisen parameter  $\gamma=2.2$  and the dashed lines for  $\gamma=1.0$  for  $T=6000$  K; bold solid ( $\gamma=2.0$ ) and dashed ( $\gamma=1.0$ ) lines represent  $Fe_3C$  at 6000 K; the rhomb shows  $K_s$  and  $\rho$  for the inner core boundary value. The inset shows the calculated athermal bulk and shear moduli vs. pressure for  $Fe_7C_3$ . The elastic anomaly at  $\sim 65$  GPa is associated with the magnetic collapse.

We compare density and adiabatic bulk modulus systematics ( $K_S - \rho$ ) for  $\text{Fe}_7\text{C}_3$  and  $\text{Fe}_3\text{C}$  at 6000 K with that of the inner core (Fig. 3.1-10). The adiabatic bulk modulus,  $K_S$ , is related to the isothermal bulk modulus,  $K_T$ , by  $K_S = K_T(1 + \alpha\gamma T)$ , where  $\alpha$  is the thermal expansion and  $\gamma$  refers to Grüneisen parameter. We have considered  $\gamma$  in the range of 1 to 2.2 and used  $\alpha = 3 \times 10^{-5} \text{ K}^{-1}$ . From the comparison (Fig. 3.1-10) it is evident that neither  $\text{Fe}_3\text{C}$  nor  $\text{Fe}_7\text{C}_3$  are likely inner core candidates. If the magnitude of  $\alpha$  is reduced, it will improve the agreement in density; at the same time, however, it is likely to enhance the discrepancy in  $K_S$  for  $\text{Fe}_3\text{C}$  and  $\text{Fe}_7\text{C}_3$  to that of the inner core.

### 3.2 Geochemistry

The earliest differentiation events to shape the Earth's chemical composition are the subject of the first 5 studies in this section. The nebular gas which cooled and condensed to form the solar system was expelled from the inner solar system by increased solar activity before temperatures were low enough for complete condensation. This differentiation event left the region where Earth formed depleted in elements that condense at temperatures  $< 1200$  K, referred to as volatile elements in this context. Many volatile elements are also siderophile (metal loving), however, and were stripped from the silicate portion of the Earth into the metallic core as it differentiated from the mantle. The first study in this section shows how the differences in volatile element fractionation between the Earth and Moon are consistent with core-mantle equilibration at very high pressures in the Earth. This indicates that volatile elements may have only been added to the Earth in the later stages of its formation, once internal pressures were significant. The second study shows how the relative depletions of alkali elements in the mantle (K, Rb and Cs) may have been established through core formation, rather than through volatility as previously assumed, while the 3 following studies examine the possibility that Si and O may be major light elements in the core. An interesting result is that Si changes its metal-silicate partitioning behaviour strongly in the presence of O. This means that at high pressures both Si and O could have entered the core, where as they are mutually exclusive at lower pressures.

The next 7 contributions focus on carbon, which is an important volatile element in the mantle when oxidised as  $\text{CO}_2$  or carbonates but behaves in a refractory manner when reduced as graphite or diamond. The first three of these studies deal with measuring the redox conditions at which this transition of carbon from reduced diamond to oxidised carbonate minerals and melts occurs. An interesting result is that at the redox conditions of the deep lower mantle carbonate minerals may be stable rather than diamond. Two further contributions examine mineral inclusions in natural diamonds with the aim of identifying the redox conditions at which the diamonds were formed and the medium from which they were produced. The 2 final carbon contributions deal with the melting behaviour of carbonated peridotite and the genesis of carbonate magmas (carbonatites). The first documents a decrease in the melting temperature of carbonated rocks in the Earth's transition zone, which may act to slow seismic waves in this region. The second presents evidence that immiscible silicate and carbonatitic melts may coexist at conditions close to those where the bulk of basalt genesis is considered to occur.

The following 2 reports deal with the origin of trace element signatures in island arc magmas. The first uses experimentally determined fluid-melt and fluid-mineral partition coefficients to explain the commonly high U/Th-ratios of arc magmas relative to mid-ocean ridge basalts. It is shown that high U/Th-ratios are favoured in settings where partial melts are generated by saline and oxidized fluids leaving the subducting slab. Similarly, the next report shows that the Nb/Ta-ratio of subduction zone melts is mainly a function of temperature and melt  $\text{H}_2\text{O}$  content. The results can explain the low Nb/Ta ratio observed in continental crust and Archean granitic magmas.

The partitioning of metals between sulphide phases and silicate melts is the subject of the next 2 reports. The first examines the partitioning of ore-forming elements between mafic alkaline melts and sulphide minerals and sulphide melts at lithospheric mantle conditions. The results have implications for ore formation as well as for chalcophile element distribution on a global scale. In the second study, the solubility of a molybdenum-bearing mineral in silicate magma is investigated, with the aim of developing a thermodynamic model that allows the oxygen and sulphur fugacities of natural, molybdenite saturated melts to be estimated.

Sulphides are formed in marine and fresh water sediments as a result of redox reactions at the interface between oxic and anoxic waters. The final contribution in this section seeks to identify experimentally the reaction pathways for the formation of iron sulphides in these settings. The reactions are complex and involve many metastable intermediate nano-scale products, which can be successfully identified, however, using a transmission electron microscope. The results provide important insights into the stability and growth mechanism of iron sulphides, that may have the ability to adsorb harmful elements from contaminated waters, particularly in mining regions.

**a. Accretion of volatile elements to the Earth and Moon (D.C. Rubie, and D.J. Frost; F. Nimmo/Santa Cruz, D. O'Brien/Tucson, U. Mann/Zürich, and H. Palme/Frankfurt)**

Our recent work on modelling accretion and core-mantle differentiation of the Earth has shown that the bulk composition of the Earth can be represented by solar-system (CI chondritic) relative abundances of non-volatile elements but with an enhancement of the concentrations of the refractory elements Ca, Al, V, Nb, W and Ta by ~ 22 %. This suggests that the material that accreted to form the Earth was enriched in an early-condensing refractory component. Volatile elements, in contrast, are strongly depleted in the Earth's mantle relative to CI abundances by factors of 5-10 (*e.g.*, Fig. 3.2-1).

The elements Mn, Cu, Ga, Na, Zn and In are depleted in the various types of carbonaceous chondrites relative to CI abundances (Fig. 3.2-1). The degree of depletion generally increases with decreasing condensation temperature (*i.e.*, with increasing volatility). The depletion trend of volatile elements in these meteorites is a consequence of incomplete condensation of the more volatile elements. Differentiation processes such as planetary core formation cannot explain this trend. With the exception of Cu, the depletion in Earth's mantle is almost identical to the carbonaceous chondrite trends, which strongly suggests that they have been accreted to the Earth in material that closely resembled the carbonaceous chondrites. There are, however, differences in the isotopic composition of some elements between carbonaceous chondrites and the Earth which excludes carbonaceous chondrites as Earth parental material. The one element in the Earth's mantle that does not fit into the depletion trend is Cu (Fig. 3.2-1). But Cu is a siderophile (metal-loving) element. Its depletion in the Earth's mantle must therefore be affected by metal-silicate segregation during core formation. The depletions of

Cu and other siderophile volatile elements show that volatile elements were accreted to the Earth before core formation was complete.

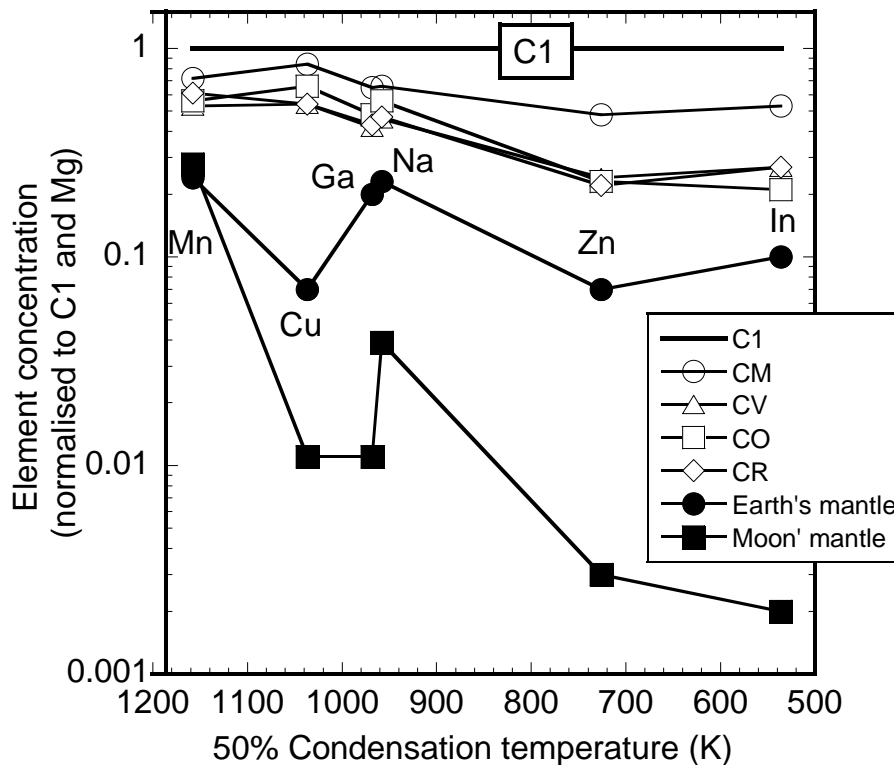


Fig. 3.2-1: Concentrations of the volatile elements Mn, Cu, Ga, Na, Zn and In in carbonaceous chondrites (groups CM, CV, CO, and CR) and the mantles of the Earth and Moon, based on published data. Element concentrations, which are normalized to CI abundances and Mg content, are plotted against their 50 % condensation temperatures – which decrease with increasing volatility.

Our recent published work on the partitioning of the volatile elements Mn, Ga, Zn and In between liquid Fe-rich metal and silicate melt at high pressures provides additional important new constraints on the timing of the accretion of volatile elements to the Earth. The similarity of the depletion pattern of Mn, Ga, Zn and In in the Earth and carbonaceous chondrites (Fig. 3.2-1) indicates that these elements were not fractionated by core formation in the Earth. At low pressures (*e.g.*, < 2 GPa), however, our experimental studies have shown that  $D(\text{Ga}) \gg D(\text{Mn})$  and  $D(\text{In}) \gg D(\text{Zn})$ , where the metal-silicate partition coefficient  $D = (\text{concentration in metal}/\text{concentration in silicate})$ . Under such conditions, Ga would have been depleted relative to Mn and In relative to Zn, which is not observed. In order to explain the lack of fractionation of these elements in the Earth's mantle, it is necessary that  $D(\text{Ga}) \approx D(\text{Mn})$  and  $D(\text{In}) \approx D(\text{Zn})$ . Based on our experimental results, the similarity of these pairs of partition coefficients requires pressures of at least 40-60 GPa. This means that the volatile elements were added to the Earth at a late stage of accretion because otherwise metal-silicate equilibration pressures would have been too low.

The Moon also formed late in the Earth's accretion history as the result of a giant impact between the Earth and a Mars-sized planetary embryo. This raises the question of the timing of volatile element addition relative to the timing of the Moon-forming giant impact. Concentrations of volatile elements in the Moon's mantle are on average two orders of magnitude below those in the Earth's mantle, but they also show some marked differences compared with their concentrations in the Earth's mantle (Fig. 3.2-1). The concentration of Mn, the least volatile of the elements discussed here, is identical in the Earth and Moon. In contrast to the Earth, Ga is strongly depleted in the Moon relative to Mn and In is depleted relative to Zn-depletions that could be a consequence of core formation in the Moon at low pressure (see above).

**b. *The partitioning of alkali metals between liquid metallic Fe and silicate melt (K. Tsuno/Houston, D.J. Frost, and D.C. Rubie)***

Compared to CI carbonaceous chondrite meteorites, which are considered to be representative of the primitive solar nebula, the combined silicate portions of the Earth are depleted in alkali metals. It has long been argued that this depletion results from volatile behaviour of these elements, either during nebula condensation or during vaporisation of condensed material during energetic accretion. As shown in Fig. 3.2-2, however, the depletion of alkali metals in the Earth is much stronger than in other volatile depleted meteorites and recent stable isotope studies imply that very little vaporisation could have occurred during accretion. The Rb/Cs ratio of the Earth, for example, is much higher than in meteorites and rather than resulting from a volatile process an alternative explanation would be that this results from partitioning of alkali elements into the Earth's core. Many previous studies have examined K partitioning between Fe-metal and silicate as there are important implications for the core's heat budget if it contains significant concentrations of the radioactive isotope  $^{40}\text{K}$ . The metal silicate partitioning of Cs has also been examined, however, most studies have only found significant K or Cs to enter Fe metal when S concentrations in Fe metal were unrealistically high *i.e.*, approximately FeS. Previous studies have indicated that the metal silicate fractionation of volatile elements in the mantle probably occurred during the later stages of accretion at high pressures (> 25 GPa) and temperatures (> 2600 K) at the base of a deep silicate magma ocean. In this study we are examining whether alkali metals could have been similarly fractionated between the mantle and core at these conditions.

The starting material for the experiments comprised an oxide mix of peridotite composition ground together with an aluminosilicate glass doped with percent levels of alkali metal oxides. This was mixed with either Fe metal or mixtures of Fe metal with FeS or FeSi. Starting powders were placed in MgO single crystal capsules, which were positioned inside 10 mm edge length octahedra and compressed to 25 GPa using 4mm edge length WC anvils in the multianvil press. Experiments were performed at temperatures up to 3000 K. Heating was for approximately 1 minute. The recovered samples were mounted in epoxy resin and polished in the absence of water. Metal silicate partition coefficients were determined from electron microprobe analyses of the quenched metal and silicate melts. The results of two

such experiments are shown in Fig. 3.2-3. At 3000 K in the absence of S, partition coefficients for all alkali metals remain below 1. However, partition coefficients at these conditions are higher than in previous S-free experiments performed at lower pressures and temperatures. At lower temperatures of 2600 K in the presence of 9 mol.% S all partitioning coefficients except those of Na are higher and Cs has a partition coefficient greater than 1 and is therefore siderophile. These results indicate that alkali metal partition coefficients increase with pressure, temperature and metal S-content. Given the trends observed in these experiments it is quite plausible that the strong fractionation of Rb and Cs in the Earth's mantle results from core-mantle equilibration at pressures exceeding 25 GPa.

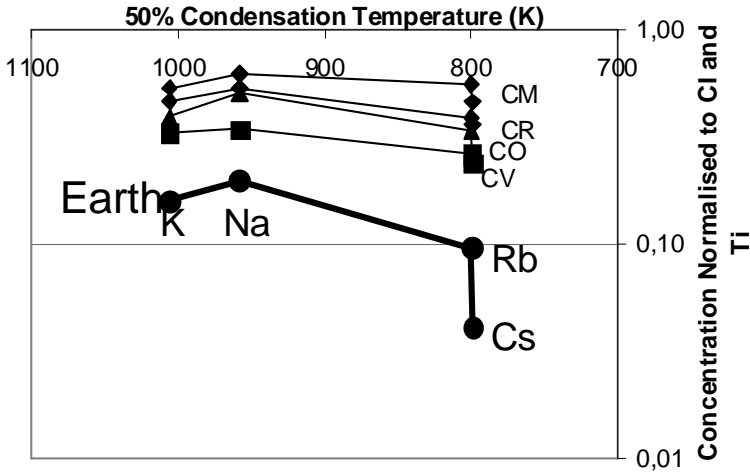


Fig. 3.2-2: Concentrations of alkali metals in carbonaceous chondrites (CM, CR, CO and CV) and the silicate Earth, normalised against the concentration in CI chondrites and Ti, plotted against the temperature at which 50 % of the elements are calculated to condense from the solar nebula.

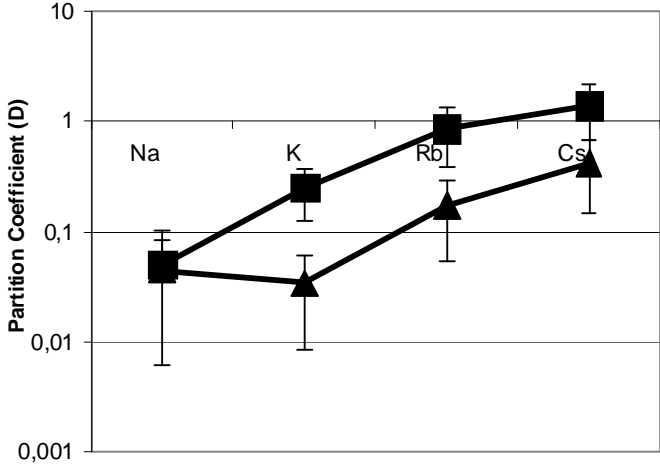


Fig. 3.2-3: Liquid metal-liquid silicate partition coefficients for alkali metals at 25 GPa. Squares are for experiments at 2600 K where the metallic Fe melt contained 9 mol.% S, triangles are from 3000 K in the absence of S.

c. The effect of Si on O partitioning between the Earth's silicate mantle and core (K. Tsuno/Houston, D.J. Frost, and D.C. Rubie)

In order to understand reactions at the core-mantle boundary (CMB), it is necessary to be able to determine how oxygen and silicon would partition between the Earth's silicate mantle and metallic core at the current CMB conditions. Here we present new experimental results that examine the effect of the Si content of liquid Fe on the partitioning of oxygen between liquid metal and liquid silicate. The results are also required for modelling core formation and for the calibration of thermodynamic models that can be extrapolated to CMB conditions.

High-pressure experiments were performed in order to determine experimentally the partitioning of oxygen and silicon between liquid Fe-alloy, ferropericlase, and liquid silicate as a function of pressure, temperature and composition. The experiments were performed in a multianvil apparatus at 25 GPa and 2773-3300 K. Starting compositions were mixtures of Fe powder and  $(\text{Mg,Fe}_{0-0.18})\text{SiO}_3$ , enclosed in single crystal MgO capsules. The partitioning of O between ferropericlase and liquid Fe metal is expressed as  $\text{FeO}^{fp} = \text{Fe}^{met} + \text{O}^{met}$  where the O distribution coefficient is defined as

$$K_d(\text{O}) = \frac{X_{\text{Fe}}^{\text{met}} X_{\text{O}}^{\text{met}}}{X_{\text{FeO}}^{\text{fp}}}$$

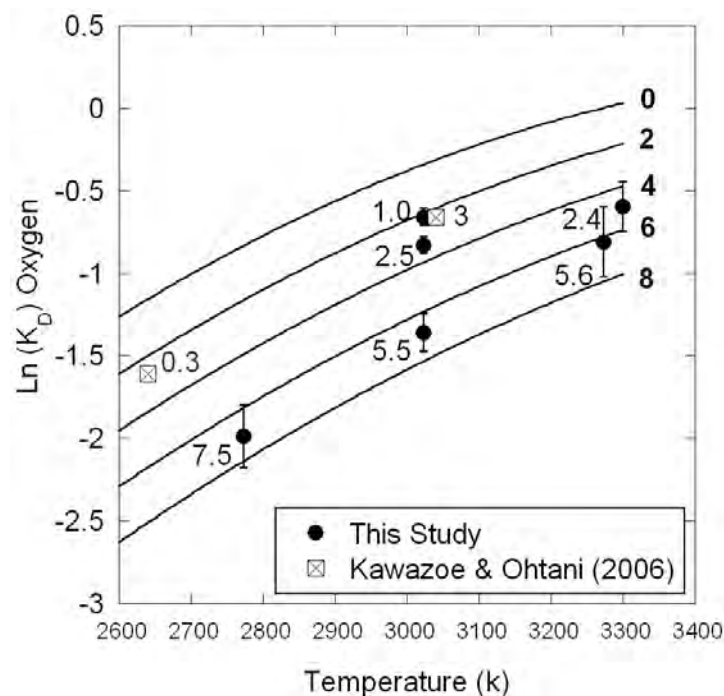


Fig. 3.2-4: The distribution coefficient ( $K_d$ ) of oxygen between ferropericlase and liquid Fe metal. The experimental data are from this study and Kawazoe and Ohtani (Phys. Chem. Miner. 33, 227, 2006). Numbers next to each data point are the Si content of the metal in mol.%. The curves indicate the results of a model fit to these data calculated for different Si contents of the metal, as indicated by the numbers by each curve.

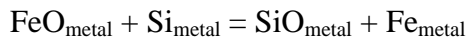
The partitioning of oxygen between ferropericlase and liquid Fe has been studied previously in Si-free systems using both multianvil and DAC techniques. The results of these experiments are summarised in Fig. 3.2-4 by the curve marked 0 % Si. In comparison to the 0 % Si curve, the current results shown in Fig. 3.2-4 along with those of a previous study are consistent with a lowering of the oxygen  $K_d$  with increasing Si content of the metal. Although the oxygen content of the metal decreases with increasing Si content due to a decrease in the oxygen fugacity, this oxygen fugacity effect should be removed through the use of  $K_d$ , which for Si free experiments is independent of oxygen fugacity. A model has been fit to these data and its predictions are shown as solid curves in Fig. 3.2-4 calculated for different liquid Fe Si contents (in mol.%). The presence of Si lowers the O content below levels observed at similar oxygen fugacities in the absence of Si, which must result from a strong interaction in the liquid metal between Si and O. This interaction probably means that Si will tend to dominate as the light element in the core because its presence makes liquid Fe a less favourable environment for the presence of O.

**d.** *An associated solution model describing the Si and O content of liquid core-forming metal at high pressure and temperature (D.J. Frost, D.C. Rubie, and K. Tsuno/Houston)*

Oxygen and silicon are both potential light-alloying elements in the Earth's outer core. At low pressures, along the silicate liquidus, O and Si are mutually exclusive in Fe metal as the Si content of the metal only starts to increase at oxygen fugacities where the O concentration has already dropped to low levels. Low pressure data from the Iron and Steel literature indicate the highest equal levels of each element in liquid Fe metal are approximately 0.2 wt.% at a temperature of 2300 K. At high pressures and temperatures the combined concentration of O and Si in Fe metal increases. As seen in the previous contribution O and Si interact strongly in liquid Fe, which causes O concentrations to be lowered in the presence of Si, below levels that would be expected from the effects of low oxygen fugacity. In Figure 3.2-5 experimental data on the Si liquid metal-silicate partition coefficient are shown at 3 different pressures and temperatures. At 2 and 25 GPa and temperatures up to 2500 K data fall on a linear trend with a gradient of approximately -1. The gradient is constrained by the stoichiometry of the Si-Fe exchange reaction between silicate and metal and implies that Si dissolves in silicate liquid in the 4+ oxidation state. At 25 GPa and 3000 K, however, the gradient is much closer to -0.5. The only plausible explanation is that this change in partitioning behaviour results from non-ideal interactions between Si and O in Fe metal. The O content of the metal exceeds 10 mol.% at the highest oxygen fugacity and this must affect the Si partitioning. It is crucial to be able to understand and model this behaviour in order to constrain the light elements in the core and reactions at the core mantle boundary.

For the presence of O in metal to influence  $D_{Si}$  there must be a favourable interaction between O and Si, *i.e.*, the presence of O makes it energetically more favourable for Si to enter the liquid. However, in the previous contribution in this section by K. Tsuno *et al.* the presence of

Si clearly had the opposite effect on the O partitioning *i.e.*, the presence of Si made the partitioning of O less favourable. For Si and O to interact so differently with each other over relatively small concentration ranges requires large non-linear compositionally dependent interaction coefficients in the Fe-O-Si system. An alternative model is to consider the presence of an associated species that forms an additional component in the liquid. We found the model that provided the best fit to the data was one that considered FeO, SiO, Si and Fe species in the metal *i.e.*, with the speciation of SiO being controlled by the internal equilibrium



The parameters for fitting the experimental data to this model are the corresponding equilibrium constant and interaction parameters between SiO, Si and FeO. The resulting speciation in the Fe liquid is shown in Fig. 3.2-6. The corresponding fit of this model to the  $D_{\text{Si}}$  data is shown by the curve for the 3000 K data in Fig. 3.2-5. The model also fits the O partitioning in the previous contribution. The results imply that species formed with O in liquid Fe at high pressures and temperature can cause very strong deviations from the partitioning behaviour for some elements. Extrapolating metal silicate partitioning data up to conditions where significant O starts to enter the Fe liquid may, therefore, be unrealistic. This may have very important implications for metal silicate partitioning at the base of a deep magma ocean during Earth's accretion.

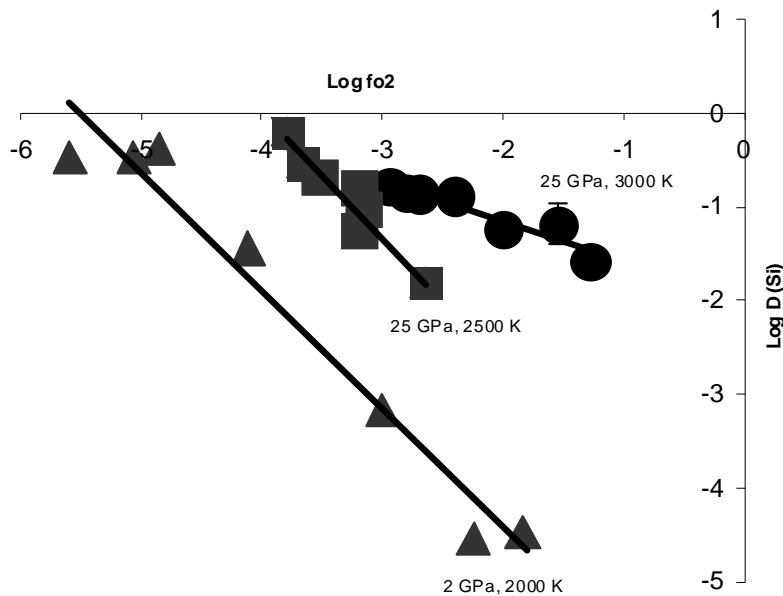


Fig. 3.2-5: The Si partition coefficient (D) between liquid metal and liquid silicate plotted against the oxygen fugacity in experiments performed at 3 pressures and temperatures. Significant O concentrations are only found in experiments at 3000 K, which likely causes the change in slope of the partitioning data.

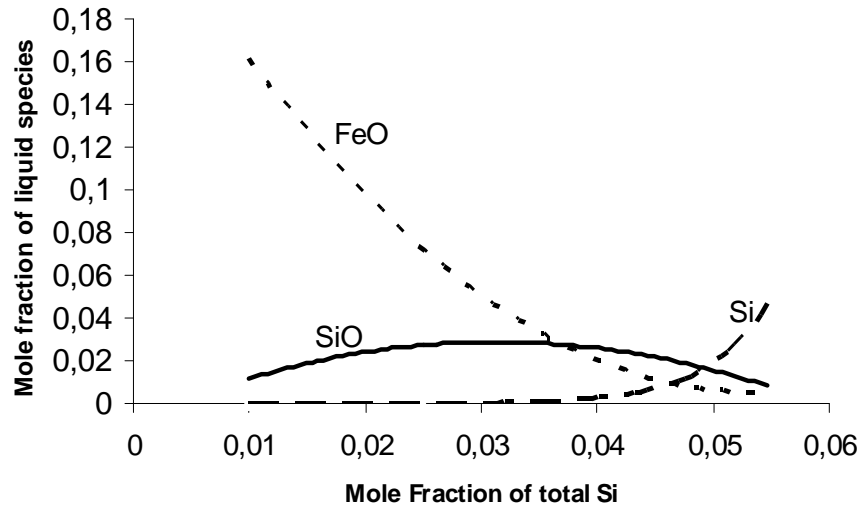


Fig. 3.2-6: The speciation of components in liquid Fe metal at 25 GPa and 3000 K considering that a Si-O associated species is formed. This model successfully explains the low gradient for the  $\log D_{\text{Si}}$  versus  $\log f\text{O}_2$  relationship in Fig. 3.2-5.

*e. Element partitioning between metal and silicates at high pressure during formation of the Earth's core (Y. Nakajima, D.J. Frost, and D.C. Rubie)*

In addition to Fe and Ni, the Earth's core contains 10-20 % of one or more light alloying elements, such as H, C, O, Si, and S. Experimental data on the partitioning behaviour of siderophile elements such as Ni and Co between liquid iron and mantle minerals indicate that pressures of equilibration between core forming metal and the silicate mantle may have been in the range 20-70 GPa. At these conditions the nature of the dominant light element in the core will depend strongly on the oxygen fugacity at which equilibration occurred. In this study we have investigated element partitioning behaviour between liquid Fe and lower mantle minerals (Mg,Fe)SiO<sub>3</sub>-perovskite (Pv) and ferropericlase (Fp).

High-pressure experiments were performed using a Kawai-type multianvil apparatus at 25 GPa and at 2400-2700 K. The starting material, comprising metallic Fe (or FeSi alloy) and San Carlos olivine, (Mg<sub>0.9</sub>,Fe<sub>0.1</sub>)<sub>2</sub>SiO<sub>4</sub>, was packed into an MgO container and placed at the center of a LaCrO<sub>3</sub> furnace. The olivine breaks down to form perovskite (Pv) and ferropericlase (Fp) at 2400-2600 K and melts to form silicate-melt and Fp at 2700 K. The silicates and oxides also react with the liquid Fe during heating. Recovered samples were analyzed by an electron microprobe.

In Figure 3.2-7a the Fe-Mg distribution coefficients  $K_D = (X_{\text{FeSiO}_3}^{\text{Pv}} / X_{\text{MgSiO}_3}^{\text{Pv}}) / (X_{\text{FeO}}^{\text{Fp}} / X_{\text{MgO}}^{\text{Fp}})$  between Pv and Fp coexisting with liquid Fe are shown, where  $X_i^j$  is the mole fraction of component i in phase j. The  $K_D$  values increase slightly with increasing temperature and with decreasing  $X_{\text{FeO}}$  in Fp. In order to evaluate the oxygen fugacity effect on Si partitioning

between liquid Fe and silicate-perovskite or -melt, the Si molar partitioning coefficients  $D_{Si}^{metal/silicate} = X_{Si}^{metal} / X_{SiO_2}^{silicate}$  were plotted as a function of oxygen fugacity  $fO_2$  relative to the iron-wüstite buffer ( $\Delta IW$ ) (Fig. 3.2-7b). The  $fO_2$  was obtained from the chemical compositions of liquid Fe and Fp. The  $D_{Si}^{metal/silicate}$  values increase with increasing temperature and with decreasing oxygen fugacity. Our data show that the oxidation conditions as well as the temperature and pressure at which metal/silicate fractionation occurred will have strongly influenced the Si concentration in the Earth's core.

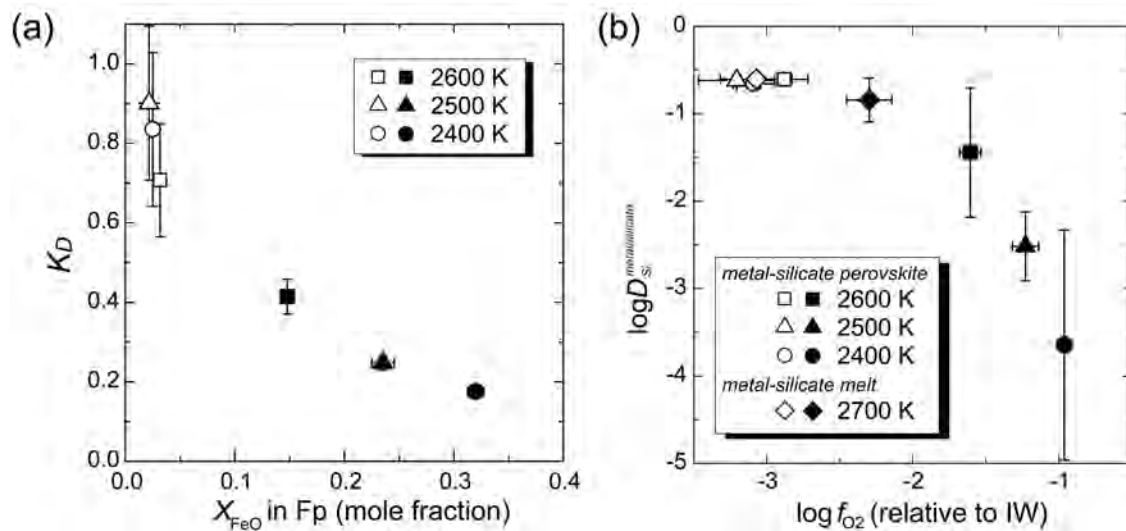
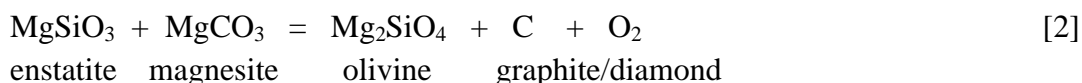
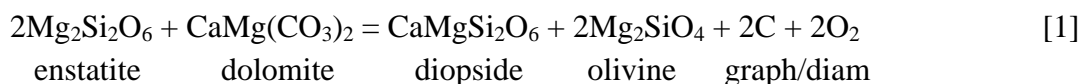


Fig. 3.2-7: Element partitioning obtained at 25 GPa with starting materials of Fe + olivine (filled symbols) and FeSi alloy + olivine (open symbols). (a) The Fe-Mg distribution coefficients between silicate-perovskite (Pv) and ferropericlase (Fp) as a function of FeO mole fraction in Fp. (b) The molar partitioning coefficients between liquid Fe and Pv at 2400-2600 K (or silicate-melt at 2700 K) for Si plotted as a function of oxygen fugacity relative to the iron-wüstite buffer ( $\Delta IW$ ).

**f.** *The carbon/carbonate equilibria in the Earth's mantle as a function of pressure, temperature, oxygen fugacity and melt composition (V. Stagno, and D.J. Frost)*

The speciation of carbon in the mantle is controlled to a large extent by oxygen fugacity. Under relatively oxidized conditions carbonate-bearing minerals and melts (*e.g.*, carbonatites and kimberlites) will be stable, while under more reduced conditions diamond, graphite or  $CH_4$  may form. The aim of this study is to determine the oxygen fugacity buffered by equilibria involving carbon (graphite/diamond) and carbonate (minerals and melts) within typical mantle bulk compositions. Most importantly we have measured the oxygen fugacity of this equilibrium for carbonate melt-bearing assemblages that evolve at high temperature towards more  $SiO_2$ -rich compositions. By comparing the oxygen fugacity of this equilibria with that expected for the mantle we can constrain the speciation of C in the mantle.

Experiments have been performed in the systems Fe-Ca-Mg-Si-C-O and Fe-Ca-Mg-Al-Si-C-O at pressures from 3 to 25 GPa and temperatures from 1100-1600 °C. In the range between 3 and 11 GPa the oxygen fugacity of a Ca- bearing assemblage is imposed by the following simplified equilibria,



that describe the stability of elemental carbon with respect to the carbonate (dolomite or magnesite depending on pressure) in equilibrium with mantle silicates. We added 5 wt.% of iridium to the starting material as a sliding redox sensor. During the experiments the extent to which Ir and Fe alloy depends on the oxygen fugacity. Therefore, the use of iridium-iron alloy allowed us to determine the oxygen fugacity of the above buffering reactions at higher pressures and temperatures than previous studies and above the carbonated solidus.

Recovered lherzolitic samples contained clino- and orthopyroxene, olivine and either carbonate minerals or melts (Fig. 3.2-8a). Graphite was also dispersed throughout the material. Textural observations of the sectioned run products were performed by scanning electron microscope whereas the chemical composition of the melts and mineral phases were obtained using a Jeol JXA-8200 electron microprobe.

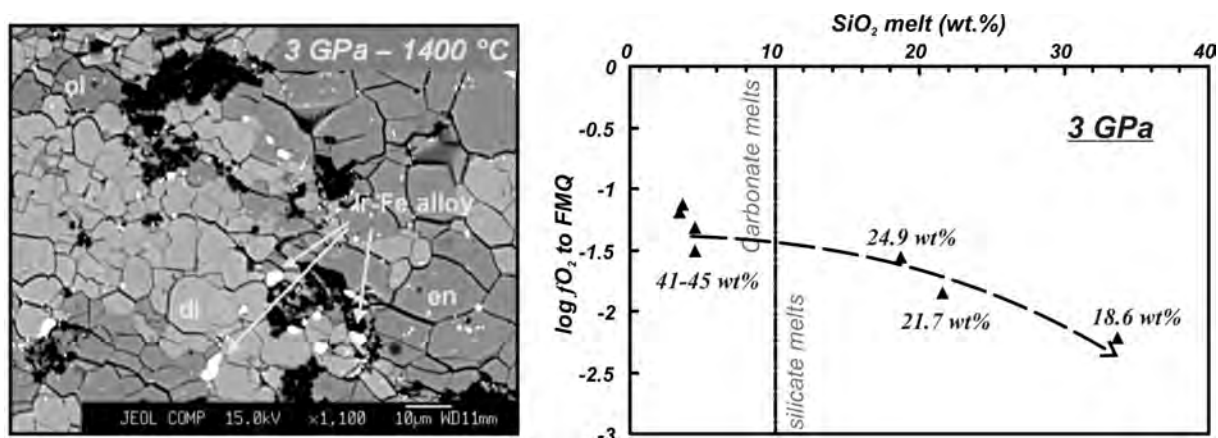


Fig. 3.2-8: a) Scanning electron microscope image of an experimental assemblage containing enstatite (en), olivine (ol), graphite (black platelets), carbonate melt (melt) and Ir-Fe alloy (bright white grains) recovered from 1400 °C and 3 GPa. b) The oxygen fugacity relative to the FMQ oxygen buffer decreases with increasing temperature, as the melt becomes less carbonate rich and more SiO<sub>2</sub> dissolves in the melt. The CO<sub>2</sub> content of the melt at each run is also indicated (italic numbers).

In Figure 3.2-8b results are shown from experiments performed at 3 GPa. The SiO<sub>2</sub> content of the melt phase increases with increasing temperature as the melt evolves from a pure carbonate melt at the solidus towards more SiO<sub>2</sub>-rich melts at higher temperatures. In turn, as the temperature increases the activity of the carbonate component in the melt decreases, which drives the equilibrium oxygen fugacity down compared to the extrapolations at higher temperature. As shown in Fig. 3.2-8b, as the silicate content increases from ~3 to 35 wt.% in the melt, the  $fO_2$  drops by approximately 1 log units.

At 3 GPa, 1200 °C, which is just at the carbonated solidus, the determined oxygen fugacity is very similar to the previously published values for the same Ca-bearing equilibrium [1]. The same effect is observed at higher pressure. At 6 GPa (Fig. 3.2-9b), for instance, the  $fO_2$  drops by 1 log unit when SiO<sub>2</sub>-rich melts with kimberlitic composition are in equilibrium with silicates.

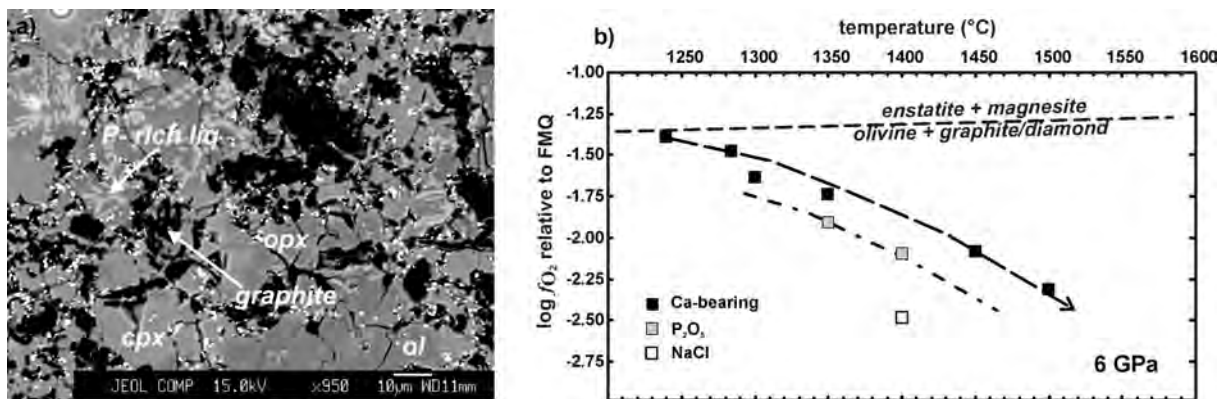


Fig. 3.2-9: a) Back Scattered Electron image of a run at 6 GPa and 1400 °C showing P-rich melt with quenched texture, in equilibrium with silicate minerals and graphite (dark platelets). b) The effects of adding P and NaCl on equilibrium [2] are shown. As observed, the curve dividing carbon and carbonate drops by 1 to ~2 log units as phosphorous and chlorine dissolve in the melt.

In addition, high pressure and temperature experiments have focused on the role played by components such as chlorine, phosphorous, sulphur and water on the oxygen fugacity of carbon/carbonate equilibria, since they may also partition strongly into small degree carbonate-rich melts in the mantle (Fig. 3.2-9). Several geophysical studies argue for the presence of melts at depths up to 300 km. If this is the case then our results mean that either the mantle must be more oxidized than fertile mantle xenoliths indicate at this depth or other components must act to stabilize carbonate-rich melts with respect to diamond at high pressures. We have studied many such components to examine whether they actually partition into carbonate melts and therefore dilute the carbonate component and whether the mineral/melt partition coefficients are low enough for typical mantle abundances of these elements to suitably effect the compositions of carbonatite melts in adiabatically up welling magma.

Results show that, at redox conditions where diamond and carbonate melt coexist in equilibrium with apatite ( $\text{Ca}_5(\text{PO}_4)_3(\text{F},\text{Cl},\text{OH})$ ) carbonate melts are stabilized at lower oxygen fugacity and contain up to 20 wt.%  $\text{P}_2\text{O}_5$ . However, coexisting olivine also contains ~0.8 wt.%  $\text{P}_2\text{O}_5$ , which means the  $\text{P}_2\text{O}_5$  contents of carbonate melts of realistically small melt fractions are likely to be relatively small.

Our results imply that: (1) the effect of melt composition on the carbon/carbonate  $f\text{O}_2$  is relatively modest and up welling mantle will only cross from the graphite to the carbonate melt stability field at pressures below approximately 4 GPa; (2) deep (> 100 km) carbonate rich melts are only stable in more oxidized regions with an unusually high  $\text{Fe}^{3+}/\Sigma\text{Fe}$  ratio, although  $\text{P}_2\text{O}_5$  and Cl may also help to stabilize carbonate liquids; (3) the effect of pressure on the carbon/carbonate equilibria indicates that carbonates might be stable in the lower mantle.

*g. High pressure and temperature experiments on a carbonated lower mantle assemblage using sintered diamond anvils in a multianvil apparatus (V. Stagno, and D.J. Frost; Y. Tange, and T. Irifune/Ehime)*

The stability of carbonate in the mantle relative to diamond depends on oxygen fugacity. In the Earth's lower mantle it is likely that the oxygen fugacity is sufficiently low enough for Fe-Ni metal to be stable, however, high pressure and temperature experiments are required in order to test whether this means diamond is the only form of carbon present in the lower mantle. Although relatively large volumes ( $1\text{mm}^3$ ) of starting material can be employed in multianvil experiments compared to the laser-heated diamond anvil cell (LHDAC), the experimental pressure is limited to below 28 GPa when tungsten carbide anvils are used. Recent technical developments in experiments with sintered diamond (SD) anvils allow us to achieve pressures compatible with the Earth's mid lower mantle (approximately 50 GPa) using a DIA-type multianvil guide block system. We have examined the stability of carbonate relative to diamond in an Fe-Ni metal bearing system at mid-lower mantle conditions (~ 1100 km). Such an approach allows us to estimate the likely redox conditions occurring in the lower mantle at which elemental carbon (diamond) is in equilibrium with carbonate.

An experiment was performed at 45 GPa and 1700 °C using the MADONNA D-DIA (1500 tons) apparatus with sintered diamond anvils installed at the Geodynamics Research Center, Ehime University. The advantage of the MADONNA press is that the displacements of all the six anvils can be measured and the differential ram pressures can be controlled with the main ram load. Therefore, higher pressures as well as a homogenous and stable hydrostatic regime are reached during compression. Starting powder was made by grinding magnesite, pure graphite powder, MgO, FeO and Ni metal. The powder was placed in a graphite capsule. High-pressure cell assemblies have been optimized for use with SD anvils and employ an MgO pressure medium doped with 5 wt.% Cr with fired pyrophyllite gaskets. High temperatures were reached using a cylindrical  $\text{LaCrO}_3$  furnace. Temperature was measured with a  $\text{W}_{97}\text{Re}_3$ - $\text{W}_{75}\text{Re}_{25}$  thermocouple in contact with the bottom of the graphite capsule. The experiment was run for 1 hour. After quenching, a long decompression rate (30 hrs) was

employed in order to prevent breakage of the sintered diamond anvils. Pressure was accurately determined using a calibration based on using the same assembly at the SPEED-Mk.II multi-anvil press installed at BL04B1 beam line in SPring-8. *In situ* X-ray diffraction (XRD) measurements with synchrotron radiation were carried out using Au as an internal pressure standard.

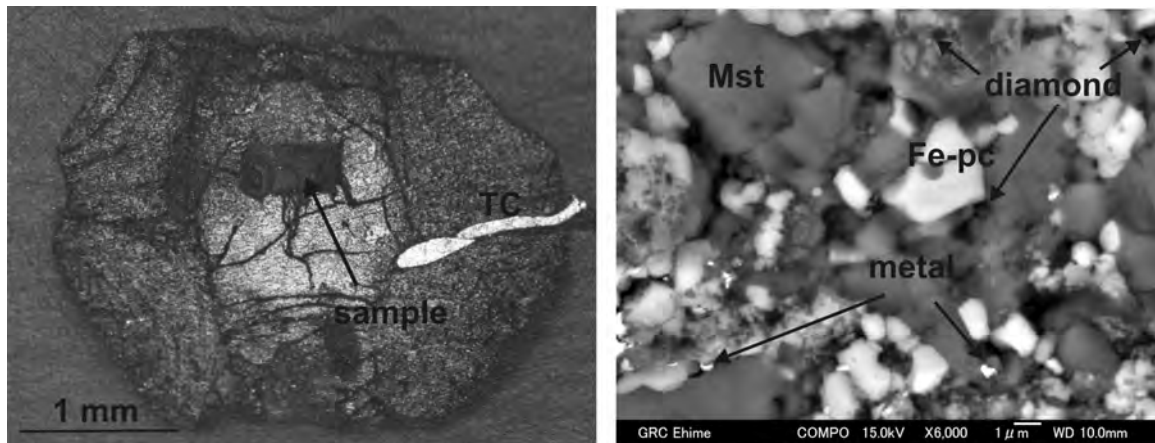


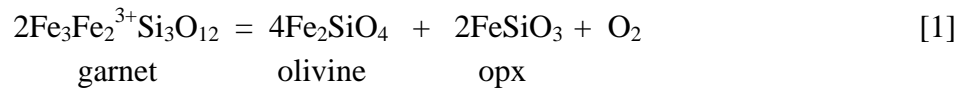
Fig. 3.2-10 (left): Recovered sectioned run product under the optical microscope. (right): BSE image with high resolution taken by FE-SEM showing a heterogeneous mineral assemblage with: magnesite (mst), Fe-periclase (Fe-pc), diamond grains and small metal grains with uncertain composition.

First observations using a scanning electron microscope with qualitative chemical analysis show typical equilibrium textures with the coexistence of carbonates and diamond with ferropericlase and a metal phase randomly distributed between the main phases (Fig. 3.2-10). The oxide phase is characterized by the presence of ~ 6 wt.% of nickel and a Fe/Fe+Mg value of about 0.17. Mass balance calculations suggest the presence of an Fe-rich metal phase, although the chemical composition will be determined more accurately through further analyses. Using an accurate measurement of the Ni content of both oxide and metal we will be able to determine the oxygen fugacity at which carbonate and diamond coexist in the lower mantle. However these preliminary results suggest that carbonate rather than diamond may be the most stable C-bearing phase within the lower mantle, even if oxygen fugacities are compatible with the presence of Fe-Ni metal.

**h.** *Fe<sup>3+</sup>/Fe<sub>tot</sub> measurements on garnets in carbon-bearing lherzolite assemblage and implications for the redox conditions of the Earth's upper mantle (V. Stagno, C.A. McCammon, and D.J. Frost)*

The oxygen fugacity of the mantle exerts a controlling influence over the speciation of volatiles in the interior, which can affect the mantle solidus and physical properties of the

segregated liquids. Oxy-thermobarometry measurements on garnet peridotite xenoliths can be performed using the equilibria



and employing the appropriate activity-composition models for each iron-bearing phase. The volume change of this reaction favours the formation of the  $2\text{Fe}_3\text{Fe}_2^{3+}\text{Si}_3\text{O}_{12}$  garnet (skiagite) component with increasing pressure, which drives down the oxygen fugacity with depth. When applied to natural xenoliths from various cratons, the calculated oxygen fugacities are more reduced than values imposed by carbon/carbonate equilibria (EMOD buffer), implying that most of the mantle is in the graphite/diamond stability field.

In this study, the  $\text{Fe}^{3+}/\Sigma\text{Fe}$  ratios of garnet buffered at an oxygen fugacity controlled by a carbonate and graphite/diamond bearing assemblage have been measured using Mössbauer spectroscopy. A knowledge of the oxygen fugacity and the garnet composition allows a test of the  $f\text{O}_2$  determined from equilibrium [1] to be performed. Mg, Fe- and Ca, Fe, Mg- bearing garnets were synthesized from glasses quenched from 1600 °C and then reduced in a gas mixing furnace employing a mixture of  $\text{CO}_2/\text{H}_2$  gases so that minimal  $\text{Fe}^{3+}$  was present. The experiments were performed in a multi anvil apparatus at pressures from 3 to 11 GPa and temperatures from 1400 - 1600 °C. In the experimental graphite capsule a 0.3 mm thick layer of garnet was placed sandwiched between layers of the buffering carbon/carbonate bearing assemblages, in either a lherzolitic or harzburgitic assemblage. In many experiments 10 % of the buffering carbon-carbonate assemblage was mixed within the garnet layer to ensure equilibrium. 5 wt.% of iridium metal was also added to the starting charge as a sliding redox sensor in order to measure the oxygen fugacity. The ferric iron contents of the garnet layers in the run products were determined by  $^{57}\text{Fe}$ -Mössbauer spectroscopy and the chemical composition of the mineral phases including garnet were obtained using the electron microprobe (Fig. 3.2-11).

The  $\text{Fe}^{3+}/\Sigma\text{Fe}$  ratio of the sample can be assessed in Fig. 3.2-11b where the Mössbauer spectrum of the garnet layer is compared to the spectrum from the entire sample (bulk). The  $\text{Fe}^{3+}$  content of the bulk is much lower than the garnet layer, indicating a very low  $\text{Fe}^{3+}$  content in the lherzolite assemblage *i.e.*, olivine, opx and cpx. As shown in Fig. 3.2-12 the oxygen fugacity estimated for the garnet-peridotite assemblage using equilibrium [1] is lower than that determined for the carbon-carbonate buffer using the Ir- sliding redox sensor. This difference increases with pressure from approximately 1 log unit at 3 GPa to 5 log units at 11 GPa. The origin of this difference is unclear but could potentially arise from inaccuracies in the calibration of equilibrium [1] for redox measurements.

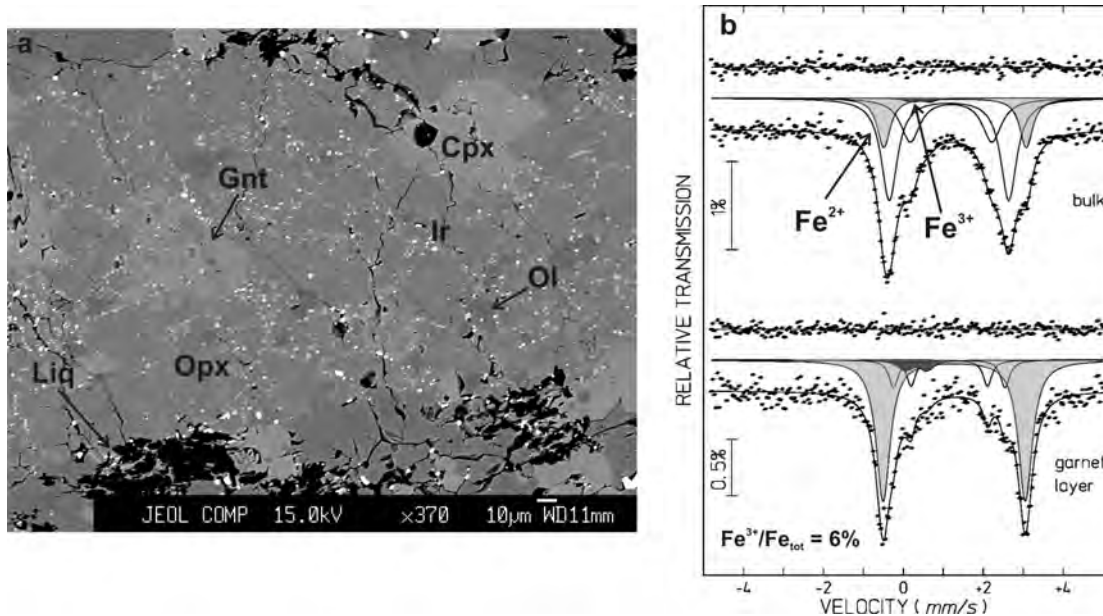


Fig. 3.2-11: a) Back scattered electron image of the garnet layer showing ortho (Opx) and clinopyroxenes (Cpx), olivine (Ol) and a CO<sub>2</sub>- rich melt (Liq). Bright spots are Iridium-Iron alloys used for  $fO_2$  measurement. b) Mössbauer spectra collected at 298 K of the entire sample (bulk) and the Ca- bearing garnet layer after experiments at 3 GPa and 1400 °C. The doublet corresponding to Fe<sup>3+</sup> is shown in bold in both spectra.

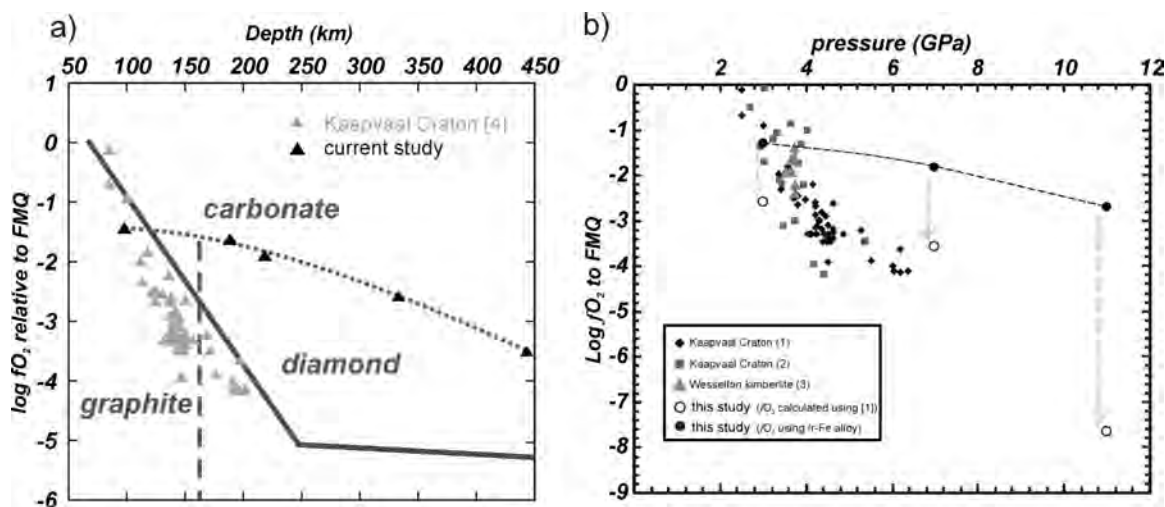


Fig. 3.2-12: a) The oxygen fugacity profile for the upper mantle calculated for a fertile garnet peridotite assemblage using equilibrium [1] is shown by the solid grey line. The experimentally determined oxygen fugacities of the appropriate carbon - carbonate equilibria in a lherzolite composition assemblage are shown by black triangles and a dotted curve. Grey triangles are oxygen fugacities determined for Kaapvaal craton xenoliths. b) Oxygen fugacities determined for the carbon-carbonate assemblage (solid circles) using Ir-Fe metal analyses are compared with those calculated from the garnet-lherzolite assemblage in the same experiment (open circles) using equilibrium [1]. Vertical dashed arrows indicate the differences between these two determinations. Oxygen fugacities of mantle xenoliths also calculated with equilibrium [1] are shown for comparison.

**i.** *Oxygen fugacities determined from iron oxidation state in natural (Mg,Fe)O ferropericlasite: new insights into lower mantle diamond formation (M. Longo, C.A. McCammon, G. Bulanova/Bristol, F. Kaminsky/West Vancouver, and R. Tappert/Adelaide)*

Mineral inclusions in diamonds reflect the chemical composition and mineral assemblages of the two principal rock types occurring in the deep lithosphere, peridotite and eclogite. However, in the past two decades, the discovery of rare diamonds containing inclusions such as former Mg,Si-perovskite and (Mg,Fe)O ferropericlasite led to the possibility that diamonds can form also at greater depths. (Mg,Fe)O ferropericlasite is the most commonly found inclusion in lower mantle diamonds (more than 50 % of the occurrences). Since the  $\text{Fe}^{3+}$  concentration in (Mg,Fe)O is sensitive to oxygen fugacity also at high pressures (see previous BGI Annual Reports), the determination of  $\text{Fe}^{3+}/\sum\text{Fe}$  in such inclusions provides a direct method for investigating lower mantle redox conditions during diamond formation. The goal of this study is to explore whether variations in mantle oxygen fugacity exist as a function of chemical, physical and geographic parameters, by studying (Mg,Fe)O inclusions in lower mantle diamonds from a wide range of localities.

Eighteen (Mg,Fe)O ferropericlasite inclusions from lower mantle diamonds selected from worldwide locations were measured by the flank method using the calibration that we previously established for synthetic ferropericlasite (see previous BGI Annual Reports). The  $\text{Fe}^{3+}/\sum\text{Fe}$  measured in (Mg,Fe)O inclusions of the present work (Juina, Brazil, Machado River, Brazil and Orroroo, Australia) were compared to data already available for other inclusions of larger size previously measured by Mössbauer spectroscopy. In order to estimate the oxygen fugacity at which the inclusions were last equilibrated, we calculated the cation vacancy concentrations required to balance the charge based on the chemical compositions and  $\text{Fe}^{3+}/\sum\text{Fe}$  values, and then compared the resulting vacancy concentrations with results obtained from (Mg,Fe)O synthesized at high P,T with oxygen fugacity controlled by different buffers. The vacancy concentrations in the (Mg,Fe)O inclusions range from relatively low (*i.e.*, similar to those observed in high P,T experiments in equilibrium with Fe metal) to relatively high (*i.e.*, similar to those observed in high P,T experiments controlled at the Re-ReO<sub>2</sub> buffer) (Fig. 3.2-13). While actual oxygen fugacity values cannot be calculated for the individual inclusions, the trend shown in Fig. 3.2-13 from reducing to oxidizing is reliable. The results show a dependence on geographical location, and in particular, inclusions from the African province (Kankan Guinea) seem to record more reducing mantle conditions than the inclusions measured from the other provinces, which cover a larger range of  $f\text{O}_2$  conditions.

It is noteworthy that a variation of oxygen fugacity was registered in multiple inclusions extracted from the same host diamonds. However, because the inclusions were removed from the host without textural control, information on the direction of any redox gradient that may have evolved, and possible correlation with diamond growth or anomalies in the variation of

the redox conditions through time, were lost. In fact, different growth zones of the diamond record information regarding environments through which it has gone before reaching the surface.

Recent published studies suggested that the ultimate source of the Australian diamonds is oceanic lithosphere of the proto-Pacific plate subducted during the Permian period. The Juina and São Luiz regions (Brazil) and Kankan (Guinea) are relatively young (around 95 Ma) compared to the Australian kimberlite occurrences (dated 170 Ma), and moreover, the Brazilian localities are at the opposite margins of the subduction of the proto-Pacific plate with respect to the Australian localities. In addition to these observations, the Kankan area is away from the subduction front. The differences encountered between these localities in terms of mineral assemblages and  $Fe^{3+}/\sum Fe$  ratio (with the apparent redox gradient observable in Australian diamonds), may therefore suggest a combination of different processes that determined their formation and subsequent emplacement at different geologic times. Based on existing models for lower mantle diamond formation, the variation in the oxygen fugacity recorded by ferropicrlase inclusions may reflect interactions between carbonates in subduction zones and melts and/or fluids locally present in the deep Earth. Moreover, the gradient in oxygen fugacity estimated from Kankan, Guinea (youngest occurrence and more reduced conditions) to Orroroo, Australia (oldest occurrence and highest variation in redox conditions) may indicate different residence times at lower mantle conditions as well as different depths at which crystallization occurred.

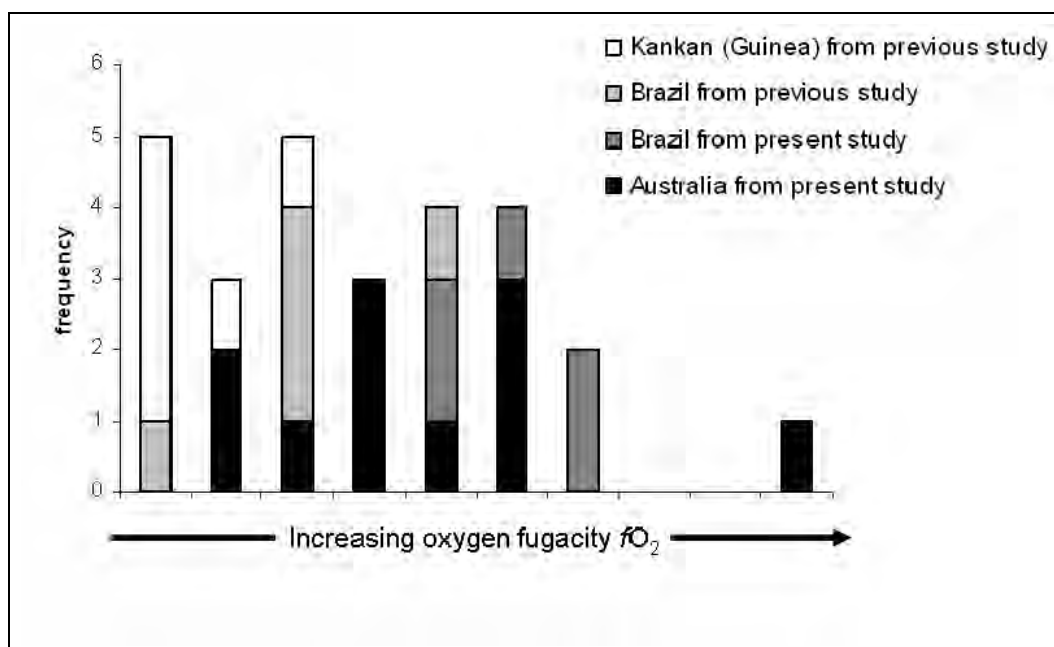


Fig. 3.2-13: Estimated relative oxygen fugacity of (Mg,Fe)O ferropicrlase inclusions in diamonds (see text for details of the estimation)

**j.** *Investigation of diamond-forming media by transmission electron microscopy of sections produced by focused ion beam technique (V. Stagno, N. Miyajima, and C.A. McCammon; H. Ohfuji, T. Sanehira, and T. Irifune/Ehime; A. Shiryayev/Moscow)*

Natural diamonds represent an important and unique tool to study geochemical processes occurring in the Earth's deep interior. During their growth, diamonds may trap fluids and/or mineral inclusions, which are considered pristine witnesses of the surrounding diamond forming-media. Further, the composition of these inclusions allows us to infer the chemical and physical conditions at which diamond is stable in the mantle relative to carbonates.

In this study, TEM assisted by the Focused Ion Beam (FIB) technique has been employed to investigate micro to nano inclusions in a natural diamond (BR5) from Brazil. The diamond, fibrous and cubic in shape, was previously laser-cut into a plate for other scientific investigations (*e.g.*, isotopic signatures, speciation of nitrogen and bulk chemical composition of the inclusions). This diamond is remarkable because the chemistry of micro-inclusions suggests a gradual evolution of growth medium as previously discussed in the literature: the inner part grew from silicic fluid while the outer part grew from carbonate-rich fluids.

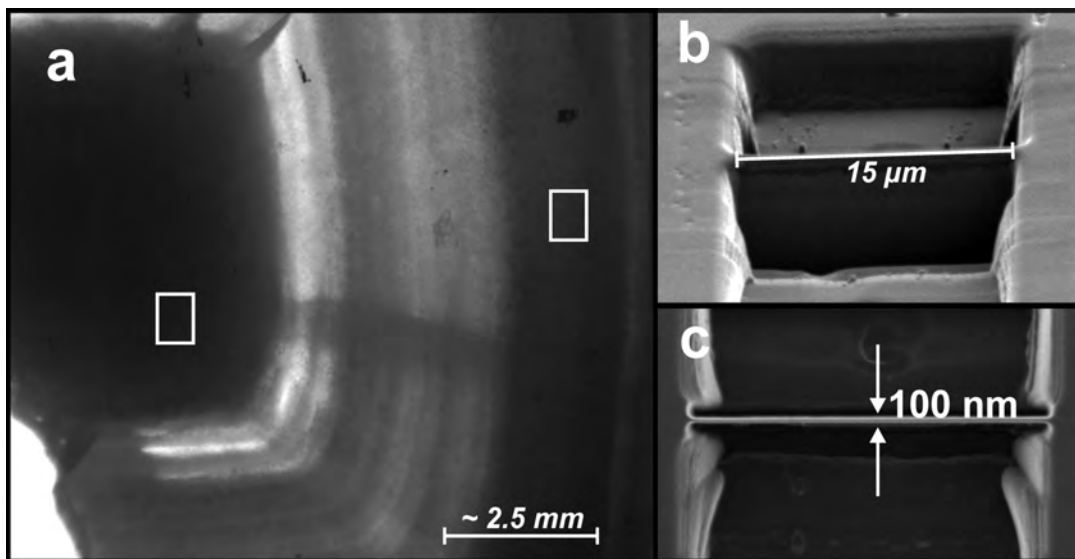


Fig. 3.2-14: (a) BR5 diamond observed using an optical microscope. Squares indicate the two selected areas for the FIB-based TEM foil preparation. (b), (c) Secondary electron images of the two final milling pits showing the typical size of FIB foils ready to be removed.

The FIB technique is an ideal tool for TEM sample preparation as it allows fabrication of electron-transparent foils from any region of interest. Foils were prepared with typical dimensions of  $15 \times 10 \times 0.1 \mu\text{m}$  from both the inner and outer part of the diamond (Fig. 3.2-14) using a JEOL 9310 Focused Ion Beam instrument with an ion beam generated from a gallium

(Ga) liquid-metal ion source. Removal of the foil from its excavation pit was performed using an optical microscope with micromanipulator on which a glass needle was attached. The foil was then placed on a standard TEM copper grid with a carbon film. Structural and mineralogical information on the inclusions in the diamond foils were obtained using selected area electron diffraction (SAED) that provides diffraction patterns from very small volumes. Qualitative analysis of chemical composition was obtained by EDX analysis.

Our first results of FIB/TEM studies on BR5 diamonds reveal the presence of many crystalline and fluid inclusions. One inclusion from the inner part was identified as coesite based on its chemistry and the diffraction pattern. Inclusions in a foil from the outer part of BR5 are chemically complex, containing Ti, P, K, Si, Fe, Mg, Ca and O as shown by EDX analysis. Electron diffraction patterns on these inclusions suggest the presence of both Si- rich and CO<sub>2</sub>- rich phases (Fig. 3.2-15). An amorphous inclusion found in the outer part of the diamond is interpreted to represent residues of evaporated fluids, impregnated by the Ga beam during FIB foil preparation.

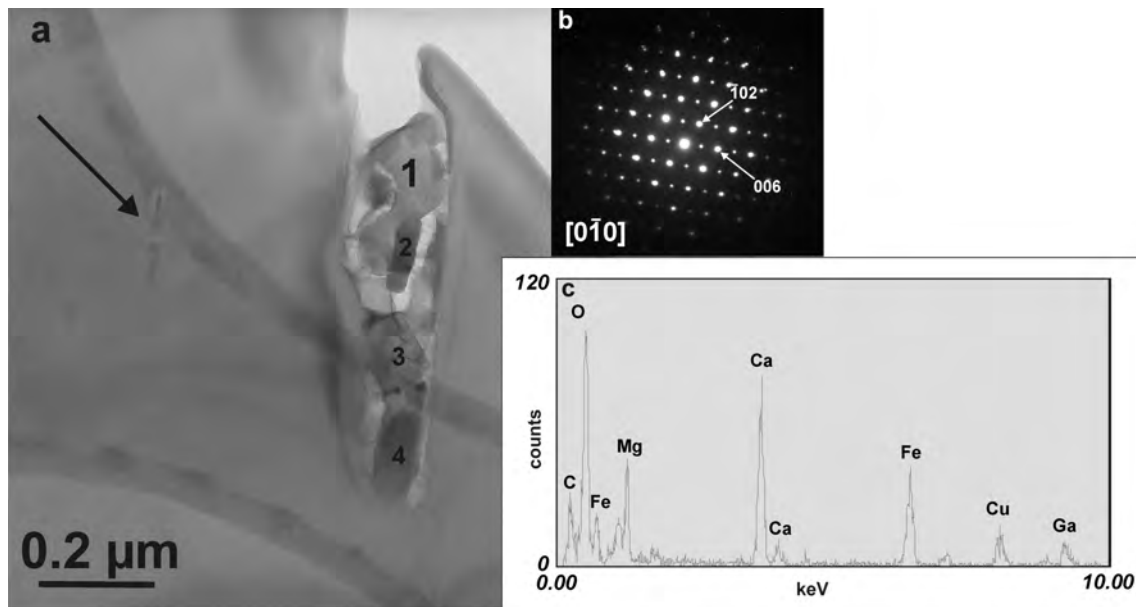


Fig. 3.2-15: (a) Bright Field TEM image showing many mineral inclusions with different contrast and relief. The arrow shows nano-inclusions oriented parallel to the investigated micro-inclusions. In (b) the electron diffraction pattern from grain 1 is shown, suggesting a CO<sub>2</sub>-rich phase with a calcite-like structure. In (c) an EDX spectrum of the same grain is displayed. The Ga peak occurs as a consequence of its implantation into the sample surface during the sputtering process. The thickness of this “amorphous” layer is about 5-15 nm on both surfaces and does not affect the physical properties of the bulk sample.

Chemical analyses assisted by electron diffraction patterns of a foil recovered from the outer part of BR5 demonstrate the coexistence of silicic inclusions (*i.e.*, a 10Å phase) with apatite

and CO<sub>2</sub>- rich inclusions which may suggest an origin due to precipitation from saturated fluids in the diamond stability field. In order to determine the redox conditions at which the BR5 diamond may have formed, further measurements will be carried out by Electron Energy Loss Spectroscopy to measure Fe<sup>3+</sup>/Fe<sup>2+</sup> ratios on Fe-bearing mineral phases. These ratios will be compared to experimental data on the distribution coefficients of iron in rock-forming minerals equilibrated with elemental carbon at mantle conditions.

**k. Highly calcic carbonatites at moderate depths in the Earth and solidus reactions of simplified carbonated peridotite in the system CaO-MgO-Al<sub>2</sub>O<sub>3</sub>-SiO<sub>2</sub>-CO<sub>2</sub> (S. Keshav, G.H. Gudfinnsson/Reykjavík, and D.C. Presnall/Texas)**

In an effort to clarify melting phase relations and solidus reactions of carbonated peridotite at moderate depths (350-750 km) in the Earth, last year, we published results in the system CaO-MgO-SiO<sub>2</sub>-CO<sub>2</sub> (CMS-CO<sub>2</sub>; annual report 2008, BGI). In this system it was observed that while the melting curve (solidus) of simplified carbonated peridotite had a positive clapeyron slope between 12 and 14 GPa, the same underwent a rather steep decline between 14 and 16 GPa. In other words, the melting curve of carbonated peridotite had a negative clapeyron slope between the aforementioned pressures. However, after 16 GPa, the solidus of carbonated peridotite resumed its positive trajectory in pressure-temperature space. With increasing pressure, the solidus (univariant) of carbonated peridotite in the system CMS-CO<sub>2</sub> intersects the following phase assemblage:

12 GPa/1565 °C - forsterite + clinoenstatite + clinopyroxene + magnesite + melt

14 GPa/1625 °C - wadsleyite + majorite + cpx + magnesite + melt

16 GPa/1510 °C - wadsleyite + majorite + cpx + magnesite + melt

20 GPa/1725 °C - ringwoodite + majorite + calcium perovskite + magnesite + melt

26 GPa/1875 °C - magnesium perovskite + periclase + calcium perovskite + magnesite + melt

Therefore, if correct, such a ‘dip’ in the solidus of carbonated peridotite would have consequences not only for the seismically imaged low-velocity zones at such depths (400-550 km), but also might indicate carbonate-rich areas in the Earth’s mantle. Hence, by merely tracking the solidus of carbonated peridotite in pressure-temperature projections, one might be in a position to identify geochemical heterogeneity at moderate depths in the Earth.

With an aim to sequentially add more chemical components and to test if such a dip in the solidus of carbonated peridotite really exists at depths approaching the Earth’s transition zone, here we report solidus reactions of carbonated peridotite in the system CaO-MgO-Al<sub>2</sub>O<sub>3</sub>-SiO<sub>2</sub>-CO<sub>2</sub> (CMAS-CO<sub>2</sub>). All the experiments were performed in traditional, split-sphere, multianvil devices at BGI. Starting compositions were composed of a mixture of silicate glass plus magnesite.

In the CMS-CO<sub>2</sub> system the solidus of simplified carbonated peridotite is univariant. As alumina is added to the system, however, the variance increases and melting relations of a

peridotitic composition change from being isobarically invariant at 14 GPa (six phases) to isobarically univariant at 16-26 GPa (five phases). The reason for the change in variance is that there are six phases present at the solidus at 14 GPa, forsterite + orthopyroxene (opx) + clinopyroxene + garnet + magnesite + melt. However, since opx disappears from the peridotitic mantle after 14 GPa, there are only 5 phases (as listed below) that take part in defining the solidus reactions at 16-26 GPa. Hence, in pressure-temperature space, the solidus at 16-26 GPa occurs along divariant surfaces, meaning that a particular phase assemblage is stable over a certain temperature interval. This also means that the solidus, to some degree, depends on the bulk composition of the peridotite analog in the system CMAS-CO<sub>2</sub>. The main influence of adding Al<sub>2</sub>O<sub>3</sub> to CMS-CO<sub>2</sub> is to only very slightly dilute the liquid compositions produced here. In the system CMAS-CO<sub>2</sub>, all the alumina is hosted in opx, cpx, garnet, calcium silicate perovskite, and magnesium silicate perovskite. Peridotitic mantle has approximately 4 % Al<sub>2</sub>O<sub>3</sub>, an amount that only has a small effect on the melting phase relations and liquid compositions. Hence, the solidus of a mantle composition with this amount of Al<sub>2</sub>O<sub>3</sub> will be only slightly lower than in the system CMS-CO<sub>2</sub>. With increasing pressure in the system CMAS-CO<sub>2</sub>, we encounter the following assemblages:

- 14 GPa - forsterite + orthopyroxene + clinopyroxene + garnet + magnesite + melt (univariant)
- 16 GPa - wadsleyite + clinopyroxene + garnet + magnesite + melt (divariant)
- 20 GPa - ringwoodite + garnet + calcium perovskite + magnesite + melt (divariant)
- 26 GPa - magnesium perovskite + periclase + calcium perovskite + magnesite + melt (divariant)

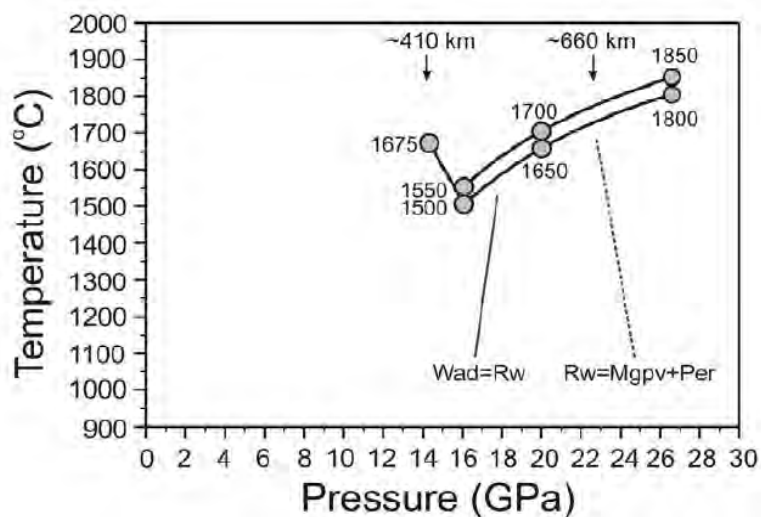


Fig. 3.2-16: Pressure-temperature projection displaying the solidus curve for carbonated peridotite in the system CMAS-CO<sub>2</sub> as determined in this study. The sole, filled, grey circle at 14 GPa represents isobaric invariance, while the rest of the data-set is characterized by divariant nature (P-T divariant solidus surface) of melting phase relations. Numbers next to the grey circles denote temperature in centigrade. For clarity, only boundary lines denoting phase transformations in wadsleyite-to-ringwoodite and the dissociation of ringwoodite to a mixture of Mgpv plus periclase, are shown.

As in the system CMS-CO<sub>2</sub>, the most remarkable feature of the phase relations in CMAS-CO<sub>2</sub> is the abrupt drop of ~ 150 °C in the solidus of model carbonated peridotite between 14 and 16 GPa (Fig. 3.2-16). The solidus has a positive P-T slope above 16 GPa, and up to at least 26 GPa (Fig. 3.2-16). Concomitant with the temperature drop between 14 and 16 GPa, the composition of the melt also changes dramatically (Fig. 3.2-17). At 14 GPa, the solidus melts are magnesiocarbonatites with Ca# (molar Ca/Ca+Mg\*100) of ~ 37, while at 16 and 20 GPa, the melts change to become highly calcic with Ca# of ~ 61. This dramatic change in the melt composition, within an interval of 2-6 GPa, is surprising because the coexisting carbonate continues to be nearly end-member magnesite with a limited amount of calcite solid solution. Hence, although magnesite contributes all the CO<sub>2</sub> to the melt, the melting reaction must include a large contribution from a Ca-rich silicate. This behaviour differs from that observed for the solidus of carbonate-bearing garnet lherzolite in the system CMAS-CO<sub>2</sub> at lower pressures (3-8 GPa), where contributions from magnesite are a larger part of the melting reaction.

The shape of the carbonated peridotite solidus in the CMS-CO<sub>2</sub> system is maintained in CMAS-CO<sub>2</sub>. At 16-26 GPa, the upper and lower filled grey circles in Fig. 3.2-16 indicate the presence of magnesite at both of these temperatures. At higher temperatures magnesite disappears from the assemblage. Once magnesite disappears the solidus is no longer contained in the P-T plane and liquid compositions are no longer tied in the P-T plane. Compositions of liquid coexisting with the correct buffering assemblage in the system CMAS-CO<sub>2</sub>, are almost identical to those observed in the system CMS-CO<sub>2</sub> (annual report 2008, BGI).

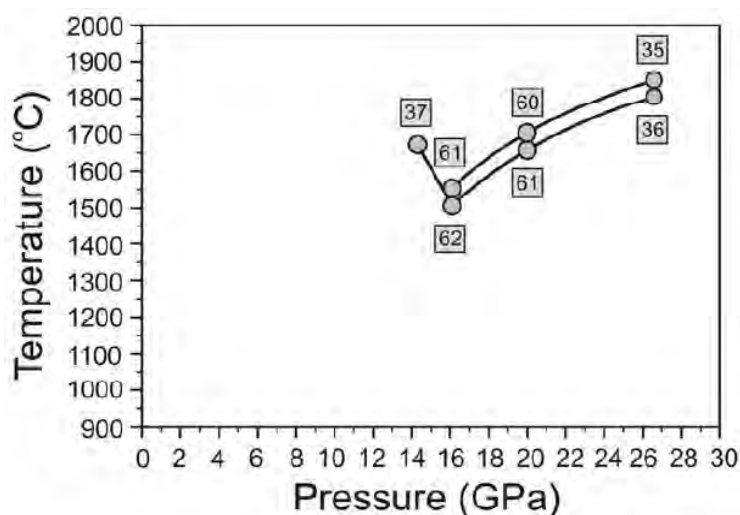


Fig. 3.2-17: Liquid (melt) compositions in terms of Ca# (molar [Ca/Ca+Mg]\*100) as determined here in the system CMAS-CO<sub>2</sub>. Numbers enclosed in grey squares represent Ca# of liquid compositions. Note that owing to isobaric invariance at 14 GPa, only one liquid composition is shown, while in the range 16-26 GPa wherein melting phase relations are divariant, two liquid compositions are projected. Of particular relevance is the striking similarity in liquid compositions in the two systems, CMS-CO<sub>2</sub> (annual report 2008, BGI) and CMAS-CO<sub>2</sub> studied, very significantly demonstrating, that addition of alumina to CMS-CO<sub>2</sub> causes only slight differences in solidus temperature at these pressures.

**1. Some complications in the melting of carbonated peridotite at 2-3 GPa (D. Novella, and S. Keshav)**

Carbonatite magmas are composed almost entirely of Ca, Mg, Fe and Na carbonates. Although carbonatites are a volumetrically minor component, they are considered to have a strong impact on the Earth's mantle. For example, carbonatitic melts may influence the trace element geochemistry of mid-oceanic ridge basalts, and combined with their high mobility, carbonatitic melts represent very effective metasomatic agents (influencing the mantle either chemically or modally), and may also play a part in affecting velocities of seismic waves in the mantle.

Different theories on the origin of carbonatites have been proposed: (1) production by liquid immiscibility from alkaline melts, (2) fractional crystallization from alkaline-silicate melts, and (3) incipient melting of upper mantle peridotite containing CO<sub>2</sub>. In the light of this complexity, experiments on model systems are extremely useful in order to understand the genesis of these unusual magmas. Previous experimental studies indicate that the temperatures at which calcic carbonatites are produced extend nearly to the CO<sub>2</sub>-free solidus at a pressure of 3.0-3.2 GPa, but are considerably lower than this solidus at higher pressures. Hence, based on these studies, it appears that the region wherein calciocarbonatites are being produced might be expanding with decreasing pressure.

Against this background, we have focused on melting phase relations of simplified, carbonated peridotite in the system CMAS-CO<sub>2</sub>. Piston-cylinder experiments to determine phase relations at 2-3 GPa were conducted. Starting mixtures (silicate glass + magnesite) were prepared and confined in Pt capsules. The melting experiments were performed at temperatures ranging from 1325 °C to 1550 °C, which corresponds to the temperature interval between the carbonated and the dry peridotite solidus (Fig. 3.2-18). Each experiment was kept at the desired P-T conditions for roughly 6 hours.

The present work started with the determination of melting reactions at 3 GPa. Experiments conducted along this isobar show that carbonatitic melts are produced at 1475 °C and 1500 °C, temperatures close to the dry peridotite solidus (Fig. 3.2-19). These runs contain highly-calcic melts (10 wt.% MgO, 1 wt.% Al<sub>2</sub>O<sub>3</sub>, 40 wt.% CaO, 4 wt.% SiO<sub>2</sub> and 42 wt.% CO<sub>2</sub>) in equilibrium with the peridotite buffer assemblage consisting of forsterite (fo), orthopyroxene (opx), clinopyroxene (cpx) and garnet (gt). Therefore, there is good agreement between our data and previous work performed at 3 GPa in the Al<sub>2</sub>O<sub>3</sub>-free system CMS-CO<sub>2</sub>.

At 2.8 GPa the carbonatitic-melt region extends also over a considerable temperature range. Carbonatitic melts are produced from 1325 °C to 1525 °C (Fig. 3.2-19), and are in equilibrium with forsterite, opx, cpx, and garnet. The production of basaltic melt at this pressure is observed only at 1550 °C, 10 °C lower than the melting point of dry, simplified peridotite (Fig. 3.2-19). At this pressure, the change in melt composition, from calcic-carbonatitic to silica-rich glass, is dramatic, occurring in a temperature range of only 25 °C.

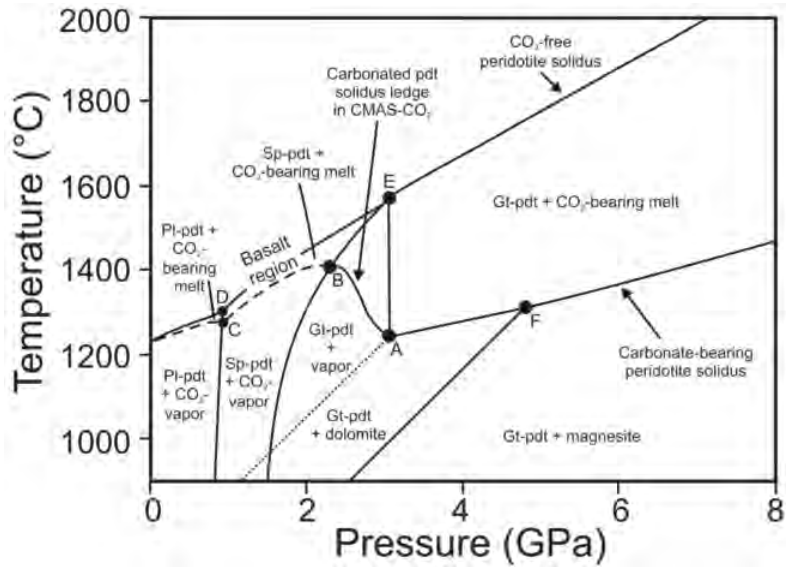


Fig. 3.2-18: Pressure-temperature diagram showing the solidus of model plagioclase, spinel and garnet peridotite in the presence or absence of  $\text{CO}_2$  (corresponding to the systems CMAS- $\text{CO}_2$  and CMAS, respectively). The curve between the invariant points A and B is the so-called  $\text{CO}_2$ -ledge. Subsolidus curves determining the stability field of plagioclase, spinel and garnet in equilibrium with the peridotite phase assemblage (forsterite + clinopyroxene + orthopyroxene) and melt, are also shown.

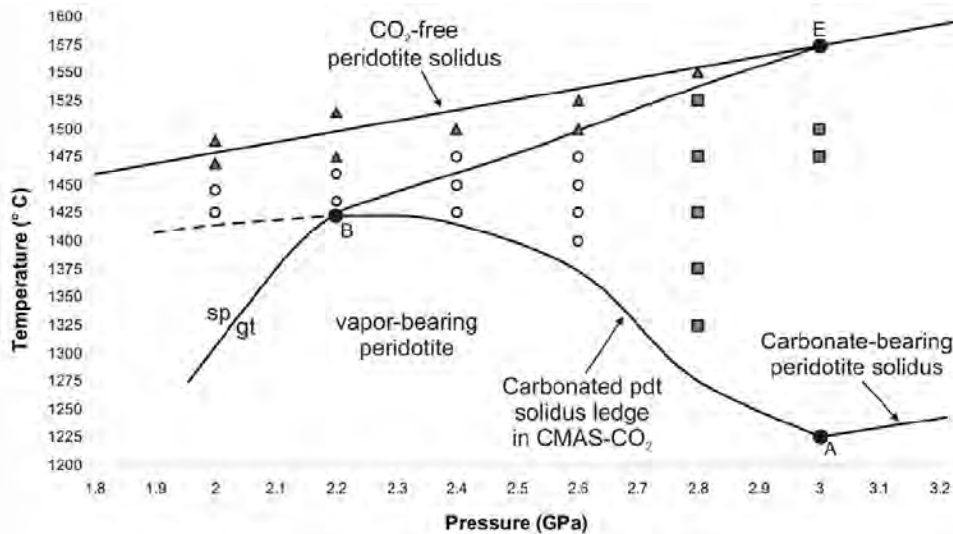


Fig. 3.2-19: Pressure-temperature diagram displaying melting curves for volatile free (in CMAS) and carbonated (CMAS- $\text{CO}_2$ ) peridotite, and the subsolidus univariant reaction curve for the spinel-to-garnet peridotite transition. The latter curve intersects the carbonated and dry peridotite solidus curves in the systems CMAS- $\text{CO}_2$  and CMAS at points B and E, respectively. Our experimental data are shown by different symbols: filled, grey squares - carbonatitic melts; filled, grey triangles - silicate melts; open, white circles - experiments containing both carbonatitic and silicate melt. Filled circles named A, B, and E are invariant points. They correspond to the following phase assemblage. A: fo + cpx + opx + gt + dolomite +  $\text{CO}_2$  + melt; B: fo + cpx + opx + sp + gt +  $\text{CO}_2$  + melt; E: fo + cpx + opx + sp + gt + melt.

At lower pressures, from 2.0 to 2.6 GPa, complexities in the melting of carbonated peridotite were discovered. In the experiments conducted over this pressure range (2.0-2.6 GPa), the melting behaviour of carbonated peridotite shows similar behaviour, and thus can be considered together. For instance, starting at temperatures 10-25 °C higher than the carbonate ledge (Fig. 3.2-19), the crystalline phases forsterite, cpx, and spinel/garnet appear to be in equilibrium with two liquids, one broadly basaltic (10-20 wt.% CO<sub>2</sub>; 30-40 wt.% SiO<sub>2</sub>), and one carbonatitic (40-45 wt.% CO<sub>2</sub>; < 6 wt.% SiO<sub>2</sub>). These two liquids are never observed in equilibrium with opx (Fig. 3.2-20). Even when opx was artificially saturated in the starting materials, this phase was never found as a stable phase when the two liquids were present. At higher temperatures only one type of melt was found to be in equilibrium with forsterite, and sometimes cpx/CO<sub>2</sub>-vapor. This silicate melt contains approximately 10 wt.% dissolved CO<sub>2</sub>. The transition from the two-liquids region to the one in which only a single, silicate melt phase exists occurs between 1445 °C and 1500 °C, depending on the pressure conditions.

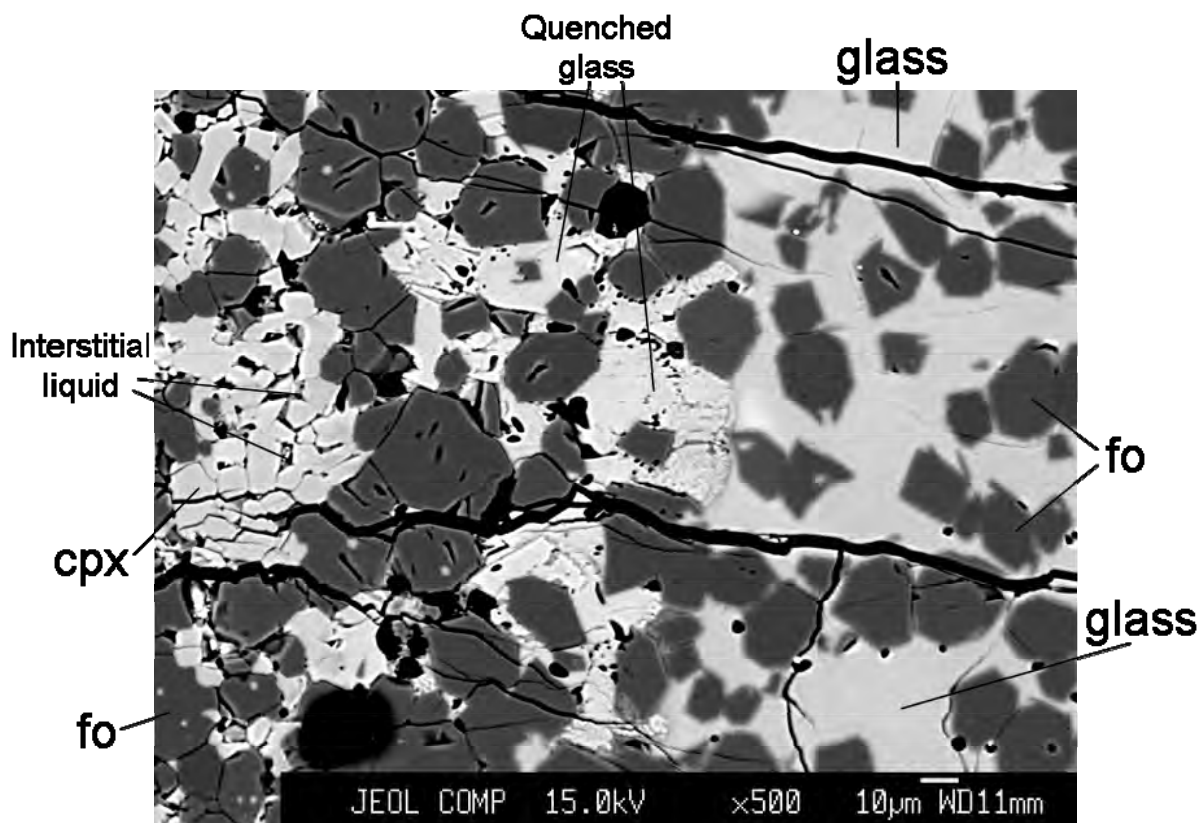


Fig. 3.2-20: Backscattered electron (BSE) image showing the run products of an experiment performed at 2.2 GPa and 1435 °C. Both silicate glass and an interstitial, carbonatitic liquid are observed in equilibrium with fo and cpx, with spinel occurring as tiny, high relief crystals contained in forsterite. The black-holes are possibly vapor bubbles or crystals removed during polishing. Also, it is possible to recognize quenched features in silicate melt. In BSE images, the quenched silicate melt appears slightly lighter compared with the normal glass but substantial differences in chemical composition are not observed (maximum difference of 4 wt.% of oxides, relative).

To date, immiscibility between carbonatites and silicate melts has been experimentally produced only when carbonatitic and silicate melts are alkalic. Such experiments, although useful, are far from realistic mantle compositions. In contrast, our experiments should be quite representative, showing for the first time that basaltic-carbonatitic liquid immiscibility in simplified peridotite is possible also in alkali-free systems. Moreover, the stability field of carbonatitic magmas at pressures of 2-3 GPa covers a wide temperature range starting at the CO<sub>2</sub>-ledge and ending 25-60 °C below the dry peridotite solidus. From this observation, we can conclude that the region where calcio-carbonatite magmas can exist as primary melts in the Earth's mantle dramatically expands at shallower depths, with the production of such magmas possible at pressures as low as 2 GPa (corresponding to depths of roughly 60 km in the Earth).

**m. Partitioning of U and Th between diopside, pyrope and aqueous fluid, and its implication to the composition of island arc magmas (E. Bali, A. Audétat, and H. Keppler)**

The solubility of U and Th in aqueous solutions at P-T-conditions relevant for subduction zones was studied by trapping uraninite or thorite saturated fluids in the form of synthetic fluid inclusions in quartz and analyzing their composition using laser-ablation ICPMS. Our experimental results demonstrate that uranium is virtually insoluble in aqueous fluids at reducing conditions imposed by the Fe-FeO buffer, whereas its solubility increases with increasing  $fO_2$  buffered by Co-CoO to Re-ReO<sub>2</sub>, at 2.6 GPa and 800 °C. Furthermore, U solubility in the fluid phase strongly increases with fluid salinity. In contrast, Th solubility does not vary significantly with changing oxidation conditions or changing fluid salinity. In order to quantify the effect of fluid-rock interaction in the subducted slab and mantle wedge the solubility of U and Th in diopside and garnet equilibrated with uraninite/thorite saturated fluid was also determined.

Knowing the maximum solubility of U and Th in the silicate phases and in the aqueous fluid we can estimate the solid/fluid partition coefficients. Figure 3.2-21a-c shows the variation of U and Th partitioning between fluid and diopside or pyrope. Uranium partitions into the fluid phase at elevated fluid salinities with respect to both diopside and garnet. Moreover, at oxidation conditions above the FMQ buffer  $D_{U}^{cpx/fluid}$  is below unity.  $D_{U}^{cpx/fluid}$  increases with decreasing  $fO_2$  at all fluid salinities. Decreasing fluid salinity also leads to an increase in  $D_{U}^{cpx/fluid}$ . In the case of garnet, the same relationships with  $fO_2$  conditions and fluid salinity can be observed. Moreover, U becomes compatible in garnet at fluid salinities below 5 wt.% NaCl<sub>equiv</sub>. In terms of Th partitioning no apparent change is observed with any of the studied variables, as the solubility of Th in both the fluid phase and silicate minerals seem to be independent of fluid salinity and  $fO_2$  conditions.

Figure 3.2-21d shows calculated, primitive mantle normalized U/Th(N) ratios in aqueous fluids equilibrated with MORB eclogite. These values were calculated by assuming that only garnet and clinopyroxene are present in the eclogitic assemblage. The enrichment of U over Th in the fluid phase increases if the modal amount of clinopyroxene in the eclogite increases.

The fluid phase is always enriched in U over Th compared to primitive mantle if the fluid contains significant amount of chlorine. In Cl-free fluids and  $fO_2$  conditions between Co-CoO and Re-ReO<sub>2</sub>, U enrichment over Th occurs only if the eclogite is clinopyroxene-rich.

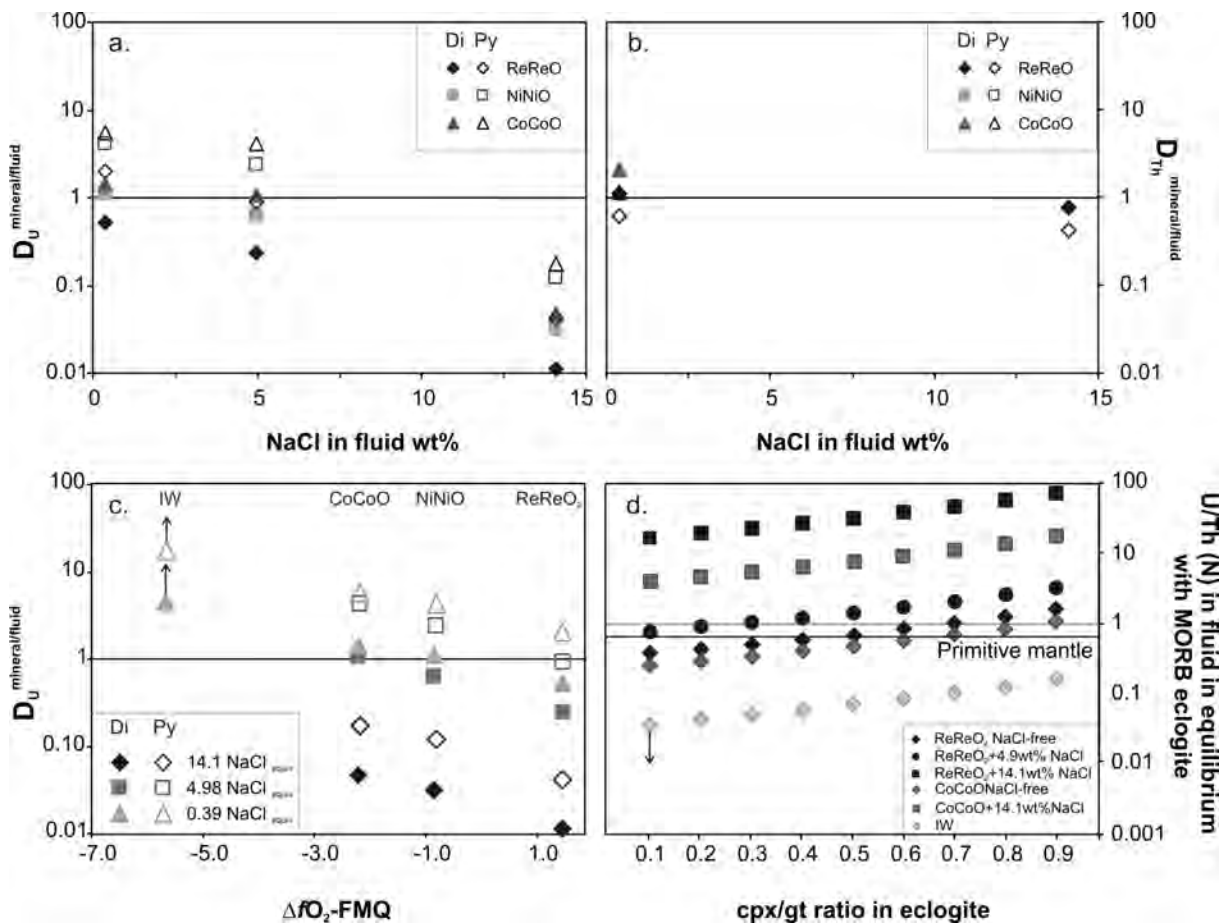


Fig. 3.2-21: Partition coefficients of U and Th between diopside (Di), pyrope (Py) and aqueous fluid as a function of fluid salinity (a, b) and  $fO_2$ -conditions (c) at 26.1 kbar and 800 °C. IW: iron-wüstite buffer; CoCoO: Co-CoO buffer; NiNiO: Ni-NiO buffer; ReReO<sub>2</sub>; Re-ReO buffer. The partition coefficients for U at oxidation conditions buffered by iron-wüstite in (c) are minimum values, as the U concentration in the fluid was below the detection limit. (d) shows the composition of aqueous fluid in equilibrium with MORB eclogite as a function of oxidation conditions, fluid salinity, and the clinopyroxene/garnet ratio in the eclogite. Fluid compositions were calculated by assuming that only clinopyroxene and garnet are present as solid phases.

Silicate melt inclusions studied in primitive arc magmas commonly contain up to 5 wt.% H<sub>2</sub>O, with some even reaching values up to 10wt.%. Figure 3.2-22 shows how the dissolution of 5 to 10wt.% aqueous fluid into the melt changes its U/Th(N) ratio compared to that of dry spinel or garnet peridotite partial melts. Dissolution of Cl-free fluid does not change the melt composition, as it is too dilute in both U and Th at any studied  $fO_2$  conditions. Similarly, the contribution of strongly reduced fluid will not lead to significant enrichment of Th over U in

the melt, as the absolute Th content of the fluid is very low. In contrast, if the dissolved fluid is saline, it can significantly increase the U/Th(N) ratio of the melt even at moderate oxygen fugacities. This is in accordance with previous results suggesting that subduction zone fluids require chlorine concentrations on a weight percent level to explain the H<sub>2</sub>O-K<sub>2</sub>O-Cl systematics observed in arc and back arc lavas.

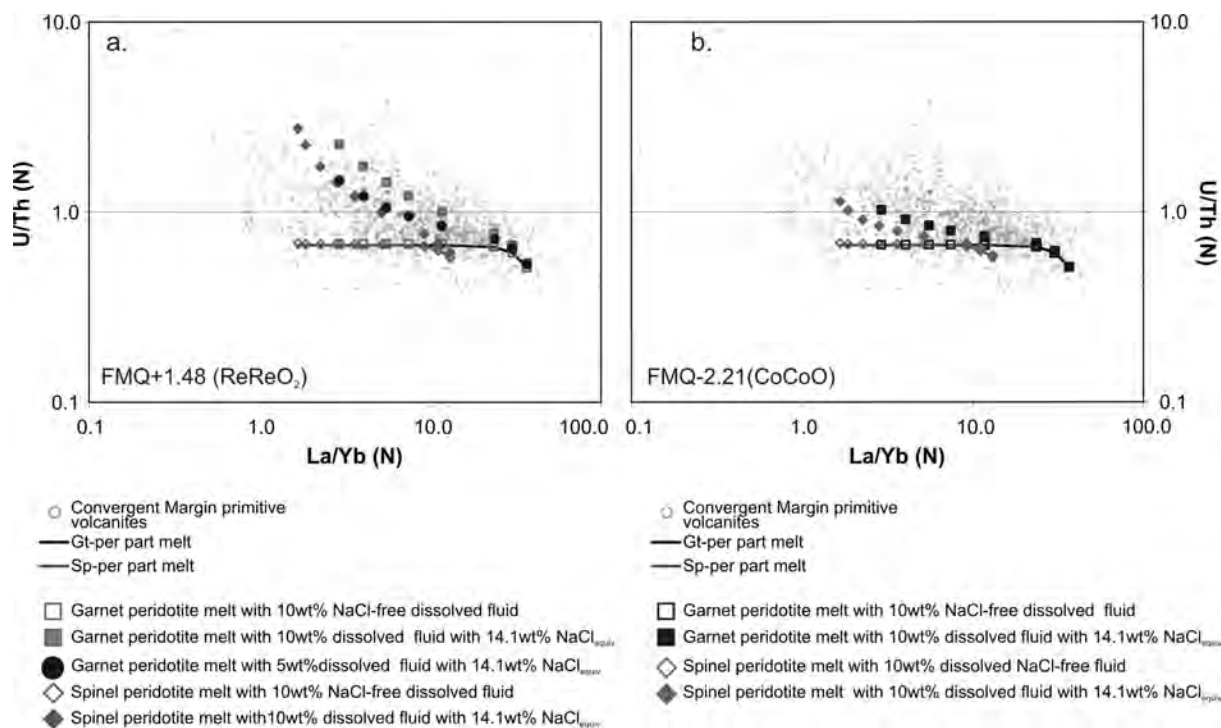


Fig. 3.2-22: Distribution of MORB-normalized U/Th and La/Yb ratios in primitive basalts from convergent margins compared to dry partial melts of garnet and spinel lherzolites and partial melts containing 5 to 10wt.% of dissolved aqueous fluid with different salinities and oxidation conditions. A fluid composition in equilibrium with MORB eclogite having a clinopyroxene:garnet ratio of 60:40 was used for this calculation (see Fig. 3.2-21d). Note that Cl-free fluids are too U and Th-poor to change the melt compositions, whereas saline fluids have the capacity to increase the U/Th (N) of the melt even at relatively reducing conditions (FMQ-2.21). Data source of the basalt analyses is the Georock database at <http://georoc.mpch-mainz.gwdg.de/georoc/>.

**n.** Partitioning of Nb and Ta between rutile and felsic melt and the fractionation of Nb/Ta during slab melting (X.L. Xiong, H. Keppler, A. Audétat, H. Ni, and Y. Li)

Rutile is the major carrier of Nb and Ta in eclogites and controls the budget and distribution of Nb and Ta during slab melting, which produces felsic crustal magmas and refractory rutile-bearing eclogites. The partitioning of trace elements between crystal and melt is a complex function of several parameters, such as pressure, temperature, water content, oxygen fugacity,

crystal composition, and melt composition. Many experiments on rutile/melt Nb and Ta partitioning have been conducted over a range of conditions. Existing data show that the rutile/melt partition coefficient  $D_{\text{Nb}}$  is always lower than  $D_{\text{Ta}}$  ( $D_{\text{Nb}}/D_{\text{Ta}} < 1.0$ );  $D_{\text{Nb}}$ ,  $D_{\text{Ta}}$  and perhaps  $D_{\text{Nb}}/D_{\text{Ta}}$  increase with increasing melt polymerization and melt alumina saturation index; oxygen fugacity appears to have no effect on the partitioning. The effects of temperature, pressure and  $\text{H}_2\text{O}$  are rarely systematically investigated. The existing rutile/melt partitioning results ( $D_{\text{Nb}}/D_{\text{Ta}} < 1.0$ ) predict that rutile will impart higher Nb/Ta to the melts, but lower Nb/Ta to the rutile-bearing residues and thus exclude the refractory rutile-bearing eclogites produced by slab melting as a possible reservoir of superchondritic Nb/Ta (Nb/Ta = 14.2 in the average MORB and 19.9 in chondrite). They also fail to account for the general low Nb/Ta ratios of continental crust and Archean TTG magmas (tonalities-trondhjemites-granites) relative to their basalt precursors.

Temperature and  $\text{H}_2\text{O}$  are the key factors for triggering slab melting and the breakdown of amphibole has been widely accepted to be the most important water source for the melting of subducting slabs. However, we note that nearly all the existing experiments on rutile/melt Nb and Ta partitioning were conducted at temperatures higher than 950 °C, which overlap little with the P-T field of amphibole breakdown and leave a temperature space of more than 200 °C above the solidus not investigated. Furthermore, we have demonstrated using data on  $\text{TiO}_2$  solubility in melts and minerals that slab melting at the amphibolite to eclogite transition nearly always occurs in the presence of rutile, and that melting temperatures for TTG generation are generally lower than 950 °C. Therefore, the existing rutile/melt Nb and Ta partitioning experiments at temperatures higher than 950 °C probably provide limited insight into Nb/Ta fractionation during slab melting. Clearly, more studies, especially on the effects of temperature and  $\text{H}_2\text{O}$ , are required.

In order to fully assess the role of rutile in fractionation of Nb/Ta during slab melting and crust-mantle differentiation, rutile/felsic melt partition coefficients for Nb and Ta at 1.5-3.5 GPa, 850-1350 °C and ~ 5.0-30 wt.%  $\text{H}_2\text{O}$  were measured using a piston cylinder press.  $D_{\text{Nb}}$ ,  $D_{\text{Ta}}$  and  $D_{\text{Nb}}/D_{\text{Ta}}$  range from 17 to 246, 34 to 232 and 0.51 to 1.06, respectively. For the tonalitic to trondhjemitic compositions investigated, melt composition appears to have no observable effect on the partitioning; the effect of pressure is also slight; while temperature and  $\text{H}_2\text{O}$  have marked effects.  $D_{\text{Nb}}$ ,  $D_{\text{Ta}}$  and  $D_{\text{Nb}}/D_{\text{Ta}}$  increase with decreasing temperature and  $\text{H}_2\text{O}$  content (Fig. 3.2-23), leading to a reversal of  $D_{\text{Nb}}/D_{\text{Ta}}$  from  $< 1.0$  to  $> 1.0$ . Using the data that approached equilibrium and obeyed Henry's law, expressions describing the dependences of  $D_{\text{Nb}}$ ,  $D_{\text{Ta}}$  and  $D_{\text{Nb}}/D_{\text{Ta}}$  on temperature, pressure and melt  $\text{H}_2\text{O}$  content were obtained:

$$\ln (D_{\text{Nb}})_{\text{rutile/melt}} = -2.589 + 9263/T + 0.185P - 0.041\text{H}_2\text{O} \quad (1)$$

$$\ln (D_{\text{Ta}})_{\text{rutile/melt}} = -0.704 + 6872/T + 0.134P - 0.010\text{H}_2\text{O} \quad (2)$$

$$\ln (D_{\text{Nb}}/D_{\text{Ta}})_{\text{rutile/melt}} = -1.885 + 2377/T + 0.059P - 0.032\text{H}_2\text{O} \quad (3)$$

where  $T$  is in Kelvin,  $P$  is in GPa, and  $H_2O$  is in wt.%. These expressions are applicable to calculate Nb and Ta partitioning coefficients between rutile and felsic melts and Nb/Ta fractionation during partial melting of metabasalt under  $P < 3.5$  GPa and hydrous conditions.

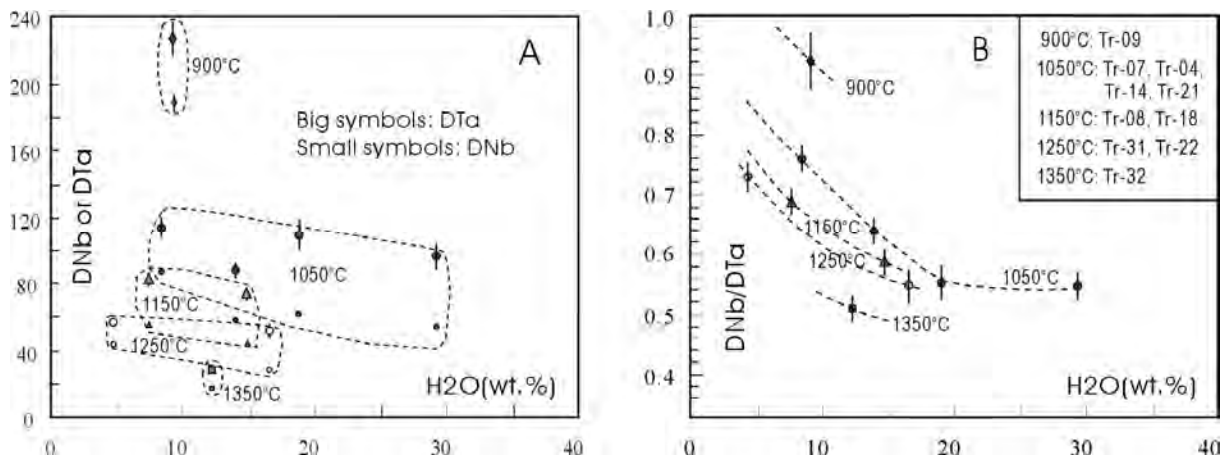


Fig. 3.2-23: Rutile/melt  $D_{Nb}$  or  $D_{Ta}$  vs.  $H_2O$  (A) and  $D_{Nb}/D_{Ta}$  vs.  $H_2O$  (B) for experiments at 2.0 GPa and 900-1350 °C, showing that  $D_{Nb}$ ,  $D_{Ta}$  and  $D_{Nb}/D_{Ta}$  increase with decreasing temperature and  $H_2O$  content.

Our data provide new insights on how rutile controls the Nb/Ta ratios of refractory eclogites and TTG magmas produced by slab melting. The calculated results show that low-temperature and low-degree (< 20 %) melting cannot substantially change the Nb/Ta ratio of rutile-bearing eclogite residues relative to their basalt precursors, whereas high-temperature and high-degree melting leads to lower Nb/Ta ratios in the residues. These results confirm that partial melting of hydrous metabasalt cannot produce rutile-bearing eclogites with superchondritic Nb/Ta. The calculated results also show that Nb/Ta fractionation for the melts relative to their basalt precursors can occur during low-temperature and low-degree melting due to the high  $D_{Nb}$  and  $D_{Ta}$  and variable  $D_{Nb}/D_{Ta}$ , but the fractionation direction depends on  $H_2O$ . Nb/Ta in partial melts will be elevated at melt  $H_2O$  contents higher than ~ 20 %, but will be lowered at lower melt  $H_2O$  contents. In general, dehydration melting leads to low melt  $H_2O$  contents and thus lower Nb/Ta in melts, explaining the low Nb/Ta characteristic of continental crust and Archean granitic magmas.

o. *Sulphide-silicate melt partitioning of ore metals during partial melting of the metasomatized lithospheric mantle (Y. Li, and A. Audétat)*

Studies on mantle xenoliths and orogenic peridotites have shown that metasomatic veins within these rocks almost invariably are enriched in sulphide phases such as monosulphide solid solution and sulphide liquid. Because most ore-forming metals are chalcophile and

concentrated in sulphide, the sulphide-melt partitioning coefficient is a key factor controlling the metal content of magmas generated during partial melting of metasomatized mantle rocks.

Mafic alkaline magmas are considered to be derived by partial melting of metasomatized mantle in intraplate settings or above subduction zones. A major role of mafic alkaline magmas in the formation of epithermal Au deposits and Au-rich porphyry copper deposits has been stressed recently, and it has been suggested that mafic alkaline magmas intruding into the base of large, composite magma chambers may not only supply the ligands (S, Cl, F) necessary for later metal transport by fluids, but also the ore-forming metals themselves.

In addition to the implications for ore genesis, the geochemical behaviour of elements such as Mo, W, As, Ag, Sb, Bi, Sn, Pb, and Zn is generally not well constrained during partial melting of the upper mantle. The fact that element ratios such as Ce/Pb, Sb/Pr, Sn/Sm, W/Ba, Mo/Nd are relatively constant in MORBs and OIBs indicate these elements behave incompatibly, which is consistent with the experimentally determined partition coefficients between silicate melts and residual silicate minerals. However, little is known about the effects of sulphide saturation on the geochemical behaviour of these elements.

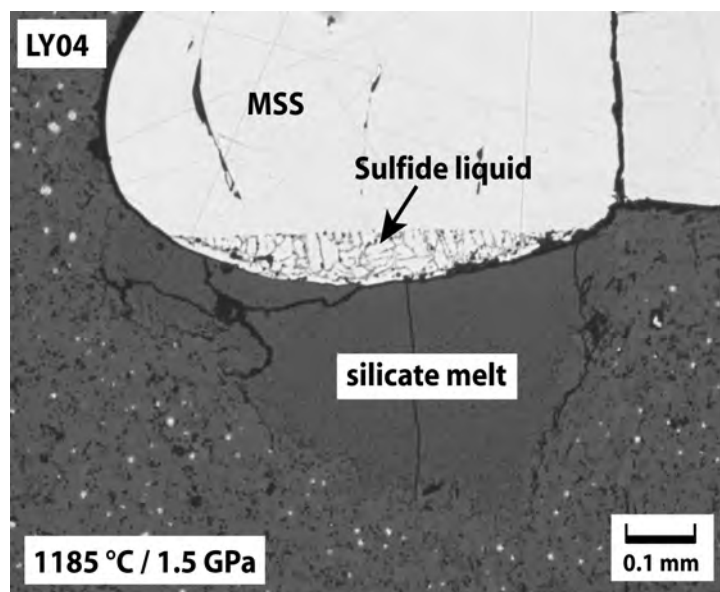


Fig. 3.2-24: Reflected light photomicrograph of a typical run product. Visible are the crystalline starting material with intermixed sulphide grains (on the lower left and lower right), a pool of silicate partial melt, a large grain of monosulphide solution (MSS), and a thin layer of sulphide liquid (unmixed into several phases during quenching) attached to it.

Experiments to measure the partition coefficients between sulphide and alkaline silicate melt were conducted in a piston cylinder apparatus at pressures of 1.5 GPa and temperatures of 1185-1300 °C. The oxygen fugacity was varied between CoCoO and ReReO, covering the

range of  $fO_2$  values reported for mantle rocks in different tectonic settings. The experimental results show that monosulphide solid solution and sulphide liquid both or individually stably coexist with silicate melts. Figure 3.2-24 shows a typical run product consisting of coexisting silicate melt, monosulphide solution and sulphide liquid. All phases were analyzed for their major and trace element contents by LA-ICP-MS. Partition coefficient data show that Cu, Au, Ag, Bi, and Ni are strongly compatible in sulphide phases, with variable preferences for the sulphide liquid relative to monosulphide solid solution. Sn and Sb are slightly compatible in sulphide liquid, but strongly incompatible in monosulphide solid solution. V, Mn, (As, Mo), W, and Zn are strongly incompatible in both sulphide phases, with W, Mo, and As showing a trend of increasing compatibility with decreasing oxygen fugacity. Pb is moderately compatible in sulphide liquid, but strongly incompatible in monosulphide solid solution (see Fig. 3.2-25).

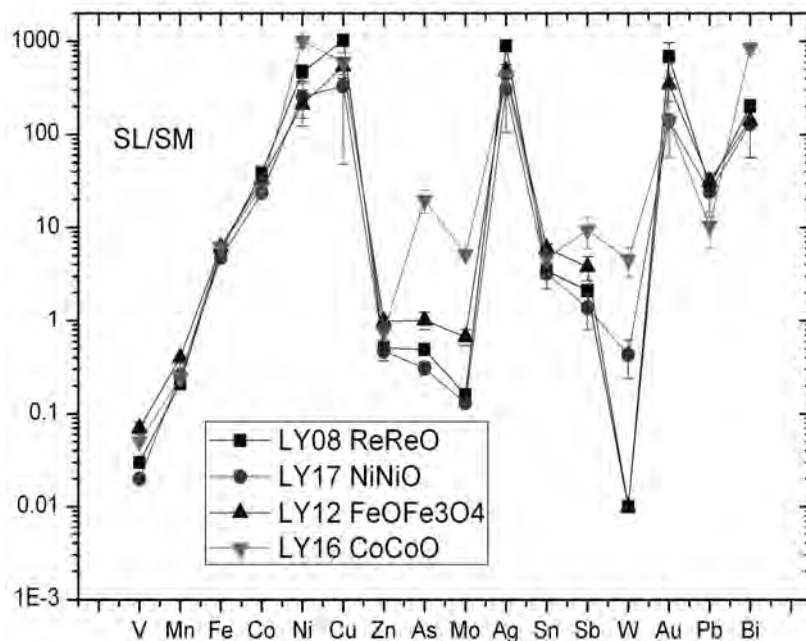


Fig. 3.2-25: Calculated sulphide liquid – silicate melt partition coefficients. Note that except for W, As and Mo, the partition coefficients show only little or no dependence on oxygen fugacity.

With these partitioning data two models are put forward to constrain the metal content in silicate melts during partial melting of lithospheric mantle. In model one it is assumed that there is no sulphide liquid present (only residual MSS). The low partition coefficients between MSS and silicate melts would thus cause the segregated magmas to be richer in Cu, Ag, Bi, and Au than magmas that are equilibrated with a sulphide liquid phase. Model Two assumes that MSS, sulphide liquid and silicate melt coexist in the source region. If the segregated magma ascends rapidly and sulphide liquid is physically entrained in it, then this magma would be even richer in Au, Cu, Bi, and Ag than the one in model one. On the other

hand, if no sulphide liquid is entrained (or is later segregated again), then the magma would be depleted in these elements.

The addition of water from subducted oceanic crust and associated lowering of the mantle solidus in arc settings renders it possible that MSS could be the only sulphide phase present. Thus, model one could explain the formation of gold-rich porphyry copper deposits or epithermal gold deposits in arc settings. Alternatively, the formation of these deposits could also be explained by model two if Au-enriched sulphide is physically entrained in the ascending mafic magmas.

**p.** *Molybdenite solubility in hydrous, pyrrhotite-saturated rhyolite melt at 2 kbar/800 °C (W. Sun, and A. Audétat)*

Recent observations have shown that natural rhyolite magmas are commonly saturated in molybdenite, and that the presence of this mineral could potentially be used as an indicator of magmatic  $fO_2$  and  $fS_2$ . However, no experimental data on molybdenite solubility in silicic magmas is currently available. In this study,  $MoS_2$  solubility in a fluid-saturated, pyrrhotite-saturated haplogranitic melt at 2 kbar / 800 °C was explored as a function of  $fO_2$  and  $fS_2$ .

Powdered haplogranitic glass of the 1 kbar and 720 °C minimum melt composition was sealed with molybdenite,  $\pm$ magnetite and pyrrhotites of variable compositions (to impose variable  $fS_2$ ) into gold or platinum capsules, together with aqueous solutions containing 2 wt.% NaCl, 2.5 wt.% KCl and 1.2 wt.% HCl. Oxygen fugacity was either buffered at NiNiO or CoCoO, or – in those runs in which magnetite was added – was calculated from the pyrrhotite composition after the run. The amount of added fluid was 4.1-11.3 wt.%, which was enough to ensure fluid saturation but was too little to significantly change the melt composition. The prepared capsules were loaded into a hydrothermal rapid-quench autoclave and equilibrated at 800 °C and 2 kbar for seven days, after which they were quenched by *in situ* rapid-quenching to avoid pyrrhotite re-equilibration and exsolution of fluids from the hydrous melt.

The run products consisted of silicate glass, subhedral grains of pyrrhotite, flakes of molybdenite and minor amounts of quartz, feldspar (both crystallized from the melt) and fluid inclusions. A few runs additionally contained magnetite and/or newly formed pyrite. Laser-ablation ICPMS was used to analyze the major and trace element composition of the quenched glass, whereas electron microprobe was used to determine the Fe-S-ratio of the pyrrhotite. Because  $fS_2$  is extremely sensitive to small changes in the Fe-S ratio we used only analyses with totals deviating less than 0.3 wt.% from 100 wt.% for the  $fS_2$  calculation. Measured molybdenum concentrations in the silicate melt ranged from 0.1 to 34  $\mu\text{g/g}$ , showing a clear trend of increasing  $MoS_2$  solubility with increasing  $fO_2$  or decreasing  $fS_2$ . The results are summarized in Fig. 3.2-26.

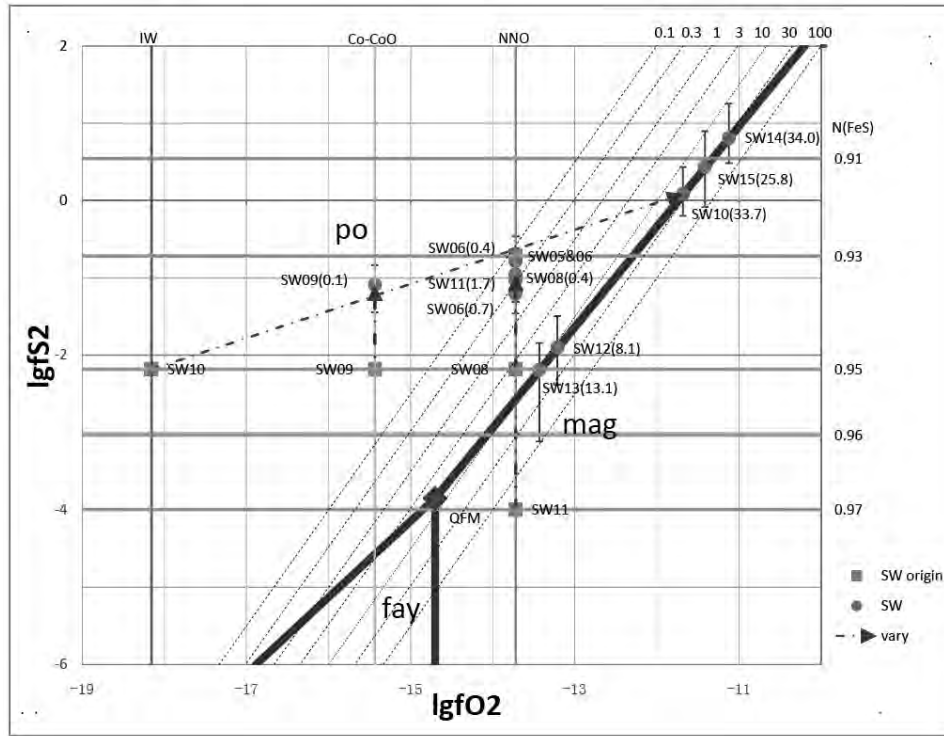
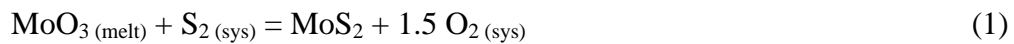


Fig. 3.2-26: Phase relations in the system Fe-Si-S-O and measured molybdenite solubilities in haplogranitic melts saturated in pyrrhotite and fluid ( $\pm$ magnetite,  $\pm$ pyrite) at 800 °C and 2 kbar. Phase boundaries between pyrrhotite (po), magnetite (mag) and fayalite (fay) are shown as dark, thick lines. Experimental data points are shown in round and square symbols, with squares denoting starting conditions imposed by  $f_{O_2}$  buffers and pyrrhotite compositions, and circles denoting the final conditions as implied by mineralogy and EMPA-measurements of pyrrhotite compositions. Average molybdenum contents of the silicate melt (in ppm) measured by LA-ICP-MS are shown in parentheses next to the run numbers. Pyrrhotite compositions are indicated on the right axis and are expressed in  $N(\text{FeS})$ , which is defined as mole fraction FeS in the system  $\text{FeS-S}_2$ . Also shown are dashed lines of constant Mo concentrations in the silicate melt (in ppm) calculated based on equation (2).

Based on available information on the speciation of Mo in silicate melts, molybdenite solubility in silicate melts can be expressed as:



Thus, our experimental data were fitted by an equation of the form  $C_{Mo} = k \times 10^{1.5 \log f_{O_2} - \log f_{S_2}}$ , in which  $k$  is a constant. Assuming that the activity coefficient of  $\text{MoO}_3$  did not vary in concentration range covered by our experiments, we obtained the following, empirical fit (correlation coefficient  $R^2 = 0.973$ ):

$$C_{Mo} [\text{ppm}] = 9.935 \times 10^{18} \times 10^{1.5 \log f_{O_2} - \log f_{S_2}} \quad (2)$$

Molybdenite solubilities at 800 °C and 2kbar calculated from this equation are shown in Fig. 3.2-26 as dashed lines. It is noted that the solubility of molybdenite is extremely sensitive to small variations in  $fO_2$  and  $fS_2$ , changing by one order of magnitude if  $fS_2$  changes by 1 log unit, or if  $fO_2$  changes by 0.6 log units.

Natural rhyolite magmas saturated in molybdenite and magnetite at similar P-T-conditions display a relatively narrow range of Mo concentrations of 2-10 ppm. Most of this compositional range plots close the pyrrhotite-magnetite boundary within the pyrrhotite-only field, suggesting that these magmas were pyrrhotite saturated (or at least close to pyrrhotite saturation). However, further experiments are necessary to constrain the effects of temperature, pressure and melt composition on molybdenite solubility.

**q. The formation of iron sulphide in sediments: Abiotic anaerobic sulphur oxidation by ferric (oxyhydr)oxides (K. Pollok, K. Hellige, and S. Peiffer)**

The formation of sulphides at the oxic/anoxic interface in marine and fresh water sediments as well as in regions of remediation, involves coupled redox reactions linked by the elemental cycles of sulphur and iron. At low temperature, the reaction pathway is complex and involves nanoparticles and metastable phases. For example, acid volatile sulphide (AVS), which is conventionally associated with the black-coloured layers in recent anoxic sediments, is widely assumed to indicate particulate FeS and mackinawite as a major component, which transforms to the stable disulphide pyrite with time. Coprecipitation and adsorption of divalent trace metals on or into FeS may be a common process during the sulphidization of iron oxide minerals by dissolved  $H_2S$  and thus provide an important sink for a number of harmful elements.

Inorganic batch experiments with different ferric (oxyhydr)oxides (lepidocrocite, goethite, ferrihydrite) and dissolved sulphide at pH 7 under anoxic conditions have been performed. Dissolved sulphide diminishes in the first minutes of the reaction with lepidocrocite and ferrihydrite, while the reaction with goethite proceeds considerably slower (1-2 h). All solutions turn black. Chemical analyses indicate the formation of  $S^0$  and acid extractable  $Fe^{2+}$  during the reaction. However, both species drop in concentration at the end of the experiments (2 weeks) and the black colour of the solution disappears. TEM analyses reveal the formation of crystalline mackinawite as 10-20 nm thick sulphur-rich rims on the surfaces of lepidocrocite and goethite after 2h (Fig. 3.2-27). In contrast, no crystalline FeS phase can be detected in experiments with ferrihydrite after 2h reaction. Rims on lepidocrocite exclusively show a continuous, 4 nm thick layer of magnetite.

After two weeks no sulphide rim could be detected on iron oxides. In contrast, the phases (iron sulphide and oxides) are spatially separated. Pyrite is the dominant sulphide phase with a grain size of 200-500 nm potentially formed by oriented aggregation (Fig. 3.2-27).

Mackinawite is no longer present. Ferrihydrite has been transformed to a nanocrystalline aggregate of goethite, hematite and magnetite. In summary, the experiments show that reaction pathways and rates of conversion are not uniform for different ferric (oxyhydr)oxides and can not be inferred by solution chemistry alone. “Time-resolved” TEM analyses are able to trace these pathways and thus allow for a more reliable parameterisation of mineral reactions relevant for element cycles.

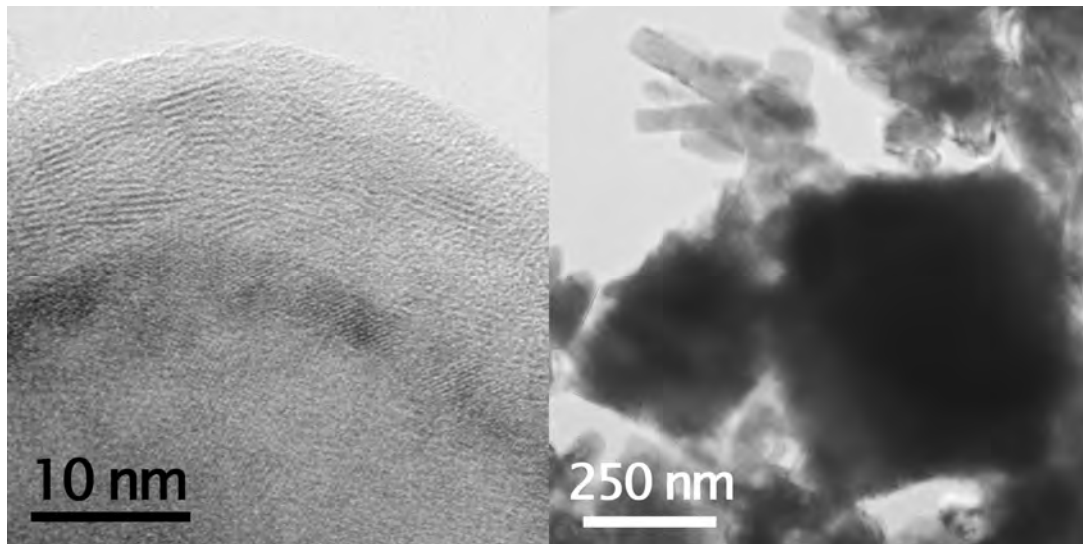


Fig. 3.2-27: High resolution TEM image of lepidocrocite after 2 h reaction with dissolved sulphide. A rim of nanocrystalline mackinawite (FeS) has formed at the surface. Furthermore, a second 4 nm thick layer of magnetite can be found between the rim and the lepidocrocite crystal (left). Bright-field TEM image of iron disulphide aggregates (square-like) and smaller lepidocrocite (lath-like) after 2 weeks of reaction. No mackinawite can be found at the surface of the iron oxyhydroxide.

### 3.3 Mineralogy, Crystal Chemistry and Phase Transformations

Studying the response of crystal materials to changing pressure, temperature and chemical compositions is fundamental to understanding the behaviour of the rock-forming minerals in the Earth. One of the major efforts of mineralogy is to determine the mineral phase relations to better constrain the phase stability at conditions of the Earth's interior that cannot be obtained by direct observation of the rocks present on the surface. Phase relations and phase transformation to high-pressure polymorphs are directly related to the atomic structure of the material and therefore it is not surprising that the study of crystal structures is still a significant contribution to this chapter. The following eleven contributions make use of several different techniques in order to synthesize and analyze crystal structures, phase transformations and chemical reactions of a variety of minerals.

The first four contributions (a - d) of this chapter report *phase relations* obtained at high pressure either by synthesizing the minerals at the desired conditions using different high-pressure apparatuses (*e.g.*, piston-cylinder and multianvil presses) and then characterizing the quenched run products or by *in situ* measurements using diamond anvil cells (DAC).

The Al solubility in TiO<sub>2</sub> polymorphs and the related structural modifications are studied in the Al<sub>2</sub>O<sub>3</sub>-TiO<sub>2</sub> system, which is important for understanding ultra high-pressure metamorphism. The crystal structure of the high-pressure polymorphs of Gypsum and its behaviours are also investigated using *in situ* synchrotron X-ray diffractions. A low temperature neutron diffraction study of wüstite gives new insight into its magnetic and structural phase transformations. The *in situ* study of carbon solubility in Fe<sub>1-x</sub>Ni<sub>x</sub> alloy at high pressures and high temperatures may give important constraint on the main constituents of the Earth's core. However, detectable carbon contamination during laser-heating in DAC experiments has been found to affect the phase relations in the Fe-Ni alloy system.

The next five contributions (e - i) experimentally investigate *the crystal structures and the crystal chemistry* of high-pressure anhydrous and hydrous polymorphs of (Mg,Fe)<sub>2</sub>SiO<sub>4</sub>, of dense Al-rich hydrous phases and of incommensurate pyrrhotites. The Mössbauer spectroscopy of  $\gamma$ -Fe<sub>2</sub>SiO<sub>4</sub> phase indicates a possible magnetic transition at high pressures. A new finding of super-aluminous phase D may be important for understanding the storage of H<sub>2</sub>O in subducted slab into the Earth's lower mantle. X-ray diffraction and <sup>29</sup>Si NMR technique are used to give insight into the water incorporation and order-disorder processes of Mg<sub>2</sub>SiO<sub>4</sub> wadsleyite and ringwoodite. Finally, an extensive electron diffraction study (TEM) succeeded in developing a method to index and parameterize the complicated arrangement of satellite reflections of non-integral NC-pyrrhotites.

The last three contributions (i - k) study the *chemical reactions* in cation layers of aluminosilicate minerals and the alteration of pyrochlore using MAS-NMR spectroscopy and transmission electron microscopy (TEM). The NMR study demonstrates that this technique is

a powerful probe to examine local environments of Al and Si, whereas the TEM study is indispensable for investigating the nanometer-scale alteration in pyrochlore.

**a. Phase relations in the  $\text{Al}_2\text{O}_3 - \text{TiO}_2$  system at pressures up to 20 GPa (A. Escudero, K. Tsuno, and F. Langenhorst)**

Aluminium is one of the trace elements in rutile that may provide information on the  $P$ - $T$  conditions of rutile-bearing metamorphic rocks. In fact, exsolved corundum lamellae have been reported in diamondiferous eclogites from South Africa. It has also been suggested that the accommodation of trivalent cations can enhance the hydrogen solubility in rutile and thus influence the water transport into the mantle. On the other hand,  $\text{TiO}_2$  is widely used, due to its photoconductive and catalyst characteristics, in both research and industrial applications, *i.e.*, hydrogen production and UV-induced oxidation of organic compounds in wastewater.  $\text{TiO}_2$  is also used as a white pigment. It is well-known that the photocatalyst properties of  $\text{TiO}_2$  can be modified by introducing small amounts of impurities in its structure. For example, the introduction of Al in rutile reduces its photoactivity and prevents the degradation of paints and other coatings by forming oxygen vacancies that can trap charge carriers, whereas the addition of Fe enhances the  $\text{TiO}_2$  absorption in the visible range. The effect of the pressure on the solubility of both elements in  $\text{TiO}_2$  remains unexplored up to now. In this experimental project we want to evaluate the Al solubility in  $\text{TiO}_2$  and the influence of Al on phase stabilities and structures at high pressures.

High-pressure experiments have been performed using commercial  $\text{Al}_2\text{TiO}_5$  (= 50 mol.%  $\text{TiO}_2$  + 50 mol.%  $\text{Al}_2\text{O}_3$ ) nanopowder. The experiments were run from 0.5 to 3 GPa and 1300 °C for 24 hours in a piston cylinder and from 5 to 20 GPa and 1300 °C for 3 hours in a 1200 tonne MA8 Kawai-type multianvil press. The samples were subsequently characterised by XRD,  $^{27}\text{Al}$  MAS-NMR, SEM and TEM.

XRD data show that  $\text{Al}_2\text{TiO}_5$  is only stable at atmospheric pressure; it decomposes into  $\text{TiO}_2$  +  $\text{Al}_2\text{O}_3$  with increasing pressure. Rutile is the stable polymorph of  $\text{TiO}_2$  until 7 GPa. However, the splitting of the signals at high  $2\theta$  suggests a loss of symmetry, from tetragonal to orthorhombic at pressures larger than 2 GPa. The change in symmetry is due to the increasing isomorphic substitution of  $\text{Ti}^{4+}$  by  $\text{Al}^{3+}$  and accommodation of  $\text{Al}^{3+}$  in unoccupied octahedral interstices at the  $(0 \frac{1}{2} 0)$  positions. For geometrical reasons, the incorporation of  $\text{Al}^{3+}$  into these interstices expands the lattice in the  $[\bar{3}20]$  direction, which is the tie line along the two closest oxygens of an octahedron. At 10 GPa rutile transforms into  $\alpha - \text{PbO}_2$  structured  $\text{TiO}_2$ . The further transformation of  $\text{TiO}_2$  into the baddeleyite-type structure, expected at about 17 GPa at 1300 °C, is not observed. Corundum is the stable  $\text{Al}_2\text{O}_3$  phase observed at each pressure.

Figure 3.3-1 shows  $^{27}\text{Al}$  Magic Angle Spinning Nuclear Magnetic Resonance (MAS-NMR) spectra of the 1 and 3 GPa samples, consisting of two signals. The peak centered at 12.5 ppm

has been previously assigned to  $\alpha$ - $\text{Al}_2\text{O}_3$ , corundum, while the other one centered at -5.7 ppm corresponds to isolated Al in normal octahedral (Oh) Ti sites of rutile. The intensity ratio of both signals indicates that  $\text{Al}^{3+}$  substitution for  $\text{Ti}^{4+}$  in rutile increases with the pressure, thus the global solubility of  $\text{Al}_2\text{O}_3$  in  $\text{TiO}_2$  increases. The signals corresponding to Al in octahedral interstices should appear at ca. 6 ppm but, according to the XRD data, almost no Al in these positions is expected at 3 GPa. No signals in the tetrahedral (Td) chemical shift region have been observed. Previous studies have demonstrated that the aluminium in this coordination shows high quadrupolar interaction that can cause the well-known effect of invisible aluminium. This hypothesis must be confirmed by using high magnetic field or multiple quantum experiments.

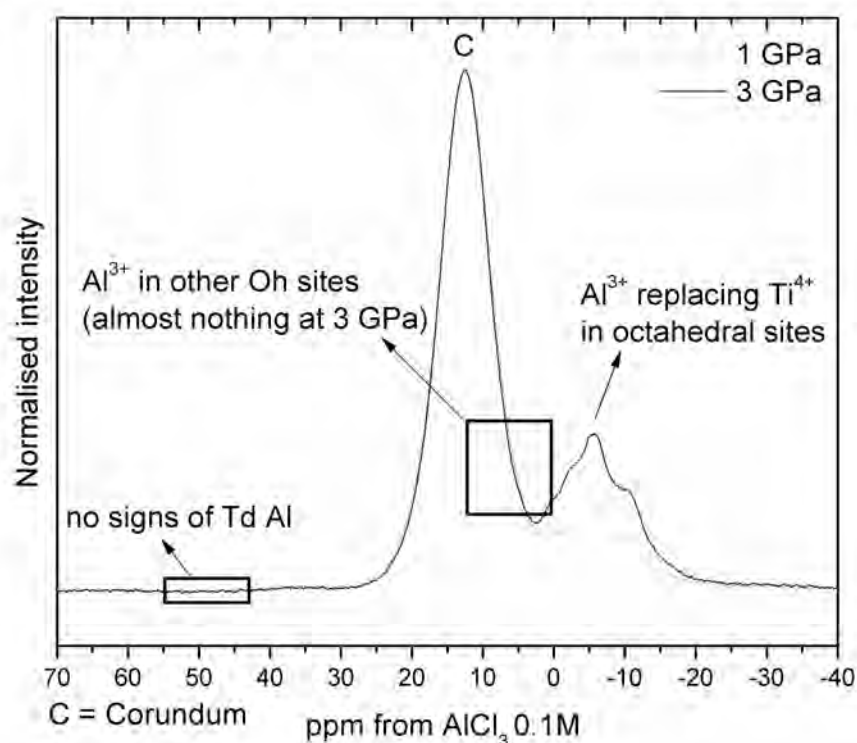


Fig. 3.3-1:  $^{27}\text{Al}$  MAS NMR spectra of the samples treated at 1 (light gray) and 3 GPa (black). The intensity of the signal centered at -5.7 ppm, associated with  $\text{Al}^{3+}$  replacing  $\text{Ti}^{4+}$ , increases with pressure.

HRTEM and EDX studies on rutile single crystals confirm that  $\text{Al}^{3+}$  is incorporated into the rutile structure and does not occur as a separate phase. Figure 3.3-2 shows the microstructure of a Al-doped  $\text{TiO}_2$  single crystal of the sample synthesised at 7 GPa. It contains multiple twins on the [110] rutile plane, which are produced by the decrease of the rutile symmetry at these pressures, as it was indicated by XRD data. In conclusion, this study is the first one indicating that the uptake of trivalent cations into the rutile structure can reduce the symmetry from tetragonal to orthorhombic.

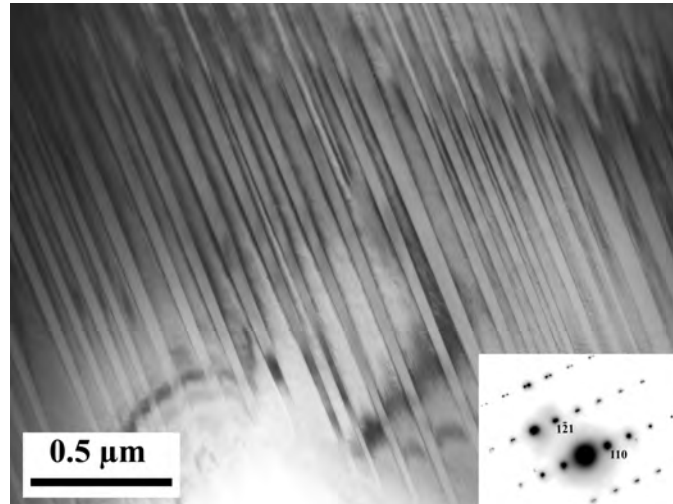


Fig. 3.3-2: TEM image and electron diffraction pattern of a Al-doped  $\text{TiO}_2$  single crystal of the sample synthesised at 7 GPa, showing a microstructure consisting of [110] twins.

**b. Effect of carbon on the phase relations in Fe-Ni system at high pressures and temperatures (O. Narygina, L. Dubrovinsky, C.A. McCammon, and D.J. Frost; N. Dubrovinskaia/Heidelberg, I.Yu. Kantor/Chicago, and V. Dmitriev/Grenoble)**

The phase diagram of  $\text{Fe}_{1-x}\text{Ni}_x$  ( $0.05 \leq x \leq 0.20$ ) alloy, which is thought to be the main constituent of the Earth's core, as well as the effect of the incorporation of light elements such as O, Si, S, C, H on the phase relations in the Fe-Ni system at high pressures and temperatures have been addressed by a large number of experimental and theoretical studies. However, the structural phase of Fe-enriched alloys at the conditions of the Earth's core remains unconstrained, mainly due to the lack of experimental results at the relevant pressures and temperatures. Most of the current knowledge on this subject derives from extrapolations of high-pressure data collected at room temperature to the temperatures of the core-mantle boundary. Nowadays the  $P$ - $T$  conditions close to those thought to be relevant for the Earth's core can be achieved in diamond anvil cells with *in situ* laser heating (LH-DAC), however this kind of experiment is still very challenging in terms of sample preparation, stability and alignment of a the laser spot, maintaining an acceptable temperature gradient, measurements of the temperature itself, etc. In contrast, the large-volume press (LVP) technique allows more homogeneous heating, which can be maintained for a several hours, providing more equilibrated conditions but at a significantly lower pressures and temperatures. In this study, we combined the advantages of both of the above mentioned high-pressure and high-temperature techniques to perform a comparative study of the phase diagram of  $\text{Fe}_{1-x}\text{Ni}_x$  ( $0.10 \leq x \leq 0.22$ ) alloy and the effect of carbon incorporation (as one of the plausible light constituent of the Earth's core) on the phase relations in the system at pressures from 0.5 to 31 GPa and temperatures up to 2600 K using LH-DAC and LVP (multianvil and piston-cylinder) techniques.

The  $\text{Fe}_{1-x}\text{Ni}_x$  alloy was initially compressed to the required pressure (10 - 31 GPa, depending on the run) and then, after heat treatment during 5-10 min (1700 K - 2600 K, depending on the run), it was quenched to room temperature at high pressure. The recovered samples were analysed by X-ray diffraction, Mössbauer spectroscopy and Scanning Electron Microscopy.

Laser heating to 1700-2600 K of the *bcc*  $\text{Fe}_{1-x}\text{Ni}_x$  alloy in DACs pressurised to different pressures in the range between 10 and 35 GPa leads to the formation of an additional antiferromagnetic *fcc* Fe-bearing phase (Figs. 3.3-3a,b), whereas the quenched products of multianvil runs, performed using the same starting material at practically the same *P-T* conditions (15-20 GPa and 1700-2200 K), consisted only of the single initial *bcc* Fe,Ni phase (Figs. 3.3-3c,d). A possible explanation for the discrepancy between the results obtained using the two different high-pressure techniques may be the presence of contaminating material in the LH-DAC experiments which may have reacted with the sample. However, careful preparation of a DAC experiment enables the elimination of any possible contaminating material, except, of course, carbon which is provided by the diamond anvils. We simulated the conditions of a DAC experiment in the preparation of a multianvil press experiment by adding diamond powder into the starting material. Analyses of the recovered sample after the

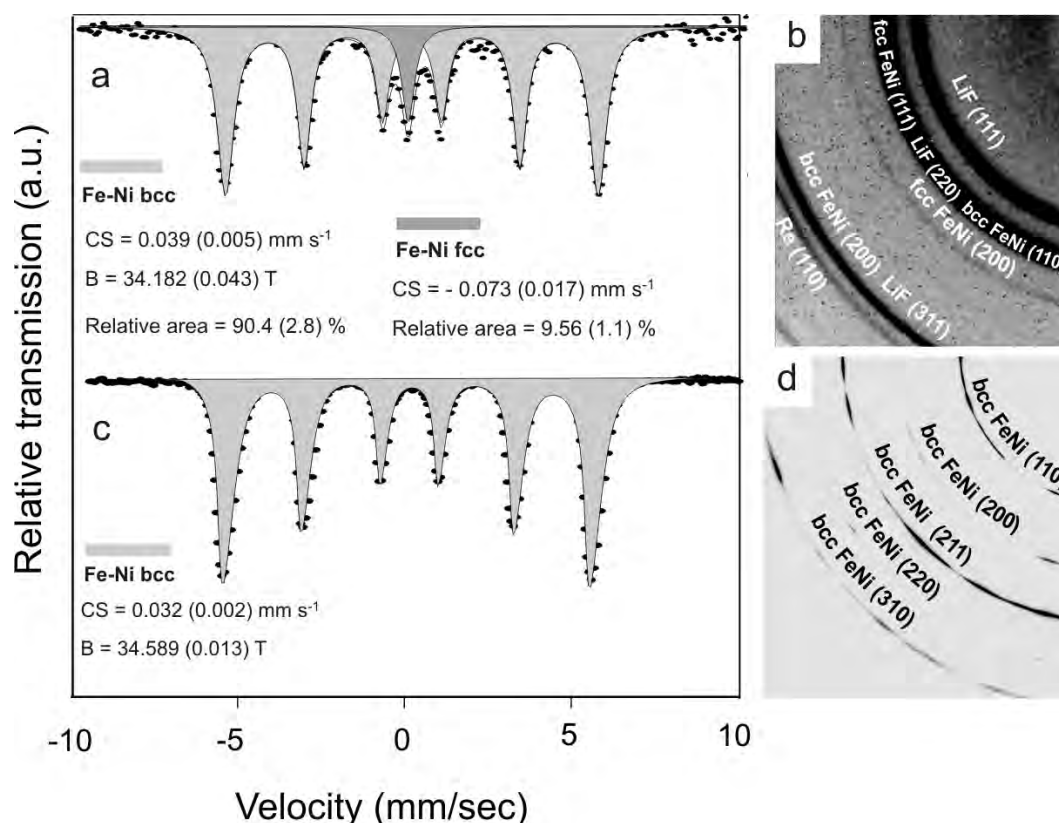


Fig. 3.3-3: Mössbauer spectra and X-ray diffraction patterns of a  $\text{Fe}_{0.90}\text{Ni}_{0.10}$  alloy recovered after heating to 2000(50) K at 20(1) GPa. a,b) experiments in LH-DAC; c,d) experiment in a multianvil press.

multianvil press experiment at 20 GPa and 2100-2200 K in the presence of 1 wt.% of diamond powder, revealed the formation of a *fcc* phase along with *bcc* -Fe,Ni and Fe<sub>3</sub>C carbide (Fig. 3.3-4), confirming our hypothesis regarding carbon contamination in the case of LH-DAC experiments, which leads to the decomposition of the sample to *bcc* and *fcc* Fe-Ni-C phases, stable at ambient conditions. The reason why we did not observe formation of Fe<sub>3</sub>C carbide in the LH-DAC experiments is most probably related to the much smaller amount of dissolved carbon (in comparison with 1 wt.% carbon in the case of the DAC-simulating multianvil run).

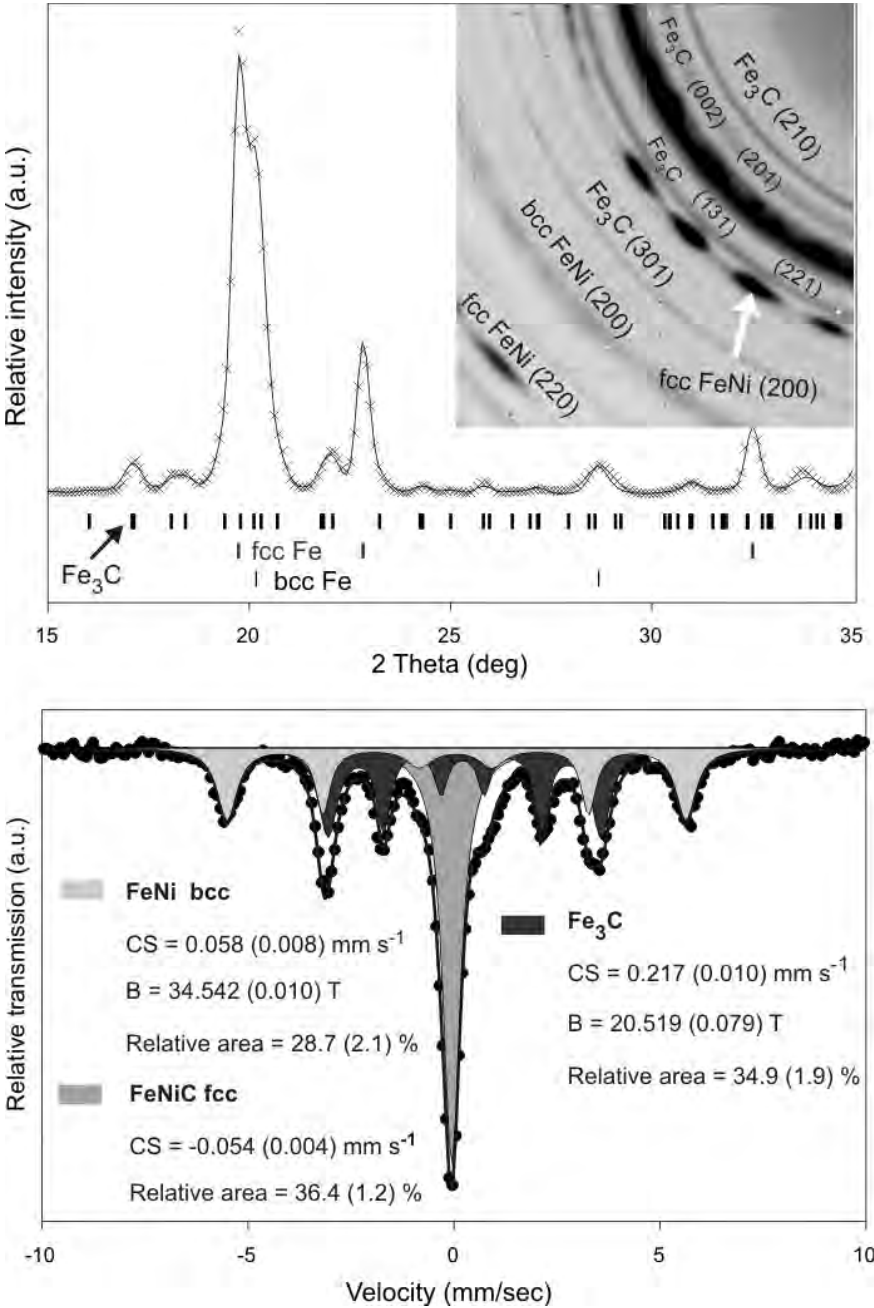


Fig. 3-3.4: XRD pattern (top) and Mossbauer spectra (bottom) of a Fe<sub>0.90</sub>Ni<sub>0.10</sub> alloy recovered after heating to 2000(50) K at 20(1) GPa in multianvil press in the presence of 1 wt.% of diamond powder.

In order to estimate the solubility of carbon in the Fe-Ni system at high pressures and temperatures, we performed a series of quenched LVP runs with  $\text{Fe}_{0.90}\text{Ni}_{(0.10-x)}\text{C}_x$  ( $0.01 < x < 0.05$ , corresponding to  $0.2 < x < 1.1$  wt.% carbon) at pressures between 0.5 and 20 GPa and temperatures of 2050-2300 K. We showed that at pressures up to 9.0(5) GPa and 2300(20) K *fcc*-FeNi alloy can still incorporate as much as 0.9(2) wt.% carbon, while at 20.0(5) GPa and 2300 (20) K this value drops to 0.7(2) wt.%, which coincides with the previously reported decrease of the carbon solubility in the Fe-Ni system upon compression.

To summarise, we showed that laser heating in the DAC can induce diffusion of carbon from the diamond anvils, which can then react with the sample (in our case it was FeNi alloy), and therefore interfere with the experimental data. The results of experiments performed in LH-DAC should therefore be treated with caution.

**c. High-pressure induced polymorphism on gypsum (S. Nazzareni and P. Comodi/Perugia; L. Bindi/Firenze, and L. Dubrovinsky)**

Gypsum ( $\text{CaSO}_4 \cdot 2\text{H}_2\text{O}$ ) is one of the most common sulfate minerals and one of many minerals with water molecules in its structure. Because of its importance in many geological and industrial processes, gypsum has been the subject of a wealth of studies on thermal and pressure stability. In regard to the behaviour of gypsum with increasing pressure, X-ray powder diffraction, infrared and Raman spectroscopic studies suggest a reversible polymorphic phase transition at 4-5 GPa, however, the structure of the high-pressure polymorph has yet not been solved.

We therefore performed an HP X-ray synchrotron diffraction experiments at APS (Chicago) and ESRF (Grenoble), on both powder and single-crystals of gypsum, to study the structure of the gypsum polymorph and the structural behaviour at high pressure.

The high-pressure gypsum polymorph (gypsum-II) is stable in the pressure range between 4 and 8 GPa; above 8 GPa changes in the diffraction patterns of both powder and single-crystal gypsum are observed. The lattice parameters of gypsum-II obtained from both powder and single-crystal data, show a strong anisotropy in the axial compressibilities with  $\beta_a: \beta_b: \beta_c = 4:1:2.5$  in contrast with the isotropic behaviour of gypsum-I ( $\beta_a: \beta_b: \beta_c = 1.1:1.1:1$ ). The bulk modulus  $K_0 = 58(1)$  GPa with  $K'$  fixed to the value of 4, increases with respect to that of gypsum-I ( $K_0 = 44(3)$  with  $K' = 3.3$ ).

The crystal structure of gypsum-II at 5.35 (5) and 6.74(5) GPa has been solved from single-crystal synchrotron X-ray diffraction data collected at the beamline ID09 at ESRF (Fig. 3.3-5). Gypsum-II is monoclinic, space group  $P2_1/n$ , with lattice parameters  $a = 5.865(12)$ ,  $b = 15.045(14)$ ,  $c = 5.478(12)$  Å,  $\beta = 115.3(2)^\circ$  and  $V = 437.0(1)$  Å<sup>3</sup> at 5.35(5) GPa, and  $a = 5.776(2)$ ,  $b = 15.017(2)$ ,  $c = 5.473(2)$  Å,  $\beta = 114.98(4)^\circ$  and  $V = 430.3(2)$  Å<sup>3</sup> at 6.74(5) GPa.

The crystal structure has been refined to a discrepancy factor,  $R_1 = 3.7\%$  at 5.35(5) GPa and 3.9% at 6.74(5) GPa. It closely resembles that of the room pressure gypsum with stacking of  $\text{CaO}_8$  and  $\text{SO}_4$  polyhedra along the  $b$ -axis to form layers. With increasing pressure, a continuous increase in the distortion of the  $\text{SO}_4$  tetrahedron as well as a large variation in the bonding style of the water molecules have been observed (Figs. 3.3-6a,b). According to reported HP-spectroscopic data the transition results from the repulsion between O-H...O atoms. Above 4 GPa the water molecules rearrange themselves in order to reduce the repulsion with consequent change of symmetry from the C-centered to the primitive lattice.

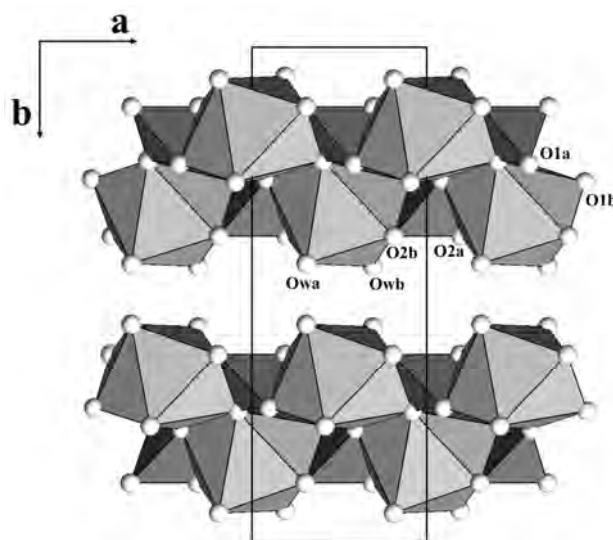


Fig. 3.3-5: The structure of gypsum-II projected down the [001] direction.

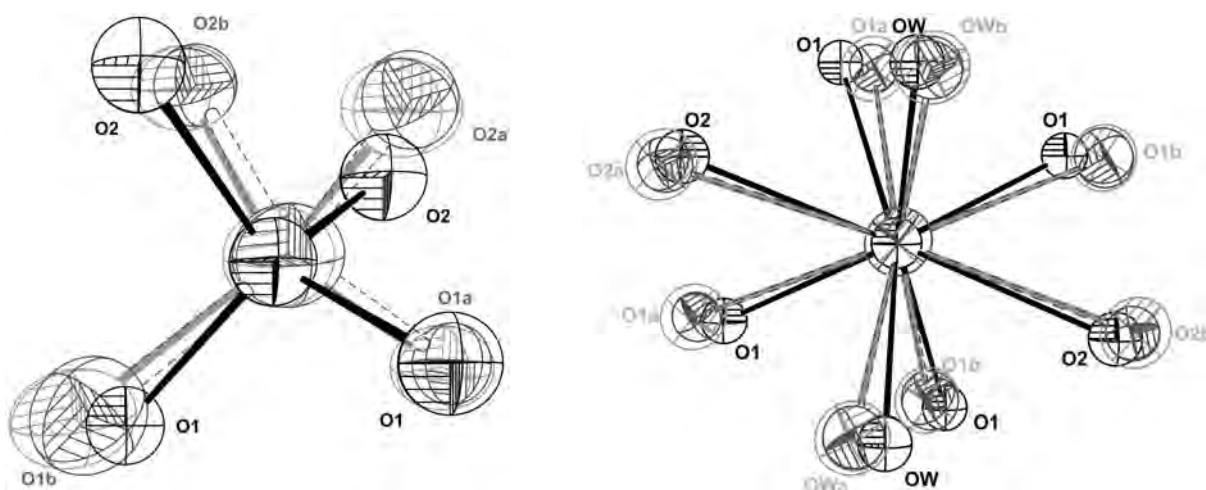


Fig. 3.3-6: Coordination polyhedra of gypsum at different pressures projected down the [001] direction. (a)  $\text{SO}_4$  tetrahedron; (b)  $\text{CaO}_8$  polyhedron. Black, grey and light grey colors refer to the structure at 0.00, 5.35 and 6.74 GPa, respectively. Displacement parameters are drawn at the 70% probability level.

**d. Insight on the low-temperature – high-pressure phase diagram of wüstite (K. Glazyrin, and L. Dubrovinsky; S. Klotz/Paris)**

Wüstite ( $\text{Fe}_{1-x}\text{O}$ ) is one of the simplest antiferromagnetic Mott-Hubbard insulators which have been at the center of interest of the solid state community for decades. This material has also considerable importance in Earth sciences since it is an end-member of the periclase-wüstite ( $\text{Mg,Fe}$ )O system which is a major constituent of the Earth's lower mantle. At ambient conditions this material is paramagnetic and crystallise to a NaCl-type structure. At low temperatures (190-200 K, depending on composition) an antiferromagnetic ordering occurs (PM-AFM). Ambient pressure experiments have shown that the Néel transition is accompanied by a structural distortions from the cubic NaCl-type structure of wüstite to a rhombohedral (C-RH) structure. Up to now it was generally believed that the PM-AFM coincides with the C-RH transitions.

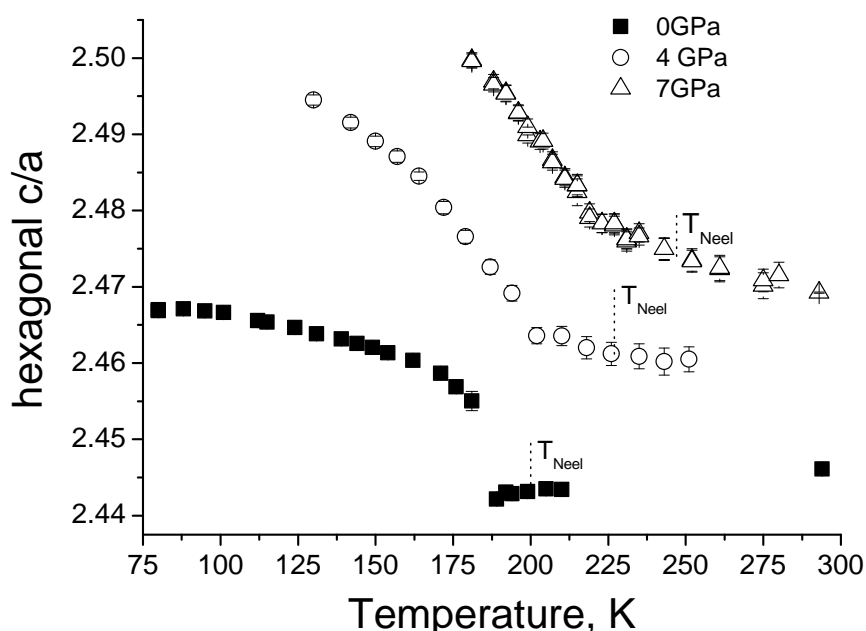


Fig. 3.3-7: The  $c/a$  ratio of  $\text{Fe}_{1-x}\text{O}$  ( $x=0.06$ ) at different pressures. The dashed lines ( $T_{\text{Neel}}$ ) represent the onset of the magnetic transitions at the various pressures.

We have performed low temperature experiments using  $\text{Fe}_{1-x}\text{O}$  ( $x=0.06$ ) at the neutron powder diffraction D20 beam line ILL, Grenoble, France. The scans were done at three different pressures (0 GPa, 4 GPa, and 7 GPa). To get a better precision on the critical temperatures for the magnetic transition, the variation of the individual magnetic peaks (and in particular of the most intense magnetic peak  $[3/2, 1/2, 1/2]$ ) were followed as a function of temperatures. The lattice parameters  $a$ , and  $c$  and their ratio  $c/a$ , as well as the magnetic moments on the iron sites were obtained from Rietveld analysis using the Fullprof software

package. The structure of  $\text{Fe}_{1-x}\text{O}$  was refined as rhombohedral at all temperatures. The anomaly in the evolution of the  $c/a$  ratio with decreasing pressures (Fig. 3.3-7) is therefore indicative of the structural (C-RH) transition. The analysis of the obtained data allows us to plot the low-temperature/high-pressure phase diagram of  $\text{Fe}_{1-x}\text{O}$  ( $x=0.06$ ) (Fig. 3.3-8). The critical temperatures of the magnetic and structural phase transitions are clearly not coincident and their difference becomes larger with increasing pressure.

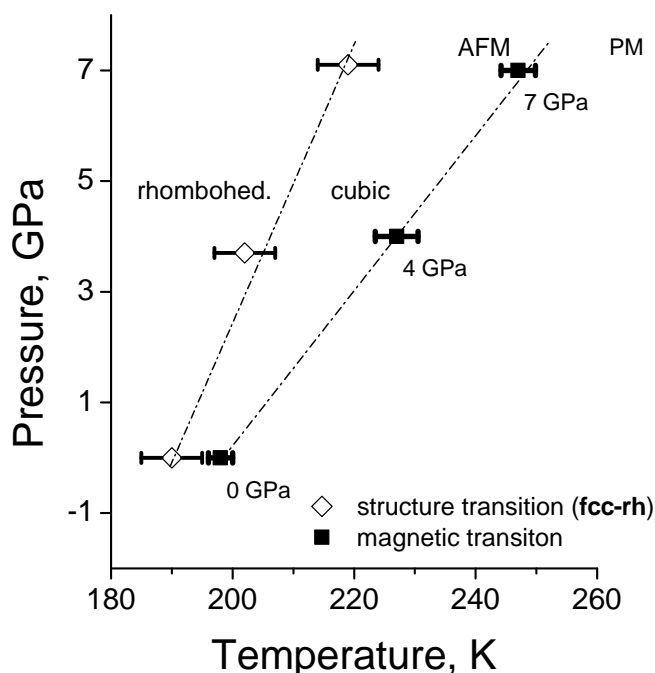


Fig. 3.3-8: Low  $T$ - high  $P$  phase diagram of  $\text{Fe}_{1-x}\text{O}$  ( $x=0.06$ )

**e.** *High-pressure Mössbauer spectroscopy studies of  $\gamma\text{-Fe}_2\text{SiO}_4$  ringwoodite (E. Greenberg, L.S. Dubrovinsky, and C.A. McCammon)*

One of the most abundant constituents of Earth's upper mantle is olivine  $(\text{Fe,Mg})_2\text{SiO}_4$ , which transforms to the spinel structure (Ringwoodite  $\gamma\text{-(Fe,Mg)}_2\text{SiO}_4$ ) at pressures below 20 GPa. This transformation of olivine to spinel and the transformation of spinel to post-spinel at higher pressures are reported to be the cause of seismic discontinuities at depths of around 400 and 660 km, respectively.

Mössbauer spectroscopy (MS) was used as a probe for detecting changes in the magnetic and quadrupole hyperfine interactions at the Fe nucleus. High-pressure (HP) measurements, utilizing diamond anvil cells (DACs), on the Fe end-member of Ringwoodite ( $\gamma\text{-Fe}_2\text{SiO}_4$ ) were performed up to pressures of 72 GPa.

At low pressures the observed spectra include one component with a quadrupole splitting, as expected for the spinel structure, which includes one crystallographic site for all the Fe atoms

in the unit cell. However, at pressures above 20 GPa a 2<sup>nd</sup> component with smaller quadrupole splitting and isomer shift values is required in order to achieve a reasonable fit to the data (Fig. 3.3-9). Between 20 and 40 GPa the relative abundance of the new component increases rapidly and saturates at ~ 75 %. The original component increases its quadrupole splitting (Fig. 3.3-10) while decreasing in abundance. A further increase of pressure results in an additional component with a relatively low abundance. However, higher pressures are required in order to completely characterize this new component. X-ray diffraction (XRD) studies, using a conventional X-ray source, show no structural change in this pressure range.

Future studies include HP synchrotron XRD studies, for confirming the absence of structural changes and for obtaining an equation of state for  $\gamma$ -Fe<sub>2</sub>SiO<sub>4</sub> in a large pressure range. High-temperature (HT) XRD studies are also planned for determining the HP-HT stability of  $\gamma$ -Fe<sub>2</sub>SiO<sub>4</sub>, expecting a disproportionation into FeO and either FeSiO<sub>3</sub> perovskite or FeSiO<sub>3</sub> post-perovskite, or a completely new Fe<sub>2</sub>SiO<sub>4</sub> structure. These studies under HP-HT conditions are important because they represent conditions in the Earth's lower mantle and the core-mantle boundary.

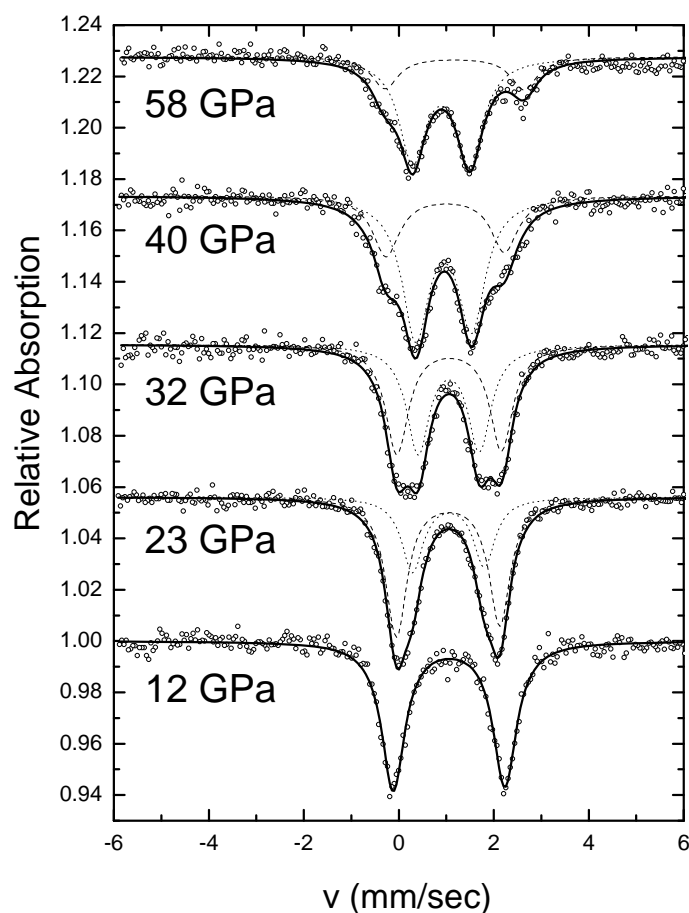


Fig. 3.3-9: Mössbauer spectra of  $\gamma$ -Fe<sub>2</sub>SiO<sub>4</sub> at different pressures describing the relative absorption as a function of the source's energy shift (in units of velocity). Solid lines represent the total least squares fit to the spectra, dashed and dotted lines represent the original and new components, respectively.

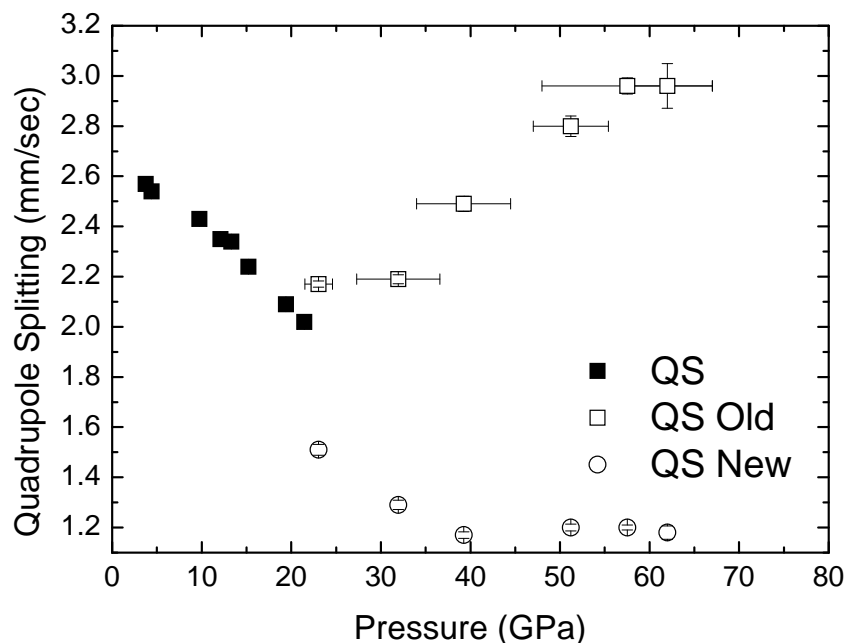


Fig. 3.3-10: Quadrupole splitting (QS) as a function of pressure for  $\gamma$ - $\text{Fe}_2\text{SiO}_4$ . Filled squares represent the QS at low pressure, empty squares and empty circles represent the two QS values observed above 20 GPa.

**f.** *The structure of a super-aluminous version of the dense hydrous magnesium silicate phase D (T. Boffa Ballaran, and D.J. Frost)*

The depth and extent to which  $\text{H}_2\text{O}$  can be transported into the Earth's mantle at convergent plate boundaries depends largely on the stability of hydrous-bearing phases at the pressures and temperatures encompassed by subducting oceanic lithosphere. A number of hydrous phases in the  $\text{MgO-SiO}_2\text{-H}_2\text{O}$  system have been synthesized in high pressure and temperature experiments that could be stable in subduction zones at depths compatible with the Earth's transition zone and lower mantle. Among these dense hydrous magnesium silicates (DHMS) phases, phase D, which has the ideal formula  $\text{MgSi}_2\text{H}_2\text{O}_6$  but varies significantly in stoichiometry depending on synthesis conditions, is the highest pressure phase yet reported with a stability field extending from 20 to 44 GPa. Phase D, along with most other DHMS phases, has also been synthesized within complex peridotitic bulk compositions where it has been found to contain up to 7 wt.%  $\text{Al}_2\text{O}_3$  and 5 wt.%  $\text{FeO}$ .

We have synthesized a new Al-rich form of phase D using a multianvil device at approximately 1300 °C and 25 GPa. The phase, with the formula  $\text{H}_{1.8}\text{Mg}_{0.2}\text{Fe}_{0.15}\text{Al}_{1.8}\text{SiO}_6$ , was initially produced in a bulk composition designed to synthesize Al-rich magnesium silicate perovskite with a composition similar to that found in experiments on mid ocean ridge basalt bulk compositions at lower mantle conditions. A second starting composition based on the Al-rich phase was fabricated from oxides and hydroxides and single crystals up to 60-70  $\mu\text{m}$  were recovered. The composition of these crystals is slightly richer in  $\text{H}_2\text{O}$

( $\text{H}_{3.1}\text{Mg}_{0.2}\text{Fe}_{0.12}\text{Al}_{1.5}\text{Si}_{0.92}\text{O}_6$ ) and their unit-cell lattice parameters are very similar to those of magnesium silicate phase D. Refinement of the crystal structure has been carried out in the  $P\bar{3}1m$  space group and it shows a more disordered cation distribution than magnesium silicate phase D. All cation-oxygen distances are very similar suggesting a large degree of Si / Al disordered. The difference-Fourier maps of super-aluminous phase D show very little residual electron density, however for each crystal the largest residual peak is at about 0.9-1.0 Å from the oxygen atom. Since this position has symmetry  $m$ , it requires disorder of the protons among 6 different positions. The O-H bonds point toward the B octahedral sites (Fig. 3.3-11). The longer O...H bond is about 1.98 Å, *i.e.*, larger than that assumed in the phase D model, however the O-H...O distance is practically the same for both structures. The different position of the H in super-aluminous phase D, assuming our model to be correct, may be explained by the partial occupancy of the A site which would cause a strong repulsion with the H atoms occupying the position assumed in the phase D model.

These results demonstrate a remarkable flexibility of the phase D structure that can accommodate a significant range of cation substitutions. Although the stability field of this new variant of phase D is yet to be determined, this phase may be an important host for  $\text{H}_2\text{O}$  within portions of subducted oceanic crust in the lower mantle.

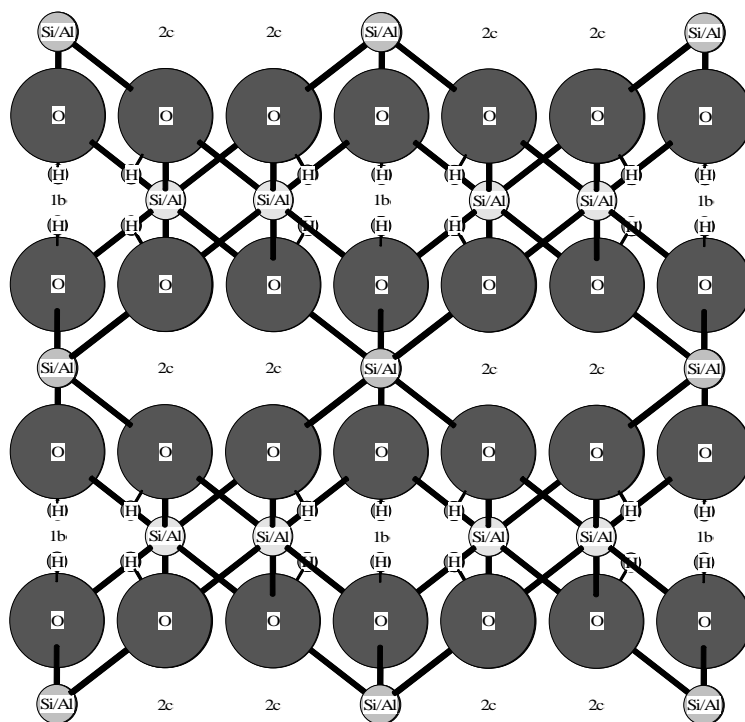


Fig. 3.3-11: Crystal structure of super-aluminous phase D projected down to the  $a$  axis. The Si/Al balls are positions equivalent to the Si and Mg sites of magnesium silicate phase D. The 2c and 1b octahedral sites which are vacant in magnesium silicate phase D are partially occupied in super-aluminous phase D. The largest residual in the difference-Fourier maps of the structural refinements is here included as a possible H position.

**g. The crystal chemistry of wadsleyite hydration (J.R. Smyth, and Y. Ye/Boulder; D.J. Frost)**

Wadsleyite ( $\beta$ -Mg<sub>2</sub>SiO<sub>4</sub>) is potentially a major host for H and thus water in the Earth's transition zone at depths of 410-525 km. Refinements of the crystal structure with up to 16600 ppm H<sub>2</sub>O have been reported and elastic properties measured both at ambient conditions and at elevated pressures. Water contents in wadsleyite in excess of 3 weight percent have been reported. However crystal structures and elasticity of wadsleyites with more than 2 weight percent H<sub>2</sub>O have not been reported.

Crystals of hydrous pure Mg wadsleyite containing about 2.8 percent H<sub>2</sub>O by weight were synthesized at 15 GPa and 1250 °C in the 5000 tonne multianvil press using a 2 mm welded Pt capsule and in an 18/8 mm assembly. Single crystals up to 250  $\mu$ m were obtained. Unit cell parameters obtained from centering of 40 X-ray reflections between 15 and 25° in both positive and negative 2 $\theta$  are:  $a=5.6635(12)$  Å,  $b=11.5726(19)$  Å,  $c=8.2302(59)$  Å;  $V=539.42(32)$  Å<sup>3</sup>. This gives a  $b/a$  ratio of 2.04337, which yields an H<sub>2</sub>O content of 28300 ppm. A single crystal of this material was mounted on a Bruker AXS P4 diffractometer with an APEX II CCD detector system. An intensity data set consisting of 2247 reflections was measured. The crystal structure was refined in space group *Imma* to an R factor of 0.038 using ionized atomic scattering factors. The final occupancy and positional parameters were determined. Selected interatomic distances are shown below along with comparable distances for an anhydrous wadsleyite (Tab. 3.3-1).

Table 3.3-1: Interatomic distances in hydrous and anhydrous wadsleyites

	Anhydrous	Hydrous
Mg1- O3 (x 2)	2.112(1)	2.117(1)
Mg1- O4 (x 4)	2.050(1)	2.058(1)
<M1-O>	2.071	2.078
M1 Octahedral Vol.	11.76	11.89
Mg2 – O1 (x 1)	2.025(1)	2.105(1)
Mg2 – O2 (x 1)	2.101(1)	2.098(1)
Mg2 – O4 (x 4)	2.092(1)	2.083(1)
<Mg2-O>	2.082	2.089
M2 Octahedral Vol.	11.95	12.04
Mg3 – O1 (x 2)	2.018(1)	2.071(1)
Mg3 – O3 (x 2)	2.124(1)	2.098(1)
Mg3 – O4 (x 2)	2.131(1)	2.099(1)
<Mg3-O>	2.091	2.089
M3 Octahedral Vol.	12.07	12.08

With hydration, the vacancies are concentrated in the Mg3 position, which appears to be about 23 % vacant. The *b*-axis expands from 11.440 Å in the anhydrous sample to 11.573 Å, whereas the *a*-axis contracts from 5.701 Å to 5.664 Å. The proton appears to be principally located on O1. The distances around O1, the non-silicate oxygen, expand dramatically, whereas those around the other oxygen positions decrease slightly so there is minimal volume expansion in the Mg1 and Mg2 octahedra and a small expansion in the M3 octahedron.

These conclusions are consistent with the major substitution mechanism in the nominally anhydrous high-pressure Mg silicates being  $2\text{H}^+$  for  $\text{Mg}^{2+}$  which is seen in forsterite, wadsleyite, and ringwoodite. The results for wadsleyite show ordering of vacancies in M3 and a clear indication of protonation of O1, the non-silicate oxygen. Samples of this material will be made available for compression and elastic property measurements and other spectroscopic methods.

**h.** *NMR studies of anhydrous and hydrous forsterite, wadsleyite and ringwoodite ( $\text{Mg}_2\text{SiO}_4$ ) (J.R. Smyth/Boulder, D.J. Frost, W.R. Panero/Columbus, and J.F. Stebbins/Stanford)*

Forsterite, wadsleyite, and ringwoodite phases of  $(\text{Mg,Fe})_2\text{SiO}_4$  probably make up most of the Earth's upper mantle. A number of details of their structures, however, remain unknown but are important to understanding their properties and behaviour in Earth processes. Si-29 nuclear magnetic resonance (NMR) offers considerable potential in resolving such questions.

Using 99 % Si-29 enriched forsterite as starting material, we synthesized 5 to 10 mg samples of anhydrous wadsleyite and ringwoodite, and hydrous samples of forsterite, wadsleyite and ringwoodite containing up to 1 %  $\text{H}_2\text{O}$ . These were characterized by XRD and EPMA, and studied in detail with both magic-angle spinning (MAS) and cross-polarization (CPMAS) Si-29 NMR. The isotopic enrichment provided greatly enhanced signal-to-noise ratios over those obtained in previous studies.

Because ringwoodite has the spinel structure, it has long been suggested that some Mg/Si disorder could occur, resulting in the formation of six-coordinated Si ( $^{\text{VI}}\text{Si}$ ). NMR spectra on quenched samples do not show any octahedral Si. Theoretical modeling indicates that several per cent of cation disorder should occur at mantle temperatures, these results, therefore, may suggest that rapid re-ordering can take place during quenching, as it has been observed above a certain temperature range in  $\text{MgAl}_2\text{O}_4$  spinels. Several small, unknown peaks for tetrahedral Si ( $^{\text{IV}}\text{Si}$ ) were observed, however, which may be related to defects formed during the reordering process. Theoretical work is in progress to help assign these chemical shifts.

The extremely high signal-to-noise ratios (>1000:1) obtained for the forsterite starting material led to the discovery of a number (>10) of very small, "anomalous" NMR peaks, many of which have chemical shifts outside the known range for  $^{\text{IV}}\text{Si}$ , and which have spin-

lattice relaxation rates much faster than the main peak. After additional study, including observation of large temperature effects on these peak positions (25 to 160 °C, shifts linear with 1/T), we concluded that they can be attributed to interactions with paramagnetic impurity cations (known to be present at the 10-50 ppm level), probably through the “pseudocontact” interaction. This opens the possibility of new types of NMR constraints on short-range ordering involving transition metal cations in silicate minerals. We also observed such features in wadsleyite, but not in ringwoodite, possibly because of the high symmetry of the latter mineral.

Si-29{H-1} CPMAS NMR, including systematic results on cross-polarization dynamics, supports the protonation of the O1 oxygens in hydrous wadsleyite without the formation of a large numbers of Si-OH groups. However, new peaks were observed in hydrous ringwoodite that cross-polarize much more rapidly, suggesting short Si-H distances and hence Si-OH groups, as expected if most H<sup>+</sup> substitutes into vacant Mg<sup>2+</sup> sites. In the hydrous forsterite, if such peaks are present, they overlap closely with the main Si-29 peaks, limiting the information that can be extracted.

Detailed studies of spin-lattice relaxation in these samples show that a stretched exponential function (with exponent “beta” of 0.5) fits data much better than the commonly used single exponential (“beta” of 1). This is expected when the predominant relaxation mechanism is through-space dipolar coupling to unpaired electron spins on paramagnetic impurity cations.

**i. TEM study of natural non-integral NC-pyrrhotites (D. Harries, K. Pollok, and F. Langenhorst)**

Pyrrhotite (Fe<sub>1-x</sub>S with x < 0.125) is one of the principal iron sulfides in ore deposits and crustal rocks and contributes significantly to rock magnetisation and the paleomagnetic record. Its NiAs-derivative structure contains sequences of hexagonal close-packed S atom layers stacked along the crystallographic *c* axis in alternation with layers of Fe atoms in octahedral coordination. Non-stoichiometric compositions arise from the presence of vacancies within Fe layers due to the presence of nominal Fe<sup>3+</sup>. Observed compositions in nature span the range between 47 and 50 at.% Fe (Fe<sub>7</sub>S<sub>8</sub> to FeS), whereas most structural complexity occurs in the narrow compositional range between 47 and 48 at.% Fe (‘intermediate pyrrhotites’). At temperatures below 300 °C various structural variants within this range are thought to result from vacancy ordering among and within Fe layers. The many possible arrangements are intimately coupled to the deficiency of Fe resulting in a large number of possible structures with distinct Fe/S ratios and widely varying physicochemical and magnetic properties. Owing to slow ordering kinetics and pronounced phase heterogeneity on microscopic scales, detailed knowledge on structures and ordering mechanisms is lacking, despite many potentially important implications in the fields of geomagnetics, environmental mineralogy, and technical mineral processing.

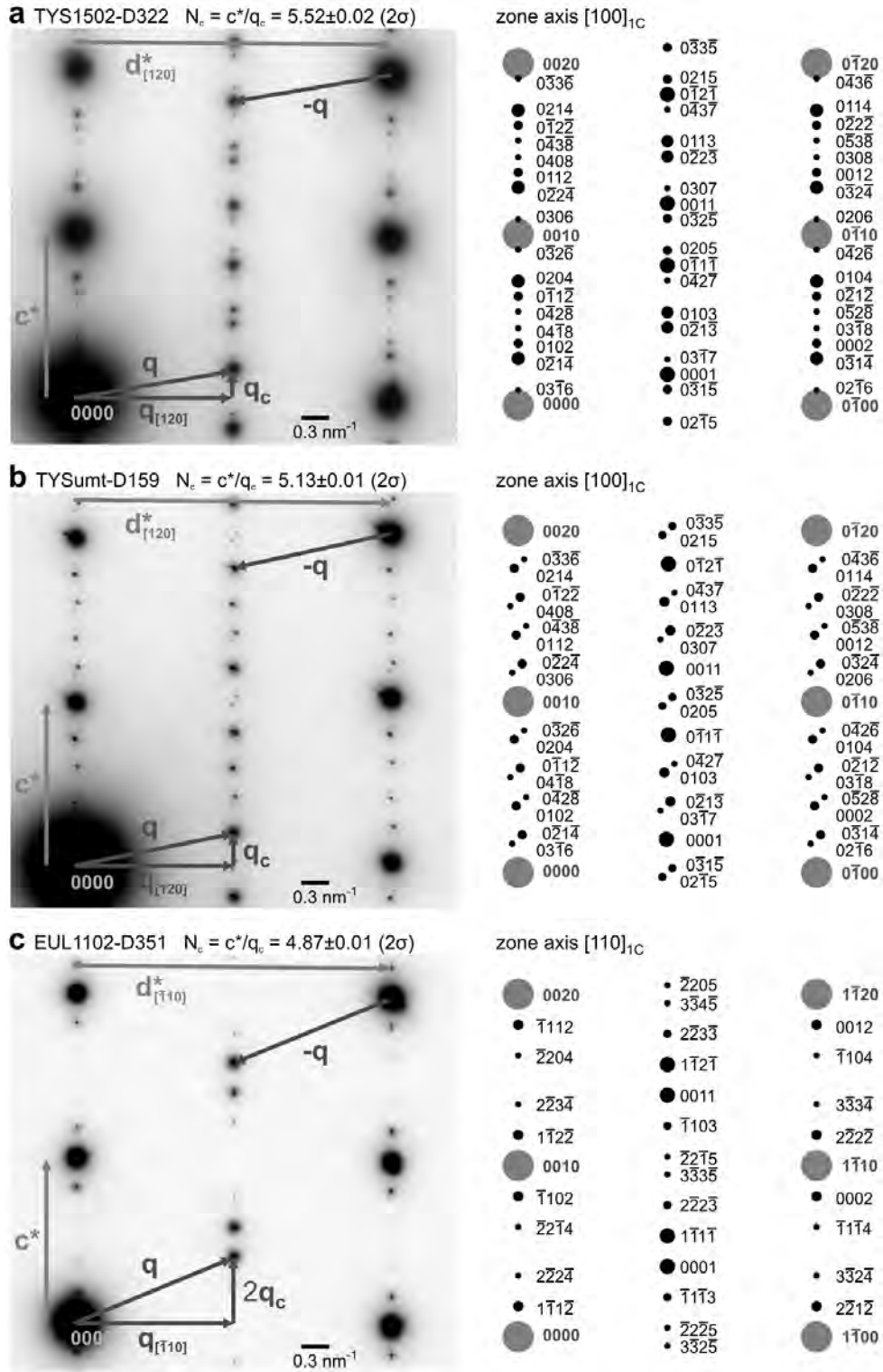


Fig. 3.3-12: SAED pattern of non-integral NC-pyrrhotites and schematic representations with  $hklm$  indices. Large grey spots belong to substructure, black spots are satellites. (a) Tysfjord (Norway), non-integral  $N_c$ , integral  $N_{[120]} = 2$ . (b) Tysfjord (Norway), non-integral  $N_c$  and non-integral  $N_{[120]}$  which is slightly larger than 2. (c) Sta. Eulalia (Mexico), non-integral  $N_c$  and slightly non-integral  $N_{[110]}$  which becomes apparent by close inspection of weak 4<sup>th</sup> and 5<sup>th</sup> order satellite spots.

Non-integral NC-pyrrhotites are the most perplexing structural variants existing within the range of intermediate pyrrhotites at room temperature and ambient pressure. Electron diffraction patterns show complicated arrangements of generally very sharp satellite diffraction maxima around the NiAs substructure spots. We developed a system allowing us to index and parameterise the highly variable diffraction pattern obtained by TEM-SAED. In given zone axes perpendicular to  $c$  the satellites can be indexed by use of a single specific vector  $\mathbf{q}$  originating at the substructure spots (Fig. 3.3-12). This gives rise to four digit ( $hklm$ ) indices in which  $m$  signifies the satellite order in terms of multiples of  $\mathbf{q}$ . In non-integral NC-pyrrhotites at least one vector component of  $\mathbf{q}$  along principle crystallographic directions (within the  $ab$  plane or along  $c$ ) is related to the substructure repeat in a non-integral manner. Characteristic parameters are the positive ratios of vector lengths  $N_c = c^*/q_c$  and  $N_{[uv0]} = d^*_{[uv0]}/q_{[uv0]}$ , where  $c^*$  and  $d^*_{[uv0]}$  represent lattice spacings of the NiAs substructure in directions of  $\mathbf{q}_c$  and  $\mathbf{q}_{[uv0]}$  which are the components of  $\mathbf{q}$  in zone axes perpendicular to  $c$  (see Fig. 3.3-12). In most cases  $N_{[uv0]}$  is 2 and  $N_c$  shows non-integral values in the range of 4.7 to 5.5. Interestingly no integral 5C-pyrrhotite ( $N_c = 5$ ) could be found, although it is proposed to be a common and stable intermediate pyrrhotite. SAED pattern in which both  $N$  parameters are non-integral are described for the first time (Fig. 3.3-12b). Determination of the  $N_c$  parameter is generally possible with standard uncertainties of less than 0.02, allowing us to recognise spatial heterogeneity in all four investigated samples from various geological environments. Besides this, exsolution lamellae of integral 4C- or 2C-pyrrhotite ('monoclinic pyrrhotite' and troilite respectively) frequently occur in the NC matrices and also twinning of NC structures is observed (60 or 120° rotation about  $c$ ). The extreme structural variability within and among natural pyrrhotite samples as observed by TEM-SAED challenges published models of vacancy superstructures involving modular stacking and polytypic formation, commensurate/incommensurate occupancy modulations or order/disorder transitions of antiphase domain arrangements. Because  $q_c$  is mostly around 0.35 nm<sup>-1</sup>, corresponding to roughly 3 nm in direct space, many proposed structure models of non-integral NC pyrrhotites involve very long range ordering apparently incompatible with simple coulombic short range interactions of vacancies.

**j.** *Application of <sup>29</sup>Si and <sup>27</sup>Al MAS-NMR spectroscopy to the study of the reaction mechanism of kaolinite to illite/muscovite (M. Mantovani/Sevilla, A. Escudero, and A.I. Becerro/Sevilla)*

Understanding the mechanisms for illitization of clay minerals has important applications in reconstructing geologic histories and determining the origins of physical and chemical characteristics of buried sediments. While many studies have been carried out on this topic, few have focused on the mechanism of illite formation from kaolinite. The purpose of this study was to investigate more deeply the illitization of kaolinite in KOH solution at a high solid/liquid ratio (1000 mg/ml).

The methodology followed consists in the hydrothermal treatment, at 500 bars, of a powdered kaolinite in a 2.5 M KOH solution, using a solid/liquid ratio = 1000 and increasing reaction

times (from 1 to 24 hours). X-ray diffraction (XRD) and infrared spectroscopy were used to follow the formation of new crystalline phases and the composition of the octahedral sheet, while the transformation of the Si and Al local environments was analyzed by  $^{29}\text{Si}$  and  $^{27}\text{Al}$  magic angle spinning nuclear magnetic resonance spectroscopy (MAS NMR).

The XRD patterns of the samples treated for 1, 4, and 7 h showed only unmodified reflections of kaolinite, as well as an extra reflection at  $\sim 30^\circ 2\theta$ . The patterns of the samples treated for 13 and 24 h revealed, in addition to the characteristic kaolinite reflections, a set of new reflections that indicate the crystallization of illite/muscovite, more pronounced in the sample treated for 24 h. The positions of the illite/muscovite basal reflections indicate a basal spacing of 10.2 Å, characteristic of TOT layers with dehydrated interlayer  $\text{K}^+$  ions. The location of the (060) reflection corresponds to a  $d_{060}$  value of 1.50 Å, slightly larger than that of the parent kaolinite. The reflections corresponding to kaolinite were unchanged throughout the process.

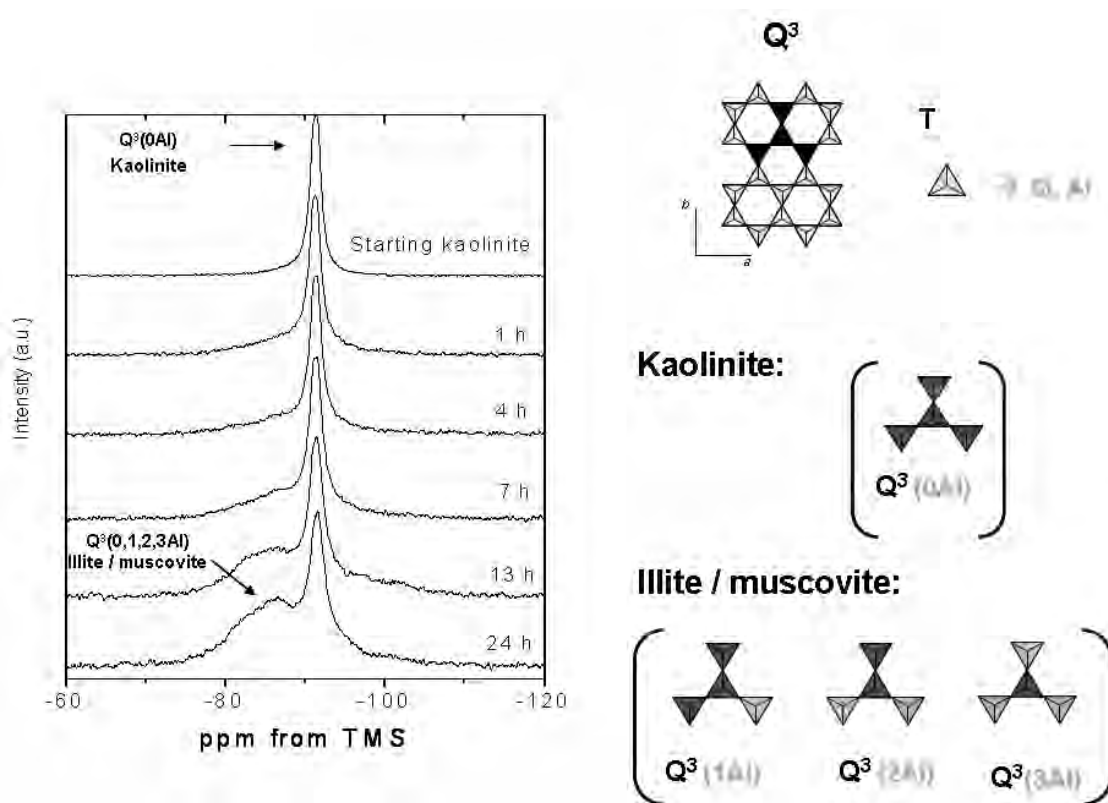


Fig. 3.3-13:  $^{29}\text{Si}$  MAS NMR spectra of kaolinite before and after hydrothermal treatment in KOH solution at increasing reaction times. The dotted line indicates the constant-frequency value of the main signal. The positions expected for the different  $\text{Q}^3(1-3\text{Al})$  in muscovite/illite are marked with arrows.

The  $^{29}\text{Si}$  MAS NMR spectrum of the starting and treated samples are shown in Fig. 3.3-13. The spectrum of the starting kaolinite contained a single, symmetric  $^{29}\text{Si}$  resonance at -91.26 ppm, corresponding to the unique Si environment in the sample, consisting of Si atoms

surrounded by three  $\text{SiO}_4$  tetrahedra  $-\text{Q}^3(0\text{Al})-$  (nomenclature from Liebau, 1985), in good agreement with the chemical formula of the kaolinite sample. The position of this signal does not change with the treatment, although an increase in the FWHM value was observed with reaction time, indicating a progressive disorder in the local environment of the Si nuclei of the remnant kaolinite particles. As reaction progressed, a new broad contribution developed on the high-frequency side of the main resonance, which was appreciable after only 1 h of treatment and the intensity of which increased with increasing reaction time. The new band is located in the ppm range characteristic of  $\text{Q}^3(1\text{Al})$ ,  $\text{Q}^3(2\text{Al})$ , and  $\text{Q}^3(3\text{Al})$  environments. The low resolution of the signal fails to provide reliable results in terms of the percentage of each environment.

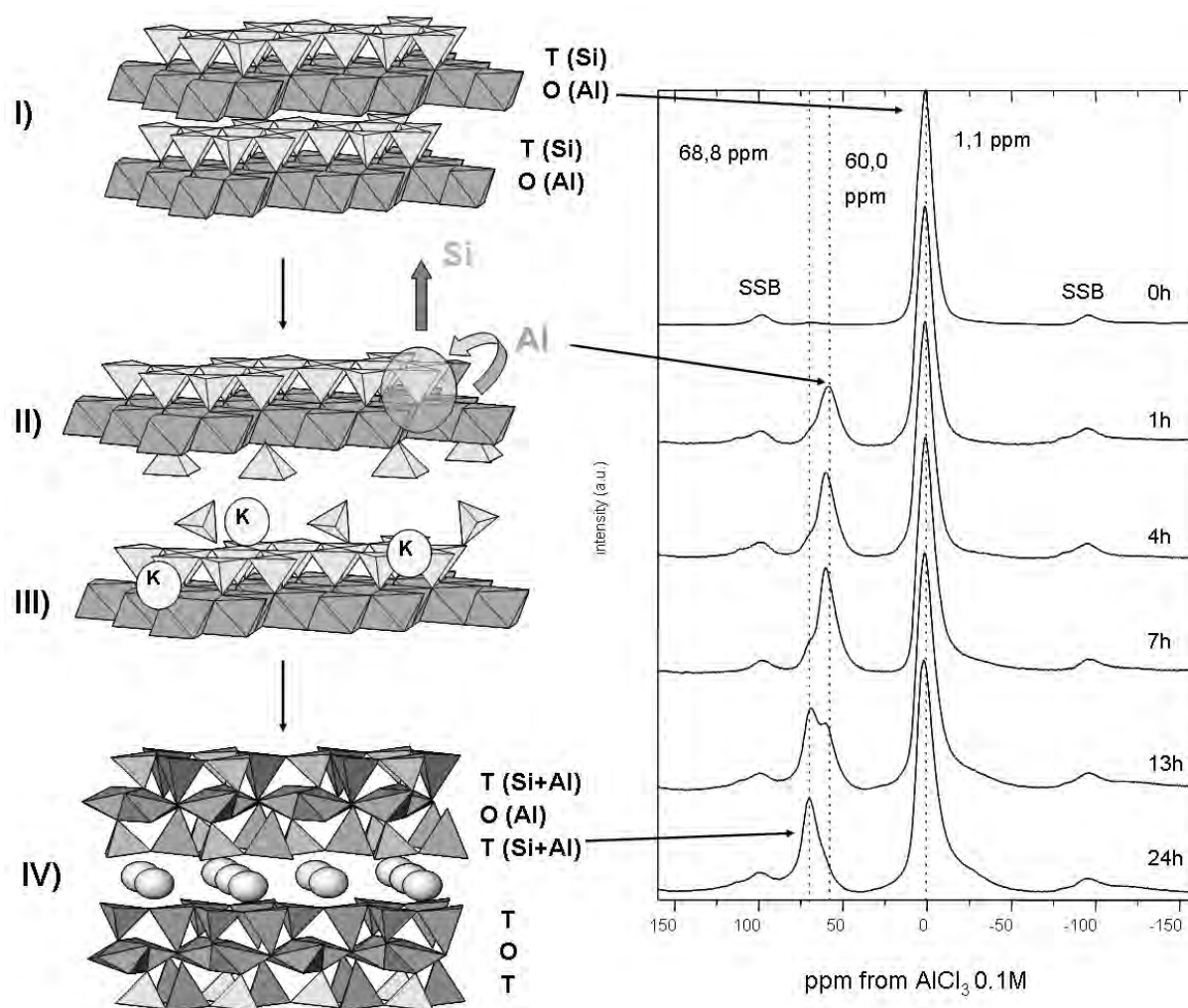


Fig. 3.3-14: Left: I) Starting kaolinite. II) Diffusion of Al from the octahedral to the tetrahedral sheet. III) Second tetrahedral sheet condensation does not take place until a minimum Al content is reached in the tetrahedral sheet of the TO structure. IV) Illite/muscovite; Right:  $^{27}\text{Al}$  MAS NMR spectra of kaolinite before and after hydrothermal treatment in KOH solution at increasing reaction times. The low-intensity signals at 98.2 ppm and 95.7 ppm are spinning side bands (SSB) of the Al resonance at 1.1 ppm.

The  $^{27}\text{Al}$  MAS NMR spectrum of the starting kaolinite and of the treated samples are shown in Fig. 3.3-14. The spectrum of the starting kaolinite consisted of a signal at 1.1 ppm, corresponding to Al in the octahedral sheet of the clay. When the sample was submitted to hydrothermal treatment for 1 h, a new signal was clearly observed at 60.0 ppm, which progressively decreased in intensity with increasing reaction time, giving rise to a second signal at 68.8 ppm. Both signals coexisted with the resonance at 1.1 ppm in all samples. The signals at 60.0 and 68.8 ppm are both in the frequency range characteristic of tetrahedral Al, denoting, therefore, that a partial change in the coordination polyhedron of Al was produced as a consequence of the treatment, the reaction products containing Al in both octahedral and tetrahedral coordination.

These results suggest that the first reaction stage consists of the diffusion of Al from the octahedral to the tetrahedral sheet of the kaolinite TO layers, giving rise to the precursors of the illite/muscovite nuclei. A minimum amount of tetrahedral Al is required in the original TO layer before condensation of a second tetrahedral sheet occurs to complete the formation of the illite/muscovite TOT layers. These nuclei require the condensation of an additional Si-Al tetrahedral sheet to be formed. Illite/muscovite coherent diffraction domains only form after 13 hours treatment; at shorter reaction times, proper illite/muscovite layers, with a basal spacing of 10 Å characteristic of TOT layers with interlayer  $\text{K}^+$ , are not observed as indicated by the absence of any reflection at  $8.6^\circ 2\theta$  on the XRD patterns.

**k. TEM study of hydrothermally altered pyrochlore from Zomba Malosa, Malawi (A. Soman, and T. Geisler/Münster; K. Pollok)**

Pyrochlore has been proposed as a promising candidate for the immobilization of weapons-grade plutonium. The investigation of the long-term performance of pyrochlore-group minerals and related pyrochlore-based ceramic waste forms is thus critical and mainly related to their aqueous durability. Studies of the alteration features in natural pyrochlore samples can provide such information for relevant geological conditions. It can help to interpret experimental data from leaching or dissolution studies performed under controlled physicochemical conditions and to deduce relevant reaction mechanisms and kinetics.

A naturally altered pyrochlore crystal from Zomba Malosa, Malawi, was investigated in the present study. It is of pegmatitic origin and has experienced multiple hydrothermal events. Its composition is complex and can be generalized based on a  $^{\text{VIII}}\text{A}_2^{\text{VI}}\text{B}_2^{\text{IV}}\text{X}_6^{\text{IV}}\text{Y}$  structural formula. The A site consists mainly of Ca and Na, while the B site is occupied by Nb, Ta, and Ti with  $\text{Nb} + \text{Ta} > 2\text{Ti}$ . The Y site is occupied by OH and F, and some amount of  $\text{H}_2\text{O}$ . Three different domains are evident in backscattered electron images (Fig. 3.3-15). Primary pyrochlore appears homogeneous without any pores. Stage I alteration domains are characterized by micrometer sized pores and are depleted in Ta, Ti, and U, but are relatively enriched in Nb. Radiometric U-Pb dating suggests that the stage I alteration occurred shortly

after the crystallisation of the pyrochlore parent. Stage II alteration domains appear as finger-shaped or cauliflower-like structures and are compositionally heterogeneous. They crosscut both the primary and the stage I alterations and are thus more recent, as also indicated by U-Pb dating results. All three stages have received an alpha-decay dosage of  $1.4 \times 10^{16}$   $\alpha$ -events/mg, which is above critical limit of amorphization ( $1 \times 10^{16}$   $\alpha$ -events/mg).

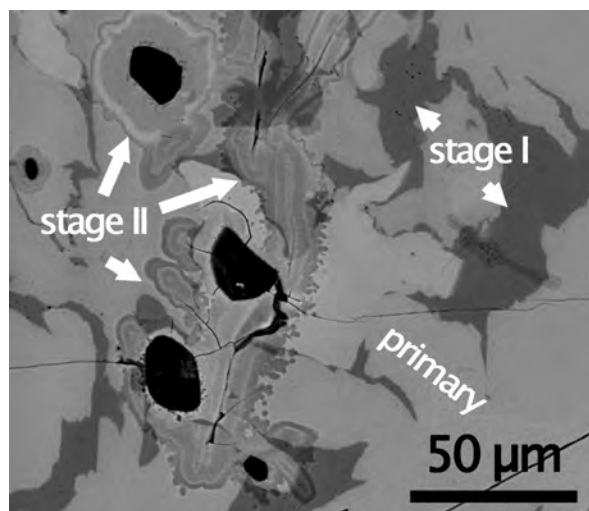


Fig. 3.3-15: Back scattered electron image of the pyrochlore sample indicating primary and altered parts. Primary and stage I yield an indistinguishable age, whereas stage II alterations are considerably younger.

Transmission electron microscope (TEM) work has so far been focused on the stage II domains to obtain information about the structural state and the elemental distribution. Special care has been taken to precisely trace the location of the interfaces between the altered domains and the pristine pyrochlore during ion milling sample preparation.

The primary pyrochlore is completely amorphous due to the metamictization as verified by selected electron diffraction area (Fig. 3.3-16 left). Primary and altered parts are marked by a sharp interface on the nano-scale. The altered stage II domains adjacent to the interface consists of polycrystalline particles with grain size of 10-50 nm embedded in a glassy matrix. However, the diffraction pattern suggests a preferred orientation of the grains. Towards the centre of the finger-shaped alteration, a single crystal with pores and inclusions has been found (Fig. 3.3-16 right). It is sharply marked off from the partly crystalline area. High resolution TEM reveals an amorphous band with a width of 150 nm right at the centre of the alteration which may represent an original fluid channel. EDX mapping in scanning TEM mode shows a Na depletion and Fe enrichment in the channel. Inclusions in the surrounding matrix show a Ca and F signal, suggesting nano-crystalline fluorite inclusions.

The textural observation made on the stage II domains indicate a diffusion-controlled leaching process that is associated with the nucleation and growth of new pyrochlore at the expense of

the amorphous phase. Accordingly, crystallinity is increasing towards the assumed fluid channel. Nano-crystalline particles with a preferred crystallographic orientation have also been observed in an experimentally altered natural, radiation-damaged zircon, suggesting a similar mechanism for both radiation-damaged materials. However, more work is necessary to fully understand the effect of radiation-damage on the alteration of pyrochlore.

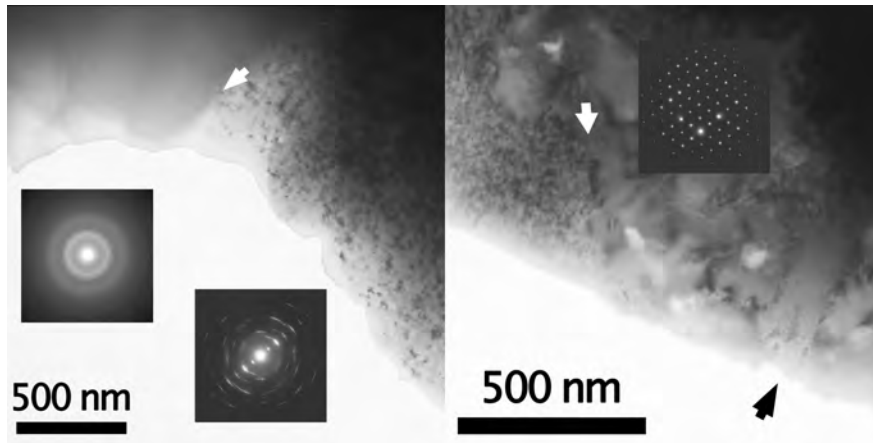


Fig. 3.3-16: Bright-field TEM images of selected area with electron diffraction patterns as insets. **Left:** The amorphous primary part is separated by a sharp interface (white arrow) from a partly crystalline area with preferred grain orientation. **Right:** The inner part of the alteration is a single crystal with pores and inclusions. It also exhibits an amorphous fluid channel (black arrow) and a well defined change to the partly crystalline area (white arrow). Inclusions show a significant enrichment of Ca and F suggesting secondary fluorite.

### 3.4 Physical properties of minerals

Structure-property relations of solids are of fundamental scientific and technological importance in Earth and material sciences. The knowledge of the physical properties of mantle minerals is important to understand the structure, dynamics, and processes in Earth's interior. For example, the interpretation of seismic data from the deep Earth's interior is based on laboratory measurements of sound and shear wave velocities of mantle minerals. Data on such physical properties of mantle minerals are however scarce and often not well constrained because *in situ* measurements at high pressures and temperatures on very small sample volumes are experimentally challenging. Advances in the development of experimental setups and the use of large-scale synchrotron and neutron facilities provided recently however an improved data set on physical properties of mantle materials.

Examples for such studies are given in this chapter. The first three contributions focus on the determination of sound and shear wave velocities of mantle phases in multianvil and diamond anvil cell experiments using ultrasonic interferometry, nuclear inelastic scattering, and Brillouin spectroscopy. The first contribution reports the measurements of seismic wave velocities of garnet, one of the major phases in the lower crust, upper mantle and transition zone. Since garnets form a majorite-pyrope solid-solution in the deep Earth interior, this study addresses the question on how the chemistry of this mantle phase influences its elastic properties. The second contribution focuses on the lower mantle phase ferropericlase and the potential influence of spin transitions on the elastic properties of this iron-bearing mineral, while the third contribution investigates the effect of an amorphous – amorphous transition in  $\text{TiO}_2$  on the sound wave velocities.

Compressibility is a further fundamental property of solids that is needed to interpret seismic data. The compressibility of ringwoodite and the effect of Mg-Fe substitution on the bulk modulus have been investigated by two X-ray diffraction studies. These investigations are particularly relevant for Fe-richer planetary mantle with an extended transition zone such as the Martian mantle. The results of our X-ray studies indicate that Fe incorporation into the ringwoodite structure does not significantly affect its bulk modulus and that the oxygen sublattice is the limiting factor for the compressibility.

Thermal diffusivities and conductivities as well as magnetic properties are addressed in the third part of this chapter. Thermal diffusivities and conductivities are important to model the thermal state and profile of the Earth's interior. Measurements of these properties on lower mantle phases are very demanding due to the small sample sizes. We present here two ways to circumvent this problem by performing experiments at lower pressures on analog materials ( $\text{CaGeO}_3$  perovskite) and by using first-principles molecular dynamics calculations. The final contribution of this chapter demonstrates that the crystal structure of hematite exerts an important control on the anisotropy of its magnetic properties. Thus metamorphic rocks with pronounced textures may show a strong orientation-dependence of magnetic properties.

**a.**  $V_p$  and  $V_s$  measurements of polycrystalline pyrope ( $Mg_3Al_2Si_3O_{12}$ ) up to 16 GPa (J. Chantel and D.J. Frost)

Garnet is one of the major constituents of the lower crust, upper mantle and transition zone. Although most natural garnets are complex solid solutions, the most significant component in garnets of mantle origin is pyrope. Knowledge of the elasticity of pyrope is directly relevant for the mineralogical interpretation of seismic velocity profiles. Chemical variations in the mantle resulting from partial melting and the subduction of oceanic lithosphere will mainly vary the mode and composition of garnet in the upper mantle and transition zone. In order to ultimately study the effects of chemistry on the elasticity of garnet, we are first studying the elasticity of the dominant end member pyrope.

Earlier studies of the elastic properties of pyrope using ultrasonic techniques were performed up to 10 GPa. In this study, we report new measurements of the elastic compressional ( $P$ ) and shear ( $S$ ) wave velocities for synthetic polycrystalline pyrope [ $Py_{100} = Mg_3Al_2Si_3O_{12}$ ] determined by ultrasonic interferometry at pressures up to 16 GPa. We compare our wave velocity data to those of previous investigations.

$P$  and  $S$  wave velocities as functions of pressure to 16 GPa were obtained in experiments using a multianvil apparatus (Zwick-5000) with an 18mm edge length octahedron and 11 mm anvil truncations. In order to provide a pseudohydrostatic pressure environment, the specimen was placed inside the MgO octahedral assembly on top of a disk of AgCl and surrounded by a BN sleeve. To define precisely velocity – pressure relations, the experiment includes the two pressure calibrants Bi and Manganin wire. The electrical resistance of Manganin was measured under pressure up to 9 GPa and calibrated against well-known fixed points, the Bi phase transitions (Bi I–Bi II at 2.55 GPa and Bi III–Bi IV at 7.70 GPa). Obtained results show a, previously defined, linear relationship between the resistance and the pressure up to 6.4 GPa. However, at 6.4 and 7 GPa two sharp discontinuities appear with good reproducibility in the electrical resistance of Manganin.

To obtain the  $P$  and  $S$  wave velocities we use the phase-comparison method of ultrasonic interferometry. The output from a continuous wave source is gated to produce a pair of phase-coherent MHz pulses, which serve as input signals to excite the transducer. The transducer is glued to one polished truncated surface of the cube, opposite the truncation used to pressurize the experiment. The elastic waves generated by each pulse are reflected and transmitted at the WC cube, then at the alumina buffer rod and finally at the sample, resulting in a series of ‘sample’ echoes following the buffer rod echo. As the carrier frequency is varied, alternate constructive and destructive interference between the superimposed buffer rod and sample signals will occur, resulting in a series of maxima and minima in the amplitude spectrum modulated by the transducer response envelope. Frequencies for  $p$ th and  $(p+n)$ th interference extrema,  $f_p$  and  $f_{p+n}$  respectively, can be used to estimate the apparent travel time by  $t_{est} = n / (f_{p+n} - f_p)$ .  $P$  and  $S$  wave velocities from this study have been plotted as a function of

pressure (Fig. 3.4-1), and compared with previous data on the same mineral. Within the observed scatter in these data sets and the measured experimental uncertainties, all of these velocity data are mutually consistent. The ultimate goal of this project is to determine the effects of chemistry on the elastic properties of garnet at high pressures and temperatures, and use these data to assess the origins of seismic velocity heterogeneity in the upper mantle and transition zone.

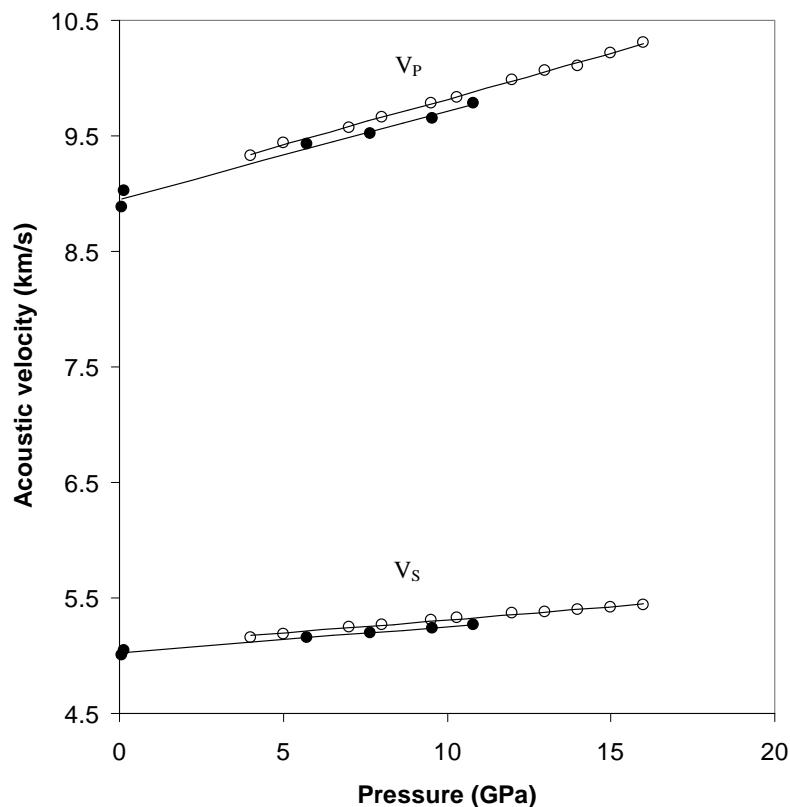


Fig. 3.4-1: Acoustic compressional wave velocity ( $V_p$ ) and shear wave velocity ( $V_s$ ) at room T for pyrope garnet as a function of increasing pressure. Open circles are the ultrasonic data for polycrystalline aggregate synthesized at BGI. Solid circles are values from the literature.

**b.** Bulk sound velocity measurements of lower mantle phases at high  $P,T$  using nuclear inelastic scattering (C. McCammon, L. Dubrovinsky, K. Glazyrin, O. Narygina, and E. Greenberg; I. Sergueev, and A. Chumakov/Grenoble)

Comparison of laboratory measurements of sound and shear wave velocities of mantle minerals with seismic data constitutes one of the foundations upon which knowledge of the Earth's interior is based. *In situ* measurements are important, because some transitions (for example, spin transitions) are not quenchable, and may influence the elastic properties of iron-containing minerals. Nuclear inelastic scattering (NIS) offers the possibility to determine bulk

sound velocities of iron-containing minerals in the diamond anvil cell through direct measurement of the partial density of states. Both dominant lower mantle phases, silicate perovskite and ferropericlaase, have been reported to undergo spin transitions at pressure and temperature conditions of the Earth's lower mantle, although their nature remains controversial. The resulting uncertainty regarding their influence on mantle properties is bypassed, however, by making direct bulk sound velocity measurements at high pressure and temperature that can be compared with seismic data.

Using a newly developed approach, we performed NIS measurements in laser-heated diamond anvil cells, coupled with nuclear forward scattering (NFS) to determine spin populations and X-ray diffraction to observe crystal structures. All nuclear resonance synchrotron experiments were performed on beamline ID18 at the European Synchrotron Radiation Facility. To investigate the effect of spin transitions on bulk sound velocities of lower mantle minerals, our first study focused on high pressure and temperature measurements of  $\text{Mg}_{0.8}\text{Fe}_{0.2}\text{O}$  ferropericlaase. We collected both NIS and NFS data from 0 to 113 GPa at temperatures up to 2200 K, where pressure was measured using either ruby fluorescence or from the Raman spectrum of diamond, and temperature was measured directly from analysis of the NIS data (Fig. 3.4-2). The NFS data enabled the spin state population at each pressure and temperature to be determined (Fig. 3.4-3). Preliminary analysis of the NIS data to extract the Debye sound velocities shows that velocity reduction as a function of temperature is smaller than expected, which may have important implications for the interpretation of fast and slow regions in seismic tomography data.

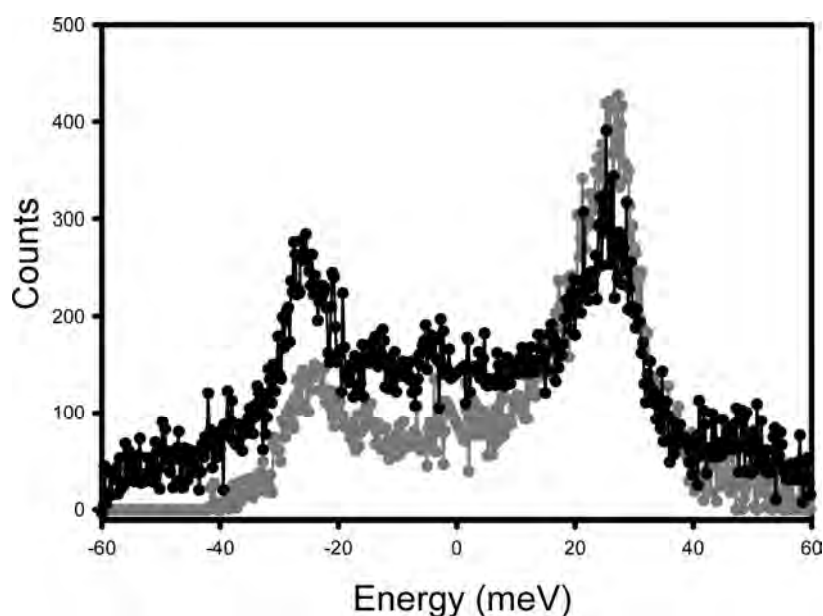


Fig. 3.4-2: Nuclear inelastic scattering (NIS) spectra of  $\text{Mg}_{0.8}\text{Fe}_{0.2}\text{O}$  at 40 GPa and room temperature (grey) and 2200 K (black). Note the increased intensity of the anti-Stokes component (scattering at negative energies) in the black spectrum, which can be used to determine the sample temperature. For clarity the central resonance lines have been removed.

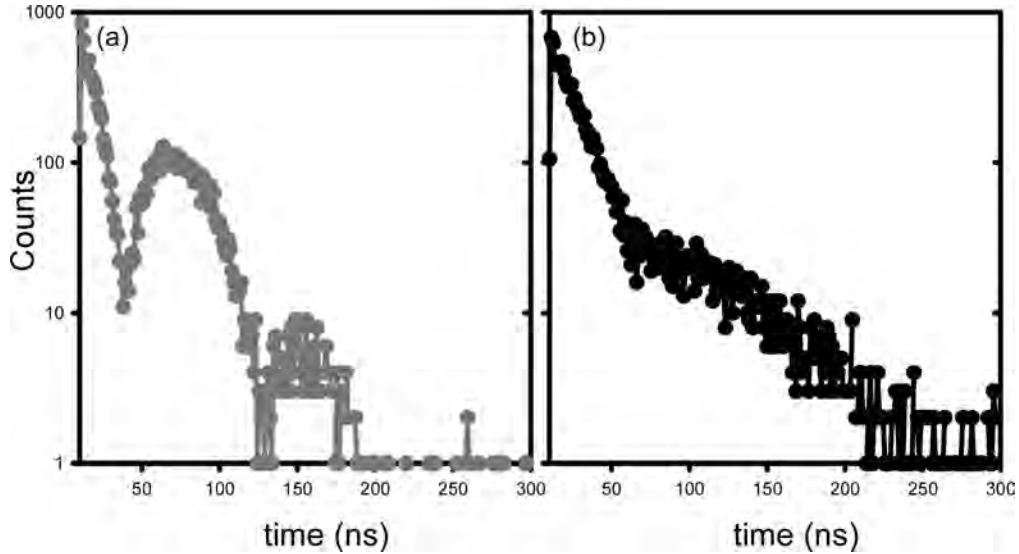


Fig. 3.4-3: Nuclear forward scattering (NFS) spectra of  $\text{Mg}_{0.8}\text{Fe}_{0.2}\text{O}$  at 40 GPa at (a) room temperature, and (b) 2200 K, collected at the same conditions as the NIS spectra. The room temperature NFS spectrum shows high frequency quantum beats (= quadrupole splitting) associated with high-spin  $\text{Fe}^{2+}$ , while the high temperature NFS spectrum shows low frequency quantum beats (= quadrupole splitting) which is expected for low-spin  $\text{Fe}^{2+}$ .

**c.** *Elastic behaviour of nanocrystalline anatase  $\text{TiO}_2$  under compression (A. Kantor, I. Kantor, and V. Prakapenka/Chicago)*

Pressure-induced amorphization, which is a metastable transformation of crystalline material into amorphous solids, is a well-known phenomenon for many materials. Some of them (*e.g.*,  $\text{H}_2\text{O}$ , Si) even undergo a further amorphous-amorphous transition upon compression from a low to a high density phase. Pressure-induced amorphization leading to high- and low-density amorphous forms were recently also reported for nanocrystalline titanium dioxide. To examine how this transition influences the elastic behaviour of titanium dioxide we have carried out diamond anvil cell experiments and simultaneously collected not only X-ray diffraction data but also Brillouin scattering spectra. The investigation was conducted at the GSECARS (Sector 13, Advanced Photon Source, Argonne, USA) synchrotron beamline. The nanopowder sample was loaded along with a couple ruby spheres and a piece of gold for the precise pressure determination.

The diffraction patterns were collected upon compression (to about 50 GPa) and decompression. The amorphization of the material was well-pronounced during the compression of the sample at about 18 GPa. There were no drastic changes in the main broad peak position during decompression, which could possibly show the high- to low-density amorphous-amorphous transition. However further experiments are required in the low-pressure regime ( $< 18$  GPa) to assess the structural behaviour of titanium oxide upon decompression.

Collected Brillouin spectra allowed calculating sound velocities – pressure dependencies of both bulk  $V_P$  and  $V_S$  (Fig. 3.4-4 and Fig. 3.4-5, respectively). After pressure-induced amorphization both sound velocities are changing smoothly during compression and decompression; no elastic discontinuities were observed. Altogether our study could not yet confirm the presence of an amorphous-amorphous transition but it demonstrates that combined Brillouin scattering and X-ray diffraction experiments on materials pressurized in a diamond anvil cell allows us to gain important structural and elastic data at elevated pressures.

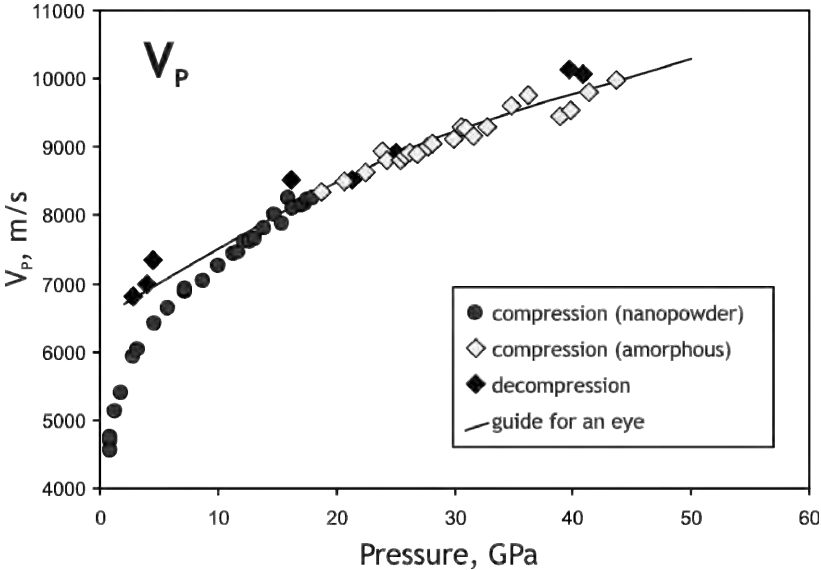


Fig. 3.4-4: Longitudinal sound wave velocities – pressure dependence for nanocrystalline titanium dioxide.

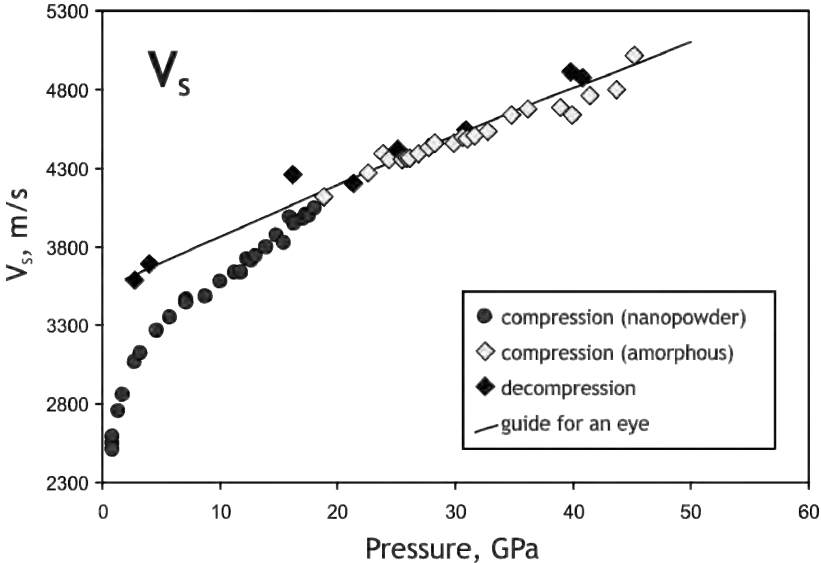


Fig. 3.4-5: Transverse sound wave velocities – pressure dependence for nanocrystalline titanium dioxide.

**d.** *Effect of iron on the compressibility of hydrous ringwoodite (G. Ganskow, T. Boffa Ballaran, and F. Langenhorst)*

Ringwoodite (Mg,Fe)<sub>2</sub>SiO<sub>4</sub> is thought to be the most abundant mineral in the Earth's transition zone as well as in the deeper Martian mantle. Nominally anhydrous minerals such as Mg-ringwoodite are able to accommodate up to 2.4 wt.% H<sub>2</sub>O as OH-groups in their structure, implying a potentially enormous water reservoir in the Earth's mantle. Since the compressibility and density of ringwoodite are relevant for the interpretation of seismic velocities in the transition zone, anhydrous and hydrous Mg<sub>2</sub>SiO<sub>4</sub> ringwoodites have been intensively studied using a variety of techniques, including Brillouin spectroscopy, ultrasonic interferometry and X-ray diffraction. Anhydrous iron-bearing ringwoodite containing up to 10 mol.% iron appears to have a slightly higher bulk modulus ( $K_{T0} = 188(3)$  GPa) than the pure Mg-endmember. In contrast, hydrous Mg-ringwoodite with 2.3 wt.% H<sub>2</sub>O has a smaller isothermal bulk modulus with  $K_{T0}$  ranging between 155(4) and 165.8(5) GPa. Water and iron substitution into the ringwoodite structure appears therefore to have an opposite effect on its compressibility. To better constrain such results, we have determined the compressibility of iron-rich hydrous ringwoodite in a diamond anvil cell by single-crystal X-ray diffraction. Knowledge of the effect of iron on the compressibility of ringwoodite is particularly important for the interpretation of the structure of iron-rich planetary mantles such as those of Mercury and Mars.

Samples of hydrous ferroan ringwoodite were synthesized from a stoichiometric MgFeSiO<sub>4</sub> starting mixture (Fe<sub>2</sub>SiO<sub>4</sub> + Mg(OH)<sub>2</sub> + SiO<sub>2</sub>) at 15 GPa and 1150 °C (run 3854) as well as at 20.5 GPa and 1400 °C (run 4218) using a multianvil press. Ringwoodite samples were characterized using EPMA, infrared spectroscopy and electron energy loss spectroscopy. The compositions of the two examined hydrous ringwoodites are as follows: Mg<sub>0.97</sub>Fe<sub>0.99</sub>Si<sub>0.98</sub>H<sub>0.14</sub>O<sub>4</sub> (run 3854) and Mg<sub>1.23</sub>Fe<sup>2+</sup><sub>0.67</sub>Fe<sup>3+</sup><sub>0.1</sub>Si<sub>0.98</sub>H<sub>0.07</sub>O<sub>4</sub> (run 4218). Unit-cell lattice parameters were measured at room temperature and different pressures up to about 9 GPa by means of X-ray single-crystal diffraction. The *P-V* data were fitted to a second-order Birch-Murnaghan equation of state ( $K'$  fixed to the value of 4).

The lattice parameters of hydrous ferroan ringwoodite at ambient conditions are  $a = 8.1597(6)$  Å and  $V = 543.28(13)$  Å<sup>3</sup> (GG 3854), and  $a = 8.1384(3)$  Å and  $V = 539.03(7)$  Å<sup>3</sup> (GG 4218). The refined EoS parameters are:  $V_0 = 543.32(8)$  Å<sup>3</sup> and  $K_{T0} = 186.5(9)$  GPa for run 3854 and  $V_0 = 539.01(5)$  Å<sup>3</sup> and  $K_{T0} = 184.1(7)$  GPa for run 4218.

The bulk modulus of hydrous ferroan ringwoodites obtained in this study are very similar ( $K_{T0} = 186.5(9)$  and  $K_{T0} = 184.1(7)$  GPa for sample 3854 and 4218 respectively) and have values close to those reported for anhydrous Mg-ringwoodite. Also, a recent study on Fe<sub>2</sub>SiO<sub>4</sub>-ringwoodite presents a value of the bulk modulus very similar to that of (Mg,Fe)<sub>2</sub>SiO<sub>4</sub>-ringwoodite examined in this study, suggesting therefore that the Fe substitution has little

effect on the compressibility of ringwoodite. This would suggest therefore that the oxygen closed-packing of the spinel structure is the decisive parameter in determining its compressibility.

e. Equation of state of  $Fe_2SiO_4$  ringwoodite (F. Nestola/Padova, T. Boffa Ballaran, and M. Koch-Müller/Potsdam)

Ringwoodite is among the most investigated phases in Earth sciences due to its high abundance in the transition zone of the Earth's mantle and to the characteristic polymorphic transformations, which are probable causes of seismic discontinuities at depths of 410 km (olivine to wadsleyite transformation) and 525 km (wadsleyite to ringwoodite transformation). In the last decade several experimental and computational works have mainly focused on the effect that water could have on the thermodynamic properties of pure  $Mg_2SiO_4$  ringwoodite; less constrained is instead the effect of Fe substitution, which is however important not only for the Earth interior but also for iron-rich planetary mantles. Thermodynamic data (e.g., bulk modulus, thermal expansion, molar volume) for iron-rich ringwoodites are scarce and show some discrepancies. For instance, experimental works reported for pure  $Fe_2SiO_4$  ringwoodite values of bulk modulus,  $K_{T0}$ , ranging between 201 and 207 GPa with a first pressure derivative,  $K'$ , ranging between 4 and 5.6.

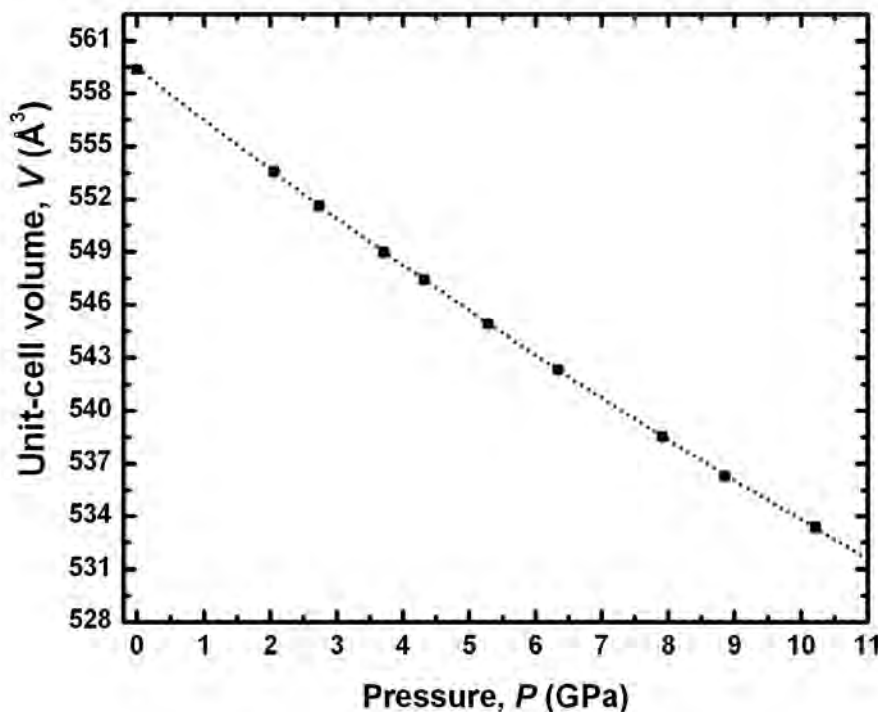


Fig. 3.4-6: Variation of the unit-cell volume of  $Fe_2SiO_4$  ringwoodite up to 10 GPa and at room temperature.

In order to clarify the effect of the Mg-Fe substitution on compressibility, we have conducted high-pressure *in situ* measurements on a single-crystal of Fe<sub>2</sub>SiO<sub>4</sub> ringwoodite up to 10.2 GPa carrying out X-ray diffraction experiments in a diamond anvil cell. The measurements allowed to determine accurate values of the unit-cell lattice parameters at different pressures and to calculate a precise value of both bulk modulus and its first pressure derivative. The pressure – volume data (see Fig. 3.4-6), measured at 10 different pressures, did not show any evidence of a phase transformation and were fit using a third-order Birch-Murnaghan equation of state (dashed line in Fig. 3.4-6). The refinement allowed obtaining simultaneously the following coefficients:  $V_0 = 559.44(6) \text{ \AA}^3$ ,  $K_{T0} = 187.3(1.7) \text{ GPa}$ , and  $K' = 5.5(4)$ . This result implies that the Mg-Fe substitution along the Fo-Fa ringwoodite join does not affect significantly the bulk modulus. However, with respect to the Mg<sub>2</sub>SiO<sub>4</sub> end-member and intermediate compositions along the Fo-Fa join, which always show a  $K'$  close to 4. An increase in the first pressure derivative seems to be evident, as well.

**f.** *Compressibility of the Ca<sub>2</sub>Sb<sub>2</sub>O<sub>7</sub> weberite-like compound: In situ high-pressure single-crystal X-ray diffraction study (L. Chelazzi/Firenze, T. Boffa Ballaran, F. Nestola/Padova, L. Bindi/Firenze, and P. Bonazzi/Firenze)*

The A<sub>2</sub>B<sub>2</sub>O<sub>7</sub> oxides (A=M<sup>2+</sup>; B=M<sup>5+</sup>) have a broad range of chemical and physical properties and great technological potential. Most of these compounds and minerals adopt a zirconolite-polytype (commonly pyrochlore-like) or a weberite-polytype structure, depending on the kind of cations (ionic radius, electronegativity, etc.), as well as the pressure and/or temperature of crystallization. Therefore, investigation of their thermodynamic properties (*e.g.*, thermal expansion and compressibility) is crucial in determining their stability fields. Nonetheless, no data of compressibility of weberite-type structures have been reported in the literature so far, except for the natural ingersonite, Ca<sub>3</sub>MnSb<sub>4</sub>O<sub>14</sub>, which adopts a weberite-3*T* structure. It is known from previous works that the Ca<sub>2</sub>Sb<sub>2</sub>O<sub>7</sub> compound occurs in both pyrochlore and weberite-2*O* structure types depending on the pressure applied during the synthesis, with pressure higher than 6 GPa favouring the cubic pyrochlore structure. In this work we have investigated this compound, having a weberite-2*O* structure, by means of *in situ* single crystal X-ray diffraction at high pressure using a diamond anvil cell. The high-pressure data were collected at room temperature up to  $P_{\text{max}} = 9.2 \text{ GPa}$  and unit-cell data were measured at 16 different pressures. No phase-transition was observed in the range of pressure investigated. The  $P$ - $V$  data, as suggested by the relative  $F_E$ - $f_E$  plot, were fitted using a second-order Birch-Murnaghan Equation of State (EoS). The refined EoS coefficients are:  $V_0 = 555.8(1) \text{ \AA}^3$  and  $K_0 = 155(1) \text{ GPa}$ . The value of the bulk modulus obtained for Ca<sub>2</sub>Sb<sub>2</sub>O<sub>7</sub> appears to be identical to that reported for ingersonite [154 (2) GPa]. Nonetheless, their respective high-pressure behaviour seems to be significantly different with respect to their axial compressibility. Indeed, ingersonite compresses almost isotropically, whereas Ca<sub>2</sub>Sb<sub>2</sub>O<sub>7</sub> shows a marked anisotropic compression (Fig. 3.4-7).

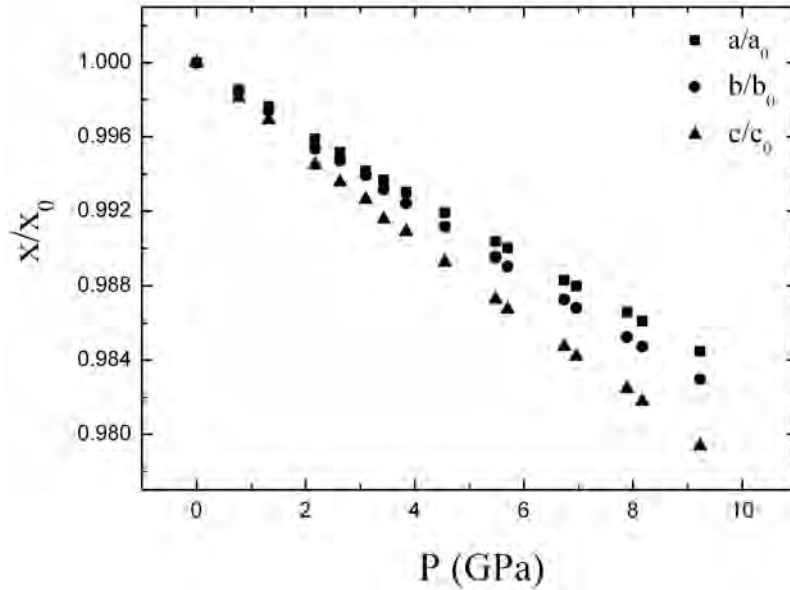


Fig. 3.4-7: Evolution of the unit-cell lattice parameters of  $\text{Ca}_2\text{Sb}_2\text{O}_7$  normalised with respect to the room pressure values. The symbols used are larger than the errors.

**g. Thermal diffusivity of  $\text{CaGeO}_3$  perovskite (G. Manthilake, N. de Koker, and D.J. Frost)**

Knowledge of the thermal diffusivity of mantle minerals is essential for understanding the dynamic properties in the Earth's mantle. A number of studies on heat-transfer properties of mantle minerals have been made so far at high pressures in addition to theoretical approaches that address lattice anharmonicity and use Debye theory or the results of infrared spectroscopy. The thermal diffusivity of perovskite is poorly known due to the difficulty of synthesizing an adequately large sample volume required for measurements within its stability field. Analog materials have been commonly used to characterize the physical properties of perovskite at more easily achievable lower pressures. Calcium germanate ( $\text{CaGeO}_3$ ) has served as an excellent analog for  $\text{MgSiO}_3$  perovskite, as both structures exhibit a similar sequence of phase transformations.

Here we present the thermal diffusivity of  $\text{CaGeO}_3$  perovskite, measured at pressures of 8, 10, and 14 GPa, up to 1473 K using a 5000 tonne multianvil apparatus. The measurements were based on the Ångström method, in which, the thermal diffusivity can be determined from both the phase and the amplitude of the periodic temperature wave propagated through the sample. Calcium germanate-perovskite samples were synthesized for the thermal diffusivity measurements at 8 GPa and 1373 K for 2 hours, from wollastonite-  $\text{CaGeO}_3$  powder. The dimensions of the sample used for the measurements were  $\sim 3.5$  mm in diameter and  $\sim 3.5$  mm in length. A 25/15 multianvil assembly was employed with a  $\text{LaCrO}_3$  furnace. Cylindrical samples were cut into two halves in the axial direction and a vertical groove was made to accommodate an inner thermocouple. The outer thermocouple was placed along the surface of the sample. Thermocouples were fabricated from 0.05 mm diameter  $\text{W}_{97}\text{Re}_3$ - $\text{W}_{75}\text{Re}_{25}$  wires.

Measurements were performed at frequencies of 0.1, 0.4, 0.7, 1.0 and 1.3 Hz during heating and subsequent cooling at intervals of 100 K. We fitted 10 sinusoidal cycles to obtain amplitude and phase at each modulation frequency (Fig. 3.4-8a). Thermal diffusivity (Fig. 3.4-9) was calculated from the amplitude ratio and phase shift of the two temperature waves. Thermal conductivity was obtained from calculated thermal diffusivity  $D$ , adopting  $\kappa = D\rho C_p$ , where  $\rho$  is the density function and  $C_p$  is the heat capacity (Fig. 3.4-10).

The thermal diffusivity and the thermal conductivity of  $\text{CaGeO}_3$  perovskite increases with increasing pressure. Our thermal diffusivity data of  $\text{CaGeO}_3$  perovskite is in good agreement with that of  $\text{MgSiO}_3$  perovskite, but it is lower than the thermal diffusivity of ringwoodite and majorite garnet. These results suggest the association of low thermal conductivity with transformation of majorite and ringwoodite into perovskite in the lower mantle.

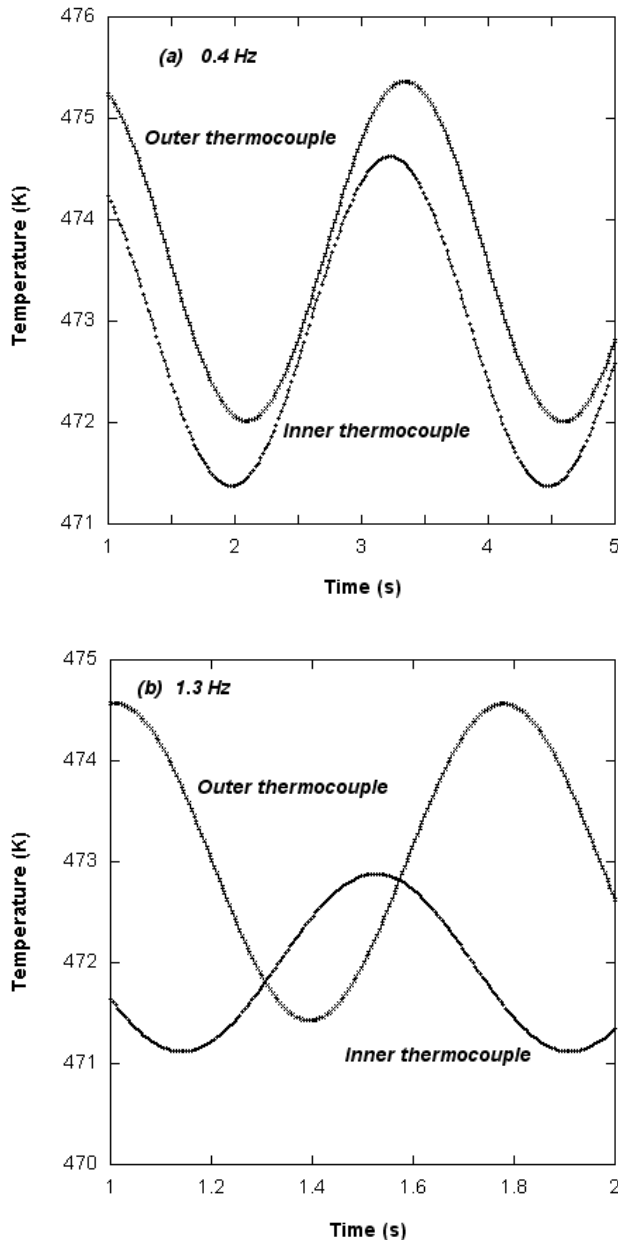


Fig. 3.4-8: Examples of fitted sine waves for the measured data at frequencies 0.4 Hz (a) and 1.3 Hz (b) at 10 GPa and 473 K.

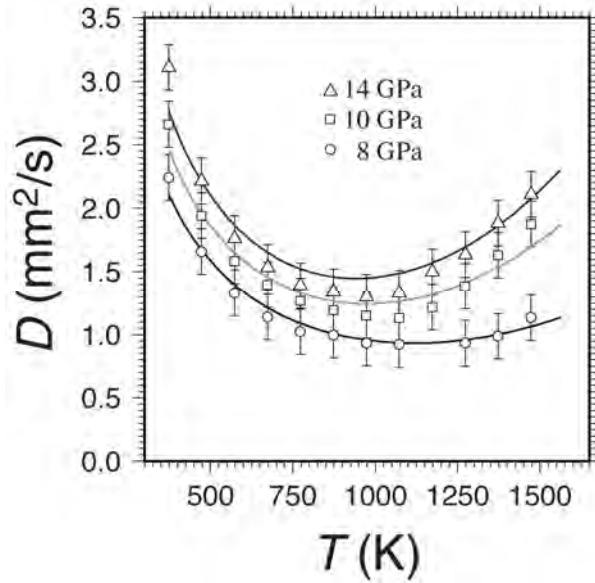


Fig. 3.4-9: Comparison of thermal diffusivities of CaGeO<sub>3</sub> perovskite at pressures 8, 10, and 14 GPa.

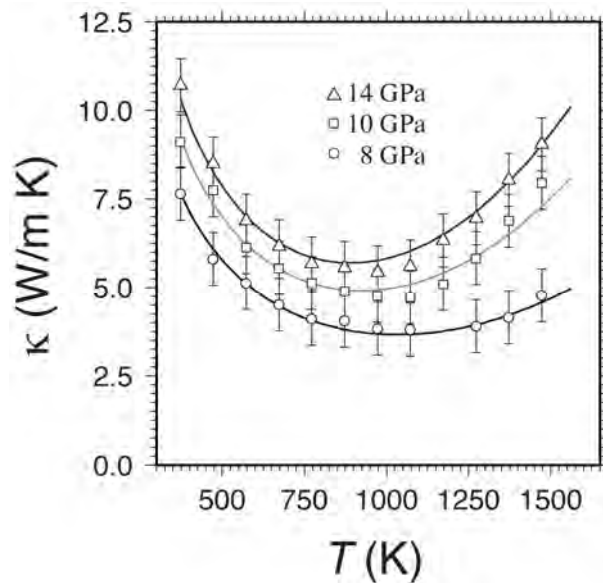


Fig. 3.4-10: Thermal conductivities of CaGeO<sub>3</sub> perovskite at 8, 10, and 14 GPa.

**h.** *Lattice thermal conductivity in MgO periclase computed using equilibrium first-principles molecular dynamics (N. de Koker)*

Thermal conductivity ( $\mathcal{K}$ ) of candidate deep-Earth mineral phases at high pressure and temperature represents a key parameter for understanding the thermal state of the deep Earth, and places important boundary constraints on convection in the outer core by which Earth's

magnetic field is generated. Current estimates for  $\mathcal{K}$  in the lower mantle are very poorly constrained, ranging from 4-16 W/m/K. The large uncertainty results mainly from two factors. Firstly, measurements of  $\mathcal{K}$  at pressure are extremely challenging and often not mutually consistent, resulting in notable low pressure uncertainties. Secondly, there is no consensus on how to represent the pressure dependence of  $\mathcal{K}$ ; different models yield rather different extrapolations. Due to the large uncertainties and a relatively small range in pressure in the experimental data, distinguishing among these various models has not been possible.

First-principles computational methods present an ideal solution to this dilemma, as they are reliable and robust at both ambient and high pressures. Unfortunately, these methods are very demanding on computational resources. Because existing methods by which thermal conductivity can be computed require large system sizes and long simulation times, the first principles determination of lattice thermal conductivity has remained a difficult challenge.

We have implemented a simple, computationally efficient method for computing lattice thermal conductivity from first principles. The basis for the method is the Peierls-Boltzmann transport equation

$$\mathcal{K} = \sum_s \int_{\mathbf{q}} v_{\mathbf{q},s}^2 c_{\mathbf{q},s} \tau_{\mathbf{q},s} d\mathbf{q}, \quad (1)$$

where  $\tau_{\mathbf{q},s}$  is the lifetime of phonons of mode  $s$  at wave vector  $\mathbf{q}$ ,  $v_{\mathbf{q},s} = |\mathbf{v}_{\mathbf{q},s}|$  is the phonon group velocity

$$\mathbf{v}_{\mathbf{q},s} = \frac{\partial v_{\mathbf{q},s}}{\partial \mathbf{q}}, \quad (2)$$

and  $c_{\mathbf{q},s}$  is the modal heat capacity

$$c_{\mathbf{q},s} = \frac{k_B}{V} \frac{x^2 e^x}{(e^x - 1)^2}; \quad x = \frac{h v_{\mathbf{q},s}}{k_B T}. \quad (3)$$

To compute  $\mathcal{K}$  from equation (1), phonon lifetimes times and frequencies must be known at all wave vectors within the Brillouin zone. The method evaluates these properties by combining equilibrium first-principles molecular dynamics (FPMD) and first-principles lattice dynamics (FPLD), both of which are well established methods for characterizing thermal effects in solids.

Recognizing that phonon lifetimes are directly related to the decay of the wave-vector dependent velocity autocorrelation function, values for  $\tau_{\mathbf{q},s}$  are computed at a subset of wave vectors using FPMD. Anharmonic vibrational frequencies thus obtained are in close agreement with the harmonic frequencies computed at all wave vectors within the Brillouin zone by FPLD.

Low pressure  $\mathcal{K}$  values for MgO periclase, computed via (1) by FPMD using 64 and 216 atom simulation cells, show excellent agreement with available experimental measurements

(Fig. 3.4-11), although direct comparison is possible only between 500-1200 K, where theoretical pressures are comparable to those at which experimental measurements are available. Comparison to higher temperature experimental values suggests that the radiative conductivity is significant above about 1500 K.

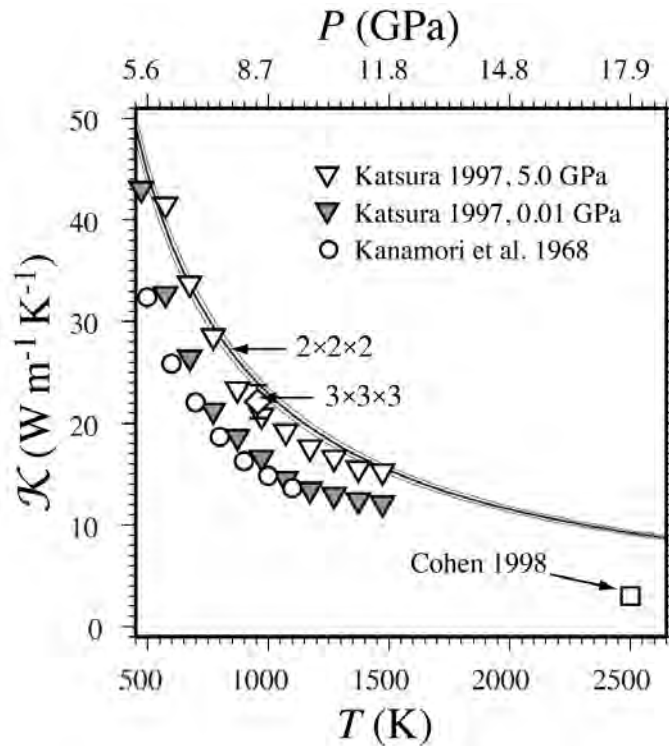


Fig. 3.4-11: Thermal conductivity of MgO at the LDA relaxed volume (10.998 cm<sup>3</sup>/mol). Thick line with uncertainty envelope – 64 atom cell; Diamond – 216 atom cell. Pressures to which various temperatures correspond are indicated on the top axis, and include a correction for overbinding due to the LDA.

**i.** *The magnetic signature of basal plane anisotropy in hematite (K. Fabian, P. Robinson, and S.A. McEnroe/Trondheim; F. Heidelberg)*

At the Morin-transition,  $T_M \sim 260\text{K}$ , the magnetic symmetry of hematite changes from c-axis parallel magnetic ordering to c-axis perpendicular ordering. Above  $T_M$  the crystal symmetry of hematite in the basal plane predicts three easy magnetization axes for the antiferromagnetic spins. Spin canting then leads to three preferred magnetization axes perpendicular to these easy axes. The threefold atomic symmetry in the basal plane creates three equivalent a-axes corresponding to three equivalent magnetic states. The magnetic anisotropy energy in the basal plane therefore shows six-fold symmetry. Along the c-axis susceptibility is low, coercivity is extremely high, and magnetization can be moved out of the basal plane only under the influence of very strong fields. Of interest here, however, is the detection of magnetic variations within the basal plane, and the relationships, if any, between the

orientations of magnetic sublattices and the structure of  $\text{Fe}^{3+}$  octahedrons in the basal plane related to the positions of the crystallographic  $a$ -axes. This has become a recent focus of interest in the study of single hemo-ilmenite crystals, where the natural remanent magnetization (NRM), strictly confined to the basal plane, appears to be derived from a vector sum of the lamellar magnetization parallel to the direction of the sublattice magnetizations, and the spin-canted magnetization of the hematite, which is normal to the mean of the sublattice magnetizations.

The present study was conducted on a  $2 \times 3 \times 4 \text{ mm}^3$  natural hematite crystal, on which one shiny face is parallel to the basal plane. The orientation of the single crystal hematite was determined by electron backscatter diffraction (EBSD) in the scanning electron microscope (SEM). The measured basal-plane surface is homogeneous in orientation within an angle of about  $0.5^\circ$  with the reference edge being parallel to one of the  $a$ -axes (Fig. 3.4-12). The angular-dependent magnetic measurements were performed using a vibrating-sample magnetometer (PMC Micromag 3900) equipped with a computer -controlled continuous rotation about its Z-axis, allowing a maximum applied field of 1.4 T. For each rotation step of

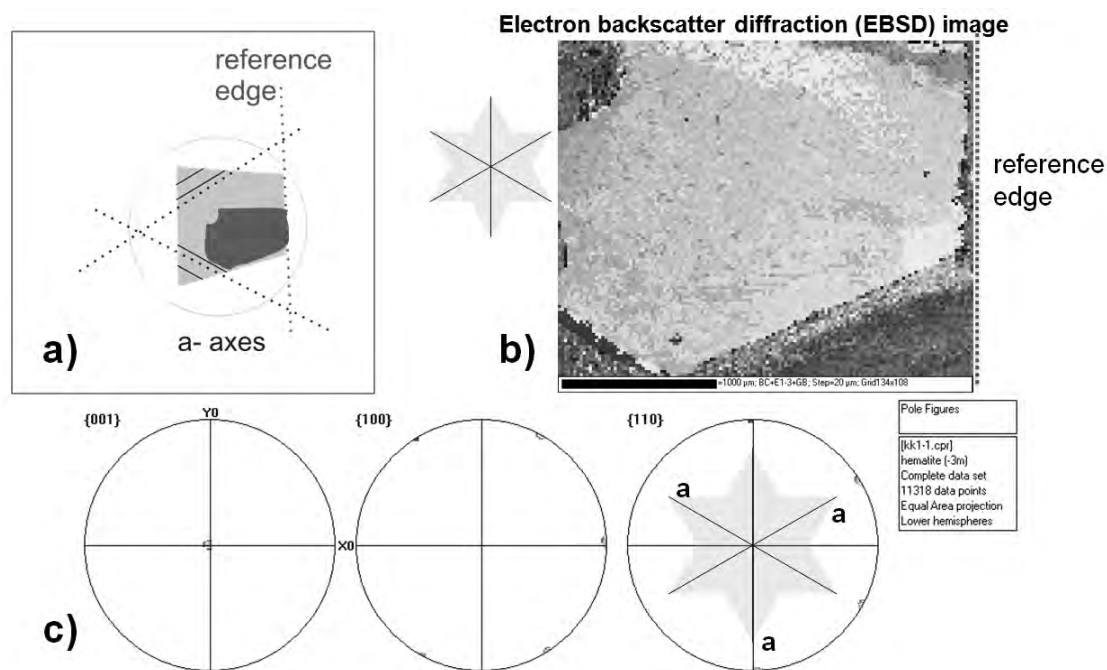


Fig. 3.4-12: EBSD mapping of the basal plane of the investigated hematite crystal, (a) schematic drawing; (b) EBSD map showing orientation differences as gray levels; (c) pole figures.

$2^\circ$  between  $0$  and  $358^\circ$  we measured (1) the high-field hysteresis branch from zero field to  $+1$  T in steps  $10 \text{ mT}$ , (2) the low-field branch from zero field to  $+10 \text{ mT}$  in steps of  $0.5 \text{ mT}$ , and (3) the back-field curve from zero to  $-100 \text{ mT}$  in steps of  $10 \text{ mT}$ . From the first measurement it is possible to infer a slope-corrected estimate for  $M_s$ , the value of  $M_{rs}$  and high-field, as well

as low-field slope of the hysteresis branch. The second measurement gives a more precise determination of the low-field slope, which can be used as a value for the saturation-remanence-aligned susceptibility  $\chi_r$ . The back-field curves are used to determine approximations for the coercivity of remanence,  $H_{cr}$ .

Figure 3.4-13 shows two extreme back-field curves in the basal plane, one measured at  $8^\circ$ , approximately perpendicular to an  $a$ -axis and one at  $22^\circ$ , at an intermediate peak of  $H_{cr}$ . The values of  $H_{cr}$  as a function of angle (Fig. 3.4-13b) show that it has a six-fold periodicity and also that  $H_{cr}$  is always at a minimum whenever an  $a$ -axis is aligned perpendicular to the field, and at a maximum when the field is aligned with an  $a$ -axis. There are also additional peaks with six-fold symmetry which may be related to twins which do not appear at the measured surface. The saturation magnetization  $M_s$  is determined by a straight line fit to the high-field curve above 0.85 T; for the saturation remanence  $M_{rs}$  the zero-field value of the high-field curve is used (Fig. 3.4-14 left). Whereas  $M_s$  is almost constant as a function of angle,  $M_{rs}$  varies with a six-fold periodicity, in phase with  $H_{cr}$  (Fig. 3.4-14 right). A crude estimate of magnetic susceptibility is given by the slope of the high-field curve at zero (Fig. 3.4-14 left); this rather noisy data set varies in anti-phase with  $M_{rs}$ .

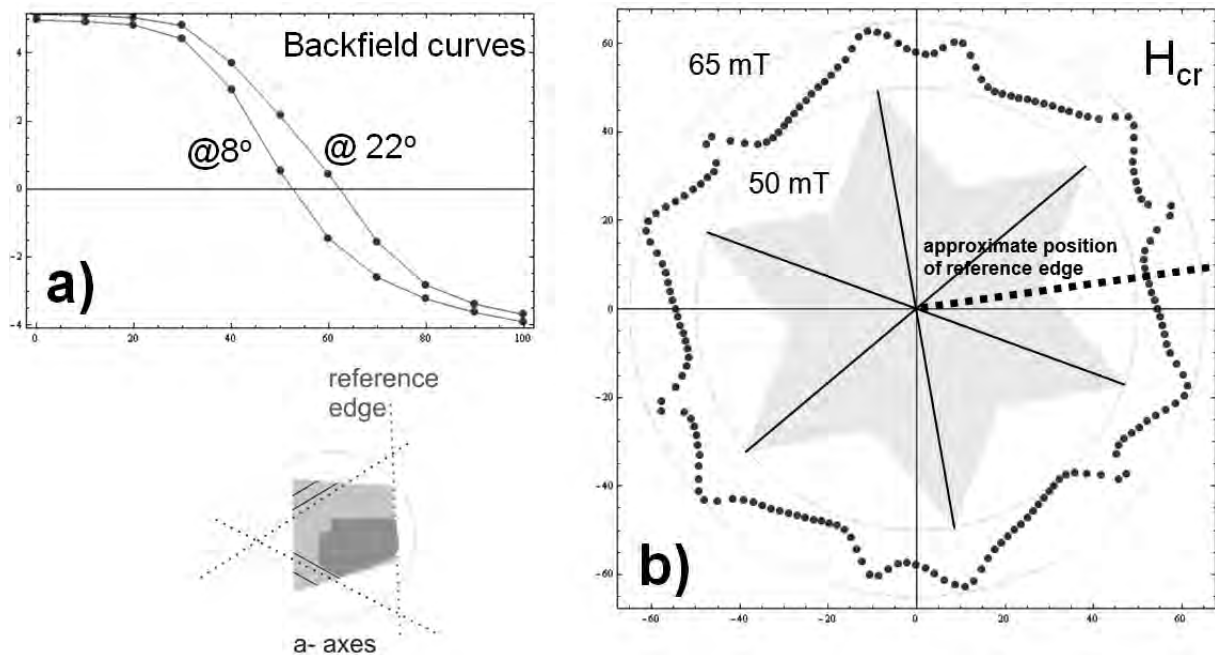


Fig. 3.4-13: (a) Two typical back-field curves, the position at  $8^\circ$  is about perpendicular to an  $a$ -axis; (b) variation of remanence coercivity  $H_{cr}$  as a function of rotation angle.

The measurements show that the remanence coercive force  $H_{cr}$  is maximal along, and minimal perpendicular to the  $a$ -axes, whereas  $M_s$  is independent of field direction indicating easy rotation of the spins away from the easy  $a$ -axes. The high-field slope is probably due to field-

induced spin canting. The canting angle is doubled in 1.6 T.  $M_{rs}$  is maximal along and minimal perpendicular to the  $a$ -axes. Results of the weak-field measurements (not shown here) indicate that the weak-field susceptibility after saturation is minimal along and maximal perpendicular to the  $a$ -axes. Its variation approximately agrees with a  $(\cos 30^\circ)^2$  field angle dependence. If the high-field extrapolation is also valid for low fields, spin flip is an unlikely coercivity mechanism below 1.5 T.

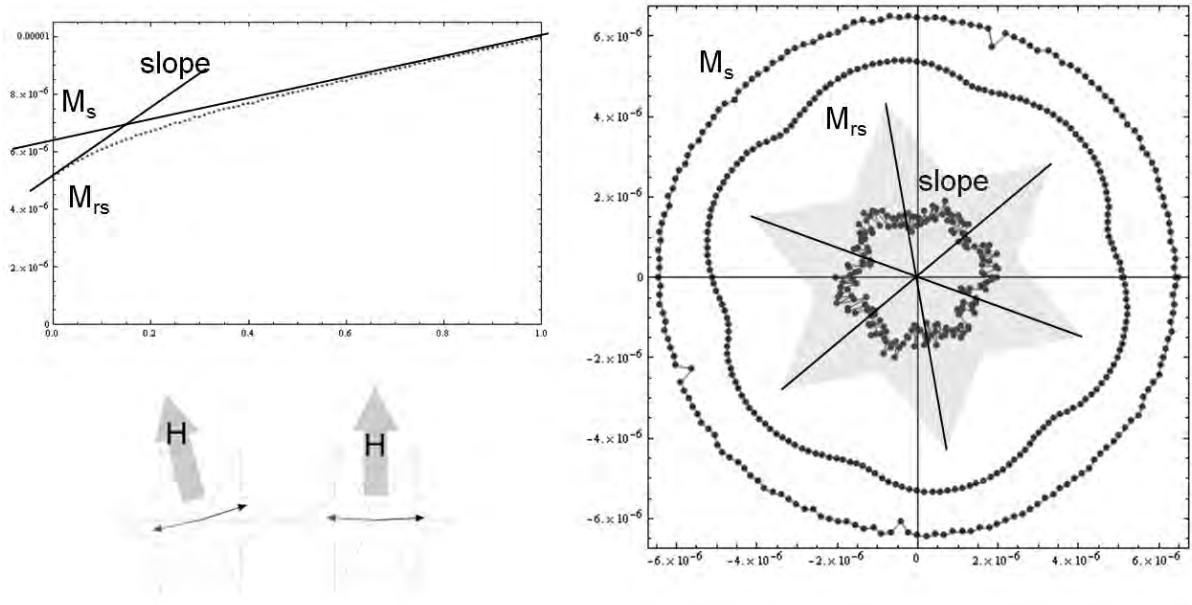


Fig. 3.4-14: Measurements of  $M_s$ ,  $M_{rs}$  and the slope of the high-field curve near zero.

### 3.5 Fluids and their Interaction with Melts and Minerals

Aqueous fluids play a fundamental role in mass and energy transfer in the Earth's interior. The fluid-mediated mass transfer is manifested by distinct trace element depletion-enrichment patterns in subduction-zone metamorphism and arc magmas, fluid flow and metamorphic veining in convergent orogens, alteration reactions in ore-forming and contact metasomatic environments, or recorded in small-scale dissolution-precipitation phenomena.

The thermodynamic properties and the structure of fluids at elevated temperatures and pressures are generally not very well known. Two contributions in this section of the annual report try to address this problem. A first contribution develops a new equation of state for dissolved species in aqueous fluids. Mineral solubilities predicted from this equation of state are clearly related to speciation: While the solubilities of neutral species only gently increase with fluid density, this increase is much more pronounced for those minerals that likely form charged species or ion pairs in solution. Another interesting prediction from this model is that at constant pressure, the solubilities of many minerals first increase with temperature, but subsequently drop again. The relationship between speciation and solubility is further elaborated in a second contribution. Here, measurements of the Raman spectra of aqueous fluids in equilibrium with corundum show that the dissolution mechanism of aluminium in aqueous fluid is fundamentally different from silica. While silica preferentially dissolves as monomeric  $\text{Si}(\text{OH})_4$ , aluminium appears to occur predominantly in polymeric species in high temperature aqueous fluids. This tendency of Al to promote polymerization may be important for the mobilization of high field strength elements as well as for the onset of critical behaviour in silicate-water systems.

Aqueous fluids in volcanic and subvolcanic systems are responsible for the formation of hydrothermal ore deposits as well as for the global cooling events and possibly for the stratospheric ozone depletion observed after major volcanic eruptions. In one contribution of this section, new data are reported that demonstrate that copper can be preferentially enriched in an aqueous vapor phase coexisting with a brine, probably due to complexing with hydrogen sulfide. Two small research projects carried out by a student during a EU Marie Curie training visit show that HCl is significantly absorbed by volcanic ashes and that sulfur is strongly partitioned into aqueous fluids, even if they coexist with an Fe-bearing silicate melt. These data will help predicting the environmental impact of volcanic eruptions.

The weathering of sulfides, and particularly the role of microorganisms played in these processes is the subject of the two last research projects reported in this section. A very interesting result of these studies is that *Acidithiobacillus ferrooxidans* does not only greatly accelerate the oxidation of pyrrhotite – but this bacterium seems to develop different dissolution rates for different structure types of pyrrhotite.

**a.** *An equation of state for mineral dissolution in aqueous fluids at high temperatures and pressures (D. Dolejš/Prague, and C.E. Manning/Los Angeles)*

The thermodynamic properties of dissolved aqueous species at elevated temperatures and pressures are frequently described by the Helgeson-Kirkham-Flowers model but this equation of state is limited to liquid-like densities, pressures below 5 kbar, it is not applicable at near-critical conditions and it becomes particularly inaccurate for gaseous nonelectrolytes. In addition, the static permittivity of water, which is required for the solute thermodynamic properties, has not been calibrated experimentally at  $T > 600$  °C or  $P > 20$  kbar, and current formulations strongly diverge in these regions.

We have developed a thermodynamic model for dissolution of minerals in aqueous fluids at high temperatures and pressures. The model incorporates thermodynamic contributions from lattice breakdown, ionization and chemical hydration, which depend on temperature, and the effects associated with the compression in the hydration sphere and electrostatic solute-solvent interactions, which are formulated as a function of solvent volumetric properties. The standard Gibbs energy of lattice breakdown, ionization and chemical hydration is represented by conventional caloric expansion,

$$\Delta_{cl}G = \Delta H + \int_{T_{ref}}^T c_p dT - T \left( \Delta S + \int_{T_{ref}}^T \frac{c_p}{T} dT \right), \quad (1)$$

where  $T$  and  $T_{ref}$  represent the temperature of interest and reference temperature (*e.g.*, 298 K), respectively. Eq. (1) accommodates the standard Gibbs energy of formation of hydrated species in the ideal gas state at 1 bar from a solid phase. The contribution to the Gibbs energy resulting from conversion of standard state,  $\Delta_{ss}G$ , represents  $PV$  work performed between an ideal gas state at 1 bar, and a 1 molal standard state at the pressure of interest:

$$\Delta_{ss}G = RT \ln \frac{RT\rho}{1000} \quad (2)$$

where  $RT$  is the volume of an ideal gas at 1 bar, with the universal gas constant given in  $\text{bar cm}^3 \text{ K}^{-1} \text{ mol}^{-1}$ , and  $1000/\rho$  is the volume of 1 kg of water, with density in  $\text{g cm}^{-3}$ . Differentiation of  $\Delta_{ss}G$  with respect to pressure provides the standard molar volume of transfer to aqueous solvent,

$$\Delta_{ss}V = \left( \frac{\partial \Delta_{ss}G}{\partial P} \right)_T = \beta RT, \quad (3)$$

where  $\beta$  is the compressibility of  $\text{H}_2\text{O}$ . It should be noted that

$$A = \frac{\Delta_{ss}V}{\beta RT}, \quad (4)$$

where  $A$  is the generalized Krichevskii parameter. It has the advantage of behaving as a finite smooth function in the vicinity of the critical point, it is nearly independent of temperature when applied to both electrolyte and non-electrolyte inorganic and organic systems, and it has a simple, linear scaling with the reduced Born energy.

The standard properties of dissolution,  $\Delta_{\text{ds}}G$ , are obtained by combining the caloric and standard-state contributions. Truncating the heat capacity function in Eq. (1) after the term linear in temperature and adding Eqs. (1) and (2) leads to:

$$\Delta_{\text{ds}}G = a + bT + cT \ln T + dT^2 + eT \ln \rho \quad (5)$$

and

$$\ln K = -\frac{1}{R} \left\{ \frac{a}{T} + b + c \ln T + dT + e \ln \rho \right\}, \quad (6)$$

where  $a$  through  $e$  are parameters of the model. This relationship suggests a linear dependence of logarithm of equilibrium constant and logarithm of solvent density at constant temperature, with slope independent of temperature.

We fitted the experimental solubilities of quartz, corundum, rutile, calcite, apatite, fluorite and portlandite in pure water to the thermodynamic model (Table 3.5-1). The experimental data cover temperature range of 100-1100 °C at pressures up to 20 kbar. The solubilities vary by up to six orders of magnitude on the molality concentration scale and are reproduced by the model to better than 5 %, or 0.1 log molality units. The solubilities of six minerals were reproduced satisfactorily by a three-parameter function only whereas quartz required two additional terms describing the heat capacity and its linear dependence on temperature.

In all cases, the mineral solubilities increase with the H<sub>2</sub>O density at constant temperature. The magnitude of this increase,  $d \log m/d \log \rho$ , depends on parameter  $e$  only, *i.e.*, it is dictated by the combination of the generalized Krichevskii and Born parameter of the solute species. Quartz, corundum and rutile, which congruently dissolve as neutral hydroxyspecies at neutral conditions, such as Si(OH)<sub>4</sub> or Ti(OH)<sub>4</sub>, show relatively small increase in solubility with increasing water density at constant temperature,  $d \log m/d \log \rho = 1.6-4.5$ . By contrast, the solubilities of Ca-bearing minerals – calcite, apatite, fluorite and portlandite, exhibit much stronger dependence of their solubilities on the water density,  $d \log m/d \log \rho = 7.2-11.4$ . These phases form upon congruent dissolution a variety of charged species and ion pairs (*e.g.*, Ca<sup>2+</sup>, CO<sub>3</sub><sup>2-</sup>, HCO<sub>3</sub><sup>-</sup>, OH<sup>-</sup>, F<sup>-</sup>, CaF<sup>+</sup>, H<sub>2</sub>PO<sub>4</sub><sup>-</sup> etc.), which cause much stronger electrostriction effects in the hydration shell as demonstrated previously by dependence of the species Born parameter on its charge. This effect is then reflected in more negative partial molar volumes of dissolution. At 298.15 K and 1 bar, the partial molar volumes of

Table 3.5-1: Parameters of the thermodynamic model, Eqs. (5) and (6)

	a (kJ mol <sup>-1</sup> )	b (J K <sup>-1</sup> mol <sup>-1</sup> )	c (J K <sup>-1</sup> mol <sup>-1</sup> )	d (J K <sup>-2</sup> mol <sup>-1</sup> )	e (cm <sup>3</sup> mol <sup>-1</sup> )
apatite-F	63.36	3.903			-89.318
calcite	57.43	-35.710			-72.983
corundum	80.34	-29.315			-37.011
fluorite	56.43	-24.888			-59.726
portlandite	13.09	10.052			-94.741
quartz	23.63	-52.921	10.933	-0.0463	-18.515
rutile	103.98	-33.722			-13.316

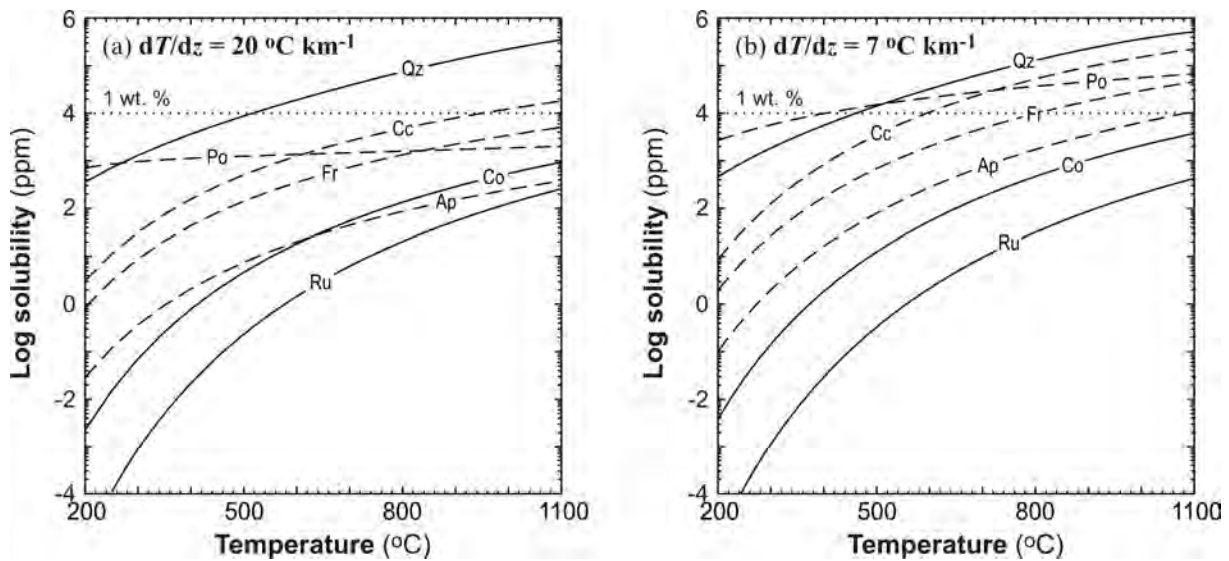


Fig. 3.5-1: Solubilities of rock-forming minerals in pure H<sub>2</sub>O along geothermal gradients of (a) 20 and (b) 7 °C/km. Solubilities of oxides are shown by solid curves whereas Ca-bearing phases are in dashed style.

dissolution for quartz, corundum and rutile are  $-1.8$  to  $-5.0$  cm<sup>3</sup> mol<sup>-1</sup> whereas those for Ca-bearing phases are  $-8.1$  to  $-12.8$  cm<sup>3</sup> mol<sup>-1</sup>. Consequently, electrostriction in the vicinity of the charged species promotes the solubility increase with pressure by a factor of 3 to 4.

Solubilities of all seven rock-forming minerals monotonously increase with temperature along metamorphic geotherms or water isochores (Fig. 3.5-1). The solubility of a given phase increases by 4-5 orders of magnitudes as temperature rises from 200 to 1100 °C along typical geotherms. In detail, the spacing of isotherms,  $(\partial \log m / \partial T)_p$ , varies between  $7.7 \cdot 10^{-3}$  and  $6.1 \cdot 10^{-2}$ , and  $5.9 \cdot 10^{-4}$  and  $4.7 \cdot 10^{-3}$  K<sup>-1</sup> at 25 and 800 °C, respectively, and  $\rho = 1$  g cm<sup>-3</sup>. The caloric terms of all minerals broadly overlap at 25 °C but quartz, corundum and rutile are more endothermic at 800 °C. Consequently, solubilities of these three minerals increase by a greater degree with temperature than the Ca-bearing minerals along isochores. Since an

increase in mineral solubility with temperature at constant density is free of physical hydration effects, this behaviour is related either to distinct lattice enthalpies of oxides vs. other minerals considered in this study, or to variably endothermic nature of chemical hydration of neutral vs. charged aqueous species.

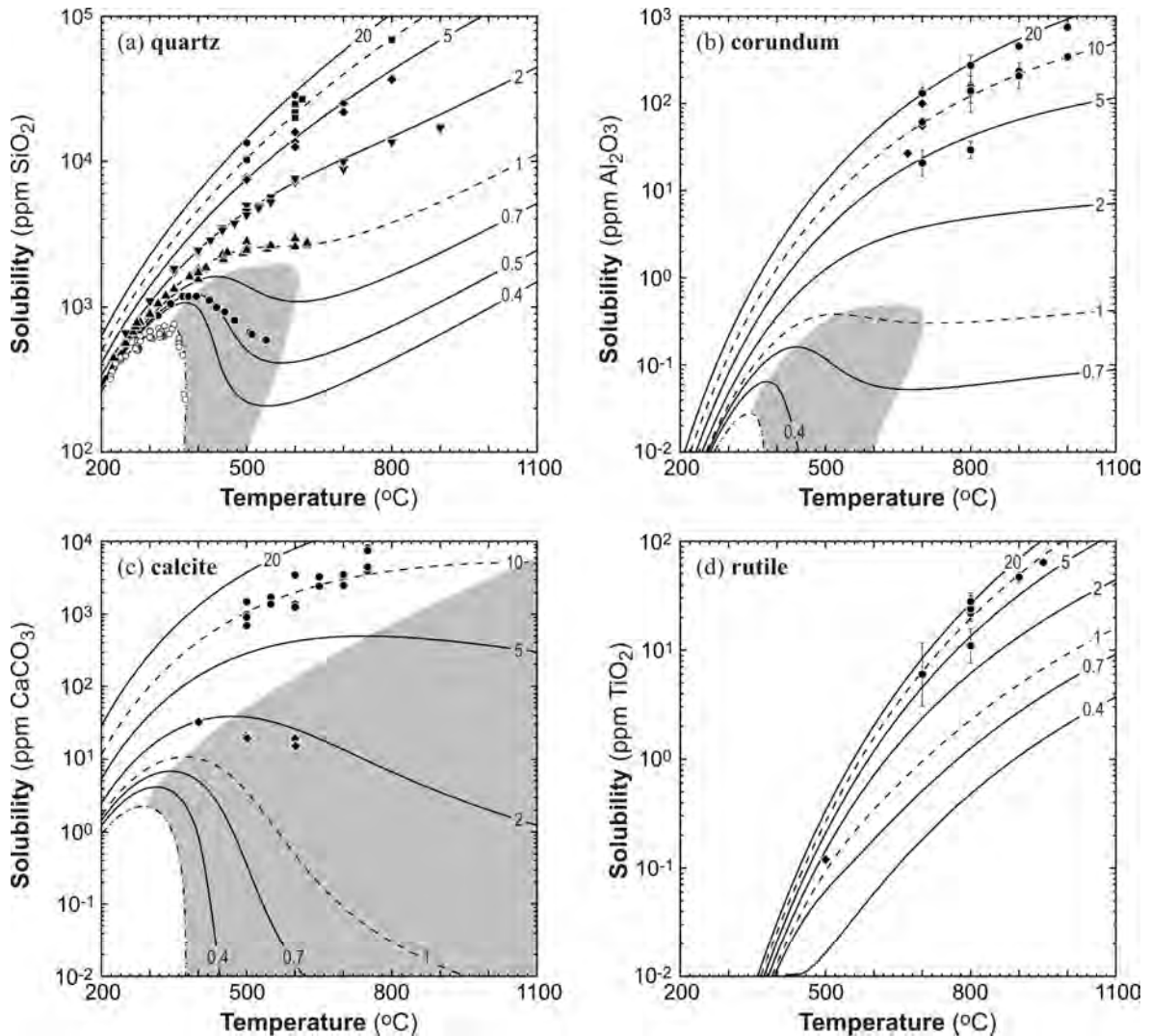


Fig. 3.5-2: Retrograde solubility behaviour illustrated for (a) quartz, (b) corundum, (c) calcite, and (d) rutile at selected pressures and the liquid-vapor coexistence curve: (a) open circles – liquid-vapor coexistence curve, solid circles – 0.5 kbar, upright triangles – 1 kbar, inverted triangles – 2 kbar, diamonds – 5 kbar, squares – 10 kbar, hexagons – 20 kbar; (b) diamonds – 5, 10 and 20 kbar, circles – 10 and 20 kbar; (c) diamonds – 2 kbar, circles – 10 kbar; (d) circles – 10, 15 and 20 kbar.

At constant pressure, however, mineral solubilities initially increase with rising temperature but often subsequently drop (Fig. 3.5-2). This effect is caused by a reversal in isobaric expansivity of the aqueous solvent, which propagates into the enthalpy of dissolution. The

onset and extent of the isobaric retrograde solubility is directly related to the combined, generalized Krichevskii and Born parameter ( $e$ ) of aqueous solute. For Ca-bearing minerals, the isobaric retrograde solubility appears from  $\sim 300$  °C and it covers the moderate- and high-temperature space through the granulite facies. For oxide minerals, the retrograde solubility is suppressed because neutral solutes have very low electrostriction volume and it appears as a transient feature above the critical temperature of H<sub>2</sub>O. In these cases the retrograde behaviour is limited to very low pressures: rutile – 403 bar, quartz – 972 bar, corundum – 1231 bar.

Application of solute transport theory to our thermodynamic model permits calculation of time-integrated fluid fluxes, which are necessary to precipitate mineral veins during fluid flow events. The integrated fluid fluxes along geotherms of 20 and 7 °C km<sup>-1</sup> vary from 10<sup>4</sup> to 10<sup>15</sup> m<sup>3</sup> m<sup>-2</sup> in the following sequence: quartz, calcite, fluorite, corundum and apatite, and rutile. This is in broad agreement with observations of high mobility and veining of quartz and calcite as the most mobile predicted phases in many metamorphic environments. Conversely, typical integrated fluid fluxes in crustal shear zones produce a transfer of quartz and calcite in quantities of several to tens vol.% whereas the solubility of apatite or rutile lies below 1000 ppm, which may still be important for the trace element budget in metasomatized rocks.

**b. Aluminium speciation in aqueous fluids at high pressures and high temperatures (M. Mookherjee, H. Keppler, and C. Manning/Los Angeles)**

The solubility of corundum in water is low even at high pressure and temperature. Therefore, it was often assumed that alumina remains essentially immobile during fluid-rock interaction. However, both field evidence and experimental studies suggest that alumina solubility is strongly enhanced in the presence of silica as well as in alkaline solutions. In order to understand the dependence of alumina solubility on fluid composition, we have carried out a systematic Raman-spectroscopic study of Al speciation in aqueous fluids at high pressure and temperature.

Experiments were carried out in an externally heated diamond cell equipped with low-fluorescence diamonds and iridium gaskets. Raman spectra were collected with a Horiba Jobin-Yvon Labram HR spectrometer using the 514 nm line of an argon laser for excitation.

We have conducted three separate sets of experiments. In the first, speciation of alumina was studied in a 1 M KOH aqueous solution in equilibrium with corundum up to 1 GPa and 700 °C. The Raman spectra show a prominent band at 618 cm<sup>-1</sup>, which is due to Al-O stretching in the  $[Al(OH)_4]^{1-}$  monomer species. At higher pressure and temperature, additional vibrational modes appear at 200 cm<sup>-1</sup> and 374 cm<sup>-1</sup>. These features are most likely due to bending modes of  $[(OH)_3Al-O-Al(OH)_3]^{2-}$  or similar polymeric species (Fig. 3.5-3, left). Upon cooling from high pressure and high temperature, some oversaturation of the

solutions appears to occur. Often, peaks at 930 and 1066  $\text{cm}^{-1}$  are observed upon cooling, which are probably due to some colloidal aluminium hydroxide. In a second set of experiments, Al speciation was studied in pure  $\text{H}_2\text{O}$  in equilibrium with solid corundum to 2 GPa and 1000  $^\circ\text{C}$ . The Raman spectra are devoid of features corresponding to  $[\text{Al}(\text{OH})_4]^-$ . However, at relatively high temperatures bands at 374  $\text{cm}^{-1}$  appear that suggest the presence of polymeric species (Fig. 3.5-3, right). This might indicate a very high equilibrium constant for the polymerization reaction. It therefore appears that the dissolution mechanism of alumina in water is radically different from the dissolution mechanism of silica, which is predominately dissolved as monomeric  $\text{Si}(\text{OH})_4$  under similar conditions.

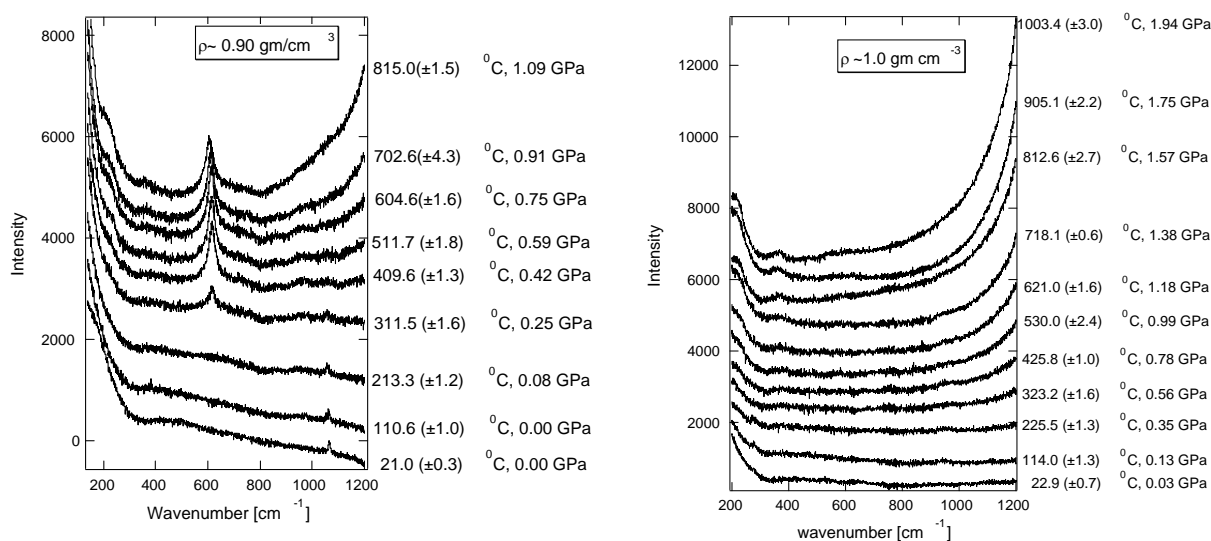


Fig. 3.5-3: Raman spectra of aqueous fluid (left: 1 M KOH; right: pure  $\text{H}_2\text{O}$ ) in equilibrium with solid  $\text{Al}_2\text{O}_3$ . Spectra were collected during heating. The spectra are shifted along the intensity axis for clarity. Note the absence of the  $[\text{Al}(\text{OH})_4]^-$  monomer peak at 618  $\text{cm}^{-1}$  in the spectra for pure water (right).

In a third set of experiments, Al speciation was studied in an aqueous solution in equilibrium with corundum and quartz, up to 1 GPa and 900  $^\circ\text{C}$  (Fig. 3.5-4). The Raman spectrum at 375  $^\circ\text{C}$ , shows a prominent band 766  $\text{cm}^{-1}$  which is due to Si-O stretching in the  $[\text{Si}(\text{OH})_4]$  monomer. At higher pressures and temperatures, additional bands appear at 944  $\text{cm}^{-1}$ , 608  $\text{cm}^{-1}$ , 360  $\text{cm}^{-1}$  and 200  $\text{cm}^{-1}$ , which might be attributed to various alumino-silicate polymeric species, including  $[(\text{OH})_3\text{Al}-\text{O}-\text{Si}(\text{OH})_3]^{2-}$ . Comparing these data with previous measurements in the  $\text{SiO}_2\text{-H}_2\text{O}$  system again suggest that in the presence of Al, polymerization is enhanced. These observations may therefore explain, why the solubility of high field strength elements in fluids are strongly enhanced by Al and they also suggest that that the presence of Al should lower the critical curve in silicate – water system.

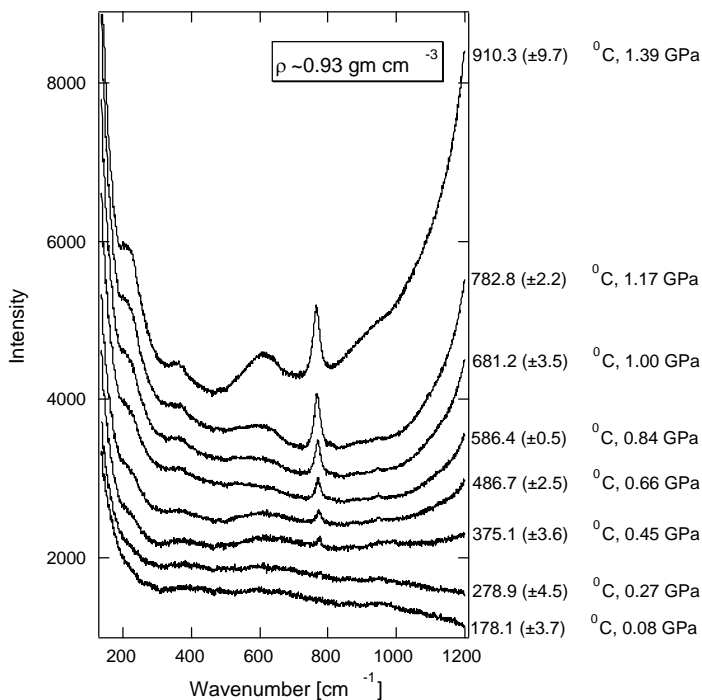


Fig. 3.5-4: Raman spectra of aqueous fluid in equilibrium with solid  $\text{Al}_2\text{O}_3$  and solid  $\text{SiO}_2$ . Spectra were collected during cooling. The spectra are shifted along the intensity axis for clarity.

**c. Partitioning of Cu in a two-phase fluid system at 600 °C and 700 bar (L. Lerchbaumer, and A. Audéat)**

Studies on natural assemblages of coexisting vapor and brine inclusions revealed that certain ore-forming elements (Cu, Au, As,  $\pm\text{Ag}$ ,  $\pm\text{Mo}$ ) sometimes occur in higher concentrations in the vapor phase than in the brine. It is believed that these elements are enriched in the vapor phase by some sort of hydrosulfide complex, but so far no experimental study was able to reproduce this phenomenon at geologically realistic conditions.

Here we report the results of a particularly interesting experiment at 600 °C / 700 bar. In this experiment, a fluid containing 5.2 wt.% NaCl, 4.0 wt.%  $\text{FeCl}_2$ , 0.9 wt.% HCl, 1.2 wt.%  $\text{Na}_2\text{S}$ , 0.8 wt.%  $\text{Cu}^{(I)}\text{Cl}$  and 225-555 ppm of Pb, Co, and As was filled into a gold capsule, together with a pre-fractured quartz core and powdered  $\text{SiO}_2$  glass. The gold capsule was then equilibrated at 600 °C and 700 bar for 11 days in a cold-seal pressure vessel. During heating, the starting materials were anticipated to form  $\text{H}_2\text{S}$  and Cu-hydrosulfide according to the reaction:  $2 \text{Na}_2\text{S} + \text{CuCl} + 3 \text{HCl} = 4 \text{NaCl} + \text{Cu}(\text{HS}) + \text{H}_2\text{S}$ . Lead and cobalt were added to monitor relative time sequences of inclusion formation, as their concentration in the fluid drops with increasing run time due to alloying of Pb and Co with the Au-capsule. The recovered quartz core was cut and polished, and 25 fluid inclusions were analyzed by both microthermometry and LA-ICP-MS. For internal standardization of the latter measurements we used microthermometrically derived  $\text{NaCl}_{\text{equiv}}$  salinities that were corrected for  $\text{FeCl}_2$ .

As in all previous runs, a large range of Cu-concentrations was observed in both vapor and brine inclusions. These variation could have been caused by the following processes: (1) loss

of Cu from the fluid through alloying with the gold capsule or precipitation of a Cu-bearing mineral phase, (2) incomplete separation of brine and vapor during fluid entrapment (co-entrapment of small amounts of brine is very common in vapor inclusions), (3) loss of a Cu-bearing daughter crystal during LA-ICP-MS analysis, and (4) gain of Cu through accidental entrapment of a Cu-bearing mineral phase. Processes 3 and 4 are unlikely because the fluid inclusions were opened in a very controlled fashion, and because no solid inclusions were observed in the quartz sample. Processes (1) and (2) probably both occurred, hence it is essential to be able to differentiate between the two. The amount of brine co-entrapment in vapor inclusions can be quantified based on measured Na concentrations and assuming that the lowest value is representative of the pure vapor endmember. After subtracting this effect the re-calculated vapor inclusions still show a large scatter in Cu concentrations. However, in many experiments these corrected Cu concentrations correlate positively with the concentrations of Co and Pb, suggesting that the vapor inclusions with the highest Cu contents were trapped earliest and thus most closely approach the initial conditions before Cu started to be lost to the gold capsule. Similar trends can be observed also in brine inclusions, although less pronounced due to apparently faster closure times compared to vapor inclusions. By mass balance calculations it further can be demonstrated that the brine inclusions with the highest Cu content did not lose any Co until they were closed off, hence also their Cu content should be representative of the initial conditions. The latter is of great importance, as it allows the initial Cu content of the vapor phase to be calculated by mass balance.

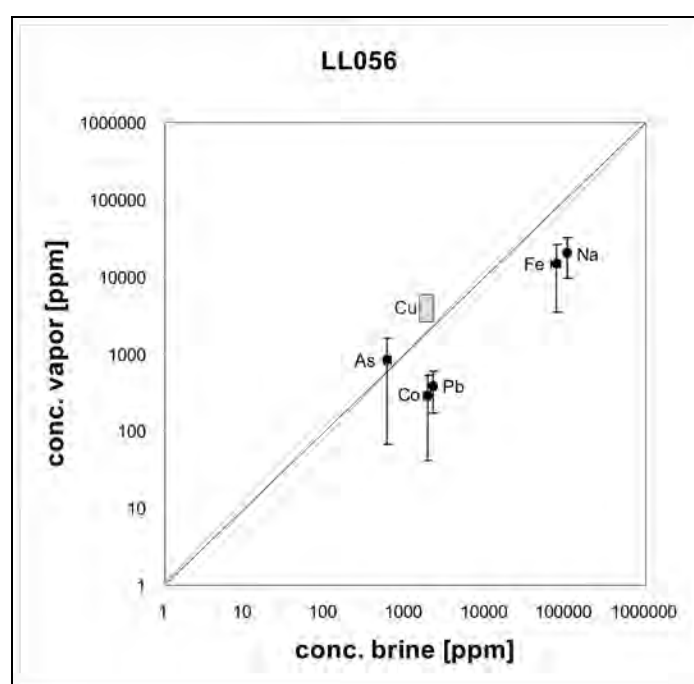


Fig. 3.5-5: Measured element concentrations in brine inclusions versus vapor inclusions. Note that Co, Pb, Fe and Na are concentrated in the brine, whereas Cu and As occur in higher concentrations in the vapor. The Cu content of the vapor phase is bracketed between the highest measured value and a maximum theoretical value that calculated by mass balance (as described in the text). The three most Cu-rich brines were used to define the range of initial Cu concentration in the brine.

The initial Cu content of the vapor phase was thus constrained as follows: (i) a maximum value was calculated by mass balance, assuming that the most Cu-rich brine is representative of the initial stage and that no Cu has been lost to the gold capsule yet, and (ii) a minimum value is provided by the highest actually measured Cu value (which might represent a fluid which was already depleted in this element). The weight fractions of vapor and brine that were used to calculate the maximum value were determined by mass balance from the Na-content of the bulk fluid, the Na-content of the brines and the lowest measured Na-concentration in a vapor inclusion.

The results of this experiment are summarized in Fig. 3.5-5. Copper partitions into the vapor phase over the entire uncertainty interval displayed by the gray box, with an average  $D_{Cu}^{vap/brine}$  of 2.6. Arsenic shows an affinity to the vapor phase, too, although the measured values display a large scatter. Again, the highest As values in the vapor phase seem to be most representative. Bracketing in the manner described above was not possible in this case due to some contamination problem. All other elements occur at about eight times higher concentration in the brine than in the coexisting vapor phase.

**d. Partitioning of sulfur dioxide between dacitic melt and aqueous fluid phases (L. Hobbs, and H. Keppler)**

Sulfur dioxide from explosive volcanic eruptions can cause a global cooling of climate. Previous research indicates that SO<sub>2</sub> emissions are far higher than predicted from the mass of magma erupted, suggesting that “extra” sulphur might be extracted from the entire magma reservoir by hydrous fluid at the top of the chamber, which is then erupted. However, there is still some controversy about the fluid/melt distribution coefficient of sulfur in these systems. While sulfur strongly partitions into the fluid in Fe-free haplogranite systems, it has been suggested that the partitioning may strongly change in the presence of iron. We have therefore carried out an exploratory study on the fluid/melt partitioning of sulfur using natural, Fe-bearing melt compositions.

Starting glasses were synthesized according to compositional data available in the literature for the Mount St. Helens (1980) and Pinatubo (1991) eruptions. Partitioning experiments were carried out in TZM rapid-quench autoclaves, using gold capsules, H<sub>2</sub>SO<sub>4</sub> of varying concentration as the source of sulfur, and Re-ReO<sub>2</sub> or Fe<sub>3</sub>O<sub>4</sub>-Fe<sub>2</sub>O<sub>3</sub> external buffers to control oxygen fugacity. Each experiment was run for 7 days at 950 °C and 1000 bar pressure. Electron microprobe analysis of run products for sulfur content allowed a partition coefficient ( $D_S^{fluid/melt}$ ) between the melt and fluid to be calculated by mass balance.

In addition to glass, anorthite was the dominant mineral present in all run products, with spinel forming when the less oxidising Re-ReO<sub>2</sub> buffer was used. Anhydrite formed as a quench product from the fluid under Re-ReO<sub>2</sub> buffer conditions, while it appeared to be a stable phase at Fe<sub>3</sub>O<sub>4</sub>-Fe<sub>2</sub>O<sub>3</sub> buffer conditions.

The Re-ReO<sub>2</sub> buffer experiments produced a result of  $D_S^{\text{fluid/melt}} = 79.9$ , while for the MH buffer  $D_S^{\text{fluid/melt}} = 37.2$  was observed. These preliminary data suggest that at least under oxidizing conditions, the presence of some iron does not fundamentally change the fluid/melt partitioning of sulfur.

*e. Adsorption of HCl onto volcanic ash (L. Hobbs, and H. Keppler)*

HCl molecules emitted from volcanoes break down to form chlorine free radicals via heterogeneous chemical reactions and photolysis, which act as catalysts to the breakdown of ozone in the stratosphere. Antarctic ozone depletion of up to 2-7 % was estimated in the literature following the Pinatubo 1991 eruption. Moreover; the ozone layer directly above Mt. Pinatubo was completely destroyed in the days after the eruption. However, only stratospheric HCl is dangerous to ozone, and the amount of HCl that reaches these levels is often lower than expected. This suggests that HCl is removed from the eruption column at tropospheric levels.

In order to investigate the removal of HCl from the atmosphere by adsorption onto ash in volcanic plumes, glass with the composition of dacite from the Pinatubo (1991) eruption was synthesized and ground to sub-micrometer sized particles using a planetary mill. The ash was then placed in a simple volumetric vacuum device, which was purged with HCl gas to a desired pressure. The ash was connected to the system and the adsorption of HCl onto the ash surface recorded by the resulting pressure drop until an equilibrium pressure was reached.

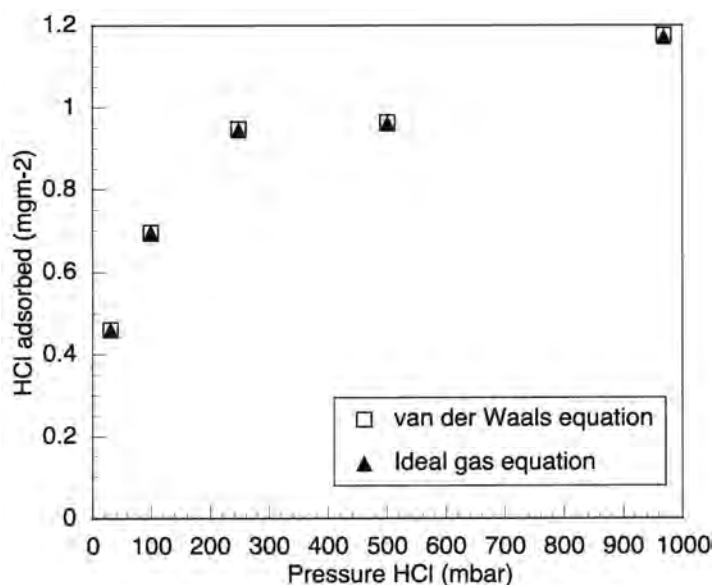


Fig. 3.5-6: Adsorption isotherm for HCl adsorption experiment

Preliminary results from experimental runs beginning with an HCl gas pressure of 31 mbar, 100 mbar, 250 mbar, 504 mbar and 975 mbar indicate that adsorption on the order of 0.5 mgm<sup>-2</sup> occurs even at low partial pressures of HCl. The adsorption isotherm (Fig. 3.5-6)

suggests that multilayer adsorption occurs; adsorption initially increases with increasing pressure, reaches a plateau then increases again. No significant desorption was observed. Our data imply that adsorption of HCl on ash particles is indeed a mechanism that may greatly reduce the amount of HCl injected into the stratosphere by major explosive eruptions.

**f. Dissolution experiments on sphalerite and galena and the role of secondary phases (K. Etzel, and K. Pollok)**

Mining of sulfide ores transfers large amounts of rocks to heap dumps and thus to an oxidizing environment. Weathering of these deposited sulfides often results in acid mine drainage with the production of sulfuric acid and the release of high concentrations of metals into ground and surface waters. However, hazardous element release is not only controlled by the reactivity of the primary sulfides but also by the formation of secondary mineral assemblages. The secondary phases can influence the dissolution kinetics of the primary sulfide via coating or adsorption. For example, the dissolution of galena is closely related to the formation of secondary phases with low solubility (anglesite, lead oxides), which can passivate the reactive surface area.

In this study, the dissolution of natural sphalerite and galena has been investigated. Microprobe analyses yield variable amounts of iron in sphalerites (< 0.5 up to 11 wt.%) and of trace element compositions (*e.g.*, Ag, Sb) in galenas (< 1 up to 8 wt.%). For investigations of dissolution kinetics and mineral dependent effects on alteration, sulfide powders and two acidic solutions were used at pH=2, both solutions are based on a growth medium for mesophilic microbes. One type of solution was acidified using sulfuric acid, the second enriched with iron sulfate to investigate the effect of ferric iron on dissolution. After four weeks of sulfide dissolution remaining phases were analyzed and quantified using XRD (Rietveld), SEM and TEM.

In all experiments, the formation of secondary phases, like elemental sulfur and sulfates, were observed, however, the amount of secondary phases depends strongly on the type of mineral and its composition as well as on the oxidant. The quantity of secondary phases in experiments on sphalerite treated with iron-free solution is negligible. However, secondary phases make up 30 and 60 wt.% of the charge in dissolution experiments with Fe-bearing solution for iron-free and iron-rich sphalerite, respectively. Observed secondary phases are jarosite ( $\text{KFe}_3(\text{SO}_4)_2(\text{OH})_6$ ) and sulfur, forming reaction rims around sphalerite grains. No Zn-bearing secondary phase has formed, but the content of Zn in solution increased up to 3 g/L after exposure of iron-rich sphalerite to the Fe-bearing solution.

Reactions of galena yield up to ~ 5 wt.% of secondary phases in the Fe-free solution and up to > 85 wt.% in Fe-bearing solution. Observed secondary phases are jarosite, anglesite ( $\text{PbSO}_4$ ) and sulfur. The texture of secondary phase formation is considerably different. In dissolution

experiments with the Fe-free solution anglesite occurs as separate grains (Fig. 3.5-7 a), while precipitated secondary phases form microporous rims around parent grains when the Fe-bearing solution is involved. Rims formed during experiments involving sphalerite are homogeneous and consist of jarosite and sulfur, while reaction rims of galena are split into an inner rim of anglesite and an outer rim of jarosite (Fig. 3.5-7 b).

This experimental study shows that iron in the solvent can enhance the dissolution of sulfides and thus affects metal mobilization. It also influences the formation and texture of secondary phases. Zn remains dissolved in the solution, while Pb precipitates as anglesite, but does not passivate the surface of the primary phase.

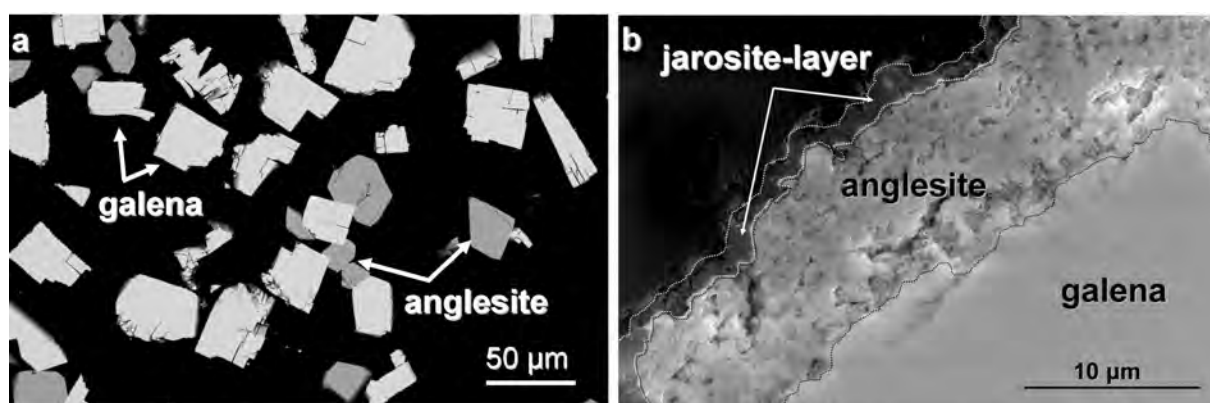


Fig. 3.5-7: SEM image (a) shows remaining galena and anglesite grains after four weeks exposure to the iron-free solution; no jarosite was formed and the secondary phase anglesite crystallizes as separate grains. SEM image (b) shows a cross section of a galena grain including reaction rims formed during four weeks of exposure to the iron-rich oxidation solution. The outer rim consists of jarosite and the inner shows fine-grained anglesite.

**g. Oxidative dissolution of pyrrhotite by *Acidithiobacillus ferrooxidans* (J. Hopf, D. Harries, F. Langenhorst, and K. Pollok; M.F. Hochella/Blacksburg)**

Pyrrhotites represent a series of non-stoichiometric iron sulfides ( $\text{Fe}_{1-x}\text{S}$ ;  $0 < x \leq 0.125$ ) with NiAs structure. The most iron-deficient endmember ( $\text{Fe}_7\text{S}_8$ ) has a monoclinic symmetry, whereas the intermediate and stoichiometric members ( $\text{FeS}$ ) have hexagonal and orthorhombic structures. Ordering of cation vacancies generates a number of superstructures, but their thermodynamic stability at low temperatures is arguable. Natural pyrrhotites are commonly found as intergrowth of different superstructures in association with other metal sulfides (pyrite, sphalerite, galena, chalcopyrite). The oxidation of pyrrhotite (in air or aqueous solution), is of substantial environmental interest, as it contributes to acid mine drainage (AMD). Microorganisms play a dominant role in AMD systems but studies related to biotic pyrrhotite oxidation are rare and neglect a direct examination of textural and

chemical changes of the reacting surface. *Acidithiobacillus ferrooxidans* is one of the predominant metal-sulfide-dissolving microorganisms and the cells of this acidophilic iron (II) oxidizing bacterium are able to attach directly to mineral surfaces.

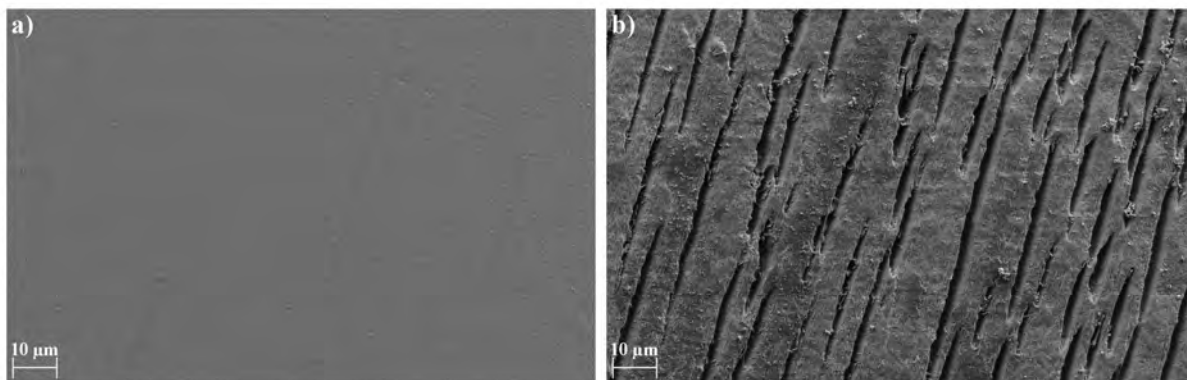


Fig. 3.5-8: Surfaces of pyrrhotite after exposure to an acid solution for 40 days, (a) in the absence of microorganisms (b) in the presence of *Acidithiobacillus ferrooxidans*.

A massive pyrrhotite (Tysfjord, Norway) was cut into cubes with approximate dimensions of ca. 3×3×3 mm and four faces were polished to a smooth mirror finish. The starting material is an intergrowth of two different superstructures with 1-3µm wide, fine exsolution lamellae of the well ordered 2C type in a host of the NC type. The lamellae are close to stoichiometric FeS and contain about 2 wt.% more iron than the surrounding matrix. Cultures of *A. ferrooxidans* cells were grown in 50 ml inorganic salt solution (0.4 g each of (NH<sub>4</sub>)<sub>2</sub>SO<sub>4</sub>, K<sub>2</sub>HPO<sub>4</sub>, and MgSO<sub>4</sub> · 7H<sub>2</sub>O per liter; acidified to pH 2.0 with H<sub>2</sub>SO<sub>4</sub>) supplemented with sterilized pyrrhotite cubes. Flasks were incubated at 30 °C on a rotary shaker. Apart from the biological treatment, an abiotic experiment was performed, serving as a control. The duration of the experiments was 1, 4, 9, 14, 17, 21, 28 and 40 days. The samples were analyzed by X-ray photoelectron spectroscopy (XPS), atomic force microscopy (AFM), and scanning electron microscopy (SEM).

The surfaces of the control pyrrhotite cubes were visually unaltered after exposure for 40 days to growth medium (Fig. 3.5-8 a). In contrast, *A. ferrooxidans* develops a thick whitish biofilm on the cubes within 40 days. The surface underneath shows deep and extremely long trenches with a width of ca. 3.5 µm (Fig. 3.5-8 b). Obviously, bacterial activity preferentially dissolved the embedded lamellae of the 2C pyrrhotite. The surface between these trenches shows a layered and frayed structure which indicate that pyrrhotite surface alteration has been enhanced significantly. To investigate the evolution of the surface area between the trenches AFM was used. Within 21 days the biologically altered pyrrhotite forms a grooved surface with a peak to valley distance of over 1 µm, which is at the limit of accurate AFM surface measurement. The relative surface area (ratio of measured surface area and a perfectly flat area) has more than doubled during that period, whereas the control surface is close to a flat

surface. Both, the biotic and the control experiment start with an initial pH of 2, which slightly decreased to pH 1.8 (within 40 days) indicating that the different dissolution behaviour is not related to proton activity. XPS was used to monitor pyrrhotite surface oxidation as function of time. The S 2p spectrum of the starting material shows the presence of monosulfide and disulfide, with minor polysulfide. Oxide species, hydroxide groups, and chemically and physically attached water are represented in the relatively wide O 1s spectrum. Fe 2p, O 1s, and S 2p spectra of the control experiment do not change significantly during 28 days. The biological treatment significantly shifts the sulfur and iron spectra. The S 2p spectra exhibit an enhanced polysulfide line and a reduced one of monosulfide. Additionally binding energy contributions attributed to sulfur bonded to oxygen (sulfate) developed. A gradual reduction of the Fe(II)-S peak with a simultaneous rise of the Fe(III)-S and Fe(III)-O bands highlights the chemical changes at the bioleached surface. Furthermore, the surface bound oxygen content increases enormously with time in the biotic experiment.

The results indicate that *A. ferrooxidans* drastically enhance the oxidation of Fe(II) to Fe(III) on the pyrrhotite surface and thus the rate of dissolution whereas the pure abiotic oxidation show no alteration, neither morphological nor chemical, under the given conditions. Surprisingly, the biotic activity favors the dissolution of the slightly more iron-rich lamellae. Future work will evaluate whether this effect is due to a preference of the microorganisms to the higher iron constant or to kinetic factors related to mineral stability.

### 3.6 Physics and Chemistry of Melts and Magmas

Throughout the Earth's history, melting and the production of magma (molten or partially-molten rock) have played a major role in the evolution of the planet. The migration and subsequent crystallization of magma is the main process by which the Earth has differentiated, to produce, for example, its compositionally distinct crust and mantle. At the Earth's surface, volcanic eruptions are an important consequence of magma production at depth in the crust or upper mantle. In addition to being a serious natural hazard that threatens the lives of the inhabitants of volcanic regions, large volumes of gases are released into the atmosphere by volcanism which subsequently play a major role in affecting climate evolution.

The production, transport and crystallisation of magma in the Earth are processes that are controlled by the physical and chemical properties of melts. Such properties include transport properties such as viscosity, chemical diffusion and electrical conductivity, as well as fundamental physical properties such as density. In order to fully understand magmatic processes in the Earth, the effects of parameters such as temperature, pressure and composition of melt properties are investigated through laboratory experiments and by using computational methods. Three examples of such studies are presented in this section.

The very early history of the Earth was characterized by large impacts with other planetary bodies. A consequence of such high-energy collisions was large scale melting of the early Earth and the formation of one or more "magma oceans" with depths of hundreds of kilometers or more. The evolution of a magma ocean is strongly dependent on convection dynamics which is controlled primarily by viscosity. Experimentally, it is very difficult to measure the viscosity of silicate melts at pressures above about 12 GPa and an alternative is to use *ab initio* computational methods. The first contribution below presents the results of a computational study of the viscosity of  $\text{Mg}_2\text{SiO}_4$  melt up to 35 GPa and discusses the implications for a deep magma ocean.

The details of how magma crystallises are poorly understood because direct observations of textures during melt crystallisation experiments are difficult. An alternative, as presented in the second contribution below, is to perform experiments on analogue materials that crystallise at relatively low temperatures. By using nitrate and chloride salts at moderately-high temperatures (250-900 °C), a very detailed study of textural evolution has been made. Such studies will make the interpretation of the textures of magmatic rocks in terms of crystallisation history much more reliable.

The final contribution in this section presents the results of a study of the electrical conductivity of a silicate melt at high pressure. The aim of such studies is to produce data that can be combined with geophysical measurements in order to monitor the state of magma bodies in volcanic regions. Ultimately such methods will help in predicting the nature of forthcoming eruptions.

**a. Transport properties of  $Mg_2SiO_4$  melt at high pressure – Viscosity of the magma ocean (O. Adjaoud/Potsdam, G. Steinle-Neumann, and S. Jahn/Potsdam)**

The viscosity of silicate melts is of central importance in many geological settings as it determines how magma bodies cool, flow and erupt. Knowing the dependence of viscosity on temperature ( $T$ ), pressure ( $P$ ), composition and water content is hence of great importance in geochemistry and geophysics. In the early Earth, the thermal and chemical evolution of our planet was governed by the physical properties of the melt that made up the deep magma ocean that likely formed as a result of high-energy impacts with other planetary bodies. The viscosity of a magma ocean is central to the understanding of its convective dynamics and thermal evolution.

With a ratio  $(MgO+FeO)/SiO_2 \sim 1.7$  for the primitive Earth and the eutectic point moving towards  $Mg_2SiO_4$  at higher pressures, melts in the Earth are dominated by  $Mg_2SiO_4$ . As the major component in the magma ocean, the properties of liquid  $Mg_2SiO_4$  are hence of fundamental interest for understanding its structure and dynamics. Despite this importance, the knowledge of the thermodynamic and transport properties of  $Mg_2SiO_4$  melt from experimental studies is limited because temperatures have to be extremely high.

Molecular dynamics (MD) simulations provide a complementary route to explore the high  $P$  and  $T$  behaviour of silicate melts. *Ab initio* computations based on density functional theory are accurate and transferable, but they are computationally demanding, and simulations for silicate melts have been restricted to a few hundred atoms and run durations to a few picoseconds (ps). This allows for sufficiently accurate determination of structural and thermodynamic properties, but in order to obtain good statistics for transport properties - and hence geophysically relevant precision - much longer run durations and larger simulation cells are required. Here we have applied a flexible potential model to perform large-scale molecular dynamics simulations (2016 atoms and run durations of 200 ps) in order to investigate diffusivity and viscosity of  $Mg_2SiO_4$  melt up to 32 GPa and over a  $T$  range of 2600-3200 K (Fig. 3.6-1). Diffusivity of  $Mg_2SiO_4$  in our simulations increases slightly with  $T$  and decreases uniformly with  $P$  (Fig. 3.6-1), being reduced by  $\sim 0.3$  log-units from 0 to 32 GPa at 3000 K. Similarly, viscosity  $\eta$  decreases with  $T$  and increases with  $P$  (Fig. 3.6-1). Both diffusivities and viscosities can readily be fit with a closed Arrhenius expression.

Using the previously reported thermodynamic model from the simulations we have computed an adiabat for the magma ocean (Fig. 3.6-2), with a potential temperature of 2163 K (the melting point of forsterite) together with slightly colder ( $T_0=2000$  K) and hotter ( $T_0=2400$  K) adiabats as envelopes for the likely thermal profile in the magma ocean. Using this thermal profile, we can estimate viscosity ( $\eta$ ) as a function of depth for the magma ocean using the computed viscosities (Fig. 3.6-1) and find that  $\eta$  increases from  $\sim 2 \times 10^{-2}$  Pa s at the surface, to  $\sim 6 \times 10^{-2}$  Pa s at 32 GPa ( $\sim 700$  km depth). Using the hotter and colder adiabats cause viscosity to be offset by  $\sim 0.1$  log-units at low pressure and  $\sim 0.2$  log units at high pressure.

Using these values for viscosity we can compute an upper bound on the Prandtl number (Pr) and a lower bound on the Rayleigh number (Ra) for the terrestrial magma ocean to explore its convection dynamics. Using reasonable numerical values for the parameters entering Pr and Ra we obtain  $Pr_{\max}=75$  and  $Ra_{\min}=10^{27}$  which places the convection dynamics of the magma ocean in the regime of hard turbulence, similar to the current state of the giant gas planets.

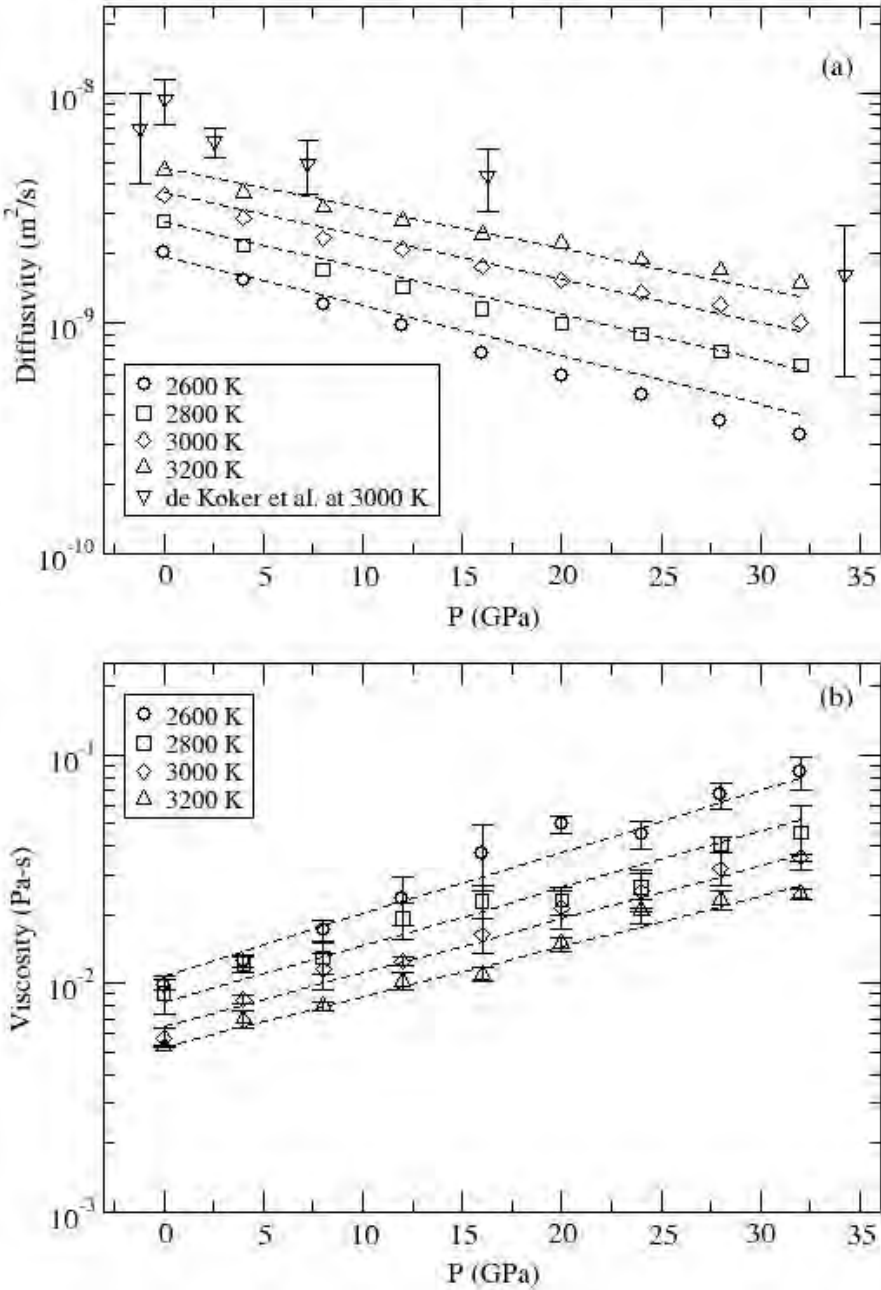


Fig. 3.6-1: Pressure and temperature dependence of diffusivity (a) and viscosity (b) of Mg<sub>2</sub>SiO<sub>4</sub> melt. Results for different temperatures are shown by the different symbols. For comparison we have included previously computed diffusivity values from DFT-based simulations at 3000 K, including the uncertainties. The dashed lines show Arrhenius fits to both diffusivity and viscosity.

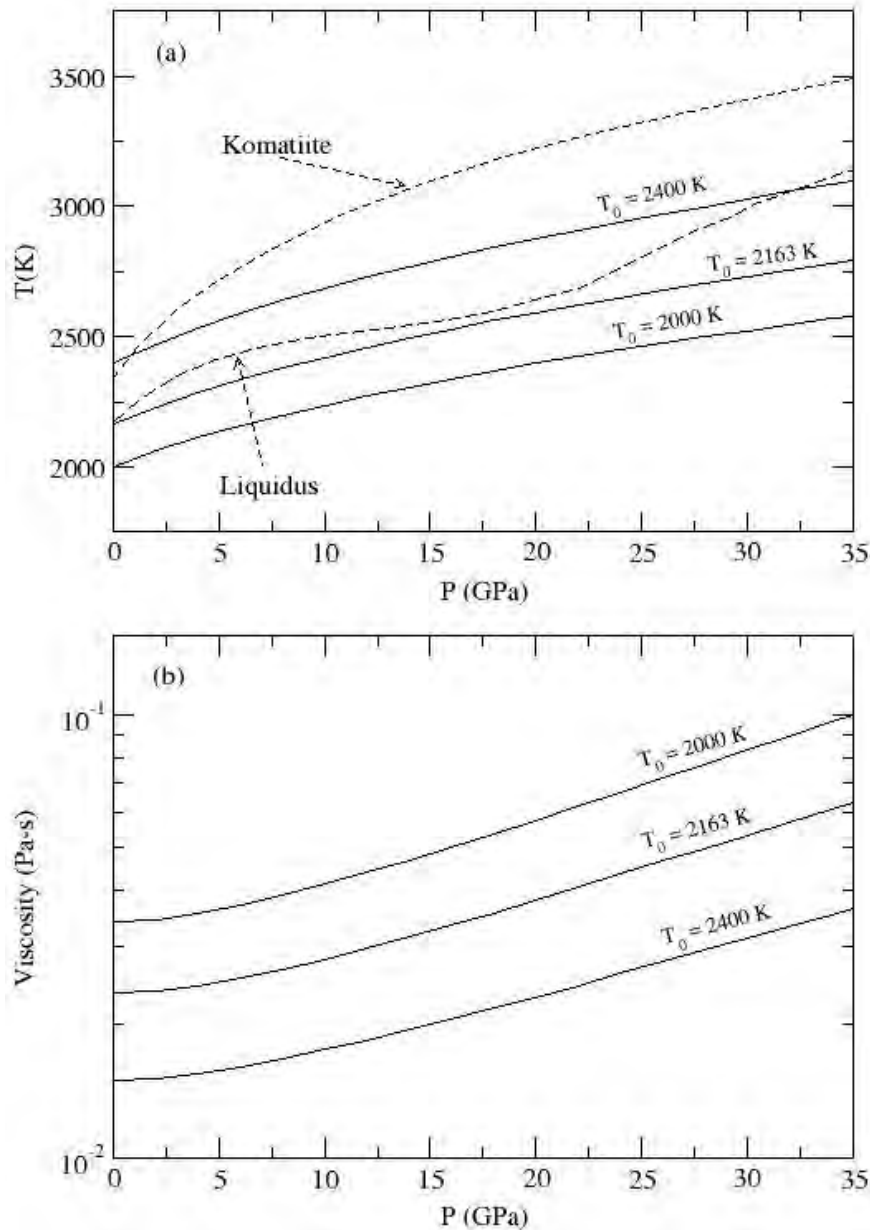


Fig. 3.6-2: (a) The adiabatic temperature profile for a  $\text{Mg}_2\text{SiO}_4$  magma ocean with a potential temperature of 2163 K (melting point of forsterite), as well as alternative potential temperatures of 2000 K and 2400 K. For comparison a dry liquidus and a komatiite adiabat are shown. (b) Corresponding viscosity profiles for the three adiabats shown in (a).

**b. Observation of low-anisotropy crystal aggregates undergoing static grain growth and melting in the moissanite cell (F. Schiavi, N. Walte, and H. Keppler)**

Static grain growth, a common process that occurs in igneous and metamorphic rocks at elevated temperatures, has profound implications for the texture of rocks. In melt-bearing rocks, changes in grain-size as well as temporal departures from textural equilibrium can

strongly affect melt distribution and the physical properties of rocks. We performed experiments on nitrate and chloride salts at moderately high temperatures (250-900 °C) in the moissanite cell in order to directly observe texture-controlling mechanisms during crystallization, textural coarsening, and melting of crystal aggregates. Both nitrate and chloride salts have previously been used as analogs for minerals with low surface energy anisotropy, such as olivine and quartz.

A first series of experiments was conducted on a crystalline aggregate consisting of a mixture of ~ 80 wt.% KNO<sub>3</sub> and ~ 20 wt.% LiNO<sub>3</sub>. During a rapid reduction in temperature (3 °C/min) from the liquidus (~ 265 °C) to 245 °C followed by subsequent annealing, the crystallizing aggregate underwent a complex evolution involving dendritic and vermicular growth, abnormal grain-growth, and normal grain growth. Most notably, the final foam texture preserved no evidence of the early evolutionary stages. During normal grain-growth, topological changes such as neighbor switching and grain dissolution took place and led to the temporary formation of irregularly-shaped melt pockets (Fig. 3.6-3). The importance of subgrains and gas bubbles for pinning migrating grain boundaries confirms the results of earlier studies conducted, using conventional methods, on partially molten olivine aggregates. Notably, crystal-melt contacts were characterized by curved boundaries and roundish shapes (Fig. 3.6-3) and straight facets did not develop. During re-melting, melt formed at triple junctions and along grain boundaries simultaneously (at a fast heating rate of 3.4 °C/min) or melting began at three-grain junctions (at a slow heating rate of 0.1 °C/min). This is due to a decrease in effective dihedral angle during heating: at fast melting the effective angle is decreased to 0°, which causes a very early loss of cohesion of the grain matrix.

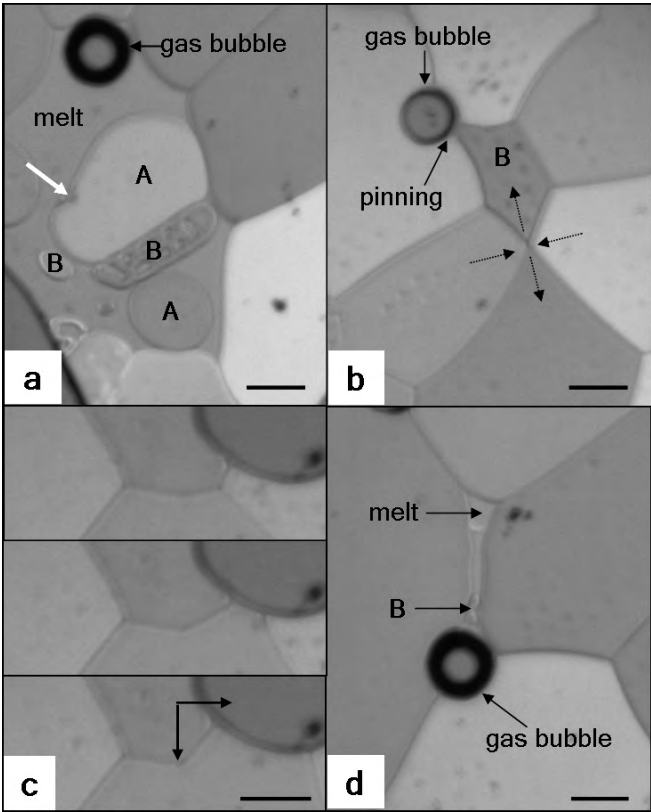


Fig. 3.6-3: Textures that developed in the nitrate aggregate. Growing and dissolving crystals are indicated by “A” and “B”, respectively. (a) Pinning mechanism exerted by a subgrain is indicated by the arrow. (b) A “neighbor switching” mechanism is indicated by dotted arrows. (c) Formation of a step-shaped grain boundary caused by pinning exerted by two bubbles (black arrows). (d) The final melt was squeezed out of the triple junction that formed in the upper part of the pocket. Scale bars correspond to 50 μm.

A second series of experiments was conducted on a mixture of NaCl and KCl in relative proportions of ~ 90-95 and 10-5 wt.%, respectively. Textural coarsening of the starting aggregate was investigated during annealing experiments at temperatures just below the liquidus temperature (~ 785 °C). The melt-solid dihedral angle is < 60°. During grain-growth, the system locally formed a foam texture with smooth grain boundaries at locations with little melt (Fig. 3.6-4). A major result concerns the first *in situ* detailed observation of grain-coalescence (Fig. 3.6-4). Shrinking grains assumed spherical shapes before resorption; in some cases they were directly resorbed in the liquid phase, but more often they were consumed by large grains (Fig. 3.6-4). The observed distribution of the liquid phase in the aggregate was influenced by the rapid continuous rearrangement of growing grains. The migration of curved grain boundaries combined with the resorption of small grains was responsible for the development of melt lenses and strongly distorted, melt-filled triple junctions. Melt disequilibrium driven by grain growth in an ionic crystalline system at high temperature suggests the likely importance of such a process for natural systems with a low to moderate surface energy anisotropy (*i.e.*, olivine-melt, quartz-melt) and may therefore be relevant for asthenospheric permeability and seismic properties.

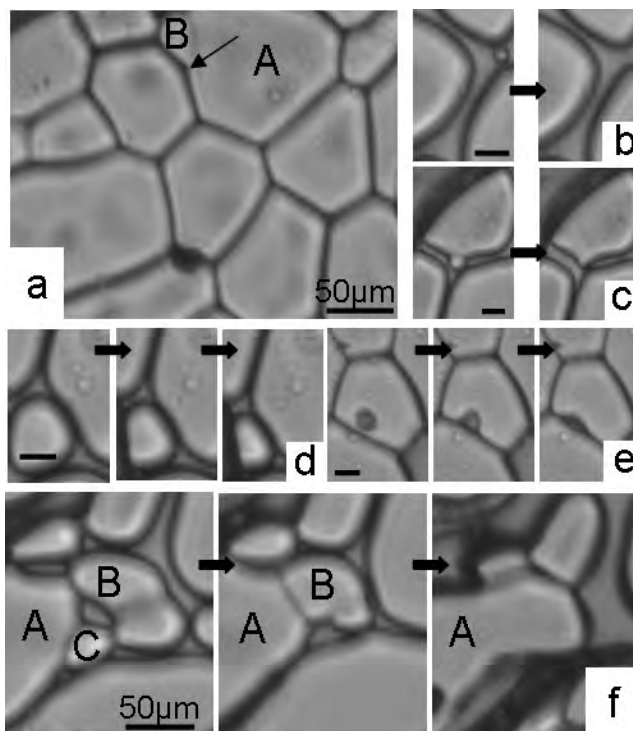


Fig. 3.6-4: (a) Foam texture in NaCl-KCl aggregates. The arrow indicates a step in the grain boundary related to the absorption of a smaller grain (B) by a larger grain (A). (b-e) Resorption mechanisms of small grains and the formation of melt lenses. Scale bars correspond to 25 µm. (f) Coalescence between the grains “A” and “B”: the interposed grain boundary does not migrate but “dissolves” leaving a single grain behind. Note a small grain (C) that is consumed by a larger grain (A) through Ostwald ripening.

**c. Electrical conductivity of anhydrous and hydrous albite-composition melts at high pressures (H. Ni, and H. Keppler)**

High electrical conductivity observed from magnetotelluric/geomagnetic depth sounding is probably associated with the presence of magma. Conductivity measurements on silicate melts with various compositions at different temperatures and pressures are therefore

necessary for fully understanding the physicochemical state of magma at depths in the Earth's crust. We have investigated the electrical conductivity of albite-composition ( $\text{NaAlSi}_3\text{O}_8$ ) melts, both anhydrous (with 0.02 wt.%  $\text{H}_2\text{O}$ ) and hydrous (with 2.0-5.4 wt.%  $\text{H}_2\text{O}$ ), at 300-1500 °C and 0.9-1.8 GPa in a piston-cylinder apparatus.

Anhydrous glass was synthesized by fusing oxides and carbonates in a 1-bar furnace, and hydrous glasses were prepared by fusing a mixture of the glass powder and water at high pressure in a TZM vessel. For the conductivity measurements, a glass cylinder was contained in a  $\text{Pt}_{95}\text{Rh}_5$  capsule, which acted as an outer electrode, and contained a centrally-located platinum rod, which acted as an inner electrode (Fig. 3.6-5). Platinum wires were used to connect both electrodes to a Solartron 1260 impedance analyzer for electrical conductivity measurements over a frequency range of 3 MHz to 3 Hz. A type-S thermocouple was used to monitor temperature. Furthermore, a Mo foil was employed to reduce interference from the heating circuit (Fig. 3.6-5).

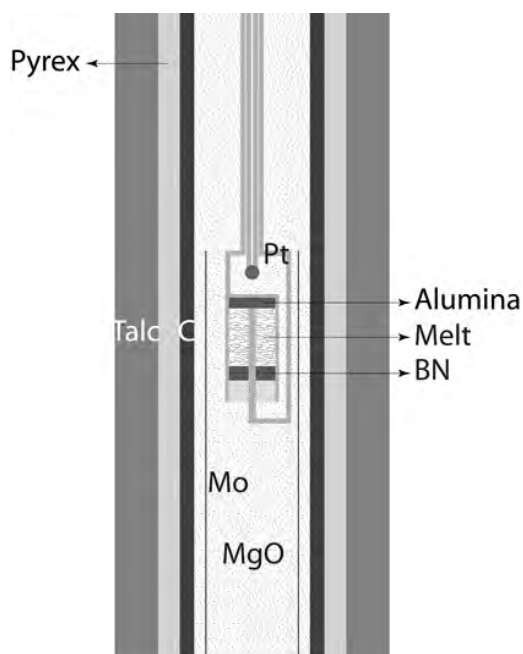


Fig. 3.6-5: Sketch of the sample assembly used for electrical conductivity measurements in a piston-cylinder apparatus. The pressure medium consists of a composite talc-pyrex sleeve in which a cylindrical graphite heater (C) is located. Albite-composition glass (melt at high temperature) is located between the inner and outer electrodes and two ceramic alumina plugs.

For the anhydrous melt, electrical conductivity  $\sigma$  increases with temperature  $T$  following an Arrhenius relationship (linear relationship between  $\log \sigma$  and  $10000/T$ ) in both the 300-800 °C and 800-1500 °C temperature ranges (Fig. 3.6-6), with an inflection point (an increase in activation energy towards high  $T$ ) at the glass transition temperature of  $\sim 800$  °C. Loosely bonded sodium cations are the dominant charge carriers for electrical conduction in anhydrous albite-composition melt.

Electrical conductivity of hydrous melts is markedly higher than that of the anhydrous melt, which is probably because adding  $\text{H}_2\text{O}$  facilitates the transport of sodium cation, although hydrogen-associated species may also contribute to conduction. For melt with 5.4 wt.%  $\text{H}_2\text{O}$ ,

the transition from low  $T$  (300-650 °C) to high  $T$  (1100-1500 °C) is rather gradual and the activation energy is lower in the high  $T$  region. In addition, electrical conductivity drops by a factor of  $\sim 2$  when pressure is reduced from 1.8 GPa to 0.9 GPa.

When combined with geophysical observations, experimental data from this study could provide information concerning the physical and chemical state of felsic magma reservoirs, such as temperature, sodium/water content, or crystal proportions.

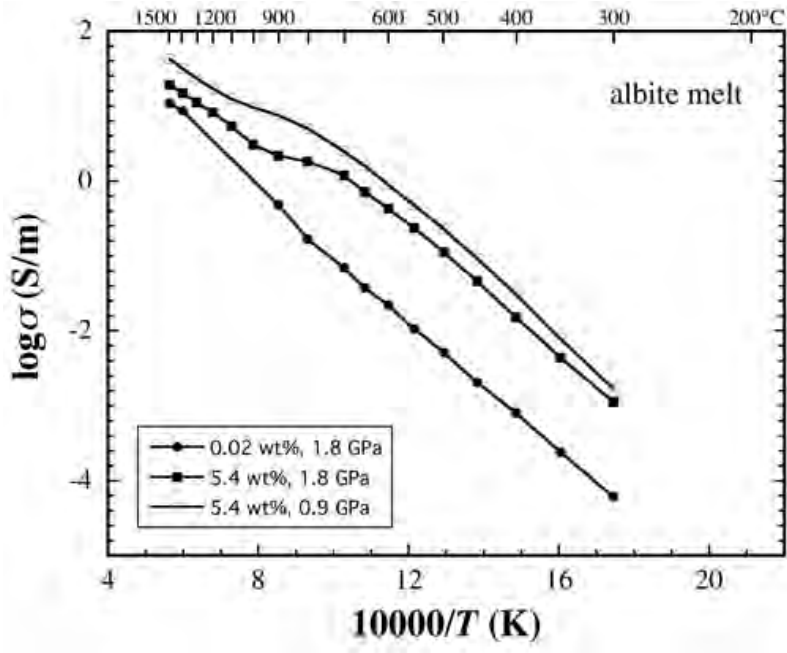


Fig. 3.6-6: Electrical conductivities of anhydrous (0.02 wt.% H<sub>2</sub>O) and hydrous (5.4 wt.% H<sub>2</sub>O) albite-composition melts at 0.9-1.8 GPa.

### 3.7 Rheology

The rheology of minerals and rocks in the Earth's deep interior has consequences for a large number of processes that shaped the Earth's past history and present state. Dynamic processes such as mantle flow and plate movements are a function of rheology as well as chemical mixing behaviour and mechanical coupling between different shells in the Earth's interior. Two aspects of rock deformation are of interest in the Earth sciences: 1) the mechanical response (strain rate) to an applied stress as described in flow laws and 2), the change in microstructure and physical properties (especially their orientational dependence, anisotropy), which tends to develop during large strain deformation. The physical anisotropies may in turn be detectable by geophysical methods allowing inferences about the deformation state of otherwise inaccessible regions of the Earth's deep interior. If the actual sample material is available, thorough fabric analysis coupled with measurements of the physical properties of the rock may allow to reconstruct the deformation history.

Since experimental equipment for quantitative deformation experiments (*i.e.*, the derivation of experimental flow laws) is presently lacking at the Geoinstitut, deformation studies are focussing on the effect of deformation at high pressure on the microstructures and physical anisotropies of minerals present in the Earth's mantle. The pressure dependence and transition of slip systems in olivine can be used to explain the presence and disappearance of seismic anisotropies with increasing depth in the upper mantle. Coesite ( $\text{SiO}_2$ ) and lingunite ( $\text{KAlSi}_3\text{O}_8$ ) are both high pressure minerals that form in felsic or  $\text{SiO}_2$ -rich rocks that have been subducted to great depths during continental collision. Their deformation behaviour as well as their ability to inherit their deformation fabrics to their low pressure polymorphs on the retrograde path is important when we try to understand and reconstruct p,T paths of deep subduction of continental material during orogenesis.

The recognition of the dominant slip systems in high pressure minerals is crucial for the understanding of the material behaviour in dislocation creep, a wide-spread deformation mechanism in the Earth's interior which also produces characteristic anisotropy patterns. Only transmission electron microscopy (TEM) can provide this microstructural information unambiguously, but it needs to be adapted especially for high pressure minerals which are often metastable and extremely sensitive to beam damage.

Magnetic anisotropies (especially AMS, anisotropy of magnetic susceptibility) in deformed rocks are often a good proxy for their deformation history. Detailed analysis of the fabric of its different magnetic components allows to decipher the complex signals derived from rock magnetic measurements and interpret quantitatively the amount of strain in a deformed rock sequence.

**a. High pressure and temperature deformation experiments on San-Carlos olivine and implications for upper mantle anisotropy (S. Shekhar, D.J. Frost, N. Walte, N. Miyajima, and F. Heidelbach)**

The mineral olivine is the major constituent of Earth's upper mantle, which comprises the top 410 km of the mantle. Below this olivine transforms to wadsleyite in the transition zone. Crystallographic preferred orientation developed in olivine due to shearing in the mantle is thought to be the prominent reason behind seismic anisotropy in the upper mantle. Seismic anisotropy in upper mantle can be observed down to a depth of ~ 350 km with a marked drop in the strength of anisotropy seen around 250 km. In addition a regional seismic discontinuity known as the Lehman discontinuity can be also seen at about 220 km and has also been argued to be related to changes in anisotropy in the mantle. One-dimensional seismic models of the Earth indicate that P-waves traveling horizontally have higher velocity than the P-waves traveling vertically; however the velocity difference decreases monotonically to a depth of 350 km and below this depth the mantle appears seismically isotropic. Anisotropy studies using S-waves indicate that horizontally polarized S-waves travel faster than vertically polarized S-waves down to a depth of 250 km, whereas between 300 km to 400 km vertically polarized S-waves are faster but with a significantly reduced velocity difference.

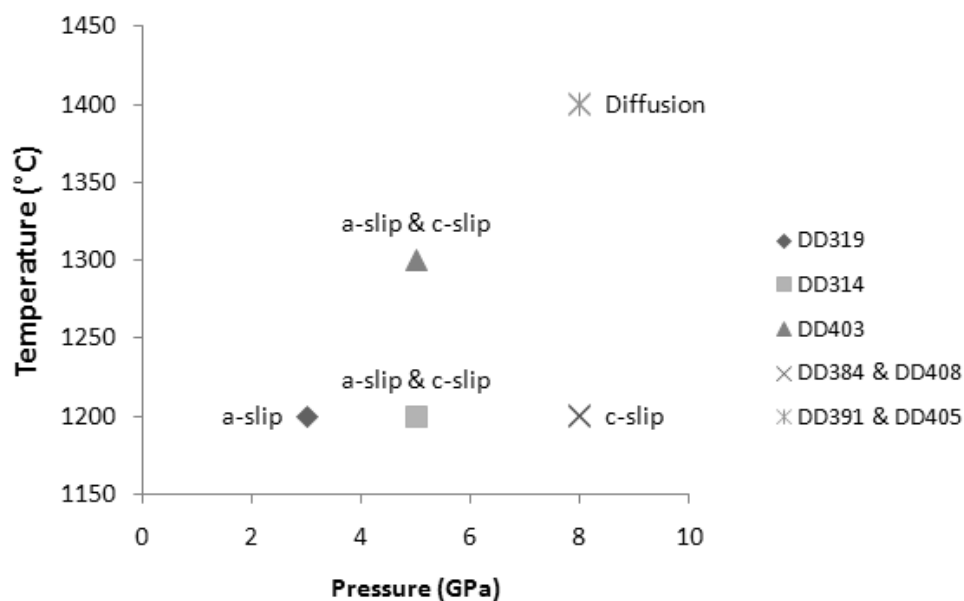


Fig. 3.7-1: Experiments performed at various pressures and temperature conditions and the resultant fabric as observed using EBSD. Diffusion refers to the diffusion creep deformation mechanism.

In the last few decades studies on natural rock samples from the mantle and deformation experiments performed on olivine have revealed that olivine deforms mainly through dislocation creep with Burgers vectors parallel to the [100] crystallographic axis under low-pressure conditions (up to 3 GPa). Under similar pressures, evidence of [001] slip has been

reported due to the presence of water. To understand the deformation mechanism in olivine at pressures higher than 3 GPa, a number of experiments have been performed using the deformation DIA.

The experimental setup consists of a hot-pressed slice of dry polycrystalline San-Carlos olivine of 0.2 mm thickness cut from a 1.2 mm diameter core at 45°. This slice is sandwiched between alumina pistons also cut at 45° in a simple shear geometry. Experiments have been performed at 3, 5 and 8 GPa at a deformation anvil strain rate of  $1.0 \times 10^{-4} \text{ s}^{-1}$  and various temperatures, as depicted in the Fig. 3.7-1. Deformed samples were cut normal to the shear plane and parallel to the shear direction. Then the sample was polished and analyzed using electron back scattered diffraction (EBSD) to identify the crystallographic preferred orientation (CPO). The fabric that developed in olivine deformed at 3 GPa and 1200 °C mainly resulted from the [100] axes being aligned subparallel to the shear direction with the (010) planes subparallel to the shear plane indicating the a-slip. Samples deformed at 5 GPa in addition had many crystallites with [100] axes aligned with the shear direction along with [100] axes indicating combined a- and c-slip. This was true for deformation experiments both at 1200 °C and 1300 °C.

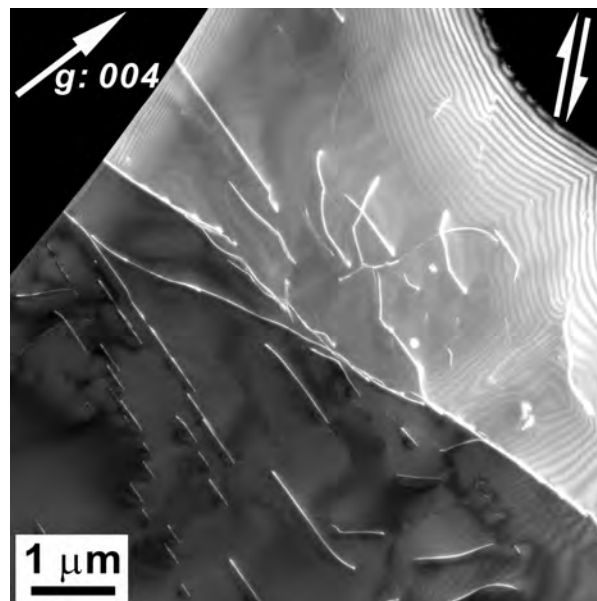


Fig. 3.7-2: TEM image of the sample DD384 deformed at 8 GPa and 1200 °C shows edge dislocation preserved, which indicates that screw segments were more mobile than the edge segments. Sense of shear has been indicated by the double arrows at the top-right section of the picture.

Samples deformed at 8 GPa and 1200 °C indicate deformation through slip along the [100] axes on the family of {hk0} planes. These observations can be interpreted as resulting from the progressive hardening of [100] slip with respect to [001] slip with increasing pressure. In

the samples deformed at 8 GPa and 1400 °C, very little CPO was developed implying that diffusion creep may be the deformation mechanism.

TEM observations have been made on several of the recovered samples in order to correlate the observed CPO with the action of specific dislocations. Sample DD384 deformed at 8 GPa and 1200 °C shows dislocations with a [001] Burgers vector; straight edge dislocations dominate indicating that screw segments were more mobile (Fig. 3.7-2). The sample deformed at 8 GPa and 1400 °C shows reduced dislocation densities and more evidence of dislocation climb consistent with deformation being largely accommodated by diffusive processes.

These results lead us to believe that the transition that occurs between a-slip to c-slip with increasing pressure is rather a gradual process, which goes to completion at pressures approaching 8 GPa. If such a gradual change occurs it would be difficult for such a transition to cause a seismic discontinuity such as the Lehman discontinuity. On the other hand our results imply that at depths over 200 km in the upper mantle, temperatures may be sufficiently high for diffusion creep to become the dominant mechanism for deformation. If diffusion creep dominates very little CPO will develop and the mantle will become seismically isotropic at these depths. This is exactly what is observed below 250 km depth from S-wave anisotropy studies. It is important to point out that mantle rocks can also contain up to 40 % pyroxene and 20 % garnet. While these minerals do not exhibit elastic anisotropy at the level of olivine they may still have a prominent effect on the bulk mantle anisotropy once the role of olivine becomes insignificant and may also influence the development of olivine CPO. In order to get a better understanding of mantle anisotropy more experiments will be performed in the future to examine the effects of water, stress, oxygen fugacity and the role of other major minerals in the upper mantle on seismic anisotropy.

**b. Deformation and crystallographic preferred orientation of coesite and retrograde quartz (N. Walte, F. Heidelbach, P. Cordier/Lille, and D. Rubie)**

Coesite, a high-pressure polymorph of SiO<sub>2</sub> is a major constituent of felsic ultra-high pressure metamorphic rocks that were subducted to great depths during continental collision. Even though the transfer to depths greater than 100 km followed by rapid exhumation must have involved a large amount of deformation, very little evidence for deformation of coesite has been found in relict UHP assemblages so that the deformation behaviour of this important mineral is still in question. Based on optical investigation of experimentally deformed samples a dominant (010)<001> slip system was suggested for coesite. Two investigations using transmission electron microscopy (TEM) suggested a range of different Burgers vectors with a possible (110) glide plane but could not confirm a (010) glide plane. In this study we present an electronic backscatter detection (EBSD) study of experimentally deformed coesite to solve the apparent contradiction between the previous studies. Since most coesite is back-

transformed to quartz during exhumation of the UHP rocks, it is of great interest whether there is a potential for texture inheritance in newly grown quartz that might allow drawing conclusions regarding deformation in the coesite field.

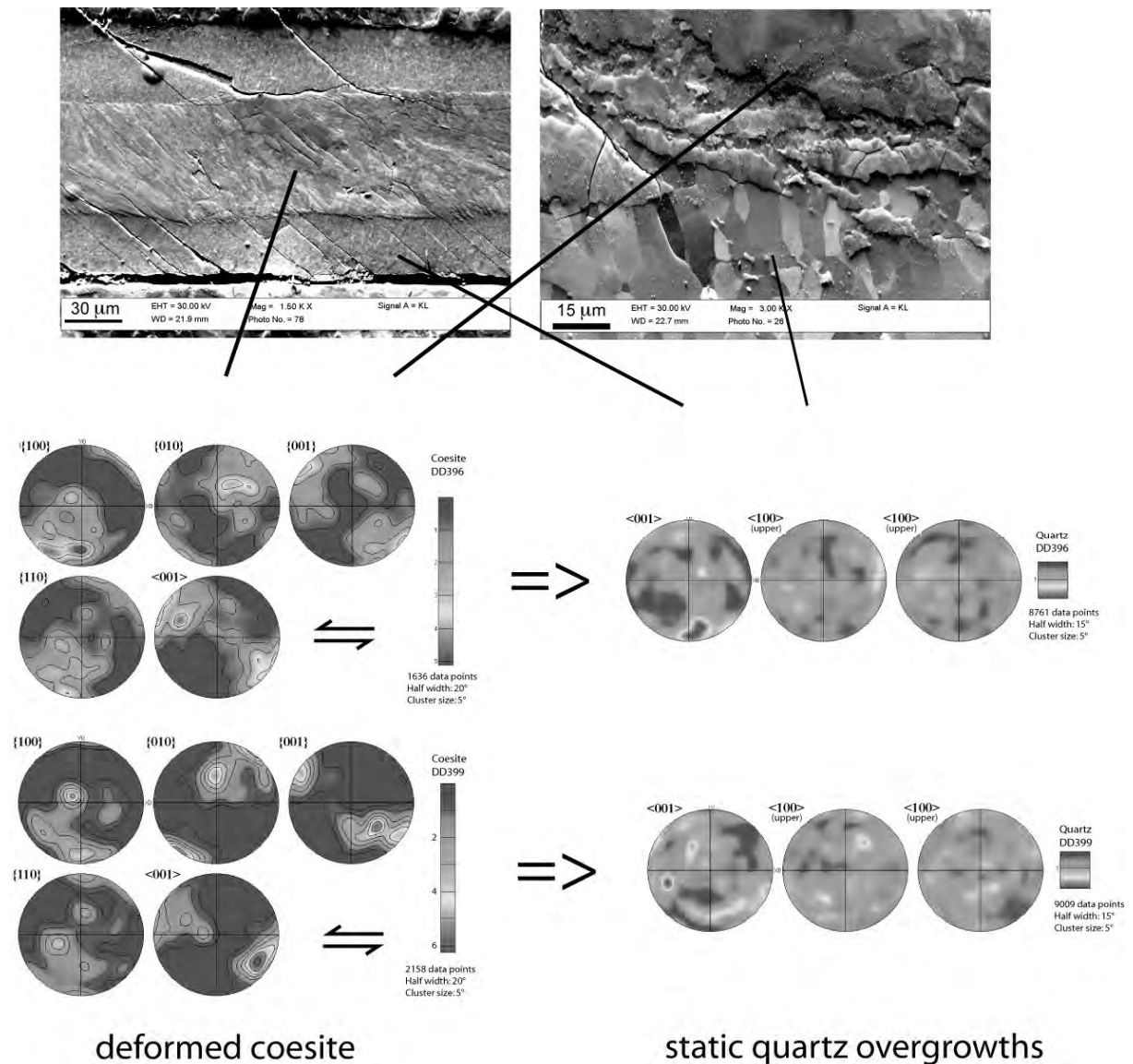


Fig. 3.7-3: Microstructure and pole figures of deformed coesite (left, high relief on SEM images) and of retrograde quartz palisades (right, low relief). Coesite displays a deformation LPO, quartz shows no LPO, *i.e.*, it does not show texture inheritance from coesite.

Experiments were performed with a deformation-DIA (d-DIA) at 1173K or 1373K and at a pressure of 3.5 GPa. After deformation, the experiments were quenched or deformation was stopped and the sample was statically decompressed into the quartz field and annealed at constant temperature to investigate quartz overgrowth and texture inheritance. The recovered

samples were cut in the centre and prepared for SEM and EBSD analysis. EBSD analysis revealed a deformation induced lattice preferred orientation (LPO) in all deformed samples usually with an alignment of the (010) planes in the shear plane (Fig. 3.7-3). Additionally, in simple shear coesite often displays an alignment of  $\langle 001 \rangle$  in the shear direction and a rough alignment of (100) and/or (110) in the shear plane. The strongly deformed coesite is replaced by elongated quartz palisades that do not inherit a texture from the coesite (Fig. 3.7-3).

Our results suggest the activation of (010), (110), and (100) glide planes for the deformation of coesite. The alignment of the (010) poles appears to be the most dominant in many experiments. This corresponds to a preferential alignment of the tabular coesite crystals in the shear plane, which can be observed in some microstructures and confirms earlier reports. On the other hand, the alignment of (110) poles is in agreement with the reports of previous TEM investigations. It is currently unclear why (010) could not be confirmed by TEM investigations. One possibility may be a grain boundary sliding component in coesite deformation that causes a passive rotation of the elongated grains; a (010) glide plane could also be masked by dislocation climb. The lack of texture inheritance in new quartz confirms previous reports of heterogeneous quartz nucleation interpreted from natural samples. Unfortunately, it means that no information about deformation in the coesite field can be extracted from the textures of retrograde quartz from natural rocks.

**c. Characterization of the dislocations and slip systems in lingunite (P. Cordier, and A. Mussi/Lille; D.J. Frost)**

Lingunite ( $\text{KAlSi}_3\text{O}_8$  hollandite) is likely to be a major phase in continental crust and marine sediment lithologies, as well as in some basalts, at depths equivalent to the deeper part of the upper mantle and throughout the mantle transition zone. This mineral may be a host phase for K in the mantle.

Lingunite exhibits an interesting crystal structure which may have strong implications on its plastic deformation properties. Cell parameters exhibit with very different moduli (9.315 and 2.723 Å). [001] is thus, from the elastic point of view, the most likely shear direction (Burgers vectors with the shortest modulus). The space group of lingunite being  $I 4/m, \frac{1}{2}\langle 111 \rangle$  are other translation vectors in the structure and hence can be potential Burgers vectors. The table below summarizes the various possibilities.

Possible Burgers vectors	Moduli (Å)	Possible slip planes
[100], [010]	9.315	(001)
$\frac{1}{2}\langle 111 \rangle$	6.726	{110}
[001]	2.723	{110}, (100), (010)

Examination of the structure suggests several possible glide planes for dislocations in this structure (see table). Figure 3.7-4 below shows possible slip planes for [001] dislocations.

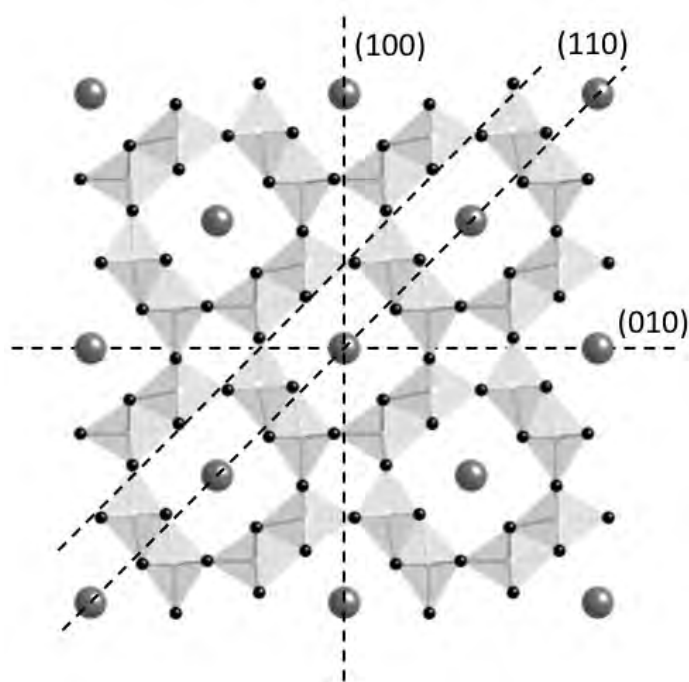


Fig. 3.7-4: Structure of  $\text{KAlSi}_3\text{O}_8$  lingunite viewed down [001]; K atoms: dark spheres;  $(\text{Si,Al})\text{O}_6$ : light octahedra with O atoms in black; possible glide planes containing the [001] direction are highlighted.

We have performed deformation experiments on lingunite with the multianvil apparatus. Lingunite was synthesized from a  $\text{KAlSi}_3\text{O}_8$  glass at 17 GPa and 1400-1600 °C. Specimens containing the high-pressure phase were recovered and placed in a second high-pressure cell designed to induce deviatoric stresses during compression (the specimen was located between two alumina pistons). The deformation conditions corresponding to this second run were 17 GPa and 1300 °C. After deformation, the specimen was prepared for Transmission Electron Microscopy (TEM) investigation. Observations were carried out with a FEI CM30 microscope operated at 300 kV. Lingunite is extremely sensitive to beam damage, such that observations were conducted at liquid nitrogen temperature in a Gatan cold stage and under low illuminating conditions.

Although there is some dispersion, a grain size of  $65 \pm 20 \mu\text{m}$  was observed which is suitable for deformation by dislocations and, more importantly here, for the characterization of their microstructures by TEM. These microstructures are heterogeneous. Some grains are free of dislocations (usually the smallest) but a large number of grains contain clear evidences of dislocation activities. We observed free dislocations with a density of the order of  $3 \times 10^{12} \text{ m}^{-2}$ . We also observed a significant number of subgrain boundaries. Considering that the deformation experiment corresponds to a stress relaxation test, these dislocations are likely to

reflect the large deformation event at the beginning of the experiments and the fact that, after stress decreased, dislocations in excess had to be annihilated or re-arranged in subgrain boundaries (recovery). The occurrence of well-organized subgrain boundaries demonstrates that atomic diffusion is active at 1300 °C in lingunite. TEM analyses in weak beam conditions reveal that dislocations are mostly [001] dislocations gliding in (010) and {110} and  $\frac{1}{2}\langle 111 \rangle$  dislocations gliding in {110} (Fig. 3.7-5). This information can be incorporated in a further modeling of the contribution of lingunite to the seismic anisotropy of subducted sediments integrating the possible crystallographic preferred orientations (CPOs) of this mineral.

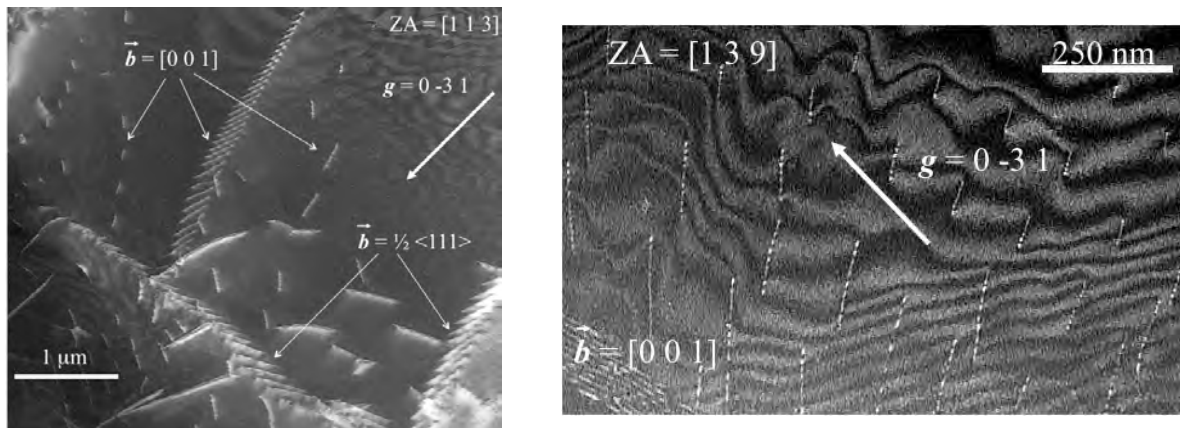


Fig. 3.7-5: TEM micrographs (weak-beam dark-field. ZA: zone axis.  $g$  diffraction vector.  $b$ : Burgers vector) showing the deformation microstructures and illustrating the pervasive occurrence of [001] dislocations (left and right) followed by  $\frac{1}{2}\langle 111 \rangle$  dislocations (left).

**d. Burgers vector determination in deformed materials using thickness-contour fringes in weak-beam dark-field TEM images (N. Miyajima, and N. Walte)**

Dislocations are the most important agents in dislocation creep which may be one of dominant deformation mechanisms in the Earth’s mantle. Dislocations are line defects and defined by the line direction and the slip vector, Burgers vector, which are identified with these two directions as “screw”, “edge” or “mixed” characters. The dislocation line can be visible by selecting diffraction conditions in TEM, but Burgers vector is invisible, to be not directly determined. So we need a proper method to determine it by using a TEM imaging technique.

The thickness-contour fringe method has been performed in materials deformed under high pressure and temperature conditions. The advantage of the method is to enable a complete determination of the character of a dislocation Burgers vector (sign and magnitude) by counting the number of terminating thickness fringes at the extremity of a dislocation from a wedge-shaped thin-foil specimen in weak-beam dark-field (WBDF) TEM images (see an example in Fig. 3.7-6). The visibility criteria,  $g \cdot b = n$  ( $g$ : diffraction vector,  $b$ : Burgers vector and  $n$ : Integral) in TEM images are clearly demonstrated to be superior in unambiguity to

conventional invisibility criteria,  $\mathbf{g}\cdot\mathbf{b} = 0$ , which can be comparable with large-angle convergent-beam electron diffraction techniques. Large deviation error ( $s \gg 0$ ) in WBDF images, *i.e.*, pseudo-kinematical diffraction conditions, is also an advantage compared to using  $\mathbf{g}\cdot\mathbf{b} = 0$  ( $s = 0$ ) criterion for invisibility of dislocations in elastically anisotropic materials (*i.e.*, almost natural minerals). In addition, the pseudo-parallel beam technique involves only a low-dose illumination of the specimen, which is a critical advantage in applications to sensitive high-pressure minerals to high electron doses.

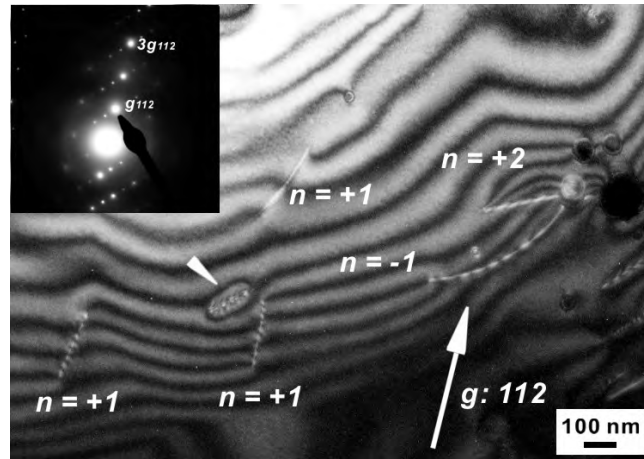


Fig. 3.7-6: Weak-beam dark-field (WBDF) TEM micrograph showing dislocations in a  $\text{CaIrO}_3$  perovskite (courtesy sample from K. Ohgushi/Tokyo). The given number ( $\mathbf{n}$ ) indicates scalar product of diffraction vector ( $\mathbf{g}$ ) and Burgers vector ( $\mathbf{b}$ ) in each dislocation. The arrowhead indicates a partial dislocation. The inset is a selected area diffraction pattern indicating the diffraction condition on the image with  $\mathbf{g}_{112}/3\mathbf{g}_{112}$  under the systematic reflections of the type  $n\mathbf{g}_{112}$  (where  $n$  is an integral).

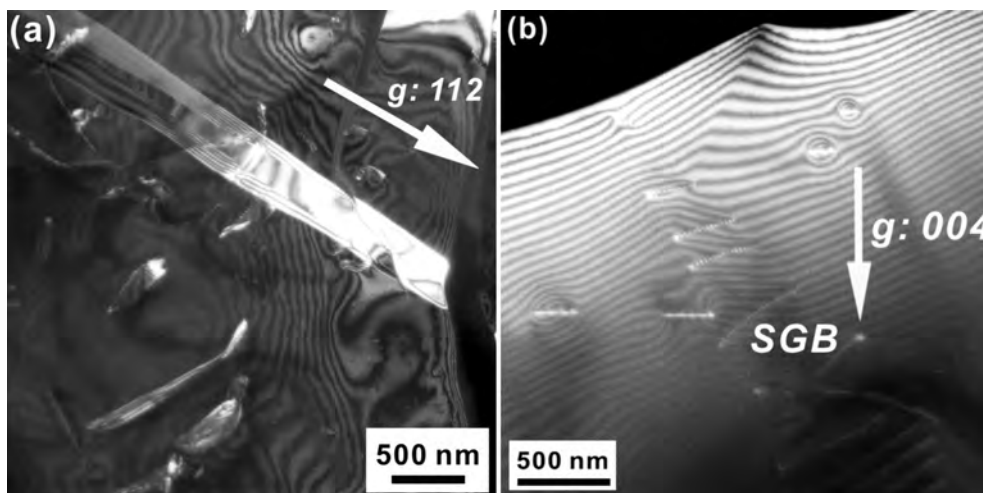


Fig. 3.7-7: WBDF-TEM micrographs of (a) a silicate perovskite (a courtesy sample from S. Shcheka/BGI) and (b) olivine (from S. Shekhar/BGI). A  $\{110\}$  twin and widely dissociated dislocations are clearly visible in the perovskite. A sub-grain boundary (SGB) consists of  $[001]$  edge dislocations in the olivine.

Currently we are applying the thickness-fringe method to several rock-forming minerals in the Earth's mantle, such as olivine and synthetic high-pressure phases (*e.g.*, Fig. 3.7-7). The WBDF-TEM image is also very useful for evaluating dislocation microtextures, because we can obtain much finer line contrast in a dislocation, which is much closer to the dislocation core than in a conventional dark-field TEM image.

*e. Magnetofabric and textural analysis from highly anisotropic magnetite-bearing mylonitic garnet micaschist of the Scandinavian Caledonides (R. Engelmann, A. Kontny, and J. Grimmer/Karlsruhe; F. Heidelberg)*

The very high anisotropies ( $P'$ -values up to 4.5) of the magnetic susceptibility (AMS) of mylonitic garnet micaschists of the Seve nappe N and W of Lake Slipsiken (Swedish Caledonides) raises questions about their origin. The study of shear zones with very high AMS provides a chance to monitor systematic changes of rock magnetic parameters and petrofabrics - quantified by low- and high-field AMS, isothermal remanent magnetization (IRM), and anisotropy of anhysteretic remanent magnetization (AARM) - and to link them with field observations, and meso- to microscale structural data, textural data (EBSD), magnetomineralogy (SEM, EMP), and image analysis. The goal of the present study is the characterization of the magnetic minerals and their fabrics in order to better understand the parameters that control the very high AMS.

The AMS is related to the distribution, preferred orientation and grain shape of minerals. The advantage of this method in comparison with conventional macroscopic, microscopic, and X-ray diffraction techniques, is its high sensitivity to weak differences in the crystallographic orientation of paramagnetic minerals (*e.g.*, phyllosilicates, amphiboles, pyroxenes, olivine) and in the grain shape and distribution of ferrimagnetic minerals (*e.g.*, magnetite, pyrrhotite).

Microscopic investigations revealed that white mica and quartz are the major phases of the mylonitic garnet micaschists. Minor phases are garnet, feldspar, biotite, magnetite, ilmenohematite, and in relictic abundance epidote, chlorite, pyrite, zircon and tourmaline. The metamorphic foliation is defined by muscovite and biotite. The matrix is formed by fine-grained quartz with grain sizes  $< 10 \mu\text{m}$ . Mica fish and S-C fabrics indicate top-to-the-NW ductile shearing. Magnetite and ilmenohematite comprise less than 3 vol.% of the rock, however they are the main carriers of the magnetic moments in these rocks. Most ilmenohematite grains show exsolution lamellae of fine hematite in ilmenite hosts. Magnetite and ilmenohematite are aligned subparallel to the mica fabric, forming flattened and elongated mineral grains of 20 to 250  $\mu\text{m}$  size. Their long grain axes are aligned in the plane of metamorphic foliation.

From AMS investigations we distinguished the dataset into three types of rocks (Fig. 3.7-8): type I: low  $P'$ -values ( $P' < 1.8$ ) and  $k_{\text{mean}}$ -values of  $0.5 \cdot 10^{-3}$  to  $5 \cdot 10^{-3}$  SI;

type II: intermediate  $P'$ -values ( $1.5 < P' < 3.2$ ) and  $k_{\text{mean}}$ -values  $5 \cdot 10^{-3}$  to  $20 \cdot 10^{-3}$  SI  
 type III: very high  $P'$ -values ( $P' > 3.2$ ) and  $k_{\text{mean}}$ -values of  $20 \cdot 10^{-3}$  to  $60 \cdot 10^{-3}$  SI

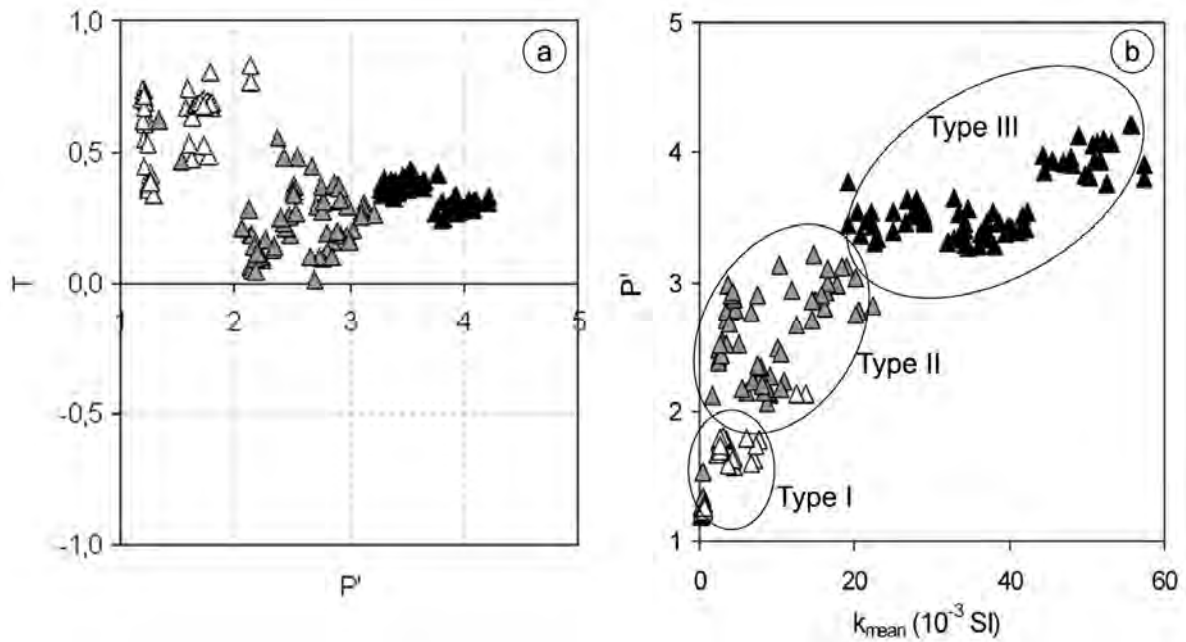


Fig. 3.7-8: AMS data of the different magnetic fabric types (open triangle: type I; grey triangle: type II; solid triangle: type III). (a) Shape factor ( $T$ ) versus degree of anisotropy ( $P'$ ), (b)  $P'$  versus mean susceptibility ( $k_{\text{mean}}$ ).

The AMS ellipsoids of all samples show an oblate shape ( $T > 1$ ) and the  $P'$ -values correlate positively with the mean susceptibility ( $k_{\text{mean}}$ ). Independent of rock type the orientation of the ellipsoid axis from low- and high-field AMS and AARM measurements are nearly coaxial. The  $k_{\text{max}}$  direction of the AMS ellipsoid is NW-SE and coaxial with metamorphic lineation. The magnetic foliation is parallel to the subhorizontal petrofabric. This observation clearly confirms a syntectonic formation of mica minerals and Fe-Ti oxides during the main stage of shear zone deformation. We observed a field dependency (up to 10 %) of magnetic susceptibility parallel to  $k_{\text{max}}$ , especially for samples with high  $P'$ -values.

Temperature dependent susceptibility measurements ( $\chi$ - $T$  curves) show significant differences between the rock types. The  $\chi$ - $T$  curves of type II and type III indicate magnetite as dominant magnetic phase with Curie-temperatures between 575 °C and 580 °C whereas  $\chi$ - $T$  curves of type I show more paramagnetic behaviour superimposed by magnetite. This observation is in accordance with the increase of  $k_{\text{mean}}$  from type I to type III, which is effected by an increase of magnetite content, also confirmed by microscopical observations. But not only the magnetite content of the three rock types is different, but also the arrangement and the shape of the magnetite grains change. Type III exhibits elongated magnetite aggregates created by magnetite grains with grain sizes up to 30  $\mu\text{m}$  and a grain-

grain-distance < 15  $\mu\text{m}$ . The aggregate size is up to 250  $\mu\text{m}$ . Type II exhibits elongated or isometric magnetite grains arranged in clusters. The magnetite grain size is up to 80  $\mu\text{m}$ , the cluster size is more than 250  $\mu\text{m}$ . The grain-grain-distance between the magnetite grains is often more than 50  $\mu\text{m}$ . The magnetite content of type I is very small. Magnetite only occurs as small (< 10  $\mu\text{m}$ ) grains in the matrix. Exsolved ilmenohematite is the dominant oxide phase in type I with grains up to 80  $\mu\text{m}$  in size.

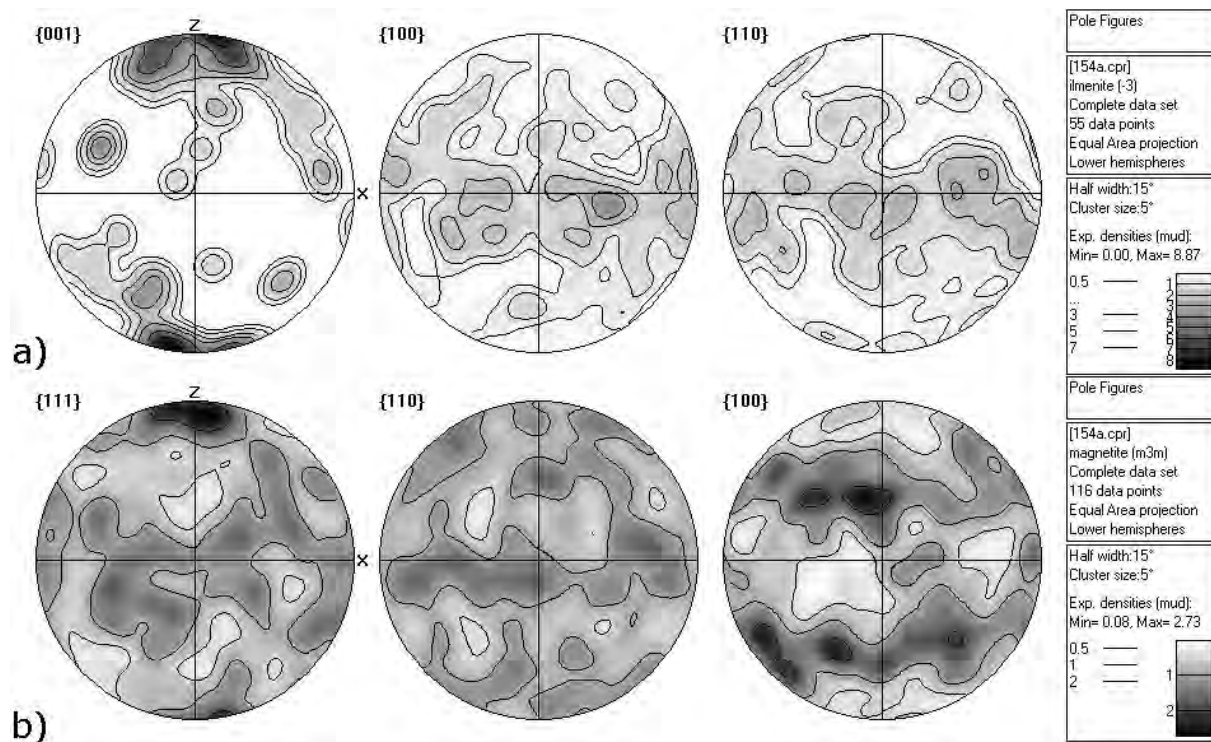


Fig. 3.7-9: Pole figures of crystallographic orientations of a) ilmenohematite and b) magnetite; **z** and **x** refer to the position of the pole of the foliation and the lineation respectively.

The electron backscattered diffraction (EBSD) study at the BGI aimed at the question if the high magnetic anisotropy has any relation with lattice preferred orientation (LPO) of magnetite or ilmenohematite. All samples show a LPO for magnetite as well as for ilmenohematite grains independent of magnetic fabric type (Fig. 3.7-9). Magnetite shows an axisymmetric LPO with the  $\langle 111 \rangle$  axes aligned coaxial to  $k_{\min}$ , and the  $\langle 110 \rangle$  axes aligned in the plane of magnetic and metamorphic foliation. Ilmenohematite also displays an axisymmetric LPO with the  $\langle 001 \rangle$  axis coaxial to  $k_{\min}$  and  $\{100\}$  and  $\{110\}$  oriented in the plane of magnetic and metamorphic foliation.

This observation confirms that the LPO could produce a magnetic anisotropy in the garnet mica schists but it is more probable that the high AMS and the field dependency of susceptibility are produced by flattened and elongated magnetite aggregates with magnetic interaction between the magnetite grains if the grain-grain-distance is less than half grain size.

### 3.8 Metamorphism

During geological processes Earth and planetary material experience changing temperature (T) and pressure (P) conditions that may alter the chemical composition of the minerals or change the mineral assembly. Metamorphic phase assemblies are often preserved in rocks from the upper mantle or in meteorites so that an investigation of these samples allows drawing conclusions regarding the natural conditions during their formation.

Solid-state diffusion is an important process during metamorphism that determines the rate at which mineral reactions can take place. In the first study diffusion of majorite component in garnet was investigated, which is one of the important reactions that occurs in the lowermost upper mantle and in the transition zone at a depth of 410-660 km. It was found that diffusion coefficients for pyrope and majorite garnets are similar and that diffusion is strongly pressure sensitive, which confirms earlier studies that were performed at the BGI. In the second study a detailed investigation of  $\text{Fe}^{3+}/\Sigma\text{Fe}$  ratios was performed for different minerals in a metasomatized mantle peridotite. In the study a relatively high  $f\text{O}_2$  for these peridotites compared to other sub-cratonic peridotites was confirmed. However, it was also shown that additional factors usually not considered may have played a role for the measured  $\text{Fe}^{3+}/\Sigma\text{Fe}$  distribution between the different minerals.

While metamorphism normally takes place in geological time-scales of millions of years the special case of shock metamorphism causes metamorphic reaction in only seconds to minutes during an impact of planetary bodies. Release of  $\text{SO}_x$  during a huge bolide impact 65 million years ago is considered to be one of the major causes for one of the most severe global extinctions in the Earth's history. The stability and decomposition of anhydrite ( $\text{CaSO}_4$ ) was investigated during experimental shock metamorphism to quantify this process. It was found that anhydrite is decomposed at an experimental pressure of 31-40 GPa, which is in accordance with previous thermodynamic modeling.

For the following studies meteorites that have undergone shock metamorphism were investigated. These meteorites represent the only natural samples in which mineral reactions such as the olivine to wadsleyite transition that usually takes place in great depths of the Earth below 410 km can be investigated directly. One interesting example for the strength of detailed petrographic inspection is a study on maskelynite glass in a Martian meteorite. Maskelynite is generally thought to be produced by direct shock-induced solid-state amorphization of plagioclase feldspar and is used as an impact pressure indicator. However, the new study showed evidence for flow textures in the glass, which means that it quenched from a flowing melt. As a result, the use of maskelynite as a reliable impact pressure indicator was questioned.

**a.** *Diffusion of majorite in garnet (W. van Mierlo, F. Langenhorst, N. Miyajima, D.J. Frost, and D. Rubie)*

Majorite ( $\text{MgSiO}_3$ ) is a high-pressure polymorph of enstatite and possesses the garnet structure. Due to the increased solubility of a majorite component in alumina-silicate garnets with increasing pressure, the amount of enstatite that can be dissolved into garnet, forming a majoritic garnet, is strongly increasing with depth. As a result, garnet is the second most abundant phase of the Earth's transition zone after the high-pressure polymorphs of olivine, wadsleyite and ringwoodite, probably constituting about 40 volume percent. However, the transport properties of this majoritic garnet phase are not well understood. Therefore diffusion experiments were conducted at upper mantle to transition zone conditions.

The diffusion experiments consisted of diffusion couples made either from polished pyrope – enstatite couples or pyrope – majoritic pyrope ( $\text{Mj}_{40-50}$ ) couples. Enstatite and majoritic garnet have been synthesized from fused oxide powders in the piston-cylinder apparatus and multianvil apparatus, respectively. Two multianvil experiments have been performed at 10 GPa and 1400 °C and 1600 °C. In the 1400 °C experiment, no diffusion profiles could be obtained using either the electron microprobe or analytical transmission electron microscopy (TEM), probably because of the low aluminium solubility in enstatite and lack of nucleation of a majoritic garnet phase. In the second experiment at 1600 °C only one newly formed garnet grain with a composition of  $\text{Mj}_{15}\text{Py}_{85}$  could be found, from which a diffusion profile into the surrounding pyrope could be obtained using analytical TEM. Diffusion coefficients were determined from these profiles using a diffusion model, where concentrations at the boundaries are kept fixed (Fig. 3.8-1a).

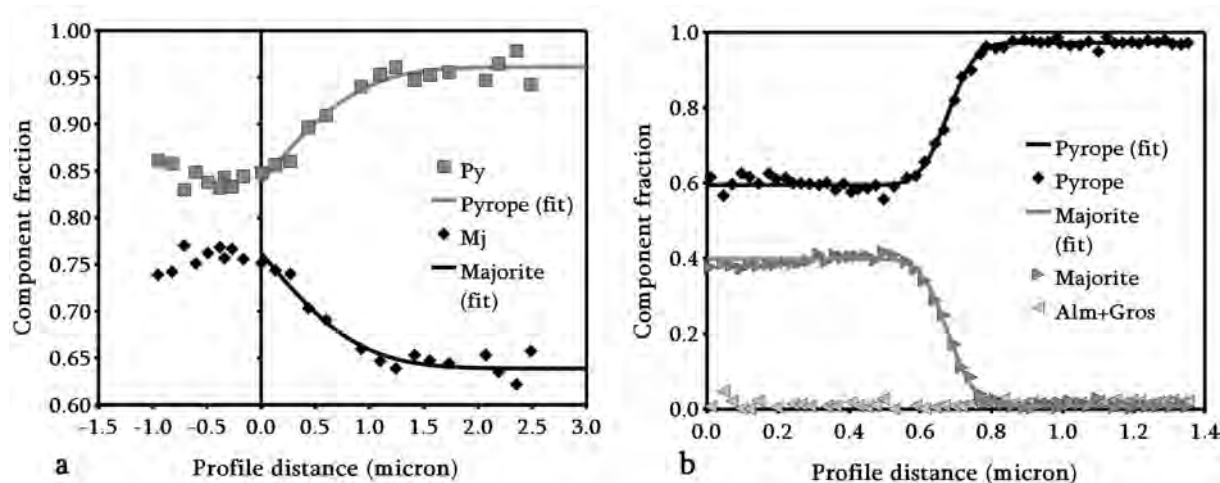


Fig. 3.8-1: Plot of diffusion profiles obtained by EDS analyses using a TEM. (a) Diffusion profile for the sample run at 10 GPa, 1600 °C. The majorite profile has been shifted up by 0.6 units, *i.e.*, a majorite component in the graph of 0.75 corresponds to an actual majorite component of 0.15 . The location of the grain boundary is at  $x = 0$ . (b) Diffusion profile obtained from the majorite – pyrope couple, run at 15 GPa and 1600 °C.

The pyrope – majorite interdiffusion coefficients are determined to be  $D_{\text{Py-Mj}} = 3.0(4) \times 10^{-14} \text{ cm}^2 \text{ s}^{-1}$  (errors are at the  $1\sigma$  level) at 1600 °C and 10 GPa for 24 hours. The lack of nucleation of a majoritic garnet phase near the interface indicates that nucleation of this phase is suppressed at the conditions of the experiment. The reported value is thus a minimum value, since nucleation of a majoritic phase is required before diffusion can occur.

To overcome the problem of nucleation, diffusion experiments using natural Dora Maira pyrope – majorite couples have been conducted at 15 GPa and 1600 °C for 4 hours. Diffusion profiles could be measured around the interface and have been fitted against a diffusion model, where two finite half spaces with contrasting compositions have been put together, and subsequently let to homogenize for 4 hours (Fig. 3.8-1b). The diffusion coefficients for pyrope and majorite were determined to be identical ( $D_{\text{Mj}} = D_{\text{Py}} = 1.3(1) \times 10^{-15} \text{ cm}^2 \text{ s}^{-1}$ ). Diffusion at 15 GPa is thus at least one order of magnitude slower than at 10 GPa. This would correspond to an activation volume for pyrope – majorite interdiffusion of at least  $10 \text{ cm}^3 \text{ mol}^{-1}$ , which is similar to values found by Chakraborty and Rubie (1996) for Mg tracer diffusion in garnets ( $8 \text{ cm}^3 \text{ mol}^{-1}$ ).

**b.  $\text{Fe}^{3+}/\text{Fe}^{2+}$  equilibria in subduction zone metasomatized garnet peridotites (N. Malaspina, S. Poli, and P. Fumagalli/Milano; F. Langenhorst)**

Redox equilibria in the Earth's mantle control many chemical and physical processes such as magma genesis, chemical differentiation and fluid-related metasomatism. Garnet peridotites from subduction environments can be important witnesses of the processes occurring in the deep sub-arc mantle, the site where the fluid phases metasomatize and re-fertilize the upper mantle by transferring elements from the slab to the mantle wedge. However, the redox state determination of most metasomatized garnet peridotites is a demanding task because of the large number of phases that may incorporate both ferric and ferrous iron, and that may show zonations.  $f\text{O}_2$  in high-pressure peridotites is traditionally determined from the  $\text{Fe}^{2+}$ - $\text{Fe}^{3+}$  content of garnet in equilibrium with olivine and orthopyroxene, but the  $\text{Fe}^{3+}$  partitioning among the peridotite mineral phases is often neglected. An increasing  $\text{Fe}^{3+}$  content in garnet can also be the consequence of a redistribution of  $\text{Fe}^{3+}$  from clinopyroxene into the garnet with increasing temperature and pressure. This implies that the  $\text{Fe}^{3+}$  enrichment in garnet is not necessarily indicative of high whole-rock oxygen contents or of the interaction with more oxidized metasomatic agents.

We studied orogenic peridotites from the ultra-high-pressure (UHP) Sulu belt (Eastern China) corresponding to a slice of metasomatized mantle wedge, equilibrated at  $\sim 5$  GPa and 900 °C. They show two UHP mineral assemblages: a high-temperature porphyroclastic garnet, coarse exsolved clinopyroxene and phlogopite association, and finer-grained olivine + clinopyroxene + orthopyroxene  $\pm$  magnesite  $\pm$  phlogopite equilibrated at lower temperature with neoblastic garnet. The  $\text{Fe}^{3+}/\Sigma\text{Fe}$  ratio of garnet, clino- and orthopyroxene and phlogopite was measured by two combined techniques: the “Flank Method”, acquired on garnets with an electron

microprobe at the University of Milano, and Electron Energy Loss Spectroscopy, at the Bayerisches Geoinstitut, employed to analyze pyroxenes and phlogopite. These two methods enable to check possible  $\text{Fe}^{3+}$  zonation and occurrence of magnetite lamellae in pyroxenes.

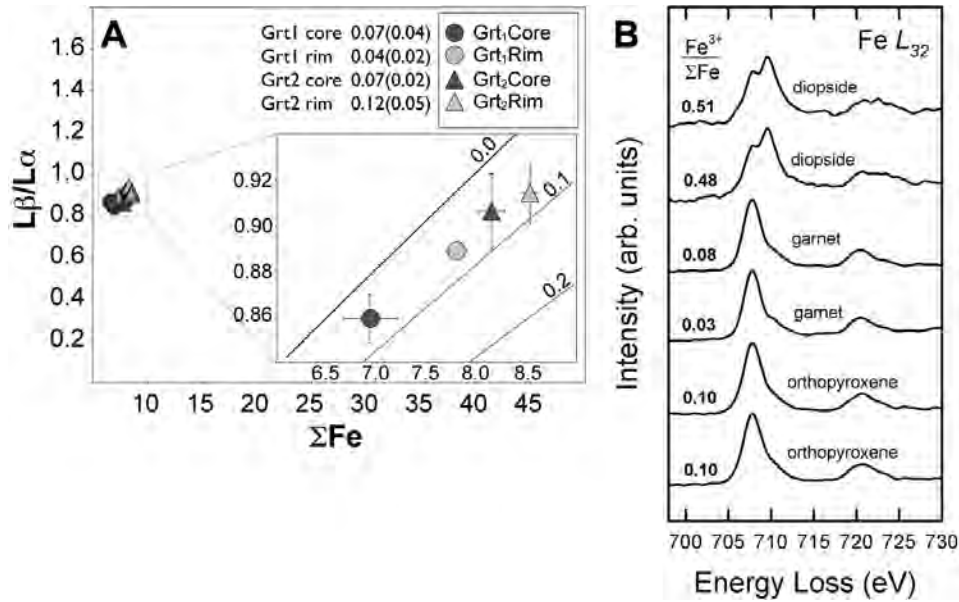


Fig. 3.8-2: A: Fe  $L\beta/L\alpha$  intensity ratios measured in garnets plotted vs total Fe content (wt.%) and average  $\text{Fe}^{3+}/\Sigma\text{Fe}$  microprobe measurements with Flank Method (standard deviations in brackets). The inset is a close-up of the data showing averages of  $L\beta/L\alpha$  intensity ratios vs  $\Sigma\text{Fe}$  compared with  $\text{Fe}^{3+}/\Sigma\text{Fe}$  regression lines. B: Fe  $L_{23}$  electron energy-loss near-edge structure of garnets, clinopyroxene and orthopyroxene.

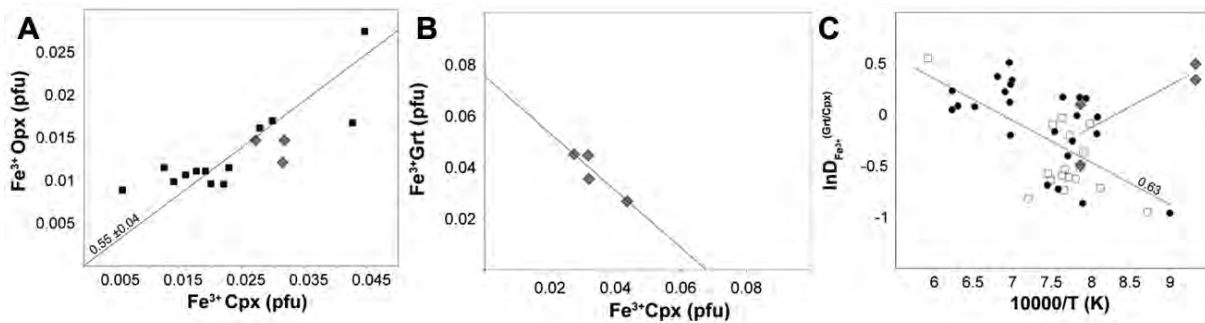


Fig. 3.8-3: Correlation of  $\text{Fe}^{3+}$  cations in coexisting clinopyroxenes and garnets (A) and clinopyroxenes and garnets (B). C:  $\ln D_{\text{Fe}^{3+}}^{\text{grt/cpx}}$  for  $\text{Fe}^{3+}$  plotted as a function of reciprocal temperature. The data from Sulu peridotites (gray diamonds) are compared with lherzolite xenoliths from sub-cratonic mantle.

The measurements shown in Fig. 3.8-2a indicate that the pyrope-rich garnets are zoned and contain  $\text{Fe}^{3+}/\Sigma\text{Fe}$  up to 0.12-0.14. Clinopyroxene contains relatively high  $\text{Fe}^{3+}$  ( $\text{Fe}^{3+}/\Sigma\text{Fe}=0.48-0.51$ ), while  $\text{Fe}^{3+}$  in phlogopite is below the detection limits. It should be noted that also orthopyroxene contains  $\text{Fe}^{3+}/\Sigma\text{Fe}$  up to 0.10, a percentage comparable to that

of garnet (Fig. 3.8-2B). Garnet/clinopyroxene and orthopyroxene/clinopyroxene qualitative partitioning are reported in Fig. 3.8-3A and B. The  $D_{\text{Fe}^{3+}(\text{Grt/Cpx})}$  of our sample apparently do not follow the same temperature trend described in the literature for sub-cratonic garnet peridotite xenoliths (Fig. 3.8-3C). This suggests that, besides temperature (and pressure), the redistribution of  $\text{Fe}^{3+}$  between garnet and pyroxenes could depend on additional variables. The  $\text{Fe}^{3+}/\Sigma\text{Fe}$  content of garnet is therefore consistent with the relatively high oxygen fugacities (FMQ to FMQ+2) recorded by the Sulu peridotites, compared with garnet peridotite xenoliths from the sub-cratonic mantle equilibrated at similar pressures. However, despite the  $\text{Fe}^{3+}$  content in orthopyroxene is usually neglected in  $f\text{O}_2$  calculations, it is worth noting that this could potentially play an important role in the relationships between  $f\text{O}_2$  and phase assemblages in a multi-component mantle system.

*c. Experimental study on shock metamorphism of anhydrite (C. Prescher, F. Langenhorst, and U. Hornemann/Weil am Rhein)*

The ejection of huge amounts of  $\text{SO}_x$  gases due to a bolide impact at Yucatan peninsula, Mexico, is the most probable cause for the global extinction at the KT-boundary. However, the devolatilization conditions of anhydrite ( $\text{CaSO}_4$ ), a main constituent in target rocks, have been predominantly inferred from thermodynamic considerations, because experimental data are scarce and previous investigations are controversial. To obtain a better understanding of the shock metamorphism of anhydrites, we conducted six shock recovery experiments from 12 to 85 GPa at the Ernst-Mach-Institut, Freiburg. The peak shock pressures were reached by the reverberation method. Thus, the energy gain in the sample is lower than in case of impedance shock experiments. Recovered samples were investigated by Raman spectroscopy, X-ray diffraction and transmission electron microscopy (TEM).

The Raman spectra of the samples revealed no variation in peak positions or breadths, which implies that there is no phase transition or change in the short-range order structure of the recovered shock-loaded anhydrites.

In the low-pressure regime up to 20 GPa the shock temperatures and stresses are relatively low; the sample reacts by multiple mechanical twinning and formation of straight dislocations. The dislocation density increases from  $10^{13} \text{ m}^{-2}$  at 12 GPa to  $10^{16} \text{ m}^{-2}$  at 33 GPa. At 46.5 GPa dislocations start to polygonize resulting finally in low dislocation densities and grain coarsening at 85 GPa. These TEM observations are in accord with the line broadening analysis of the X-ray diffraction patterns. The strain first increases up to 33 GPa and decreases then in the interval from 46.5 GPa to 85 GPa. The domain size stays constant up to 64 GPa and shows a marked jump to large sizes at 85 GPa.

A high density of voids can be observed in the samples shocked to 64 GPa and 85 GPa (Fig. 3.8-4). However, no decomposition products, melts, or crystallization from melts were observed in the experimentally shocked anhydrites. The closed container may have inhibited

the release of the  $\text{SO}_x$  gases, which could have resulted in a back-reaction with CaO. The degassing of anhydrite is only affected by the energy gained. The pressures of incipient degassing might be higher in our experiments than in nature because of the different loading paths. If we calculate the energies gained by multiple reflections of the shock wave in our samples and estimate the impedance shock pressure that is needed to result into the same energy increase, the onset of degassing would be between 30 and 41 GPa. This is within the error in the range of a previously reported value of 33 GPa calculated by entropy method.

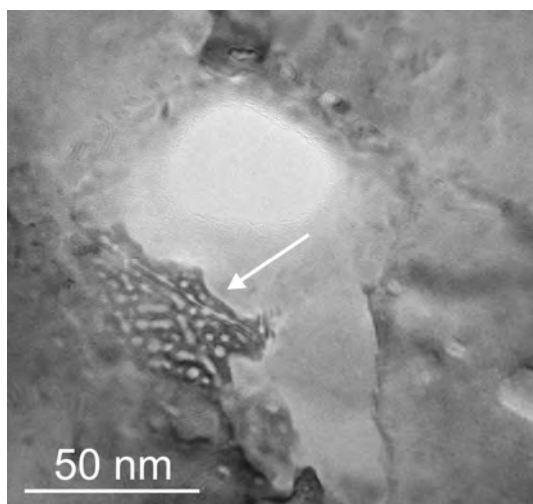


Fig. 3.8-4: HRTEM image of a degassing structure next to a void in the sample shocked to 85 GPa.

The sample shocked to 64 GPa also shows indications for different kinds of phase transformations. Planar defects on the (010) plane indicate an incipient martensitic phase transition probably to the monazite type structure. Multiple lens- and wedge-shaped twins are possibly remnants of a ferroelastic phase transition.

This work supports the constraints delivered from thermodynamic considerations for the calculation of the amount of  $\text{SO}_x$  gases released by the impact at the KT-boundary. Our study also revealed the presence of two phase transitions, which may affect the equation of state of  $\text{CaSO}_4$ .

**d.** *Ample evidence for shock-induced melting of labradorite and quenching to maskelynite glass in Martian shergottites: Fundamental consequences to equilibrium shock pressure estimates and to the age conundrum of Martian meteorites (A. El Goresy; M. Miyahara, E. Ohtani, and S. Ozawa/Sendai; P. Gillet/Lyon, P. Beck/Grenoble, G. Montagnac/Lyon, and T. Nagase/Sendai)*

Maskelynite, a glass with labradorite composition, was first recognized in 1872 in the Shergotty meteorite by Gustav Tschermack. Tschermack interpreted his finding that melting and quenching of parental plagioclase feldspar produced the labradorite glass (maskelynite).

In the last 40 years the refractive index (IR) of maskelynite was used to estimate the peak-shock pressure to which the shergottites were subjected to in belief, that the glass was produced by shock-induced solid-state amorphization of plagioclase, hence its RI could have fingerprinted the peak-shock pressure. Recent laboratory high-pressure and -temperature investigations on labradorite indicate that dynamic experiments are inadequate in obtaining reliable information on the amorphization of this feldspar due to enormous kinetic effects of amorphization not considered in the dynamic experiments.

Figure 1b NWA856

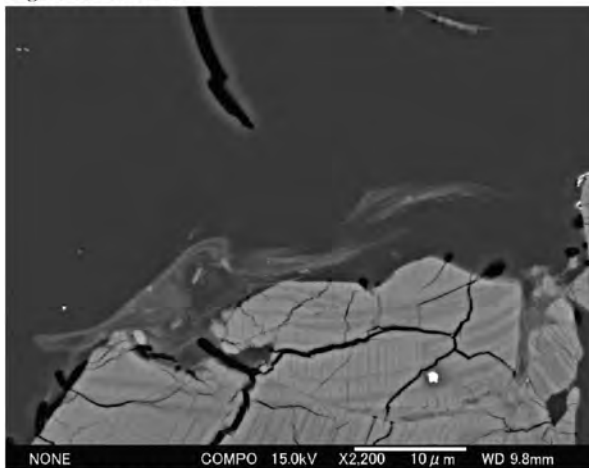


Figure 1a NWA856

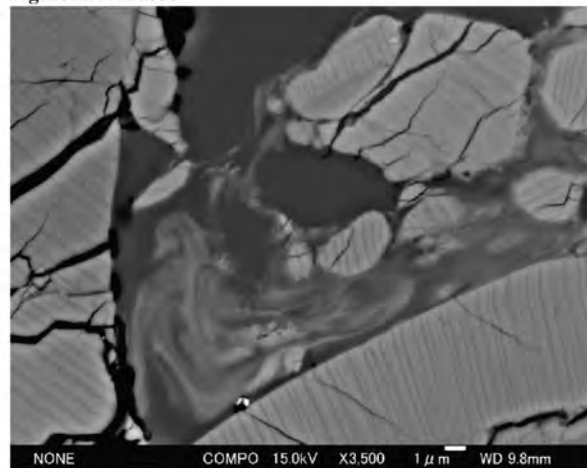


Figure 1c NWA856

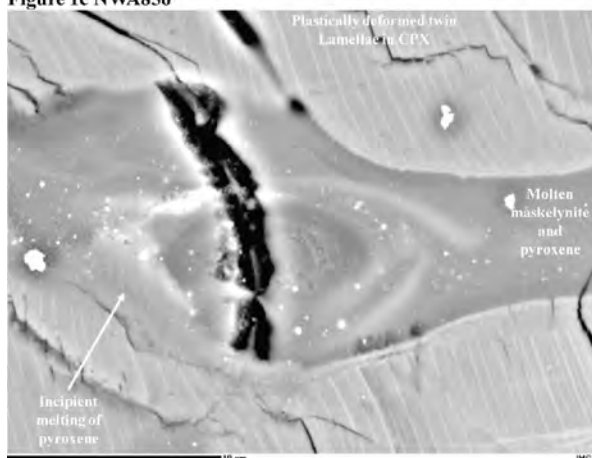


Fig. 3.8-5: BSE-SEM pictures of maskelynite-pyroxene assemblages from the shocked Martian basaltic shergottite NWA856 showing evidence of melting of plagioclase and quenching to maskelynite glass. a) Fragmented and partially molten clinopyroxene with schlieren of the melt depicting flow texture in the maskelynite melt. Clinopyroxene shows shock-induced twin lamellae // (100) planes.; b) Heavily fragmented clinopyroxene showing partial melting and migration of the melt schlieren in flow texture in the maskelynite melt. The short migration dimension of the flow texture in maskelynite indicates low turbulence during the impact event.; c) A detail of maskelynite vein inside clinopyroxene depicting an oval schlieren of molten clinopyroxene in the maskelynite.

We conducted a detailed study of several shergottites in attempt to (1) uncover the nature of maskelynite and its mode of formation if diaplectic glass or glass quenched from shock-induced melt; (2) search for shock-induced high-pressure assemblages that should allow a meaningful estimate of the equilibrium peak-shock pressures, and (3) test the reliability of maskelynite as a pressure indicator in comparison to the high-pressure inventory encountered in the Martian rocks.

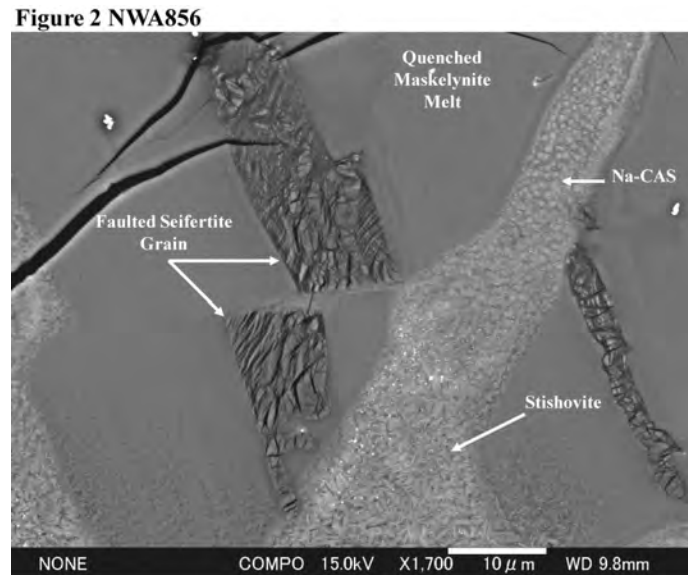


Fig. 3.8-6: A Back-Scattered-Electron image of a shock-induced high-pressure assemblage enclosed in quenched maskelynite glass in the Martian basaltic shergottite NWA856. The figure depicts a faulted seifertite grain ( $\alpha$ - $\text{PbO}_2$  structured dense polymorph of silica;  $\rho = 4.29 \text{ gm/cm}^3$ ) formed by solid-state inversion of tridymite during the shock event on Mars. Adjacent to the two seifertite segments is a long melt pocket consisting of liquidus Na-CAS phase ( $\text{CaAl}_4\text{Si}_2\text{O}_{11}$ - $\text{NaAl}_3\text{Si}_3\text{O}_{11}$  solid solution) and acicular stishovite. The high-pressure assemblage is embedded in quenched maskelynite glass of labradorite origin and composition. The segments of the faulted seifertite grain are not separated by an open fault fracture thus unambiguously evidencing that faulting took place at high pressure and temperature while maskelynite was molten. The faulting of seifertite dragged material from the melt pocket now visible as dragged schlieren between the two-seifertite segments without mixing of the two melts. The assemblage and the host maskelynite constrain the nature of maskelynite and the equilibrium shock pressure during the shock event: (1) Maskelynite is a glass quenched from plagioclase melt at high pressure and not diaplectic glass as erroneously claimed since 1986; (2) The liquidus assemblage  $\text{CaAl}_4\text{Si}_2\text{O}_{11}$ - $\text{NaAl}_3\text{Si}_3\text{O}_{11}$  solid solution + stishovite realistically constrain the equilibrium shock-pressure of the event in this Martian rock at  $\leq 22 \text{ GPa}$  at  $2000\text{-}2200 \text{ }^\circ\text{C}$  at least  $20 \text{ GPa}$  below previous reports.

Maskelynite in the Martian shergottites **Shergotty Zagami, NWA480, NWA856, NWA1068, ALHA84001** depict clear evidence for formation by melting and quenching to glass at high

pressure. Contrary to many previous reports, maskelynite is characterized by a flow texture and partial mixing of pyroxene melts with schlieren (Fig. 3.8-5). The glass is surrounded by radiating fractures in the neighboring pyroxene as a result of relaxation after decompression. This is also manifested in its lower RI reported in the last decades indicating a lower density than the parental crystalline feldspar. Maskelynite is hence not a diaplectic glass as has been believed in the last 37 years. Hence, the RI of maskelynite cannot be a reliable indicator for estimation of the peak-shock pressure because it was first established after quenching of the liquid and decompression at the closure temperature of relaxation. RI of maskelynite has hence no relevance to the shock history of shergottites.

All studied shergottites, except ALH770055 were found to contain the liquidus high-pressure assemblage Na-CAS ( $\text{CaAl}_4\text{Si}_3\text{O}_{11}$ - $\text{NaAl}_3\text{Si}_3\text{O}_{11}$  solid solution), stishovite and seifertite in many shock-melt pockets (Fig. 3.8-6). The Na-CAS phase contains 75 % of the  $\text{NaAl}_3\text{Si}_3\text{O}_{11}$  molecule. Recent experimental investigations on the binary system  $\text{CaAl}_4\text{Si}_3\text{O}_{11}$ - $\text{NaAl}_3\text{Si}_3\text{O}_{11}$  indicate that the Na-CAS with 75 mol.% of the Na-end member is stable at or just below 22 GPa and at  $T > 1900 \leq 2200$  °C. This phase dissociates at pressures higher than 22 GPa to the assemblage  $\text{NaAlSiO}_4$  Ca-ferrite + stishovite. We did not encounter any evidence for dissociation of Na-CAS to the assemblage  $\text{NaAlSiO}_4$  Ca-ferrite + stishovite in any of the studied shergottites. Our findings unambiguously indicate that the Martian shergottites were subjected to a shock event at 22 GPa and a shock temperature of  $>1900 \leq 2200$  °C in the shock-melt pockets. All previously reported estimates (30-to more than 45 GPa) using RI of maskelynite as an “indicator” are unrealistically high and discrepant with both results of static experiments and our results. A direct consequence of this discovery is that shock melting of feldspar and pyroxene must have lead to considerable resetting of the radiometric systems (*e.g.*,  $^{39}\text{Ar}$ - $^{40}\text{Ar}$ ;  $^{87}\text{Rb}$ - $^{86}\text{Sr}$ ) at the impact time on Mars. Any meaningful radiometric dating of the igneous crystallization and impact resetting ages requires careful sample selection of pristine unmelted and shock-melted parts, respectively, of the meteorites. Melted parts can only reveal partial or total resetting at the time of the shock event.

*e. First natural occurrence of ringwoodite exsolution lamellae in fractionally crystallized Mg-rich wadsleyite from shock-induced olivine melts in L6 chondrites (A. El Goresy; M. Miyahara, E. Ohtani, S. Ozawa, T. Nagase, and M. Nishijima/Sendai)*

High-pressure phase transformations reported from shocked chondrites and investigated in laboratory static high-pressure experiments may mimic mechanisms operating in planetary interiors. The formational mechanisms in melt veins in shocked chondrites were investigated to constrain the magnitude of the equilibrium shock pressure and eventually the time scales of the dynamic events.

Recently, wadsleyite-ringwoodite (Wds-Rgt) assemblages produced by fractional crystallization of homogeneous olivine melts ( $\text{Fa}_{24-26}$ ) generated by the shock event were

reported in porphyritic olivine chondrules in a shock-melt vein of the Peace River L6 chondrite. The Wds-Rgt crystallites interface displayed a large compositional gap of  $\leq 32$  mol.% fayalite, with no evidence for inter-diffusion of Mg and Fe between them. Although it was recognized that wadsleyite and ringwoodite were produced by fractional crystallization of individual olivine melts produced during the impact event on the parent body, details of the melting process and the conditions of formation of the diverse textures remained unclear.

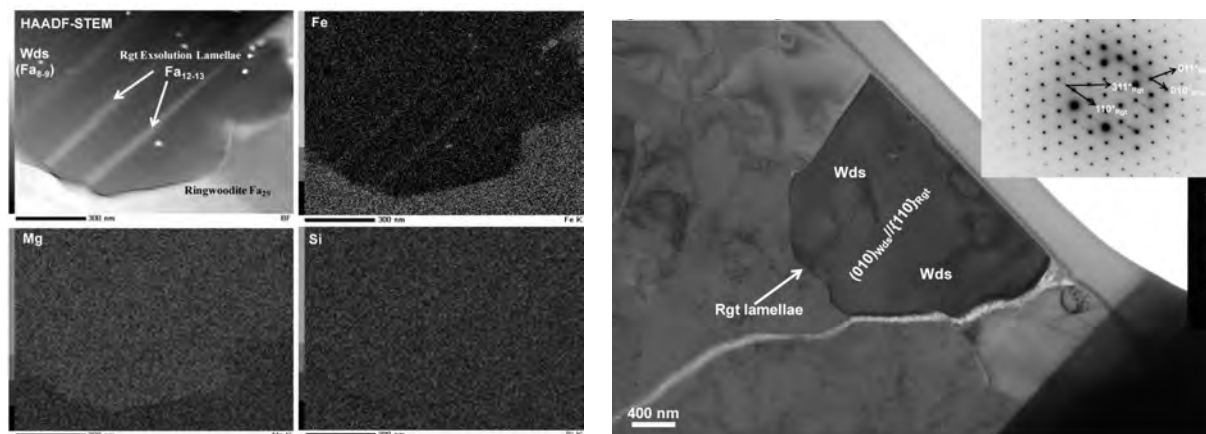


Fig. 3.8-7: (A) wadsleyite crystallite ( $\text{Fa}_{8-9}$ ) from a porphyritic olivine chondrule in the Peace River L-6 chondrite with exsolution lamellae of ringwoodite ( $\text{Fa}_{12-13}$ ): 1a: Dark Field pictures of an FIB- slice across a wadsleyite crystallite depicting exsolution lamellae of ringwoodite; a) A TEM High Angular Annular Dark Field (HAADF) picture of the intergrowth and X-ray distribution maps for Fe, Mg and Si of the same slice. (B) A TEM picture of the same slice depicting the crystallographic orientation of the ringwoodite exsolutions in the wadsleyite crystallites:  $\text{Rgt}_{\{110\}} // \text{Wds}_{(010)}$ . The inset is a SAED pattern of the ringwoodite lamellae and the wadsleyite host crystallite confirming the crystallographic relationship.

We investigated with FIB-HRTEM techniques the Wds-Rgt assemblages in porphyritic olivine chondrules and individual olivine grains entrained in the same shock-melt vein of the Peace River L-6 chondrite to scrutinize the details of preferential melting of olivines and the stages of the fractional crystallization of Mg-rich wadsleyite and Fe-rich ringwoodite in the two different settings. While the mechanism of melting of the porphyritic olivines in the chondrules seems to have been induced by considerable increase of local strain, melting in large individual olivines took place through friction along fractures. The equilibrium shock-pressure in both settings should be the same, since the chondritic liquid in which both objects were originally cold entrained is a perfect pressure-transmitting medium.

We studied FIB-slices of individual liquidus wadsleyite and ringwoodite crystallites both in molten former olivine porphyritic crystals in a chondrule and in ringwoodite-wadsleyite veins in an olivine grain in the same shock melt vein of the Peace River L6 chondrite. Wadsleyite crystallites in both settings are large and idiomorphic (up to 3  $\mu\text{m}$  in length). The wadsleyites

in the chondrule are very low in Fe (Fa<sub>8-9</sub>), a consequence of being the first phase to crystallize from the homogeneous olivine melt (Fa<sub>24-26</sub>). They depict one set of ringwoodite exsolution lamellae (Fig. 3.8-7) with slightly higher fayalite content (Fa<sub>12</sub>) than in the parental wadsleyite crystallites. SAED patterns of the Wds-Rgt intergrowth indicate that the ringwoodite lamellae are topotaxially intergrown with the wadsleyite with the crystallographic orientation  $\{110\}_{\text{rgt}} // (010)_{\text{wds}}$  (Fig. 3.8-7b) The wadsleyite crystallites in the ringwoodite-wadsleyite veins in the large olivine grain show in contrast a higher fayalite-content (Fa<sub>14-16</sub>) than their counterparts in the chondrule (Fa<sub>08-09</sub>). Wadsleyites in the veins also depict ubiquitous ringwoodite exsolution lamellae along one crystallographic direction (Fig. 3.8-8). The ringwoodite lamellae in these wadsleyites have much higher fayalite contents (Fa<sub>30-37</sub>) than their counterparts in the chondrule (Fig. 3.8-7). The compositional gap between the wadsleyite parental crystal and the ringwoodite lamellae in the olivine grain (21 mol.%) is much wider than in the assemblage in the chondrule (3 mol.% only).

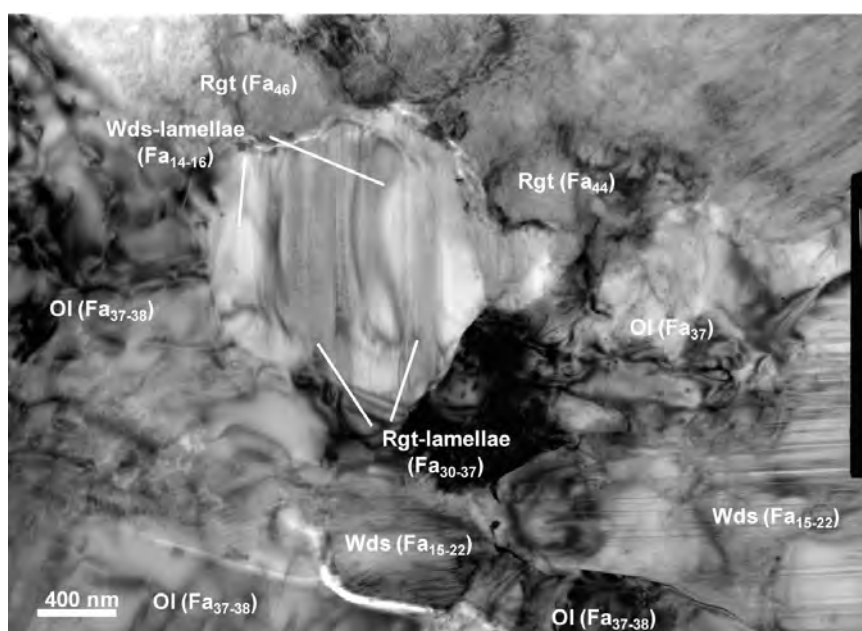


Fig. 3.8-8: A TEM photograph of the assemblage wadsleyite-ringwoodite extracted from a large olivine grain in the same shock melt vein in the Peace River L-6 chondrite. The figure shows a large wadsleyite crystallite (Fa<sub>14-16</sub>) with one set of ringwoodite (Fa<sub>30-37</sub>) exsolution lamellae.

The dichotomy in the chemical compositions of the liquidus wadsleyite crystallites and the ringwoodite exsolution lamellae in the chondrule on the one hand and in the wadsleyite-ringwoodite vein in the olivine crystal on the other, although both assemblages originally emerged from olivines of the same compositions and at the same equilibrium shock pressure possibly reflects the diversity of the fractional crystallization paths in both settings. We anticipate that the higher fayalite-content of the assemblage in the olivine grain probably resulted from continuous contributions of additional melts produced by remelting of some

wadsleyite and ringwoodite crystallites due to the continuous friction along the two-phase vein. Olivine melts produced in the olivine porphyritic crystals were closed systems and had quite confined volumes whose liquids fractionally crystallized without additional melt contributions until completion of the fractional crystallization process. In contrast, melting in the large olivine grain was not produced from the parental olivines alone but probably from remelted some wadsleyite and ringwoodite that just emerged from the fractional crystallization in a repeated process.

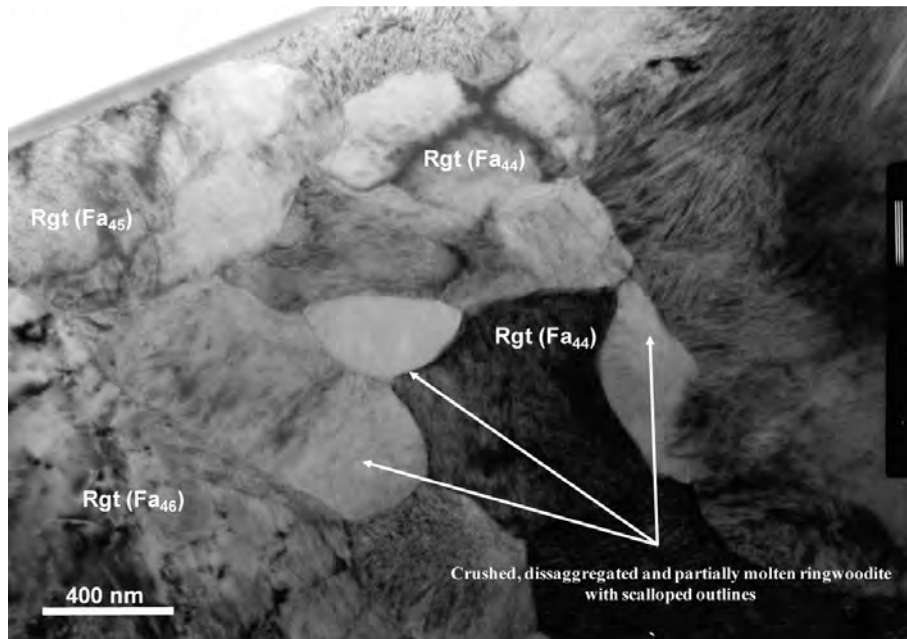


Fig. 3.8-9: A BF TEM photograph of an aggregate of liquidus ringwoodite grains from a ringwoodite-wadsleyite vein in the large olivine grain in Peace River L-6 chondrite. The individual grains in the assemblage depict scalloped outlines evidencing partial remelting after reassembly from a disaggregated ringwoodite pegs in the veins.

Hence, the olivine melts here were not closed systems and did not have limited volumes, because continuous friction along the fractures produced new melts from parental olivine (Fa<sub>24-26</sub>) compositions in addition to some melts of the already crystallized wadsleyite and ringwoodite so that the liquid along the fracture did not have a confined volume but was continuously fed with new melts different in composition from the Fe-rich residual melt. Consequently, the liquid along the fractures did not get enriched in Fe with the same magnitude as in the chondrule because it was continuously fed with fresh melts with olivine stoichiometry but with contrasting compositions. We observed that some fractionally crystallized ringwoodite and wadsleyite originally crystallized as pegs vertical to the walls of the veins were fragmented and remelted due to the continuous flattening and friction thus repeatedly enhancing the composition of the olivine liquid in Mg. The ringwoodite crystallites in the wadsleyite-ringwoodite vein have a very narrow composition range (Fa<sub>44-46</sub>) and depict scalloped outlines (Fig. 3.8-9) thus evidencing partial melting and equilibration after

accumulation. The results demonstrate the complexity of the mechanisms producing liquidus wadsleyite and ringwoodite both of entirely different compositions from olivine melts in different settings but at the same equilibrium pressure.

**f. Coherent ringwoodite growth in olivine of Yamato 791384 L6 chondrite (M. Miyahara, and E. Ohtani/Sendai; M. Kimura/Mito; A. El Goresy; S. Ozawa, T. Nagase, M. Nishijima, and K. Hiraga/Sendai)**

Transformation mechanisms from olivine to ringwoodite have been studied at high static pressure using fine-grained olivine powder or single olivine crystals as starting materials. These studies proposed that principally, solid-state phase transformation from olivine to ringwoodite can take place in two ways; 1) incoherent grain-boundary nucleation and growth and 2) coherent intracrystalline lamella ( $\{111\}_{\text{Rgt}} // (100)_{\text{Ol}}$ ) growth. Previous reports show that most ringwoodite in shocked chondrites occurs as polycrystalline aggregates. On the other hand, Ohtani *et al.* (2004) and Chen *et al.* (2004) reported the existence of ringwoodite lamellae in original olivine grains adjacent to the shock-melt veins of Yamato 791384 and Sixiangkou L6 chondrites, respectively for the first time. A TEM study of slices extracted by Focused Ion Beam (FIB) indicates that ringwoodite lamellae in parental olivine in the Sixiangkou chondrite indeed consist of polycrystalline ringwoodite, thus suggesting incoherent growth mechanism. Although some static laboratory experiments demonstrated that the coherent intracrystalline lamellae could play an important role as nucleation sites for incoherent ringwoodite, such a mutual correlation was not observed in any naturally shocked sample so far. Accordingly, we conducted a detailed investigation of olivines in and around shock-melt veins of Yamato 791384 with a high-resolution field emission gun (FEG)-SEM and FIB-TEM technique to clarify its transformation mechanisms and their sequence of nucleation.

Olivine grains adjacent to the shock-melt veins of Yamato 791384 revealed diverse olivine to ringwoodite transformation textures. We observed in these olivines three distinct textures arranged in a spatial successive arrangement from the wall of the shock-melt vein: (1) polycrystalline, (2) oriented several sets of lamellae and (3) single oriented set of lamellae (Fig. 3.8-10). The polycrystalline parts are adjacent to the walls of the shock-melt veins, and their widths vary ( $< \sim 30 \mu\text{m}$  to the vein walls). The olivine part bearing oriented sets of lamellae depicts 2 or 3 different orientations of lamellae. Some lamellae appear to occur along or parallel to fractures. Some of them display lens-shaped structures.

We extracted many FIB-TEM slices from (1) the polycrystalline region, (2) the region with several oriented sets of lamellae and (3) the area with single oriented set of lamella (Fig. 3.8-10 b-c). TEM images show that the polycrystalline parts consist of ringwoodite with a grain-size  $< \sim 300 \text{ nm}$ . The several oriented sets of lamellae also consist of polycrystalline ringwoodite crystallites with the crystallites depicting preferred orientations in several

neighboring lamellae. Many sub-grain boundaries exist in the surrounding original olivine. We could not find a specific crystallographic relationship between the original olivine and the oriented sets of ringwoodite lamellae. In most cases, each polycrystalline ringwoodite lamella consists of oriented sets of nm-sized slabs with approximately similar orientation. On the other hand, in some cases, each polycrystalline ringwoodite lamella consists of randomly oriented sub-grains. These textures imply that some thick ringwoodite lamellae are formed only through the incoherent mechanism while those depicting oriented ringwoodite slabs may be related to a coherent or semi-coherent mechanism. In contrast, the single set of oriented lamellae consists of a group of very thin ringwoodite platelets with a width  $< \sim 10$  nm (Fig. 3.8-11). TEM study indicates that the platelets unambiguously depict coherent crystallographic orientation with the parental olivine:  $(100)_{\text{Ol}} // \{111\}_{\text{Rgt}}$ . We unambiguously identified the preferred ringwoodite orientation in slices SP1FIB2, SP1FIB3 and SP2FIB1 (Fig. 3.8-10 b-c). Some ringwoodite platelets are intersected by the oriented sets of lamellae consisting of polycrystalline ringwoodite.

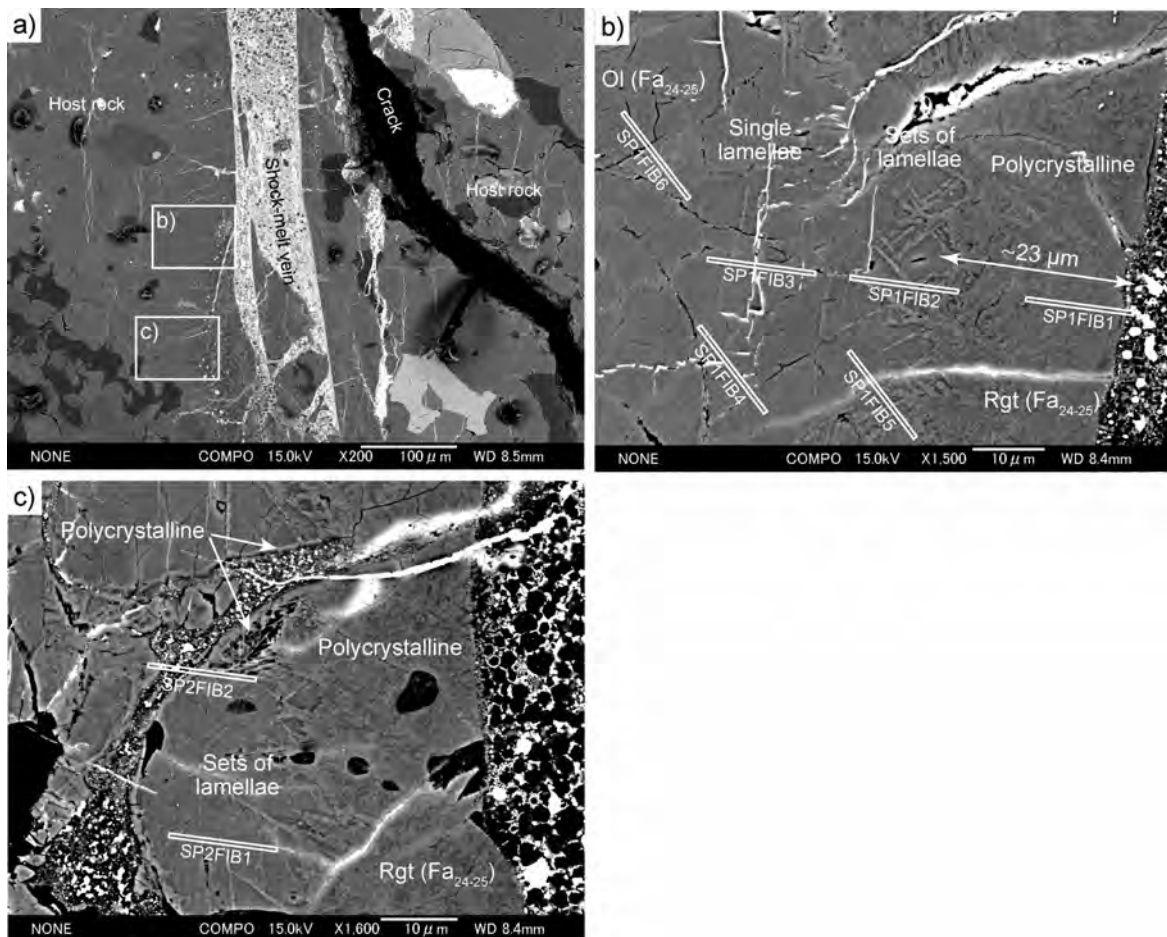


Fig. 3.8-10: Back-scattered electron (BSE) image of a shock-melt vein of Y-791384. a) Low-magnification image. b) Magnified image of a box in a). Original olivine adjacent to the shock-melt vein is replaced with polycrystalline ringwoodite, sets of ringwoodite lamellae and single ringwoodite lamellae. TEM foils extracted by FIB are indicated by white boxes. c) Magnified image of a box in a).

Our FEG-SEM observations reveal that ringwoodite lamellae are ubiquitous in olivine grains adjacent to the shock-melt veins. No significant differences in the chemical compositions between the original olivine (Fa<sub>24</sub>) and ringwoodite (Fa<sub>25</sub>) are detected, indicating that the mechanism encountered is not diffusion controlled as thought before. The crystallographic relationship  $(100)_{Ol} // \{111\}_{Rgt}$  was theoretically predicted by Poirier (1981), and subsequently experimentally produced in static high-pressure experiments in olivine and olivine-analog. Our finding is the first report of the intracrystalline coherent olivine-ringwoodite intergrowth in nature.

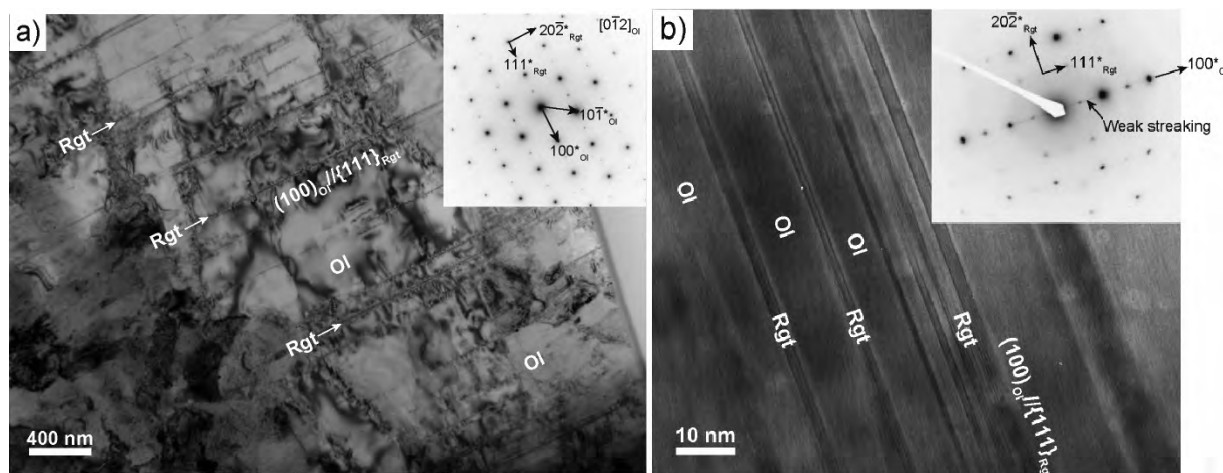


Fig. 3.8-11: Bright-field (BF) TEM images. a) Single thin lamellae consist of ringwoodite platelets with a width of  $< \sim 10$  nm (SP1FIB2). Crystallographic relation  $(100)_{Ol} // \{111\}_{Rgt}$  exist. b) High-resolution (HR) TEM image of ringwoodite platelets (SP2FIB1).

### 3.9 Materials Science

Historically experiments at high pressures and temperatures have been mainly used to model processes in the deep Earth's interior. Subsequently, physicists, chemists and now materials scientists have used the methodology developed by Earth scientists to study different classes of compounds at extreme conditions. BGI, an institution whose goals include developing unique high pressure equipment and methods, is involved in sophisticated and challenging materials research at extreme conditions.

Boron is one of the most enigmatic elements of the periodic system, and even its ground state structure is not fully understood. Recently in BGI a method was developed to synthesise a high-pressure high-temperature phase of boron ( $B_{28}$ ) which combines a number of useful properties – superhard, semiconducting, and optically transparent. Such grown single crystals of the  $B_{28}$  phase enabled a detailed Raman spectroscopy study and assignment of vibration modes, and opens the possibility to investigate the behaviour of boron at high pressures.

Titanium oxides attract attention due to their potential technological importance for hydrogen conversion cells and electrochemical applications. Synthesis of a new dense semiconducting  $Ti_2O_3$  phase with low compressibility and with the  $Th_2S_3$ -type structure has added a new dimension to the crystal chemistry of transition metal sesquioxides.

Rare-earth manganites exhibit a rich variety of physical properties that depend on their composition. Compounds with larger lanthanides crystallize in the orthorhombic structure, while manganites of rare-earth elements with smaller ionic radius have a hexagonal structure. Hexagonal manganites belong to an unusual class of multiferroic materials showing the coexistence of ferroelectric behaviour and magnetic ordering. New experiments on  $YMnO_3$  demonstrate that pressure can induce the transition from the hexagonal to the orthorhombic structure.

In addition to allowing synthesis of new compounds and phase, high pressure also allows a drastic modification of properties of well known materials. An important goal in optical glass technology is to produce material with a high refractive index while maintaining a low dispersion. As demonstrated by experiments on commercially available Schott glasses, high-pressure annealing leads to significant increase of the refractive index, while dispersion remains unchanged. The high pressure treatment therefore allows access to a region of glass properties that have been otherwise hard to achieve.

**a.** *Assignment of Raman active modes of  $B_{28}$  (E.Yu. Zarechnaya, L. Dubrovinsky, and N. Dubrovinskaia/Heidelberg)*

Elemental boron and boron-rich compounds have various allotropes. Recently, a high-pressure high-temperature form of boron was synthesized at 14 GPa and  $\sim 1500$  °C which

crystallizes in a structure with  $Pn\bar{m}$  space group and contains 28 atoms in the unit cell (referred to here as  $B_{28}$ ). The structure consists of  $B_{12}$  icosahedra linked covalently with each other and  $B_2$  dumbbells. Theoretically the phase transition  $B_{28} \rightarrow \alpha\text{-Ga}$  is suggested to occur at about 90 GPa.

Because boron is a weak scatterer, investigation of boron structures and structural relations using X-ray diffraction is problematic. Raman spectroscopy could be one of the most convenient and useful techniques for studying structural changes in boron, provided that its Raman modes are assigned. The comparison of Raman spectra of  $\alpha$ -boron as the most studied polymorph (its structure consists of only  $B_{12}$  icosahedra) with those of  $B_{28}$ , which are very strong and distinct, provides an opportunity to discuss possible atomic vibrations in  $B_{28}$ .

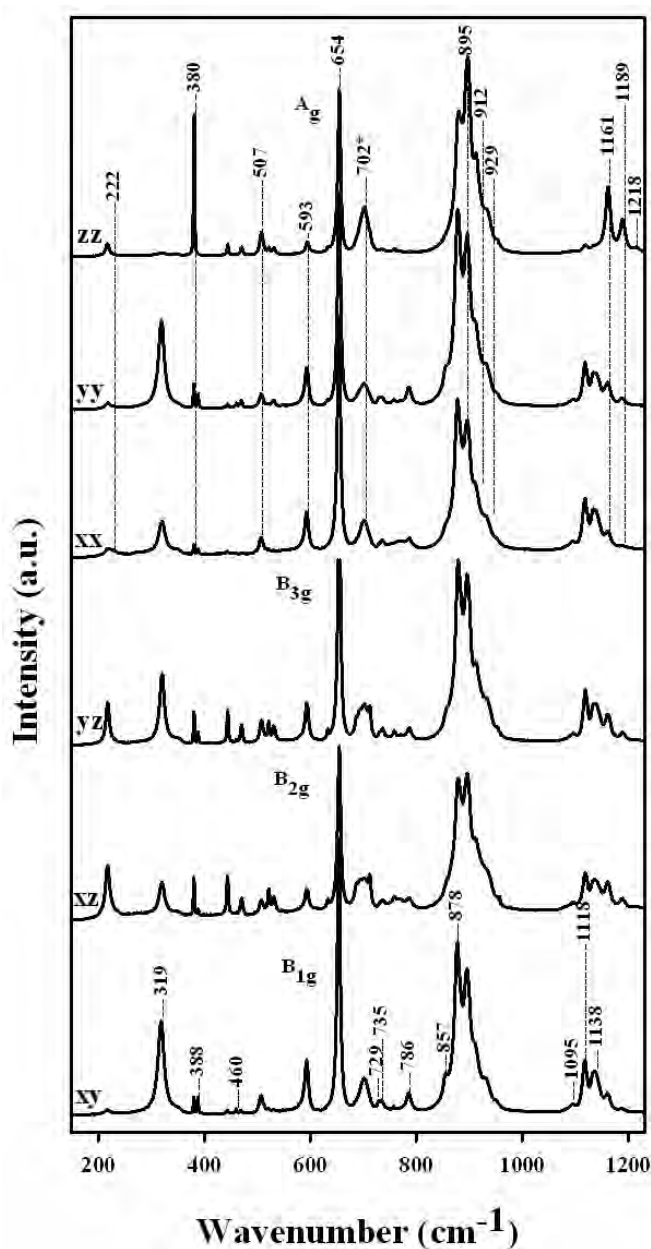


Fig. 3.9-1: Polarised Raman spectra of  $B_{28}$  single crystals obtained at room temperature in several scattering geometries. The polarisation components are expressed according to Porto's notation. The ambiguously assigned modes are labelled with stars.

Using single crystal X-ray diffraction, B<sub>28</sub> crystals (~5 x 5 x 25 μm<sup>3</sup>) were first pre-oriented and then polished. Raman spectra of B<sub>28</sub> were collected in backscattered geometry with polarisers in both cross and parallel polarisation configurations with respect to the incident laser polarisation vector and described according to Porto's notations. A LabRam spectrometer (with a resolution of 2 cm<sup>-1</sup>) and a He-Ne laser (632.8 nm) with a power of 15 mW for excitation and a ×50 objective were used. The positions of Raman peaks were determined by fitting experimental data using PeakFit© v4.12 software.

Figure 3.9-1 shows the measured polarised Raman spectra. For orthorhombic (*Pnmm*) B<sub>28</sub> crystals the A<sub>g</sub> modes are allowed with parallel scattering configurations (xx), (yy) and (zz), while the B<sub>1g</sub>, B<sub>2g</sub>, and B<sub>3g</sub> modes should be clearly visible in the crossed (xy), (xz) and (yz) scattering geometries. In some cases the mode assessment is difficult. There are modes which are visible in all or some geometries. In this case a procedure of peak assessment is carried out by choosing the most intense peak among all scattering configurations. Thus, modes at 593 cm<sup>-1</sup>, 654 cm<sup>-1</sup>, 895, 929 cm<sup>-1</sup>, 1189 cm<sup>-1</sup>, and 1218 cm<sup>-1</sup> were attributed to A<sub>g</sub>. The modes at 878 cm<sup>-1</sup>, 1133 cm<sup>-1</sup> and 1138 cm<sup>-1</sup> were assigned as B<sub>1g</sub> vibrations. In case of weak, poorly resolved and broad peaks (between 686 and 729 cm<sup>-1</sup> in (xz) and (yz) geometries), we cannot unambiguously conclude if modes are B<sub>2g</sub> or B<sub>3g</sub>, or a mixture. We were able to determine 12A<sub>g</sub> and 12B<sub>1g</sub> lines, while unique assignment of B<sub>2g</sub> and B<sub>3g</sub> modes was problematic.

By analogy with α-boron, the mode at 319 cm<sup>-1</sup> could correspond to B<sub>12</sub> icosahedra vibrations. Modes observed between 507 cm<sup>-1</sup> and 1200 cm<sup>-1</sup> can be attributed to icosahedra vibrations (intericosahedral and intraicosahedral). From comparison with highly ordered pnictides (B<sub>12</sub>As<sub>2</sub>, B<sub>12</sub>P<sub>2</sub>) and boron carbide (B<sub>4</sub>C), the A<sub>g</sub> (380 cm<sup>-1</sup>) and B<sub>1g</sub> (388 cm<sup>-1</sup>) modes could be associated with icosahedron-dumbbell and B<sub>2</sub> dumbbells vibrations, respectively.

**b. Synthesis and equation of state of a high density phase Ni<sub>3</sub>S** (*D. Chareev, in collaboration with E. Osadchii, and Yu. Litvin/Chernogolovka; L. Dubrovinsky, A. Kurnosov, E. Zarechnaya, O. Narygina*)

According to the chondritic model, Fe and Ni sulphides are the main possible sulphide components of the Earth's core, the cores of the other terrestrial planets and even the heterogenetic mantle of the Earth. But phase relations of the Fe-Ni-S system at high pressures and temperatures still not fully understood. The main task of the work was to investigate experimentally the phase relations and properties of phases in the Ni-S system at high pressures and temperatures.

As starting materials for synthesis the homogeneous mixtures of Ni and Ni<sub>3</sub>S<sub>2</sub> were used. All of synthesis experiments were carried out in multianvil presses (1000 and 1200 tonnes) at pressures between 15 and 20 GPa and temperatures from 700 to 800 °C. Starting mixtures

were heated at the desired pressure-temperature conditions for 3 to 5 hours and then quenched. The chemical composition of the samples after quenching was investigated using an electron microprobe (JEOL JXA-8900).

We observed formation of a new phase in the system Ni-S with a chemical composition close to Ni<sub>3</sub>S. The measured composition of the sulphide is Ni<sub>2.95</sub>S according to the electron microprobe data. Depending on the starting compositions of the samples, we obtained either pure homogeneous Ni<sub>3</sub>S, or Ni<sub>3</sub>S in equilibrium with metal Ni, or Ni<sub>3</sub>S in equilibrium with Ni<sub>3</sub>S<sub>2</sub> (heazlewoodite) (Fig. 3.9-2). According to X-ray diffraction data from samples quenched from 800°C and 3.5 GPa (piston cylinder press, BGI) and from 8.5 GPa (toroidal device “anvil with mine hole”, IEM RAS, Russia), the stable association is Ni+Ni<sub>3</sub>S<sub>2</sub>. This result suggests that the low stability limit of Ni<sub>3</sub>S is between 9 and 15 GPa.

X-ray powder diffraction of Ni<sub>3</sub>S was collected at the APS synchrotron radiation facility (GSECARS, IDD13 station,  $\lambda = 0.2480 \text{ \AA}$ ). The phase has a Ni<sub>3</sub>P-type structure (like the high-density phase of Fe<sub>3</sub>S), space group  $I\bar{4}$ ,  $Z = 8$ , and the unit cell parameters are  $a = 8.831(5) \text{ \AA}$ ,  $c = 4.455(3) \text{ \AA}$ . The average phase composition based on atomic occupation determined from a refinement of powder X-ray diffraction data is Ni<sub>2.75</sub>S. The atomic coordinates and average occupation are given in Table 3.9-1. Since Ni<sub>3-x</sub>S and Fe<sub>3</sub>S have the same structural type and similar chemical properties, these two compounds might form a continuous solid solution.

Table 3.9-1: Atomic coordinates and site occupation of Ni<sub>3-x</sub>S without thermal factor effects.

Atom	Occupancy	X	Y	Z
Ni1	0.87	0.081	0.109	0.276
Ni2	1	0.129	0.479	0.021
Ni3	0.88	0.335	0.276	0.262
S	1	0.304	0.047	0.008

The equation of state of Ni<sub>3</sub>S has been investigated in a diamond anvil cell experiment at pressures up to 50 GPa (Re gasket, Ne pressure transmitting medium). The pressure was determined using ruby fluorescence. *In situ* diffraction was carried out using a X-ray Rigaku diffractometer with rotating anode (MoK $\alpha$ ) (OSMIC focusing X-ray optics, 2D Bruker detector with 512 x 512 matrix). Because Ni<sub>3</sub>S has low symmetry and its main peaks overlap with reflections of rhenium, processing of the X-ray data was difficult. The Ni<sub>3</sub>S volume change was calculated using the positions of the (222), (312) and (321) peaks. A fit of the Ni<sub>3</sub>S pressure-volume relation with a Birch-Murnaghan equation of state gives a value of the bulk modulus of 143(10) GPa, assuming  $K' = 4$ .

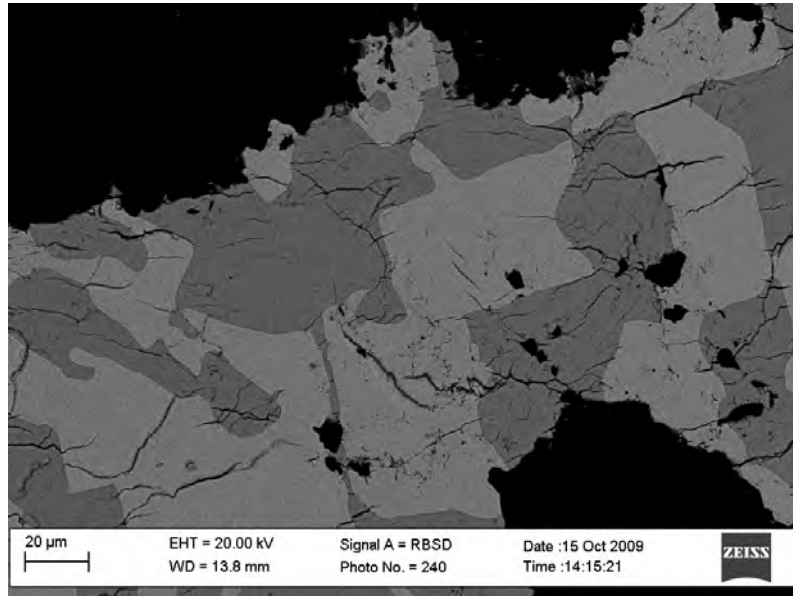


Fig. 3.9-2: Reflected light photomicrograph of an assemblage consisting of  $\text{Ni}_3\text{S}$  (light grey) and  $\text{Ni}_3\text{S}_2$  (dark grey) synthesised at 20 GPa and 620°C.

**c. Pressure-induced phase transitions of iron-phosphor alloys: Ab initio calculations (X. Wu, G. Steinle-Neumann, L. Dubrovinsky, M. Kanzaki/Misasa, S. Qin/Beijing)**

Iron-phosphor alloys are often found in meteorites and terrestrial garnet peridotites, therefore phosphor is proposed to be a potential light element (circa 0.2 % weight) in the Earth's core. In addition, iron-phosphor alloys are also interesting in materials science because a novel high-temperature superconductor has been found in the iron-based pnictide compounds. Here we explored the structural stabilities of  $\text{FeP}_2$ ,  $\text{FeP}$ ,  $\text{Fe}_2\text{P}$  and  $\text{Fe}_3\text{P}$  at high pressure using theoretical calculations based on density functional theory. The full potential linearised augmented plane wave method was used within the local spin density approximation, the generalized gradient approximation and plus Hubbard U, implemented in the WIEN2k code.

Four polymorphs of  $\text{FeP}_2$  were constructed: marcasite-type ( $Pn\bar{m}$ ,  $Z=2$ ) which is the stable phase at ambient conditions,  $\alpha\text{-PbO}_2$ -type ( $Pbcn$ ,  $Z=4$ ), pyrite-type ( $Pa\bar{3}$ ,  $Z=4$ ), and  $\text{CuAl}_2$ -type ( $I4/m\bar{c}m$ ,  $Z=4$ ). Theoretical results indicate that the shortest axis ( $c$ -axis) of the marcasite-type  $\text{FeP}_2$  cell is the most compressible due to softening of edge-shared octahedra along the  $c$ -axis. The marcasite-type phase transforms to the  $\text{CuAl}_2$ -type at 108 GPa rather than to the pyrite-type, accompanying by a semiconductor-to-metal crossover transition.

$\text{FeP}$  with MnP-type structure ( $Pnma$ ,  $Z=4$ ) is isostructural with the post-troilite structure of  $\text{FeS}$ , which has many other polymorphs at high pressure. All polymorphs of  $\text{FeS}$  were computed for the case of  $\text{FeP}$ ; however MnP-type  $\text{FeP}$  still came out to be the stable phase in the pressure range up to 60 GPa.

Fe<sub>2</sub>P and Ni<sub>2</sub>P have the same space group (*P-62m*, *Z*=3), but Co<sub>2</sub>P is an orthorhombic phase (*Pnma*, *Z*=4) at ambient conditions. Compared with the enthalpies of *P-62m* and *Pnma*, the stable phase of Fe<sub>2</sub>P should be the one with *Pnma* space group which has the lowest total energy at low pressure, rather than *P-62m*. This result is consistent with previous experimental results that show that *P-62m* transforms to *Pnma* at 8.0 GPa upon heating and that the *Pnma* phase could be quenched to ambient conditions. A magnetic moment collapse is observed at about 28 GPa in the *P-62m* phase. A further transformation to the *P-3m* phase which has a higher iron coordination number of eight would occur from the *P-62m* and *Pnma* phases of Fe<sub>2</sub>P at 125 GPa and 153 GPa, respectively.

Theoretical results of Fe<sub>3</sub>P demonstrate that there is a new high-pressure phase (*I-42m*) in addition to the earlier described modifications with *I-4* and *Pm3m* space groups. The phase transition from the *I-4* structure to the *I-42m* structure occurs at 75 GPa, which is a second-order transition. The mechanism of the structural change is revealed to be of a displacement type (Fig. 3.9-3). Magnetic collapse in Fe<sub>3</sub>P is observed around 15 GPa, and the magnetic moments of all iron sites become zero when Fe<sub>3</sub>P transforms to the *I-42m* phase.

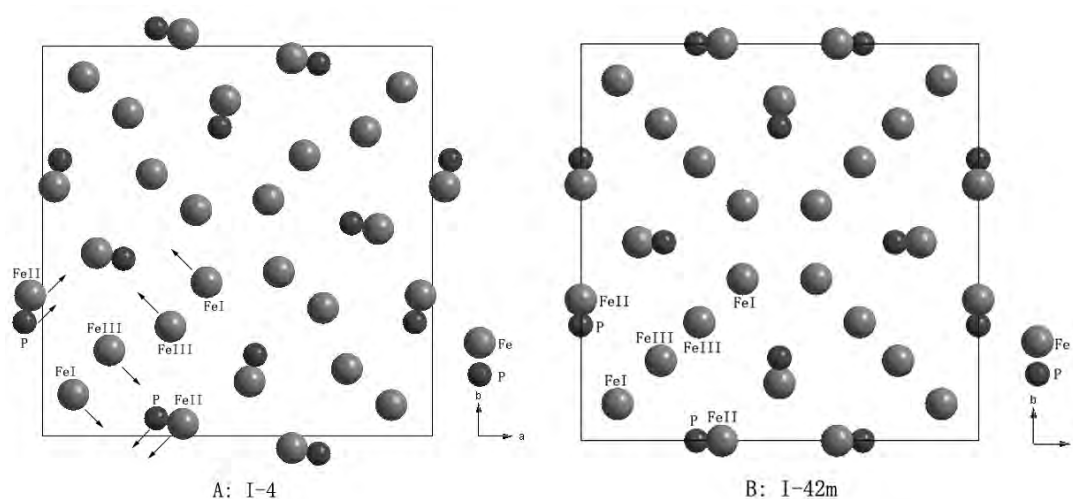


Fig. 3.9-3: Projection along the *c* axis of the *I-4* structure (A) and the *I-42m* structure (B). The atomic shift directions of the *I-4* phase are labelled by arrows.

**d. Compression of *Pnma*-structured Ti<sub>2</sub>O<sub>3</sub> to 67 GPa: X-ray diffraction and Raman studies (S.V. Ovsyannikov, X. Wu, L. Dubrovinsky, and N. Dubrovinskaia/Heidelberg)**

Titanium oxides attract attention owing to their potential technological importance. A 2-3 system (*i.e.*, Ti<sub>2</sub>O<sub>3</sub>) is representative of sesquioxides that are of special importance for geosciences. At ambient conditions sesquioxides normally adopt the corundum-type structure, while high-pressure studies (*e.g.*, in Al<sub>2</sub>O<sub>3</sub>, Fe<sub>3</sub>O<sub>3</sub>, etc.) have revealed transitions to a post-corundum phase (presumably of Rh<sub>2</sub>O<sub>3</sub> (II)-type) and then to a CaIrO<sub>3</sub>-type. A U<sub>2</sub>S<sub>3</sub>-type structure was considered as the potential endpoint of this transition sequence in the accessible pressure range (below 3-4 Mbars). Very recently it was shown that other sesquioxides of both

‘transient’ (*e.g.*,  $\text{Sc}_2\text{O}_3$  and  $\text{Ti}_2\text{O}_3$ ) and heavier cations (*e.g.*,  $\text{In}_2\text{O}_3$ ) deviate from the proposed sequence. Thus, a new phase found in  $\text{Ti}_2\text{O}_3$  has been refined in  $Pnma$  symmetry (standard notation –  $Pnma$ ) and the  $\text{Th}_2\text{S}_3$  structural type; this phase appeared to be quenchable to ambient conditions. Likewise, those in  $\text{Sc}_2\text{O}_3$  and  $\text{In}_2\text{O}_3$  have been refined in the  $\text{Gd}_2\text{S}_3$ -type structure. Further compression of sesquioxides, and in particular the new phases, could lead to a discovery of a new transition sequence.

This study focused on the new orthorhombic form of  $\text{Ti}_2\text{O}_3$  synthesised under high-pressure and high-temperature conditions at BGI with the goal to investigate its stability under pressure through structural and optical studies. We performed: (i) an X-ray diffraction study on a polycrystalline sample at ID09 line at ESRF under pressures up to 57 GPa, and (ii) a Raman spectroscopy study on a single crystal under pressures up to 67 GPa. A diamond anvil cell with a culet of 250  $\mu\text{m}$ , a rhenium gasket and a neon pressure-transmitting medium were employed in both cases. At the maximum pressure during both high pressure runs the samples were heated with a YAG-laser to temperatures of  $\sim 2000$  K for 30 minutes.

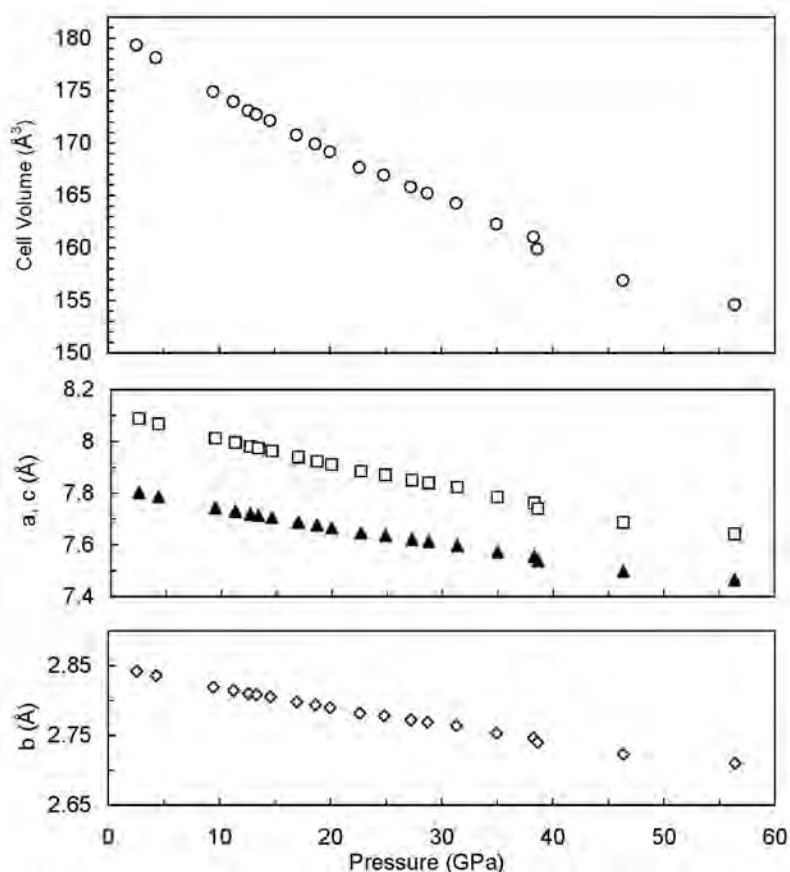


Fig. 3.9-4: Pressure dependence of the unit cell volume and the lattice parameters  $a$ ,  $b$ ,  $c$  of  $Pnma$ - $\text{Ti}_2\text{O}_3$  at ambient temperature.

Some results are shown in Figs. 3.9-4 and 3.9-5. X-ray diffraction (XRD) data show the persistence of the  $\text{Th}_2\text{S}_3$ -type structure in  $\text{Ti}_2\text{O}_3$  up until the highest pressure reached in the

experiment (57 GPa). The only unusual behaviour is a small drop in volume at about 39 GPa (Fig. 3.9-4). The  $Pnma$ - $Ti_2O_3$  phase exhibits numerous sharp Raman peaks ( $\sim 20$ ), which have not yet been assigned. A Raman study of this polymorph could therefore be a sensitive tool for detection of changes in the crystal structure. To the highest pressure reached (67 GPa), no apparent changes in the spectra were detected (Fig. 3.9-5), and prolonged laser annealing up to 2000 K at the maximum pressure did not produce any changes. In summary, our work has demonstrated that the  $Pnma$ - $Ti_2O_3$  phase is stable to 67 GPa and 2000 K.

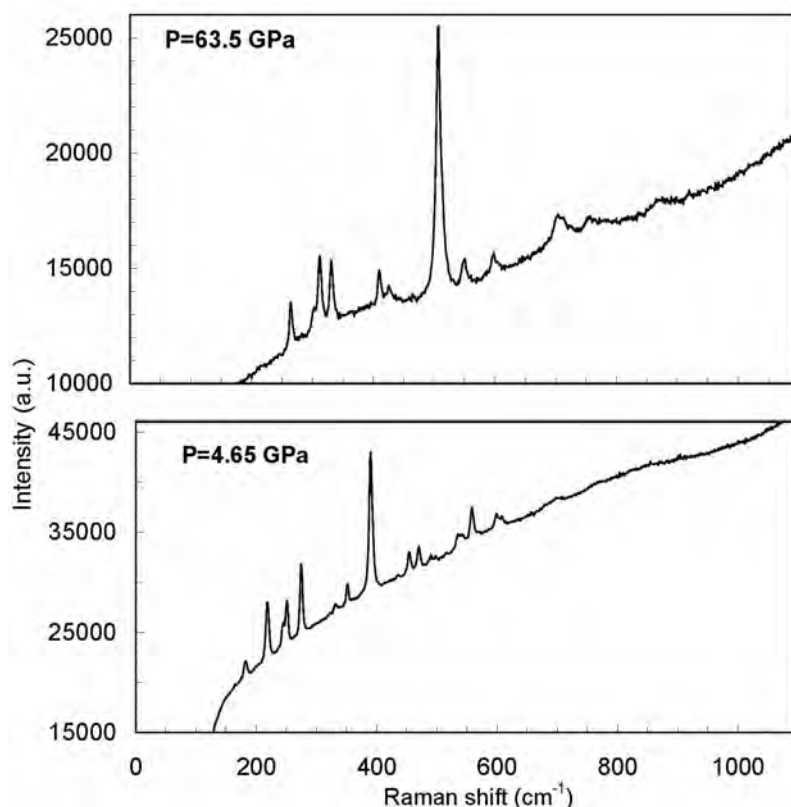


Fig. 3.9-5: Raman spectra of  $Pnma$ -structured  $Ti_2O_3$  at two different pressures.

**e.** *Pressure-induced structural phase transition in  $YMnO_3$  (D.P. Kozlenko, and E.V. Lukin/Dubna; L.S. Dubrovinsky; B.N. Savenko/Dubna, and J.-G.Park/Suwon)*

Manganites,  $RMnO_3$ , exhibit a rich variety of physical properties depending on the rare-earth (R) element. Compounds with larger ionic radius (La, Pr, Nd, Sm, Eu, Gd, and Tb) crystallise in the orthorhombic structure with  $Pnma$  symmetry. In compounds with smaller ionic radius (Y, Ho, Er, Tm, Yb, Lu, Sc and In) a hexagonal structure with  $P6_3cm$  symmetry is stabilised. Hexagonal manganites belong to an unusual class of multiferroic materials showing the coexistence of ferroelectric behaviour and magnetic ordering. The ferroelectric transition temperature is found to be much higher,  $T_C \sim 600$ -900 K, than the antiferromagnetic (AFM) ordering temperature,  $T_N \sim 70$ -130 K.

Recent high pressure structural studies revealed a number of structural and magnetic phase transitions in orthorhombic manganites. In contrast, the high-pressure structural behaviour of hexagonal manganites remains unclear. In order to elucidate this question, an X-ray diffraction (XRD) study of polycrystalline hexagonal YMnO<sub>3</sub> was performed at pressures up to 45 GPa and ambient temperature. Typical measured XRD patterns are shown in Fig. 3.9-6. At pressures up to 33 GPa, they correspond to a hexagonal crystal structure with *P*6<sub>3</sub>*cm* symmetry. At higher pressures, we observed the appearance of a new diffraction peak at  $2\theta \approx 12.8^\circ$  and the simultaneous disappearance of peaks (002) and (102) located at  $2\theta \approx 7.5$  and  $11.2^\circ$ , followed by splitting of the peak located at  $2\theta \approx 15^\circ$  (Fig. 3.9-6). Data analysis has shown that these modifications of the diffraction patterns correspond to a structural phase transition from the hexagonal phase to an orthorhombic phase with *Pnma* symmetry. The estimated lattice parameters at 45 GPa are  $a = 5.13$ ,  $b = 6.80$ , and  $c = 4.72$  Å.

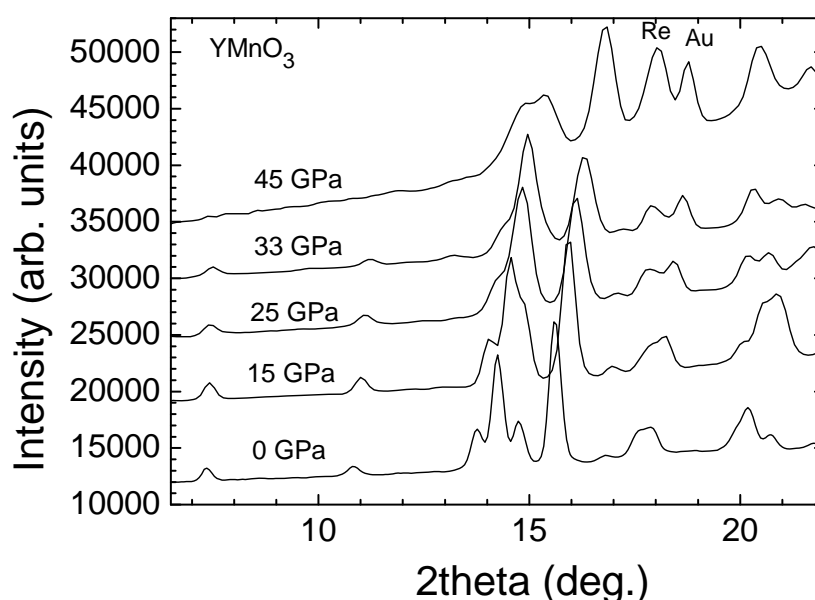


Fig. 3.9-6: X-ray diffraction patterns of YMnO<sub>3</sub> measured experimentally at room temperature and pressures up to 45 GPa.

**f.** *A high-pressure Raman investigation of CaFe<sub>2</sub>O<sub>4</sub> (E. Greenberg, L.S. Dubrovinsky, and C.A. McCammon)*

The ternary oxide CaFe<sub>2</sub>O<sub>4</sub> has gathered much interest in recent years because many spinel compounds have been claimed to transform to a CaFe<sub>2</sub>O<sub>4</sub> (CFO) type structure under high pressure (HP). This includes MgAl<sub>2</sub>O<sub>4</sub> (spinel), Fe<sub>3</sub>O<sub>4</sub> (magnetite), Mn<sub>3</sub>O<sub>4</sub> and FeTi<sub>2</sub>O<sub>4</sub>. Studying the HP behaviour of CaFe<sub>2</sub>O<sub>4</sub> could provide a better understanding of other oxides which adopt the CFO structure at high pressures. Recent reports claim that above 50 GPa CaFe<sub>2</sub>O<sub>4</sub> undergoes a structural phase transition to the same space group (*Pnam*) with a

martensitic transformation every 3<sup>rd</sup> layer, resulting in a unit cell containing three times the number of atoms. The new HP phase exhibits a large volume drop, resulting in an increase of the density by 9.4 %.

Raman spectroscopy was used as a probe for subtle structural changes. A diamond anvil cell was used to induce pressures up to ~ 51 GPa. With increasing pressure the observed modes shifted to higher wavenumbers, as expected. However, at ~ 50 GPa most of the modes were no longer observed (Fig. 3.9-7). Upon decompression, at ~ 46 GPa, all the previously observed modes reappeared, implying a reversible transition.

Current ongoing Mössbauer spectroscopy measurements will help determine if the increase in density at the transition pressure is due to a high-spin to low-spin transition. Other future work on this topic includes synthesising single crystal samples of  $\text{CaFe}_2\text{O}_4$  and performing polarised Raman measurements in an attempt to precisely determine which modes remain above the transition pressure.

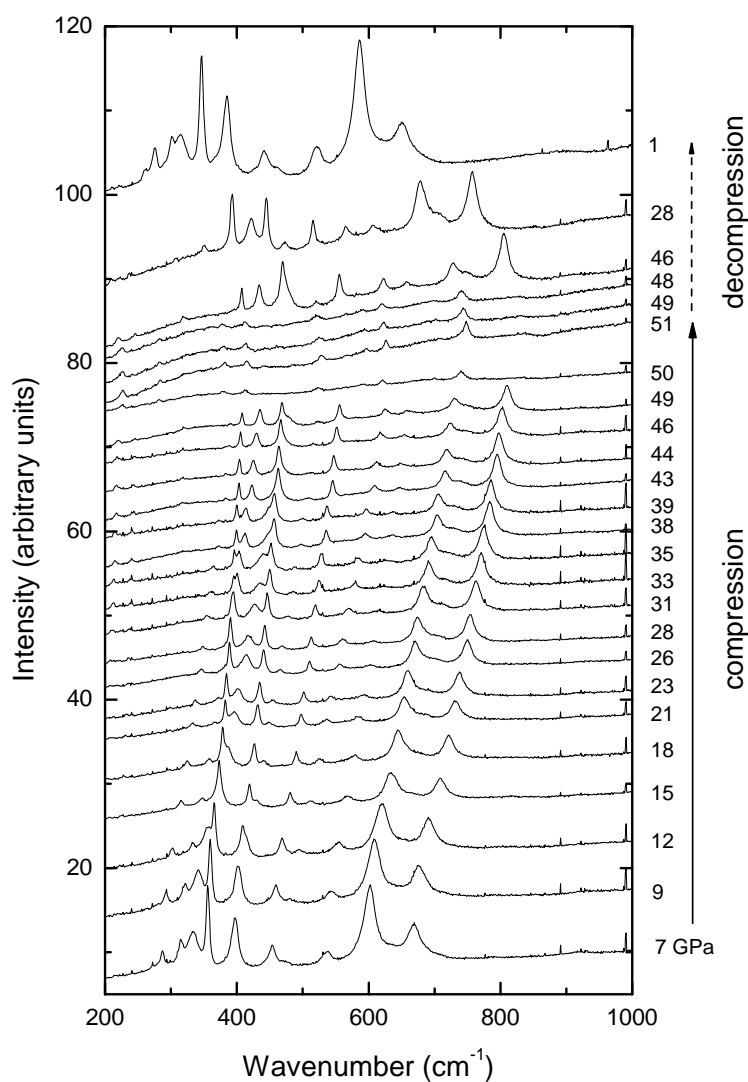


Fig. 3.9-7: Evolution of Raman spectra of  $\text{CaFe}_2\text{O}_4$  as a function of pressure. Numerical values on the right represent the pressure for each spectrum.

**g.** *Optical and volumetric measurements on glass densified by high pressure annealing (D.J. Frost, in collaboration with U. Fotheringham, O. Sohr, P. Fischer, G. Westenberger/Schott AG, Mainz; C. Bienert, and R. Weißmann/Erlangen; K. Richardson/Clemson)*

An important goal in optical glass technology is to produce material with a high refractive index while maintaining a low dispersion, *i.e.*, the variation of refractive index with wavelength. A negative aspect of dispersion, for example, is chromatic aberration in lenses, which prevents all light wavelengths from focusing at the same spot. Dispersion is measured using the Abbe-number ( $V$ ) or similar relation such as,

$$V_s = \frac{n_s - 1}{n_s - n_y}, \quad (3.9-1)$$

where  $n_s$  and  $n_y$  are the refractive indices of the materials at specific wavelengths of interest. Although there is a general relationship between the refractive index of glasses and density, an increase in density is, in most cases, also coupled with an increase in dispersion. In this study we have attempted to densify optical glass samples by annealing them below the glass transition temperature at 5 and 10 GPa. The effects of densification on the refractive index and dispersion have then been determined.

Three samples of commercially available Schott glasses (N-LaK33A, N-LaSF35, LaSF46A) were cored into cylinders of 3.8 mm diameter and 3.8 mm long. These glasses are borosilicates with varying proportions of lanthanum, barium and potassium oxide. Each sample was wrapped in Re foil and placed in a 25 mm MgO octahedron and compressed to either 5 or 10 GPa using WC anvils with 15 mm edge length truncations. At the desired pressure samples were heated at 2°/min using an internal LaCrO<sub>3</sub> cylindrical furnace. After 30 min of annealing at maximum temperatures between 530 and 680 °C the samples were cooled at 2°/min to 200 °C then quenched to room temperature. Properties of the recovered samples were measured at Schott AG, Mainz.

All glasses densified during the high pressure annealing with densification of approximately 5 % during annealing at 5 GPa. Initial glass densities could be recovered, however, by room pressure annealing for 1 hour at the same high pressure annealing temperature. Raman spectroscopy revealed no evidence for crystalline precipitates in the recovered high-pressure samples. Refractive index and dispersion measurements are shown in Fig. 3.9-8 compared to a range of commercial glasses. The recovered samples show an increase in refractive index of approximately 0.05, but no significant change in dispersion. Densification has therefore increased the refractive index significantly, while the influence on the dispersion is significantly lower. The high-pressure treatment therefore allows access to a region of glass properties that have otherwise been hard to achieve.

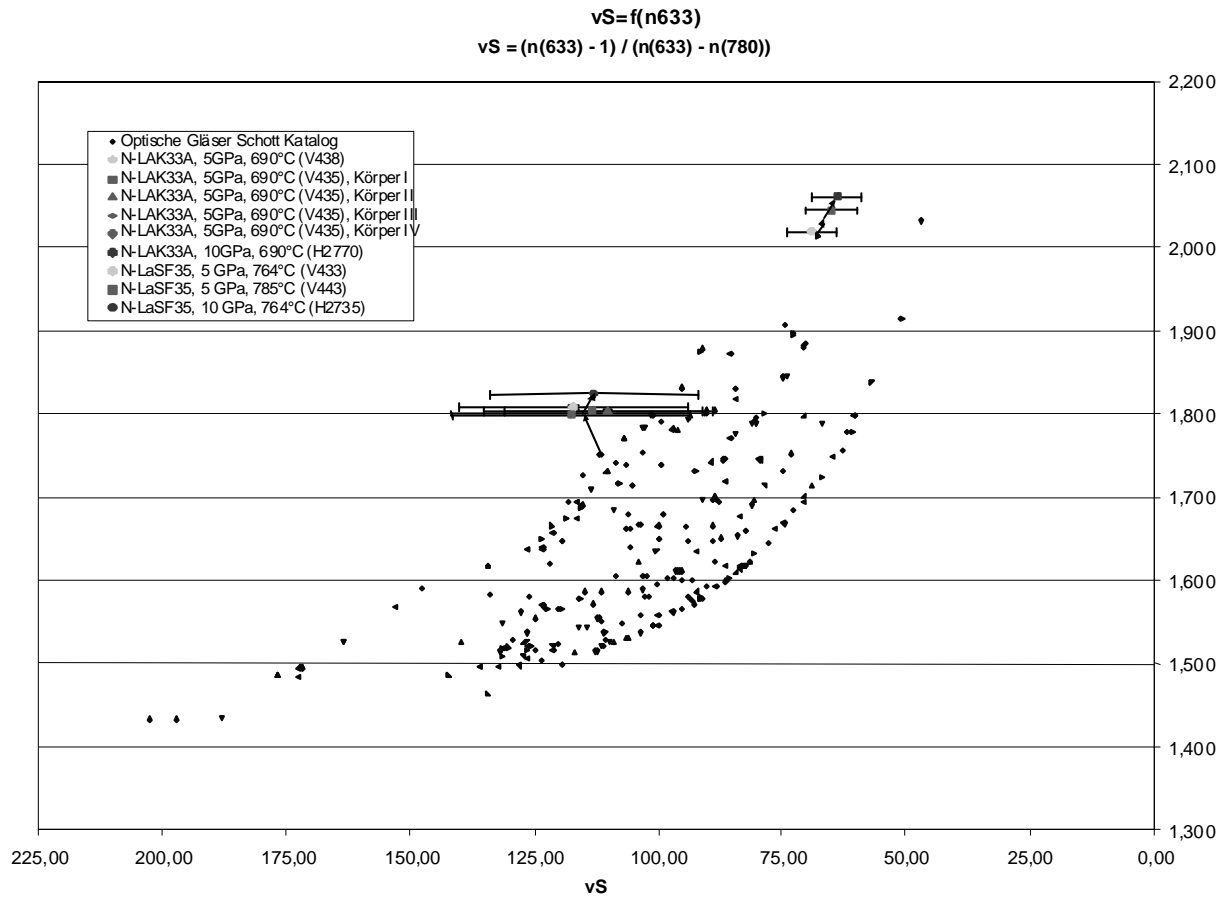


Fig. 3.9-8: The refractive index at 633 nm versus dispersion for a range of optical glasses compared with the samples annealed at high pressure.

### 3.10 Methodological Developments

Geoscience research, particularly at high pressure and high temperature, has changed dramatically over the past decade, where increasingly sophisticated tools are available to investigate the properties of matter under extreme pressures and temperatures. The capabilities of large scale facilities, for example modern synchrotron and neutron sources, have presented enormous opportunities for new types of experimentation at high pressure, and Bayerisches Geoinstitut has been closely involved in a number of these developments. Laser heating has for many years been the premier method for reaching mantle temperatures at high pressure in the diamond anvil cell; however the relative immovability of setups has limited its versatility. Here a newly developed unique portable system is described, and first results of X-ray absorption spectra at mantle pressures and temperatures are presented. Another innovation involving synchrotron measurements is the development of an energy domain version of synchrotron Mössbauer spectroscopy that will provide the energy resolution required to study multiphase mantle assemblages, combined with the high intensity required to collect data at megabar pressures. Developments are also reported in the use of neutrons to study the properties of materials at high pressure, and promising results are reported for measurements in the diamond anvil cell.

Bayerisches Geoinstitut also continues to develop in house facilities. Newly installed equipment includes a multianvil press that incorporates six independently acting hydraulic rams, opening the possibility for innovative deformation experiments as well as the use of diamond sintered anvils to greatly expand the pressure capabilities of the multianvil press. Another new experimental setup involves the combination of Brillouin spectroscopy with a high-brilliance X-ray diffraction system to enable the simultaneous collection of structure and elastic property information, with the goal to establish an absolute pressure scale as well as a more rigorous approach to the interpretation of seismic data.

Further innovations at Bayerisches Geoinstitut affect a new assembly for the D-DIA press that overcomes previous limitations, and enables simple shear experiments to be performed up to deep upper mantle pressures. A new method of sample preparation is described that allows a detailed cross sectional view of reactions at mineral surfaces, and finally a new approach is described for the modelling of sharp boundaries in geodynamic flow fields that overcomes previous limitations.

**a.** *Application of portable laser heating system for in situ diamond anvil cell experiments at synchrotron radiation facilities (L. Dubrovinsky, K. Glazyrin, O. Narygina, and C. McCammon; N. Dubrovinskaia/Heidelberg; A.I. Chumakov, and S. Pascarelli/Grenoble; J. Bock/Gaggenau)*

The diamond anvil cell (DAC) technique coupled with laser heating has become the most successful method to study materials in the multimegabar pressure range at high temperatures. However, so far all DAC laser-heating systems were stationary; they are linked either to

certain equipment or a beam-line. Studies of various physical properties and chemical reactions at high pressures and temperatures in diamond anvil cells require mobility of the laser-heating system, for example, the ability to move laser heating equipment (preferably together with the same DAC, at the same pressure) between different analytical facilities, including transfer from in-house to a synchrotron or between synchrotron beamlines. We have developed a portable laser heating system for DACs with these capabilities.

The clearest test of portability of our system is an experiment performed at the ID18 and ID24 beamlines at the European Synchrotron Radiation Facility (ESRF, Grenoble, France). The entire system was transferred from Germany to France in a car, and then mounted and aligned in a hutch of the beamline over a period of about 2 hours (Fig. 3.10-1).

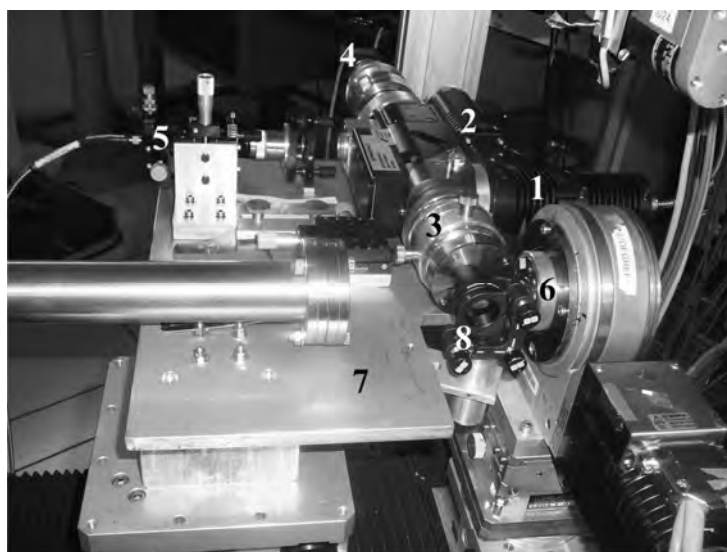


Fig. 3.10-1: The Universal laser-heating head (UniHead) mounted on beamline ID24 at ESRF for XANES spectroscopy measurements. (1 – connector for SPI100 fiber laser, 2 – illumination unit, 3 – lens unit for focusing the incoming laser light, 4 – digital video camera, 5 – module for spectroscopic measurements, 6 – diamond anvil cell mounted inside the holder; 7 – mounting plate; 8 – holder for carbon laser mirror).

Nuclear inelastic scattering (NIS) of geophysically and geochemically important materials - iron-nickel alloy  $\text{Fe}_{0.9}\text{Ni}_{0.1}$ , ferropericlae  $(\text{Mg}_{0.875}\text{Fe}_{0.125})\text{O}$ , and silicate perovskite  $(\text{Mg}_{0.88}\text{Fe}_{0.12})\text{SiO}_3$  - were studied at beamline ID18 at pressures over 100 GPa and temperatures up to 2000 K. Measurements of the energy dependences of NIS spectra of  $\text{Fe}_{0.9}\text{Ni}_{0.1}$  alloy allowed us to extract information on changes of the sound velocities at high pressures and elevated temperatures and indicate that sound velocities of *hcp*- $\text{Fe}_{0.9}\text{Ni}_{0.1}$  at pressures up to 50 GPa and high temperatures do not follow a linear relation with density (Birch's law).

At the energy dispersive X-ray absorption spectroscopy ID24 beam line at ESRF, the portable laser-heating system was used for a Fe *K*-edge X-ray absorption near-edge structure

(XANES) study of  $(\text{Mg}_{0.85}\text{Fe}_{0.15})\text{SiO}_3$  majorite at high pressure and temperature. We found that the strong  $\sim 7$  keV X-ray radiation was sufficient to excite ruby fluorescence and we were able to measure pressure using the spectroscopic module of the UniHead. Temperatures were measured spectroradiometrically during data collection.

The beam was focused horizontally using a curved polychromator Si(111) crystal in Bragg geometry and vertically with a bent Si mirror placed at 2.8 mrad with respect to the direct beam. The Bragg diffraction peaks arising from the diamond anvils were removed from the energy range of interest by changing the orientation of the diamond anvil cell and following in real time the intensity of the transmitted beam on a two-dimensional detector. The measured XANES spectra were analyzed using the VIPER program. The flat part of the pre-edge region of the spectrum was fitted to the Victoreen function ( $F=a+bE^{-3}$ , where  $E$  is the absorption energy, and  $a$  and  $b$  are fit parameters) and this baseline was extended over the entire energy region. The post-edge jump in X-ray absorption was then normalized to one.

In experiments at the ID24 beam line we employed the UniHead in “perpendicular” geometry (Fig. 3.10-1) with a carbon mirror. Glassy carbon used as substrate for silver coating does not introduce any structure in the XANES spectra, but the thickness of the mirror appears to be critical for success of the experiment. With a mirror of 2 mm thickness we were not able to collect any spectra, while with a mirror of 0.9 mm thickness, the quality of the spectra are acceptable (Fig. 3.10-2): we could clearly observe the transition from  $(\text{Mg}_{0.85}\text{Fe}_{0.15})\text{SiO}_3$  majorite to silicate perovskite at 30(2) GPa and 1750(50) K.

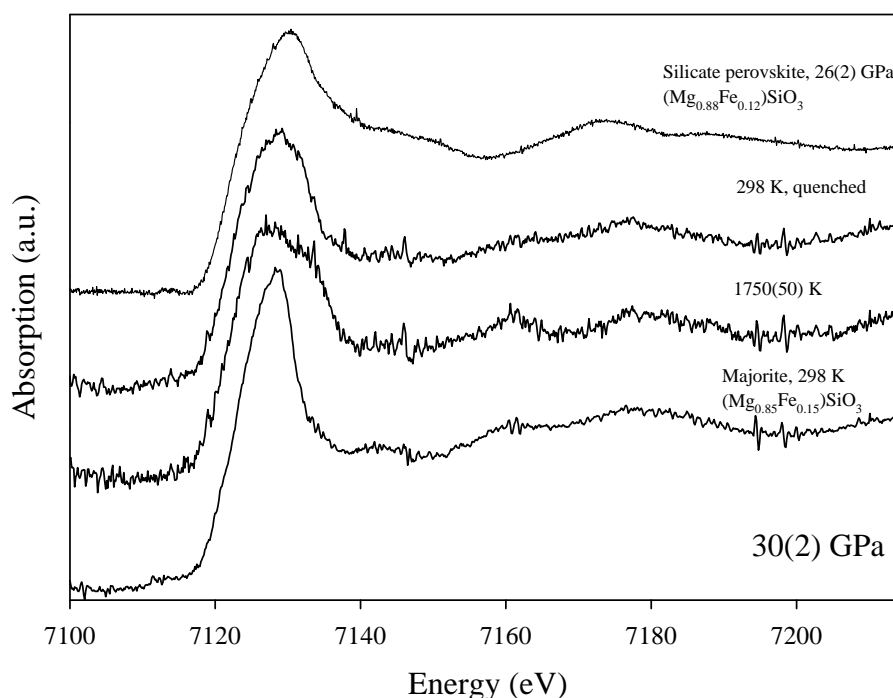


Fig. 3.10-2: XANES spectra (from bottom to top) of  $(\text{Mg}_{0.85}\text{Fe}_{0.15})\text{SiO}_3$  majorite at 30(2) GPa before, during, and after laser heating, and for comparison,  $(\text{Mg}_{0.88}\text{Fe}_{0.12})\text{SiO}_3$  silicate perovskite collected at ambient temperature at 26(2) GPa.

**b. Development of synchrotron Mössbauer source for geophysical studies at the ESRF (V. Potapkin, A.I. Chumakov, and R. Rüffer/Grenoble; G.V. Smirnov, and S.L. Popov/Moscow; L. Dubrovinsky, and C. McCammon)**

Nuclear resonant scattering of synchrotron radiation brought to life a time-differential analogue of conventional energy-resolved Mössbauer spectroscopy. This allowed for significant progress in many fields of research, especially in surface science, materials science, biophysics and geophysics. Progress in geophysics, however, is somewhat moderated by “inconvenient” magnetic and electronic properties of many geophysically-relevant materials for studying in time-domain mode. Indeed, the advantages of time-resolved Mössbauer spectroscopy are most evident for systems with well-resolved hyperfine structures. However, many relevant materials in geophysical studies either do not have large hyperfine interactions, or the splitting collapses at high pressure. In these cases, conventional energy-resolved Mössbauer spectroscopy would be more suitable.

However, energy-resolved Mössbauer spectroscopy utilizes radioactive sources whose brilliance is several orders of magnitude lower than that of synchrotron radiation. Therefore, high-pressure studies with Mössbauer spectroscopy require very long counting times and are limited to moderate pressures. Earth’s lower mantle minerals contain only 5 to 20 wt.% of iron, which makes the measurements even more time consuming. Therefore, there are only a few reported works on *in situ* Mössbauer spectroscopy of samples relevant to the Earth’s mantle, and nearly none of them were conducted under high-pressure and high-temperature conditions simultaneously.

The problem can be solved by combining the outstanding properties of synchrotron radiation with the energy-resolved approach. The possibility to develop a synchrotron source of Mössbauer radiation was demonstrated at the Nuclear Resonance Beamline ID18 at the European Synchrotron Radiation Facility (ESRF) in 1997. The key element of the source is a perfect single crystal of iron borate  $\text{FeBO}_3$  grown out of the resonant isotope  $^{57}\text{Fe}$ . Iron borate is a canted antiferromagnet with Néel temperature 75.35 °C. The period of the magnetic structure is two times larger than that of the crystallographic structure. Therefore, all ( $NNN$ ) reflections with odd  $N$  are forbidden for electronic scattering but allowed for nuclear scattering. These reflections select from a white spectrum of synchrotron radiation only X-ray photons in the energy range around the nuclear resonance.

Such a beam is not yet suitable for Mössbauer spectroscopy, because it consists of four energy components of the magnetically split nuclear levels. In order to achieve a single line source, one needs to heat the crystal close to its Néel temperature, where the collapse of the magnetic structure provides a single line spectrum with an energy width of  $\sim 15$  neV.

Recently, the same approach has been implemented at the SPring-8 synchrotron, where an intensity of the Synchrotron Mössbauer Source (SMS) of  $\sim 20\,000$  photons per second was

reached. In addition, they successfully developed the experimental scheme where the Doppler shift was achieved not by vibrating the sample, but by vibrating the iron borate crystal. This allows for a complex sample environment, which is especially important for geophysical studies under extreme conditions using a diamond anvil cell.

We are constructing a powerful SMS for geophysical applications at the ESRF. The source is planned to have convenient in-line geometry, high intensity, and it should allow for focusing of the X-ray beam to a spot size of a few microns. Furthermore, it should work in any mode of the storage ring operation.

In order to create such a source, we have performed several experimental runs. During these studies, we successfully developed the prototype of the device that has convenient in-line geometry of scattering and produces a single-line source of synchrotron radiation with a narrow linewidth and a high count rate.

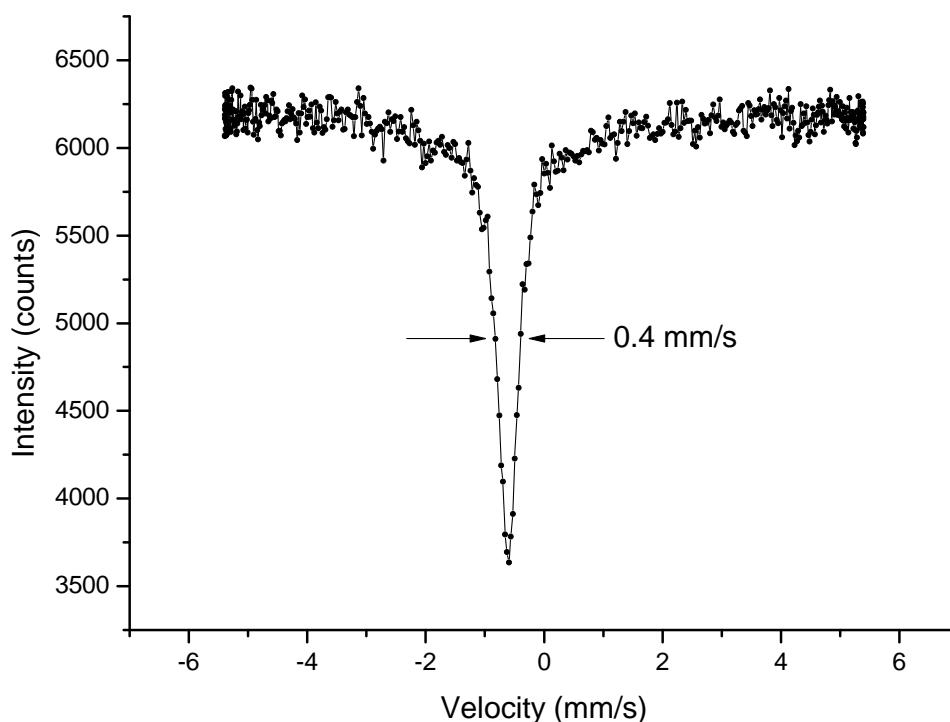


Fig. 3.10-3: Mössbauer spectrum of the standard single-line  $\text{Na}_4\text{Fe}(\text{CN})_6\cdot 10\text{H}_2\text{O}$  absorber collected using the synchrotron Mössbauer source over a period of 10 minutes.

During the most recent experiments we obtained an energy width of the SMS radiation around  $2.3\Gamma_0$ , where  $\Gamma_0$  is the natural linewidth of the  $^{57}\text{Fe}$  nuclear resonance. Figure 3.10-3 shows the Mössbauer spectrum of the standard single line  $\text{Na}_4\text{Fe}(\text{CN})_6\cdot 10\text{H}_2\text{O}$  absorber with a density of the resonant  $^{57}\text{Fe}$  nuclei of  $0.50 \text{ mg/cm}^2$ . The width of the line of the spectrum is a sum of the width of the SMS radiation and of the linewidth of the absorber. The measured linewidth is  $4.3\Gamma_0$ , and the estimated linewidth of the absorber is  $2.0\Gamma_0$ , thus the estimated linewidth of the

source is  $2.3\Gamma_0$ . The intensity of the obtained radiation was around  $2.4 \times 10^4$  photons/s. The achieved parameters were obtained through a compromise between the quality of the linewidth and the count rate. Lowering of temperature in an attempt to increase the count rate increases the linewidth, and increase of temperature leads to a narrowing of linewidth but decreases the count rate. Further improvement of the device performance can be obtained with design of the special high resolution monochromator to have higher throughput and better stability. In addition, improving the temperature control system should allow us to optimize the compromise between the count rate and the value of the linewidth.

In these studies we have obtained a deeper understanding of the physics of the SMS. Firstly, the performance of the SMS strongly depends on the angular position of the iron borate crystal. The rocking curve of the iron borate crystal near the Néel temperature has two peaks and the best position for an optimal single line is located in the minimum between these two peaks. Secondly, the radiation provided by the SMS consists nearly 100 % of resonance radiation. Thirdly, the operation of the device requires a high resolution monochromator, because the intense incident beam causes a temperature gradient on the iron borate crystal.

*c. Neutron diffraction at high pressures using Stress-Spec diffractometer at FRM II (N. Dubrovinskaia/Heidelberg, M. Hofmann/Garching, and L. Dubrovinsky)*

The use of neutrons has several advantages for carrying out high quality powder diffraction measurements. Being nuclear particles, neutrons interact *via* strong interaction with the particles of the nucleus of the atom, an assemblage of protons and neutrons, and scatter predominantly from the nuclei of atoms assuming them to be scatterers of point dimension. Although in general neutron scattering is weak, the values of the neutron scattering length  $b_n$  depend sensitively on the order number  $Z$  and the mass number  $A$  of the scattering atom. Since  $b_n$  varies unsystematically through the periodic table, a large scattering contrast between elements with similar  $Z$  or between different isotopes (same  $Z$ , different  $A$ ) can be readily obtained with neutrons that is not possible with X-rays. Moreover, the interaction of neutrons with atoms is not always limited to the nucleus. In the case of magnetic materials, the magnetic dipole moment of the neutron leads to an additional interaction with any magnetic moment in the shells of the atoms, which is of similar magnitude to the nuclear interaction. For this reason neutrons are the classical probe of magnetic structures.

The nuclear reactor at the Institute Laue Langevin (ILL) in Grenoble, France, produces the world's highest continuous neutron flux for research use. The neutron powder diffraction beam line D20 at ILL for many years has been adapted to high-pressure experiments and allows the use of on-line large volume Paris-Edinburgh (PE) presses. The sample volume, which is on the order of  $10 \text{ mm}^3$ , allows one to obtain high quality neutron diffraction patterns over a reasonable data collection time. This facility can be considered as a "benchmark" for developing further instruments. Figure 3.10-4 (upper curve) shows a neutron powder

diffraction pattern of wüstite  $\text{Fe}_{1-x}\text{O}$  ( $x=0.06$ ) which was collected at D20, ILL, at 7.7 GPa and 130 K in a PE press for 2 hours. Low intensity magnetic peaks are clearly observable. However, application of the PE press is limited by its inability to generate pressures above about 25 GPa. One solution is the use of diamond anvil cells (DACs) which can generate pressures well above 100 GPa.

Neutron diffraction experiments in a diamond anvil cell are challenging, because they involve a dramatic decrease of the sample volume that leads to dramatic deterioration of the data quality. Until recently such experiments were conducted at the powder diffraction instrument G4 at the Leon Brillouin Laboratory (LLB) located around the Orpheus nuclear reactor in the CEA-Saclay Centre (Gif-sur-Yvette), France. On some strongly scattering magnetic materials, measurements at pressures as high as 50 GPa have been performed. However, at comparable experimental pressure-temperature conditions such as those in the ILL experiment on wüstite, but with a considerably reduced (by an order of magnitude) sample volume (about  $1 \text{ mm}^3$ ) in a DAC, we could not obtain any reasonable data, even if the data collection time was increased up to 36 hours (lower curve in Fig. 3.10-4).

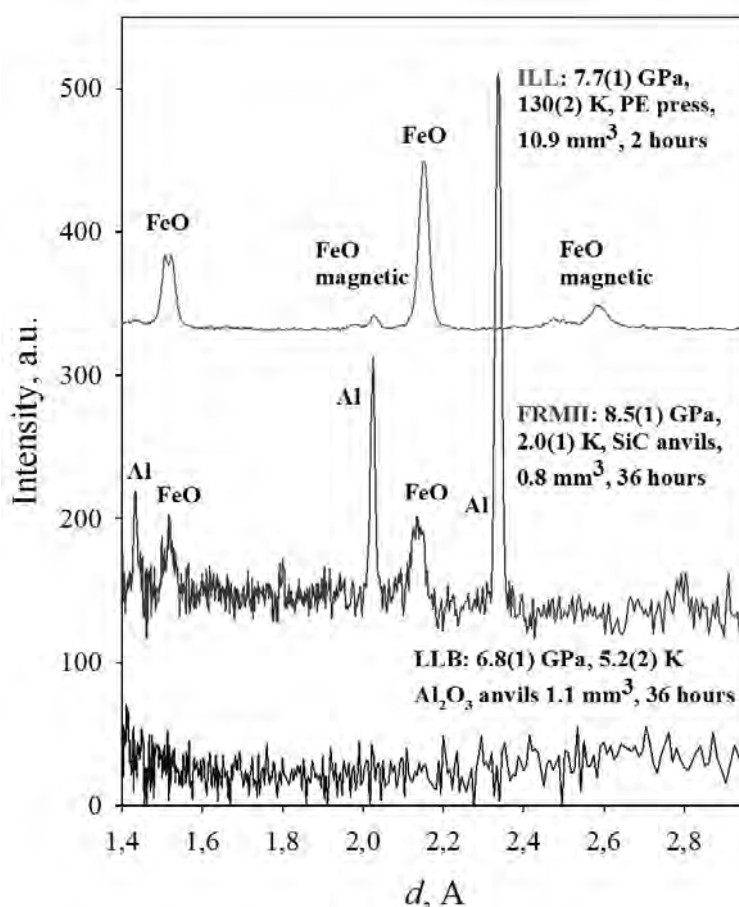


Fig. 3.10-4: Comparison of powder neutron diffraction patterns obtained from wüstite samples at various laboratories.

The Munich research reactor FRM II (Forschungsreaktor München) is now the most powerful neutron source in Germany. Most of the instrumentation at beam tubes or in the neutron guide hall are dedicated to materials science, but so far not at high pressure. Due to the high thermal flux, the Stress-Spec materials diffractometer is dedicated to stress and texture measurements on small probe volumes (smaller than  $1 \text{ mm}^3$ ) inside the sample chamber. To check its capabilities for powder diffraction at high pressures in DACs, we conducted low temperature pilot experiments on  $\text{Fe}_{1-x}\text{O}$  ( $x=0.06$ ) at about the same pressure conditions as those at ILL and LLB. We used a DAC with a wide opening (about 110 degrees in the gasket plane) (Fig. 3.10-5). Figure 3.10-4 (middle curve) shows a diffraction pattern of wüstite that we collected from a sample with a size below  $1 \text{ mm}^3$  for 36 hours. Although detection of magnetic peaks remains ambiguous, the quality of the data is clearly better than that which we obtained at LLB. These first results show the feasibility of DAC neutron diffraction experiments using the German high flux neutron source FRM II.



Fig. 3.10-5: Diamond anvil cell mounted on the top of the cryostat cold finger for a HP experiment at FRM II using Stress-Spec diffractometer.

**d.** *The design and calibration of a multianvil press employing six independently acting 800 tonne hydraulic rams (D.J. Frost, and G. Manthilake, in collaboration with the firm of Vogenreiter GmbH/Mainleus)*

Pressure and displacement calibrations have been performed on the new six-ram multianvil press installed at the institute in October. The concept was to create a device capable of compressing an inner high-pressure chamber with six square faceted anvils that could each be advanced independently. By precisely measuring the position of each anvil the high-pressure chamber can be adjusted under high loads to preserve or deform its cubic geometry. In this way deformation experiments on cubic sample assemblies can be performed in addition to

experiments employing eight sintered diamond inner anvils, which require a high level of symmetry in the distribution of force in order to prevent tensile stresses from damaging the anvils.

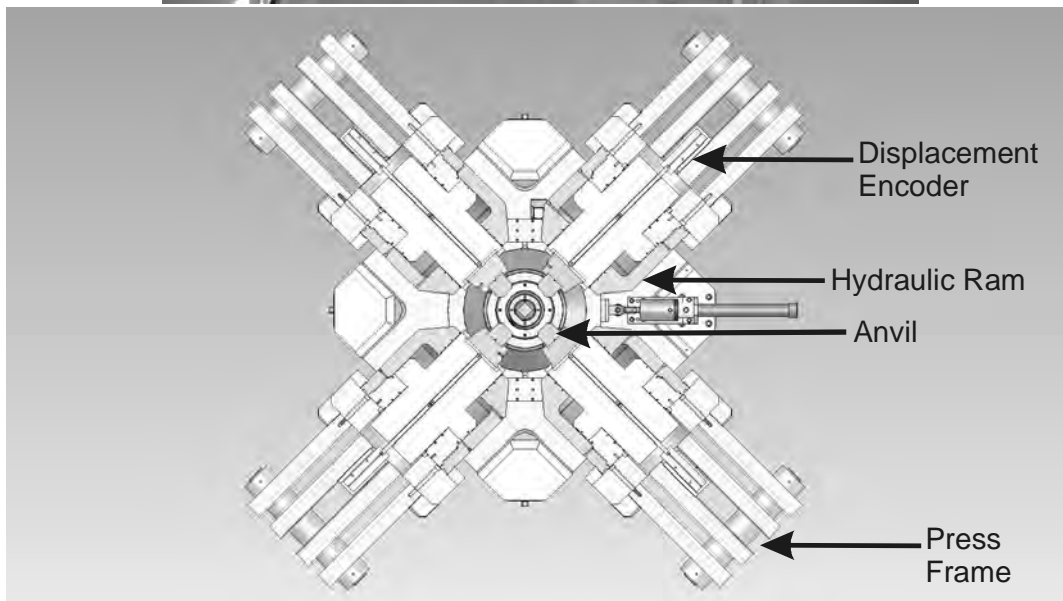


Fig. 3.10-6: The Mavo 6-ram press in the deformation laboratory of the BGI (top). Four of the six hydraulic cylinders can be seen at the centre of the image. A horizontal section through the centre of the press (bottom) shows four of the hydraulic rams with rods passing through them, which connect the displacement encoders with the rear surface of the anvils.

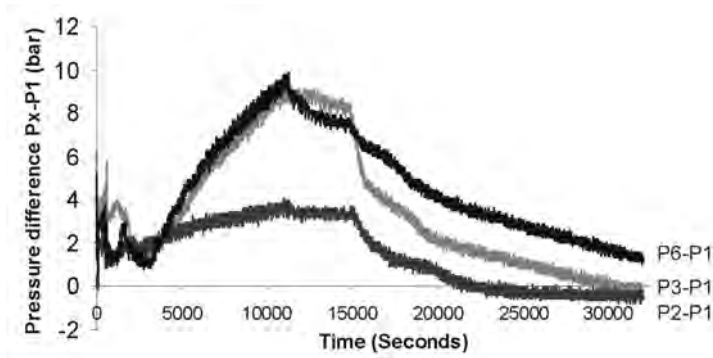
In detail the device comprises six 800 tonne hydraulic rams approaching at right angles inside a composite steel plate frame (Fig. 3.10-6). A servo-controlled spindle-pumping system independently maintains the pressure in each ram. Connected to each ram is an outer square

faceted hardened tool steel anvil with 60 mm edge length, which is currently being used with eight inner tungsten carbide anvils and octahedral pressure media. For deformation experiments on cubic pressure media or use with eight sintered diamond anvils, the six outer tool steel anvils will be replaced with tungsten carbide. The position of each anvil is measured relative to the frame of the press using a Heidenhain linear displacement encoder, positioned on the rear surface of the frame behind each hydraulic ram. The linear encoders are connected to the rear surface of each anvil by a rod, which passes through the centre of each hydraulic ram.

For experiments designed to compress an inner packet of anvils the lower ram follows an oil-pressure ramping profile, while the remaining five rams follow the position of this first ram, determined from the linear displacement encoders. A small correction is applied to the position of the horizontal rams compared to the two vertical rams to account for the fact that the press frame expands slightly more in the horizontal direction as a linear function of the applied load. This expansion has been calibrated up to maximum load. Figure 3.10-7a shows the pressure on three of the hydraulic rams relative to the pressure in the lower ram (P1) in an experiment where an MgO octahedral pressure assembly was compressed to an oil pressure of 200 bars. Differences in pressure relative to P1 in the horizontal rams P3 and P6 are generated in order to maintain the cubic inner geometry. This must be due to the inner octahedral assembly being stiffer in these horizontal directions, which probably results from relatively small deviations in the geometry of the initial MgO octahedra and pyrophyllite gaskets. Figure 3.10-7b shows the position of two horizontal anvils relative to that of the lower anvil (P1). The deviation in this relative position, and therefore in the cubic geometry, is less than 1 micron, and in general close to  $\pm 0.5$  microns, during the entire cycle of the experiment. This can be compared with traditional guide block multianvil systems where differences in thickness between deformed shims on various faces of a steel cube can be  $> 20$  microns at even smaller loads. Heating experiments using  $\text{LaCrO}_3$  furnaces have also been performed and even during rapid quenching the anvil deviations remain of the order of  $\pm 0.5$  microns. The inclusion of a cylindrical furnace introduces further anisotropy in the compression profiles compared to those shown in Fig. 3.10-7a.

Pressure calibrations have been performed in the press using 18 mm and 10 mm edge length octahedra with 11 and 4 mm edge length WC cube truncations. The fixed-point transitions in Bi, ZnTe and ZnS have been measured by monitoring changes in electrical resistance. In order to compare the efficiency of the load in the six-ram press with a conventional single ram 6/8 multianvil guide block system, the force calculated from one of the six rams must be multiplied by  $3\sqrt{3}$  to account for the difference in orientation of the inner anvils compared to the principle load direction. Such a comparison between the two types of multianvil systems is shown in Fig 3.10-8. This shows that the remarkable improvement in the control of the strain is not achieved at the expense of efficiency in sample pressure transmission, which is comparable in both types of systems.

A



B

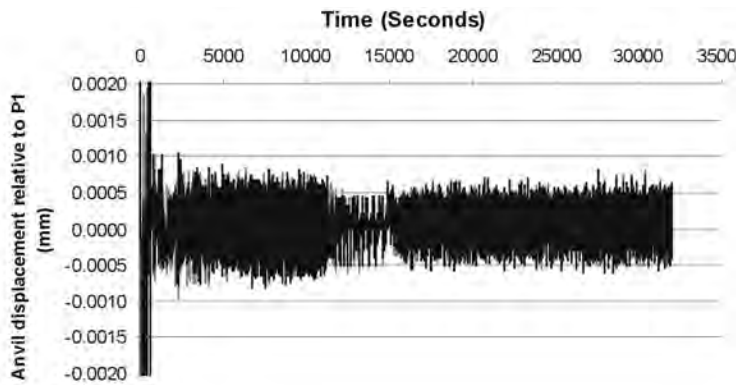


Fig. 3.10-7: (A) The difference in pressure between two horizontal rams (P3 and P6) and the vertical ram (P2) relative to the main lower ram (P1) is shown for an experiment compressed to 200 bars on an 18 mm edge length MgO octahedra. (B) The difference in displacement between two horizontal rams and the main lower ram is shown for the same experiment.

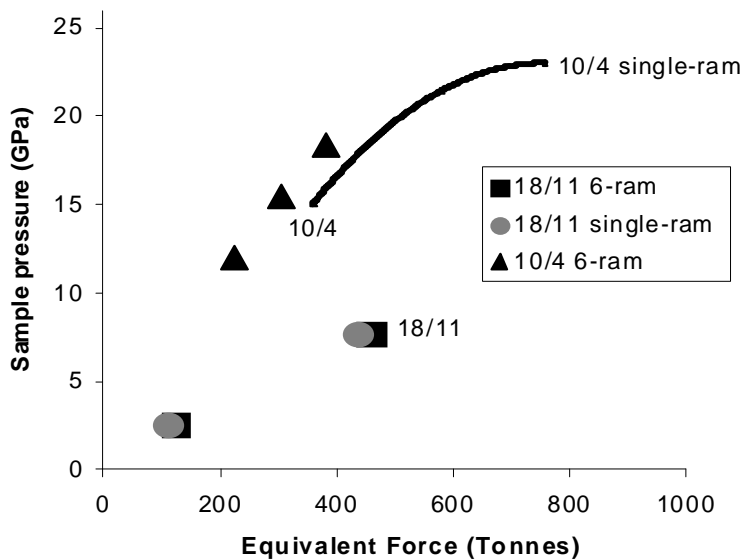


Fig. 3.10-8: Room temperature fixed-point pressure calibrations in the 6-ram press compared to those made in a conventional single-ram 6/8 multianvil. A conversion factor of  $3\sqrt{3}$  is applied to the 6-ram load to allow the different systems to be compared.

e. Single-crystal diffractometer with an ultrahigh intensity rotating anode X-ray source (D. Trots, A. Kurnosov, T. Boffa Ballaran, and D.J. Frost)

The main focus of the Brillouin spectroscopy and single crystal X-ray diffraction laboratory is obtaining the elastic properties of minerals under extreme conditions for the calibration of an

absolute high-temperature-pressure scale and an interpretation of seismic data of the deep Earth. The new diffractometer system is installed in a separate experimental hutch equipped with a door interlock and climate control systems. The X-ray source is an ultrahigh-intensity rotating anode FR-E<sup>+</sup> SuperBright from Rigaku, with MoK $\alpha$  radiation. The rotating anode assembly is mounted on a lifting stage with the X-ray exit window protected by a beam shutter positioned at a height of about 1260 mm from the floor. A VariMax<sup>TM</sup> focusing optics unit is mounted on the front of the exit window. The VariMax<sup>TM</sup> optics unit is realized as a two-dimensional reflection system consisting of an optic housing assembly with two focusing parabolic-curved mirrors in a “side-by-side” Kirkpatrick-Baez scheme. Rough positioning and centring of the optics is achieved by X, Y and Z adjustment stages as well as by pivot screws. In order to optimize the performance parameters including flux, spectrum and divergence, both focusing mirrors can be separately aligned using stepping motors connected to a controller. The beam intensity during the fine adjustment can be monitored either by a CCD camera or a PIN diode. The Eulerian four-circle diffractometer from Huber is equipped with the new SMC9300 programmable motor controller. It can be controlled via either the certified scientific software SPEC or the code SINGLE written by Ross Angel, which allows 8-position centring for accurate measurements of lattice parameters (the precision in lattice parameter values is 1 part in 80000). The chi circle has an inner diameter of 362 mm which allows enough space for the components of a Brillouin spectrometer or a laser heating system to be mounted around a diamond anvil cell. The diffractometer is installed together with the Brillouin spectrometer on a separate optic table top. The X-ray counting system, consisting of a YAP:Ce scintillator coupled to photomultiplier, amplifier and two discriminators, is placed onto the detector arm at a distance of about 600 mm from the centre of the goniometer. The estimated beam size at the sample position is about 200 microns.

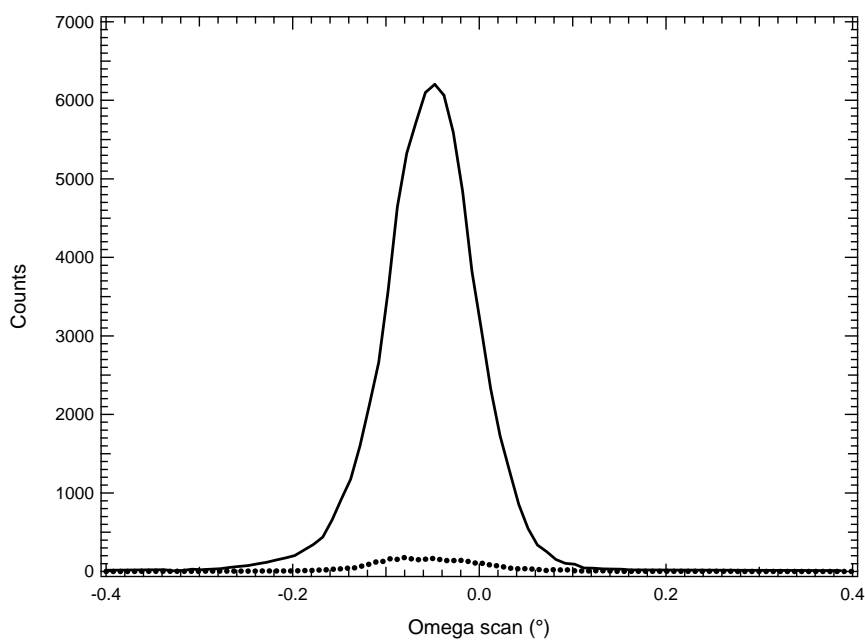


Fig. 3.10-9: Comparison of the (111) diffraction peak of a standard crystal measured on the conventional Huber diffractometer (dotted profile) and on the new Huber diffractometer coupled with a rotating anode system (solid profile).

A test measurement of X-ray diffraction from a reference crystal revealed excellent instrumental resolution. The full width at half maximum of the (111) diffraction peak measured on the new system is exactly the same as that measured for the same crystal on the conventional Huber diffractometer at the BGI; however we obtained 60 times more intensity (Fig. 3.10-9). Such improvement is due to the coupling of the brighter X-ray source with the new optics designed specifically to reduce the large divergence usually associated with a rotating anode system. We therefore expect to be able to collect accurate and precise data for very small single crystals (dimensions less than  $\sim 20$  microns) in a diamond anvil cell at pressures much higher than can usually be reached in a laboratory.

**f.** *On-line Brillouin spectroscopy at BGI: Development of in-house research facility for simultaneous measurement of acoustic velocities and densities at high pressures (A. Kurnosov, A. Trzaskowska/Poznań, D. Trots, D.J. Frost, and T. Boffa Ballaran)*

Recent development of ultra high-pressure diamond anvil cells and the use of highly hydrostatic pressure media allow measurements of lattice parameters using X-ray diffraction and acoustic velocities using Brillouin spectroscopy at megabar pressures. A prevailing problem with separate measurements using these techniques is the uncertainty in pressure. The uncertainty arises from the different pressure scales normally employed by X-ray and optical measurements, which introduces considerable uncertainties in the determination of the pressure dependence of physical properties, especially at simultaneously high temperatures.

This problem can be solved by simultaneous measurements of density (using X-ray diffraction) and sound velocities (using Brillouin scattering), which allows the determination of an absolute pressure scale. The equation of state and velocity as a function of pressure can be determined without requiring a secondary pressure standard. Recently, such types of experiments have been available at some synchrotrons, such as APS and SPRING-8. Here we report a new Brillouin spectrometer coupled with an in-house high brilliance X-ray source based on a rotating anode and focusing X-ray optics.

The feature of the Brillouin spectrometer installed together with a single crystal X-ray diffractometer is that the sample position is fixed, so to align the system for Brillouin measurements both the focusing and collecting optics has to be adjustable. At the same time the angular relation in the system should be preserved. Thus, we divided the system into two parts: the horizontal optical part of the Brillouin system assembled on the optical table and vertical collecting and focusing plates.

The components of the Brillouin spectrometer include a laser, a Fabry-Pérot interferometer, alignment fixtures, and part of the signal transmitting optics. We chose a Coherent Verdi V2 laser with 532 nm single wavelength output. The heart of the Brillouin spectrometer is a six-pass Sandercock-type piezoelectrically scanning tandem Fabry-Pérot interferometer. The interferometer is dynamically stabilized in order to maintain parallel alignment of the mirrors and to correct for thermal drift of the spectrum. The stabilization is achieved by using a

reference laser beam which is selected from the main laser beam and directed to the interferometer.

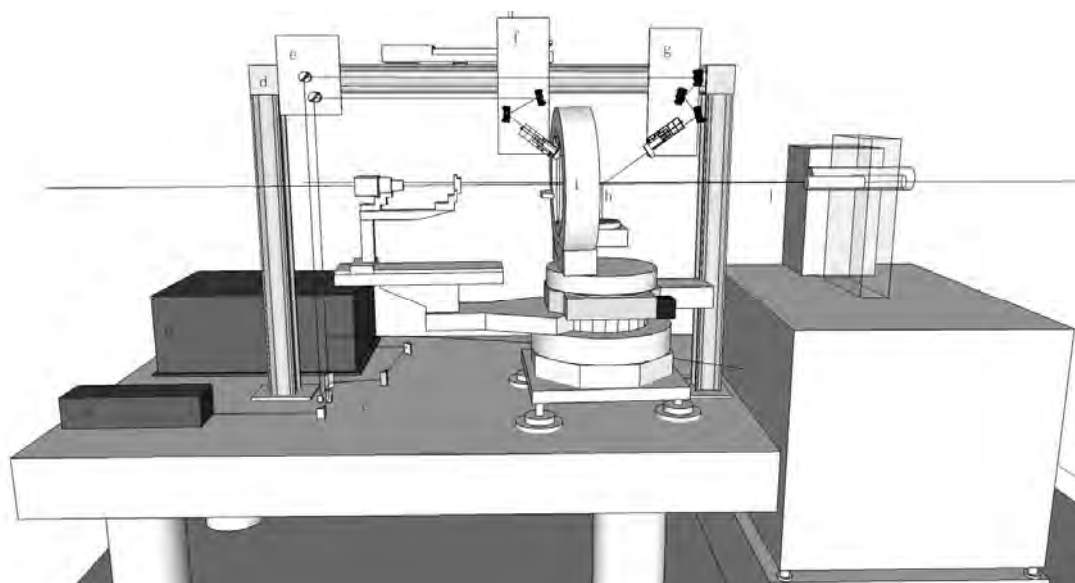


Fig. 3.10-10: Setup of the Brillouin spectrometer. a – laser, b – interferometer, c – horizontal assembly of optical elements (schematic), d - arm for mounting of vertical optical assemblies, e – periscope plate, g – vertical plate with focusing optical assembly, including two adjustable mirrors and focusing lens on motorized stage for focus adjustment, f – vertical plates with collecting optical assembly, including three adjustable mirrors and collecting lens on motorized stage for focus adjustment, h – sample position, i – diffractometer, j – X-ray beam.

The focusing/collecting optical components are mounted on symmetrical vertical metal plates, and the plates are mounted on the stable arm (see Fig. 3.10-10), connected to the optical table. The positions of both plates are adjustable in the plane perpendicular to the X-ray beam, which gives the possibility to focus the laser beam onto a selected point on the sample and to collect a spectrum from the desired point without changing the sample position. The focusing and collecting lenses are adjustable along the focusing and collecting directions in order to provide focusing and to preserve the scattering geometry. The angle between the incident and scattered beam is currently  $100^\circ$ . This angle is limited by the opening angle of the DAC; however our system allows the possibility for the future to vary the geometry to enable the use of different types of cells or samples.

**g.** *Design and calibration of a new D-DIA assembly for conducting deformation experiments in simple shear up to 8 GPa (S. Shekhar, and D.J. Frost)*

The deformation-DIA (D-DIA) is widely used for conducting deformation experiments on materials to study their viscosity and fabric development under high-pressure/-temperature

conditions. Of the six square faceted anvils of the apparatus, two (top and bottom) can be driven independently such that a principal stress can be applied to the cubic pressure media once all anvils have been compressed to high pressure and the sample is heated. An important use of the D-DIA is to study fabric development in minerals such as olivine, pyroxene and garnet deformed in simple shear at upper mantle conditions. For these experiments a sample must be deformed between alumina pistons, cut at 45°, inside a cylindrical furnace, which is in turn placed inside a cubic pressure medium. The materials surrounding the sample and pistons must be mechanically compliant at high temperature, so that the compressive action of the D-DIA is converted into shear of the sample. During room temperature compression, however, compressive forces should not be transferred into shearing of the sample. The new 4/6 mm assembly (4 mm anvil and 6 mm cubic assembly edge lengths) design presented here can be employed with the simple shear configuration up to a confining pressure of 8 GPa and 1673K.

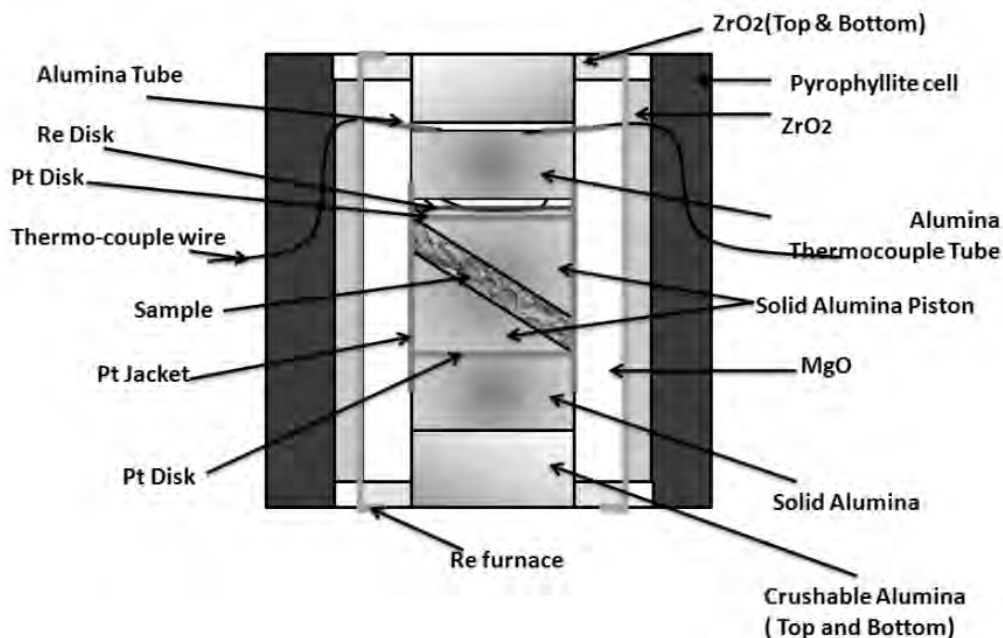


Fig. 3.10-11: The new 4/6 mm simple shear deformation assembly showing its various components. This assembly has been successfully used to conduct deformation experiments on olivine at pressures up to 8 GPa and 1673K.

The new assembly consists of a pyrophyllite cubic pressure cell, fired at 1000 °C for 5 hours. We found the  $\text{LaCrO}_3$  furnaces employed in previous designs to be too susceptible to failure once deformation progresses. This is because deformation of the furnace itself results in the formation of localized hot spots, which cause melting. In the current design (Fig. 3.10-11) a rhenium metal foil furnace is employed, which can be deformed without significantly changing its heating characteristics. Crushable alumina cylinders are placed on either side of the sample, with lengths chosen to minimize the deformation of the sample during cold compression. The lengths of the alumina thermocouple tube and solid alumina tube below the

lower alumina piston are identical (in this case 0.5 mm), and the same is true for the crushable alumina cylinders at the top and bottom (1.7 mm) of the sample column. This ensures a symmetric configuration in the assembly, so that during the deformation process the sample does not translate and thus stays in the hot spot throughout the experiment. We also glue a set of 12 trapezoidal-shaped Teflon gaskets on the edges of the anvils. The thickness and width of each gasket is 1 mm and 1.5 mm, respectively, and the sides are cut at 45° to the base.

Cell pressure calibrations were performed at room temperature using phase transitions in bismuth metal, detected electrically, and Manganin-wire resistivity measurements. At high temperature the coesite-stishovite phase transition has been employed. Bismuth undergoes phase transitions at 2.54 GPa (Bi I-II), 2.7 GPa (Bi II-III) and 7.7 GPa (Bi III-IV), which causes a change in the resistivity; whereas the resistivity of the Manganin wire changes linearly with pressure. The change in Manganin resistivity with confining pressure can be expressed as the pressure coefficient of the resistance change given by  $(\delta R/R_0)(1/P) = (2.322 \pm 0.008) \times 10^{-2} \text{ GPa}^{-1}$ , where  $\delta R$  is the change in resistance and  $R$  is the resistance at any pressure  $P$  measured in GPa. The resistivity must be calibrated with a known pressure, for which we used the Bi I-II transition. As shown in Fig. 3.10-12 the pressure at room temperature determined using Manganin wire reaches a plateau just over 7 GPa, consistent with the observation that we were unable to observe the Bi III-IV transition at 7.7 GPa. This plateau is typical of most multianvil assemblies and results from the gasket supporting an ever-increasing proportion of the load. The assembly is more efficient at temperatures of 1000 °C as shown by the coesite/stishovite transition, which occurs at approximately 110 bars.

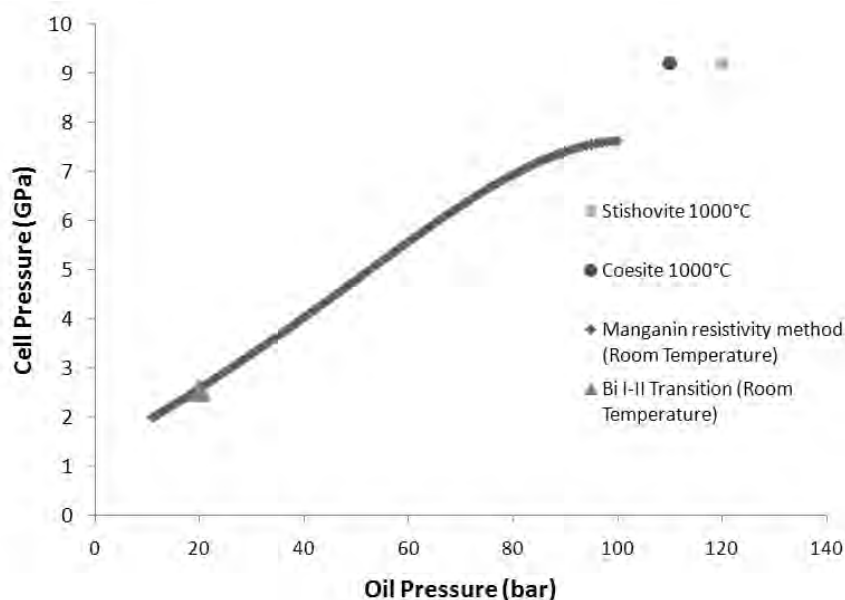


Fig. 3.10-12: D-DIA pressure calibrations for a 6 mm cube employing 4 mm anvil truncations. The oil pressure versus cell pressure relationship is determined from calibrations performed at room temperature and 1000 °C. Manganin resistivity values were related to the cell pressure using the Bi I-II transition point as an internal pressure reference.

**h. FIB-SEM preparation of nm-sized alteration layers and adsorbed nanoparticles on sulfide surfaces for TEM study (D. Harries, K. Pollok, and F. Langenhorst)**

The study of processes at mineral surfaces is generally pursued by a top view onto the specimen surfaces under consideration; however in many cases a more detailed cross sectional view is desired, especially if material accumulations or replacement reactions occur. Focussed ion beam (FIB) preparation renders such views accessible by TEM.

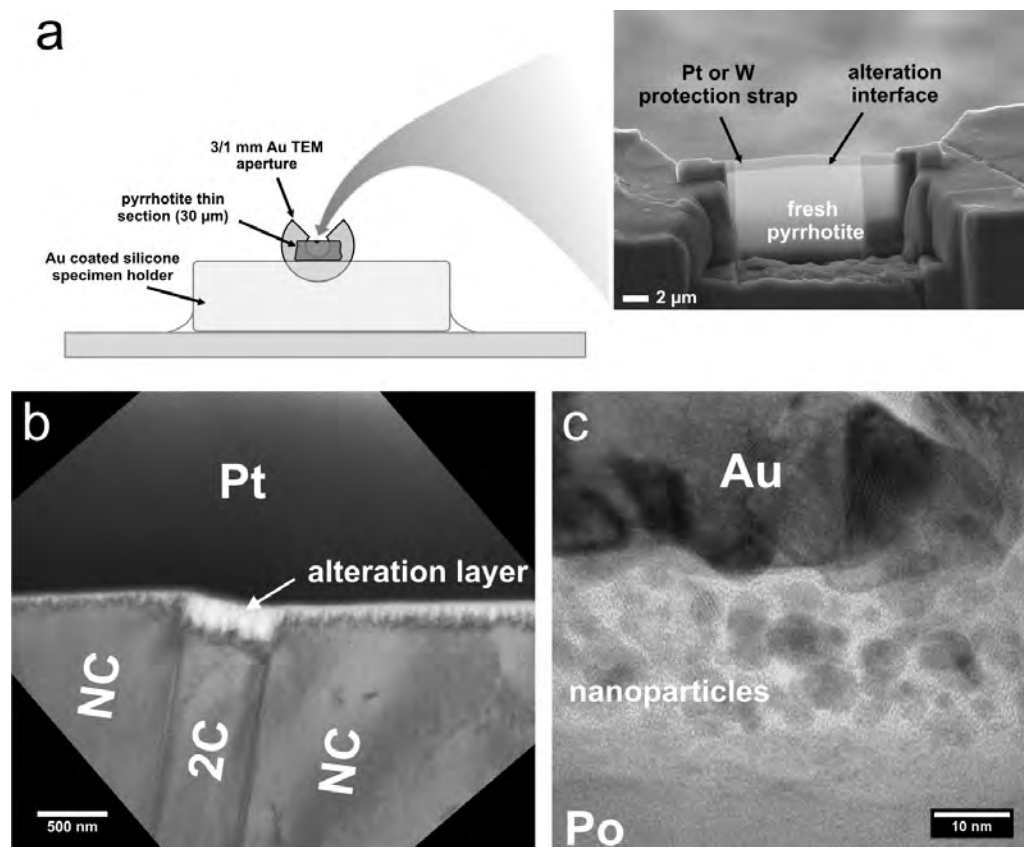


Fig. 3.10-13: (a) Schematic sample assembly and final preparation result. (b) TEM image of alteration layer on NC-type pyrrhotite with a troilite exsolution lamella (2C). (c) HR-TEM image of nanoparticles adsorbed on a pyrrhotite (Po) surface and covered by a protective gold film applied by Ar sputtering. Following FIB cross sectioning the specimen was thinned by Ar milling to allow for HR-TEM.

The assembly is prepared by gluing a 2 mm fragment of a dismantled 30 μm thick sulphide thin section onto a TEM Au aperture (3 mm outer diameter, 0.6 or 1 mm hole), from which a 90-120° sector had been removed. The fresh and exposed cleavage surface of the thin section fragment is oriented towards the open sector of the aperture, and after curing of the epoxy glue the assembly is clamped (cleavage surface facing upwards) into a 10 x 10 mm<sup>2</sup> silicone rubber block mounted on top of a glass slide (Fig. 3.10-13a). For alteration of the pyrrhotite surface, the entire assembly is immersed into the reactive fluid and afterwards transferred into

the FIB-SEM for cross sectioning by means of an H-bar technique. This involves deposition of a Pt or W metal strap ( $2 \times 20 \mu\text{m}^2$ ) onto the middle of the  $30 \mu\text{m}$  wide surface and the subsequent removal of the pyrrhotite to both sides until electron transparency for TEM is attained. Because the deposition of the protective metal strap is the most critical step in terms of potential damage to alteration phases by the focussed  $\text{Ga}^+$  ion beam, we found it useful to deposit a 100-200 nm thick Pt or Au film onto the pyrrhotite surface by conventional and relatively gentle Ar sputtering (as commonly used for electron microscopy) before starting FIB work. For high resolution (HR-)TEM observations, further thinning of the specimen can be done precisely by Ar milling using a Gatan PIPS ion polisher operated at low beam currents and energies (2-3 keV).

Application of this technique to pyrrhotite ( $\text{Fe}_{1-x}\text{S}$ ) surfaces experimentally altered in acidic aqueous solutions shows clear differences in reactivity of different structural variants coexisting on  $\mu\text{m}$  scales (Fig. 3.10-13b), and illustrates how nanoparticles present in the solution attach on the mineral surface and potentially influence the reaction rates (Fig. 3.10-13c).

**i. Fast and accurate modelling of sharp discontinuities in geophysical flows using Lagrangian implicit surfaces (H. Samuel)**

Advection is one of the major processes that commonly acts on various scales in geodynamics. When diffusion is negligible this transport mode, in its simplest form, can be described by the following differential equation:

$$\partial_t C + \mathbf{U} \cdot \nabla C = 0, \quad (3.10-1)$$

where  $t$  is the time,  $C$  is a scalar quantity (*e.g.*, temperature or a chemical component) being advected by a given velocity field  $\mathbf{U}$ . Various geodynamic scenarios involve the presence of sharp discontinuities in  $C$  (core formation processes, mantle convective stirring, multiphase flows in magma chambers, salt diapirism ...). Unfortunately in these cases solving for Eq. 3.10-1 is very challenging, because sharp discontinuities lead to numerical instabilities, which prevent the local use of high order numerical schemes.

Several approaches have been used in computational geodynamics in order to overcome this difficulty, with variable amounts of success. Despite the use of correcting filters or non-oscillatory, shock-preserving schemes, Eulerian (fixed grid) techniques generally suffer from artificial numerical diffusion. Lagrangian approaches (dynamic grids or particles) tend to be more popular in computational geodynamics because they are not prone to excessive numerical diffusion. However these approaches are generally computationally expensive, especially in 3D, and can suffer from spurious statistical noise. As an alternative to these aforementioned approaches, I have applied the recently developed *Particle Level set* method for solving Eq. 3.10-1 in the presence of sharp discontinuities. I have adapted this improved numerical method and tested it for the first time against geodynamic flows.

The basic principle of this hybrid Eulerian-Lagrangian method consists in the use of an *implicit surface*, as part of a smooth *level set* function  $\phi$  of higher dimension, which replaces  $C$  in Eq. 3.10-1. The *level set* function  $\phi$  is conveniently maintained as a signed distance to the interface. This guaranties that  $\phi$  remains smooth and it enables a straightforward reconstruction of the interface  $S$  as it corresponds exactly to the location of the 0 level set function  $S \equiv \phi=0$ . A major advantage of the *level set* method lies in the smoothness of  $\phi$ , for which high order accurate schemes can be efficiently applied. In addition, this formulation allows a straightforward calculation of critical geometric quantities such as the unit normal vector to the interface  $N = \nabla \phi / |\nabla \phi|$  and the curvature  $\kappa = \nabla \cdot N$ , which are required in order to evaluate surface tension acting on the interface  $S$ . Moreover, the method is computationally cheap since Eq. 3.10-1 only needs to be solved in the vicinity of the zero level set function, instead of in the whole domain. An additional advantage of this hybrid method is the use of tracer particles to improve the accuracy of the *level set* solution to Eq. 3.10-1 by limiting errors due, for instance, to numerical diffusion.

A first experiment was performed to test the ability of the *Level Set* method to evaluate surface tension between two fluids. While traditional Lagrangian methods can track the interface with relatively good accuracy, they often fail in defining accurately critical geometric quantities such as the curvature, as illustrated in Fig. 3.10-14. The *Level Set* method is found to be successful in tracking accurately the interface and in evaluating surface tension (Fig. 3.10-14).

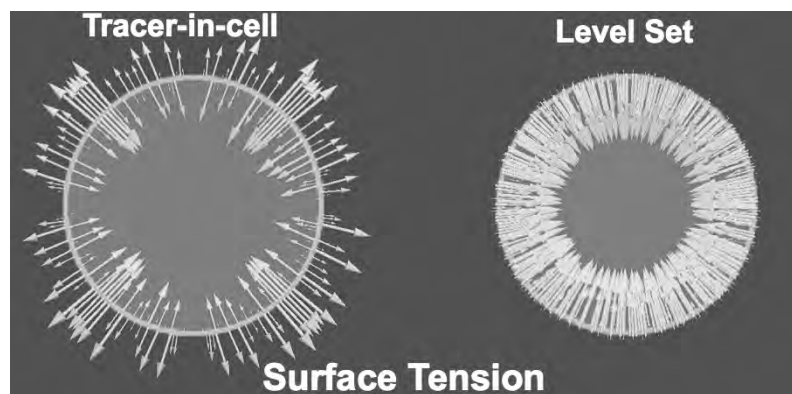


Fig. 3.10-14: Comparison of the *Tracer-in-cell* (left) and the *Level Set* (right) methods, for estimating surface tension acting at the interface between two fluids. The domain is discretized using 200x200 square cells. Although the *Tracer-in-cell* method is able to track the interface accurately, the corresponding surface tension at the interface shows large errors in both magnitude and direction. In contrast, the *Level Set* method allows for both accurate tracking of the interface and estimation of surface tension.

Additional tests of the *Particle Level Set* method against various geodynamic flows including thermo-chemical benchmarks (Figs. 3.10-15 and 3.10-16) were successfully performed. In each case I found that the *Particle Level Set* method accuracy equals or is better than other Eulerian and Lagrangian methods, and leads to significantly smaller computational cost.

Future work will focus on adapting the *Particle Level Set* method to three-dimensional flows where the reduction of computational time in solving Eq. 3.10-1 is most needed.

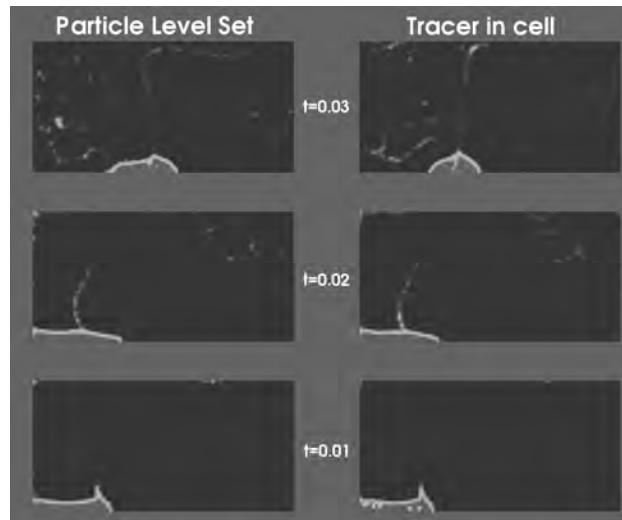


Fig. 3.10-15: Comparison of the *Tracer-in-cell* and the *Particle Level Set methods*, in the frame of a classical thermo-chemical convection benchmark. The bottom surface is hotter than the top surface, leading to convective upwelling and downwelling currents. The light gray material is 150 % denser than its surrounding and tends to be entrained by upwellings. For both cases, the  $2 \times 1$  domain is discretized using  $120 \times 60$  square cells and 25 tracers per cell are used for the *Tracer-in-cell* method. The same amount is used for the *Particle Level Set* method, except that tracer particles are placed only in the vicinity of the interface, therefore reducing significantly the computational expenses. Both methods show very good qualitative agreement, and also agree well with published benchmark values.

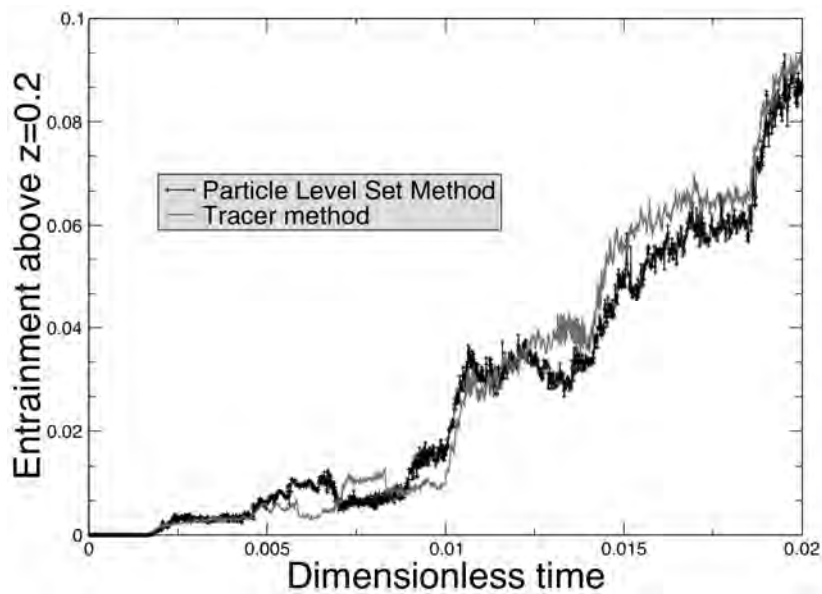


Fig. 3.10-16: Quantitative comparison of entrainments of a dense layer corresponding to the experiment displayed in Fig. 3.10-15. Both methods show very good quantitative agreement, and are also in good agreement with published benchmark values.

#### 4. International Graduate School – Elitenetzwerk Bayern/Elite Network of Bavaria "Structure, Reactivity and Properties of Oxide Materials" (OXIDES)

The interdisciplinary Graduate School is funded by the State of Bavaria and it encompasses three cooperating institutes: Bayerisches Geoinstitut (BGI), Institute of Inorganic Chemistry 1 (LAC), both in Bayreuth, and the Fraunhofer Institute for Silicate Research (ISC) in Würzburg. These institutes provide their experimental and analytical facilities, complementary expertise in basic and applied material research, and commitment to capitalize on synergies as well as international contacts to other leading research institutes all over the world.

The Graduate School is chaired by Prof. Dr. Hans Keppler/BGI (since the retirement of Prof. David Rubie, Ph.D. at the end of 2008) and it includes ten other faculty members and one coordinator. Enrolment in 2009 was ten doctoral students on a full-time basis at all three institutes (BGI, LAC, ISC) and, in addition, sixteen doctoral students have associate status in the school which provides them with full access to all educational activities. Research projects include physical and chemical properties of oxides and mineral assemblages at P-T conditions of the deep Earth, synthesis and investigation of new layer silicates, polymer coatings, transition metal oxides and polyoxometalates as well as the development of new methods in NMR crystallography.

During 2009, seven students have graduated:

<i>Alexander Konschak</i> (Dipl.-Geol. 2003, Freiberg) on 26.02.2009	CO <sub>2</sub> in silicate melts <u>Supervisor:</u> Prof. Hans Keppler
<i>Ram Sai Yelamanchili</i> (M.Sc. in Chemistry 2002, I.I.T. Madras/India) on 30.03.2009	New approaches to the synthesis of porous and/or high surface area transition metal <u>Supervisor:</u> Prof. J. Breu
<i>Alexander Baumgartner</i> (Dipl.-Chem. 2005, Regensburg) on 30.04.2009	Synthesis, characterization and modification of transition metal containing layered silicates <u>Supervisor:</u> Prof. J. Breu
<i>Omar Adjaoud</i> (M.Sc. in Physics 2005, Tizi Ouzou/Algeria) on 10.06.2009	First principles phase diagram calculations in group IV carbides and Mg <sub>2</sub> SiO <sub>4</sub> liquid from molecular dynamics <u>Supervisors:</u> Prof. D. Rubie, Dr. G. Steinle-Neumann
<i>Mohammad Lutful Arefin</i> (M.Sc. in Mat. Science 2005, Ulm) on 21.07.2009	An observation of liquid-phase sintering of ZnO-based Varistor ceramics <u>Supervisors:</u> Dr. F. Raether, Prof. G. Müller
<i>Xian-Liang Huang</i> (M.Sc. Eng. 2006, Beijing/China) on 03.12.2009	Sintering kinetics and properties of highly pure lead zirconate and titanate ceramics <u>Supervisor:</u> Dr. F. Raether

*Micaela Longo*  
(Laurea Sci. Nat. in Mineralogy  
2004, Rome/Italy)  
on 04.12.2009

Iron oxidation state in (MgFe): Calibration of the flank  
method on synthetic samples and application on natural  
inclusions from lower mantle diamonds.  
Supervisors: Dr. C. McCammon, Prof. D. Rubie

*Olga Narygina* has submitted her thesis with the title "Investigation of the properties of iron-bearing alloys and silicates and their implications for the Earth's lower mantle and core" towards the end of 2009 and will graduate early in 2010.

In 2009 seven new students were accepted to the doctoral program:

*Veronika Schmitt*  
(Dipl.-Min. 2008, Würzburg)  
since 11.02.2009

Lead-free piezoceramics  
Supervisors: Dr. F. Raether, Prof. G. Sestl

*Thomas Lunkenbein*  
(Dipl.-Chem. 2009, Bayreuth)  
since 01.06.2009

Synthesis, characterization and applications of  
mesoporous transition metal oxides and  
polyoxometalates using crosslinked wormlike micelles  
Supervisor: Prof. J. Breu

*Julia Wack*  
(Dipl.-Chem. 2009, Bayreuth)  
since 01.06.2009

Development of solid-state NMR pulse sequences for the  
use in NMR crystallography  
Supervisor: Prof. J. Senker

*Nicolas Brockmann*  
(Dipl.-Chem. 2008, Würzburg)  
since 01.06.2009

Development and characterization of catalytic active  
microporous hybrid materials  
Supervisors: Prof. G. Sestl, Dr. K. Rose

*Yuan Li*  
(M.Sc. Exp. Geosc. 2009, Bayreuth)  
since 01.11.2009

Nitrogen solubility in silicate melts, mantle minerals and  
the core  
Supervisor: Prof. H. Keppler

*Clemens Prescher*  
(Dipl.-Geol. 2009, Jena)  
since 11.11.2009

Chemistry of the Earth's lower mantle  
Supervisors: Prof. F. Langenhorst, Prof. L. Dubrovinsky

*Tina Örtel*  
(Dipl. Bau.-Ing. 2009, Weimar)  
will start January 2010

Reactivity of inorganic nanoparticles on ultra-high  
performance concrete  
Supervisors: Dr. C. Gellermann, Prof. G. Sestl

Two new associate students were accepted to the doctoral program in 2009:

*Eran Greenberg*  
(M.Sc. 2009, Tel Aviv)  
since 02.02.2009

Mössbauer spectroscopy and XRD studies of ferrite  
oxides under high pressure  
Supervisor: Prof. L. Dubrovinsky

*Thomas Chust*  
(Dipl.-Geophys. 2009, München)  
since 01.03.2009

Mineral physics, computational thermodynamics and  
mantle convection simulations  
Supervisors: Prof. H.-P. Bunge, Dr. G. Steinle-Neumann

Descriptions of some of the student research projects are listed in Chapter 3 of this yearbook. Students also gave presentations at major international meetings in 2009. The list of presentations and publications may be found in Chapter 5.

As part of program requirements, all students undergo an intensive training program, in addition to their research project, that encompasses lectures, short courses, research colloquium, doctoral seminar, seminars by invited leading experts and weekend seminars on soft skills such as scientific writing, ethics and team work. Invited speakers from overseas and Europe gave 18 lectures during the last year and presented novel experimental techniques and current research results.

The following courses and seminars were offered by ENB in 2009:

- 4<sup>th</sup> Joint Student Meeting on Geo- & Material Sciences, Thurnau; Graduate School Oxides (Univ. Bayreuth, ISC Würzburg) and Master Course Advanced Materials and Processes (MAP), Univ. Erlangen; 31.01.-01.02.2009
- Workshop on multianvil techniques and applications, Bayreuth; 09.-12.03.2009
- Visit to the nuclear research reactor (FRM II) and the Max-Planck-Institut for Plasma Physics with its supercomputing centre in Garching; 08.05.2009
- Geological field trip to the Ries impact crater; 01.-03.06.2009
- Thermodynamics in geochemistry, Bayreuth; 27.-30.07.2009
- Presentation techniques (soft skills seminar), Bayreuth; 22.-23.10.2009



Five students (*A. Baumgartner, X.L. Huang, A. Konschak, S. Kumbar, M. Longo*), the speaker and the coordinator of the graduate school, *Prof. H. Keppler* and *Dr. F. Heidebach*, participated in the Graduation Ceremony of the Elite Network of Bavaria with the State Minister *Dr. W. Heubisch* (3<sup>rd</sup> from right) and *B. Brossardt*, Vice-President of the Bavarian Marketing Board (5<sup>th</sup> from right) in Regensburg on October 30, 2009.

Students of the graduate school participated in several external short courses/seminars during 2009:

- Job hunting in the academic world, DAAD-Seminar, Bonn, 09.02.2009
- Workshop on thermodynamics; Sevilla, 02.-03.03.2009
- Presentation techniques (soft skills - in English), Beilngries, 21.-24.05.2009
- Topbewerbung aus Unternehmersicht (soft skills), Kloster Plankstetten, 11.-12.07.2009
- BWL-Workshop, Fraunhofer ISC Würzburg, 14.07.2009
- Management training (soft skills), Bayreuth, 28.-29.09.2009
- Scientific Writing (soft skills), Herrsching, 21.-22.11.2009
- Konflikte lösen (soft skills), Beilngries, 01.-04.10.2009
- HT-in-situ-XRD Workshop, ICT Pfinztal, 05.-06.11.2009
- Röntgenabsorptionsspektroskopie (XAFS) in der Materialforschung, TU Berlin (Prof. Ressler); 09.-10.12.2009

In fulfillment of the program requirements, one graduate student carried out a research stay at an institute abroad:

<i>Vincenzo Stagno</i>	14.09.-28.12.2009	Geodynamic Research Center, Ehime University, Matsuyama, Japan <i>Stability of diamonds and carbonates – experimental investigations</i>
------------------------	-------------------	--

Students and members of the graduate program received international awards for their research presentation excellence; these awards are listed in Section 7.2.

Detailed information on the Graduate School "Structure, Reactivity and Properties of Oxide Materials" can be found at <http://www.uni-bayreuth.de/elitenetzwerk/oxides>.

## 5. Publications, Conference Presentations, Seminars

### 5.1 Publications (published)

Supplement to **2008** (papers published at the end of 2008):

ZARECHNAYA, E.YU.; DUBROVINSKY, L.; DUBROVINSKAIA, N.; MIYAJIMA, N.; FILINCHUK, Y.; CHERNYSHOV, D.; DMITRIEV, V. (2008): Synthesis of an orthorhombic high pressure boron phase. *Science and Technology of Advanced Materials* 9, 044209, doi: 10.1088/1468-6996/9/4/044209

## 2009

### a) Refereed international journals

ADJAOUD, O.; STEINLE-NEUMANN, G.; BURTON, B.P.; WALLE, A.v.d. (2009): First-principles phase diagram calculations for the HfC-TiC, ZrC-TiC and HfC-ZrC solid solutions. *Physical Review B* 80, 134112, doi: 10.1103/PhysRevB.80.134112

AQUILANTI, G.; PASCARELLI, S.; MATHON, O.; MANOZ, M.; NARYGINA, O.; DUBROVINSKY, L. (2009): Development of micro-XANES mapping in the diamond anvil cell. *Journal of Synchrotron Radiation* 16, 376-379

AREFIN, M.L.; RAETHER, F.; DOLEJŠ, D; KLIMERA, A. (2009): Phase formation during liquid phase sintering of ZnO ceramics. *Ceramics International* 35, 3313-3320

BECERRO, A.I.; MANTOVANI, M.; ESCUDERO, A. (2009): Mineralogical stability of phyllosilicates in hyperalkaline fluids. Influence of layer nature, octahedral occupation and presence of tetrahedral Al. *American Mineralogist* 94, 1187-1197

BECERRO, A.I.; MANTOVANI, M.; ESCUDERO, A. (2009): Hydrothermal synthesis of Kalsilite: A simple and economical method. *Journal of the American Ceramic Society* 92, 2204-2206

BECERRO, A.I.; ESCUDERO, A.; MANTOVANI, M. (2009): The hydrothermal conversion of kaolinite to kalsilite: Influence of time, temperature and pH. *American Mineralogist* 94, 1672-1678

BOFFA BALLARAN, T.; NESTOLA, F.; TRIBAUDINO, M.; OHASHI, H. (2009): Bulk modulus variation along the diopside-kosmochlor solid solution. *European Journal of Mineralogy* 21, 591-597

CHEMIA, Z.; SCHMELING, H.; KOYI, H. (2009): The effect of the salt viscosity on future evolution of the Gorleben salt diapir, Germany. *Tectonophysics* 473, 446-456

COMODI, P.; NAZZARENI, S.; DUBROVINSKY, L.; MERLINI, M. (2009): The high pressure-high temperature behavior of bassanite. *American Mineralogist* 94, 1596-1602

CREIGHTON, S.; STACHEL, T.; MATVEEV, S.; HÖFER, H.; MCCAMMON, C.; LUTH, R.W. (2009): Oxidation of the Kaapvaal lithospheric mantle driven by metasomatism. *Contributions to Mineralogy and Petrology* 157, 491-504

- DE KOKER, N.; STIXRUDE, L. (2009): Self-consistent thermodynamic description of silicate liquids, with application to shock melting of MgO periclase and MgSiO<sub>3</sub> perovskite. *Geophysical Journal International* 178, 162-179
- DE KOKER, N. (2009): Thermal conductivity of MgO periclase from equilibrium first principles molecular dynamics. *Physical Review Letters* 103, 125902
- DEGTYAREVA, V.F.; DUBROVINSKY, L.; KURNOSOV, A. (2009): Structural stability of the sigma phase FeCr under pressure up to 77 GPa. *Journal of Physics: Condensed Matter* 21(7), 075706
- DUBROVINSKY, L.; GLAZYRIN, K.; MCCAMMON, C.; NARYGINA, O.; GREENBERG, E.; ÜBELHACK, S.; CHUMAKOV, A.I.; PASCARELLI, S.; PRAKAPENKA, V.; BOCK, J.; DUBROVINSKAIA, N. (2009): Portable laser-heating system for diamond anvil cells. *Journal of Synchrotron Radiation* 16, 737-741
- ELLIOTT, P.; KOLITSCH, U.; GIESTER, G.; LIBOWITZKY, E.; MCCAMMON, C.; PRING, A.; BIRCH, W.D.; BRUGGER, J. (2009): Description and crystal structure of plimerite, ZnFe<sup>3+</sup><sub>4</sub>(PO<sub>4</sub>)<sub>3</sub>(OH)<sub>5</sub>, the Zn-analogue of rockbridgeite and frondelite, from Broken Hill, New South Wales, Australia. *Mineralogical Magazine* 73, 131-148
- FAJARDO-CAVAZOS, P.; LANGENHORST, F.; MELOSH, H.J.; NICHOLSON, W. (2009): Bacterial spores in granite survive hypervelocity launch by spallation: implications for lithospanspermia. *Astrobiology* 9(7), 647-657
- FROST, D.J.; MCCAMMON, C.A. (2009): The effect of oxygen fugacity on the olivine to wadsleyite transformation: Implications for remote sensing of mantle redox state at the 410 km seismic discontinuity. *American Mineralogist* 94 (7), 872-882
- GATTA, G.D.; ROTIROTI, N.; BOFFA BALLARAN, T.; SANCHEZ VALLE, C.; PAVESE, A. (2009): Elastic behavior and phase-stability of pollucite, a potential host for nuclear waste. *American Mineralogist* 94, 1137-1143
- GOLOSOVA, N.O.; KOZLENKO, D.P.; DUBROVINSKY, L.S.; DROZHZHIN, O.A.; ISTOMIN, S.Ya.; SAVENKO, B.N. (2009): Spin state and magnetic transformations in Sr<sub>0.7</sub>Y<sub>0.3</sub>CoO<sub>2.62</sub> at high pressures. *Physical Review B* 79, 104431
- GUILLAUME, C.; SERGHIOU, G.; THOMSON, A.; MORNIROLI, J.P.; FROST, D.J.; ODLING, N.; MEZOUAR, M. (2009): Tuning between mixing and reactivity in the Ge-Sn system using pressure and temperature. *Journal of the American Chemical Society* 131 (22), 7550
- HANKARD, F.; GATTACCECA, J.; FERMON, C.; PANNETIER-LECOEUR, M.; LANGLAIS, B.; QUESNEL, Y.; ROCHETTE, P.; MCENROE, S.A. (2009): Magnetic field microscopy of rock samples using a Giant Magneto Resistance-based scanning magnetometer, *Geochemistry, Geophysics, Geosystems*, doi: 10.1029/2009GC002750
- HEIDELBACH, F.; TERRY, M.P.; BYSTRICKY, M.; HOLZAPFEL, C.; MCCAMMON, C. (2009): A simultaneous deformation and diffusion experiment: Quantifying the role of deformation in enhancing metamorphic reactions. *Earth and Planetary Science Letters* 278, 386-394
- HOLZAPFEL, C.; CHAKRABORTY, S.; RUBIE, D.C.; FROST, D.J. (2009): Fe-Mg interdiffusion in wadsleyite: The role of pressure, temperature and composition and the magnitude of jump in diffusion rates at the 410 km discontinuity. *Physics of Earth and Planetary Interiors* 172 (1-2), 28-33

- HOPF, J.; LANGENHORST, F.; POLLOK, K.; MERTEN, D.; KOTHE, E. (2009): Influence of microorganisms on biotite dissolution: an experimental approach. *Chemie der Erde – Geochemistry* 69 (S2), 45-56
- HUNT, S.A.; WEIDNER, D.J.; LI, L.; WANG, L.; WALTE, N.P.; BRODHOLD, J.P.; DOBSON, D.P. (2009): Weakening of  $\text{CaIrO}_3$  during the perovskite-post perovskite transformation. *Nature Geoscience* 2, 794-797
- HUSHUR, A.; MANGHNANI, M.H.; SMYTH, J.R.; NESTOLA, F.; FROST, D.J. (2009): Crystal chemistry of hydrous forsterite and its vibrational properties up to 41 GPa. *American Mineralogist* 94 (5-6), 751-760
- IRIFUNE, T.; SHINMEI, T.; MCCAMMON, C.; MIYAJIMA, N.; RUBIE, D.; FROST, D. (2009): Iron partitioning and density changes in pyrolite in Earth's lower mantle. *Science* 327, No. 5962, 193-195, doi: 10.1126/science.1181443
- JACOB, D.; STODOLNA, J.; LEROUX, H.; LANGENHORST, F.; HOUELIER, F. (2009): Pyroxenes microstructure in comet 81P/Wild2 terminal Stardust particles. *Meteoritics & Planetary Science* 44(10), 1475-1488
- KANTOR, I.; DUBROVINSKY, L.; MCCAMMON, C.; STEINLE-NEUMANN, G.; KANTOR, A.; SKORODUMOVA, N.; PASCARELLI, S.; AQUILANTI, G. (2009): Short-range order in  $(\text{Mg,Fe})\text{O}$ : Evidence for Fe clusterization under high pressure. *Physical Review B* 80, 014204, doi: 10.1103/PhysRevB.80.014204
- KATSURA, T.; SHATSKIY, A.; MANTHILAKE, M.A.G.M.; ZHAI, S.M.; FUKUI, H.; YAMAZAKI, D.; MATSUZAKI, T.; YOSHINO, T.; YONEDA, A.; ITO, E.; SUGITA, M.; TOMIOKA, N.; KUWATA, A.; UEDA, A.; TANGE, Y.; NOZAWA, A.; ANDFUNAKOSHI, K. (2009): P-V-T relations of wadsleyite determined by *in situ* X-ray diffraction in a large-volume high-pressure apparatus. *Geophysical Research Letters* 36, L11307
- KATSURA, T.; YOKOSHI, S.; KAWABE, K.; SHATSKIY, A.; MANTHILAKE, M.A.G.M.; ZHAI, S.-M.; FUKUI, H.; HEGODA, A.C.I.H.; YOSHINO, Y.; YAMAZAKI, D.; MATSUZAKI, T.; YONEDA, A.; ITO, E.; SUGITA, M.; TOMIOKA, N.; HAGIYA, K.; NOZAWA, A.; FUNAKOSHI, K. (2009): P-V-T relations of  $\text{MgSiO}_3$  perovskite determined by *in situ* X-ray diffraction using a large-volume high-pressure apparatus. *Geophysical Research Letters* 36, L01305
- KATSURA, T.; SHATSKIY, A.; MANTHILAKE, M.A.G.M.; ZHAI, S.-M.; FUKUI, H.; YAMAZAKI, D.; MATSUZAKI, T.; YONEDA, A.; ITO, E.; KUWATA, A.; UEDA, A.; NOZAWA, A.; FUNAKOSHI, K. (2009): Thermal expansion of forsterite at high pressures determined by *in situ* X-ray diffraction: the adiabatic geotherm in the upper mantle. *Physics of the Earth and Planetary Interiors* 174, 86-92
- KEPLER, H. (2009): Plate tectonics: Why only on Earth? *Europhysics News* 40 (4), 27-30
- KICHANOV, S.E.; KOZLENKO, D.P.; WASICKI, J.; DUBROVINSKY, L.; CZARNECKI, P.; NAWROCIK, W.; SAVENKO, B.N.; POGORELIY, D.K.; PODURETS, K.M. (2009): Structural phase transitions and Raman spectra of pyridinium perrhenate at high pressures. *Journal of Molecular Structure* 921, 68-71

- KIMURA, M.; MIKOUCHI, T.; SUZUKI, A.; MIYAHARA, M.; OHTANI, E.; EL GORESY, A. (2009): Kushiroite,  $\text{CaAlAlSiO}_6$ : A new mineral of the pyroxene group from the ALH 85085 CH chondrite, and its genetic significance in refractory inclusions. *American Mineralogist* 94, 1479-1482
- LEE, K.K.M.; STEINLE-NEUMANN, G.; AKBER-KNUTSON, S. (2009): *Ab initio* predictions of potassium partitioning between Fe and Al-bearing  $\text{MgSiO}_3$  perovskite and post-perovskite. *Physics of the Earth and Planetary Interiors* 174, 247-253, doi: 10.1016/j.pepi.2008.09.003
- LI, Y.; AUDÉTAT, A. (2009): A method to synthesize large fluid inclusions in quartz at controlled times and under unfavorable growth conditions. *American Mineralogist* 94, 367-371
- LI, Y.; AUDÉTAT, A.; LERCHBAUMER, L.; XIONG, X.L. (2009): Rapid Na, Cu exchange between synthetic fluid inclusions and external aqueous solutions: evidence from LA-ICP-MS analysis. *Geofluids* 9, 321-329
- MANN, U.; FROST, D.J.; RUBIE, D.C. (2009): Evidence for high-pressure core-mantle differentiation from the metal-silicate partitioning of lithophile and weakly siderophile elements. *Geochimica et Cosmochimica Acta* 73, 7360-7386, doi: 10.1016/j.gca.2009.08.006
- MANTHILAKE, M.A.G.M.; MATSUZAKI, T.; YOSHINO, T.; YAMASHITA, S.; ITO, E.; KATSURA, T. (2009): Electrical conductivity of wadsleyite as a function of temperature and water content. *Physics of the Earth and Planetary Interiors* 174, 10-18
- MANTOVANI, M.; ESCUDERO, A.; ALBA, M.D.; BECERRO, A.I. (2009): Stability of phyllosilicates in  $\text{Ca(OH)}_2$  solution. Influence of layer nature, octahedral occupation, presence of tetrahedral Al and degree of crystallinity. *Applied Geochemistry* 24, 1251-1260
- MANTOVANI, M.; ESCUDERO, A.; BECERRO, A.I. (2009): Application of  $^{29}\text{Si}$  and  $^{27}\text{Al}$  MAS NMR spectroscopy to the study of the reaction mechanism of kaolinite to illite/muscovite. *Clays and Clay Minerals* 57, 302-310
- MARIANI, E.; MECKLENBURGH, J.; WHEELER, J.; PRIOR, D.J.; HEIDELBACH, F. (2009): Microstructure evolution and recrystallization during creep of MgO single crystals. *Acta Materialia* 57, 1886-1898
- MARQUARDT, H.; SPEZIALE, S.; REICHMANN, H.J.; FROST, D.J.; SCHILLING, F.R.; GARNERO, E.J. (2009): Elastic shear anisotropy of ferropericlasite in Earth's lower mantle. *Science* 324, No. 5924, 224-226
- MCCAMMON, C.A.; MCENROE, S.A.; ROBINSON, P.; FABIAN, K.; BURTON, B.P. (2009): High efficiency of natural lamellar remanent magnetisation in single grains of ilmeno-hematite calculated using Mössbauer spectroscopy. *Earth and Planetary Science Letters* 288, 268-278
- MIYAHARA, M.; EL GORESY, A.; OHTANI, E.; KIMURA, M.; OZAWA, S.; NAGASE, T.; NISHIJIMA, M. (2009): Fractional crystallization of olivine melt inclusion in shock-induced chondritic melt vein. *Physics of the Earth and Planetary Interiors* 177, 116-121

- MIYAJIMA, N.; YAGI, T.; ICHIHARA, M. (2009): Dislocation microstructures of MgSiO<sub>3</sub> perovskite at a high pressure and temperature condition. *Physics of the Earth and Planetary Interiors* 174, 153-158
- MIYAJIMA, N.; WALTE, N. (2009): Burgers vector determination in deformed perovskite and post-perovskite of CaIrO<sub>3</sub> using thickness fringes in weak-beam dark-field images. *Ultramicroscopy* 109, 683-692
- MOOKHERJEE, M.; STEINLE-NEUMANN, G. (2009): Elasticity of phase-X at high pressure. *Geophysical Research Letters* 36, L08307, doi: 10.1029/2009GL037782
- MOOKHERJEE, M.; Stixrude, L. (2009): Proton behaviour, structure and elasticity of serpentine at high-pressure. *Earth and Planetary Science Letters* 279, 11-19
- MOSENFELDER, J.L.; ASIMOW, P.D.; FROST, D.J.; RUBIE, D.C.; AHRENS, T.J. (2009): The MgSiO<sub>3</sub> system at high pressure: Thermodynamic properties of perovskite, postperovskite, and melt from global inversion of shock and static compression data. *Journal of Geophysical Research*, 114, B01203, doi: 10.1029/2008JB005900
- NARYGINA, O.; KANTOR, I.; WU, X.; PASCARELLI, S.; AQUILANTI, G.; MCCAMMON, C.; DUBROVINSKY, L. (2009): XANES study of spin crossover in Fe-bearing silicate perovskite. *Phase transitions* 82(4), 336-343
- NARYGINA, O.; KANTOR, I.; MATTESINI, M.; WU, X.; PASCARELLI, S.; AQUILANTI, G.; MCCAMMON, C.; DUBROVINSKY, L. (2009): High-pressure experimental and computational XANES studies of (Mg,Fe)(Si,Al)O<sub>3</sub> perovskite and (Mg,Fe)O ferropicrinite as in the Earth's lower mantle. *Physical Review B* 79, 174115
- NIGROVSKI, B.; SCHOLZ, P.; KRECH, T.; QUI, N.V.; POLLOK, K.; KELLER, T.; ONDRUSCHKA, B. (2009): The influence of microwave heating on the texture and catalytic properties of oxidized multi-walled carbon nanotubes. *Catalysis Communications* 10, 1473-1477
- OVSYANNIKOV, S.V.; SHCHENNIKOV, V.V.; MANAKOV, A.Y.; LIKHACHEVA, A.Y.; PONOSOV, Y.S.; MOGILENSKIKH, V.E.; VOKHMYANIN, A.P.; ANCHAROV, A.I.; SKIPETROV, E.P. (2009): Unusual B1 – B2 transition in PbSe under high pressure: evidences for two intermediate phases; transport, structural, and optical properties. *Physica Status Solidi B* 246, 615-621
- OVSYANNIKOV, S.V.; SHCHENNIKOV, V.V.; MISIUK, A.; KOMAROVSKY, I.A. (2009): Electronic properties and phase transitions in Si, ZnSe, and GaAs under pressure cycling up to 20-30 GPa in a high-pressure cell. *Physica Status Solidi B* 246, 604-611
- PONOSOV, Y.S.; OVSYANNIKOV, S.V.; STRELTSOV, S.V.; SHCHENNIKOV, V.V.; SYASSEN, K. (2009): A Raman study of high-pressure phases of lead chalcogenides PbX (X = Te, Se, S). *High Pressure Research* 29, 224-229
- PONOMAREVA, A.V.; RUBAN, A.V.; DUBROVINSKAIA, N.; DUBROVINSKY, L.; ABRIKOSOV, I.A. (2009): Influence of global magnetic state on chemical interactions in high-pressure high-temperature synthesis of B2 Fe<sub>2</sub>Si. *Applied Physics Letters* 94, 181912
- ROSE-WESTON, L.; BRENAN, J.M.; FEI, Y.; SECCO, R.A.; FROST, D.J. (2009): Effect of pressure, temperature, and oxygen fugacity on the metal-silicate partitioning of Te, Se, and S: Implications for earth differentiation. *Geochimica et Cosmochimica Acta* 73 (15), 4598-4615

- ROZENBERG, G.; PASTERNAK, M.P.; GORODETSKY, P.; XU, W.M.; DUBROVINSKY, L.S.; LE BIHAN, T.; TAYLOR, R.D. (2009): Pressure-induced structural, electronic, and magnetic phase transitions in FeCl<sub>2</sub> studied by X-ray diffraction and resistivity measurements. *Physical Review B* 79, 214105
- SAIKIA, A.; BOFFA BALLARAN, T.; FROST, D.J. (2009): The effect of Fe and Al substitution on the compressibility of MgSiO<sub>3</sub>-perovskite determined through single-crystal X-ray diffraction. *Physics of Earth and Planetary Interiors* 173 (1-2), 153-161
- SCHIAVI, F.; WALTE, N.; KEPPLER, H. (2009): First *in situ* observation of crystallization processes in a basaltic-andesitic melt with the moissanite cell. *Geology* 37, 963-966
- SCHIAVI, F.; KOBAYASHI, K.; MORIGUTI, T.; NAKAMURA, E.; POMPILIO, M.; TIEPOLO, M.; VANNUCCI, R.: Degassing, crystallization and eruption dynamics at Stromboli: trace element and lithium isotopic evidence from 2003 ashes. *Contributions to Mineralogy and Petrology* (published online), doi: 10.1007/s00410-009-0441-2
- SCHOLLENBRUCH, K.; WOODLAND, A.; FROST, D.; LANGENHORST, F. (2009): Detecting the spinel post-spinel transition in Fe<sub>3</sub>O<sub>4</sub> by *in situ* Electrical Resistivity Measurements. *High-Pressure Research* 29(10), 520-524
- SCHUBERTH, B.S.A.; BUNGE, H.-P.; STEINLE-NEUMANN, G.; MODER, C.; OESER, J. (2009): Thermal versus elastic heterogeneity in high-resolution mantle circulation models with pyrolite composition: High plume excess temperatures in the lowermost mantle. *Geochemistry, Geophysics, Geosystems* (G-cubed) 10, Q01W01, doi: 10.1029/2008GC002235
- SEIFERT, D.; TÖPFER, J.; LANGENHORST, F.; LE BRETON, J.-M., CHIRON, H.; LECHEVALLIER, L. (2009): Synthesis and magnetic properties of La-substituted M-type Sr hexaferrites. *Journal of Magnetism and Magnetic Materials* 321(24), 4045-4051
- SERGHIOU, G.; GUILLAUME, C.L.; THOMSON, A.; MORNIROLI, J.P.; FROST, D.J. (2009): Synthesis of a nitrogen-stabilized hexagonal Re<sub>3</sub>ZnN<sub>x</sub> phase using high pressures and temperatures. *Journal of the American Chemical Society* 131(42), 15170-15175
- SHCHENNIKOV, V.V.; OVSYANNIKOV, S.V.; KARKIN, A.E.; TODO, S.; UWATOKO, Y. (2009): Galvanomagnetic properties of fast neutron bombarded Fe<sub>3</sub>O<sub>4</sub> magnetite: A case against charge ordering mechanism of the Verwey transition. *Solid State Communications* 149, 759-762
- SHCHENNIKOV, V.V.; OVSYANNIKOV, S.V. (2009): Is the Verwey transition in Fe<sub>3</sub>O<sub>4</sub> magnetite driven by a Peierls distortion? *Journal of Physics: Condensed Matter* 21, 271001
- SHCHERBAKOV, V.P.; FABIAN, K.; MCENROE S.A. (2009): A mechanism of exchange bias for nanoparticles embedded in an antiferromagnetic matrix. *Physical Review B* 80, 174419
- SKÁLA, R.; STRNAD, L.; MCCAMMON, C.; CADA, M. (2009): Moldavites from the Cheb Basin, Czech Republic. *Geochimica et Cosmochimica Acta* 73, 1145-1179
- STEBBINS, J.F.; PANERO, W.R.; SMYTH, J.R.; FROST, D.J. (2009): Forsterite, wadsleyite, and ringwoodite (Mg<sub>2</sub>SiO<sub>4</sub>): <sup>29</sup>Si NMR constraints on structural disorder and effects of paramagnetic impurity ions. *American Mineralogist* 94(4), 626-629

- STEBBINS, J.F.; SMYTH, J.R.; PANERO, W.R.; FROST, D.J. (2009): Forsterite, hydrous and anhydrous wadsleyite and ringwoodite ( $\text{Mg}_2\text{SiO}_4$ ):  $^{29}\text{Si}$  NMR results for chemical shift anisotropy, spin-lattice relaxation, and mechanism of hydration. *American Mineralogist* 94(7), 905-915
- STIXRUDE, L.; DE KOKER, N.; SUN, N.; MOOKHERJEE, M.; KARKI, B.B. (2009): Thermodynamics of silicate liquids in the deep Earth. *Earth and Planetary Science Letters* 278, 226-232
- STRELTSOV, S.V.; MANAKOV, A.Y.; VOKHMYANIN, A.P.; OVSYANNIKOV, S.V.; SHCHENNIKOV, V.V. (2009): Crystal lattice and band structure of the intermediate high-pressure phase of PbSe. *Journal of Physics: Condensed Matter* 21, 385501
- SWAMY, V.; KUZNETSOV, A.Y.; DUBROVINSKY, L.S.; KURNOSOV, A.; PRAKAPENKA, V.B. (2009): Unusual compression behavior of anatase  $\text{TiO}_2$  nanocrystals. *Physical Review Letters*, 103(7), 075505
- SZABÓ, Cs.; HIDAS, K.; BALI, E.; ZAJACZ, Z.; KOVÁCS, I.; YANG, K.; GUZMICS, T.; TÖRÖK, K. (2009): Mafic melt peridotite wall rock interaction as shown by silicate melt inclusions in upper mantle xenoliths from the central Pannonian Basin. *The Island Arc* 18, 375-400
- TALBOT, C.; AFTABI, P.; CHEMIA, Z. (2009): Potash in a salt mushroom at Hormoz Island, Hormoz Strait, Iran. *Ore Geology Reviews* 35, 317-332
- TALYZIN, A.V.; SZABO, T.; DEKANY, I.; LANGENHORST, F.; SOKOLOV, P.S.; SOLOZHENKO, V.L. (2009): Nanocarbons by high-temperature decomposition of graphite oxide at various pressures. *Journal of Physical Chemistry C* 113(26), 11279-11284, doi: 10.1021/jp9016272
- TSUNO, K.; OHTANI, E. (2009): Eutectic temperatures and melting relations in the Fe-O-S system at high pressures and temperatures. *Physics and Chemistry of Minerals* 36, 9-17
- UVAROVA, Y.; SOKOLOVA, E.; HAWTHORNE, F.C.; MCCAMMON, C.; KAZANSKY, V.I.; LOBANOV, K.V. (2009): Amphiboles from the Kola Superdeep Borehole:  $\text{Fe}^{3+}$  contents from crystal-chemical analysis and Mössbauer spectroscopy. *Mineralogical Magazine* 71, 651-669
- WALTE, N.P.; HEIDELBACH, F.; MIYAJIMA, N.; FROST, D.J.; RUBIE, D.C.; DOBSON, D.P. (2009): Transformation textures in post-perovskite: Understanding mantle flow in the D" layer of the Earth. *Geophysical Research Letters* 36, L04302, doi: 10.1029/2008GL036840
- WENDLER, F.; BECKER, J.K.; NESTLER, B.; BONS, P.D.; WALTE, N.P. (2009): Phase-field simulations of partial melts in geological materials. *Computers & Geosciences* 35, 1907-1916
- WILLIAMS, H.M.; NIELSEN, S.G.; RENAC, C.; GRIFFIN, W.L.; O'REILLY, S.Y.; MCCAMMON, C.A.; PEARSON, N.; VILJOEN, F.; ALT, J.C.; HALLIDAY, A.N. (2009): Fractionation of oxygen and iron isotopes in the mantle: implications for crustal recycling and the source regions of oceanic basalts. *Earth and Planetary Science Letters* 283, 156-166

- WOODLAND, A.B.; BAUER, M.; BOFFA BALLARAN, T.; HANRAHAN, M. (2009): Crystal chemistry of  $\text{Fe}^{2+}_3\text{Cr}_2\text{Si}_3\text{O}_{12}$  -  $\text{Fe}^{2+}_3\text{Fe}^{3+}_2\text{Si}_3\text{O}_{12}$  garnet solid solutions and related spinels. *American Mineralogist* 94, 359-366
- WU, X.; STEINLE-NEUMANN, G.; NARYGINA, O.; KANTOR, I.; MCCAMMON, C.; PASCARELLI, S.; AQUILANTI, G.; PRAKAPENKA, V.; DUBROVINSKY, L. (2009): Iron oxidation state of  $\text{FeTiO}_3$  under high pressure. *Physical Review B* 79, 094106, doi: 10.1103/PhysRevB.79.094106
- WU, X.; STEINLE-NEUMANN, G.; NARYGINA, O.; KANTOR, I.; MCCAMMON, C.; PRAKAPENKA, V.; SWAMY, V.; DUBROVINSKY, L. (2009): High-pressure behavior of perovskite:  $\text{FeTiO}_3$  dissociation into  $(\text{Fe}_{1-\delta}, \text{Ti}_\delta)\text{O}$  and  $\text{Fe}_{1+\delta}\text{Ti}_{2-\delta}\text{O}_5$ . *Physical Review Letters* 103, 065503, doi: 10.1103/PhysRevLett.103.065503
- WU, X.; STEINLE-NEUMANN, G.; QIN, S.; KANZAKI, M.; DUBROVINSKY, L. (2009): Pressure-induced phase transitions of AX(2)-type iron pnictides: an *ab initio* study. *Journal of Physics: Condensed Matter* 21, 185403, doi: 10.1088/0953-8984/21/18/185403
- WU, X.; KANZAKI, M.; QIN, S.; STEINLE-NEUMANN, G.; DUBROVINSKY, L. (2009): Structural study of  $\text{FeP}_2$  at high pressure. *High Pressure Research* 29, 235-244, doi: 10.1080/08957950802597221
- XIONG, X.; KEPPLER, H.; AUDÉTAT, A.; GUDFINNSSON, G.; SUN, W.; SONG, M.; XIAO, W.; YUAN, L. (2009): Experimental constraints on rutile saturation during partial melting of metabasalt at the amphibolite to eclogite transition, with applications to TTG genesis. *American Mineralogist* 94, 1175-1186
- YANG, H.X.; KONZETT, J.; DOWNS, R.T.; FROST, D.J. (2009): Crystal structure and Raman spectrum of a high-pressure Li-rich majoritic garnet,  $(\text{Li}_2\text{Mg})\text{Si}_2(\text{SiO}_4)_3$ . *American Mineralogist* 94(4), 630-633
- YANG, H.X.; KONZETT, J.; FROST, D.J.; DOWNS, R.T. (2009): X-ray diffraction and Raman spectroscopic study of clinopyroxenes with six-coordinated Si in the  $\text{Na}(\text{Mg}_{0.5}\text{Si}_{0.5})\text{Si}_2\text{O}_6$ - $\text{NaAlSi}_2\text{O}_6$  system. *American Mineralogist* 94(7), 942-949
- YELAMANCHILI, R.S.; LU, Y.; LUNKENBEIN, T.; MIYAJIMA, N.; YAN, LI-T.; BALLAUFF, M.; BREU, J. (2009): Shaping colloidal rutile into thermally stable and porous mesoscopic titania-balls. *Small* 5, 1326-1333
- ZARECHNAYA, E.YU.; DUBROVINSKY, L.; DUBROVINSKAIA, N.; FILINCHUK, Y.; CHERNYSHOV, D.; DMITRIEV, V.; MIYAJIMA, N.; EL GORESY, A.; BRAUN, H.F.; VAN SMAALEN, S.; KANTOR, I.; KANTOR, A.; PRAKAPENKA, V.; HANFLAND, M.; MIKHAYLUSHKIN, A.S.; ABRIKOSOV, I.A.; SIMAK, S. I. (2009): Superhard semiconducting optically transparent high pressure phase of boron. *Physical Review Letters* 102, 185501
- ZARECHNAYA, E.YU.; DUBROVINSKY, L.; DUBROVINSKAIA, N.; MIYAJIMA, N.; FILINCHUK, Y.; CHERNYSHOV, D.; DMITRIEV, V. (2008): Synthesis of an orthorhombic high pressure boron phase. *Science and Technology of Advanced Materials* 9, 044209, doi: 10.1088/1468-6996/9/4/044209
- ZÖLLER, L.; BLANCHARD, H.; MCCAMMON, C. (2009): Can temperature assisted hydrostatic pressure reset the ambient TL of rocks? – A note on the TL of partially heated country rock from volcanic eruptions. *Ancient TL* 27, 15-22

ZVORISTE, C.E.; DUBROVINSKY, L.S.; HERING, S.; HUPPERTZ, H.; RIEDEL, R.; KINSKI, I. (2009): Diamond anvil cell syntheses and compressibility studies of the spinel-structured gallium oxonitride. *High Pressure Research* 29, 389-395

*b) Popular scientific magazines*

LANGENHORST, F. (2009): Der Schwabenstein und seine edlen Steine – Über die Diamanten des Nördlinger Rieses. In: *Der Stein der Schwaben – Zur Natur- und Kulturgeschichte des Suevits* (Eds. Wilfried Rosendahl & M. Schieber), Staatsanzeigerverlag Stuttgart 50-53

RUMMEL, R.; DREWES, H.; KEPPLER, H.; VÖLKSEN, C. (2009): Geographische Finsternisse vertreiben. *Akademie Aktuell* 2009, 2, 58-61

*5.2 Publications (submitted, in press)*

AUDÉTAT, A.; BALI, E.: A new technique to seal volatile-rich samples into platinum capsules. *European Journal of Mineralogy* (in press)

AUDÉTAT, A.; DOLEJS, D.; LOWENSTERN, J.B.: Molybdenite saturation in silicic magmas. *Geology* (submitted)

AUDÉTAT, A.: Source and evolution of molybdenum in the porphyry-Mo(-Nb) deposit at Cave Peak, Texas. *Journal of Petrology* (submitted)

BLÄß, U.; LANGENHORST, F.; MCCAMMON, C.: Microstructural investigations on strongly stained olivines of the chassignite NWA 2737 and implications to its shock history. *Earth and Planetary Science Letters* (submitted)

BOFFA BALLARAN, T.; LIU, J.; DUBROVINSKY, L.; CARACAS, R.; CHRICHTON, W.: High-pressure ferroelastic phase transition in aluminosilicate hollandite. *Physical Review B* (in press)

BORISOV, A.; MCCAMMON, C.: The effect of silica on ferric/ferrous ratio in silicate melts: An experimental investigation. *American Mineralogist* (in press)

COMODI, P.; BOFFA BALLARAN, T.; ZANAZZI, P.F.; CAPALBO, C.; ZANETTI, A.; NAZZARENI, S.: The effect of oxo-component on the high-pressure behavior of amphiboles. *American Mineralogist* (submitted)

DE KOKER, N.: Structure, thermodynamics, and diffusion in  $\text{CaAl}_2\text{Si}_2\text{O}_8$  liquid from first-principles molecular dynamics. *Geochimica et Cosmochimica Acta* (submitted)

DE KOKER, N.; STIXRUDE, L.: Theoretical computation of diffusion in minerals and melts. – In: ZHANG, Y.; CHERNIAK, D. (Eds.): *Reviews of Mineralogy and Geochemistry: Volume 72, Diffusion in Minerals and Melts* (submitted)

DÉGI, J.; ABART, R.; TÖRÖK, K.; BALI, E.; WIRTH, R.; RHEDE, D.: Symplectite formation during decompression induced garnet breakdown in lower crustal mafic granulite xenoliths: mechanisms and rates. *Contributions to Mineralogy and Petrology* (in press)

- DOLEJŠ, D.; MANNING, C.E.: A new equation of state for mineral dissolution in aqueous fluids: theory, calibration, and application to model fluid-flow systems. *Geofluids* (submitted)
- EL GORESY, A.; DUBROVINSKY, L.; GILLET, Ph.; GRAUP<sup>†</sup>, G.; CHEN, M.: Akaogiite: An ultra-dense polymorph of TiO<sub>2</sub> with seven-coordinated titanium, in shocked garnet gneisses from the Ries Crater, Germany. *American Mineralogist* (submitted)
- FABIAN, K.; ROBINSON, P.; MCENROE, S.A.; HEIDELBACH, F.: Experimental study of the magnetic signature of basal-plane anisotropy in hematite. Springer Monograph, IAGA (submitted)
- FROST, D.J.; ASAHARA, Y.; RUBIE, D.C.; MIYAJIMA, N.; DUBROVINSKY, L.S.; HOLZAPFEL, C.; OHTANI, E.; MIYAHARA, M.; SAKAI, T.: The partitioning of oxygen between the Earth's mantle and core. *Journal of Geophysical Research* (in press), doi: 10.1029/2009JB006302
- GALADÍ-ENRÍQUEZ, E.; DÖRR, W.; ZULAUF, G.; GALINDO-ZALDÍVAR, J.; HEIDELBACH, F.; ROHRMÜLLER, J.: Variscan deformation phases in the southwestern Bohemian Massif: new constraints from sheared granitoids. *Zeitschrift der Deutschen Geologischen Gesellschaft* (submitted)
- GANSKOW, G.; BOFFA BALLARAN, T.; LANGENHORST, F.: Effect of iron on the compressibility of hydrous ringwoodite. *American Mineralogist* (submitted)
- GAVRILENKO, P.; BOFFA BALLARAN, T.; KEPPLER, H.: The effect of Al and water on the compressibility of diopside. *American Mineralogist* (submitted)
- GLAZYRIN, K.; NARYGINA, O.; STEINLE-NEUMANN, G.; MCCAMMON, C.; DUBROVINSKY, L.; HEWENER, B.; WOLNY, J.A.; MUFFLER, K.; SCHÜNEMANN, V.; CHUMAKOV, A.; TASNÁDI, F.; EKHOLM, M.; VILDOSOLA, V.; POUROVSKII, L.V.; AICHHORN, M.; RUBAN, A.V.; ABRİKOSOV, I.A.: Electronic transition in hexagonal closed packed iron ( $\epsilon$ -Fe) at high pressure. *Nature Physics* (submitted)
- GREENBERG, E.; ROZENBERG, G.Kh.; XU, W.; ARIELLY, R.; PASTERNAK, M.P.; MELCHIOR, A.; GARBARINO, G.; DUBROVINSKY, L.S.: On the compressibility of ferrite spinels: a high-pressure X-ray diffraction study of  $M\text{Fe}_2\text{O}_4$  ( $M=\text{Mg, Co, Zn}$ ). *High Pressure Research* (in press)
- HAMMOUDA, T.; CHANTEL, J.; DEVIDAL, J-L.: Apatite solubility in carbonatitic liquids and trace element partitioning between apatite and carbonatite at high pressure. *Geochimica et Cosmochimica Acta* (submitted)
- HARRISON, R.H.; MCENROE, S.A.; ROBINSON, P.; HOWARD C.: Spin orientation in a natural Ti-bearing hematite: evidence for an out-of plane component. *American Mineralogist* (in press)
- HEIDELBACH, F.; TERRY, M.P.: Inherited fabric in an eclogite symplectite: evidence for deformation under ultra-high pressure conditions. *Mineralogical Magazine* (submitted)
- IRIFUNE, T.; SHINMEI, T.; MCCAMMON, C.; MIYAJIMA, N.; RUBIE, D.; FROST, D.: Iron partitioning and density changes in pyrolite in Earth's lower mantle. *Science* (in press)
- KALO, H.; MÖLLER, M.W.; ZIADEH, M.; DOLEJŠ, D.; BREU, J.: Large scale melt-synthesis in an open crucible of Na-fluorohectorite with superb charge homogeneity and particle size. *Applied Clay Science* (in press)

- KARKI, B.B.; BHATTARAI, D.; MOOKHERJEE, M.; STIXRUDE, L.: Visualization and analysis of structural and dynamical properties of simulated hydrous silicate melt. *Physics and Chemistry of Minerals* (accepted)
- KATSURA, T.; YOSHINO, T.; MANTHILAKE, M.A.G.M.; MATSUZAKI, T.: Electrical conductivity of the major upper mantle minerals, a review. *Russian Geology and Geophysics* (in press)
- KEPLER, H.: The distribution of sulfur between haplogranitic melts and aqueous fluids. *Geochimica et Cosmochimica Acta* (in press, published online October 2009)
- KESHAV, S.; GUDFINNSSON, G.H.; PRESNALL, D.C.: Melting phase relations of simplified carbonated peridotite at 12-26 GPa in the systems CaO-MgO-SiO<sub>2</sub>-CO<sub>2</sub> and CaO-MgO-Al<sub>2</sub>O<sub>3</sub>-SiO<sub>2</sub>-CO<sub>2</sub>: highly calcic magmas at moderate depths in the Earth. *Journal of Petrology*, *Wyllie volume* (submitted)
- KESHAV, S.; GUDFINNSSON, G.H.; GHOSH, S.: The carbonated peridotite solidus ledge in the system CaO-MgO-Al<sub>2</sub>O<sub>3</sub>-SiO<sub>2</sub>-CO<sub>2</sub>, reconsidered. *Journal of Petrology*, *Wyllie volume* (submitted)
- KESHAV, S.; GUDFINNSSON, G.H.: Experimentally dictated stability of carbonated oceanic crust to moderately great depths in the Earth: results from the solidus determination in the system CaO-MgO-Al<sub>2</sub>O<sub>3</sub>-SiO<sub>2</sub>-CO<sub>2</sub>. *Journal of Geophysical Research* (in press)
- MANNING, C.E.; ANTIGNANO, A.; LIN, H.A.: Premelting polymerization of crustal and mantle fluids, as indicated by solubility of albite + paragonite + quartz in H<sub>2</sub>O at 1 GPa and 350-620 °C. *Earth and Planetary Science Letters* (submitted)
- MCCAMMON, C.; DUBROVINSKY, L.; NARYGINA, O.; KANTOR, I.; WU, X.; GLAZYRIN, K.; SERGUEEV, I.; CHUMAKOV, A.: Low-spin Fe<sup>2+</sup> in silicate perovskite and a possible layer at the base of the lower mantle. *Physics of the Earth and Planetary Interiors* (in press)
- MECKLENBURGH, J.; HEIDELBACH, F.; MARIANI, E.; MACKWELL, S.; SEIFERT, F.: Rheology and microstructure of (Ca,Sr)TiO<sub>3</sub> perovskite deformed in compression and torsion. *Journal of Geophysical Research* (in press)
- MINCH, R.; DUBROVINSKY, L.; KURNOSOV, A.; EHM, L.; KNORR, K.; DEPMEIER, W.: Raman spectroscopic study of PbCO<sub>3</sub> at high pressures and temperatures. *Physics and Chemistry of Minerals* (in press), doi: 10.1007/s00269-009-0308-0
- MIYAHARA, M.; OHTANI, E.; KIMURA, M.; EL GORESY, A.; OZAWA, S.; NAGASE, T.; NISHIJIMA, M.; HIRAGA, K.: Coherent with subsequent incoherent ringwoodite growth in olivine of shocked L6 chondrites. *Earth and Planetary Science Letters* (submitted)
- MIYAJIMA, N.; HOLZAPFEL, C.; ASAHARA, Y.; DUBROVINSKY, L.; FROST, D.J.; RUBIE, D.C.; DRECHSLER, M.; NIWA, K.; ICHIHARA, M.; YAGI, T.: Combining FIB milling and conventional Argon ion milling techniques to prepare high quality site-specific TEM samples for quantitative EELS analysis of oxygen in molten iron. *Journal of Microscopy* (in press), doi: 10.1111/j.1365-2818.2009.03341.x

- MIYAJIMA, N.; NIWA, K.; HEIDELBACH, F.; YAGI, T.; OHGUSHI, K.: Deformation microtextures in  $\text{CaIrO}_3$  post-perovskite under high stress conditions in a laser heated DAC. *Journal of Physics: Conference Series* (submitted)
- MOLLO, S.; GAETA, M.; FREDA, C.; DI ROCCO, T.; MISITI, V.; SCARLATO, P.: Carbonate assimilation in magmas: A reappraisal based on experimental petrology. *Lithos* (in press)
- MOOKHERJEE, M.; STEINLE-NEUMANN, G.: Detecting deeply subducted crust from elasticity of hollandite. *Earth and Planetary Science Letters* (in press) doi: 10.1016/j.epsl.2009.09.037
- NAKASHIMA, D.; OTT, U.; EL GORESY, A.; NAKAMURA, T.: Heavily fractionated noble gases in an acid residue from the KLE 98300 EH3 chondrite. *Earth and Planetary Science Letters* (submitted)
- NARYGINA, O.; KANTOR, I.; MCCAMMON, C.; DUBROVINSKY, L.: Electronic state of  $\text{Fe}^{2+}$  in  $(\text{Mg,Fe})(\text{Si,Al})\text{O}_3$  perovskite and  $(\text{Mg,Fe})\text{SiO}_3$  majorite at pressures up to 86 GPa and temperatures up to 800 K. *Physics and Chemistry of Minerals* (accepted)
- NARYGINA, O.; DUBROVINSKY, L.S.; GLAZYRIN, K.; MCCAMMON, C.A.; PASCARELLI, S.; AQUILANTI, G.; KANTOR, I.Y.; HANFLAND, M.; PRAKAPENKA, V.: Chemically homogeneous spin transition zone in Earth's lower mantle. *Earth and Planetary Science Letters* (submitted)
- NAZZARENI, S.; COMODI, P.; BINDI, L.; DUBROVINSKY, L.: The crystal structure of gypsum-II by single-crystal synchrotron X-ray diffraction data. *American Mineralogist* (submitted)
- OTSUKA, K.; MCCAMMON, C.A.; KARATO, S.-I.: Tetrahedral occupancy of ferric iron in  $(\text{Mg,Fe})\text{O}$ : Implications for point defects in the Earth's lower mantle. *Physics of the Earth and Planetary Interiors* (in press)
- OVSYANNIKOV, S.V.; SHCHENNIKOV, V.V.: High-pressure routes in the thermoelectricity or how one can improve a performance of thermoelectrics (review). *Chemistry of Materials* (in press)
- OVSYANNIKOV, S.V.; SHCHENNIKOV, V.V. SHVETSOVA, M.A.; DUBROVINSKY, L.S.; POLIAN, A.: Tuning of a stoichiometry in  $\text{Fe}_{1-x}\text{O}$  wustite by compression. *Physical Review Letters* (submitted)
- OVSYANNIKOV, S.V.; POLIAN, A.; GAUTHIER, M.; MUNSCH, P.; CHERVIN, J.C.; LE MARCHAND, G.; ASELAGE, T.: Raman spectroscopy of doped  $\alpha$ -boron ( $\text{B}_{12}\text{P}_2$  and  $\text{B}_{12}\text{As}_2$ ) to 120 GPa: Evidences for a structural distortion. *Physical Review Letters* (submitted)
- ROBINSON, P.; FABIAN, K.; MCENROE, S.A.: The geometry of ionic arrangements and magnetic interactions in ordered ferri-ilmenite solid solutions and its effect on low-temperature magnetic behavior. *Geochemistry, Geophysics, Geosystems* (in press)
- RUBIE, D.C.; FROST, D.J.; MANN, U.; ASAHARA, Y.; TSUNO, K.; NIMMO, F.; KEGLER, P.; HOLZHEID, A.; PALME, H.: Accretion, composition and core-mantle differentiation of the Earth. *Science* (submitted)

- RUSKOV, T.; SPIROV, I.; GEORGIEVA, M.; YAMAMOTO, S.; GREEN, H.; MCCAMMON, C.; DOBRZHINETSKAYA, L.: Mössbauer spectroscopy studies of the valence state of iron in chromite from the Luobusa massif of Tibet. *Journal of Metamorphic Geology* (submitted)
- SAMUEL, H.; TACKLEY, P.J.; EVONUK, M.: Heat partitioning in terrestrial planets during core formation by negative diapirism. *Earth and Planetary Science Letters* (in press)
- SCHIAVI, F.; WALTE, N.; KONSCHAK, A; KEPPLER, H: A new moissanite cell apparatus for *in situ* observation of crystallizing melts at high temperature. *American Mineralogist* (submitted)
- SHCHENNIKOV, V.V.; OVSYANNIKOV, S.V.: Phase transitions from mechanical contraction: direct observation of phase-transition-related volumetric effects in crystals of ZnO, GaAs, CaCO<sub>3</sub>, and CeNi under compression up to 25 GPa. *High Pressure Research* (in press)
- SHCHENNIKOV, V.V.; OVSYANNIKOV, S.V.; MANAKOV, A.Y.: Measurement of Seebeck effect (thermoelectric power) at high pressure up to 40 GPa. *Journal of Physics and Chemistry of Solids* (submitted)
- SHIRYAEV, A.A.; ZUBAVICHUS, Y.V.; MCCAMMON, C.; VELIGZHANIN, A.A.: Iron in fibrous diamonds from different localities: X-ray absorption and Mössbauer data. *Russian Geology and Geophysics* (submitted)
- TERRY, M.P.; HEIDELBACH, F.; COUVY, H.; BROMILEY, G.D.; CARSWELL, D.A.: Deformation and metamorphism of the Kvalvika peridotite, Norway: Conditions and timing for olivine c-slip and exhumation at ultrahigh pressure. *Journal of Metamorphic Petrology* (submitted)
- TRONCHE, E.J.; KAN, M.V.; VRIES, J.D.; WANG, Y.; SANEHIRA, T.; LI, J.; CHEN, B.; GAO, L.; KLEMME, S.; MCCAMMON, C.A.; WESTRENNEN, W.V.: The thermal equation of state of FeTiO<sub>3</sub> ilmenite based on *in situ* X-ray diffraction at high pressures and temperatures. *American Mineralogist* (submitted)
- WEIGEL, C.; MCCAMMON, C.; KEPPLER, H.: High-temperature Mössbauer spectroscopy: A probe for the relaxation time of Fe species in silicate melts and glasses. *American Mineralogist* (submitted)
- WU, X.; STEINLE-NEUMANN, G.; NARYGINA, O.; MCCAMMON, C.; DUBROVINSKY, L.: Structural evolution and iron oxidation state of LiNbO<sub>3</sub>-type FeTiO<sub>3</sub> at high pressure. *American Mineralogist* (submitted)
- XIONG, X.; KEPPLER, H.; AUDÉTAT, A.; NI, H.; SUN, W.; YUAN, L.: Partitioning of Nb and Ta between rutile and felsic melt and the fractionation of Nb/Ta during partial melting of hydrous metabasalt. *Geochimica et Cosmochimica Acta* (submitted)
- ZHANG, Y.; NI, H.: Diffusion of H, C, and O in silicate melts. *Review in Mineralogy and Geochemistry* (in press)
- ZHANG, Y.; NI, H.; CHEN, Y.: Effective binary diffusion in silicate melts. *Review in Mineralogy and Geochemistry* (in press)
- ZHANG, Y.: Geochemical kinetics. *Trans. (Chinese) Ni, H.; Wang, H.; Liu, Y.; Chen, Y.; Hui, H.; Wang, L., Higher Education Press, Beijing* (in press)

### 5.3 Presentations at scientific institutions and at congresses

- ADJAOUD, O.; STEINLE-NEUMANN, G.; JAHN, S.: 21.-26.06.2009, Goldschmidt 2009, Davos, Switzerland<sup>\*2</sup>: "Structure, thermodynamics and transport properties of Mg<sub>2</sub>SiO<sub>4</sub> liquid under high pressure from molecular dynamics", *Geochimica et Cosmochimica Acta*, 73 (13), Supp. 1, A11
- AUDÉTAT, A.: 21.-26.06.2009, Goldschmidt 2009, Davos, Switzerland<sup>\*2</sup> (*keynote lecture*): "Source and evolution of Mo in the porphyry-Mo(Nb) deposit at Cave Peak, Texas", *Geochimica et Cosmochimica Acta*, 73 (13), Supp. 1, A62
- AUDÉTAT, A.: 29.08.-02.09.2009, MAPT (Micro-Analysis, Processes, Time) Conference, Edinburgh, U.K. (*plenary lecture*): "Laser-ablation ICP-MS analysis of solid, melt and fluid inclusions: techniques and applications", Abstract p. 79
- AUDÉTAT, A.: 09.09.2009, Guangzhou Institute of Geochemistry, Guangzhou, China: "Source and evolution of Mo in the porphyry-Mo(Nb) deposit at Cave Peak, Texas"
- AUDÉTAT, A.: 16.09.2009, State Key Laboratory for Mineral Deposits Research, Nanjing University, Nanjing, China: "Laser-ablation ICP-MS analysis of solid, melt and fluid inclusions: techniques and applications"
- BALI, E.; AUDÉTAT, A.; KEPPLER, H.: 21.-26.06.2009, Goldschmidt 2009, Davos, Switzerland<sup>\*2</sup>: "Mobility of U and Th in subduction zone fluids – A synthetic fluid inclusion study", *Geochimica et Cosmochimica Acta*, 73 (13), Supp. 1, A80
- BALI, E.; AUDÉTAT, A.; KEPPLER, H.: 21.-30.09.2009, XX European Current Research on Fluid Inclusions – ECROFI 2009, Granada, Spain: "Solubility of Uranium and Thorium at high pressure and temperature – a synthetic fluid inclusion study", Abstract book, 17-18
- BERNINI, D.: 31.01.2009, ENB Workshop, Thurnau, Germany<sup>\*1</sup>: "Zircon solubility in aqueous fluids at high pressures and temperatures"
- BERNINI, D.; DOLEJŠ, D.; KEPPLER, H.: 21.-26.06.2009, Goldschmidt 2009, Davos, Switzerland<sup>\*2</sup>: "The distribution of halogens between fluids and upper-mantle minerals", *Geochimica et Cosmochimica Acta*, 73 (13), Supp. 1, A116
- BOFFA BALLARAN, T.: 04.-14.06.2009, International School of Crystallography, Erice, Italy (*invited*): "Compressibility, EOS – applications in geosciences"
- BOFFA BALLARAN, T.; LIU, J.; DUBROVINSKY, L.S.; CARACAS, R.; CRICHTON, W.: 06.-11.09.2009, 47<sup>th</sup> EHPRG International Conference, Paris, France: "High-pressure ferroelastic transition in K<sub>0.8</sub>Na<sub>0.2</sub>AlSi<sub>3</sub>O<sub>8</sub> hollandite"
- BOFFA BALLARAN, T.; NESTOLA, F.; ANGEL, R.J.; OHASHI, H.: 09.-11.09.2009, Geitalia 2009, VII Forum Italiano di Scienze della Terra, Rimini, Italy: "Low-temperature C2/c to P2<sub>1</sub>/c phase transition in Li(Ga<sub>0.73</sub>Al<sub>0.27</sub>)Si<sub>2</sub>O<sub>6</sub>"
- BOFFA BALLARAN, T.: 23.11.2009, Institut Mineralogie und Kristallographie, University of Vienna (*invited*): "MORB mineralogy at the conditions of the Earth's lower mantle"
- BOFFA BALLARAN, T.; FROST, D.J.; MIYAJIMA, N.: 14.-18.12.2009, AGU Fall Meeting, San Francisco, USA<sup>\*3</sup>: "A new water rich aluminumsilicate phase stable at the Earth's lower mantle conditions", *EOS Trans. AGU*, 90(52), Fall Meet. Suppl., Abstract MR31B-1655, 2009

- BUISMAN, I.; WALTER, M.J.; KESHAV, S.: 14.-18.12.2009, AGU Fall Meeting, San Francisco, USA <sup>\*3</sup>: "Non-potassic melts in CMAS-CO<sub>2</sub>-H<sub>2</sub>O-K<sub>2</sub>O peridotite", EOS Trans. AGU, 90(52), Fall Meet. Suppl., Abstract MR43A-1871, 2009
- BUNGE, H.; SCHUBERTH, B.; STEINLE-NEUMANN, G.; OESER, J.: 14.-18.12.2009, AGU Fall Meeting, San Francisco, USA <sup>\*3</sup>: "Stark temperature contrasts in the lowermost mantle", EOS Trans. AGU, 90(52), Fall Meet. Suppl., Abstract MR22C-07, 2009
- CAILLET KOMOROWSKI, C.; BOUDOUMA, O.; EL GORESY, A.; MIYAHARA, M.; ÖZEL, M.E.: 13.-18.07.2009, 72<sup>nd</sup> Annual Meeting of the Meteoritical Society, Nancy, France: "Sub-microscopic study of Cu- and Hg-bearing opaque assemblages in unshocked primitive H chondrites: Origin and first occurrence of native Hg in a meteorite"
- CHANTEL, J.; KOGA, K.; HAMMOUDA, T.; KATSURA, T.; YOSHINO, T.: 04.-06.03.2009, c2c mid-term review meeting, Sevilla, Spain: "Infiltration rate measurements at HP-HT using *in situ* electrical resistivity: Application to a carbonatite melt in a forsterite aggregate"
- CHANTEL, J.; KOGA, K.; HAMMOUDA, T.; KATSURA, T.; YOSHINO, T.: 18.-20.06.2009, Marie Curie Research Training Network Crust to Core – The Fate of Subducted Material Workshop 'The Deep Carbon Cycle', ETH Zurich, Switzerland "Infiltration rate measurements at HP-HT using *in situ* electrical resistivity: Application to a carbonatite melt in a forsterite aggregate"
- CHELAZZI, L.; BOFFA BALLARAN, T.; NESTOLA, F.; BINDI, L.; BONAZZI, P.: 20.-23.09.2009, XXXVIII National Congress of the Italian Crystallography Association, Salerno, Italy: "Compressibility of Ca<sub>2</sub>Sb<sub>2</sub>O<sub>7</sub> weberite-like compound: *In situ* high-pressure single-crystal X-ray diffraction study"
- CHEMIA, Z.; SCHMELING, H.; KOYI, H.: 04.-06.03.2009, c2c mid-term review meeting, Sevilla, Spain: "The effect of the salt viscosity on future evolution of the Gorleben salt diapir, Germany"
- CHEMIA, Z.; BUITER, S.: 28.06.-03.07.2009, 11<sup>th</sup> International Workshop on Modeling of Mantle Convection and Lithospheric Dynamics, Braunwald, Switzerland: "Discussion on resolving sediment subduction"
- COCHAIN, B.; NEUVILLE, D.R.; MCCAMMON, C.; HENDERSON, G.S.; DE LIGNY, D.; PINET, O.; RICHEL, P.: 24.-27.05.2009, 2009 Joint Assembly 'The Meeting of the Americas', Toronto, Canada: "Tetraedrally coordinated Fe<sup>3+</sup> in silicate glasses: A Mössbauer, iron K-edge XANES and Raman spectroscopies study"
- COMODI, P.; BOFFA BALLARAN, T.; ZANAZZI, P.F.; CAPALBO, C.; ZANETTI, A.; NAZZARENI, S.: 09.-11.09.2009, Geoitalia 2009, VII Forum Italiano di Scienze della Terra, Rimini, Italy: "The effect of H-deficiency on the baric behavior of amphiboles"
- COMODI, P.; KURNOSOV, A.; NAZZARENI, S.; DUBROVINSKY, L.: 09.-11.09.2009, Geoitalia 2009, VII Forum Italiano di Scienze della Terra, Rimini, Italy: "The dehydration of gypsum: a HP-HT Raman study"
- DECARLI, P.S.; EL GORESY, A.; XIE, Z.; SHARP, T.G.: 13.-18.07.2009, 72<sup>nd</sup> Annual Meeting of the Meteoritical Society, Nancy, France: "High-pressure mineralogy of shock veins in meteorites does constrain the equilibrium shock pressure and its duration"

- DE KOKER, N.; STIXRUDE, L.: 04.-06.03.2009, c2c mid-term review meeting, Sevilla, Spain: "Self-consistent thermodynamic description of silicate liquids"
- DE KOKER, N.: 21.-26.06.2009, Goldschmidt 2009, Davos, Switzerland\*<sup>2</sup> (*invited*): "Thermal conductivity of MgO periclase from equilibrium first principles molecular dynamics", *Geochimica et Cosmochimica Acta*, 73 (13), Supp. 1, A274
- DE KOKER, N.: 20.-24.07.2009, 'From Core to Crust: Towards an Integrated Vision of Earth's Interior', International Center for Theoretical Physics, Trieste, Italy: "Thermal conductivity of MgO periclase from equilibrium first principles molecular dynamics"
- DE KOKER, N.: 15.-18.11.2009, 'Out of Africa: 140 years with Kevin Burke and Lew Ashwal', University of the Witwatersrand, Johannesburg, South Africa: "First-principles computations of thermal conductivity at high pressure and temperature - Implications for the deep Earth"
- DE KOKER, N. 15.-18.11.2009, 'Out of Africa: 140 years with Kevin Burke and Lew Ashwal', University of the Witwatersrand, Johannesburg, South Africa: "Physics of silicate melts at deep mantle conditions"
- DE KOKER, N.: 20.11.2009, University of Johannesburg, Department of Physics, Johannesburg, South Africa: "First-principles computations of lattice thermal conductivity: Implications for the deep Earth"
- DE KOKER, N.: 14.-18.12.2009, AGU Fall Meeting, San Francisco, USA\*<sup>3</sup>: "Thermal conductivity of major mantle minerals at the core-mantle boundary", *EOS Trans. AGU*, 90(52), Fall Meet. Suppl., Abstract MR22C-06, 2009
- DOLEJŠ, D.: 27.-29.04.2009: Physics of Geological Processes, University of Oslo, Norway: "Halogens in silicic magmas: Experimental constraints and thermodynamic models"
- DOLEJŠ, D.; STAGNO, V.: 21.-26.06.2009, Goldschmidt 2009, Davos, Switzerland\*<sup>2</sup>: "Halogens in silicic magmas, from the upper mantle to the crust", *Geochimica et Cosmochimica Acta*, 73 (13), Supp. 1, A297
- DUBROVINSKY, L.S.; EL GORESY, A.; GILLET, Ph.; WU, X.; SIMIONOVICI, A.: 13.-18.07.2009, 72<sup>nd</sup> Annual Meeting of the Meteoritical Society, Nancy, France: "A novel natural shock-induced high-pressure polymorph of FeTiO<sub>3</sub> ilmenite with the Li-niobate structure from the Ries Crater, Germany"
- EL GORESY, A.; MIYAHARA, M.; OHTANI, E.; NAGASE, T.; NISHIJIMA, M.; FERROIR, T.; GILLET, Ph.: 13.-18.07.2009, 72<sup>nd</sup> Annual Meeting of the Meteoritical Society, Nancy, France: "Micro-surgical FIB-TEM study of diverse liquidus wadsleyite-ringwoodite pairs fractionally crystallized from olivine melt inclusions in L6 chondrites"
- EL GORESY, A.; DUBROVINSKY, L.S.; GILLET, Ph.; WU, X.; SIMIONOVICI, A.: 06.10.2009, Tohoku University, Sendai, Japan: "Shock-induced high-pressure polymorph of FeTiO<sub>3</sub> ilmenite with the Li-niobate structure from the Ries Crater, Germany"
- EL GORESY, A.; MIYAHARA, M.; OHTANI, E.; NAGASE, T.; NISHIJIMA, M.; FERROIR, T.; GILLET, Ph.: 13.10.2009, Tohoku University, Sendai, Japan: "Micro-surgical FIB-TEM study of diverse liquidus wadsleyite-ringwoodite pairs fractionally crystallized from olivine melt inclusions in shock melt veins in L6 chondrites"

- EL GORESY, A.; OZAWA, S.; MIYAHARA, M.; GILLET, Ph.; OHTANI, E.; BECK, P.; MONTAGNAC, G.: 20.10.2009, Tohoku University, Sendai, Japan: "Shock-induced melting of maskelynite and the high-pressure mineral inventory of shergottites: Implications to evaluation of the shock history of martian meteorites"
- EL GORESY, A.; OZAWA, S.; MIYAHARA, M.; GILLET, Ph.; OHTANI, E.; BECK, P.; MONTAGNAC, G.: 14.-18.12.2009, AGU Fall Meeting, San Francisco, USA<sup>\*3</sup>: "Shock-induced melting of maskelynite and the high-pressure mineral inventory of shergottites: Implications to evaluation of the shock history of Martian meteorites", EOS Trans. AGU, 90(52), Fall Meet. Suppl., Abstract MR12A-03, 2009
- ESCUADERO, A.: 04.-07.02.2009, c2c Meeting, Seville, Spain: "Microstructural and chemical characteristics of TiO<sub>2</sub> in ultra-high pressure metamorphic rocks"
- ESCUADERO, A.: 07.-11.09.2009, CSIC Postgraduate Course 'Structure determination of real solids. Nuclear Magnetic Resonance Technique', Universidad de Sevilla, Instituto de Ciencia de Materiales de Sevilla, Spain (*invited*): "Magnetic interactions in solid state. Magic angle spinning", "Dmfit: a program to simulate and fit NMR spectra"
- ESCUADERO, A.; TSUNO, K.; LANGENHORST, F.: 13.-16.09.2009, DMG 2009, 87. Meeting of the German Mineralogical Society, Halle, Germany: "Phase relations in the Al<sub>2</sub>O<sub>3</sub> – TiO<sub>2</sub> system at pressures up to 20 GPa", Hallesches Jahrbuch für Geowissenschaften 31, 54
- ETZEL, K.; HARRIES, D.; POLLOK, K.; DEPMEIER, W.: 25.-27.02.2009, Rundgespräch der Arbeitsgruppe geowissenschaftlicher Nachwuchs der DFG-Geokommission, Mühlthal, Germany: "Metall-Sulfide und deren Verwitterung"
- ETZEL, K.; POLLOK, K.: 21.-26.06.2009, Goldschmidt 2009, Davos, Switzerland<sup>\*2</sup>: "Effects of microstructure and secondary phases on the dissolution of Fe-rich sphalerite", Geochimica et Cosmochimica Acta, 73 (13), Supp. 1, A343
- ETZEL, K.; POLLOK, K.: 13.-16.09.2009, DMG 2009, 87. Meeting of the German Mineralogical Society, Halle, Germany: "How do microstructure and secondary phases affect sulfide dissolution"
- ETZEL, K.; HOPF, J.; HOHELLA Jr., M.; LANGENHORST, F.; POLLOK, K.: 10.-11.11.2009, Geotechnology Seminar 'Mineral Surfaces', Universität Bayreuth, Hydrologie, Bayreuth: "Experimentelle Ansätze zur abiotischen und biotischen Alteration von Monosulfiden"
- FERROIR, T.; MIYAHARA, M.; OHTANI, E.; BECK, P.; SIMIONOVICI, A.; GILLET, Ph.; EL GORESY, A.: 13.-18.07.2009, 72<sup>nd</sup> Annual Meeting of the Meteoritical Society, Nancy, France: "P-T conditions and mechanisms of enstatite to akimotoite transformations in the shocked L-6 chondrite Tenham"
- FROST, D.J.: 12.-13.02.2009, Mineralogical Society of London Meeting 'New Views on the Earth's Interior', London, U.K.: "Chemical reactions at the core mantle boundary"
- FROST, D.J.: 17.-20.05.2009, CIDER '09 Community Workshop, Marconi Center, Marshall, California, USA: "The onset of deep mantle melting"
- FROST, D.J.; RUBIE, D.C.; TSUNO, K.: 21.-26.06.2009, Goldschmidt 2009, Davos, Switzerland<sup>\*2</sup>: "Chemistry of the Earth's core and reactions at the core-mantle boundary", Geochimica et Cosmochimica Acta, 73 (13), Supp. 1, A400

- FROST, D.J.: 13.07.2009, University of Münster, Institute of Geophysics, Münster, Germany: "Interpreting seismic observations of the Earth's interior using the results of high pressure and temperature laboratory experiments"
- FROST, D.J.: 16.11.2009, University of Oxford, Department of Earth Sciences, Oxford, U.K.: "Accretion of the Earth according to experimental petrology"
- GANSKOW, G.; LANGENHORST, F.; FROST, D.: 08.-11.01.2009, Kumamoto University Global COE Program 'Global Initiative Center for Pulsed Power Engineering', International COE Forum on Pulsed Power Engineering & Young Researcher Training Camp, Kumamoto, Japan: "Stability of hydrous mantle phases in the MgFeSiO<sub>4</sub>-H<sub>2</sub>O system"
- GANSKOW, G.: 31.01.2009, ENB Workshop, Thurnau, Germany<sup>\*1</sup>: "TEM study of a quenched high-pressure polymorph of spinel"
- GILLET, Ph.; FERROIR, T.; BECK, P.; EL GORESY, A.: 13.-18.07.2009, 72<sup>nd</sup> Annual Meeting of the Meteoritical Society, Nancy, France: "Pressure-temperature-time records of shock in meteorites"
- GLAZYRIN, K.: 31.01.2009, ENB Workshop, Thurnau, Germany<sup>\*1</sup>: "Electronic transition in hcp Fe and Fe<sub>0.9</sub>Ni<sub>0.1</sub>"
- GLAZYRIN, K.; NARYGINA, O.; STEINLE-NEUMANN, G.; MCCAMMON, C.; DUBROVINSKY, L.; HEWENER, B.; WOLNY, J.A.; MUFFLER, K.; SCHÜNEMANN, V.; CHUMAKOV, A.; TASNÁDI, F.; EKHOLM, M.; POUROVSKII, L.V.; VILDOSOLA, V.; AICHHORN, M.; RUBAN, A.V.; ABRIKOSOV, I.A.: 06.-11.09.2009, 47<sup>th</sup> EHPRG International Conference, Paris, France: "High pressure electronic transition in hcp Fe and Fe<sub>0.9</sub>Ni<sub>0.1</sub>"
- GLAZYRIN, K.; DUBROVINSKY, L.; MCCAMMON, C.: 06.-11.09.2009, 47<sup>th</sup> EHPRG International Conference, Paris, France: "Mössbauer study of magnetite under high pressure"
- GREENBERG, E.; XU, W.; ROZENBERG, G.Kh.; PASTERNAK, M.P.; KURNOSOV, A.; DUBROVINSKY, L.S.; HANFLAND, M.; GARBARINO, G.: 06.-11.09.2009, 47<sup>th</sup> EHPRG International Conference, Paris, France: "High-pressure studies of MFe<sub>2</sub>O<sub>4</sub> (M=Mg, Co, Zn) ferrite spinels: the dilemma of the post-spinel structure"
- HAFERBURG, G.; CARABULEA, K.; HOPF, J.; KOTHE, E.: 28.-29.09.2009, 8<sup>th</sup> Symposium on Remediation 'Geo-bio-processes at geochemical barriers', Friedrich-Schiller-Universität Jena, Germany: "Microorganisms as brick layers of minerals: How could deposit formation be linked to metal resistance?"
- HANKARD, F.; GATTACCECA, J.; FERMON, C.; PANNETIER-LECOEUR, M.; LANGLAIS, B.; QUESNEL, Y.; ROCHETTE, P.; MCENROE, S.A.: 14.-18.12.2009, AGU Fall Meeting, San Francisco, USA<sup>\*3</sup>: "Rock magnetic and paleomagnetic investigations using a Giant Magneto Resistance-based scanning magnetometer", EOS Trans. AGU, 90(52), Fall Meet. Suppl., Abstract GP11A-0744, 2009
- HARRIES, D.: 31.01.2009, ENB Workshop, Thurnau, Germany<sup>\*1</sup>: "Structural control on oxidation of pyrrhotite (Fe<sub>1-x</sub>S) surfaces"
- HARRIES, D.; POLLOK, K.; LANGENHORST, F.: 29.08.-02.09.2009, MAPT (Micro-Analysis, Processes, Time) Conference, Edinburgh, U.K.: "Pyrrhotite, polytypes and pH: A TEM study on structural complexity and its effects at the mineral-fluid interface"

- HARRIES, D.; POLLOK, K.; LANGENHORST, F.: 13.-16.09.2009, DMG 2009, 87. Meeting of the German Mineralogical Society, Halle, Germany: "Nanometer-wide magnetite lamellae in mixed 4C/NC-type pyrrhotite from Bodenmais (Bavaria, Germany) – alteration or exsolution?", Hallesches Jahrbuch für Geowissenschaften 31, 94
- HARRIES, D.; POLLOK, K.; ETZEL, K.; LANGENHORST, F.: 21.-26.06.2009, Goldschmidt 2009, Davos, Switzerland<sup>\*2</sup>: "Structural complexity in pyrrhotites: What are the implications for fluid-mineral interactions?", *Geochimica et Cosmochimica Acta*, 73 (13), Supp. 1, A495
- HEIDELBACH, F.; TERRY, M.P.: 29.08.-02.09.2009, MAPT (Micro-Analysis, Processes, Time) Conference, Edinburgh, U.K.: "Inherited fabric in an eclogite symplectite: evidence for deformation under ultra-high pressure conditions"
- HEWENER, B.; MCCAMMON, C.; DUBROVINSKY, L.; CHUMAKOV, A.; MUFFLER, K.; WOLNY, J.; TIPPELT, G.; AMTHAUER, G.; SCHÜNEMANN, V.: 19.-24.07.2009, International Conference on the Applications of the Mössbauer Effect, Vienna, Austria: "Nuclear inelastic scattering on the pyroxene mineral diopside"
- HOBBS, L.; KEPLER, H.: 21.-26.06.2009, Goldschmidt 2009, Davos, Switzerland<sup>\*2</sup>: "Adsorption of HCl onto volcanic ash", *Geochimica et Cosmochimica Acta*, 73 (13), Supp. 1, A536
- HOPF, J.; HARRIES, D.; LANGENHORST, F.; HOCELLA, M.F.; POLLOK, K.: 10.-11.11.2009, Geotechnology Seminar 'Mineral Surfaces', Universität Bayreuth, Hydrologie, Bayreuth: "Oxidative dissolution of pyrrhotite by *Acidithiobacillus ferrooxidans*: a surface approach"
- KANTOR, A.; DUBROVINSKY, L.; KANTOR, I.; PRAKAPENKA, V.; SINOGEIKIN, S.: 06.-11.09.2009, 47<sup>th</sup> EHPRG International Conference, Paris, France: "Simultaneous X-ray density and acoustic velocity measurements of titanium dioxide"
- KANTOR, A.; JACOBSEN, S.; KANTOR, I.; DUBROVINSKY, L.; REICHMANN, H.-J.: 23.-25.09.2009, Workshop on On-line Brillouin Spectroscopy at GSECARS: 'Basic Principles and Application for High Pressure Research', Argonne National Laboratory, Argonne, USA: "GHz ultrasonic interferometry at high pressure and temperature in the diamond anvil cell"
- KEGLER, P.; HOLZHEID, A.; MCCAMMON, C.; RUBIE, D.C.; PALME, H.: 23.-27.03.2009, 40<sup>th</sup> Lunar and Planetary Science Conference, The Woodlands, USA: "Pressure and temperature dependent partitioning of copper: Implications for terrestrial core formation"
- KEGLER, P.; HOLZHEID, A.; MCCAMMON, C.; RUBIE, D.; PALME, H.: 21.-26.06.2009, Goldschmidt 2009, Davos, Switzerland<sup>\*2</sup>: "Terrestrial core formation: Constraints from copper partitioning", *Geochimica et Cosmochimica Acta*, 73 (13), Supp. 1, A633
- KEPLER, H.: 23.04.2009, Public lecture in the town hall of Dresden, Germany: "Vulkaneruptione: Ursachen, Auswirkungen, Vorhersagen"
- KEPLER, H.; SHCHEKA, S.: 21.-26.06.2009, Goldschmidt 2009, Davos, Switzerland<sup>\*2</sup>: "Water, carbon and noble gases in Earth's interior", *Geochimica et Cosmochimica Acta*, 73 (13), Supp. 1, A642

- KEPPLER, H.; 05.12.2009, Bayerische Akademie der Wissenschaften, München, Germany: "Kommission für geowissenschaftliche Hochdruckforschung und Bayerisches Geoinstitut Bayreuth"
- KESHAV, S.: 23.01.2009, Ecole Normale Supérieure de Lyon, France: "Carbonatites at low pressures and kimberlites at high pressures"
- KESHAV, S.: 12.06.2009, Ruhr-Universität Bochum, Geowissenschaften, Bochum, Germany: "Making magmas in the Earth"
- KESHAV, S.; GUDFINNSSON, G.H.: 18.-20.06.2009, Marie Curie Research Training Network Crust to Core – The Fate of Subducted Material Workshop 'The Deep Carbon Cycle', ETH Zurich, Switzerland (*invited*): "The transition between basaltic and carbonatitic liquids in the Earth"
- KESHAV, S.: 21.-26.06.2009, Goldschmidt 2009, Davos, Switzerland<sup>\*2</sup> (*invited*): "A tale of two ledges in the carbonated peridotite space", *Geochimica et Cosmochimica Acta*, 73 (13), Supp. 1, A643
- KESHAV, S.: 01.10.2009, Université Montpellier, Géosciences, Montpellier, France: "Liquids derived from a hydrous, carbonated peridotite"
- KESHAV, S.; GUDFINNSSON, G.H.: 14.-18.12.2009, AGU Fall Meeting, San Francisco, USA<sup>\*3</sup>: "Absence of singularity along the wet solidus of carbonated peridotite", *EOS Trans. AGU*, 90(52), Fall Meet. Suppl., Abstract MR31C-05, 2009
- KIMURA, M.; EL GORESY, A.; MIKOUCHI, T.; SUZUKI, A.; MIYAHARA, M.; OHTANI, E.: 13.-18.07.2009, 72<sup>nd</sup> Annual Meeting of the Meteoritical Society, Nancy, France: "Kushiroite, CaAl<sub>2</sub>SiO<sub>6</sub>, a new mineral in carbonaceous chondrites: its formation conditions and genetic significance in calcium-aluminum refractory inclusions"
- KONSCHAK, A.; KEPPLER, H.: 21.-26.06.2009, Goldschmidt 2009, Davos, Switzerland<sup>\*2</sup>: "A model for CO<sub>2</sub> solubility in silicate melts", *Geochimica et Cosmochimica Acta*, 73 (13), Supp. 1, A680
- LANGENHORST, F.: 10.03.2009, Plenarvortrag, Deutsche Gesellschaft für Kristallographie, Hannover, Germany: "High-pressure phases under the electron microscope: insights into Earth's interior"
- LANGENHORST, F.: 29.04.2009, Humboldt-Universität zu Berlin, Museum für Naturkunde, Berlin, Germany: "Hochdruckphasen unter dem Elektronenmikroskop: Einblicke in das Erdinnere"
- LANGENHORST, F.: 30.04.2009, Geowissenschaftliches Kolloquium, Freie Universität Berlin, Germany: "Stardust – Sternenstaub unter dem Mikroskop?"
- LANGENHORST, F.: 13.-18.07.2009, 72<sup>nd</sup> Annual Meeting of the Meteoritical Society, Nancy, France: "Shock deformation and transformation of minerals – advances by transmission electron microscopy"
- LANGENHORST, F.: 12.10.2009, Jena School for Microbial Communication Symposium: "High-pressure experiments on minerals and microbes – aims and current research trends"
- LERCHBAUMER, L.: 31.01.2009, ENB Workshop, Thurnau, Germany<sup>\*1</sup>: "Synthetic fluid inclusions: How can copper be moved into the vapor phase?"

- LERCHBAUMER, L.; AUDÉTAT, A.: 21.-26.06.2009, Goldschmidt 2009, Davos, Switzerland<sup>\*2</sup>: "Partitioning of Cu between vapor and brine – An experimental study based on LA-ICP-MS analysis of synthetic fluid inclusions", *Geochimica et Cosmochimica Acta*, 73 (13), Suppl. 1, A744
- LI, L.; EHM, L.; MCCAMMON, C.A.; GHOSE, S.; WANG, L.: 14.-18.12.2009, AGU Fall Meeting, San Francisco, USA<sup>\*3</sup>: "Cation disorder in spinels of Fe<sub>2</sub>SiO<sub>4</sub> and FeAl<sub>2</sub>O<sub>4</sub>", *EOS Trans. AGU*, 90(52), Fall Meet. Suppl., Abstract MR13A-1659, 2009
- LIU, J.; BOFFA BALLARAN, T.; CARACAS, R.; FROST, D.J.: 09.-11.09.2009, Geoitalia 2009, VII Forum Italiano di Scienze della Terra, Rimini, Italy: "The solid solution of KAlSi<sub>3</sub>O<sub>8</sub> - NaAlSi<sub>3</sub>O<sub>8</sub> hollandite: a possible host of K and Na in the mantle"
- LONGO, M.: 31.01.2009, ENB Workshop, Thurnau, Germany<sup>\*1</sup>: "Oxygen fugacity determined from iron oxidation state of (Mg,Fe)O ferropericlasite in lower mantle diamond inclusions"
- LONGO, M.; MCCAMMON, C.; BULANOVA, G.; KAMINSKY, F.V.; TAPPERT, R.: 14.-18.12.2009, AGU Fall Meeting, San Francisco, USA<sup>\*3</sup>: "Oxygen fugacity determined from iron oxidation state in natural (Mg,Fe)O ferropericlasite: new insights for lower mantle diamond formation", *EOS Trans. AGU*, 90(52), Fall Meet. Suppl., Abstract DI23A-1675, 2009
- MCCAMMON, C.: 04.02.2009, 19<sup>th</sup> ESRF Users' Meeting, Grenoble, France: "High pressure/high temperature: A view into the deep Earth"
- MCCAMMON, C.: 31.03.-02.04.2009, Antragskolloquium of the SPP 1236: 'Structures and characteristics of crystals at extremely high pressures and temperatures', Ebernburg, Germany: "Mössbauer spectroscopy at high P,T"
- MCCAMMON, C.: 12.-13.04.2009, Biologie et Sciences de la Terre, Ecole Normale Supérieure de Lyon, France: "Oxygen Fugacity: Lecture and Practical"
- MCCAMMON, C.; DUBROVINSKY, L.; NARYGINA, O.; GLAZYRIN, K.; WU, X.; KANTOR, I.; SCHÜNEMANN, V.; HEWENER, B.; WOLNY, J.; MUFFLER, K.; SERGUEEV, I.; CHUMAKOV, A.: 19.-24.07.2009, International Conference on the Applications of the Mössbauer Effect, Vienna, Austria: "Journey to the centre of the Earth"
- MCCAMMON, C.A.; DUBROVINSKY, L.S.; NARYGINA, O.; GLAZYRIN, K.; WU, X.; KANTOR, I.; SERGUEEV, I.; CHUMAKOV, A.: 14.-18.12.2009, AGU Fall Meeting, San Francisco, USA<sup>\*3</sup>: "Bulk sound velocity measurements at high P,T using nuclear inelastic scattering: Influence of spin transitions on mantle velocity profiles", *EOS Trans. AGU*, 90(52), Fall Meet. Suppl., Abstract DI21B-04, 2009
- MCENROE, S.A.; ROBINSON, P.; FABIAN, K.; GATTACCECA, J.; LANGENHORST, F.; HEIDELBACH, F.: 07.-08.02.2009, Geological Survey of Norway, Seminar Day, Trondheim, Norway: "Mineral exploration: Bridging the gap from the mineral-scale to the airborne survey"
- MCENROE, S.A.; FABIAN, K.; ROBINSON, P.; GATTACCECA, J.; LANGENHORST, F.: 04.-05.03.2009, Research Council of Norway, Petromaks Seminar, Statoil, Trondheim, Norway: "Mineral sources of remanent crustal magnetic anomalies"
- MCENROE, S.A.; FABIAN, K.; ROBINSON, P.; GATTACCECA, J.; LANGENHORST, F.: 19.-24.04.2009, EGU General Assembly 2009, Vienna, Austria. "Understanding the mineral sources of remanent crustal magnetic anomalies"

- MCENROE, S.A.: 20.10.2009, Frontiers in Earth Sciences, Ludwig-Maximilians-Universität, München, Germany: "Crustal magnetism and rocks that remember"
- MCENROE, S.A.: 22.-23.10.2009, Research on Materials Science, University of Oslo, Norway: "Lamellar magnetism: A billion year old template for future thin films?"
- MCENROE, S.A.: 14.-18.12.2009, AGU Fall Meeting, San Francisco, USA<sup>\*3</sup> (*invited*): "Rocks that remember" Bullard Lecture, EOS Trans. AGU, 90(52), Fall Meet. Suppl., Abstract GP44A-01, 2009
- MIYAHARA, M.; OHTANI, E.; KIMURA, M.; EL GORESY, A.; OZAWA, S.; NAGASE, T.: 13.-18.07.2009, 72<sup>nd</sup> Annual Meeting of the Meteoritical Society, Nancy, France: "Detailed FIB-TEM study of ringwoodite lamellae in individual olivine grains in shock-melt veins of Yamato 791384 L6 chondrite"
- MIYAJIMA, N.; WALTE, N.: 08.-11.01.2009, Kumamoto University Global COE Program 'Global Initiative Center for Pulsed Power Engineering', International COE Forum on Pulsed Power Engineering, Kumamoto, Japan: "Dislocation microtextures of perovskite and post-perovskite: TEM studies from CaIrO<sub>3</sub> analogues to MgSiO<sub>3</sub>"
- MIYAJIMA, N.: 07.05.2009, Workshop 'Electronic Excitations Studied by Non-Resonant Inelastic X-Ray Scattering at PETRA III', HASYLAB/DESY, Hamburg, Germany: "Applications of Electron Energy-Loss Spectroscopy for high pressure mineral physics"
- MIYAJIMA, N.; WALTE, N.: 26.-31.07.2009, Joint AIRAPT-22 & HPCJ-50 Conference, Tokyo, Japan: "Dislocation microtextures of perovskite and post-perovskite: TEM studies from CaIrO<sub>3</sub> analogues to MgSiO<sub>3</sub>"
- MIYAJIMA, N.: 13.-16.09.2009, DMG 2009, 87. Meeting of the German Mineralogical Society, Halle, Germany: "Burgers vector determination in deformed minerals using thickness fringes in weak-beam dark-field TEM images"
- MOOKHERJEE, M.: 07.01.2009, Indian Institute of Technology, Bombay (Mumbai), India: "Water in Earth materials"
- MOOKHERJEE, M.; STEINLE-NEUMANN, G.: 21.-26.06.2009, Goldschmidt 2009, Davos, Switzerland<sup>\*2</sup>: "Structure and elasticity of hollandite at high pressures", *Geochimica et Cosmochimica Acta*, 73 (13), Suppl. 1, A898
- MOOKHERJEE, M.; STEINLE-NEUMANN, G.: 04.-06.03.2009, c2c mid-term review meeting, Sevilla, Spain: "Structure and elasticity of hollandite"
- MOOKHERJEE, M.: 28.10.2009, University College London, Department of Earth Sciences, London, UK: "Volatiles in the Earth's interior"
- MOOKHERJEE, M.; KEPPLER, H.; MANNING, C.E.: 14.-18.12.2009, AGU Fall Meeting, San Francisco, USA<sup>\*3</sup>: "*In situ* Raman spectroscopic study of aluminate speciation in H<sub>2</sub>O-KOH solutions at high pressures and temperatures", EOS Trans. AGU, 90(52), Fall Meet. Suppl., Abstract V52A-04, 2009
- MOOKHERJEE, M.; DE KOKER, N.; STIXRUDE, L.P.; KARKI, B.B.: 14.-18.12.2009, AGU Fall Meeting, San Francisco, USA<sup>\*3</sup>: "H<sub>2</sub>O and CO<sub>2</sub> bearing silicate melts at high-pressures", EOS Trans. AGU, 90(52), Fall Meet. Suppl., Abstract MR31C-06, 2009
- NARYGINA, O.: 31.01.2009, ENB Workshop, Thurnau, Germany<sup>\*1</sup>: "Spin state of iron in (Mg,Fe)(Si,Al)O<sub>3</sub> perovskite"

- NARYGINA, O.; KANTOR, I.Yu.; MCCAMMON, C.A.; DUBROVINSKY, L.S.: 06.-11.09.2009, 47<sup>th</sup> EHPRG International Conference, Paris, France: "Poster Electronic state of Fe<sup>2+</sup> in (Mg,Fe)(Si,Al)O<sub>3</sub> perovskite and (Mg,Fe)SiO<sub>3</sub> majorite at pressures up to 81 GPa and temperatures up to 800K"
- NAZZARENI, S.; COMODI, P.; DUBROVINSKY, L.; BINDI, L.: 09.-11.09.2009, Geoitalia 2009, VII Forum Italiano di Scienze della Terra, Rimini, Italy: "The crystal structure and HP behavior of gypsum-II from synchrotron single-crystal and powder X-ray diffraction"
- NI, H.; KEPLER, H.: 14.-18.12.2009, AGU Fall Meeting, San Francisco, USA<sup>\*3</sup>: "Electrical conductivity of albite melts at high pressures", EOS Trans. AGU, 90(52), Fall Meet. Suppl., Abstract MR43A-1867, 2009
- OTSUKA, K.; MCCAMMON, C.; KARATO, S.: 14.-19.06.2009: Gordon Research Conference 'Interior of the Earth', South Hadley, USA: "Tetrahedral occupancy of ferric iron in (Mg,Fe)O at high pressures: Implications for point defects in the lower mantle"
- OTSUKA, K.; MCCAMMON, C.; KARATO, S.: 19.-22.06.2009, 2009 COMPRES Annual Meeting, Bretton Woods, USA: "Tetrahedral occupancy of ferric iron in (Mg,Fe)O at high pressures: Implications for point defects in the lower mantle"
- OVSYANNIKOV, S.V.; SHCHENNIKOV, V.V.; MANAKOV, A.Y.; LIKHACHEVA, A.Y.; BERGER, I.F.; VORONTSOV, G.V.; ANCHAROV, A.I.: 04.-14.06.2009, International School of Crystallography, Erice, Italy: "Correlation of structural and transport properties of thermoelectric materials at high pressure", p. 668
- OVSYANNIKOV, S.V.; POLIAN, A.; GAUTHIER, M.; MUNSCH, P.; CHERVIN, J.C.; LE MARCHAND, G.: 26.-31.07.2009, Joint AIRAPT-22 & HPCJ-50 Conference, Tokyo, Japan: "Raman spectroscopy of B<sub>12</sub>As<sub>2</sub> and B<sub>12</sub>P<sub>2</sub> single crystals at pressures to 100 GPa", p. 34
- OVSYANNIKOV, S.V.; POLIAN, A.; GAUTHIER, M.; MUNSCH, P.; CHERVIN, J.C.; LE MARCHAND, G.: 06.-11.09.2009, 47<sup>th</sup> EHPRG International Conference, Paris, France: "Compression of B<sub>12</sub>As<sub>2</sub> and B<sub>12</sub>P<sub>2</sub> single crystals beyond 100 GPa: a Raman study", p. 236
- OZAWA, S.; IRELAND, T.R.; EL GORESY, A.; OHTANI, E.: 13.-18.07.2009, 72<sup>nd</sup> Annual Meeting of the Meteoritical Society, Nancy, France: "U-PB dating of baddeleyite in Shergotty, Zagami and NWA 2737: Implications for crystallization and impact ages of Martian meteorites"
- POLIAN, A.; OVSYANNIKOV, S.V.; GAUTHIER, M.; MUNSCH, P.; CHERVIN, J.C.; LE MARCHAND, G.: 28.03.-02.04.2009, SMEC2009, Study of Matter at Extreme Conditions, Miami, USA: "Boron and boron-rich solids at high pressures", p. 437-445
- POLLOK, K.; HELLIGE, K.; HARRIES, D.; PEIFFER, S.: 21.-26.06.2009, Goldschmidt 2009, Davos, Switzerland<sup>\*2</sup>: "Redox processes at the nanoscale: A TEM perspective of iron sulphide – iron (oxyhydr)oxide reactions", Geochimica et Cosmochimica Acta, 73 (13), Supp. 1, A1039
- POLLOK, K.; HARRIES, D.; HOPF, J.; HELLIGE, K.; SITTE, J.; PEIFFER, S.; KÜSEL, K.; HOHELLA Jr., M.F.; LANGENHORST, F.: 13.-16.09.2009, DMG 2009, 87. Meeting of the German Mineralogical Society, Halle, Germany: "Biotic and abiotic alteration and formation of sulfides: differences and commonalities", Hallesches Jahrbuch für Geowissenschaften 31, 187

- POLLOK, K.; HELLIGE, K.; PEIFFER, S.: 28.-29.09.2009, 8. Jenaer Sanierungskolloquium, Jena, Germany (*invited*): "The formation of sedimentary sulfides under anoxic conditions: An experimental approach"
- POLLOK, K.; HARRIES, D.; ETZEL, K.; HOPF, J.; LANGENHORST, F.: 10.-11.11.2009, 1. Status-Seminar 'Mineral Surfaces – From Atomic Processes to Industrial Application', Bayreuth, Germany: "MIMOS – Stand des Projektes"
- POTAPKIN, V.; CHUMAKOV, A.I.; RÜFFER, R.; SMIRNOV, G.V.; POPOV, S.L.; DUBROVINSKY, L.; MCCAMMON, C.: 19.-24.07.2009, International Conference on the Applications of the Mössbauer Effect, Vienna, Austria: "Development of synchrotron Mössbauer source for geophysical studies at the ESRF"
- PRESNALL, D.C.; GUDFINNSSON, G.H.: 21.-26.06.2009, Goldschmidt 2009, Davos, Switzerland<sup>\*2</sup>: "Hawaiian volcanism - Magmas from the seismic low-velocity zone", *Geochimica et Cosmochimica Acta*, 73 (13), Supp. 1, A1051
- RUBIE, D.C.: 31.01.2009, ENB Workshop, Thurnau, Germany<sup>\*1</sup>: "Experimental studies of the early evolution of the Earth"
- RUBIE, D.C.; FROST, D.J.; ASAHARA, Y.; TSUNO, K.; MANN, U.: 28.03.-02.04.2009, SMEC2009, Study of Matter at Extreme Conditions, Miami, USA: "Composition of the Earth's core and reaction at the core-mantle boundary"
- RUBIE, D.C.: 20.11.2009, Planetary Science Institute, Tucson, USA: "Accretion, composition and core-mantle differentiation of the Earth"
- SAMUEL, H.: 28.06.-03.07.2009, 11<sup>th</sup> International Workshop on Modeling of Mantle Convection and Lithospheric Dynamics, Braunwald, Switzerland (*invited keynote speaker*): "Dynamics and consequences of core formation in terrestrial Planets"
- SCHIAVI, F.; KOBAYASHI, K.; MORIGUTI, T.; NAKAMURA, E.; POMPILIO, M.; TIEPOLO, M.; VANNUCCI, R.: 11.06.-13.06.2009, Conferenza A. Rittmann 'La vulcanologia italiana: stato dell'arte e prospettive future', Nicolosi (Catania), Italy: "Degassing, crystallization and eruption dynamics at Stromboli inferred from trace elements and lithium isotopic composition of juvenile ashes from the 2003 activity"
- SCHIAVI, F.; WALTE, N.; KEPPLER, H.: 09.-11.09.2009, Geoitalia 2009, VII Forum Italiano di Scienze della Terra, Rimini, Italy: "The first direct observation of crystallization processes in a basaltic-andesitic melt with the moissanite cell", Abstract Volume, 222
- SCHIAVI, F.; KOBAYASHI, K.; MORIGUTI, T.; NAKAMURA, E.; POMPILIO, M.; TIEPOLO, M.; VANNUCCI, R.: 09.-11.09.2009, Geoitalia 2009, VII Forum Italiano di Scienze della Terra, Rimini, Italy: "Degassing, crystallization and eruption dynamics at Stromboli volcano: trace elements and lithium isotopes evidence from juvenile ashes ejected during the 2003 activity", Abstract Volume, 227
- SCHIAVI, F.; WALTE, N.; KEPPLER, H.: 14.-18.12.2009, AGU Fall Meeting, San Francisco, USA<sup>\*3</sup>: "Real-time observation of crystallization and textural evolution in magmatic systems with the moissanite cell", *EOS Trans. AGU*, 90(52), Fall Meet. Suppl., Abstract V53C-04, 2009
- SHCHENNIKOV, V.V.; OVSYANNIKOV, S.V.: 28.03.-02.04.2009, SMEC2009, Study of Matter at Extreme Conditions, Miami, USA: "Measurement of Seebeck effect (thermopower) at high pressures", p. 49-50

- SHCHENNIKOV, V.V.; OVSYANNIKOV, S.V.: 26.-31.07.2009, Joint AIRAPT-22 & HPCJ-50 Conference, Tokyo, Japan: "High-pressure thermopower technique and its application", p. 265
- SHCHENNIKOV, V.V.; VORONTSOV, G.V.; KOMAROVSKY, I.A.; SHCHENNIKOV Jr., V.V.; OVSYANNIKOV, S.V.; SHNIPOVA, E.M.: 26.-31.07.2009, Joint AIRAPT-22 & HPCJ-50 Conference, Tokyo, Japan: "Analysis of multiphase states in vicinity of pressure-induced phase transitions", p. 124
- SHCHENNIKOV, V.V.; OVSYANNIKOV, S.V.: 06.-11.09.2009, 47<sup>th</sup> EHPRG International Conference, Paris, France: "New approaches for probing of phase transitions under pressure", p. 129
- SHCHENNIKOV, V.V.; OVSYANNIKOV, S.V.; KOMAROVSKY, I.A.; VORONTSOV, G.V.; SHCHENNIKOV Jr., V.V.: 06.-11.09.2009, 47<sup>th</sup> EHPRG International Conference, Paris, France: "Multiphase states in the vicinity of phase transitions", p. 261
- SHEKHAR, S.: 31.01.2009, ENB Workshop, Thurnau, Germany<sup>\*1</sup>: "Simple shear deformation experiments on olivine at high P-T condition using the D-DIA"
- STAGNO, V.: 31.01.2009, ENB Workshop, Thurnau, Germany<sup>\*1</sup>: "Carbonates, diamonds and melts in the Earth's mantle"
- STAGNO, V.; FROST, D.J.: 21.-26.06.2009, Goldschmidt 2009, Davos, Switzerland<sup>\*2</sup>: "The carbon/carbonate equilibria in the Earth's mantle as function of pressure, temperature and oxygen fugacity", *Geochimica et Cosmochimica Acta*, 73 (13), Supp. 1, A1262
- STAGNO, V.; FROST, D.J.; MCCAMMON, C.A.: 14.-18.12.2009, AGU Fall Meeting, San Francisco, USA<sup>\*3</sup>: "The effect of the oxygen fugacity on carbon speciation in the Earth's mantle", *EOS Trans. AGU*, 90(52), Fall Meet. Suppl., Abstract V11D-1986, 2009
- STEINLE-NEUMANN, G.: 21.-26.06.2009, Goldschmidt 2009, Davos, Switzerland<sup>\*2</sup>: "Magneto-elastic effects in compressed cobalt", *Geochimica et Cosmochimica Acta*, 73 (13), Supp. 1, A1270
- STEINLE-NEUMANN, G.: 20.-24.07.2009, ICTP Workshop 'From Core to Crust: Towards an integrated vision of Earth's interior' Trieste, Italy: "Computing deep Earth structure"
- STEINLE-NEUMANN, G.: 20.10.2009, Charles University Prague, Institute of Petrology and Structural Geology, Prague, Czech Republic: "Mineralogy meets geophysics – deep earth structure"
- STEINLE-NEUMANN, G.: 21.10.2009, Charles University Prague, Department of Geophysics, Czech Republic: "Deep Earth structure from a mineralogical perspective"
- STEINLE-NEUMANN, G.; MOOKHERJEE, M.: 14.-18.12.2009, AGU Fall Meeting, San Francisco, USA<sup>\*3</sup>: "Carbon content in the Earth's inner core from the elasticity of iron carbide at high pressure", *EOS Trans. AGU*, 90(52), Fall Meet. Suppl., Abstract DI33A-1618, 2009
- TANG, Z.: 31.01.2009, ENB Workshop, Thurnau, Germany<sup>\*1</sup>: "Electronic and magnetic structure of fayalite"
- TIBBETTS, N.J.; BIZIMIS, M.; KESHAV, S.; LONGO, M.; SALTERS, V.J.; MCCAMMON, C.A.: 14.-18.12.2009, AGU Fall Meeting, San Francisco, USA<sup>\*3</sup>: "The oxygen fugacity structure of the sub-oceanic lithosphere and upper mantle as recorded by spinel peridotite and garnet clinopyroxenite xenoliths from O'ahu, Hawai'i", *EOS Trans. AGU*, 90(52), Fall Meet. Suppl., Abstract V33C-2052, 2009

- TIN, Q.D.; KEPPLER, H.: 13.-16.09.2009, DMG 2009, 87. Meeting of the German Mineralogical Society, Halle, Germany: "The origin of the lanthanide tetrad effect in granites"
- VAN MIERLO, W.; LANGENHORST, F.; MIYAJIMA, N.; FROST, D.: 08.-11.01.2009, Kumamoto University Global COE Program 'Global Initiative Center for Pulsed Power Engineering', International COE Forum on Pulsed Power Engineering & Young Researcher Training Camp, Kumamoto, Japan: "A high pressure diffusion study of the majorite component in pyrope"
- VAN MIERLO, W.; LANGENHORST, F.; MIYAJIMA, N.; FROST, D.: 31.01.2009, ENB Workshop, Thurnau, Germany<sup>\*1</sup>: "A high pressure diffusion study of the majorite component in pyrope"
- VAN MIERLO, W.; LANGENHORST, F.; MIYAJIMA, N.; FROST, D.: 04.-06.03.2009, c2c mid-term review meeting, Sevilla, Spain: "A high pressure diffusion study of the majorite component in pyrope"
- VAN MIERLO, W.; LANGENHORST, F.; MIYAJIMA, N.; FROST, D.: 04.-06.03.2009, c2c mid-term review meeting, Sevilla, Spain: "Diffusion of the majorite component in garnet"
- VAN MIERLO, W.; LANGENHORST, L.; MIYAJIMA, N.; FROST, D.; RUBIE, D.: 29.08.-02.09.2009, MAPT (Micro-Analysis, Processes, Time) Conference, Edinburgh, U.K.: "Diffusion in the pyrope – majorite system"
- WALTE, N.P.; HEIDELBACH, F.; CORDIER, P.; RUBIE, D.C.: 07.-09.09.2009, Deformation, Rheology & Tectonics 2009, Liverpool, UK: "Deformation and crystallographic preferred orientation of coesite and retrograde quartz"
- WEIGEL, C.; KEPPLER, H.; MCCAMMON, C.: 08.-11.01.2009, Kumamoto University Global COE Program 'Global Initiative Center for Pulsed Power Engineering', International COE Forum on Pulsed Power Engineering & Young Researcher Training Camp, Kumamoto, Japan: "<sup>57</sup>Fe Mössbauer spectroscopy applied to silicate glasses at extreme conditions"
- WEIGEL, C.; KEPPLER, H.; MCCAMMON, C.: 06.-13.09.2009, Conference on the Physics of Non-Crystalline Solids, Foz do Iguacu, Brazil: "<sup>57</sup>Fe Mössbauer spectroscopy applied to silicate glasses at high temperature"
- WU, X.; STEINLE-NEUMANN, G.: 21.-26.06.2009, Goldschmidt 2009, Davos, Switzerland<sup>\*2</sup>: "Phase stability and elasticity of ScAlO<sub>3</sub> at high pressure", *Geochimica et Cosmochimica Acta*, 73 (13), Supp. 1, A1454
- WU, X.; STEINLE-NEUMANN, G.; NARYGINA, O.; KANTOR, I.; MCCAMMON, C.; PRAKAPENKA, V.; SWAMY, V.; DUBROVINSKY, L.: 26.-31.07.2009, Joint AIRAPT-22 & HPCJ-50 Conference, Tokyo, Japan: "Decomposition of FeTiO<sub>3</sub> perovskite to (Fe<sub>1-δ</sub>,Ti<sub>δ</sub>)O and Fe<sub>1+δ</sub>Ti<sub>2-δ</sub>O<sub>5</sub>"
- ZARECHNAYA, E.Yu.: 20.01.2009, Universite P&M Curie, Physique des Milieux Denses, Paris, France (*invited*): "High pressure high temperature phase of boron and its properties"
- ZARECHNAYA, E.Yu.: 31.01.2009, ENB Workshop, Thurnau, Germany<sup>\*1</sup>: "High pressure high temperature phase of boron and its properties"

ZARECHNAYA, E.Yu.; DUBROVINSKY, L.; DUBROVINSKAIA, N.; MIKHAYLUSHKIN, A.; SIMAK, S.I.; ABRIKOSOV, I.A.: 26.-31.07.2009, Joint AIRAPT-22 & HPCJ-50 Conference, Tokyo, Japan: "The ground state properties of orthorhombic boron: investigation from 'first principles'"

ZARECHNAYA, E.Yu.; DUBROVINSKY, L.; DUBROVINSKAIA, N.; FILINCHUK, Y.; CHERNYSHOV, D.; DMITRIEV, V.; MIYAJIMA, N.; EL GORESY, A.; BRAUN, H.F.; VAN SMAALEN, S.; KANTOR, I.; KANTOR, A.; PRAKAPENKA, V.; HANFLAND, M.; MIKHAYLUSHKIN, A.; SIMAK, S.I.; ABRIKOSOV, I.A.: 04.-14.06.2009, International School of Crystallography, Erice, Italy: "High pressure high temperature phase of boron"

<sup>\*1</sup> **Elitenetzwerk Bayern, 4<sup>th</sup> Joint Student Workshop, Oxides (Universität Bayreuth, Fraunhofer ISC Würzburg), MAP Advanced Materials and Processes (Universität Erlangen), 31.01.2009, Schloss Thurnau, Germany**

<sup>\*2</sup> **Goldschmidt<sup>TM</sup>2009: 19<sup>th</sup> V.M. Goldschmidt<sup>TM</sup> Conference "Challenges to Our Volatile Planet", 21.-26.06.2009, Davos, Switzerland – Geochimica et Cosmochimica Acta 73, Issue 13, Supplement 1**

<sup>\*3</sup> **AGU: American Geophysical Union Fall Meeting, 14.-18.12.2009, San Francisco, USA – EOS Transactions, American Geophysical Union, 90(52), AGU Fall Meeting 2009 Supplement**

#### *5.4 Lectures and seminars at Bayerisches Geoinstitut*

AUDÉTAT, A., Bayerisches Geoinstitut, Bayreuth, Germany: "The use of fluid and melt inclusions in the study of ore deposits", 23.07.2009

AGOSTINI, C., Università degli Studi di Camerino, Dipartimento di Scienze della Terra, Camerino, Italy: "Kinetics of crystallization and dissolution of clinopyroxenes in Stromboli magmas", 20.04.2009

BOFFA BALLARAN, T., Bayerisches Geoinstitut, Bayreuth, Germany: "High-pressure behaviour of a very Fe and Al-rich MgSiO<sub>3</sub> perovskite", 16.07.2009

BOUVIER, A., Arizona State University, School of Earth and Space Exploration, Tempe, USA: "The evolution of Mars, a perspective from SNC meteorites", 08.01.2009

BUISMAN, I., Bayerisches Geoinstitut, Bayreuth, Germany: "Non-potassic melts in CMAS-CO<sub>2</sub>-H<sub>2</sub>O-K<sub>2</sub>O model peridotite", 27.10.2009

CASATI, N.P., Università degli Studi di Milano, Dipartimento di Chimica Strutturale e Stereochimica Inorganica, Milano, Italy: "Single crystal high pressure studies of molecular systems", 05.03.2009

COHEN, R., Carnegie Institution of Washington, Geophysical Laboratory, Washington D.C., USA: "Theory of minerals at high pressures beyond band theory", 13.01.2009

CÔTÉ, A., University College London, Department of Earth Sciences, London, U.K.: "The structure and composition of the Earth's inner core: An *ab initio* approach", 16.06.2009

- DIETRICH, W., Bayerisches Geoinstitut, Bayreuth, Germany: "The effect of insulating lids on the dynamics and stirring properties in Rayleigh-Bénard convective systems", 23.04.2009
- ESCUADERO, A., Bayerisches Geoinstitut, Bayreuth, Germany: "Phase relations in the  $\text{Al}_2\text{O}_3 - \text{TiO}_2$  system at pressure up to 20 GPa", 02.07.2009
- EWING, R.C., University of Michigan, Department of Geological Sciences, Ann Arbor, USA: "Nuclear energy issues: Plutonium vs. Carbon", 29.06.2009
- EWING, R.C., University of Michigan, Department of Geological Sciences, Ann Arbor, USA: "The elegant response of a simple structure to extreme conditions of irradiation and pressure", 30.06.2009
- GHOSH, S., Tohoku University, Earth and Planetary Material Physics Research Group, Sendai, Japan: "The role of volatiles ( $\text{CO}_2/\text{H}_2\text{O}$ ) in phase relations and melting of Earth's mantle", 06.07.2009
- GREENBERG, E., Bayerisches Geoinstitut, Bayreuth, Germany: "High-pressure studies of  $\text{AFe}_2\text{O}_4$  compounds", 17.12.2009
- HAWKESWORTH, C., University of Bristol, Department of Earth Sciences, Bristol, U.K.: "The generation and reworking of Hadean crust, insights from the zircon archive", 12.05.2009
- HAWKESWORTH, C., University of Bristol, Department of Earth Sciences, Bristol, U.K.: "Granites, granulites and the continental record", 13.05.2009
- HUNT, S., University College London, Department of Earth Sciences, London, U.K.: "Weakening of calcium iridate during its transformation from perovskite to post-perovskite", 12.11.2009
- INOUE, T., Ehime University, Geodynamics Research Center, Matsuyama, Japan: "Experimental partitioning of water in upper mantle, mantle transition zone and lower mantle", 25.03.2009
- KAMENETSKY, V., University of Tasmania, School of Earth Sciences, Centre of Excellence in Ore Deposits, Hobart, Tasmania, Australia: "New identity of kimberlite parental melts and implication for kimberlite magma ascent and eruption", 15.06.2009
- KAWAMOTO, T., Kyoto University, Institute for Geothermal Sciences, Graduate School of Science, Kyoto, Japan: "X-ray radiography to observe unmixing and mixing between magmas and aqueous fluids: implication to subduction zone magmatism", 19.08.2009
- KESHAV, S., Bayerisches Geoinstitut, Bayreuth, Germany: "The basalt-carbonatite transition in the Earth – revisited", 04.06.2009
- KIND, R., Helmholtz-Zentrum Potsdam, Deutsches GeoForschungsZentrum GFZ, Potsdam, Germany: "Seismic techniques to study structures in the upper mantle", 08.06.2009
- KIND, R., Helmholtz-Zentrum Potsdam, Deutsches GeoForschungsZentrum GFZ, Potsdam, Germany: "New results on seismic discontinuities in the upper mantle", 09.06.2009
- KOGURE, T., University of Tokyo, Department of Earth and Planetary Sciences, Tokyo, Japan: "High-resolution electron microscopy for silicates; its history and future", 02.04.2009
- KOGURE, T., University of Tokyo, Department of Earth and Planetary Sciences, Tokyo, Japan: "Investigation of layered materials using HRTEM and XRD simulations", 06.04.2009

- LI, Y., Bayerisches Geoinstitut, Bayreuth, Germany: "Sulfide-silicate melt partitioning of ore metals during partial melting of metasomatized mantle", 10.09.2009
- MARSH, B., Johns Hopkins University, Department of Earth & Planetary Sciences, Baltimore, USA: "Magma dynamics: Towards a unified theory", 09.11.2009
- MARSH, B., Johns Hopkins University, Department of Earth & Planetary Sciences, Baltimore, USA: "Fundamentals of a magmatic mush column: McMurdo Dry Valleys, Antarctica", 10.11.2009
- MCENROE, Bayerisches Geoinstitut, Bayreuth, Germany: "Crustal magnetism and rocks that remember", 26.11.2009
- MIYAJIMA, N., Bayerisches Geoinstitut, Bayreuth, Germany: "Rheological properties of silicate perovskite and implications for the Earth's lower mantle: TEM studies", 29.10.2009
- MOOKHERJEE, M., Bayerisches Geoinstitut, Bayreuth, Germany: "Volatiles in the Earth's interior", 19.11.2009
- MOSTEFAOUI, S., Museum National d'Histoire Naturelle, Paris, France: "NanoSIMS application in extraterrestrial research", 25.05.2009
- NAKAJIMA, Y., Tokyo Institute of Technology, Department of Earth and Planetary Sciences, Tokyo, Japan: "Experimental study on the systems Fe-C and Fe-H", 22.01.2009
- NARYGINA, O., Bayerisches Geoinstitut, Bayreuth, Germany: "Spin state of iron in lower mantle perovskite", 29.01.2009
- NOVELLA, D., Bayerisches Geoinstitut, Bayreuth, Germany: "Some complications in melting of carbonated peridotite at 2-3 GPa", 03.12.2009
- NIMMO, F., University of California Santa Cruz, Earth & Planetary Sciences Department, Santa Cruz, USA: "What's going on at Enceladus?", 27.04.2009
- NIMMO, F., University of California Santa Cruz, Earth & Planetary Sciences Department, Santa Cruz, USA: "Accretion of the terrestrial planets", 28.04.2009
- PANERO, W., Ohio State University, Mineral Physics Research Group, Columbus, USA: "Anisotropic fabric of the inner core", 15.09.2009
- PANERO, W., Ohio State University, Mineral Physics Research Group, Columbus, USA: "Water Storage and Cycling in the Earth's Mantle", 21.09.2009
- PINHEIRO, K., ETH Zürich, Departement Erdwissenschaften, Switzerland: "Mantle electrical conductivity estimates from geomagnetic jerk observations", 05.02.2009
- POLLOK, K., Bayerisches Geoinstitut, Bayreuth, Germany: "A TEM perspective on dissolution and growth of sulphides in low temperature environments", 09.07.2009
- POMMIER, A., CNRS, Institut des Sciences de la Terre d'Orléans, France: "Electrical measurements in laboratory: Methodology, concepts and applications", 07.07.2009
- POTAPKIN, V., European Synchrotron Radiation Facility, Grenoble, France: "Development of synchrotron Mössbauer source for geophysical studies at the ESRF", 24.09.2009
- QIN, J., Sichuan University, Institute of Atomic and Molecular Physics, Chengdu, China: Part I: "High pressure and high temperature behaviour of MAX phases ( $Ti_2AlC$ ,  $Ti_2AlN$ , and  $Ti_3SiC_2$ )"; Part II: "Synthesis and sintering of B-based hard and superhard materials under high pressure and high temperature", 17.09.2009
- RICARD, Y., Université de Lyon, Laboratoire de Science de la Terre, Lyon, France: "Accretion and differentiation of planets", 19.01.2009

- RICARD, Y., Université de Lyon, Laboratoire de Science de la Terre, Lyon, France: "A model of grain size evolution during deformation", 20.01.2009
- SHCHEKA, S., Bayerisches Geoinstitut, Bayreuth, Germany: "Solubility of noble gases in silicate perovskite", 15.01.2009
- STAGNO, V., Bayerisches Geoinstitut, Bayreuth, Germany: "An experimental study on the carbon-carbonates equilibria in the Earth's mantle", 12.03.2009
- STEINLE-NEUMANN, G., Bayerisches Geoinstitut, Bayreuth, Germany: "Elastic structure of minerals and the mantle", 05.11.2009
- TOSI, N., Charles University, Prague, Czech Republic: "Sensitivity of the geoid to subduction into the deep mantle", 28.05.2009
- WALTE, N., Bayerisches Geoinstitut, Bayreuth, Germany: "Strain rate dependent melt interconnection and strain localization in systems with high-dihedral-angle melt phases", 10.12.2009
- WEIGEL, C., Bayerisches Geoinstitut, Bayreuth, Germany: "High-temperature and high-pressure spectroscopic studies of Fe-bearing silicate glasses", 06.08.2009
- ZARECHNAYA, E., Bayerisches Geoinstitut, Bayreuth, Germany: "High pressure high temperature phase of boron and it's properties", 12.02.2009

*Lectures and poster presentations during the GRC\*-BGI Workshop on Deep Earth Mineralogy, Bayreuth, Germany: 17.-19.06.2009*

\* Geodynamics Research Center, Ehime University, Matsuyama, Japan

Lectures:

- BALI, E.; AUDETAT, A.; KEPPLER, H.: "Mobility of U and Th in subduction zones – a synthetic fluid inclusion study"
- CHUST, T.; STEINLE-NEUMANN, G.; BUNGE, H.-P.: "Integrated modelling of mineral physics and mantle convection"
- DE KOKER, N.: "Thermal conductivity of MgO Periclase from equilibrium first principles molecular dynamics"
- FROST, D.; TSUNO, K.; RUBIE, D.: "The light element in the Earth's core and reactions at the core mantle boundary"
- GRÉAUX, S.; NISHIYAMA, N.; KONO, Y.; OHFUJI, H.; GAUTRON, L.; IRIFUNE, T.: "High pressure and high temperature phase relation of  $\text{Ca}_3\text{Al}_2\text{Si}_3\text{O}_{12}$  grossular garnet"
- IIZUKA, R.; KAGI, H.; KOMATSU, K.; USHIJIMA, D.; NAGAI, T.; NAKANO, S.; SANO-FURUKAWA, A.: "*In situ* observation of the pressure-induced phase transition in  $\text{Ca}(\text{OH})_2$ "
- ISHIKAWA, T.; TSUCHIYA, T.; TSUCHIYA, J.: "Exploring crystal structures of iron at Earth's inner core pressure by free energy surface trekking"
- KAWAZOE, T.; NISHIYAMA, N.; NISHIHARA, Y.; IRIFUNE, T.: "Preliminary experiments using the deformation-DIA apparatus 'MADONNA'"

- KESHAV, S.; GUDFINNSSON, G.H.: "The transition between basaltic and carbonatitic liquids in the Earth"
- KOMATSU, K.: " Neutron scattering experiments in ISIS and ILL – the recent developments for the single crystal diffraction under high pressure"
- KONO, Y.; IRIFUNE, T.; HIGO, Y.; INOUE, T.; BARNHOORN, A.: "Pressure-scale-independent  $V_p$ - $V_s$ - $P$ - $V$ - $T$  relation of MgO derived by simultaneous elastic wave velocity and *in situ* X-ray measurements"
- KUNIMOTO, T.; IRIFUNE, T.: "Development of a 6-8-2 type multianvil apparatus and its application"
- KUWAYAMA, Y.; HIROSE, K.: "Phase relations of iron alloys at high pressure and high temperature"
- LONGO, M.; MCCAMMON, C.A.; BULANOVA, G.; KAMINSKY, F.; TAPPERT, R.: "Iron oxidation state in (Mg,Fe)O: Calibration of the flank method on synthetic samples and application to natural inclusions in lower mantle diamonds"
- MACHIDA, S.; HIRAI, H.; KAWAMURA, T.; YAMAMOTO, Y.; YAGI, T.: "Structural changes and intermolecular interactions for hydrogen hydrate under high pressure"
- MCCAMMON, C.; DUBROVINSKY, L.; NARYGINA, O.; GLAZYRIN, K.; WU, X.; KANTOR, I.; SCHÜNEMANN, V.; HEWENER, B.; WOLNY, J.; MUFFLER, K.; SERGUEEV, I.; CHUMAKOV, A.: "Mössbauer spectroscopy at high P,T using a synchrotron source"
- MIYAJIMA, N.; LANGENHORST, F.; HIROSE, K.: "Fe  $L_{2,3}$ -edge ELNES of high pressure minerals in a K-bearing MORB"
- MOOKHERJEE, M.; STEINLE-NEUMANN, G.: "Structure and elasticity of hollandite at high pressures"
- NARYGINA, O.; DUBROVINSKY, L.; MIYAJIMA, N.: "Phase relations in Fe-Ni-C system at high pressures and temperatures: implication to the Earth's core"
- NISHIHARA, Y.; FUNAKOSHI, K.; HIGO, Y.; TSUJINO, N.; KAWAZOE, T.; KUBO, T.; SHIMOJUKU, A.; TERASAKI, H., NISHIYAMA, N.: "Experimental study on the deep Earth rheology: Stress relaxation test of olivine and recent technical developments in deformation experiments under high pressure"
- NISHIYAMA, N.; YANBIN, Y.; IRIFUNE, T.; UCHIDA, T.; SANEHIRA, T.; KAWAZOE, T.; NISHIHARA, Y.; RIVERS, M.L.; SUTTON, S.R.: "Phase relations in harzburgite at lower part of the mantle transition zone and the uppermost lower mantle"
- ODAKE, S.; KAGI, H.; ARAKAWA, M.; OHTA, A.; HARTE, B.: "Micro-XANES study of the oxidation state of chromium in natural ferropericlae inclusions"
- SHCHEKA, S.; KEPPLER, H.: "Argon solubility in aluminous MgSiO<sub>3</sub>-perovskite"
- SHEKHAR, S.; WALTE, N.; FROST, D.; HEIDELBACH, F.: " Effect of pressure on olivine slip system"
- SHINOZAKI, A.; HIRAI, H.; HAMANE, D.; KAGI, H.; KONDO, T.; YAGI, T.: "Polarization of methane molecule and reaction between released hydrogen and olivine in the Earth's mantle"
- SPENGLER, D.; NISHIHARA, Y.: "Majorite breakdown kinetics during mantle upwelling – significance and experimental strategy"

STAGNO, V.; FROST, D.J.: "The carbon/carbonate equilibria in the Earth's mantle as function of pressure, temperature and oxygen fugacity"

TANGE, Y.: "High-pressure techniques using sintered diamond anvils in multianvil apparatus and its applications"

TSUCHIYA, J.; TSUCHIYA, T.: "First principles investigation on hydrous wadsleyite under pressure"

USUI, Y.; TSUCHIYA, T.: "Seismic anisotropy in the D" layer beneath the antarctic ocean"

WALTE, N.P.; HEIDELBACH, F.; RUBIE, D.; HUNT, S.; DOBSON, D.: "Crystallographic preferred orientation and relative viscosity of upper and lower mantle phases with the deformation DIA"

Poster presentations:

BOFFA BALLARAN, T.; FROST, D.J.; POZZOBON, R.: "Structure and density of perovskite from subducted oceanic crust in the lower mantle"

DE KOKER, N.; STIXRUDE, L.: "Self-consistent thermodynamic description of silicate liquids"

ESCUADERO, A.; MIYAJIMA, N.; LANGENHORST, F.: "Chemical and microstructural characteristics of TiO<sub>2</sub> in ultra high pressure metamorphic rocks. New insights into the estimation of pressure and temperature"

ESCUADERO, A.; TSUNO, K.; LANGENHORST, F.: "Phase relations in the Al<sub>2</sub>O<sub>3</sub> – TiO<sub>2</sub> system at pressures up to 20 GPa"

ETZEL, K.; POLLOK, K.: "Effects of microstructure on dissolution of sulfides"

GLAZYRIN, K.; DUBROVINSKY, L.D.: "High pressure electronic transition in hcp Fe and Fe<sub>0.9</sub>Ni<sub>0.1</sub>"

GRÉAUX, S.; NISHIYAMA, N.; KONO, Y.; OHFUJI, H.; GAUTRON, L.; IRIFUNE, T.: "High pressure and high temperature phase relation of Ca<sub>3</sub>Al<sub>2</sub>Si<sub>3</sub>O<sub>12</sub> grossular garnet"

HARRIES, D.; POLLOK, K.; ETZEL, K.; LANGENHORST, F.: "Structural complexity in pyrrhotites: What are the implications for fluid-mineral interactions?"

HEIDELBACH, F.; TERRY, M.P.: "Inherited fabric in a eclogite symplectite: evidence for deformation under ultra-high pressure conditions"

HOBBS, L.K.; KEPPLER, H.: "Partitioning of sulphur dioxide between dacitic melt and aqueous fluid phases"

IIZUKA, R.; KAGI, H.; KOMATSU, K.; USHIJIMA, D.; NAGAI, T.; NAKANO, S.; SANO-FURUKAWA, A.: "*In situ* observation of the pressure-induced phase transition in Ca(OH)<sub>2</sub>"

ISHIKAWA, T.; TSUCHIYA, T.; TSUCHIYA, J.: "New algorithm for exploration of crystal structures under high pressure and high temperature: free energy surface trekking"

KAWAZOE, T.; NISHIYAMA, N.; NISHIHARA, Y.; IRIFUNE, T.: "Preliminary experiments using the deformation-DIA apparatus 'MADONNA'"

KUNIMOTO, T.; IRIFUNE, T.: "Development of a 6-8-2 type multianvil apparatus and its application"

LERCHBAUMER, L.; AUDÉTAT, A.: "Partitioning of Cu between vapor and brine – an experimental study based on LA-ICP-MS analysis of synthetic fluid inclusions"

MACHIDA, S.; HIRAI, H.; KAWAMURA, T.; YAMAMOTO, Y.; YAGI, T.: "Structural changes and intermolecular interactions for hydrogen hydrate under high pressure"

MATSUKAGE, K.N.: "Origin of Mg and Si rich cratonic mantle: Does the Earth's deep mantle consist of pyrolite?"

NARYGINA, O.; DUBROVINSKY, L.S.; MIYAJIMA, N.: "Phase relations in Fe-Ni-C system at high pressures and temperatures: implication to the Earth's core"

NI, H.; KEPPLER, H.: "Electrical conductivity of albitic melts at high pressures"

ODAKE, S.; KAGI, H.; ARAKAWA, M.; OHTA, A.; HARTE, B.: "Micro-XANES study of the oxidation state of chromium in natural ferropericlasite inclusions"

POLLOK, K.; HELDIGE, K.; HARRIES, D.; PEIFFER, S.: "Redox processes at the nanoscale: Reactions of dissolved sulfide with iron(oxyhydr)oxides"

SAMUEL, H.; TACKLEY, P.J.: "Chemical equilibration and heat partitioning in terrestrial planets during core formation"

SCHIAVI, F.; WALTE, N.; KEPPLER, H.: "The first direct observation of crystallizing magmas with the moissanite cell"

SHINMEI, T.: "Facility at Geodynamics Research Center, Ehime University"

SHINOZAKI, A.; HIRAI, H.; HAMANE, D.; KAGI, H.; KONDO, T.; YAGI, T.: "Polarization of methane molecule and reaction between released hydrogen and olivine in the Earth's mantle"

STEINLE-NEUMANN, G.; LEE, K.K.M.; DOLEJŠ, D.: "Potassium partitioning in the deep Earth from *ab initio* computations"

TANG, Z.; STEINLE-NEUMANN, G.: "Magnetic and electronic structure of Fe<sub>2</sub>SiO<sub>4</sub> ringwoodite from first principles"

USUI, Y.; TSUCHIYA, T.: "Seismic anisotropy in the D" layer beneath the antarctic ocean"

VAN MIERLO, W.; LANGENHORST, F.; MIYAJIMA, N.; FROST, D.; RUBIE, D.: "The formation of majoritic garnet from aluminous enstatite at transition zone conditions"

WEIGEL, C.; KEPPLER, H.; MCCAMMON, C.: "<sup>57</sup>Fe Mössbauer spectroscopy applied to silicate glasses at extreme conditions"

WU, X.; DUBROVINSKY, L.; STEINLE-NEUMANN, G.; NARYGINA, O.; MCCAMMON, C.; PASCARELLI, S.; AQUILANTI, G.; KANTOR, I.; PRAKAPENKA, V.; SWAMY, V.: "Structural evolution and iron oxidation state of FeTiO<sub>3</sub> at high pressure"

YAMADA, A.: "Global COE program: Center for Advanced Experimental and Theoretical deep Earth Mineralogy"

ZARECHNAYA, E.; DUBROVINSKY, L.; DUBROVINSKAIA, N.; MIKHAYLUSHKIN, A.; SIMAK, S.I.; ABRIKOSOV, I.: "The ground state properties of orthorhombic boron: Investigation from 'first principles'"

### 5.5 Conference organization

- 22.-26.06.2009, Goldschmidt Conference, Davos, Switzerland: Symposium 04d: Magma Generation and Evolution and Global Tectonics – A Symposium in Honor of Peter J. Wyllie (H. KEPPLER)
- 22.-26.06.2009, Goldschmidt Conference, Davos, Switzerland: Session 03f: High Pressure Mineral Physics – a Key to Earth Structure: Symposium in honor of Ronald Cohen (G. STEINLE-NEUMANN, L. STIXRUDE)
- 31.08.-04.09.2009, Micro-Analysis, Processes, Time (MAPT) meeting, Edinburgh, UK: Symposium 5, Deep Earth mineral physics and experimental petrology I: Probing geochemical and physical processes (recent developments from nano-beam and *in situ* techniques), (A. AUZENDE, C. SANLOUP, D. DOBSON, F. LANGENHORST)
- 31.08.-04.09.2009, Micro-Analysis, Processes, Time (MAPT) meeting, Edinburgh, UK: Symposium 6, Deep Earth mineral physics and experimental petrology II: The fate of subducted material from lithosphere to core (F. LANGENHORST, A. AUZENDE, C. SANLOUP, D. DOBSON)
- 13.09.-16.09.2009, 87<sup>th</sup> Annual Meeting of the German Mineralogical Society (DMG), Halle, Germany: Symposium 2, Mineral physics/mineral chemistry/crystallography – analytical methods (P. STEMMERMANN, F. LANGENHORST)
- 14.-18.12.2009, American Geophysical Union Fall Meeting, San Francisco, USA: Masters of terrestrial igneous activity: magmas, melts, and fluids (S. KESHAV, C. LESHER, S.-k. LEE, R. CARACAS, S. DEMOUCHY)
- 14.-18.12.2009, American Geophysical Union Fall Meeting, San Francisco, USA: Sessions DI33A and DI42A, Composition, Structure and Thermodynamics of the Earth's Core (D. ANTONANGELI, A.F. DEUSS, G. STEINLE-NEUMANN)
- 07.-10.09.2009, Université Blaise Pascal, Laboratoire Magmas et Volcans, UMR CNRS 6524, Observatoire de Physique du Globe, Clermont-Ferrand, France: Microscopic course on the sulfide-mineralogy of unequilibrated enstatite chondrites (A. EL GORESY)
- 26.-29.10.2009 Tohoku University in Sendai, Japan: Microscopic course on the mineralogy of unequilibrated enstatite chondrites (A. EL GORESY)

## 6. Visiting scientists

### *6.1 Visiting scientists funded by the Bayerisches Geoinstitut*

- BHASKAR, Indian Institute of Technology, Kharagpur, India: 12.05.-18.07.2009
- BOUVIER, A., Arizona State University, School of Earth and Space Exploration, Tempe, USA: 07.-10.01.2009
- CARACAS, R., Laboratoire de Sciences de la Terre, CNRS UMR5570, Ecole Normale Supérieure de Lyon, France: 20.-31.07.2009, 12.-23.10.2009, 23.-27.11.2009
- CHAREEV, D., Institute of Experimental Mineralogy, Chernogolovka, Moscow region, Russia: 10.09.-30.10.2009
- CORDIER, P., Université des Sciences et Technologies de Lille, Laboratoire de Structure et Propriétés de l'Etat Solide, Villeneuve d'Ascq, France: 13.-25.07.2009
- CÔTÉ, A., University College London, Department of Earth Sciences, London, U.K.: 14.-17.06.2009
- DOLEJŠ, D., Charles University, Institute of Petrology and Structural Geology, Prague, Czech Republic: 16.-20.02.2009, 01.07.-31.08.2009
- FILIPPI, S., Università degli Studi di Padova, Dipartimento di Geoscienze, Padova, Italy: 10.06.-24.07.2009
- GHOSH, S., Tohoku University, Earth and Planetary Material Physics Research Group, Sendai, Japan: 03.-10.07.2009
- GIANNINI, M., Università degli Studi di Pavia, Scienze della Terra, Pavia, Italy: 08.-11.12.2009
- HUNT, S., University College London, Department of Earth Sciences, London, U.K.: 09.-13.11.2009
- KATSURA, T., Okayama University, Institute for Study of the Earth's Interior, Misasa, Japan: 01.-30.09.2009
- MANNING, C., University of California, Department of Earth and Space Sciences, Los Angeles, USA: 12.07.-20.08.2009
- MOSTEFAOUI, S., Museum National d'Histoire Naturelle, Paris, France: 24.-26.05.2009
- NAKAJIMA, Y., Tokyo Institute of Technology, Department of Earth and Planetary Sciences, Tokyo, Japan: 19.-23.01.2009
- NARDINI, L., Università degli Studi di Padova, Dipartimento di Geoscienze, Padova, Italy: 01.07.-14.08.2009
- NESTOLA, F., Università degli Studi di Padova, Dipartimento di Geoscienze, Padova, Italy: 18.05.-18.06.2009
- OZAWA, S., Tohoku University, Faculty of Science, Institute of Mineralogy, Petrology, and Economic Geology, Sendai, Japan: 12.01.-13.03.2009
- PELLIZZARI, L., Vicenza, Italy: 18.-20.11.2009
- PESCE, G., Università degli Studi di Padova, Dipartimento di Geoscienze, Padova, Italy: 01.07.-14.08.2009
- PINHEIRO, K., ETH Zürich, Departement Erdwissenschaften, Switzerland: 05.-06.02.2009
- POMMIER, A., CNRS, Institut des Sciences de la Terre d'Orléans, France: 07.-09.07.2009

PRESNALL, D., University of Texas at Dallas, Department of Geosciences, Richardson, USA: 01.06.-04.07.2009  
QIN, J., Sichuan University, Institute of Atomic and Molecular Physics, Chengdu, China: 14.-19.09.2009  
SEIFERT, F., Berlin, Germany: 26.-27.02.2009, 03.-04.12.2009  
SKÁLA, R., Academy of Sciences of the Czech Republic, Institute of Geology, Prague, Czech Republic: 19.-24.07.2009  
STIXRUDE, L., University College London, Department of Earth Sciences, London, U.K.: 10.06.2009

### 6.2 Visiting scientists supported by other externally funded BGI projects

AGOSTINI, C., Università degli Studi di Camerino, Dipartimento di Scienze della Terra, Camerino, Italy: 19.-22.04.2009 (ENB<sup>\*C</sup>)  
AGRAWAL, T., Indian Institute of Technology, Kharagpur, India: 04.05.-15.07.2009 (c2c<sup>\*B</sup>)  
ANGEL, R., Virginia Polytechnic Institute and State University, Geosciences, Blacksburg, USA: 16.-20.09.2009 (ERC<sup>\*E</sup>)  
BUISMAN, I., University of Bristol, Department of Earth Sciences, Bristol, U.K.: *"Towards a better understanding of the evolution and origin of kimberlites by investigating the melt phase relations in CMAS-CO<sub>2</sub>-H<sub>2</sub>O-K<sub>2</sub>O"*, 04.05.-04.11.2009 (AtG<sup>\*A</sup>)  
CASATI, N.P., Università degli Studi di Milano, Dipartimento di Chimica Strutturale e Stereochimica Inorganica, Milano, Italy: 04.-06.03.2009 (ERC<sup>\*E</sup>)  
CHUST, T., LMU München, Department für Geo- und Umweltwissenschaften, München, Germany: 18.-20.02.2009 (c2c<sup>\*B</sup>)  
COHEN, R., Carnegie Institution of Washington, Geophysical Laboratory, Washington D.C., USA: 12.-15.01.2009 (c2c<sup>\*B</sup>)  
DOLEJŠ, D., Charles University, Institute of Petrology and Structural Geology, Prague, Czech Republic: 14.-15.12.2009 (c2c<sup>\*B</sup>)  
EWING, R.C., University of Michigan, Department of Geological Sciences, Ann Arbor, USA: 27.06.-01.07.2009 (ENB<sup>\*C</sup>)  
HAWKESWORTH, C., University of Bristol, Department of Earth Sciences, Bristol, U.K.: 12.-14.05.2009 (ENB<sup>\*C</sup>)  
HOBBS, L., University of Bristol, Department of Earth Sciences, Bristol, U.K.: *"Exploring volcanism: Distribution of sulphur between silicate melt and aqueous fluids, and adsorption of HCl onto volcanic ash"*, 01.01.-12.02.2009 (AtG<sup>\*A</sup>)  
KAMENETSKY, V., University of Tasmania, School of Earth Sciences, Centre of Excellence in Ore Deposits, Hobart, Tasmania, Australia: 15.-20.06.2009 (DFG<sup>\*D</sup>)  
KATERINOPOULOU, A., University of Copenhagen, Institute of Geography and Geology, Copenhagen, Denmark: 27.-29.04.2009 (ERC<sup>\*E</sup>)  
KIND, R., Helmholtz-Zentrum Potsdam, Deutsches GeoForschungsZentrum GFZ, Potsdam, Germany: 08.-09.06.2009 (ENB<sup>\*C</sup>)

KOGURE, T., University of Tokyo, Department of Earth and Planetary Sciences, Tokyo, Japan: 01.-07.04.2009 (ENB<sup>\*C</sup>)

KUZNETSOV, A., INMETRO, National Institute of Metrology, Standardization and Industrial Quality, Rio de Janeiro, Brazil: 03.-06.07.2009 (DFG<sup>\*D</sup>)

LUKIN, E.; Frank Laboratory of Neutron Physics, Joint Institute for Nuclear Research, Dubna, Russia: 25.10.-11.11.2009 (industrial grant)

MARSH, B., Johns Hopkins University, Department of Earth & Planetary Sciences, Baltimore, USA: 08.-12.11.2009 (ENB<sup>\*C</sup>)

MICHALAK, P., Adam Michiewicz University, Institute of Geology, Poznań, Poland: 05.-07.08.2009 (ENB<sup>\*C</sup>)

NIMMO, F., University of California Santa Cruz, Earth & Planetary Sciences Department, Santa Cruz, USA: 26.-30.04.2009 (ENB<sup>\*C</sup>)

PANERO, W., Ohio State University, Mineral Physics Research Group, Columbus, USA: 14.-22.09.2009 (ENB<sup>\*C</sup>)

RICARD, Y., Université de Lyon, Laboratoire de Science de la Terre, Lyon, France: 18.-21.01.2009 (ENB<sup>\*C</sup>)

SPEZIALE, S., Helmholtz-Zentrum Potsdam, Deutsches GeoForschungsZentrum GFZ, Potsdam, Germany: 02.-04.03.2009 (ERC<sup>\*E</sup>)

TOSI, N., Charles University, Prague, Czech Republic: 28.-29.05.2009 (c2c<sup>\*B</sup>)

TRZASKOWSKA, A., Adam Michiewicz University, Faculty of Physics, Poznań, Poland: 23.-24.03.2009 (ERC<sup>\*E</sup>)

TROTS, D., HASYLAB at DESY, Hamburg, Germany: 12.-13.05.2009 (ERC<sup>\*E</sup>)

VLCEK, V., Charles University Prague, Institute of Petrology and Structural Geology, Prague, Czech Republic: 16.-17.09.2009 (c2c<sup>\*B</sup>)

**\*A) AtG: EU Marie Curie Actions "Atomic to Global" Training Programme**

**\*B) c2c: EU Marie Curie Research Training Network - the fate of subducted material**

**\*C) ENB: International Graduate School under the Elitenetzwerk Bayern**

**\*D) DFG: Deutsche Forschungsgemeinschaft**

**\*E) ERC: European Research Council**

### *6.3 Visitors (externally funded)*

ABRIKOSOV, I., Linköping University, Department of Physics, Chemistry, and Biology (IFM), Linköping, Sweden: 02.-03.02.2009, 16.-17.10.2009

ADJAOUD, O., Helmholtz-Zentrum Potsdam, Deutsches GeoForschungsZentrum GFZ, Potsdam, Germany: 08.-14.06.2009

ASKER, C., Linköping University, Department of Physics, Chemistry, and Biology (IFM), Linköping, Sweden: 14.-17.10.2009

BABUSHKIN, A., Ural State University, Ekaterinburg, Russia: 19.10.-06.11.2009

BORINSKI, S., Ruhr-Universität Bochum, Institut für Geologie, Mineralogie & Geophysik, Bochum, Germany: 23.-31.03.2009

BÜCHEL, G., Friedrich-Schiller-Universität Jena, Institut für Geowissenschaften, Jena, Germany: 04.05.2009

CARACAS, R., Laboratoire de Sciences de la Terre, CNRS UMR5570, Ecole Normale Supérieure de Lyon, France: 16.-20.02.2009

CHELAZZI, L., Università degli Studi di Firenze, Dipartimento di Scienze della Terra, Firenze, Italy: 04.05.-30.06.2009

COCHAIN, B., Institut de Physique du Globe de Paris, Physique des Minéraux et des Magmas, Paris, France: 15.-20.02.2009

DEMOUCHY, S., Université Montpellier II, Laboratoire Géosciences Montpellier, UMR CNRS 5243 - CC060, Montpellier, France: 04.-07.08.2009, 09.-13.11.2009

DEUTSCH, A., Universität Münster, Institut für Planetologie, Münster, Germany: 19.-22.07.2009

DOBSON, D., University College London, Department of Earth Sciences, London, U.K.: 02.-06.11.2009

ENGEL, J., TU Dresden, Germany: 14.12.2009

ENGELMANN, R., Universität Karlsruhe, Institut für Angewandte Geowissenschaften, Lehrstuhl für Strukturgeologie und Tektonophysik, Karlsruhe, Germany: 29.06.-05.07.2009

FALKENBERG, F., Max-Planck-Institut für Festkörperforschung, Stuttgart, Germany: 03.-05.08.2009

GANNOUN, M., Laboratoire Magmas et Volcans, Université Blaise Pascal, Clermont-Ferrand, France: 16.-21.03.2009

HÄNDEL, M., Friedrich-Schiller-Universität Jena, Institut für Geowissenschaften, Jena, Germany: 04.05.2009, 26.10.2009

INOUE, T., Ehime University, Geodynamics Research Center, Matsuyama, Japan: 23.-26.03.2009

IRIFUNE, T., Ehime University, Geodynamics Research Center, Matsuyama, Japan: 21.-26.03.2009, 07.-19.08.2009

JACOBSEN, S., Northwestern University, Department of Earth and Planetary Sciences, Evanston, USA: 20.-27.03.2009

KATSURA, T., Okayama University, Institute for Study of the Earth's Interior, Okayama, Japan: 08.-11.06.2009

KAWAMOTO, T., Kyoto University, Institute for Geothermal Sciences, Graduate School of Science, Kyoto, Japan: 19.-27.08.2009

KLEIN, R., Gesellschaft für Schwerionenforschung mbH, Darmstadt, Germany: 09.-13.02.2009

KOZLENKO, D.; Frank Laboratory of Neutron Physics, Joint Institute for Nuclear Research, Dubna, Russia: 25.10.-04.11.2009

LOCHERER, T., Max-Planck-Institut für Festkörperforschung, Stuttgart, Germany: 03.-05.08.2009

MALASPINA, N., Università degli Studi di Milano, Dipartimento di Scienze della Terra, Milano, Italy: 10.-14.02.2009, 26.-30.10.2009

MANTOVANI, M., Universidad de Sevilla, Instituto de Ciencia de Materiales (ICMSE), Sevilla, Spain: 02.10.-30.11.2009

MCCORMACK, R., University College London, Department of Earth Sciences, London, U.K.: 01.-14.11.2009, 06.-12.12.2009

MIYAHARA, M., Tohoku University, Graduate School of Science, Institute of Mineralogy, Petrology and Economic Geology, Sendai, Japan: 09.-27.03.2009

ODAKE, S., University of Tokyo, Geochemical Laboratory, Graduate School of Science, Tokyo, Japan: 21.-30.09.2009

OEHM, B., Universität Heidelberg, Institut für Geowissenschaften, Heidelberg, Germany: 02.-06.11.2009

OSADCHII, E., Institute of Experimental Mineralogy, Chernogolovka, Moscow region, Russia: 10.-29.09.2009

PIPPINGER, T., Universität Heidelberg, Mineralogisches Institut, Heidelberg, Germany: 19.-20.10.2009

POTAPKIN, V., European Synchrotron Radiation Facility, Grenoble, France: 23.09.-02.10.2009

SCHÄFFNER, F., Friedrich-Schiller-Universität Jena, Institut für Geowissenschaften, Jena, Germany: 04.05.2009, 26.10.2009

SCHMIDT, B., Universität Göttingen, Experimentelle und Angewandte Mineralogie, Göttingen, Germany: 16.-20.02.2009

SCHMIDT, P., LMU München, Department für Geo- und Umweltwissenschaften, Geophysik, München, Germany: 28.11.2009

SCHOLLENBRUCH, K., Johann Wolfgang Goethe-Universität Frankfurt/M., Institut für Geowissenschaften, Frankfurt/M., Germany: 11.-15.05.2009, 06.-10.07.2009, 03.-07.08.2009

SCHUSTER, B., Gesellschaft für Schwerionenforschung mbH, Darmstadt, Germany: 24.-25.09.2009

SIMAK, S., Linköping University, Department of Physics, Chemistry, and Biology (IFM), Linköping, Sweden: 02.-03.02.2009

SMYTH, J.R., University of Colorado at Boulder, Geological Sciences, Boulder, USA: 29.06.-10.07.2009

SOMAN, A., Westfälische Wilhelms-Universität Münster, Institut für Mineralogie, Münster, Germany: 19.-23.04.2009

STENETEG, P., Linköping University, Department of Physics, Chemistry, and Biology (IFM), Linköping, Sweden: 02.-03.02.2009

TROTS, D., HASYLAB at DESY, Hamburg, Germany: 29.06.-03.07.2009

XIONG, X., Guangzhou Institute of Geochemistry, Chinese Academy of Sciences, Guangzhou, China, 23.02.-09.04.2009

ZVORISTE, C., Technische Universität Darmstadt, Fachbereich Materialwissenschaft, Darmstadt, Germany: 19.01.-06.02.2009, 14.-18.09.2009, 12.-16.10.2009



## 7. Additional scientific activities

### 7.1 Theses

#### *Ph.D. theses*

ADJAOUD, Omar: First principles phase diagram calculations in group IV carbides and Mg<sub>2</sub>SiO<sub>4</sub> liquid from molecular dynamics.

KONSCHAK, Alexander: CO<sub>2</sub> in Silikatschmelzen

LONGO, Micaela: Iron oxidation state in (Mg,Fe)O: Calibration of the flank method on synthetic samples and applications on natural inclusions from lower mantle diamonds

#### *M.Sc. thesis*

LI, Yuan: Sulphide - alkaline silicate melt partitioning of ore metals during partial melting of metasomatized lithospheric mantle

### 7.2 Honours and awards

DUBROVINSKY, Leonid	Visiting Professor at Kumamoto University, Japan
GREENBERG, Eran	Poster prize at the 47 <sup>th</sup> EHPRG International Conference, Paris, France
LERCHBAUMER, Linda	Dritter Österreichischer Nationalpark-Forschungspreis für DiplomandInnen und DissertantInnen: 13.01.2009, Vienna, Austria. [for the diploma thesis: "Petrographical, geochemical and geochronological investigations on the Variscan basement in the Kleinellendtal/Hohe Tauern (eastern Tauern Window, Austria)."]
ZARECHNAYA, Evgeniya	Student Poster Award at the Joint AIRAPT-22 & HPCJ-50 Conference, Tokyo, Japan

### 7.3 Editorship of scientific journals

DUBROVINSKY, L.S.	Member of the Editorial Board of the "High Pressure Research - International Journal"
KEPPLER, H.	Editorial Advisory Board "Elements" Editorial Board "Contributions to Mineralogy and Petrology"
LANGENHORST, F.	Associate editor "Geochemistry/Chemie der Erde"
MCCAMMON, C.A.	Editor "Physics and Chemistry of Minerals"
RUBIE, D.C.	Editor-in-Chief "Physics of the Earth and Planetary Interiors"

#### *7.4 Membership of scientific advisory bodies*

- DUBROVINSKY, L.S.      Member of European High Pressure Research Group (EHPRG) Committee  
Member of the Review Panel of XAS Beam Lines at ESRF  
Elected Chair of the Special Interest Group "Crystallography at extreme conditions" of the European Crystallography Union  
Member of the Review Panel of the Canadian Light Source  
Member of the Review Panel of the European Science Foundation
- KEPPLER, H.            Chairman, Research Council of the German Mineralogical Society (Forschungskollegium Mineralogie der DMG)  
Member, Abraham Gottlob Werner Medal Committee, German Mineralogical Society (DMG)  
Member, Roebling Medal Committee, Mineralogical Society of America  
Member, Commission for Research of Bayreuth University (Präsidialkommission für Forschung und wissenschaftlichen Nachwuchs)  
Member, German National Academy of Sciences (Leopoldina)  
Member, Bavarian Academy of Sciences  
Member, ESF pool of referees
- LANGENHORST, F.      President, German Mineralogical Society (DMG)  
Member, DFG-Senatskommission für geowissenschaftliche Gemeinschaftsforschung (Geokommission)  
Member, Academia Europaea
- MCCAMMON, C.A.      IMA Medal Committee of the International Mineralogical Association, Member  
Fellows Committee of the Volcanology, Geochemistry & Petrology Section of the American Geophysical Union, Chairman  
Executive Committee of the Volcanology, Geochemistry & Petrology Section of the American Geophysical Union, Member  
Student Award Committee of the Mineral and Rock Physics Focus Group of the American Geophysical Union, Chairman  
Executive Committee of the Mineral and Rock Physics Focus Group of the American Geophysical Union, Member  
Advisory Board of "Mössbauer Information Exchange"  
International Advisory Board of the Mössbauer Effect Data Center
- RUBIE, D.C.            Member of Dana Medal Committee, Mineralogical Society of America  
Member of Forschungskollegium Physik des Erdkörpers (FKPE)

## 8. Scientific and Technical Personnel

Name		Position	Duration in 2009	Funding source
ADJAOUD, Omar	M.Sc. (Physics)	Wiss. Mitarbeiter	to 28.02.	BGI/IGS
AUDÉTAT, Andreas	Dr.	Akad. Rat z.A.		BGI
BALI, Enikő	Dr.	Wiss. Mitarbeiterin		BGI/VP
BERNINI, Diego	Dipl.-Geol.	Gastwissenschaftler		EU
BÖHM, Ulrich		Mechaniker		BGI
BOFFA BALLARAN, Tiziana	Dr.	Akad. Rätin		BGI
BROCKMANN, Nicolas	Dipl.-Chem.	Wiss. Mitarbeiter	from 01.06.	BGI/IGS <sup>1</sup>
BUCHERT, Petra		Fremdsprachen- sekretärin		BGI
CHANTEL, Julien	M.Sc.	Gastwissenschaftler		EU
CHEMIA, Zurab	Dr.	Gastwissenschaftler	from 01.02.	EU
CHUST, Thomas	Dipl. Geophys.	Wiss. Mitarbeiter	from 01.03.	DFG
DE KOKER, Nico	Dr.	Gastwissenschaftler		EU
DITTMANN, Uwe		Präparator		BGI
DUBROVINSKY, Leonid	PD Dr.	Akad. Oberrat		BGI
EL GORESY, Ahmed	Prof. Dr.			BGI/VP <sup>2</sup>
ESCUADERO, Alberto	Dr.	Wiss. Mitarbeiter	to 28.02. from 01.03.	DFG MICINN <sup>3</sup>
ETZEL, Katja	Dr.	Wiss. Mitarbeiterin		BMBF
FISCHER, Heinz		Mechaniker		BGI
FISCHER, Nicole	Reg. Inspektorin	Verwalt. Beamtin		BGI
FROST, Daniel	Dr.	Akad. Direktor		BGI
GANSKOW, Geertje	Dipl.-Geol.	Wiss. Mitarbeiterin	to 28.02. 01.03.-10.04. from 11.04.	DFG DFG <sup>4</sup> BGI/IGS
GAVRILENKO, Polina	Dr.	Wiss. Mitarbeiterin	to 30.04.	DFG
GLAZYRIN, Konstantin	Ing. Phys.	Wiss. Mitarbeiter		BGI/IGS
GOLLNER, Gertrud		Chem.-Techn. Assistentin		BGI
GREENBERG, Eran	M.Sc.	Gastwissenschaftler	from 02.02.	EU
HARRIES, Dennis	Dipl. Geosciences	Wiss. Mitarbeiter		DFG <sup>4</sup> BMBF
HEIDELBACH, Florian	Dr.	Wiss. Mitarbeiter		BGI/IGS
HERRMANN, Elisabeth	MTA	Chem.-Techn. Assistentin	to 30.04.	BGI
HIRSEMANN, Dunja	Dipl.-Chem.	Wiss. Mitarbeiterin		BGI/IGS <sup>5</sup>
HOPF, Juliane	Dipl.-Biol.	Wiss. Mitarbeiterin	01.04.-30.09. from 01.10.	DFG <sup>4</sup> DFG

HUANG, Xianliang	M.E. (Material Science)	Wiss. Mitarbeiter	to 31.03.	BGI/IGS <sup>1</sup>
KANTOR, Anastasia	Cand. of Science/Dr.	Wiss. Mitarbeiterin	to 15.08.	DFG
KEPPLER, Hans	Prof. Dr.	Leiter		BGI
KESHAV, Shantanu	Dr.	Wiss. Mitarbeiter		BGI/VP
KEYSSNER, Stefan	Dr.	Akad. Oberrat		BGI
KISON-HERZING, Lydia		Sekretärin		BGI
KLASINSKI, Kurt	Dipl.-Ing. (FH)	Techn. Angestellter		BGI
KRAUßE, Detlef	Dipl.-Inform. (FH)	Techn. Angestellter		BGI
KRIEGL, Holger		Haustechniker		BGI
KROPFGANS, Katja		Verwaltungs-angestellte	from 23.09.	BGI
KUMBAR, Suresh	M.Sc. (Inorg. Chem.)	Wiss. Mitarbeiter	to 31.10.	BGI/IGS <sup>5</sup>
KUNZ, Daniel	Dipl.-Chem.	Wiss. Mitarbeiter	to 31.03.	BGI/IGS <sup>5</sup>
KURNOSOV, Alexander	Dr.	Wiss. Mitarbeiter	from 15.06.	EU
LANGENHORST, Falko	Prof. Dr.	Stellvertr. Leiter		BGI
LERCHBAUMER, Linda	Mag. rer. nat.	Wiss. Mitarbeiterin	to 10.12. from 11.12.	DFG BGI/IGS
LI, Yuan	B.Sc. M.Sc.	Stipendiat Wiss. Mitarbeiter	to 31.10. from 01.11.	EU BGI/IGS
LIEBL, Mario	Dipl.-Chem.	Wiss. Mitarbeiter	to 31.05.	BGI/IGS <sup>5</sup>
LINHARDT, Sven		Elektrotechniker		BGI
LONGO, Micaela	Dipl.-Min.	Gastwissenschaftlerin	to 17.04.	EU
LUNKENBEIN, Thomas	Dipl.-Chem.	Wiss. Mitarbeiter	from 01.04.	BGI/IGS <sup>5</sup>
MANNING, Craig	Prof.	Forschungspreisträger	12.07.-20.08.	AvH
MANTHILAKE, Geeth	Dr.	Wiss. Mitarbeiter	from 15.04.	BGI/VP
MCCAMMON, Catherine	Dr.	Akad. Oberrätin		BGI
MCENROE, Suzanne	Dr.	Gastwissenschaftlerin	from 01.10.	EU
MIYAJIMA, Nobuyoshi	Dr.	Akad. Rat		BGI
MOOKHERJEE, Mainak	Dr.	Wiss. Mitarbeiter		BGI/VP
NAKAJIMA, Yoichi	Dr.	Wiss. Mitarbeiter	from 15.06.	BGI/VP
NARYGINA, Olga	M.Sc. (Physics)	Wiss. Mitarbeiterin	to 31.03. 01.04.-04.10.	BGI/IGS DFG
NI, Huaiwei	Dr.	Wiss. Mitarbeiter	from 07.01.	BGI/VP
NOVELLA, Davide	B.Sc.	stud. Hilfskraft		BGI
OVSYANNIKOV, Sergey	Dr.	Forschungsstipendiat	from 16.04.	AvH
PAMATO, Martha	B.Sc.	stud. Hilfskraft	to 30.04. 01.05.-31.10. from 01.11.	DFG BMBF DFG <sup>4</sup>
POLLOK, Kilian	Dr.	Akad. Rat a.Z.		BGI

POTZEL, Anke		Chem.-Techn. Assistentin		BGI
PRESCHER, Clemens		stud. Hilfskraft	01.05.-10.11.	DFG <sup>4</sup>
	Dipl.-Geol.	wiss. Mitarbeiter	from 11.11.	BGI/IGS
RAMMING, Gerd		Elektroniker		BGI
RAUSCH, Oliver		Mechaniker		BGI
ROSCHER Elisabeth		Wissensch.-Techn. Assistentin	to 28.02.	BGI
RUBIE, David C.	Prof. Dr.		to 31.03. from 01.04.	BGI EU
SAMUEL, Henri	Prof. Dr.	Juniorprofessor		Stiftung <sup>6</sup>
SCHIAVI, Federica	Dr.	Wiss. Mitarbeiterin	to 30.04.	DFG
			01.05.-31.07. from 01.08.	BGI/VP DFG
SCHMITT, Veronika	Dipl.-Min.	Wiss. Mitarbeiterin	from 11.02.	BGI/IGS <sup>5</sup>
SCHULZE, Hubert		Präparator		BGI
SHARMA, Rekha	M.Sc.	Wiss. Mitarbeiterin	01.04.-30.09.	BGI/IGS
SHCHEKA, Svyatoslav	Dr.	Wiss. Mitarbeiter		DFG
SHEKHAR, Sushant	M.Sc.	Wiss. Mitarbeiter		BGI/IGS
STAGNO, Vincenzo	Dipl.-Geol.	Gastwissenschaftler		EU
STEINLE-NEUMANN, Gerd	Dr.	Akad. Rat		BGI
SUN, Wei	B.Sc.	stud. Hilfskraft	from 01.04.	BGI/VP
TANG, Zhengning	M.E. (Material Science)	Gastwissenschaftler	to 28.11.	EU
TROTS, Dmytro	Dr.	Wiss. Mitarbeiter	from 01.09.	EU
TRZASKOWSKA, Aleksandra	Dr.	Wiss. Mitarbeiterin	15.07.-31.10.	EU
TSUNO, Kyusei	Dr.	Wiss. Mitarbeiter	to 30.04.	DFG/ BGI/VP
ÜBELHACK, Stefan		Mechaniker		BGI
VAN MIERLO, Willem	M.Sc.	Gastwissenschaftler		EU
VLCEK, Vojtech	B.Sc.	stud. Hilfskraft	from 01.10.	DFG
WACK, Julia	Dipl.-Chem.	Wiss. Mitarbeiterin	from 03.06.	BGI/IGS <sup>5</sup>
WALTE, Nicolas	Dr.	Wiss. Mitarbeiter		DFG
WEI, Qingguo	B.Sc.	stud. Hilfskraft	from 01.04.	DFG
WEIGEL, Coralie	Dr.	Wiss. Mitarbeiterin	to 31.08.	BGI/VP
WU, Xiang	Dr.	Forschungsstipendiat	to 31.07.	AvH
YANG, Xiaozhi	Dr.	Forschungsstipendiat	from 27.08.	AvH
ZARECHNAYA, Evgeniya	M.Sc.	Wiss. Mitarbeiterin	to 31.10. from 01.11.	BGI/IGS DFG

### Abbreviations/explanations:

AvH	Alexander von Humboldt Foundation
BGI	Staff Position of Bayerisches Geoinstitut
BGI/VP	Visiting Scientists' Program of Bayerisches Geoinstitut
BMBF	Federal Ministry of Education and Research
DFG	German Science Foundation
EU	European Union
IGS	International Graduate School under the Elitenetzwerk Bayern "Structure, Reactivity and Properties of Oxide Materials"
MICINN	Ministerio de Ciencia e Innovación, Gobierno de España

---

<sup>1</sup> Fraunhofer ISC Würzburg

<sup>2</sup> partially funded by the Visiting Scientists' Program of Bayerisches Geoinstitut

<sup>3</sup> funded by the Spanish Ministry of Science

<sup>4</sup> Leibniz award Prof. Langenhorst

<sup>5</sup> Chair of Inorganic Chemistry I, Prof. Breu

<sup>6</sup> Juniorprofessorship for Geodynamic Modeling funded by  
Stifterverband für die Deutsche Wissenschaft

## Index

Adjaoud, O. ....	131
Audétat, A. ....	64, 66, 68, 71, 122
Bali, E. ....	23, 26, 64
Becerro, A.I. ....	92
Beck, P. ....	155
Bienert, C. ....	175
Bindi, L. ....	81, 106
Bock, J. ....	177
Boffa Ballaran, T. ....	86, 104, 105, 106, 187, 189
Bonazzi, P. ....	106
Buiter, S. ....	29
Bulanova, G. ....	54
Bunge, H.-P. ....	31
Chantel, J. ....	99
Chareev, D. ....	167
Chelazzi, L. ....	106
Chemia, Z. ....	29
Chumakov, A. ....	100, 177, 180
Chust, T. ....	31
Comodi, P. ....	81
Cordier, P. ....	141, 143
de Koker, N. ....	107, 109
Degi, J. ....	23, 26
Dmitriev, V. ....	78
Dolejš, D. ....	29, 116
Dubrovinskaia, N. ....	78, 165, 170, 177, 182
Dubrovinsky, L.S. ....	78, 81, 83, 84, 100, 165, 167, 169, 170, 172, 173, 177, 180, 182
El Goresy, A. ....	155, 158, 162
Engelmann, R. ....	147
Escudero, A. ....	76, 92
Etzel, K. ....	126
Fabian, K. ....	111
Fischer, P. ....	175
Fotheringham, U. ....	175
Frost, D.J. ....	32, 39, 41, 43, 44, 46, 47, 50, 51, 78, 86, 88, 89, 99, 107, 139, 143, 151, ..... 175, 184, 187, 189, 190
Fumagalli, P. ....	152
Ganskow, G. ....	32, 104
Geisler, T. ....	95
Gillet, P. ....	155

Glazyrin, K. ....	83, 100, 177
Greenberg, E. ....	84, 100, 173
Grimmer, J. ....	147
Gudfinnsson, G.H. ....	58
Harries, D. ....	90, 127, 193
Heidelberg, F. ....	111, 139, 141, 147
Hellige, K. ....	73
Hiraga, K. ....	162
Hobbs, L. ....	124, 125
Hochella, M.F. ....	127
Hofmann, M. ....	182
Hopf, J. ....	127
Hornemann, U. ....	154
Irifune, T. ....	50, 56
Jahn, S. ....	131
Kaminsky, F. ....	54
Kantor, A. ....	102
Kantor, I.Yu. ....	78, 102
Kanzaki, M. ....	169
Keppler, H. ....	22, 64, 66, 120, 124, 125, 133, 135
Keshav, S. ....	58, 61
Kimura, M. ....	162
Klotz, S. ....	83
Koch-Müller, M. ....	105
Kontny, A. ....	147
Kotzlenko, D.P. ....	172
Kurnosov, A. ....	167, 187, 189
Langenhorst, F. ....	32, 76, 90, 104, 127, 151, 152, 154, 193
Lerchbaumer, L. ....	122
Li, Y. ....	66, 68
Litvin, Yu. ....	167
Longo, M. ....	54
Lukin, E.V. ....	172
Malaspina, N. ....	152
Mann, U. ....	39
Manning, C.E. ....	116, 120
Manthilake, G. ....	107, 184
Mantovani, M. ....	92
McCammon, C.A. ....	51, 54, 56, 78, 84, 100, 173, 177, 180
McEnroe, S. ....	111
Melosh, H.J. ....	33
Miyahara, M. ....	155, 158, 162

Miyajima, N. ....	139, 145, 151
Mookherjee, M. ....	35, 120
Montagnac, G. ....	155
Mussi, A. ....	143
Nagase, T. ....	155, 158, 162
Nakajima, Y. ....	46
Narygina, O. ....	78, 100, 167, 177
Nazzareni, S. ....	81
Nestola, F. ....	105, 106
Ni, H. ....	22, 66, 135
Nimmo, F. ....	39
Nishijima, M. ....	158, 162
Novella, D. ....	61
O'Brien, D. ....	39
Ohfuji, H. ....	56
Ohtani, E. ....	155, 158, 162
Osadchii, E. ....	167
Ovsyannikov, S.V. ....	170
Ozawa, S. ....	155, 158, 162
Palme, H. ....	39
Panero, W.R. ....	89
Park, J.-G. ....	172
Pascarelli, S. ....	177
Peiffer, S. ....	73
Poli, S. ....	152
Pollok, K. ....	73, 90, 95, 126, 127, 193
Popov, S.L. ....	180
Potapkin, V. ....	180
Prakapenka, V. ....	102
Prescher, C. ....	154
Presnall, D.C. ....	58
Richardson, K. ....	175
Robinson, P. ....	111
Rubie, D. ....	33, 39, 41, 43, 44, 46, 141, 151
Rüffer, R. ....	180
Qin, S. ....	169
Samuel, H. ....	33, 194
Sanehira, T. ....	56
Savenko, B.N. ....	172
Schiavi, F. ....	133
Sergueev, I. ....	100
Shekhar, S. ....	139, 190

Shiryayev, A. ....	56
Smirnov, G.V. ....	180
Smyth, J.R. ....	88, 89
Sohr, O. ....	175
Soman, A. ....	95
Stagno, V. ....	47, 50, 51, 56
Stebbins, J.F. ....	89
Steinle-Neumann, G. ....	29, 31, 35, 131, 169
Sun, W. ....	71
Szabo, C. ....	23, 26
Tange, Y. ....	50
Tappert, R. ....	54
Török, K. ....	23, 26
Trzaskowska, A. ....	189
Trots, D. ....	187, 189
Tsuno, K. ....	41, 43, 44, 76
van Mierlo, W. ....	151
Voggenreiter GmbH ....	184
Walte, N. ....	133, 139, 141, 145
Weißmann, R. ....	175
Westenberger, G. ....	175
Wu, X. ....	35, 169, 170
Xiong, X.L. ....	66
Yang, X.-Z. ....	22
Ye, Y. ....	88
Zarechnaya, E. ....	165, 167